

**Mysterious Ediacaran fossil
is an animal** *pp. 1198 & 1246*

Fighting chaos with chaos
pp. 1201 & 1225

**Evolution of the drug
overdose epidemic** *p. 1218*

Science

\$15
21 SEPTEMBER 2018
sciencemag.org

AAAS

SCIENCE UNDER SCRUTINY

Metaresearchers
study how research
is done—and
why it goes wrong
pp. 1178 & 1194



CONTENTS



1202 & 1216

An embryonic blueprint

21 SEPTEMBER 2018 • VOLUME 361 • ISSUE 6408

SPECIAL SECTION

RESEARCH ON RESEARCH

FEATURES

1178 INTRODUCTION

By M. Enserink

1180 JOURNALS UNDER THE MICROSCOPE

"Journalologists" use scientific methods to study publishing. Is their work improving science? By J. Couzin-Frankel

1184 THE METAWARS

Meta-analyses were supposed to end scientific debates. Often, they only cause more controversy By J. de Vrieze

► PODCAST

1189 THE TRUTH SQUAD

In its drive to expose weaknesses in science, an up-and-coming research group doesn't mind stepping on some toes By E. Stokstad

1192 A RECIPE FOR RIGOR

A simple strategy to avoid bias—declaring in advance what you will study, and how—is rapidly catching on By K. Kupferschmidt

POLICY FORUM

1194 TOWARD A MORE SCIENTIFIC SCIENCE

► PODCAST

ON THE COVER



A growing number of scientists are studying science itself. These "metaresearchers" are asking how researchers generate and test hypotheses; what they read, cite, and publish; and how they collaborate and network. Some hope that a better understanding of how science works will help address systemic problems such as biases and the inability to reproduce many studies. See pages 1178 and 1194. Illustration: Davide Bonazzi/@SalzmanArt

NEWS

IN BRIEF

1170 News at a glance

IN DEPTH

1172 DEADLY STORMS BREAK RECORDS, DAMAGE FACILITIES

Florence and Mangkhut hold lessons for future disasters, and omens of growing severity By F. Schembri

1173 EVIDENCE-BASED MEDICINE GROUP EXPELS INTERNAL CRITIC

Cochrane is in turmoil after ousting co-founder Peter Gøtzsche, who accused it of becoming "industry-friendly"

By M. Enserink

1174 DRUG PAIR SHOWS PROMISE FOR TREATING SLEEP APNEA

Small clinical trial revives hope for an alternative to bulky breathing machines

By M. Wadman

1175 AAAS ADOPTS NEW POLICY FOR EJECTING HARASSERS

Society may strip honors if misconduct has been found By M. Wadman

► EDITORIAL P. 1167

1176 A MODULAR BACKBONE AIDED THE RISE OF MAMMALS

Fossils show how lumbar vertebrae were freed up to adapt to myriad lifestyles By E. Pennisi

► REPORT P. 1249

1177 BRAIN SCIENTISTS DIVE INTO DEEP NEURAL NETWORKS

Increasingly skilled artificial intelligence could hold clues to human sensory systems By K. Servick

INSIGHTS

PERSPECTIVES

1198 CHEMICAL CLUES TO THE EARLIEST ANIMAL FOSSILS

Steroid biomarkers show that the Ediacaran fossil *Dickinsonia* was an animal By R. E. Summons and D. H. Erwin

► REPORT P. 1246

1199 PROGRAMMING CELLS AND TISSUES

New toolkits of biological parts allow powerful cell programming by synthetic biologists By D. S. Glass and U. Alon

► RESEARCH ARTICLE P. 1217; REPORT P. 1252

1201 FIGHTING CHAOS WITH CHAOS IN LASERS

Complex wave interference suppresses nonlinearities that destabilize beams

By L. Yang

► REPORT P. 1225

1202 A BIRD'S INNER STRIPES

Patterns of stripes on bird plumage are determined from deep under the skin

By B. Prud'homme and N. Gompel

► REPORT P. 1216

1203 A GUT FEELING

Gut-brain signaling involves neurotransmission from gut sensory epithelial cells

By B. U. Hoffman and E. A. Lumpkin

► REPORT P. 1219

1204 BANG OR WHIMPER?

The evidence for collapse of human civilizations at the start of the recently defined Meghalayan Age is equivocal

By G. D. Middleton

BOOKS ET AL.

1206 ANIMAL TRAFFICKING, UNVEILED

A nuanced treatise on illegal wildlife trade misses some opportunities to advance the conversation

By R. Cooney

1207 LISTENING TO A PANDEMIC

Stories from the 1918 flu come alive in a new podcast series By H. T. Battles

LETTERS

1208 POLLUTION THREATENS TOOTHED WHALES

By C. Sonne et al.

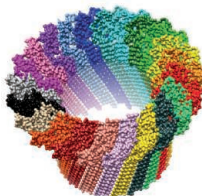
1208 GOOD GOVERNANCE FOR MIGRATORY SPECIES

By T. Aqorau et al.

1209 OUTSIDE THE TOWER: SCIENCE OUTREACH IN THE BORNEO JUNGLE

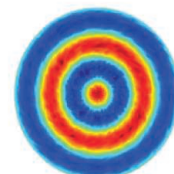
By D. Warren

1209 TECHNICAL COMMENT ABSTRACTS



1215

Bacterial arsenal



1239

Qubit readout

RESEARCH

IN BRIEF

1211 From *Science* and other journals

REVIEW

1214 SOLAR CELLS

Challenges for commercializing perovskite solar cells *Y. Rong et al.*

REVIEW SUMMARY; FOR FULL TEXT:

[dx.doi.org/10.1126/science.aat8235](https://doi.org/10.1126/science.aat8235)

1215 MICROBIOTA

Bacterial antagonism in host-associated microbial communities

L. García-Bayona and L. E. Comstock

REVIEW SUMMARY; FOR FULL TEXT:

[dx.doi.org/10.1126/science.aat2456](https://doi.org/10.1126/science.aat2456)

RESEARCH ARTICLES

1216 PATTERN FORMATION

The periodic coloration in birds forms through a prepatter of somite origin
N. Haupaix et al.

RESEARCH ARTICLE SUMMARY; FOR FULL TEXT:

[dx.doi.org/10.1126/science.aar4777](https://doi.org/10.1126/science.aar4777)

► PERSPECTIVE P. 1202

1217 SYNTHETIC BIOLOGY

Cellular checkpoint control using programmable sequential logic

L. B. Andrews et al.

RESEARCH ARTICLE SUMMARY; FOR FULL TEXT:

[dx.doi.org/10.1126/science.aap8987](https://doi.org/10.1126/science.aap8987)

► PERSPECTIVE P. 1199; REPORT P. 1252

1218 PUBLIC HEALTH

Changing dynamics of the drug overdose epidemic in the United States from 1979 through 2016

H. Jalal et al.

RESEARCH ARTICLE SUMMARY; FOR FULL TEXT:

[dx.doi.org/10.1126/science.aau1184](https://doi.org/10.1126/science.aau1184)

1219 NEUROSCIENCE

A gut-brain neural circuit for nutrient sensory transduction

M. M. Kaelberer et al.

RESEARCH ARTICLE SUMMARY; FOR FULL TEXT:

[dx.doi.org/10.1126/science.aat5236](https://doi.org/10.1126/science.aat5236)

► PERSPECTIVE P. 1203

1220 CHEMISTRY

Reconfigurable system for automated optimization of diverse chemical reactions *A.-C. Bédard et al.*

1225 APPLIED OPTICS

Suppressing spatiotemporal lasing instabilities with wave-chaotic microcavities *S. Bittner et al.*

► PERSPECTIVE P. 1201

REPORTS

1231 ASTEROSEISMOLOGY

Asteroseismic detection of latitudinal differential rotation in 13 Sun-like stars
O. Benomar et al.

1234 ORGANIC CHEMISTRY

Unlocking P(V): Reagents for chiral phosphorothioate synthesis

K. W. Knouse et al.

1239 QUANTUM ELECTRONICS

Measurement of a superconducting qubit with a microwave photon counter *A. Opremcak et al.*

1242 MICROPOROUS CRYSTALS

Self-assembly of lattices with high structural complexity from a geometrically simple molecule

H. Yamagishi et al.

1246 EARLY ANIMALS

Ancient steroids establish the Ediacaran fossil *Dickinsonia* as one of the earliest animals
I. Bobrovskiy et al.

► PERSPECTIVE P. 1198

1249 MAMMALIAN EVOLUTION

Fossils reveal the complex evolutionary history of the mammalian regionalized spine
K. E. Jones et al.

► NEWS STORY P. 1176

1252 SYNTHETIC BIOLOGY

Programmable protein circuits in living cells *X. J. Gao et al.*

► PERSPECTIVE P. 1199; RESEARCH ARTICLE P. 1217

1259 BIOTECHNOLOGY

Engineered CRISPR-Cas9 nuclease with expanded targeting space
H. Nishimasu et al.

DEPARTMENTS

1167 EDITORIAL

Address harassment now

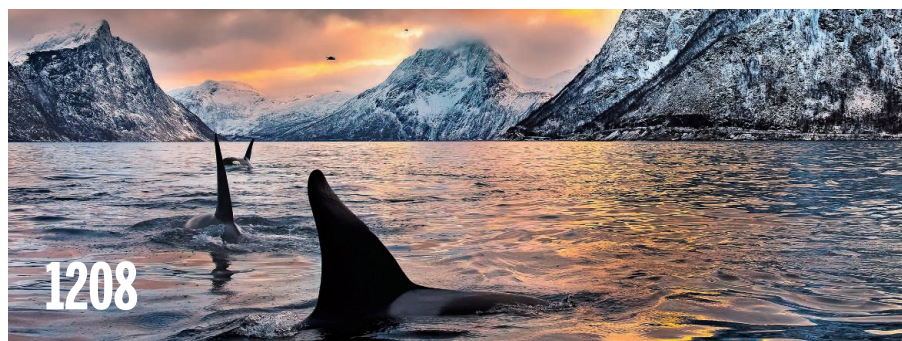
By Margaret Hamburg et al.

► NEWS STORY P. 1175

1278 WORKING LIFE

Afraid to fail? Reach out

By Barbara A. Wanchisen



SCIENCE (ISSN 0036-8075) is published weekly on Friday, except last week in December, by the American Association for the Advancement of Science, 1200 New York Avenue, NW, Washington, DC 20005. Periodicals mail postage (publication No. 484460) paid at Washington, DC, and additional mailing offices. Copyright © 2018 by the American Association for the Advancement of Science. The title SCIENCE is a registered trademark of the AAAS. Domestic individual membership, including subscription (12 months): \$165 (\$74 allocated to subscription). Domestic institutional subscription (51 issues): \$1808; Foreign postage extra: Mexico, Caribbean (surface mail) \$55; other countries (air assist delivery): \$89. First class, airmail, student, and emeritus rates on request. Canadian rates with GST available upon request. GST #125488122. Publications Mail Agreement Number 1069624. Printed in the U.S.A. Change of address: Allow 4 weeks, giving old and new addresses and 8-digit account number. Postmaster: Send change of address to AAAS, P.O. Box 96178, Washington, DC 20090-6178. Single-copy sales: \$15 each plus shipping and handling; bulk rate on request. Authorization to reproduce material for internal or personal use under circumstances not falling within the fair use provisions of the Copyright Act is granted by AAAS to libraries and others who use Copyright Clearance Center (CCC) Pay-Per-Use services provided that \$35.00 per article is paid directly to CCC, 222 Rosewood Drive, Danvers, MA 01923. The identification code for Science is 0036-8075. Science is indexed in the Reader's Guide to Periodical Literature and in several specialized indexes.



1200 New York Avenue, NW, Washington, DC 20005
Clarendon House, Clarendon Road, Cambridge, UK CB2 8FH



Editor-in-Chief Jeremy Berg

Executive Editor Monica M. Bradford

News Editor Tim Appenzeller

Editor, Insights Lisa D. Chong

Editors, Research Valda Vinson, Jake S. Yeston

Research and Insights

DEPUTY EDITORS Julia Fahrenkamp-Uppenbrink(UK), Stella M. Hurtle(UK), Phillip D. Szurmi, Sacha Vignieri **DEPUTY EDITOR, EMERITUS** Barbara R. Jasny **SR. EDITORIAL FELLOW** Andrew M. Sugden(UK) **SR. EDITORS** Gemma Alderton(UK), Caroline Ash(UK), Pamela J. Hines, Paula A. Kiberstis, Marc S. Lavine(Canada), Steve Mao, Ian S. Osborne(UK), Beverly A. Purnell, L. Bryan Ray, H. Jesse Smith, Jelena Stajic, Peter Stern(UK), Brad Wible, Laura M. Zahn **ASSOCIATE EDITORS** Michael A. Funk, Brent Grocholski, Priscilla N. Kelly, Tage S. Rai, Seth Thomas Scanlon(UK), Keith T. Smith(UK) **ASSOCIATE BOOK REVIEW EDITOR** Valerie B. Thompson **LETTERS EDITOR** Jennifer Sills **LEAD CONTENT PRODUCTION EDITORS** Harry Jach, Lauren Kmec **CONTENT PRODUCTION EDITORS** Amelia Beyna, Jeffrey E. Cook, Amber Esplin, Chris Filiatreau, Cynthia Howe **SR. EDITORIAL COORDINATORS** Carolyn Kyle, Beverly Shields **EDITORIAL COORDINATORS** Aneera Dobbins, Joi S. Granger, Jeffrey Hearn, Lisa Johnson, Maryrose Madrid, Shannon McMahon, Jerry Richardson, Alice Whaley(UK), Anita Wynn **PUBLICATIONS ASSISTANTS** Ope Martins, Nida Masulisi, Dona Mathieu, Ronnel Navas, Hilary Stewart(UK), Alana Warnke, Brian White **EXECUTIVE ASSISTANT** Jessica Slater **ASI DIRECTOR, OPERATIONS** Janet Clements(UK), **ASI SR. OFFICE ADMINISTRATOR** Jessica Waldo(CK)

News

NEWS MANAGING EDITOR John Travis **INTERNATIONAL EDITOR** Martin Enserink **DEPUTY NEWS EDITORS** Elizabeth Culotta, Lila Guterman, David Grimm, Eric Hand, David Malakoff, Leslie Roberts **SR. CORRESPONDENTS** Daniel Cley(UK), Jon Cohen Jeffrey Mervis, Elizabeth Pennisi **ASSOCIATE EDITORS** Jeffrey Brainard, Catherine Maticic **NEWS WRITERS** Adrian Cho, Jennifer Couzin-Frankel, Jocelyn Kaiser, Kelly Servick, Robert F. Service, Erik Stokstad(Cambridge, UK), Paul Voosen, Meredith Wadman **INTERNS** Frankie Schembri **CONTRIBUTING CORRESPONDENTS** Warren Cornwall, Ann Gibbons, Mara Hvistendahl, Sam Kean, Eli Kintisch, Kai Kupferschmidt(Berlin), Andrew Lawler, Mitch Leslie, Eliot Marshall, Virginia Morell, Dennis Normile(Shanghai), Charles Piller, Tania Rabesandratana(London), Emily Underwood, Gretchen Vogel(Berlin), Lizzie Wade(Mexico City) **CAREERS** Donisha Adams, Rachel Bernstein(Editor), Katie Langin **COPY EDITORS** Julia Cole (Senior Copy Editor), Cyra Master (Copy Chief) **ADMINISTRATIVE SUPPORT** Meagan Weiland

Executive Publisher Rush D. Holt

Publisher Bill Moran

Chief Digital Media Officer Josh Freeman

DIRECTOR, BUSINESS STRATEGY AND PORTFOLIO MANAGEMENT Sarah Whalen **DIRECTOR, PRODUCT AND CUSTOM PUBLISHING** Will Schweitzer **MANAGER, PRODUCT DEVELOPMENT** Hannah Heckner **BUSINESS SYSTEMS AND FINANCIAL ANALYSIS DIRECTOR** Randy Yi **DIRECTOR, BUSINESS OPERATIONS & ANALYST** Eric Knott **ASSOCIATE DIRECTOR, PRODUCT MANAGEMENT** Kris Bishop **SENIOR SYSTEMS ANALYST** Nicole Mehmedovich **SENIOR BUSINESS ANALYST** Cory Lipman **MANAGER, BUSINESS OPERATIONS** Jessica Tierney **BUSINESS ANALYSTS** Meron Kebede, Sandy Kim, Jourdan Stewart **FINANCIAL ANALYST** Julian Inari **ADVERTISING SYSTEM ADMINISTRATOR** Tina Burks **SALES COORDINATOR** Shirley Young **DIRECTOR, COPYRIGHT, LICENSING, SPECIAL PROJECTS** Emilie David **DIGITAL PRODUCT ASSOCIATE** Michael Hardesty **RIGHTS AND PERMISSIONS ASSOCIATE** Elizabeth Sandler **RIGHTS, CONTRACTS, AND LICENSING ASSOCIATE** Lili Catlett **RIGHTS & PERMISSIONS ASSISTANT** Alexander Lee **DIRECTOR, INSTITUTIONAL LICENSING** Iquo Edim **ASSOCIATE DIRECTOR, RESEARCH & DEVELOPMENT** Elisabeth Leonard **SENIOR INSTITUTIONAL LICENSING MANAGER** Ryan Rexroth **INSTITUTIONAL LICENSING MANAGERS** Marco Castellani, Chris Murawski **SENIOR OPERATIONS ANALYST** Lana Guz **MANAGER, AGENT RELATIONS & CUSTOMER SUCCESS** Judy Lillibridge **WEB TECHNOLOGIES TECHNICAL DIRECTOR** David Levy **PORTFOLIO MANAGER** Trista Smith **PROJECT MANAGER** Dean Robbins **DEVELOPERS** Liana Birke, Ryan Jensen

DIGITAL MEDIA DIRECTOR OF ANALYTICS Enrique Gonzales **MULTIMEDIA MANAGER** Sarah Crespi **MANAGING WEB PRODUCER** Kara Estelle-Powers **DIGITAL PRODUCER** Jessica Hubbard **VIDEO PRODUCER** Chris Burns **SOCIAL MEDIA PRODUCER** Brice Russ

DIGITAL/PRINT STRATEGY MANAGER Jason Hillman **QUALITY TECHNICAL MANAGER** Marcus Spiegel **DIGITAL PRODUCTION MANAGER** Lisa Stanford **ASSISTANT MANAGER DIGITAL/PRINT** Rebecca Doshi **SENIOR CONTENT SPECIALISTS** Steve Forrester, Antoinette Hodal, Lori Murphy **CONTENT SPECIALISTS** Jacob Hedrick, Kimberley Oster

DESIGN DIRECTOR Beth Rakouskas **DESIGN MANAGING EDITOR** Marcy Atarod **SENIOR DESIGNER** Chrystal Smith **DESIGNER** Christina Aycock **GRAPHICS MANAGING EDITOR** Alberto Cuadra **GRAPHICS EDITOR** Nirja Desai **SENIOR SCIENTIFIC ILLUSTRATORS** Valerie Altounian, Chris Bickel **SCIENTIFIC ILLUSTRATOR** Alice Kitterman **INTERACTIVE GRAPHICS EDITOR** Jia You **SENIOR GRAPHICS SPECIALISTS** Holly Bishop, Nathalie Cary **PHOTOGRAPHY MANAGING EDITOR** William Douthitt **PHOTO EDITOR** Emily Petersen **IMAGE RIGHTS AND FINANCIAL MANAGER** Jessica Adams

SENIOR EDITOR, CUSTOM PUBLISHING Sean Sanders: 202-326-6430 **ASSISTANT EDITOR, CUSTOM PUBLISHING** Jackie Oberst: 202-326-6463 **ADVERTISING PRODUCTION OPERATIONS MANAGER** Deborah Tompkins **SR. PRODUCTION SPECIALIST/GRAPHIC DESIGNER** Amy Hardcastle **SR. TRAFFIC ASSOCIATE** Christine Hall **DIRECTOR OF BUSINESS DEVELOPMENT AND ACADEMIC PUBLISHING RELATIONS**, ASIA Xiaoying Chu: +86-131 6136 3212, xchu@aaas.org **COLLABORATION/CUSTOM PUBLICATIONS/JAPAN** Adarsh Sandhu + 81532-81-5142 asandhu@aaas.org **EAST COAST/E. CANADA** Laurie Faraday: 508-747-9395, FAX 617-507-8189 **WEST COAST/W. CANADA** Lynne Stickrod: 415-931-9782, FAX 415-520-6940 **MIDWEST** Jeffrey Dembski: 847-498-4520 x3005, Steven Loerch: 847-498-4520 x3006 **UK EUROPE/ASIA** Roger Gonçalves: TEL/FAX +41 43 243 1358 **JAPAN** Kaoru Sasaki (Tokyo): +81 (3) 6459 4174 ksasaki@aaas.org

ASSOCIATE DIRECTOR, BUSINESS DEVELOPMENT Justin Sawyers **GLOBAL MARKETING MANAGER** Allison Pritchard **DIGITAL MARKETING ASSOCIATE** Aimee Aponte **MARKETING MANAGER, JOURNALS** Shawana Arnold **MARKETING ASSOCIATES** Mike Romano, Tori Velasquez **SENIOR DESIGNER** Kim Huynh **TRADE SHOW COORDINATOR** Andrew Clamp

GLOBAL SALES DIRECTOR ADVERTISING AND CUSTOM PUBLISHING Tracy Holmes: +44 (0) 1223 326525 **CLASSIFIED** advertise@sciencecareers.org **SALES MANAGER, US, CANADA AND LATIN AMERICA** SALES CAREERS Claudia Paulsen-Young: 202-326-6577 **EUROPE/ROW SALES** Sarah Lelarge **SALES ADMIN ASSISTANT** Kelly Grace +44 (0)1223 326528 **JAPAN** Miyuki Tani(Osaka): +81 (6) 6202 6272 mtani@aaas.org **CHINA/TAIWAN** Xiaoying Chu: +86-131 6136 3212, xchu@aaas.org

AAAS BOARD OF DIRECTORS, CHAIR Susan Hockfield **PRESIDENT** Margaret A. Hamburg **PRESIDENT-ELECT** Steven Chu **TREASURER** Carolyn N. Ainslie **CHIEF EXECUTIVE OFFICER** Rush D. Holt **BOARD** Cynthia M. Beall, May R. Berenbaum, Rosina M. Bierbaum, Kaye Husbands Fealing, Stephen P.A. Fodor, S. James Gates, Jr., Michael S. Gazzaniga, Laura H. Greene, Robert B. Millard, Mercedes Pascual, William D. Provine

SUBSCRIPTION SERVICES For change of address, missing issues, new orders and renewals, and payment questions: 866-434-AAAS (2227) or 202-326-6417, FAX 202-842-1065. Mailing addresses: AAAS, P.O. Box 96178, Washington, DC 20090-6178 or AAAS Member Services, 1200 New York Avenue, NW, Washington, DC 20005 **INSTITUTIONAL SITE LICENSES** 202-326-6730 **REPRINTS:** Author Inquiries 800-635-7181 **COMMERCIAL INQUIRIES** 803-359-4578 **PERMISSIONS** 202-326-6765, permissions@aaas.org **AAAS Member Central Support** 866-434-2227 www.aaas.org/membercentral

Science serves as a forum for discussion of important issues related to the advancement of science by publishing material on which a consensus has been reached as well as including the presentation of minority or conflicting points of view. Accordingly, all articles published in Science—including editorials, news and comment, and book reviews—are signed and reflect the individual views of the authors and not official points of view adopted by AAAS or the institutions with which the authors are affiliated.

INFORMATION FOR AUTHORS See www.sciencemag.org/authors/science-information-authors

BOARD OF REVIEWING EDITORS (Statistics board members indicated with \$)

Adriano Aguzzi, U. Hospital Zürich
Takuzo Aida, U. of Tokyo
Leslie Aiello, Wenner-Gren Foundation
Judith Allen, U. of Manchester
Sebastian Amigorena, Institut Curie
Meinrat O. Andrae, Max Planck Inst. Mainz
Paola Ariotti, Harvard U.
Johan Auwerx, EPFL
David Awschalom, U. of Chicago
Clare Baker, U. of Cambridge
Nenad Ban, ETH Zürich
Franz Bauer, Pontificia Universidad Católica de Chile
Ray H. Baughman, U. of Texas at Dallas
Carlo Beenakker, Leiden U.
Kamran Behnia, ESPCI
Yasmine Belkaid, NIAID, NIH
Philip Benfey, Duke U.
Gabriele Bergers, VIB
Bradley Bernstein, Massachusetts General Hospital
Peer Bork, EMBO
Chris Bowler, École Normale Supérieure
Ian Boyd, U. of St. Andrews
Emily Brodsky, U. of California, Santa Cruz
Ron Brookmeyer, U. of California, Los Angeles (\$) **\$**
Christian Büchel, UKE Hamburg
Dennis Burton, Scripps Research
Carter Tribble Butts, U. of California, Irvine
Gyorgy Buzsaki, New York U. School of Medicine
Blanche Capel, Duke U.
Mats Carlsson, U. of Oslo
Ib Chorkendorff, Denmark TU
James J. Collins, MIT
Robert Cook-Deegan, Arizona State U.
Lisa Coussens, Oregon Health & Science U.
Alan Cowman, Walter & Eliza Hall Inst.
Roberta Croce, VU Amsterdam
Jeff L. Dangel, U. of North Carolina
Tom Daniel, U. of Washington
Chiara Daraio, Caltech
Nicolas Dauphas, U. of Chicago
Frans de Waal, Emory U.
Stanislas Dehaene, Collège de France
Robert Desimone, MIT
Claude Desplan, New York U.
Sandra Diaz, Universidad Nacional de Córdoba
Dennis Discher, U. of Penn.
Gerald W. Dorn II, Washington U. in St. Louis
Jennifer A. Doudna, U. of California, Berkeley
Bruce Dunn, U. of California, Los Angeles
William Dunphy, Caltech
Christopher Dye, U. of Oxford
Todd Ehlers, U. of Tübingen
Jennifer Elisseeff, Johns Hopkins U.
Tim Elston, U. of North Carolina at Chapel Hill
Nader Engheta, U. of Pennsylvania
Barry Everitt, U. of Cambridge
Vanessa Ezenwa, U. of Georgia
Ernst Fehr, U. of Zürich
Michael Feuer, The George Washington U.
Toren Finkel, U. of Pittsburgh Medical Ctr.
Kate Fitzgerald, U. of Massachusetts
Peter Fratzl, Max Planck Inst. Potsdam
Elaine Fuchs, Rockefeller U.
Eileen Furlong, EMBL
Jay Gallagher, U. of Wisconsin
Daniel Geschwind, U. of California, Los Angeles
Karl-Heinz Glassmeier, TU Braunschweig
Marta Gonzalez, U. of California, Berkeley
Ramon Gonzalez, Rice U.
Elizabeth Grove, U. of Chicago
Nicolas Gruber, ETH Zürich
Kip Guy, U. of Kentucky College of Pharmacy
Taekjip Ha, Johns Hopkins U.
Christian Haass, Ludwig Maximilians U.
Sharon Hammes-Schiffer, U. of Illinois at Urbana-Champaign
Wolf-Dietrich Hardt, ETH Zürich
Louise Harra, U. College London
Michael Hasselmo, Boston U.
Jian He, Clemson U.
Martin Heimann, Max Planck Inst. Jena
Carl-Philipp Heisenberg, IST Austria
Ykä Helariutta, U. of Cambridge
Janet G. Hering, Eawag
Kai-Uwe Hinrichs, U. of Bremen
David Hodell, U. of Cambridge
Lora Hooper, UT Southwestern Medical Ctr. at Dallas
Fred Hughson, Princeton U.
Randall Hulet, Rice U.
Auke Ijspeert, EPFL
Akiko Iwasaki, Yale U.
Stephen Jackson, USGS U. of Arizona
Seema Jayachandran, Northwestern U.
Kai Johnsson, EPFL
Peter Jonas, Inst. of Science & Technology Austria
Matt Kaeblerlein, U. of Washington
William Kaelin Jr., Dana-Farber Cancer Inst.
Daniel Kammen, U. of California, Berkeley
Abby Kavner, U. of California, Los Angeles
Masashi Kawasaki, U. of Tokyo
V. Narry Kim, Seoul Nat. U.
Robert Kingston, Harvard Medical School
Etienne Kochlin, École Normale Supérieure
Alexander Kolodkin, Johns Hopkins U.

Thomas Langer, U. of Cologne
Mitchell A. Lazar, U. of Penn.
David Lazer, Harvard U.
Stanley Lemon, U. of North Carolina at Chapel Hill
Ottoline Leyser, U. of Cambridge
Wendell Lim, U. of California, San Francisco
Marcia C. Linn, U. of California, Berkeley
Jianguo Liu, Michigan State U.
Luis Liz-Marzán, CIC biomaGUNE
Jonathan Losos, Harvard U.
Ke Lu, Chinese Acad. of Sciences
Christian Lüscher, U. of Geneva
Fabienne Mackay, U. of Melbourne
Anne Magurran, U. of St. Andrews
Oscar Marin, King's College London
Charles Marshall, U. of California, Berkeley
Christopher Marx, U. of Idaho
C. Robertson McClung, Dartmouth College
Rodrigo Medellín, U. of Mexico
Graham Medley, London School of Hygiene & Tropical Med.
Jane Memmott, U. of Bristol
Tom Misteli, NCI, NIH
Yasushi Miyashita, U. of Tokyo
Richard Morris, U. of Edinburgh
Alison Motsinger-Reif, NC State U. (\$) **\$**
Daniel Neumark, U. of California, Berkeley
Kitty Nijmeijer, TU Eindhoven
Helga Nowotny, Austrian Council
Rachel O'Reilly, U. of Warwick
Harry Orr, U. of Minnesota
Pilar Ossorio, U. of Wisconsin
Andrew Oswald, U. of Warwick
Isabella Pagano, Istituto Nazionale di Astrofisica
Margaret Palmer, U. of Maryland
Steve Palumbi, Stanford U.
Jane Parker, Max Planck Inst. Cologne
Giovanni Parmigiani, Dana-Farber Cancer Inst. (\$) **\$**
Samuel Pfaff, Salk Inst. for Biological Studies
Matthieu Piel, Institut Curie
Kathrin Plath, U. of California, Los Angeles
Martin Plenio, Ulm U.
Albert Polman, FOM Institute for AMOLF
Elvira Poloczanska, Alfred-Wegener-Inst.
Philippe Poulin, CNRS
Jonathan Pritchard, Stanford U.
David Randall, Colorado State U.
Sarah Reisman, Caltech
Félix A. Rey, Institut Pasteur
Trevor Robbins, U. of Cambridge
Amy Rosenzweig, Northwestern U.
Mike Ryan, U. of Texas at Austin
Mitsunori Saitou, Kyoto U.
Shimon Sakaguchi, Osaka U.
Miquel Salmeron, Lawrence Berkeley Nat. Lab
Nitin Samarth, Penn. State U.
Jürgen Sandkühner, Medical U. of Vienna
Alexander Schier, Harvard U.
Wolfram Schlenker, Columbia U.
Susannah Scott, U. of California, Santa Barbara
Vladimir Shaleev, Purdue U.
Beth Shapiro, U. of California, Santa Cruz
Jay Shendure, U. of Washington
Brian Shoichet, U. of California, San Francisco
Robert Siliciano, Johns Hopkins U. School of Medicine
Uri Simonsohn, U. of Penn.
Lucia Sivilotti, U. College London
Alison Smith, John Innes Centre
Richard Smith, U. of North Carolina at Chapel Hill (\$) **\$**
Mark Smyth, QIMR Berghofer
Pam Soltis, U. of Florida
John Speakman, U. of Aberdeen
Tara Spire-Jones, U. of Edinburgh
Allan C. Spradling, Carnegie Institution for Science
Eric Steig, U. of Fundamental Research
Marka Stephan, Georgia State U.
V. S. Subrahmanian, U. of Maryland
Ira Tabas, Columbia U.
Sarah Teichmann, U. of Cambridge
Shubha Tole, Tata Inst. of Fundamental Research
Wim van der Putten, Netherlands Inst. of Ecology
Bert Vogelstein, Johns Hopkins U.
David Wallach, Weizmann Inst. of Science
Jane-Ling Wang, U. of California, Davis (\$) **\$**
David Waxman, Fudan U.
Jonathan Weissman, U. of California, San Francisco
Chris Wikle, U. of Missouri (\$) **\$**
Terrie Williams, U. of California, Santa Cruz
Ian A. Wilson, Scripps Research (\$) **\$**
Timothy D. Wilson, U. of Virginia
Yu Xie, Princeton U.
Jan Zaanen, Leiden U.
Kenneth Zaret, U. of Penn. School of Medicine
Jonathan Zehr, U. of California, Santa Cruz
Maria Zuber, MIT

EDITORIAL

Address harassment now

We have a problem in the academy. According to an extensive meta-analysis cited by the U.S. National Academies in their 2018 report *Sexual Harassment of Women: Climate, Culture, and Consequences in Academic Sciences, Engineering, and Medicine*, more than 50% of women faculty and staff at academic institutions in the United States report having been sexually harassed—as do some 20 to 50% of women students, depending on their field and level of study.

As troubling as this is, the problem, according to the National Academies report, is particularly egregious in the sciences, engineering, and medicine (SEM). It notes that SEM environments have four main characteristics that contribute to the problem: They have long been dominated by men; at an organizational level, they tolerate sexually harassing behavior; their mentorship structure of a hierarchy of individuals based on expertise and professional position creates dependent relationships between trainees and faculty mentors; and they often isolate faculty and trainees for considerable periods of time in labs, field sites, clinics, and hospitals.

None of this will come as a surprise to women who work or study in SEM fields. Many have experienced sexual harassment firsthand or know colleagues who have. This harassment distorts their environment and undermines the effectiveness of the communities in which they work. The problem is systemic, as are its impacts: It affects the physical and emotional health of victims and alters their career pathways and opportunities—it hinders the process and progress of science.

It's time for systemic change. The scientific community must act with urgency to create an inclusive organizational culture and professional standards of

behavior that will allow all of its members to reach their full potential. Recognizing this, last week the American Association for the Advancement of Science (AAAS, the publisher of *Science*) Council approved a new policy (www.aaas.org/FellowsRevocation) that defines sexual and gender-based harassment as a breach of professional ethics. The policy enables the revocation of elected AAAS Fellows “in cases of proven scientific misconduct, serious breaches of professional

ethics, or when the Fellow in the view of AAAS otherwise no longer merits the status of Fellow.” The policy will go into effect on 15 October 2018.

This is only one step among many that need to be taken in the months and years ahead. AAAS and other professional organizations can foster change by using their networks and influence to bring attention to policies and practices that support a culture of equality and integrity. Many scientific and engineering societies, funding organizations, and institutions are already doing important work on this front, but much remains to be done. To that end, AAAS will continue to host discussions across

the national and international scientific community to facilitate the exchange and dissemination of policies, procedures, and best practices for the adoption and enforcement of professional standards.

The goal to end sexual harassment across the scientific community is achievable only through sustained attention and commitment. Our community must no longer tolerate harassment in its labs, classrooms, clinics, hospitals, and other institutions. The health, quality of life, and productivity of all members of the scientific community depend on everyone's response to this problem.

—Margaret Hamburg, Susan Hockfield, Steven Chu

Margaret Hamburg
is president of the AAAS and foreign secretary of the U.S. National Academy of Medicine, Washington, DC, USA. mhamburg@nas.edu

Susan Hockfield
is chair of the board of directors of the AAAS and president emerita of the Massachusetts Institute of Technology, Cambridge, MA, USA. hockfield@mit.edu

Steven Chu
is president-elect of the AAAS and professor in the Department of Physics and the Department of Molecular and Cellular Physiology at Stanford University, Stanford, CA, USA. schu@stanford.edu



“The problem is systemic, as are its impacts...it hinders the process and progress of science.”

NEWS

“We stand by the science underlying our study. It is rigorous. It’s state of the art.”

Carlos Santos-Burgoa, leader of a George Washington University study criticized by President Donald Trump that put Hurricane Maria–related deaths in Puerto Rico near 3000.

IN BRIEF

Edited by **Jeffrey Brainard**

ASTRONOMY

Observatory closed for security threat



Managers have not said what led them to temporarily evacuate the Sunspot Solar Observatory.

A remote solar observatory in New Mexico reopened this week, 10 days after it was mysteriously evacuated because of an unspecified “security issue.” The operator of the site, the Association of Universities for Research in Astronomy (AURA), says it closed the facility, located on Sacramento Peak, to cooperate with a law enforcement investigation of criminal activity and because it was concerned that a suspect posed a threat to the staff. AURA has not disclosed the nature of the suspected criminal activity, but it says the threat has ended. A small number of astronomers at the Sunspot Solar Observatory make routine observations of the sun with the Richard B. Dunn Solar Telescope, run by a consortium of universities and the National Solar Observatory.

FDA eyes e-cigarette crackdown

PUBLIC HEALTH | The U.S. Food and Drug Administration (FDA) in Silver Spring, Maryland, last week said it may pull e-cigarettes from the market unless manufacturers propose satisfactory steps within 60 days to help curb an “epidemic” of use by minors. Studies indicate the addictive nature of these nicotine-containing vaping products leads youth to begin to smoke. Although e-cigarettes may help adults stop smoking, “The FDA won’t tolerate a whole generation of young people becoming addicted to nicotine as a tradeoff for enabling adults to have unfettered access to these same products,” FDA Commissioner Scott Gottlieb said in a statement. FDA also issued 1300 warning letters and fines to retailers who illegally sold e-cigarettes to minors this summer, part of what the agency called the largest coordinated enforcement effort in its history.

Industry ties prompt resignation

RESEARCH ETHICS | Breast cancer researcher José Baselga, chief medical officer at Memorial Sloan Kettering Cancer Center in New York City, resigned last week following revelations that he failed to fully report his financial ties to drug companies in his publications. ProPublica and *The New York Times* reported on 8 September that Baselga did not disclose his paid relationships with Roche and other companies in scores of published papers over the past 5 years, including articles in *Cancer Discovery*, where he is an editor-in-chief. The payments—all reported to his institution—totaled more than \$3 million. Baselga helped develop Herceptin and other molecularly targeted cancer drugs.

Brussels OA champion leaves

PUBLISHING | Robert-Jan Smits, the civil servant at the European Commission who helped hatch a radical plan to promote open access (OA) in scientific publishing, is leaving his job. Smits will become president of Eindhoven University of Technology in the Netherlands, his home country, in the spring of 2019. Smits shepherded many major reforms in EU science policy during his 25 years at the commission; in March, the commission appointed



AGRICULTURE

Virus outbreak in Belgian boars causes jitters

In another giant leap for a deadly pig virus, African swine fever (ASF) was discovered last week in Western Europe. Belgian authorities reported finding the disease's virus in two wild boars in the southeastern province of Luxembourg. No farm infections have been reported, but animal health experts worry they are inevitable if the virus becomes established in wild boars. Harmless to humans but hard to stamp out, ASF poses an increasing global threat to pig farming. It had previously been discovered in a dozen countries in Eastern Europe and has caused outbreaks in more than 20 locations in China since 1 August. The jump to Belgium suggests the disease may have reached "pandemic proportions," the University of Minnesota's Swine Health Monitoring Project in St. Paul wrote in a statement last week.

Experts worry African swine fever could jump from wild boars to pigs on Western European farms.

him its special envoy for OA. Unveiled this month, his "Plan S" seeks to finally "flip" the publishing industry to OA; it has the support of the commission and a coalition of European science funders (*Science*, 7 September, p. 957). Smits tells *Science* he's not worried about leaving his brainchild alone. An international task force will work out details by the end of the year, he says, after which it's up to funders and institutions around the European Union to implement it. Meanwhile, Smits hopes to convince traditional academic publishers opposing the plan to make the switch. "By the time I leave, my job will be finished," he says.

Spending rises for U.S. research

RESEARCH FUNDING | Congress delivered some good budget news on 13 September to several major U.S. research agencies. Lawmakers agreed on a plan to give the National Institutes of Health, the nation's largest funder of biomedical research, a 5%, \$2 billion boost, to \$39.1 billion, in the fiscal year that begins 1 October. They also agreed to increase the Department of Defense's spending on basic research by 8%, to \$2.5 billion, in 2019. The same day, they sent President Donald Trump a bill that rejects his proposed cuts to Department of Energy science programs and instead provides a 5.2% spending boost, to \$6.6 billion. But Congress is not expected to complete work on bills funding other research agencies before the current fiscal

year ends on 30 September. Instead, it plans to send Trump legislation that would extend current spending levels for those agencies through 7 December, in hopes of completing work on the 2019 budget by the end of the calendar year.

Former IPCC head to stand trial

#METOO | A court in New Delhi last week ordered Rajendra Pachauri, former head of the United Nations's Intergovernmental Panel on Climate Change (IPCC), to stand trial on criminal charges that he sexually harassed a former colleague. Pachauri, 78, stepped down from IPCC in February 2015 when a female colleague at The Energy and Resources Institute (TERI) in New Delhi, where he was director general, filed a police complaint against him, alleging he kissed and grabbed her inappropriately and threatened to retaliate against her for refusing his advances. Pachauri denies the allegations. He filed a pending defamation lawsuit against a second former TERI employee after she alleged in 2016 that he sexually harassed her a decade earlier; authorities have not charged him in that case.

Harasser's name is off glacier

#METOO | The Marchant Glacier in the Royal Society Range of Antarctica, named in 1994 for geologist David Marchant, was renamed Matataua Glacier on 10 September by the U.S. Board on Geographic Names.

Last year, Marchant, of Boston University, was found to have sexually harassed then-graduate student Jane Willenbring during field work in Antarctica nearly 20 years ago (*Science*, 13 October 2017, p. 162). The glacier sits near Matataua Peak; "*matatua*" is a Maori word meaning "a scout before the troops." Willenbring, now of the Scripps Institution of Oceanography in San Diego, California, says she was "pleased and surprised" by the move, which "sends a message that this sort of thing isn't tolerated anymore."

You published that?

SCIENCE COMEDY | Riding in the front seat of a roller coaster could help you pass a kidney stone—but even more so if you sit in back. These and other head-scratching research findings were among those honored last week by the Ig Nobel Prizes, a parody of the Nobel Prizes organized by the science humor magazine *Annals of Improbable Research*. At the awards ceremony at Harvard University, a trio of urologists won the award in reproductive medicine for a journal article for which they used postage stamps to measure nighttime erections. The Peace Prize went to researchers who surveyed Spanish drivers to determine the frequency, motivation, and effects of shouting and cursing while in a car. And the Economics Prize honored an investigation of whether employees felt better after using voodoo dolls to retaliate against abusive bosses. (They did.)

<http://science.sciencemag.org/> on September 20, 2018

PHOTO: ERICH KUCHLING/GETTY IMAGES



IN DEPTH

SEVERE WEATHER

Deadly storms break records, damage facilities

Florence and Mangkhut hold lessons for future disasters, and omens of growing severity

By **Frankie Schembri**

Weather and marine scientists were awestruck last week as they watched deadly, record-breaking storms evolve on opposite sides of the globe. Now, they are scrambling to analyze a torrent of data on the origins and impacts of the storms, collected by satellites, gauges, robotic submarines, and other instruments. They are also assessing damage to research infrastructure.

In Asia, Typhoon Mangkhut made landfall early on 15 September local time on northern Luzon in the Philippines, killing at least 70 people, many in massive mudslides. It went on to pound Hong Kong, China, with some of the strongest winds and highest storm tides recorded there in the modern era.

At about the same time in North America, Hurricane Florence came ashore near Wilmington, North Carolina. Its winds were far weaker, but it produced unprecedented rainfall and flooding, killing at least 24 people and leaving several coastal science facilities in tatters.

At the Duke University Marine Lab in Beaufort, North Carolina, the “terrifying” hurricane “peeled [the roof] off our primary teaching building” and left many dormitories “uninhabitable,” says Director Andrew Read. Florence also severely damaged Dobo

Hall, a main science building at the University of North Carolina in Wilmington. It’s not clear how long it will take to reopen the campuses, officials say.

Off Wilmington’s coast, 8-meter waves and chaotic currents dragged a buoy equipped with sensors that measure wind speeds, wave heights, and other conditions more than a kilometer from its mooring. But as of early this week, it was still transmitting data, says Debra Hernandez, executive director of the buoy’s operator, the Southeast Coastal Ocean Observing Regional Association in Charleston, South Carolina. She was waiting to find out whether an instrument that tracks ocean currents with high-frequency radar, silent since the storm, is still intact. It could take years to replace lost instruments, she notes, because her network relies mostly on federal funding that must work its way through Congress.

In China, ocean researchers at The University of Hong Kong (HKU) dodged a bullet when 175-kilometer-per-hour winds and high waves slammed into The Swire Institute of Marine Science, which is perched on an exposed peninsula. The facility “took a lot of damage,” says Director Gray Williams, an intertidal ecologist. “But it hasn’t affected us at all,” because the institute’s specimens, experiments, and major equipment were out of harm’s way. They had been moved to the main HKU campus

several months ago to allow for a major renovation and expansion. “The timing was fortuitous,” Williams says.

Other researchers are beginning to comb through data on the storms themselves. In the Pacific Ocean, monitoring networks confirmed that Typhoon Mangkhut was the most powerful seen this year, with winds peaking at 287 kilometers per hour. But the Philippines got a bit lucky, says I-I Lin, a specialist in typhoon-ocean interactions at National Taiwan University in Taipei: The storm passed over relatively cool surface waters before it made landfall, sapping some of its power.

In the United States, however, researchers say a warming climate likely contributed to Florence’s extraordinary rainfall, which totaled more than a meter in some areas and fed floodwaters that overtopped measuring gauges put in place to document the storm’s impact. Warm air simply holds more water, researchers note. On top of that, there’s evidence that warming is slowing the forward motion of storms, potentially by weakening the temperature differentials that drive steering winds, allowing the rain to linger.

That slowing, described in *Nature* earlier this year by a group led by climate scientist James Kossin of the University of Wisconsin in Madison, was certainly a factor in the flooding that Hurricane Harvey caused last year in Texas. “Now we have another textbook example with Florence,” Kossin

Hurricane Florence dawdled over North Carolina, dropping catastrophic amounts of rain.

says. "The main thing that Florence is doing is that it's not moving." At one point, the storm was creeping along at some 3 kilometers per hour, he notes. "I'm old and I can walk faster than that."

Florence also underscored the importance of winds in driving coastal flooding, says computer scientist Russell Clark of Georgia Institute of Technology in Atlanta. People tend to focus on a hurricane's maximum wind speeds, he says, but that can be "very misleading. It is the sustained onshore winds over multiple days, over a large area, that have caused the waters to pile up in the bays and rivers, leaving nowhere for this massive rainfall to go." Those winds partly explain why New Bern, North Carolina, a small town hard hit by floodwaters, "started flooding ... even before the worst of the rain had arrived."

More insight into the behavior of Florence—and future storms—could come from two automated submarine gliders and other sensors deployed along the continental shelf in the hurricane's path. The sensors "have given us a really cool view of what's happening on the shelf," including how subsurface temperatures and salinities changed as Florence churned, says Catherine Edwards, a marine researcher at the University of Georgia's Skidaway Institute of Oceanography in Savannah. She predicts the data will be useful in improving forecasts.

The pattern of blown-out windows in Hong Kong's tall building canyons may offer lessons for cities, says Deng Xiaowei, an HKU structural engineer. When wind is channeled between buildings set close together, it can accelerate and become turbulent, shattering windows. Current building codes don't "consider sufficiently the interaction of buildings in the local wind environment," Deng says.

Landslides in the Philippines highlight another shortcoming of current disaster prevention efforts. "Extreme rainfall was forecast, landslide hazard maps showing nearby safe areas were available, and yet we have many deaths," says Alfredo Mahar Francisco Lagmay, a geologist at the University of the Philippines Diliman in Quezon City. In one heartbreaking incident 200 kilometers north of Manila, dozens of miners and their families took shelter in a makeshift chapel that was buried when the slope above it collapsed. The site had been designated as dangerous, and safer locations were just several hundred meters away. But hazard maps for the region, though available online, had never been printed and distributed. ■

With reporting by Dennis Normile and Paul Voosen.

SCIENTIFIC COMMUNITY

Evidence-based medicine group expels internal critic

Cochrane is in turmoil after ousting co-founder Peter Gøtzsche, who accused it of becoming "industry-friendly"

By **Martin Enserink**

A crisis has erupted within Cochrane, an international network of scientists that promotes evidence-based medicine. On the eve of its annual conference, held earlier this week in Edinburgh, Cochrane's 13-member Governing Board voted to expel Peter Gøtzsche, director of the Nordic Cochrane Centre in Copenhagen and a board member himself, for actions "likely to have a serious adverse effect" on the organization or causing "disrepute." Four other board members then resigned in protest.

Gøtzsche, whose books have made him one of Cochrane's most widely known researchers, says he was the victim of a "show trial" likely instigated by Cochrane funders who dislike his highly critical views about pharma. But details about the procedure against him are shrouded in secrecy, and for Cochrane's members and supporters it was hard to tell this week whether the conflict is about scientific rigor, the limits of academic freedom within a large multinational organization, or a personality clash.

Formerly known as the Cochrane Collaboration, the group surveys the literature on treatments and diagnostics to produce consensus reports on their efficacy. Tens of thousands of volunteer reviewers, as well as independent Cochrane groups in 43 countries, contribute to the work, which is supported mainly by government agencies, including the U.S. National Institutes of Health; Cochrane does not accept industry money. Its Governing Board confirmed in a 15 September statement that it had expelled Gøtzsche, but did not mention him by name.

Gøtzsche had long been on a collision course with Mark Wilson, who heads Cochrane's central executive team in London. Wilson is credited with professionalizing the organization since his arrival

in 2012, but he has clashed with some in the network. The U.S. Cochrane Center decided to close down in February, says that center's former director, Kay Dickersin of the Johns Hopkins Bloomberg School of Public Health in Baltimore, Maryland, in part because "interactions with the CEO had become difficult."

In its statement, the Governing Board cited three complaints made against the unnamed board member in March—the latest of many since 2003, it noted. "Many disputes have arisen," the statement said. "Promises have been made. And broken. Some disputes have been resolved, some have not." Gøtzsche disputes the long history of problems; he says

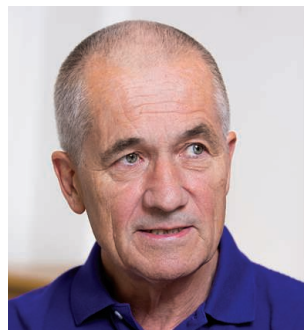
the recent complaints were about alleged violations of Cochrane's spokesperson policy, which specifies who can speak on behalf of the organization and how.

At a meeting on 13 September that Gøtzsche was asked not to attend, six board members voted to expel him, five voted against, and one abstained, according to a statement written by the four members who left the board to protest the decision.

"We consider the Board's use of its authority to expel Peter from Cochrane to be disproportionate," the four wrote. "We believe that the expulsion of inconvenient members from the Collaboration goes against Cochrane ethos."

Wilson did not respond to *Science's* requests for an interview; neither did the Governing Board's two co-chairs, Martin Burton of the University of Oxford in the United Kingdom and Marguerite Koster, a senior manager at Kaiser Permanente in Los Angeles, California.

Gøtzsche is known as a firebrand who is fiercely critical of the pharmaceutical industry and medical interventions he deems useless or harmful; he has likened the pharmaceutical industry to "organized crime." But he "has always been a very good scientist," Dickersin says. He "might be classified as



One colleague calls Peter Gøtzsche "an evidence-based medicine purist."

an evidence-based medicine purist," Trish Greenhalgh, an expert in primary health care and evidence-based medicine at Oxford, wrote in a blog post this week.

One example of that purism came in response to a favorable Cochrane review about vaccines against human papillomavirus (HPV), a common cause of cervical cancer, published in May by scientists from Belgium and the United Kingdom in the Cochrane Library, the group's in-house publication. In July, Gøtzsche and two co-authors published an attack on the review, titled "The Cochrane HPV vaccine review was incomplete and ignored important evidence of bias," in *BMJ Evidence-Based Medicine*. The critique said Cochrane's review didn't constitute the "trusted evidence" promised in the organization's motto. After an investigation, Cochrane Library editors acknowledged some shortcomings in the study but said they made little or no difference to the main outcome and that the criticism was "substantially overstated."

They also worried the debate would be fodder for the antivaccine movement: "If the result of this controversy is reduced uptake of the vaccine among young women, this has the potential to lead to women suffering and dying unnecessarily from cervical cancer," they wrote. And some found the tone of Gøtzsche's criticism too harsh. "I would not have expressed the critique in those terms myself," Greenhalgh says.

Gøtzsche says Cochrane isn't doing enough to guarantee the independence and quality of its reviews. He argues that the organization should no longer allow scientists who have financial conflicts of interest to serve as reviewers (see story, p. 1184). Gøtzsche also decries a "top-down authoritarian culture" and says Wilson has pulled the organization in a "more commercial, more industry-friendly direction." That the Cochrane leadership increasingly uses terms like "brand" and "business" is a sign of the shift, he says.

Such dissent should be possible within Cochrane, says David Hammerstein Mintz, a consumer advocate, former member of the European Parliament from Spain, and one of the four departing board members. "If it can't tolerate a few disagreements or a few headaches, that is a problem," he says. Others hope cooler heads will prevail in the interest of Cochrane's mission. "What's at stake in the current bloody fight [is] the future of reliable trustworthy evidence in a world of increasing falsity and fake news," Ray Moynihan of the Centre for Research in Evidence-Based Practice at Bond University in Gold Coast, Australia, wrote in a blog post. "To see this future threatened fore-shadows a disaster for all of us." ■

BIOMEDICINE

Drug pair shows promise for treating sleep apnea

Small clinical trial revives hope for an alternative to bulky breathing machines

By Meredith Wadman

During decades of lab experiments and dozens of clinical trials, scientists have searched in vain for drugs to defeat obstructive sleep apnea, the risky and increasingly prevalent condition in which a person's upper airway repeatedly collapses during sleep, causing them to briefly stop breathing dozens or hundreds of times each night. Now, a new drug combination has reawakened hopes.

A team led by researchers in Boston has identified a pair of medications—approved for other uses and with solid safety records—that appear to work in concert during sleep to activate the muscles that dilate the upper airway. In a study of 20 patients, the scientists found that a combination of atomoxetine and oxybutynin, taken as two pills at bedtime, reduced patients' frequency of airway obstruction—called the apnea-hypopnea index (AHI)—from a median of 28.5 hourly obstructions on placebo to 7.5 on the pills.

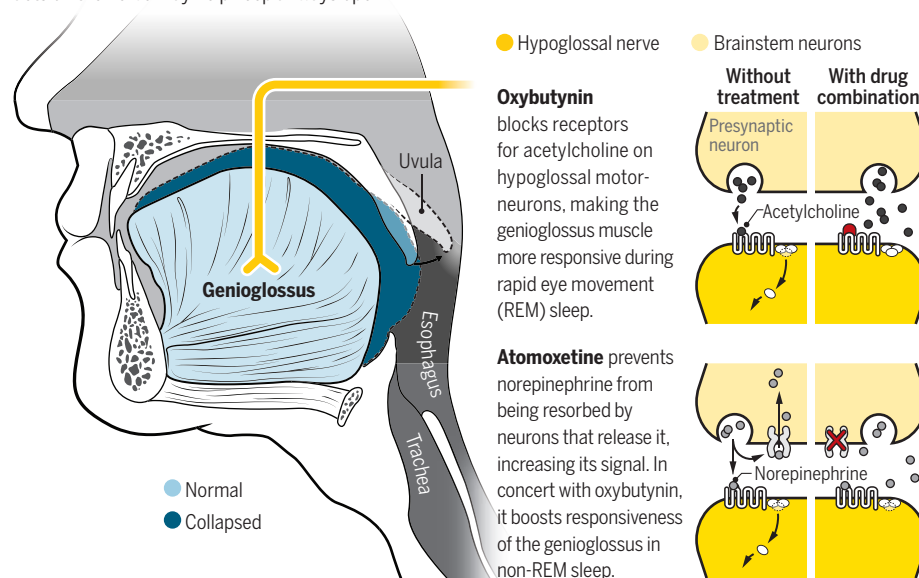
In the 15 patients with the highest AHIs, the median reduction was 74%—and every patient experienced at least a 50% reduction, Andrew Wellman and Luigi Taranto-Montemurro at Brigham and Women's Hospital in Boston reported this week at the European Respiratory Society's International Congress in Paris. Patients' blood oxygenation also improved strikingly, their group found.

"We've never had a drug combination, or any sort of a drug, that consistently improved everybody's AHI. That's actually unbelievably exciting," says Sigrid Veasey, a physician-researcher who studies sleep at the University of Pennsylvania (UPenn). It's "a great first step," adds Martina Mason, a sleep physician at the Royal Papworth Hospital in Cambridge, U.K., who co-authored a 2013 review of 30 previous, underwhelming drug trials.

The trial turned up one potentially problematic finding: Although the drug combination reduced patients' AHIs, the number of subconscious arousals—the subtle awak-

Opening a blocked airway

In obstructive sleep apnea, the muscles that maintain an open upper airway collapse repeatedly. The hypoglossal nerve controls many of these muscles, including the crucial tongue muscle, the genioglossus. A pair of drugs that acts on the nerve may help keep airways open.



enings that leave patients exhausted—remained high. But if this combination proves safe and effective in larger trials, it could free many sleep apnea patients from the current gold-standard remedy, the cumbersome continuous positive airway pressure (CPAP) machines that blow air into the throat to keep the airway open, but require users to wear a mask and headgear at night.

Mason, Veasey, and other sleep apnea experts caution, however, that the findings are extremely preliminary. They note that the pilot study, although double-blind and randomized, included just a small number of patients who took the drug combination for just 1 night.

The search for sleep apnea treatments has become pressing as its prevalence has grown, as widespread noncompliance with CPAP has been charted, and as researchers have documented the disease's long-term dangers. In addition to enduring daytime sleepiness, sleep apnea sufferers—some 13% of U.S. men and 6% of women aged 30 to 70—are at higher risk for depression, cognitive impairment, high blood pressure, heart attack, stroke, and premature death. The obesity epidemic is thought to be increasing the incidence of sleep apnea, though thin individuals can also be afflicted.

Wellman, a physician who has been studying sleep apnea since 2001, began to test various drugs for the condition in clinical trials more than 10 years ago. "I had given up, really," he recalls. Then, in 2015, Taranto-Montemurro, an enthusiastic postdoc, arrived in his lab. Wellman reluctantly let him launch a new trial of a drug combination suggested by animal studies from other labs. "I wasn't really happy about it," Wellman says, "until all of a sudden the data started coming in."

Atomoxetine, approved by the U.S. Food and Drug Administration in 2002 to treat attention deficit hyperactivity disorder, increases messaging in the brain by the excitatory neurotransmitter norepinephrine, whose levels normally fall off markedly during sleep. Giving a stimulating drug at bedtime seems counterintuitive. But animal work led by Richard Horner, a sleep physiologist at the University of Toronto in Canada, had shown that injecting rats with a norepinephrine-mimicking drug in an area of the brainstem that controls the hypoglossal nerve, which powers the upper airway muscles, improved activity of the genioglossus, a large tongue muscle that is critical for keeping the throat open. The drug was consistently effective only during nonrapid eye movement sleep, not during rapid eye movement (REM) sleep, when throat muscles are especially prone

to relaxation and collapse, making sleep apnea worse.

The other half of the combination, oxybutynin, improves genioglossus responsiveness during REM sleep. Again, work by Horner's team provided the crucial clue. It found that during REM sleep the neurotransmitter acetylcholine acts on certain receptors on the hypoglossal nerve to powerfully inhibit activation of the genioglossus. Oxybutynin, Wellman and Taranto-Montemurro knew, blocks acetylcholine's action at the same receptors—and it had a long track record as a marketed drug used for decades to treat overactive bladder.

As the drug pair progresses through clinical trials, sleep apnea specialists will watch closely whether the drugs actually reduce subconscious arousals and improve sleep quality. "What if you can improve the AHI, the obstructions, but the patients are as sleepy as they were before the treatment?" asks UPenn's Leszek Kubin, a neurophysiologist who studies the mechanisms of sleep-disordered breathing.

The study researchers propose that the patients' arousals may have been due to the invasive instrumentation attached to them during the night, and the associated discomfort. And they note that in the 13 patients with the highest AHIs, the number of arousals did decline a statistically significant amount on the pill combination.

Some are already betting that the drug pair, on which a patent for use in sleep apnea is expected to be published next month, will find a large and eager market. Apnimed, Inc., a new Cambridge, Massachusetts, company formed to commercialize the discovery, recently landed \$25 million from Morningside Venture Capital in Newton, Massachusetts. It is planning a phase II trial involving more than 100 patients, to study dosing and side effects, says CEO Larry Miller. (Wellman and Taranto-Montemurro have a financial interest in the firm but are not involved with the trial.)

Sleep physicians note that side effects unrelated to breathing may make the drug combination a nonstarter for some sleep apnea patients. In a population at risk for hypertension and heart attacks, the stimulant effects of atomoxetine will have to be watched. And oxybutynin's dampening effect on bladder muscle activity may prove problematic for a typical group with sleep apnea: "old men who have trouble urinating in the night," says J. Steven Poceta, a sleep physician at the Scripps Clinic Torrey Pines in San Diego, California. Still, he says, he's excited about the drug combination's promise. "It could be great for a lot of people." ■

SCIENCE POLICY

AAAS adopts new policy for ejecting harassers

Society may strip honors if misconduct has been found

By Meredith Wadman

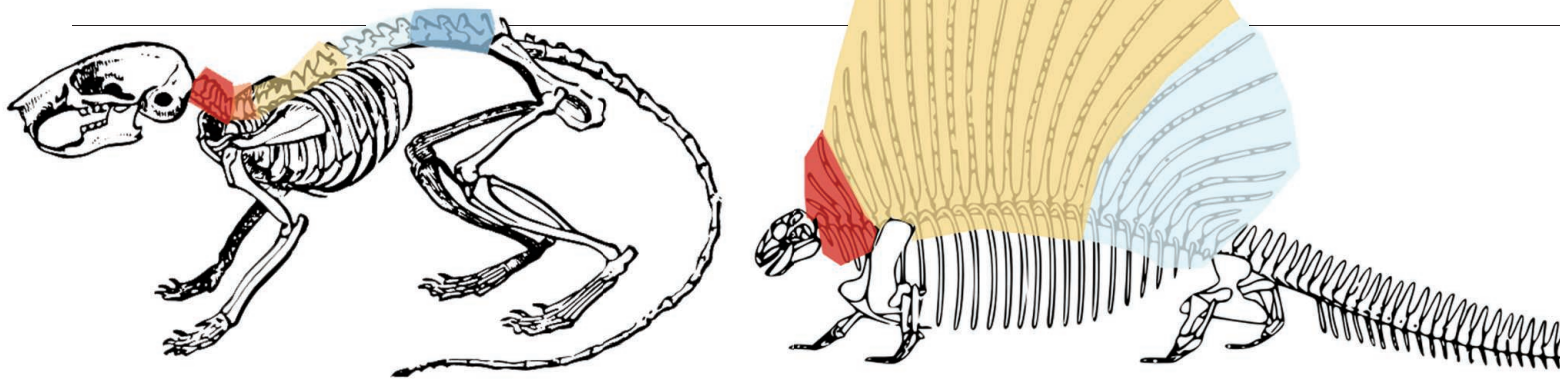
On Saturday, the governing council of AAAS (the publisher of *Science*) in Washington, D.C., unanimously adopted a policy on sexual harassment and other misconduct by scientists who have been elected as AAAS fellows. Starting on 15 October, fellows who have been found by an outside body to have violated professional ethics—which are defined as including sexual harassment—may be stripped of the prestigious honor.

"Harassment has no place in science," says Margaret Hamburg, president of AAAS. (On p. 1167, Hamburg and other AAAS officials explain the policy in an editorial.) But, she adds, "We are not going to make decisions based simply on a newspaper article, a blog, or somebody's anecdotal report."

The new policy will allow any AAAS member to request revocation of a fellow's title for breaches that range from harassment to fabricating results. AAAS will require proof in the form of investigative reports or announcements by institutions, organizations, or government agencies. AAAS has about 9000 fellows among its 120,000 members.

Advocates welcomed the policy. "I am thrilled that AAAS has shown themselves to be the leaders we knew they were," says BethAnn McLaughlin, a neuroscientist at Vanderbilt University in Nashville, who recently launched petitions urging AAAS and the National Academies of Sciences, Engineering, and Medicine (NASEM) to eject harassers. NASEM is considering revising its bylaws to allow harassers to be ousted.

AAAS fellows who have been sanctioned recently for sexual harassment or sexual misconduct include Francisco Ayala, formerly of the University of California, Irvine; Thomas Jessell, formerly of Columbia University; Lawrence Krauss of Arizona State University's Tempe campus; and Inder Verma, formerly of the Salk Institute for Biological Studies in San Diego, California. ■



EVOLUTION

A modular backbone aided the rise of mammals

Fossils show how lumbar vertebrae were freed up to adapt to myriad lifestyles

By Elizabeth Pennisi

Run, climb, breathe deep. You might not connect those abilities to your backbone. In fact, mammals owe many of their capabilities to the complex structure of their spine, which has five distinct regions, each free to adopt specialized functions. On p. 1249, Harvard University vertebrate paleontologist Stephanie Pierce and postdoc Katrina Jones report an investigation of fossils from the dawn of mammals that shows how evolution built our versatile spine.

"This is an important analysis," says Richard Blob, biomechanist at Clemson University in South Carolina. "It's tackling a fundamental problem: the origins of animal construction." And it shows how mammals ended up with a backbone that "can evolve in pieces and respond to different selective pressures at different places along the column," says Emily Buchholtz, a vertebrate paleontologist at Wellesley College in Massachusetts.

Biologists have long recognized distinct regions in the mammalian spine based on their vertebrae. For example, small cervical vertebrae make up the neck, thoracic vertebrae bear the ribs and support the chest, and the ribless, hefty lumbar vertebrae bring up the rear. In contrast, reptiles and amphibians have very uniform backbones. "All their vertebrae are essentially doing the same thing," Pierce says. She and others assumed a regionalized spine was unique to mammals.

But in 2015, a sophisticated statistical analysis of a snake spine and a look at the genetic programs controlling its development indicated this backbone, too, has very subtly defined regions. "The work showed

that regions could be distinct even if they weren't as different as in mammals," says Christian Kammerer, a paleontologist at the North Carolina Museum of Natural Sciences in Raleigh. The finding suggested a regionalized vertebral column evolved early in land animal history, even before the divergence of mammals and reptiles.

To probe its origins, Pierce, Jones, and their colleagues scoured museums for fossils with complete backbones. Ultimately, they analyzed spines from 16 synapsids, creatures that lived 200 million to 300 million years ago and include distant and immediate predecessors to mammals. They used computerized tomography scanning to get high-resolution images and worked with paleontologist David Polly from Indiana University in Bloomington to precisely measure the shapes of the vertebrae and assess regionalization within each animal.

The analysis uncovered a stepwise addition of regions. More distant ancestors of mammals, such as *Dimetrodon*, a large reptilelike synapsid with a giant sail on its back, had three regions, designated cervical, anterior dorsal, and posterior dorsal. The therapsids, creatures that just preceded mammals, had a fourth region, the pectoral. A fifth region, the lumbar, appeared after early, egg-laying mammals arose and is found today in placental and marsupial mammals.

The work also pointed to factors driving the emergence of these distinct regions. The pectoral region, for example, appeared in the therapsids as they evolved longer forelimbs, positioned under the body rather than splayed to the sides. (Think of a dog's legs compared with a lizard's.) The limb changes would have required changes in the shoulder

Distant mammal ancestors such as *Dimetrodon* (right) had three spine regions; a mouse (left) has five.

girdle and the vertebrae supporting it, resulting in a distinct region of the spine just behind the neck. The same set of changes also freed some shoulder muscles to evolve into a muscular diaphragm, which improved breathing and enabled mammals to have a higher metabolic rate, Buchholtz says.

Over time, further decoupling led to the modular spine seen in mammals today, in which individual vertebrae can change without jeopardizing the function of the whole spine. As a result, different regions can "take on new forms and functions, so they can adapt to different environments," Pierce says. Perhaps the most variable part of the spine has been the last to emerge: the lumbar region, which interacts with the pelvis and hind limbs.

The cat family illustrates the benefits of the region's evolutionary freedom. All cats look, well, catlike, but lions tend to keep their feet on the ground and hunt large prey, whereas clouded leopards live in trees, leaping on their quarry, and cheetahs chase down antelopes at high speeds. Paleontologists Marcela Randau and Anjali Goswami of the Natural History Museum in London did 3D analyses of 109 cat skeletons representing species with various hunting and living strategies. They compared the vertebrae within each species and between species, as well as the limbs, shoulders, pelvises, and skulls.

In all these cats, most of the spine looks similar. Their lumbar regions have diversified, however, suggesting this region evolved independently of the rest of the spine and skeleton, Randau said last month at the second Joint Congress on Evolutionary Biology in Montpellier, France. The size and shape of the lumbar vertebrae vary depending on what the cat does best.

"It's the lumbar region that really allows mammals to do all sorts of different things," Pierce says. On the downside, the more recently evolved parts of the back—the lumbar region in particular—are also the source of most back pain, Pierce says, so "maybe we also owe our ancestors for having back complications." ■

NEUROSCIENCE

Brain scientists dive into deep neural networks

Increasingly skilled artificial intelligence could hold clues to human sensory systems

By **Kelly Servick**, in Philadelphia, Pennsylvania

While artificial intelligence (AI) has been busy trouncing humans at Go and spawning eerily personable Alexas, some neuroscientists have harbored a different hope: that the types of algorithms driving those technologies can also yield some insight into the squishy, wet computers in our skulls. At the Conference on Cognitive Computational Neuroscience here this month, researchers presented new tools for comparing data from living brains with readouts from computational models known as deep neural networks. Such comparisons might offer up new hypotheses about how humans process sights and sounds, understand language, or navigate the world.

tems repeatedly adjust the strengths of the connections between nodes.

The complexity of these models makes it devilishly hard to figure out how they make decisions (*Science*, 7 July 2017, p. 22); speakers at the meeting variously described their innards as “mush” and “goo.” But they’re not completely inscrutable, McDermott says. “You can still look at different parts of a network—say, different layers—and ask what kinds of information can be read out.”

The answers might give scientists clues about how the brain breaks apart and processes the world around it, says cognitive neuroscientist Elissa Aminoff at Fordham University in New York City. For example, a human observer looking at a forest is aware of features such as shades of green or abundant vertical lines, she explains. But other statistical features that people are not conscious of

allow machine learning experts to include fMRI data alongside the labeled images when they train a neural network. Such models might do “much more sophisticated tasks” with the images, Aminoff says, such as using their content to reason and make future decisions.

Other neuroscientists remain ambivalent about the value of deep neural networks. “I question what exactly we learn about the brain by using them,” Baker says. He’s particularly wary of trying to make direct comparisons between network layers and brain regions. “You wouldn’t want to argue that a pitching machine is a model for the biomechanics of throwing a baseball,” he says.

AI researcher Jonas Kubilius of MIT hopes his work will help win over neuroscientists. At the meeting, he and MIT Ph.D. student Martin Schrimpf presented Brain-Score, a method for judging whether image-classifying neural networks are good models for the brain. The test relies on data the group collected from monkeys and humans as they viewed images of floating objects embedded in unrelated scenes. In the monkeys, an array of implanted electrodes recorded activity from the visual cortex. The humans saw the images for just one-tenth of a second and then had to choose which of two objects they had just seen.

A neural network’s score depends on how well it predicts both the pattern of activity from the cortical electrodes and the human response on the test—including wrong answers. The team hopes neuroscientists will submit new brain data that challenge the best models’ performance, revealing ways that they could become more like the brain.

So far, Brain-Score’s leaderboard, which went online this month, suggests the neural networks that best identify images aren’t necessarily the most brainlike. So Kubilius’s team also set out to create a set of deep neural networks that got higher Brain-Scores than many of the top-performing models. These relatively simple networks “are more penetrable and much easier to work with” than most neural networks, Kubilius says, and they have a brainlike feature that many models lack: They retain information in memory and feed it back from later layers to earlier ones. He hopes researchers put off by the inscrutability of many neural networks will buy in. His message to neuroscientists: “Don’t be scared of deep nets!” ■



Researchers compared responses of humans, monkeys, and computers to incongruous image combinations.

“People have fantasized about that since the 1980s,” says Josh McDermott, a computational neuroscientist at the Massachusetts Institute of Technology (MIT) in Cambridge. Until recently, AI couldn’t come close to human performance on tasks such as recognizing sounds or classifying images. But deep neural networks, loosely inspired by the brain, have logged increasingly impressive performances, especially on visual tasks. That “brings the question back to mind,” says neuroscientist Chris Baker of the National Institute of Mental Health in Bethesda, Maryland.

Deep neural networks work by passing information between computational “nodes” that are arranged in successive layers. The systems hone skills on huge sets of data; for networks that classify images, that usually means collections of labeled photos. Performance improves with feedback as the sys-

tems repeatedly adjust the strengths of the connections between nodes. If a neural network identifies a forest by picking up on those same features, monitoring its activity might help neuroscientists determine which brain regions use what kinds of information.

At the meeting, Aminoff and collaborators at Carnegie Mellon University in Pittsburgh, Pennsylvania, presented a new publicly available data set that may encourage such comparisons. It contains functional magnetic resonance imaging (fMRI) scans of brain activity from four people observing about 5000 images of natural scenes—a dog; rolling hills; people playing tennis. The scenes come from image collections that computer vision researchers commonly use to train and test deep neural networks, which should make it easier to compare how computer models and brains represent the images. It could also

FEATURES

RESEARCH ON RESEARCH

By Martin Enserink



Given the billions of dollars the world invests in science each year, it's surprising how few researchers study science itself. But their number is growing rapidly, driven in part by the realization that science isn't always the rigorous, objective search for knowledge it is supposed to be. Editors of medical journals, embarrassed by the quality of the papers they were publishing, began to turn the lens of science on their own profession decades ago, creating a new field now called "journalology." More recently, psychologists have taken the lead, plagued by existential doubts after many results proved irreproducible. Other fields are following suit, and meta-research, or research on research, is now blossoming as a scientific field of its own.

For some, studying how the sausage is made is a fascinating intellectual pursuit in itself. But other meta-researchers are driven by a desire to clean up science's act. Their work has spawned many initiatives to make research more robust and efficient, from preregistering studies and establishing reporting standards to the recent push to make study data freely available for others to explore. Meta-researchers sometimes need a thick skin; not all scientists are grateful when their long-standing practices are questioned. And whether the reforms actually work has become a study object in itself.

Meta-researchers are giving their fellow scientists lots of things to think about. But their underlying message is simple: If we understand better what we're doing, we might be able to do it better.

ILLUSTRATION: DAVIDE BONAZZI/SALZMANART



JOURNALS UNDER THE MICROSCOPE

"Journalologists" use scientific methods to study publishing. Is their work improving science?

By **Jennifer Couzin-Frankel**; Photography by **Ezra Marcos**

They came to Chicago from across medicine and around the world, converging on a dingy downtown hotel to witness the birth of a new field. It was a chilly May week in 1989. Guests muttered about clogged bathtubs and taps that ran cold, while a bushy-bearded Drummond Rennie, a deputy editor of *The Journal of the American Medical Association (JAMA)*, hurried the crowd away from morning bagels and coffee and into the meeting hall.

A British nephrologist who scaled mountain peaks in his spare time, Rennie had moved to a Chicago hospital from London in 1967. But while studying how the thin oxygen of high altitudes affects the kidneys, he became interested in the world of scientific publishing. Curious about how scientists report their work and how editors make their decisions, Rennie took a job at *The New England Journal of Medicine* in 1977, and later switched to *JAMA*.

He wasn't impressed by what he found. *JAMA* "was in an utter shambles. It was a laughing stock," he recalls. "Papers were ridiculous. They were anecdotes following anecdotes." And he felt it wasn't just *JAMA*—it was much of medical publishing. Some trials read like drug company ads. Patients who dropped out or suffered side effects from a drug were not always counted. Other papers contained blatant errors. Yet, all of these studies had passed peer review, Rennie says. "Every one had been blessed by the journal."

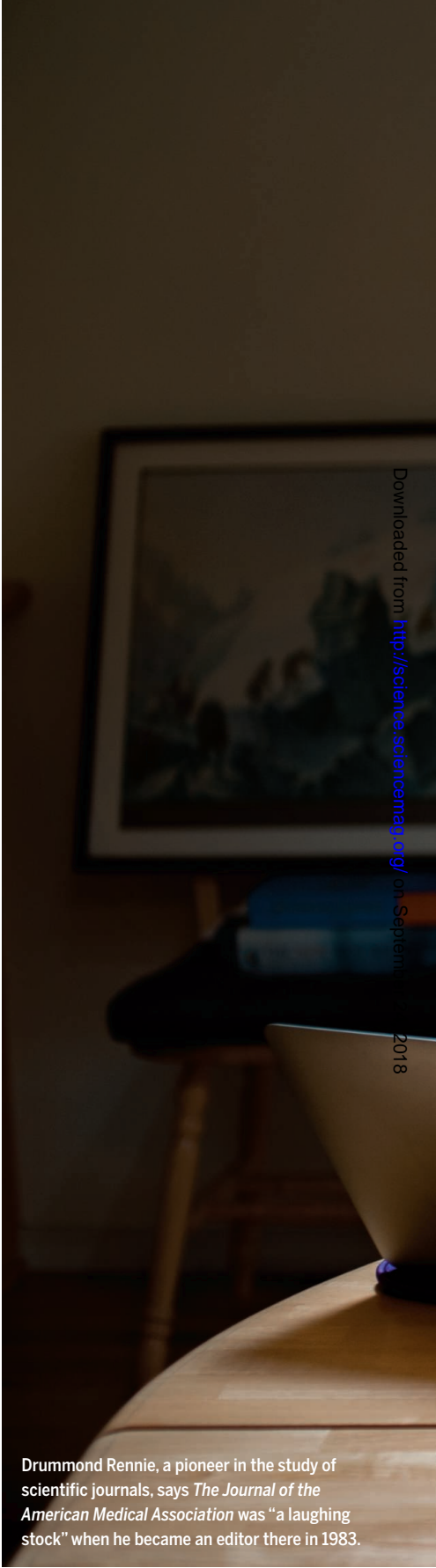
Which is why Rennie, with support from his editor-in-chief, George Lundberg, dreamed up the inaugural Peer Review Congress. He wanted to turn the lens of science onto the journals themselves. There were plenty of issues in publishing that could be studied by using scientific methods, Rennie reasoned. Are positive outcomes more likely to be published than negative ones? A study

that artificially changed the results of a clinical trial but left the rest of the paper intact could offer insight. Did peer review improve a paper's quality? A rigorous comparison of submitted papers and the published versions might provide an answer.

The Chicago, Illinois, meeting marked the birth of what is now sometimes called journalology, a term coined by Stephen Lock, a former editor of *The British Medical Journal (The BMJ)*. Its goal: improving the quality of at least a slice of the scientific record, in part by creating an evidence-based protocol for the path from the design of a study to its publication. That medical journals took a leading role isn't surprising. A sloppy paper on quantum dots has never killed anyone, but a clinical trial on a new cancer drug can mean the difference between life and death.

The field has grown steadily and has spurred important changes in publication practices. Today, for example, authors register a clinical trial in advance if they want it considered for publication in a major medical journal, so it doesn't vanish if the results aren't as hoped. And authors and journal editors often pledge to include in their papers details important for assessing and replicating a study. But almost 30 years on, plenty of questions remain, says clinical epidemiologist David Moher of The Ottawa Hospital Research Institute, a self-described journalologist. Moher—who once thought his dyslexia explained why he couldn't understand so much published research—wants to know whether the reporting standards that journals now embrace actually make papers better, for instance, and whether training for peer reviewers and editors is effective.

Finding the answers isn't easy. Journalology still hovers on the edge of respectable science, in part because it's often competing with medicine for dollars and attention. Journals are also tough to study and



Drummond Rennie, a pioneer in the study of scientific journals, says *The Journal of the American Medical Association* was "a laughing stock" when he became an editor there in 1983.



sometimes secretive, and old habits die hard. "It's hard," Moher says, "to be a disruptor in this area."

EARLY ON, RENNIE WASN'T ALONE in his qualms about scientific publishing. Kay Dickersin, an epidemiologist now at the Johns Hopkins University Bloomberg School of Public Health in Baltimore, Maryland, had been appalled by the quality of research published in the journals her doctor father left lying around the house. On the other side of the Atlantic Ocean was Iain Chalmers, a health services researcher at the University of Oxford in the United Kingdom, who had trained as an obstetrician and pediatrician. After 2 years at a clinic in the Gaza Strip in 1969 and 1970, he'd developed nagging fears that the practices taught in medical training weren't always evidence-based.

Dickersin and Chalmers were both worried that many important clinical trials were never published. To test that suspicion, they first tried to dig up unpublished trials in obstetrics and neonatology. With their colleagues, the pair asked 40,000 clinicians, obstetricians, midwives, and neonatologists in 18 countries whether they knew of other unpublished trials. Only a couple hundred people responded, and they identified 18 trials. "We knew that there were more," Chalmers says; smaller surveys had suggested at least 20% of trials are never published.

There was another big concern: Were the studies that were quietly filed away more likely to show that a treatment had failed—a phenomenon known as publication bias that could skew the scientific literature? A survey by Dickersin and colleagues of 318 authors of published trials validated these fears. The 156 respondents acknowledged 271 unpublished trials; only 14% of those favored the treatment being tested, whereas 55% of the published studies did, a pattern confirmed by other studies. "The decision as to what to include in a publication and whether to publish is largely personal, although dictated by the fashion of the times to a certain

extent," Dickersin wrote in 1990 in *JAMA*. Not publishing, Chalmers charged in the same issue, was akin to scientific misconduct.

The two papers electrified many medical researchers, engendering debate and prompting more study. That both appeared in *JAMA* was no accident: From his perch as an editor, Rennie thrived on punching holes in the veneer of scientific publishing. Not particularly diplomatic by nature, he declined to take on the prestigious post of editor-in-chief at *JAMA* or anywhere else, in part to allow him to "fight battles that go on underground," he says.

Some welcomed the scrutiny. "There are some dark corners in the way journals work that need to have some light shone on them," says Richard Horton, editor-in-chief of *The Lancet* in London since 1995. But not everybody agreed. "Some people ... wished we'd shut up," Chalmers says. One colleague accused him of being part of "an obstetric Baader-Meinhof Gang," a reference to the anarchists behind a string of bombings in West Germany. "You point out problems with the science which don't always make you popular," agrees Lisa Bero, a pharmacologist and health policy specialist now at The University of Sydney in Australia, who has spent decades studying issues such as evidence-based medicine and bias.

BUT UNPOPULARITY didn't stop them. To fight reporting bias, journalologists began to urge journals to require that clinical trials be publicly registered at inception, making it impossible to keep them secret. Journals declined to take action, until scandal forced a sea change. In 2004, the New York attorney general's office sued drug giant GlaxoSmithKline, alleging that four unpublished trials showed that the antidepressant Paxil increased the risk of suicidal tendencies in young people. (The case was later settled.) That same year, the International Committee of Medical Journal Editors began to require trial registration. Since then, more than 280,000 trials have been posted on ClinicalTrials.gov and

elsewhere. "When journals act together, they can really change behavior," says Peter Doshi, a *BMJ* associate editor and health services researcher at the University of Maryland School of Pharmacy in Baltimore.

Journalology drove other reforms. Several studies reported that published clinical trials often left out key details, prompting journal editors and others to release the Consolidated Standards of Reporting Trials (CONSORT). It included a 21-point checklist of such basics as how the sample size was chosen, any changes made to the trial design after the trial began, and the effects of the treatment on a patient's health. To date, nearly 600 journals have pledged to require authors to follow the checklist, which has been periodically updated. In 2010, a similar set of guidelines for animal studies, ARRIVE, was released.

Embracing such standards is one thing. Adhering to them is another. A study published in *PLOS ONE* in May reported that many journals that had pledged to follow ARRIVE's guidelines did not comply. Even requiring researchers to fill out and submit the checklist after filing their manuscript did little to improve adherence, a trial by researchers at The University of Edinburgh showed.

Even when new publication rules are faithfully followed, it's hard to measure their impact. "Someone once asked me at a meeting how many lives CONSORT had saved," says Douglas Altman, a medical statistician at Oxford and pioneer in the field. (Altman died in June at 69 years old, a couple of months after speaking with *Science*.) "I was tempted to say something incendiary. Something that leads to a small raising of awareness and methodological rigor is a good thing. Maybe some people's lives have been saved—but who knows."

It's equally unclear whether studies of peer review have improved the process. Researchers have examined, for instance, whether offering reviewers extra training, publishing reviewers' names, or adding statements detailing the authors' conflicts of interest improve the quality and honesty

All the research that's fit to print

The field of journalology has highlighted important problems in scientific literature and triggered reforms in academic publishing.

1989

The first Peer Review Congress is held in Chicago, Illinois, with fewer than 300 attendees and 50 abstracts. The meeting marked the launch of journalology as a new field.

1990

Papers in *The Journal of the American Medical Association* present scientific evidence of publication bias and suggest potential remedies.

1996

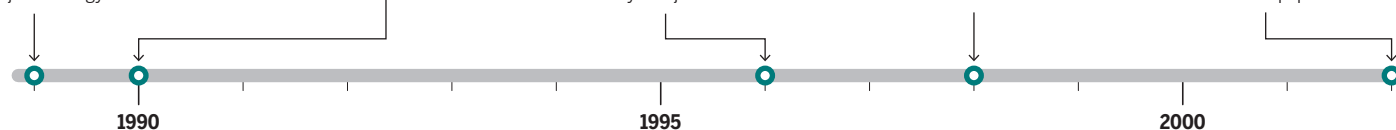
The Consolidated Standards of Reporting Trials guidelines on reporting standards for randomized controlled trials are published; they're now endorsed by 585 journals.

1998

A study of peer review across five medical journals finds no improvement in review quality when authors' identities are hidden, which some had believed might reduce reviewers' bias.

2002

An analysis of 362 scientific reviews finds that almost 40% had honorary authors, suggesting people listed as authors often didn't contribute to the paper.



of reviews. These changes have passionate advocates. "Do we want a secretive culture where it's OK to write an anonymous review that trashes your colleague, or do we want a system where everyone has to be accountable?" asks Virginia Barbour, who was an editor at *The Lancet*, helped found *PLOS Medicine*, and now works at Queensland University of Technology in Brisbane, Australia. "I feel very strongly that it should be accountable." But ethics aside, there is no evidence that the changes tested so far have improved the quality of papers.

Steven Goodman, a clinical epidemiologist at Stanford University in Palo Alto, California, and a senior statistical editor at the *Annals of Internal Medicine*, agrees it's hard to rigorously measure progress. "It's not that it's not a science," he says of journalology, but "it's very hard to say what the effect of any particular intervention is on the overall knowledge base." Moreover, even if one journal betters itself, the research it rejects may end up somewhere else. "You're squeezing a balloon," Goodman says, and shifting air—or in this case lousy research—from one place to another.

TODAY, THE WORLD OF PUBLISHING is changing rapidly. Predatory journals that release articles with little or no peer review have surged. Papers are posted as "preprints" at the same time as they are submitted to journals or even earlier, allowing others to comment. On the F1000Research publishing platform, authors submit their papers and the articles get posted after some basic checks; only then are they peer reviewed, publicly.

Publication science is struggling to keep up. "Research in this area is not fast-moving," says Sara Schroter, a senior researcher at *The BMJ*. In a recent *Nature* opinion piece, Rennie called for rigorous studies to demonstrate the pros and cons of many new developments, including open peer review and preprints. In *JAMA*, he and Executive Managing Editor Annette Flanagin lamented that few people are study-

ing "important issues and threats to the scientific enterprise, such as reproducibility, fake peer review, and predatory journals."

One big factor holding back the field: money. "If you approach government funders, foundations, often they're asking what diseases you're curing," says An-Wen Chan, a skin cancer surgeon and scientist at Women's College Research Institute in Toronto, Canada. "It is hard to convince [them] that this is directly impacting patients." (Chan believes it is: His research has shown that clinical trials in top journals often withhold or massage important

**"I THINK IT'S REALLY
HARD FOR PEOPLE TO
WRAP THEIR HEADS
AROUND USING
SCIENTIFIC METHODS
TO STUDY PUBLISHING."**

—Larissa Shamseer,
University of Maryland

information, which he says can lead doctors to prescribe the wrong treatment.)

Some grant reviewers don't even believe journalology is a science, says Larissa Shamseer, a postdoc at the University of Maryland who works with Doshi. Her proposal to study whether papers in predatory journals are more often negative than positive was part of a fellowship application that was recently rejected. "One of the peer reviewers said, 'This looks like a nice set of activities but where's the research in it?'" Shamseer says. "I think it's really hard for people to wrap their heads around using scientific methods to study publishing."

The dearth of funding is a problem for journals as well. "We're sometimes asked to take part in research studies, but there are no resources offered to help us dedicate time and staff to that work," Horton says. Other times, journal policies to protect reviewers' identities or shield communications with authors hamper research. Or journals may simply decline to offer up information to outsiders. When Peter Gøtzsche, who directs the Nordic Cochrane Centre in Copenhagen, was studying whether abstracts in journals with more industry ads were more likely to put a positive spin on the results, several journals declined to cooperate. There "is a level of secrecy that stinks," Gøtzsche says.

Still, journals are sometimes happy to help. *The BMJ* is now pairing up with researchers at Maastricht University in the Netherlands, where the journal's editor-in-chief has an honorary professorship, to set up a new Ph.D. program on responsible conduct in scientific publishing. *The BMJ* will share data from its roster of 60 journals for a range of studies on such topics as peer review, preprints, and patient and public involvement in the review process.

As godfather of the field, Rennie can reel off its limitations—but he also delights in how far it's come. Last fall, Chicago was home to the eighth edition of his meeting; it drew 600 attendees, roughly twice as many as the first. The number of abstracts had quintupled to 260, covering everything from journal data-sharing policies to gender bias in peer review. More than half the presenters were women, compared with 13% 29 years ago.

Now 82 years old and semiretired in rural Oregon, Rennie says it was his last Congress. Younger colleagues organized a session there to pay him tribute, ending in three standing ovations. With funding scarce and journals under pressure, "it has required a colossal push over the years," to get people to do this work, he says. Was it all worth it? Absolutely. "It's been exhausting, and exhilarating," he says, and now it's up to others to carry the torch. ■

2004

The International Committee of Medical Journal Editors requires registration of trials at inception to be considered for later publication.

2004

An analysis of 102 clinical trials finds major discrepancies in 51 between the protocol outcome and the outcome in the paper, suggesting researchers rewrite goals after the fact.

2010

The ARRIVE guidelines on reporting animal studies are published. Hundreds of journals have endorsed them, but studies show that compliance is spotty.

2015

The Centre for Journalology is launched at The Ottawa Hospital Research Institute, the first of its kind.

2017

A *Nature* paper analyzing nearly 2000 articles published in journals deemed predatory finds that most failed to report crucial information.

2017

The eighth International Congress on Peer Review and Scientific Publication is held in Chicago with almost 600 attendees and 260 abstracts.



Meta-analyses have failed to settle the question of whether violent video games such as *Grand Theft Auto* cause aggression.

THE METAWARES

Meta-analyses were supposed to end scientific debates. Often, they only cause more controversy

By Jop de Vrieze

After Nikolas Cruz killed 17 students and teachers and wounded 17 others early this year at Marjory Stoneman Douglas High School in Parkland, Florida, President Donald Trump had a theory about the underlying causes. "I'm hearing more and more people say the level of violence on video games is really shaping young people's thoughts," he tweeted.

He wasn't the only one to make the connection. Claims about a link to violence in movies and games surface after almost every mass shooting, and it's easy to see why, once you watch someone kill hundreds of anonymous enemies with automatic weapons and trench bombs in the bestselling game *Call of Duty*, or murder innocent drivers in the wildly popular *Grand Theft Auto*. Cruz reportedly loved such games: "It was kill, kill, kill, blow up something, and kill some more, all day," a former neighbor told *The Miami Herald*.

Yet the hundreds of scientific studies that have explored whether media violence can lead to aggressive thoughts and actions have produced conflicting results. That's why scientists have resorted to meta-analyses, studies that collect all the evidence about a scientific question, weigh it impartially, and declare a winner.

In 2009, Christopher Ferguson and John Kilburn of Texas A&M International University in Laredo published a major meta-analysis in *The Journal of Pediatrics* that

dismissed the link between games and violence. A year later, however, a team led by psychologists Brad Bushman, then at the University of Michigan in Ann Arbor, and Craig Anderson of Iowa State University in Ames published an even bigger analysis in the *Psychological Bulletin* that found the opposite: The evidence "strongly suggests" exposure to violent video games is a causal factor for increased aggressive feelings and behavior, they wrote.

a third because of alleged self-plagiarism.) Since their meta-analyses were published, Bushman, now at The Ohio State University in Columbus, and Ferguson have fought an increasingly fierce and sometimes personal battle, but the question remains unresolved. Several other meta-analyses have been published, but none has settled the matter.

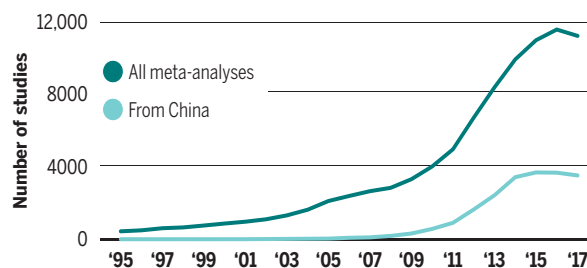
Similar fights are playing out in other fields. Although the number of meta-analyses has exploded, many don't bring clarity—whether it's on the effect of "positive parenting," the relation between antidepressants and suicide, or the health benefits of organic produce.

One reason is that, although the basic rules of the meta-analysis are simple, researchers must make many choices along the way, allowing conscious or unconscious biases to creep in. In the case of media violence, for instance, the groups dealt in different ways with the problem that many studies aren't published, and they applied different quality criteria in choosing the studies to be included.

"Meta-analyses were thought to be debate enders, but now we know they rarely are," Ferguson says. "They should be regarded as an argument, not a fact." It's a paradox, says Jacob Stegenga, a philosopher of science at University of Cambridge in the United Kingdom: "When the evidence points clearly in one direction, there is little need for a meta-analysis. When it doesn't, a meta-analysis is unlikely to give the final answer."

Eager for answers

Virtually unknown until the 1990s, meta-analyses have recently become increasingly popular. More than 11,000 were published last year, one-third of them by authors from China.



Researchers on both sides of the issue are wedded to their views. Ferguson, a gamer himself, has written, "The exaggerated focus on violent video games distracts society from much more important causes of aggression." Bushman, for his part, has consistently found a link between video games and violence in his own studies, which span 2 decades. (He retracted two papers recently, after critics exposed irregularities in the data, and

Still, some metaresearchers say there are ways to do better. The movement in some fields to ensure that all studies are published, whatever their outcome, will help ensure that meta-analyses can take the full range of evidence into account. Meta-analyses themselves can be done better. And some say researchers at odds over issues such as violence in the media should sign a truce, join hands, and design a meta-analysis that everybody can agree on.

THE TERM META-ANALYSIS was coined in 1976 by statistician Gene Glass of the University of Colorado in Boulder, who described it as “an analysis of analyses.” Glass, who worked in education psychology, had undergone a psychoanalytic treatment and found it to work very well; he was annoyed by critics of psychoanalysis,

“SCIENTISTS HAVE TO MAKE SEVERAL DECISIONS AND JUDGMENT CALLS THAT INFLUENCE THE OUTCOME OF A META-ANALYSIS. ... ANYONE WHO WANTS TO MANIPULATE HAS ENDLESS POSSIBILITIES.”

—Jos Kleijnen, Kleijnen
Systematic Reviews

including Hans Eysenck, a famous psychologist at King's College London, who Glass said was cherry picking studies to show that psychoanalysis wasn't effective, whereas behavior therapy was.

At the time, most literature reviews took a narrative approach; a prominent scientist would walk the reader through their selection of available studies and draw conclusions at the end. Glass introduced the concept of a systematic review, in which the literature is scoured using predefined search and selection criteria. Papers that don't meet those criteria are tossed out; the remaining ones are screened and the key data are extracted. If the process yields enough reasonably similar quantitative data, the reviewer can do the actual meta-analysis, a combined analysis in which the studies' effect sizes are weighed.

When Glass did this for studies of psycho-

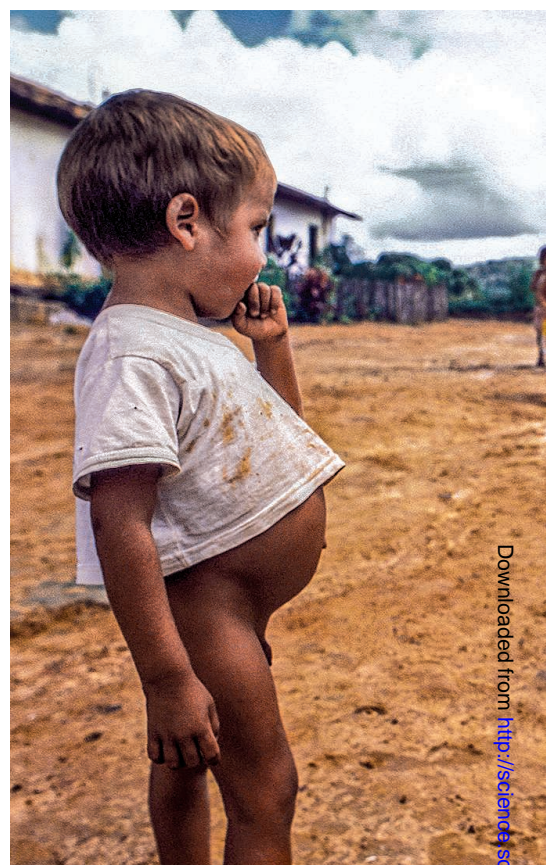
analysis, the result bore out his personal experience of its efficacy. “All the behavior therapists were outraged and all the Freudians said they knew it all along,” says Glass, now 77 and retired. Eysenck was not impressed; he called meta-analyses “an exercise in mega-silliness” and “abuse of research integration.”

Yet over the decades, the tandem of systematic review and meta-analysis has become widely accepted as a standardized, less biased way to weigh the evidence; it now guides thousands of treatment guidelines and social policies. Much of the respect it has earned reflects the work of Cochrane, a multinational organization headquartered in London that conducts systematic reviews of health care interventions and diagnostic tests, which are published in the Cochrane Library. (Cochrane was plunged into crisis last week after its Governing Board voted to expel Peter Gøtzsche, a prominent member; see story, p. 1173.) The Oslo-based Campbell Collaboration produces similar reviews for the social sciences. Both groups follow strict protocols and attempt to team up experts in the issue under study—say, cardiologists when the meta-analysis is about a heart drug—with methodological experts.

TODAY, meta-analyses are a growth industry. Their number has shot up from fewer than 1000 in the year 2000 to some 11,000 last year. The increase was most pronounced in China, which now accounts for about one-third of all meta-analyses (see graphic, p. 1185). Metaresearcher John Ioannidis of Stanford University in Palo Alto, California, has suggested meta-analyses may be so popular because they can be done with little or no money, are publishable in high-impact journals, and are often cited.

Yet they are less authoritative than they seem, in part because of what methodologists call “many researcher degrees of freedom.” “Scientists have to make several decisions and judgment calls that influence the outcome of a meta-analysis,” says Jos Kleijnen, founder of the company Kleijnen Systematic Reviews in Epswich, U.K. They can include or exclude certain study types, limit the time period, include only English-language publications or peer-reviewed papers, and apply strict or loose study quality criteria, for instance. “All these steps have a certain degree of subjectivity,” Kleijnen says. “Anyone who wants to manipulate has endless possibilities.”

His company analyzed 7212 systematic reviews and concluded that when Cochrane reviews were set aside, only 27% of the meta-analyses had a “low risk of bias.” Among Cochrane reviews, 87% were at low risk of bias.



A good meta-analysis starts with clear criteria for study inclusion and exclusion, says statistician Robbie van Aert, a post-doctoral researcher at Tilburg University in the Netherlands. “If you do it after you have collected the studies, you can get almost any result you want.” But bias can occur even when inclusion criteria are chosen beforehand; because experts in a field already know the relevant literature, they can consciously or unconsciously adjust the criteria to include studies they like or exclude ones they distrust, Van Aert says.

MONEY IS ONE POTENTIAL SOURCE of bias. It may not affect the actual results the authors produce, but it appears to affect their spin when they draw their conclusions. In 2006, for instance, the Nordic Cochrane Centre in Copenhagen compared Cochrane meta-analyses of drug efficacy, which are never funded by the industry, with those produced by other groups. It found that seven industry-funded reviews all had conclusions that recommended the drug without reservations; none of the Cochrane analyses of the same drugs did. Industry-funded systematic reviews also tended to be less transparent. Ioannidis found in a 2015 review that industry-sponsored meta-analyses of antidepressant efficacy almost never mentioned caveats about the drugs



in their abstracts. “This is a clear example of an area where meta-analyses are emerging as a powerful marketing tool,” he wrote.

Even if a study isn’t industry-funded, individual reviewers may have conflicts of interest. Cochrane’s policies sometimes allow researchers who have financial ties with a company—such as grants, fees, and stocks—to participate in a meta-analysis of that company’s products, provided a majority of the review authors and the lead author don’t have such conflicts. Most journals’ policies to prevent financial conflicts of interest are even less strict.

And Cochrane itself has been charged with bias by critics who say some reviewers have an anti-industry attitude that results in overly negative assessments of drugs and vaccines. In a 2017 review on the effect of a new generation of antiviral drugs against hepatitis C, for instance, the authors concluded that the drugs cured the patients of the virus, but called this a “surrogate outcome”; there was no evidence that the drugs led to longer survival, they said.

The findings made many headlines, but some clinicians were outraged. The studies would have to last many years to show an effect on survival, they said, but previous trials with older drugs had clearly shown that patients who eliminate the virus live

longer. “In my view, they have been too strict and they have overstated their conclusions,” says Andrew Hill of the University of Liverpool in the United Kingdom. “Due to this report, patients with hepatitis C may potentially be unable to access life-saving therapy,” a group called The Hepatitis C Coalition wrote in *The BMJ*.

EVEN WHEN NO MONEY is at stake, researchers may have an interest in the outcome of a meta-analysis—for instance because they may hope to confirm what their own studies had previously shown, or because they’ve supported certain policies.

Take the “worm wars,” over whether mass deworming campaigns among children in developing countries are clinically effective. Dozens of endemic countries have implemented mass deworming at the recommendation of the World Health Organization (WHO). But in 2015, a team led by David Taylor-Robinson of the University of Liverpool concluded in an updated Cochrane review that mass deworming does not improve kids’ average nutritional status, school performance, or survival; they called the belief in the positive impacts “delusional.” A year later, a team by economist Edward Miguel of the University of California, Berkeley, published a meta-analysis that did show clear benefits.

A child with a worm infection in Brazil (left) is at risk of malnutrition and poor school performance. But meta-analyses disagree about the effects of mass deworming campaigns like one in India (right).

For Miguel, who says the Liverpool study looked at the wrong things and lacked statistical power, there was more at stake than public health: He had headed several trials of mass deworming and had become a strong advocate of WHO’s policy.

Psychologist James Coyne of the University Medical Center Groningen in the Netherlands says scientists shouldn’t be involved in meta-analyses that include their own work; he has sharply criticized Cochrane for not taking “intellectual conflicts of interest” seriously enough. “Meta-analyses have become a tool for academics with vested interests,” he says.

Miguel says his own papers shouldn’t disqualify him. “We should judge the analysis based on the quality and have the debate on scientific terms,” he says. But Cochrane Library Editor-in-Chief David Tovey acknowledges the problem. Cochrane does not ban scientists from taking part in meta-analyses that include their own work, but they can’t be involved in the assessment of their trials—which sometimes means having to leave the room temporarily—and the conflict has to be acknowledged in the

review paper. "We recognize that this in itself is insufficient," Tovey says. "We have a new proposal coming up to make it more comprehensive. But I have to say it is jolly challenging." Finding suitable authors for a meta-analysis is hard when the people with the most expertise in an area are excluded, he explains.

BOTH SIDES IN THE WAR over media violence had a stake in the outcome. But the main reason their meta-analyses diverged was the different ways the researchers handled publication bias, the well-known phenomenon in which studies that come up empty-handed are less likely to be published.

Like other scientists who conduct meta-analyses, Ferguson and Kilburn have used several statistical methods to measure publication bias and correct for it. In one

collected in their meta-analysis. Applying a statistical method to show that the results of the studies were now distributed evenly around the mean reassured them that they had overcome publication bias. The apparent link between video games and aggression persisted.

The debate became heated. Ferguson accused his opponents of only collecting unpublished studies with desirable results and "overestimating and overadvertising" the effect—which Bushman and Anderson said was "a red herring." Many other scientists weighed in, as did game enthusiasts and opponents. Both sides also pushed their results outside science. Last year, Ferguson published a book called *Moral Combat: Why the War on Violent Video Games Is Wrong*. (The title was a play on the video game *Mortal Kombat*.) Bushman

results, they concluded in a 2017 paper in the *Psychological Bulletin* that Bushman and Anderson hadn't managed to collect all unpublished studies, and that publication bias still played a role. After correcting for that bias, the relationship between violent games and aggression turned out to be "very small," they said. Bushman and Anderson reject Hilgard's analysis and stand by the results of their meta-analysis.

THE MANY BATTLES have sobered Glass, the inventor of the meta-analysis. "I have come to think of meta-analyses as a tool to convince the undecided," he says. "To give them something useful." Psychologist Hannah Rothstein of Baruch College in New York City, a meta-analysis consultant who collaborated with Bushman in producing the 2010 meta-analysis, says she has not lost faith in the method—but she has changed her expectations. "We used to make meta-analyses as objective as possible. Now, we try to make them as transparent as possible," she says. "Anyone who disagrees with a certain decision will have to be able to redo it and see if that has an influence on the results."

Ioannidis agrees. Systematic review protocols should be published up front, he says; each analytical step and every judgment call should be reported. "If this is done, one can exactly see the degrees of freedom where the deviation is creeping in, and take that into account to attach a certain credibility to the results." In controversial cases, he adds, rival researchers should set up a meta-analysis together. Or even better, they could forget about the many studies already published and set up new ones, using standardized protocols, and then do a meta-analysis of the results, using a methodology agreed on and published in advance.





That approach was taken to settle a long-running debate over whether self-control can be depleted, just like muscles: Researchers at 23 labs around the world conducted the same standardized experiment and carried out a meta-analysis. Published in 2016, it showed that the effect is close to zero, an outcome now widely accepted.

That's exactly what Hilgard advocates to settle the debate on media violence and aggression. "We cannot bear the thought of another 30 years' stalemate," he wrote. Rothstein has no illusion that this would end the controversy, but it would at least move the discussion forward, she says. "Although I don't know if Ferguson and Bushman will be able to stay in a room together without killing each other." ■

Jop de Vrieze is a science journalist in Amsterdam. This story was supported by the Science Fund for Investigative Reporting.

When meta-analyses collide: the case of the placebo response

Some studies suggest that in recent trials of antidepressants, a growing number of patients improve just after taking a placebo, making it harder to tell whether the drug being tested is effective. Two key meta-analyses on the subject took different approaches—and reached opposing conclusions.

	FURUKAWA ET AL., LANCET PSYCHIATRY, 2016	KHAN ET AL., WORLD PSYCHIATRY, 2017
Number of studies included	 252	 85
Type of studies	Every published and unpublished randomized clinical trial done between 1978 and 2015 that the team was able to collect	Only studies reported in Food and Drug Administration reviews, for drugs approved between 1987 and 2013
Number of patients on placebo	 10,000 patients	 4,000 patients
Outcome measure	Proportion of patients who had a 50% or greater reduction of symptoms	Average decrease of symptoms, expressed as a percentage
Statistical method	Metaregression	Linear regression
Key finding	Placebo response stable since 1991; on average, 36% of patients on placebo were cured.	Average placebo response has increased by 6.4 percentage points since 2000.

method, they plotted the outcomes of all the studies against their sample size on a graph. Without publication bias, the results would have been distributed symmetrically, and the plot would look like an inverted funnel, centered on the mean. But it didn't; the plot was lopsided. To correct for this bias, they essentially added a "missing"—and supposedly unpublished—study for each study that lacked a counterpart on the other side of the mean. With that and other corrections, the evidence that games and movies made people more aggressive evaporated, they concluded in their 2009 meta-analysis.

Bushman and Anderson took a different approach: They tried to find all unpublished studies, mainly by asking the authors of published studies whether they had failed to publish others and checking Ph.D. theses for chapters not published in scientific journals. They then included what they had

was a member of former President Barack Obama's committee on gun violence, testified before the U.S. Congress on the topic of youth violence, and has frequently been interviewed on TV.

Things got even more complicated after a third researcher joined the fray in 2016: Joseph Hilgard, a psychologist at Illinois State University in Normal. Hilgard, who studies pathological aspects of gaming, including addiction, says, "I was curious: Would I be more persuaded by one or the other? So I tried to find the answer by mashing around in the data." (Questions he raised about another paper in 2017 led to one of Bushman's three retractions.)

With two colleagues, Hilgard re-examined Bushman's 2010 meta-analysis, applying several novel statistical techniques to correct for publication bias, including one developed by Van Aert. Based on those



THE TRUTH SQUAD

In its drive to expose weaknesses in science, an up-and-coming research group doesn't mind stepping on some toes

By **Erik Stokstad**, in Tilburg, the Netherlands
Photography by **Manon Bruininga**

In August 2011, Diederik Stapel, a prominent psychologist and a dean at Tilburg University here, confessed to faking data for dozens of papers over 15 years. As part of an internal investigation, Marcel van Assen, a psychologist in the university's Department of Methodology and Statistics, spent months looking into Stapel's data, methods, and results. The scope of the fraud was staggering, but just as alarming as the fabricated data, Van Assen says, were the flawed analyses, rife with statistical problems, that Stapel had performed. The fact that all his papers had been approved by co-authors and published in respectable journals meant psychology

had a larger problem, Van Assen says. "I thought, holy shit, this is not a characteristic just of Stapel or Tilburg."

Around the same time, a psychologist with a strong interest in the same issues joined his department. Jelte Wicherts, previously an assistant professor at the University of Amsterdam, wanted to find out why "smart researchers do stupid things with statistics," as he puts it. The two hit it off, and have since created what psychologist Brian Nosek, director of the University of Virginia's Center for Open Science (COS) in Charlottesville, calls "one of the leading groups" in meta-science, the study of science itself.

Metaresearchers investigate how scien-

tists operate, and how they can slip off the rails. "We've seen things that we felt were not OK," Wicherts says. "The first way to deal with it, that's our conviction, is to study these things." They're motivated by the desire to make science better, although Van Assen is drawn to the detective work. "What I like most is to solve puzzles," he

says. By scrutinizing the problems, metaresearchers aim to help scientists do more robust research. Thanks to a €2 million grant from the European Research Council (ERC), for example, the Tilburg

The metaresearch group at Tilburg University investigates how scientists operate, and how they can slip off the rails.

group is starting to build software that could help researchers explore data with less risk of bias.

That Wicherts's and Van Assen's center was built on the ruins of Stapel's deceit may seem like poetic justice, but straight-up scientific fraud is only a minor topic for the group. Its main focus is questionable research practices, such as massaging data and selective reporting of statistical tests. These misdemeanors don't get a scientist fired, but they do help explain why so many findings are hard to reproduce—the “reproducibility crisis” that has gripped not just psychology, but many areas of basic biology and clinical medicine.

For scientists who find themselves in the crosshairs, the experience can feel bruising. Several years ago, the Tilburg group—now more than a dozen faculty members and students—unveiled an algorithm, dubbed *statcheck*, to spot potential statistical problems in psychology studies. They ran it on tens of thousands of papers and posted the troubling results on PubPeer, a website for discussion of published papers. Some researchers felt unfairly attacked; one eminent psychologist insinuated that the group was part of a “self-appointed data police” harassing members of the research community.

Van Assen and Wicherts say it was worth stepping on some toes to get the message across, and to flag mistakes in the literature. Members of the group have become outspoken advocates for statistical honesty, publishing editorials and papers with tips for how to avoid biases, and they have won fans. “I’m amazed that they were able to build that group. It feels very progressive to me,” says psychologist Simone Vazire of the University of California, Davis, a past chair of the executive committee of the Society for the Improvement of Psychological Science (SIPS).

The work by the Tilburg center and others, including SIPS and COS, is beginning to have an impact. The practice of pre-registering studies—declaring a plan for the research in advance, which can lessen the chance of dodgy analyses—is growing rapidly (see story, p. 1192), as is making the

data behind research papers immediately available so others can check the findings. Wicherts and others are optimistic that the perverse incentives of careerist academia, to hoard data and sacrifice rigor for headline-generating findings, will ultimately be fixed. “We created the culture,” Nosek says. “We can change the culture.”

TILBURG MIGHT SEEM an unlikely place for academic innovation. The city, 90 kilometers south of Amsterdam, was once a center of the Dutch textile industry; after

logy in the mid-2000s, it was an open secret that many findings were irreproducible, he says, but scientists feared that discussing this would cast the whole field into doubt. Then in 2005, John Ioannidis, now co-director of Stanford University’s Meta-research Innovation Center in Palo Alto, California, published a provocative essay, “Why Most Published Research Findings Are False.” It argued that science suffers from an epidemic of small studies that try to detect modest effects, poorly designed by researchers “in chase of statistical significance.” Wicherts, inspired by the paper’s clarity and bravery, calls it a watershed event for psychology.

WICHERTS HAD his own encounter with poor scientific practices during his Ph.D. work on the rise of intelligence scores over generations. Curious about the impact of unusual data points on statistical analyses, he and his colleagues asked the authors of 141 recent papers for their data, so that they could re-analyze them. To their surprise, 73% of the authors didn’t reply or said they were not willing or able to share the data, even though the journals that published the studies stipulated they should. Wicherts dropped the study but described the experience in *American Psychologist*. The 2006 paper was an early alert about the importance of “open data,” Vazire says. “We need something better than ‘data available upon request.’”

Wicherts now co-leads the group with Van Assen, who had focused on cognitive and mathematical psychology before he

was drawn into the Stapel investigation. Its highest profile—some would say most notorious—project is *statcheck*. The algorithm, developed by Michèle Nuijten, then a Ph.D. student at Tilburg, together with Sacha Epskamp of the University of Amsterdam, scours papers for statistical results reported in standardized formats, then examines them for errors, like a mathematical spell checker. When *statcheck* scanned 30,717 papers published between 1985 and 2013, it found a “gross inconsistency” in one out of eight. Most of these results purported to be statistically significant, but in fact



The metaresearch group, co-led by Jelte Wicherts (left), created a major stir with *statcheck*, an algorithm that Michèle Nuijten (right) helped develop.

the woolen mills shut down, insurance and transportation businesses sprung up. Tilburg University was founded in 1927 as the Roman Catholic University of Commerce, but it is now best known for its social sciences departments, which fill a 10-story concrete building. Housed on a floor near the top, the metaresearchers have an expansive view of a forested 18th century park.

One morning this May, Wicherts, an energetic and talkative 42-year-old, was making a cup of strong coffee as he related how he became involved in metascience. When he was a Ph.D. student in psycho-

were not, Nuijten and colleagues reported in 2015. Statcheck can't distinguish between honest errors and deceit, but "it's not unimaginable that people do this on purpose," says Nuijten, now an assistant professor.

When Tilburg Ph.D. student Chris Hartgerink posted statcheck's evaluations of 50,000 psychology studies on PubPeer, some scientists were furious. The most vocal critics complained that statcheck had claimed an error when in fact it wasn't able to properly scan their statistics, which had been correct. "Statistical graffiti," one called it. In a column, Susan Fiske of Princeton University, a past president of the Association for Psychological Science, decried a trend of "methodological terrorism." (Fiske removed that term, which caused a tempest on social media after her draft leaked.) The German Psychological Society called for a moratorium on statcheck.

In retrospect, Nuijten says she would have written fuller explanations for the PubPeer posts, in less brusque a style. But Vazire says she handled the controversy with aplomb, showing the kind of communication skills that can "win hearts and minds" in the campaign to improve psychology. Ultimately, says Eric-Jan Wagenmakers, a statistician at the University of Amsterdam, "I think it had a really positive effect. And wouldn't have if they had done it more subtly."

Still, the episode showed how sensitive people can be to criticism. "If you make it personal," Wicherts says, "then they can't admit the errors." Rather than calling out individuals, he now believes that meta-researchers should highlight the problems, encourage best practices, and create a system where errors can be caught before publication. One sign of progress is that two psychology journals now run submissions through statcheck.

OTHER ATTEMPTS to take a hard look at psychology's practices created a backlash as well. Van Assen and two students participated in the Reproducibility Project: Psychology, a large, 4-year collaboration organized by Nosek and COS that managed to replicate only 39% of the findings in 100 studies (*Science*, 28 August 2015, p. 910). Some senior psychologists quickly pushed back; Harvard University's Daniel Gilbert and three co-authors, for instance, criticized the collaboration's methods and their "pessimistic conclusions." (A new project, published last month in *Nature Human Behaviour*, replicated 62% of experiments reported in recent papers in *Science* and *Nature*.)

Wicherts says some researchers fear such critiques could jeopardize funding or breed mistrust in science. But it's not the

group's job to protect psychology's reputation, he says. And the Tilburg studies have shaken the illusion that scientists are more objective than most people, underscoring that most researchers have a poor ability to look objectively at data and overestimate the statistical power of their studies.

With his ERC grant, Wicherts plans to develop software that will help psychologists avoid the temptation to test many hypotheses and only report those that have a significant p-value. The behavior, called data dredging, or HARKing, for "hypothesizing after results are known," generates apparently well-founded results that often can't be reproduced. Following an approach used in particle physics and other fields, the software will reveal a random sample of the data that researchers have gathered, letting them explore and gener-

**"WE'VE SEEN THINGS
THAT WE FELT WERE
NOT OK. THE FIRST
WAY TO DEAL WITH
IT, THAT'S OUR
CONVICTION, IS TO
STUDY THESE THINGS."**

—Jelte Wicherts, Tilburg University

ate hypotheses. Then it will deliver another random selection for rigorously testing those hypotheses. "I think there could be a role for this," says psychologist Dorothy Bishop of the University of Oxford in the United Kingdom, though she suspects it will require large data sets.

Wicherts's main effort right now is leading a project in which scientists at five universities take a fresh look at the data behind 200 studies, repeating the analyses in many ways to find out whether the authors chose to report specific results that matched their hypotheses. "I think we'll find quite a lot of biases in place," Wicherts says.

SINCE WICHERTS'S DISCOVERY as a student that most psychology researchers don't share their data when asked, he and others have pushed for change. Even today, only 10% of newly published psychology papers have data available, but the "open data" ethos is gaining traction in psychology and beyond. As an incentive, 41 journals now

allow authors to slap a virtual open data "badge" on a paper; after *Psychological Science* adopted the practice, the share of open-data papers rose from 3% to 39% in just over a year. (Similar badges exist for "open materials" and study preregistration.)

Like other meta-researchers, the Tilburg group has itself adopted a far-reaching open-data policy: It shares data, code, and materials, except when issues of copyright, privacy, or ownership are involved. "It's a much harder way of working—it slows you down—but it makes you more thoughtful and confident," Bishop says. Hartgerink even posted versions of chapters of his Ph.D. online as he wrote them. "I share almost everything as I do it," he says. One risk of posting entire data sets is that competitors might analyze them and come up with new findings first. Although that's arguably good for the field as a whole, some labs worry that younger scientists who have yet to make their name might lose a chance to publish a significant finding.

The reproducibility push has other potential downsides for younger researchers. Studies with respectable statistical power take major work and might fizzle. For her Ph.D., Paulette Flore, now an assistant professor at Tilburg, studied whether reminding girls of their gender hurts their performance on math tests, an effect found in many smaller studies. Flore set up the largest study of the effect ever—involving more than 2000 students at 21 Dutch high schools—only to find no evidence for it. "In earlier days, her career would have ended," Wicherts says. "Now, you do the best you can, and let the chips fall where they may. I think this is the future."

At the moment, however, negative findings "won't land you a fancy job," says Daniël Lakens, an applied statistician at Eindhoven University of Technology in the Netherlands. For that to change, science will need to put more value on good ideas, solid methods, and broadly collaborative work, and less on high-profile publications and citations. "There's a corrupting influence of our current incentive structure," Bishop says. "The pressure on younger people not to do research in a reproducible way can be quite intense."

Some of the young scientists at Tilburg are pessimistic that the situation will improve anytime soon. "At the current pace, it's going to be 2100 before things are really different," Hartgerink says. Wicherts believes avoiding bad practices in research will pay off for individual scientists in the long run. "Keep in mind that these better methods empower the truth, and that this ultimately promotes scientific progress and highlights your contributions." ■



A RECIPE FOR RIGOR

A simple strategy to avoid bias—declaring in advance what you will study, and how—is rapidly catching on

By Kai Kupferschmidt

In October 2011, Joseph Simmons, a psychologist at the Wharton School of the University of Pennsylvania, published a clearly preposterous result in the respectable journal *Psychological Science*. Together with Uri Simonsohn, also at Wharton, and Leif Nelson of the University of California, Berkeley, Simmons showed that people who listened to the Beatles song “When I’m Sixty-Four” grew younger, by nearly 18 months. But if the result was laughable, the point of the paper was serious: to show how standard scientific methods could generate scientific support for just about anything.

In the years before, the trio had slowly lost faith in the stream of neat findings in

psychology. “Leif, Uri, and I all had the experience of reading papers and simply not believing them,” Simmons says. It seemed unlikely that it could all be down to fraud. “After much discussion, our best guess was that so many published findings were false because researchers were conducting many analyses on the same data set and just reporting those that were statistically significant,” they recently wrote. They termed the behavior, which also gave them their nonsense result, “p-hacking,” a reference to the p-value, which determines whether a result is considered significant.

The paper came at a critical time for psychologists. Earlier that year, another paper using standard methods had shown

that extrasensory perception was a real phenomenon—a result the authors meant seriously, to the dismay of other psychologists. “If you use the techniques that everyone is using in their normal research ... and it supports the existence of bullshit, then there is good reason to think that that method is wrong more generally and you shouldn’t be using it,” says Chris Chambers, a neuroscientist at Cardiff University. In another blow a few months later, noted social psychologist Diederik Stapel of Tilburg University in the Netherlands admitted to faking data for dozens of papers.

The crescendo of problems has led some psychologists to adopt a radical solution: describing the research they plan to do, and

how, before they gather a single piece of data. Preregistration, in its simplest form, is a one-page document answering basic questions such as: What question will be studied? What is the hypothesis? What data will be collected, and how will they be analyzed? In its most rigorous form, a "registered report," researchers write an entire paper, minus the results and discussion, and submit it for peer review at a journal, which decides whether to accept it in principle. After the work is completed, reviewers simply check whether the researchers stuck to their own recipe; if so, the paper is published, regardless of what the data show.

Preregistration had already become the norm in clinical trials as a way to prevent publication bias, the tendency for many negative results to remain unpublished (see story, p. 1180). Now, it is spreading through psychology and into other fields, not just to ensure those results see the light of day, but also because of a different advantage: By committing researchers to a fixed plan, it takes away some of the degrees of freedom that can skew their work.

In their paper on the Beatles tune, for instance, Simmons and his colleagues had tested for significance after roughly every 10 participants, they had used other songs, and they had asked participants many questions, creating a large data set with which they could play around. As it turned out, using the age of the participants' fathers to control for variation in baseline age resulted in their statistically significant but absurd finding. That would have been impossible with a preregistered study.

Some skeptics warn about unforeseen consequences. In a 2016 blog post, Susan Goldin-Meadow, then-president of the Association for Psychological Science in Washington, D.C., wrote about her "fear that preregistration will stifle discovery." "How can we make new discoveries if our studies need to be catalogued before they are run?" she asked. Science is not just about testing pre-established hypotheses, but also about discovering them, Goldin-Meadow wrote; she also cautioned that the push to preregister might "devalue or marginalize the studies for which the preregistration procedures don't fit."

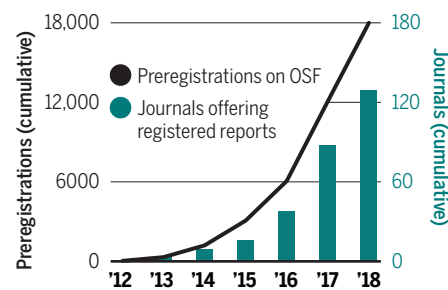
Preregistration does not preclude generating new hypotheses, counters Brian Nosek, director of the University of Virginia's Center for Open Science (COS) in Charlottesville; it just makes it transparent when researchers are doing so. Too often, a result is presented as if it confirms a hypothesis when researchers are actually doing what has become known as HARKing, he says, "hypothesizing after results are known." (For example, a researcher who rolls a die

three times and gets a six each time could report that she wanted to test her hypothesis that a die will always show a six, and that her study confirmed it.)

PREREGISTRATION CAN pay off for individual researchers as well as the broader field, advocates say. For one thing, it forces researchers to think harder about a study before it begins. "I have at least twice had the experience of realizing that my study didn't make any sense as I was writing up the analysis plan for it," Simmons says. Registered reports have the additional advantage that journals agree in advance to accept studies based on their methodological strength and the importance of the questions they address, Chambers adds. "It takes away all this pressure that you might get nonsignificant results or that your results might in some way be seen as undesirable by the editors or reviewers."

Planning ahead

Study preregistrations on the Open Science Framework (OSF) are doubling every year; more than 120 journals have introduced registered reports.



Several databases today host preregistrations. The Open Science Framework, run by COS, is the largest one; it has received 18,000 preregistrations since its launch in 2012, and the number is roughly doubling every year. The neuroscience journal *Cortex*, where Chambers is an editor, became the first journal to offer registered reports in 2013; it has accepted 64 so far, and has published results for 12. More than 120 other journals now offer registered reports, in fields as diverse as cancer research, political science, and ecology.

Still, the model is not attractive to everyone. Many journals are afraid of having to publish negative results, Chambers says. And some researchers may not want to commit to publishing whatever they find, regardless of whether it supports a hypothesis. He notes that a bit of publication bias can have advantages for scientists, some of whom essentially create a "brand" by publishing studies that support a certain theory. "A lot of scientists are more like lawyers than detectives. They

have a theory and they are trying to use the evidence to support it."

There are other drawbacks. "It can feel like a very bureaucratic burden to have to preregister every experiment," Nosek admits. The practice could also lead to a conservative shift in science, if reviewers recommend against accepting registered reports when their hypothesis runs counter to conventional wisdom. That could make it harder to do high-risk research. "This is a real concern," Nosek says.

It's not easy to tell how real preregistration's potential benefits and drawbacks are. Anne Scheel of the Eindhoven University of Technology in the Netherlands, for instance, recently set out to answer a seemingly simple question: Do registered reports lead to more negative results being published? "I'm quite shocked how hard it is," says Scheel, because it's not clear what a good control group would be. Early adopters of preregistration may be very different from other researchers, for instance, or people might choose to preregister only research more likely to have no effect. For now, she has the less ambitious goal of establishing the percentage of hypotheses in registered reports that are ultimately confirmed.

Tom Hardwicke, a meta-researcher at Stanford University in Palo Alto, California, has many questions about registered reports themselves—for instance, how detailed the initial protocols are, how often researchers deviate from them, and whether they're transparent about that. But when he tried to answer those questions recently, "the raw ingredients were not available," Hardwicke says. Many journals don't publish the protocols and don't deposit them in an independent registry such as the COS database, Hardwicke says. "The community needs access to registered protocols to conduct this kind of research and ensure that registered reports do what they say on the tin," he says.

Chambers agrees but thinks things are getting better. Already, 76% of journals that accept preregistrations agree to make protocols publicly available. At others, the reluctance "is part technical teething problems, part cultural barriers resulting from introducing preregistration for the first time to fields where it is unfamiliar," he says.

For preregistration to be a success, the protocols need to be short, simple to write, and easy to read, Simmons says. That's why in 2015 he, Nelson, and Simonsohn launched a website, *aspredicted.org*, that gives researchers a simple template for generating a preregistration. Like their 2011 paper, Simmons says, the website has been much more successful than he would ever have predicted. ■

INSIGHTS

POLICY FORUM

METARESEARCH

Toward a more scientific science

Climb atop shoulders and wait for funerals. That, suggested Newton and then Planck, is how science advances (more or less). We've come far since then, but many notions about how people and practices, policies, and resources influence the course of science are still more rooted in traditions and intuitions than in evidence. We can and must do better, lest we resign ourselves to "intuition-based policy" when making decisions and investments aimed at driving scientific progress. *Science* invited experts to highlight key aspects of the scientific enterprise that are steadily yielding to empirical investigation—and to explain how Newton and Planck got it right (and Einstein got it wrong). —**Brad Wible**

One superstar funeral at a time

By **Pierre Azoulay^{1,2}** and **Joshua Graff-Zivin^{2,3}**

Max Planck wrote that "A new scientific truth does not triumph by convincing its opponents and making them see the light, but rather because its opponents eventually die." Despite all of their contributions to science, might "superstar" scientists also use their central position to stymie the arrival of new ideas? To shed empiri-

cal light on this issue, we turned to a ghoulish natural experiment, assessing impacts of the premature deaths of 452 eminent life scientists (median age at death = 61 years). We implemented a procedure (drawing on automated analysis of keywords in publications) to delineate the boundaries of the intellectual neighborhoods in which eminent scientists worked and conceptualized the premature deaths as shocks to the structure of these neighborhoods. We found that after the deaths, the stars' expansive rosters of collaborators tend to drastically reduce their scientific output (*I*), whereas noncollaborators increase their output in the deceased stars' field



**“IF I HAVE SEEN
FURTHER THAN
OTHERS, IT IS BY
STANDING ON
THE SHOULDERS
OF GIANTS.”**

– Isaac Newton

(2). Moreover, these additional contributions are disproportionately likely to be highly cited and are more likely to be authored by scientists who were not previously active in the superstar's field before his or her death. This suggests that intellectual, social, and resource barriers impede entry into new subfields, with outsiders only entering subfields that offer a less hostile landscape for the support and acceptance of “foreign” ideas. Although the contributions of stars to the advancement of science are unassailable, our results suggest that once in control of the commanding heights of their fields, star scientists tend to hold on to their exalted position a bit too long.

Novelty and hotspots

By **Brian Uzzi^{4,5,6}** and **Dashun Wang^{4,5,6}**

Recent research on nearly 27 million scientific papers since 1950, and more than 5 million U.S. patents since 1970, shows that how scientists sample the ever-expanding literature is critical to making breakthroughs, irrespective of discipline. First, papers or patents that cite literature of a certain age range (mean of about 5 years, with a high variance) are roughly twice as likely to be a hit (in the top 5% of citations) than a field's average paper (3). By contrast, the 75% of papers and patents that combine knowledge from outside this “hotspot,” referencing the most popular or most

recent literature—work commonly sampled by search engines (4)—are not particularly likely to be hits. Second, hit papers mix highly typical and highly novel ideas and do so roughly according to a 90/10 ratio (5). Such papers referencing highly familiar knowledge—literature that historically has been cited together much more frequently than expected by chance—while at the same time citing papers that have rarely been co-cited before are at least twice as likely to be hits in their field than the average paper. Novelty is prized in science but becomes especially influential when paired with familiar, conventional thought. Sampling the literature also depends on team work. Team-authored papers are more likely to draw on work in the 5-year-old hotspot and to insert novel combinations into familiar knowledge domains than papers by solo authors (3, 5). Such insights take us closer to uncovering approaches for searching for and recombining yesterday's ideas into tomorrow's acclaimed discoveries (6, 7).

On shoulders of giants

By **Heidi Williams^{1,2}**

Isaac Newton famously noted, “If I have seen further than others, it is by standing on the shoulders of giants,” highlighting the idea that many scientific discoveries enable future discoveries. Yet although the scientific community makes tremendous investments aimed at finding new discoveries, much less attention focuses on improving access to past discoveries—efforts that could help us, like Newton, to “see further than others.” Although the idea that past discoveries may enable future discoveries is quite intuitive, measures of and mechanisms for such so-called “cumulative innovation” have traditionally proven elusive to pin down empirically. Two recent empirical studies have made progress. First, biological resource centers—“living libraries” of biological materials, such as cell lines—appear to increase follow-on research by more than 50% (8). Second, limitations on access to sequenced human genes—used by the private firm Celera during the “race” to sequence the human genome—reduced subsequent research and development on those genes by around 30% (9). These studies share two key features. Both generated novel linkages between records of scientific discoveries (such as sequenced human genes) and measures of cumulative innovation (such as gene-based medical diagnostic tests). In addition, both isolated natural experiments, in which otherwise similar scientific discoveries were “treated” by different institutions and policies—akin to a randomized controlled trial—lending credibility to a causal and policy-relevant interpretation of the results. Taken together, these findings suggest that the institutions and policies that govern how past discoveries are accessed can have dramatic effects on cumulative innovation.

A crowded frontier

By **James A. Evans⁷**

Science is a complex system in which rapid circulation of advances has resulted in scientists crowding the same frontier of accumulated knowledge, constrained to imagine the same combinations of ideas and methods that they might use to unlock discoveries, rather than exploring more broadly. Applying computational tools to massive corpora of digitized scientific texts and databases of experimental results, recent research has advanced our ability to trace the dynamic frontier of collective attention and explore how we might accelerate discovery, identifying possibilities missed by

the crowd and potentially uninferrable by any particular scientist. For example, nearly all combinations of scientific components in a given year's papers, most of them highly redundant, can be predicted by random walks across the network traced by papers published in the prior year (10). Algorithms can identify hypotheses unimagined and paths untaken, not necessarily because they lack scientific promise but because scientists are channeled away by shared institutional realities, such as the incentive to build on work familiar to one's audience (and reviewers) (11, 12). This incentive, combined with the difficulty to publish results from failed experiments, draws scientists to the same congested areas of common knowledge, pitted with unmarked failures doomed to repetition, and so dramatically slows the pace of collective discovery (13). These patterns have been exploited to generate algorithms unhampered by professional pressures for publication and promotion, which more efficiently survey the space of scientific possibilities. These findings highlight the importance of supporting diverse approaches and independence in research, and of building institutions that log failures as well as successes in order to accelerate collective advancement.

Retraction and reputation

By **Ginger Zhe Jin**^{2,8,9} and **Susan Feng Lu**⁹

Retractions of scientific articles are increasingly common. Driven by community policing and self-reported errors, retractions could reflect innocent mistakes or intentional misconduct. Although a retracted article always suffers severe losses in citations, it was not until recently that literature documented broader reputational consequences of retraction for authors. Although authors of retracted papers commonly have "clean" works that were not retracted at any time and were published before their other work was retracted, the research community may take retraction as a signal of the authors' quality and cast doubt on those prior works. Comparing such prior papers' citations after the retraction, to control papers of similar citation history, reveals a 5 to 10% citation decline for the prior works, but only if the retraction is not self-reported (14) or involves intentional misconduct (15). Reputation loss also depends on author standing. Comparing author's standing across retraction events shows that eminent scientists (as measured with cumulative citation and funding before retraction) are more harshly penalized in the citation of their prior works, if the retraction involves misconduct (16). However, within scientific teams, the blameworthy party is often nonobvious. In these cases, the most eminent team members appear to escape largely unscathed, whereas less eminent coauthors experience substantial citation declines, especially when teamed with eminent authors (17). This result holds for both absolute eminence and relative eminence within the team. In short, reputational effects for individual scientists can be substantial after retraction occurs but depend on the nature of the retraction and the author's standing.

Science across the ages

By **Benjamin F. Jones**^{*}

Einstein said, "A person who has not made his great contribution to science before the age of 30 will never do so." But was Einstein right? The relationship between age and scientific productivity matters not only for assessing one's own potential but also for science institutions deciding whom to hire, promote, and fund.



Yet although many observers have echoed Einstein's view, empirical studies have rejected it with remarkable consistency. Great achievements come at many ages and typically peak between the mid-30s and mid-40s (18). This finding holds across science, engineering, and social science fields, including for Nobel Prize-winning contributions. It also holds among celebrated inventors (19) and successful technology entrepreneurs (20). Recent research also emphasizes a dynamic view: Nobel Prize-winning contributions and great inventions came 8 years later in life at the end of the 20th century than at the beginning (19). This shift is due to a sharp decline in great contributions at very young ages. This shift also appears among more ordinary careers, for which the age at first invention is rising 0.6 years per decade (21). The increasing depth of scientific knowledge can make subsequent generations take longer to reach the research frontier (19, 21). Additionally, although an individual's best works typically come in close succession, such "hot streaks" can happen, with equal probability, anywhere in the sequence of an individual's body of work (22). Overall, although entry to science is an increasingly long road, and scientists may write fewer papers later in life, opportunity endures: The next hot streak could be just around the corner.

Modeling and mapping

By **Katy Börner**^{10,11}

Studies of science, technology, and innovation (STI) have traditionally focused on analyzing historical data. Yet increasingly, decision-makers wish to understand likely impacts of today's, for example, hires, resource allocations, and legal decisions on the unfolding of future STI scenarios. Thus, computational models are increasingly used to explore aspects of the STI system itself (23), with hundreds of ways to visualize and communicate the structure and dynamics of STI (24–26). For example, models have been used to experiment and validate alternative approaches for funding science that might

**"A PERSON WHO HAS
NOT MADE HIS
GREAT CONTRIBUTION
TO SCIENCE BEFORE
THE AGE OF 30
WILL NEVER DO SO."**

– Albert Einstein

be less subject to biases, inconsistencies, and "old-boy" network effects associated with standard peer review and reduce the time, energy, and effort spent on writing and reviewing research proposals and the overhead required to organize the review process. Under the Fund-Rank model (27), each year all eligible scholars receive an equal portion of funding but are then required to anonymously donate a certain fraction of their funding to peers. This agent-based model was validated by using large-scale citation data (37 million articles and 770 million citations), presuming that scholars would distribute funding similarly to how they distribute citations, namely to those peers who do valuable, high-quality research. Other work models the return on investment for university-supported information technology (IT) resources on winning external funding and publishing papers (28); Sankey diagrams visualize correlations of IT usage, external funding, and publications and support IT strategic decision-making. Ultimately, such predictive models help develop and refine hypotheses, explore the impact of different parameters, capture causal relationships, and pick desirable futures.

Randomized insights

By **Karim R. Lakhani**^{2,12,13}, **Kevin J. Boudreau**^{2,14}, **Eva C. Guinan**^{13,15,16}

Although there is a growing body of research that describes various aspects of the scientific enterprise, it is largely observational, which limits which questions can be investigated and what causal inferences can be drawn. We have worked closely with scientists to layer large-scale randomized field experiments onto preexisting

university research processes in order to generate causal insights (29, 30). Little is known as to how scientific collaborations form. We hypothesized that finding collaborators is a costly "search" that shapes the number and type of collaborations (31). At a research symposium related to an institutional funding opportunity, attended by 400 scientists, we randomly enabled face-to-face interactions during 90-minute scientific idea-sharing sessions. Among teams that applied for funding, the probability of collaboration increased by 75% for the treated scientists compared with controls (same idea-sharing but not face to face). However, the collaborations occurred only within the same scientific domains. This highlights the role of scientific meetings and structured information sharing for increasing collaboration (as opposed to waiting for serendipity) and the barriers to collaboration across disciplines. To understand the role of cognitive biases in peer review, we randomly assigned 150 proposals for institutional research funding to 142 faculty reviewers (~15 applications per reviewer; 2130 evaluations total) (32). Controlling for the quality of the proposals, reviewers gave poorer scores to proposals that were closer to their own field of expertise (based on automated text analysis of the applications and of reviewers' publications). More novel proposals (based on text analysis, relative to all publications in the PubMed database) also received poorer scores. This highlights the importance of constructing appropriate review panels and establishing procedures that can eliminate bias against novelty.

REFERENCES AND NOTES

1. P. Azoulay, J. G. Zivin, J. Wang, *Q. J. Econ.* **125**, 549 (2010).
2. P. Azoulay, C. Fons-Rosen, J. G. Zivin, "Does Science Advance One Funeral at a Time?" Working paper NBER, #21788, 2015 (updated June 2018).
3. S. Mukherjee, D. M. Romero, B. Jones, B. Uzzi, *Sci. Adv.* **3**, e1601315 (2017).
4. J. Evans, *Science* **321**, 395 (2008).
5. B. Uzzi, S. Mukherjee, M. Stringer, B. Jones, *Science* **342**, 468 (2013).
6. D. Wang, C. Song, A. L. Barabási, *Science* **342**, 127 (2013).
7. Y. Ma, B. Uzzi, arXiv:1808.09412 [physics.soc-ph] (2018).
8. J. Furman, S. Stern, *Am. Econ. Rev.* **101**, 1933 (2011).
9. H. L. Williams, *J. Polit. Econ.* **121**, 1 (2010).
10. F. Shi, J. Foster, J. A. Evans, *Soc. Networks* **43**, 73 (2015).
11. J. Foster, A. Rzhetsky, J. A. Evans, *Am. Sociol. Rev.* **80**, 875 (2015).
12. A. Gerow, Y. Hu, J. Boyd-Graber, D. M. Blei, J. A. Evans, *Proc. Natl. Acad. Sci. U.S.A.* **10**, 1073/pnas.1719792115 (2018).
13. A. Rzhetsky, J. G. Foster, I. T. Foster, J. A. Evans, *Proc. Natl. Acad. Sci. U.S.A.* **112**, 14569 (2015).
14. S. F. Lu, G. Z. Jin, B. Uzzi, B. Jones, *Sci. Rep.* **3**, 3146 (2013).
15. P. Azoulay, J. L. Furman, J. L. Krieger, F. Murray, *Rev. Econ. Stat.* **97**, 1118 (2015).
16. P. Azoulay, A. Bonatti, J. L. Krieger, *Res. Policy* **46**, 1552 (2017).
17. G. Z. Jin, B. Jones, F. L. Susan, B. Uzzi, *Rev. Econ. Stat.* **10**, 3386/w19489 (2018).
18. B. F. Jones, E. J. Reedy, B. A. Weinberg, in *The Wiley Handbook of Genius*, D. K. Simonton, Ed. (John Wiley & Sons, 2014), pp. 422–450.
19. B. F. Jones, *Rev. Econ. Stat.* **92**, 1 (2010).
20. P. Azoulay, B. F. Jones, J. D. Kim, J. Miranda, Age and High-Growth Entrepreneurship. Working paper, NBER #24489 (2018).
21. B. F. Jones, *Rev. Econ. Stud.* **76**, 283 (2009).
22. L. Liu et al., *Nature* **559**, 396 (2018).
23. A. Scharnhorst, K. Börner, P. van den Besselaar, Eds., *Models of Science Dynamics: Encounters Between Complexity Theory and Information Science* (Springer-Verlag, 2012).
24. K. Börner, *Atlas of Science: Visualizing What We Know* (MIT Press, 2010).
25. K. Börner, *Atlas of Knowledge: Anyone Can Map* (MIT Press, 2015).
26. scimaps.org.
27. J. Bollen, D. Crandall, D. Junk, Y. Ding, K. Börner, *EMBO Rep.* **15**, 467 (2014).
28. O. Scrivner et al., *Front. Res. Metr. Anal.* **10**, 3389/firma.2017.00010 (2018).
29. E. Guinan, K. J. Boudreau, K. R. Lakhani, *MIT Sloan Manag. Rev.* **54**, 45 (2013).
30. K. J. Boudreau, K. R. Lakhani, *Innov. Policy Econ.* **16**, 135 (2016).
31. K. J. Boudreau et al., *Rev. Econ. Stat.* **99**, 565 (2017).
32. K. J. Boudreau, E. C. Guinan, K. R. Lakhani, C. Riedl, *Manage. Sci.* **62**, 2765 (2016).

ACKNOWLEDGMENTS

K.B. is partially supported by the National Institutes of Health (NIH) under awards 1R01LM012832-01A1, P01AG039347, and U01CA198934 and the National Science Foundation under award AISL 1713567. E.C.G. is supported in part by NIH/NCATS UL1TR001102.

10.1126/science.aav2484

¹Massachusetts Institute of Technology (MIT), Cambridge, MA, USA. ²National Bureau of Economic Research (NBER), Cambridge, MA, USA. ³University of California, San Diego, San Diego, CA, USA.

⁴Kellogg School of Management, Northwestern University, Evanston, IL, USA. ⁵McCormick School of Engineering, Northwestern University, Evanston, IL, USA. ⁶Northwestern Institute on Complex Systems

(NICO), Northwestern University, Evanston, IL, USA. ⁷University of Chicago, Chicago, IL, USA. ⁸University of Maryland, College Park, MD, USA. ⁹Purdue University, West Lafayette, IN, USA. ¹⁰School of

Informatics, Computing, and Engineering, Indiana University, Bloomington, IN, USA. ¹¹Alexander von Humboldt Fellow, Technische Universität Dresden, 01062 Dresden, Germany. ¹²Harvard Business

School, Boston, MA, USA. ¹³Laboratory for Innovation Science, Harvard University, Cambridge, MA, USA. ¹⁴Northeastern University, Boston, MA, USA. ¹⁵Dana Farber Cancer Institute, Boston, MA, USA.

¹⁶Harvard Medical School, Boston, MA, USA.

PERSPECTIVES

PALEONTOLOGY

Chemical clues to the earliest animal fossils

Steroid biomarkers show that the Ediacaran fossil *Dickinsonia* was an animal

By Roger E. Summons¹ and
Douglas H. Erwin²

The Ediacara biota are a diverse assemblage of macroscopic body forms that appear in the sedimentary rock record between 570 million and 541 million years ago. First recognized in Namibia and Australia, these remarkable organisms have since been found in Russia, China, Canada, Great Britain, and other regions. Although they immediately preceded the rapid appearance and diversification of animals in the Cambrian (541 million to 485 million years ago), their position within the tree of life has long been a puzzle. Some Ediacaran fossils appear segmented, but most lack obvious characters such as appendages, a mouth, or a gut that might link them to animal clades. On page 1246, Bobrovskiy *et al.* (1) use biomarkers to confidently assign at least one Ediacaran group, *Dickinsonia* and related taxa, to the Metazoa (animals).

The Ediacara biota were first described at a time when paleontologists relied on overall similarities in form to establish phylogenetic affinities. Various Ediacaran groups were allied with later animal clades on the basis of such similarities. Thus, *Dickinsonia* and other apparently segmented taxa were considered annelids, *Rangia* a pennatulacean cnidarian, and *Parvancorina* a likely arthropod (2). In 1992, Seilacher instead proposed that most of these organisms were part of a single clade that formed a separate, independent kingdom of complex multicellular organisms, the Vendozoa (3). After this, scientists considered a range of novel solutions, and the fossils were allied with a wide array of clades.

More recent systematic inquiry has focused on identifying discrete morphological characters. There has been growing consen-

sus that the Ediacaran biota does not represent a single clade but a diversity of taxa, mostly of Metazoa (4, 5). On the basis of a detailed analysis of the features of *Dickinsonia* fossils, Gold *et al.* have suggested that they were at least bilaterian-grade animals (6). Thus, we can identify discrete groups

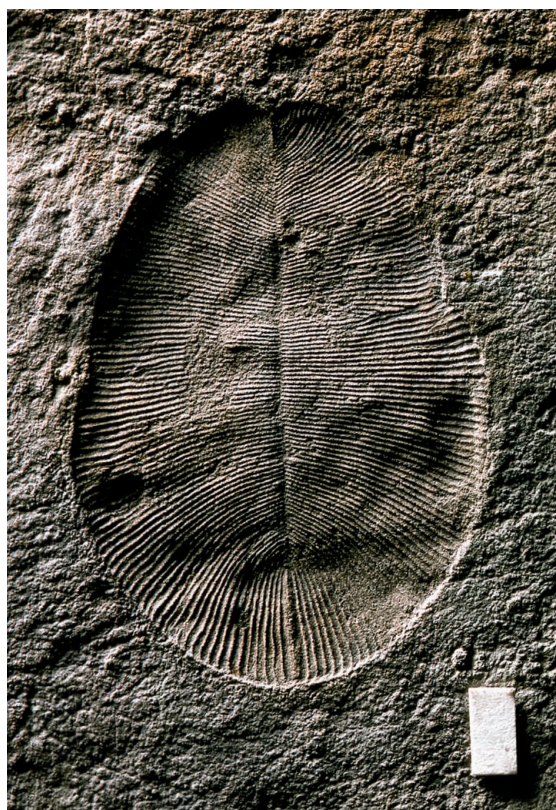
provided that they have not been highly altered by subsequent metamorphism. Sterols and steranes can be particularly useful as biomarkers because some aspects of sterol structure are specific to particular source organisms (7). For example, Love *et al.* identified 24-isopropylcholestane, which is prevalent in several sequences of rocks between 660 million and ~535 million years ago, as a steroid characteristic of demosponges (8).

Bobrovskiy *et al.* used an approach designed to identify diagnostic hydrocarbon biomarkers associated with individual fossils preserved in remarkably unaltered, fine-grained sediments of the White Sea region in Russia. In earlier work, they isolated an organic biofilm associated with circular impressions known as *Beltanelliformis*, analyzed the entrained hydrocarbons, and assigned a colonial cyanobacterial origin (9). For the current study, the authors sampled thin layers of organic material associated with fossils of *Dickinsonia* and *Andiva* from the same sequence of rocks for biomarkers. They also analyzed samples of adjacent layers of sediment to control for more broadly distributed biomarkers.

The surrounding sediments contained diverse steranes, most of which comprised compounds with 29 carbon atoms (stigmasteroids) that are diagnostic of green algae. By contrast, the steroids in the *Dickinsonia* fossil biofilms were almost exclusively composed of compounds with 27 carbon atoms (cholesteroids), a signature of

all animal phyla other than sponges and a few mollusk taxa. The steroid assemblages from the smaller *Andiva* fossils were confounded by background signals and harder to interpret.

The cholesterol predominance from *Dickinsonia* allowed Bobrovskiy *et al.* to refute alternative hypotheses of their affinities to lichens or large protists. Nevertheless, the White Sea *Dickinsonia* organic remains are enigmatic in another, biologically striking way. The sterols of living organisms are produced with a single three-dimensional



Biomarkers associated with fossils of *Dickinsonia tenuis* from the White Sea in Russia suggest metazoan affinities. Scale bar, 1 cm.

among the fossils, but how they relate to Cambrian and later clades has remained unresolved. Bobrovskiy *et al.* now resolve this controversy for *Dickinsonia* and *Andiva*, quilted forms with a medial suture, on the basis of biomarkers associated with the fossils.

Almost all eukaryotes produce and use sterols, a class of lipids that perform vital membrane behavior and cell signaling functions. After death, these sterols are transformed into more stable sterane hydrocarbons, which may be recovered from sediments

¹Department of Earth, Atmospheric and Planetary Sciences, Massachusetts Institute of Technology, Cambridge, MA 02139, USA. ²Department of Paleobiology, MRC-121 Smithsonian Institution, Washington, DC 20013, USA. Email: rsummons@mit.edu; erwind@si.edu

configuration, or stereochemistry, but the steroids preserved in sedimentary rocks are typically mixtures that include more reduced and thermodynamically stable forms, as a result of chemical transformations during burial and subsequent heating. By contrast, the *Dickinsonia* cholesteroloids mostly have the same 5 β (H) stereochemistry. The only known pathway to this steroid, informally termed coprostanol, is via the steroid coprostanol, which is produced in the gut of higher mammals (10–12). Coprostanol is thought to be unstable on geological time scales (13). Bobrovskiy *et al.* attribute the presence of these unusual steroids to reduction of *Dickinsonia* cholesterol by bacteria during the original decomposition of the animal. Yet, coprostanols are absent in much younger, exceptionally preserved animal fossils, where the dominant steranes are 5 α (H)-cholestanes (14). The association of unusual steroids associated with *Dickinsonia* suggests that it may have had a distinct metabolic physiology (see the photo).

Molecular clock evidence suggests that animals originated before 720 million years ago, although the pattern of their divergence during the Cryogenian (720 million to 635 million years ago) and Ediacaran (635 million to 541 million years ago) remains unresolved (15). Because molecular clock estimates and morphological characters from fossils offer limited resolution, our best hope for unraveling the early history of animals and the affinities of the Ediacara biota lies with identification of biomarkers that allow us to differentiate specific metazoan clades, particularly among the bilaterians. Further refining the phylogenetic signals from biomarkers may also help to resolve the early history of animals during the Cryogenian and early Ediacaran. Moreover, the fossil-specific biomarker approach taken by Bobrovskiy *et al.* promises to yield many new insights into the fossilization processes that led to soft-tissue preservation across the animal kingdom and throughout geological time. ■

REFERENCES

1. I. Bobrovskiy *et al.*, *Science* **361**, 1246 (2018).
2. R. J. F. Jenkins, in *Origin and Early Evolution of the Metazoa*, J. H. Lipps, P. W. Signor, Eds. (Plenum, 1992), pp. 131–176.
3. A. Seilacher, *J. Geol. Soc. Lond.* **149**, 07 (1992).
4. D. H. Erwin *et al.*, *Science* **334**, 1091 (2011).
5. S. H. Xiao, M. Laflamme, *Trends. Ecol. Evol.* **24**, 31 (2009).
6. D. A. Gold *et al.*, *Evol. Dev.* **17**, 315 (2015).
7. J. K. Volkman, *Org. Geochem.* **36**, 139 (2005).
8. G. D. Love *et al.*, *Nature* **457**, 718 (2009).
9. I. Bobrovskiy *et al.*, *Nat. Ecol. Evol.* **2**, 437 (2018).
10. K. Prost *et al.*, *PLOS ONE* **12**, e0164882 (2017).
11. P. Gerard, *Pathogens* **3**, 14 (2013).
12. P. Gerard *et al.*, *Appl. Env. Microbiol.* **73**, 5742 (2007).
13. G. van Graas *et al.*, *Geochim. Cosmochim. Acta* **46**, 2399 (1982).
14. I. Melendez *et al.*, *Sci. Rep.* **3**, 2768 (2013).
15. M. dos Reis *et al.*, *Curr. Biol.* **25**, 2939 (2015).

10.1126/science.aau9710

SYNTHETIC BIOLOGY

Programming cells and tissues

New toolkits of biological parts allow powerful cell programming by synthetic biologists

By David S. Glass and Uri Alon

The field of synthetic biology envisions designing genetic circuits to program cells and tissues. These circuits will enable cells to detect disease states and act to remedy them, direct cells to produce useful substances and materials, and even allow cells to self-assemble into new, user-defined tissues (1). Starting from circuits comprised of a few components (2, 3), registries of biological parts have been curated, and increasingly larger circuits have been engineered in cells (4), but the size and capabilities of these circuits have been limited. A key challenge to engineering larger systems is composability: the ability to connect any two parts and achieve predictable behavior. On page 1252 of this issue, Gao

“...the future is bright for the engineering of new capabilities in biomedicine...”

et al. (5) describe a composable protein-based system for building circuits, and on page 1217, Andrews *et al.* (6) describe a sequential logic system with many states. Recently, Toda *et al.* (7) used synthetic cell-cell signaling to drive differentiation and adhesion to form prototype tissues. These studies demonstrate that careful attention to composability can expand synthetic biology beyond its traditional limits.

Composability is a relatively subtle concept, and it is important to keep in mind several related—but distinct—concepts. Orthogonality in synthetic biology refers to parts that do not interfere or that minimally interfere with one another. This amounts to a lack of cross-talk between the parts. For example, two transcription factors are orthogonal if they do not regulate each other's promoters. Modularity refers to a system that can be divided into subsystems, each with a defined function. These concepts can apply at multiple levels—within a protein, in circuits, and in

multicellular systems (see the figure).

Composability is a more stringent criterion than either orthogonality or modularity. Parts that are composable are modular units that have matching inputs and outputs and are designed so that any two parts can be connected to each other and yield predictable behavior. Standardization of parts and their interfaces is one way to develop such “plug-and-play” capability (1). Even electronic circuits, often considered easy to engineer compared to biological ones, are not necessarily composable, and combining parts can fail if input and output impedances are not designed appropriately; a similar concept in biological circuits has been termed retroactivity (8). Natural systems show modularity and orthogonality to a first approximation but do not automatically provide parts that are composable enough for engineering purposes. Thus, synthetic biologists must carefully engineer natural parts to gain composability.

One important goal in synthetic biology has been to bring circuit design from the level of gene regulation, which takes hours owing to the slow process of making proteins, to the level of protein-protein interactions, which can occur within seconds to minutes. Protein circuits are not only faster but also provide powerful capabilities, including interfacing directly with cellular pathways and operating at distinct subcellular sites (9). The problem in producing protein-based circuits has been the lack of a toolkit of composable proteins that can regulate one another in arbitrary and predictable ways.

Gao *et al.* solved this issue using molecular scissors called viral proteases (10). They engineered these proteases to specifically regulate each other in a programmable way using binding domains, degradation tags, and orthogonal cleavage sites to define sites of protease activity. Because of the attention paid to composability, the authors were able to produce a variety of two-input Boolean logic gates encoded strictly at the protein level. They also formed more complex circuits, including a pulse generator, which benefited from the rapidity of protein-protein interactions. They even used the protease system to implement circuits that selectively kill cells harboring mutant and

Department of Molecular Cell Biology, Weizmann Institute of Science, Rehovot 76100, Israel. Email: urialon@weizmann.ac.il

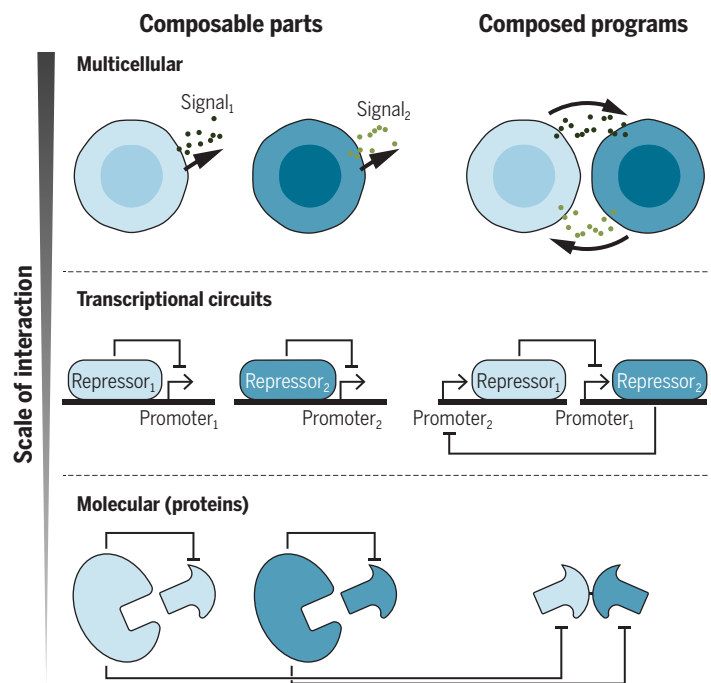
hyperactive proteins that drive cancer, all at the protein level and all encoded on a single RNA molecule. This capability expands the possibility of using synthetic circuits as therapeutics, because a protein circuit could be delivered to cells as RNA without any need to edit the genome.

Another goal of synthetic biology has been to produce sequential logic circuits that use memory storage (11). Building on their earlier work with combinatorial logic using a composable set of transcription factors (4), Andrews *et al.* engineered sequential logic with reversible states, which enabled complex circuits with behavior that depends on memory of past events. This development relied on careful characterization of a library of set-reset latches (toggle switches), each of which is composed of, regulated by, and able to regulate transcription factors. The authors composed these latches together with combinatorial logic circuits into state machines that can remember multiple events, resulting in circuits that can be set to distinct states or locked in place (known as a data latch), as well as cycle between multiple states upon distinct chemical inputs. These versatile circuits could be used to detect, for example, a sequence of "checkpoint" go-no-go events that must occur before a cellular response is appropriate.

Composability can also be applied to the multicellular level, thinking of individual cells as composable units that can be programmed to interact with one another in predictable ways. Synthetic multicellular systems hold promise to aid in tissue regeneration and to program structured living materials capable of responding to the environment (12). Key to these abilities are systems for cell-cell signaling, differentiation, and adhesion (12). Synthetic signaling (9) and differentiation (or memory) (13) have been used to produce pattern formation on sheets of cells (14). More recently, a genetically encoded system of composable cellular glues (adhesins) was used to program physical cell-cell interactions in bacteria, enabling self-assembly of three-dimensional (3D) patterns at a length scale of individual cells that persist during growth and division (12). This capability to

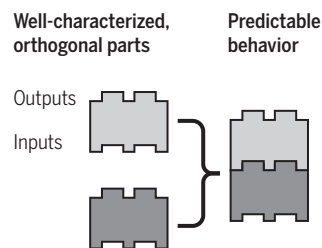
Composability at multiple scales

Composability allows predictable interaction of biological parts, which is now possible at multiple scales (proteins, transcriptional circuits, and multicellular systems). Arbitrary composability could allow programming of new cells, tissues, or even organisms.



engineer precise, 3D patterns could allow efficient separation of chemical intermediates in microbial consortia and enable bottom-up exploration of the evolutionary emergence of multicellularity.

Toda *et al.* programmed tissues to sequentially develop multicellular structures, by means of a composable set of molecular locks and keys (synthetic juxtacrine signaling) that allows neighboring cells to activate each other to express adhesion molecules and to differentiate into new cell types. Sequential steps are self-driven by the timing of adhesion-based cell sorting, a biophysical process that brings cells into direct contact to facilitate signaling. The resultant structures are reminiscent of those that occur during embryo development, with comparable behaviors such as symmetry breaking and regeneration after injury. The regulation of adhesion by synthetic signaling allows the process to be more controlled and versatile than purely adhesion-based structures (15), opening up the possibility of engineering artificial development systems for studying in vitro development.



In the future, composability is likely to accelerate synthetic biology, especially when circuits at different levels are integrated to achieve much more powerful systems than currently feasible. Memory based on rewriting or excising DNA, if easily composed with flexible, sequential logic (11), could allow scalable state machines with long-term stability that do not require active protein expression to maintain memory. Protein-based circuits combined with transcriptional logic could coordinate processes across multiple time scales, with inputs and outputs directly at the clinically relevant protein level. In a multicellular context, coupling signaling and adhesion to sequential logic could allow scalable developmental programs. These integrated processes have natural biological counterparts (for example, animal development and cell signaling networks). Synthetic circuits can shed light on these native systems: One can test in silico simulations by building the circuits within a real biological context but without the unknowns of dissecting a fully native pathway. With the long-standing limits of synthetic biology being crossed by means of composable toolkits for sequential, protein-based, and multicellular systems, the future is bright for the engineering of new capabilities in biomedicine and for gaining deeper biological understanding. ■

REFERENCES AND NOTES

1. D. Endy, *Nature* **438**, 449 (2005).
2. T. S. Gardner *et al.*, *Nature* **403**, 339 (2000).
3. M. B. Elowitz, S. Leibler, *Nature* **403**, 335 (2000).
4. A. A. K. Nielsen, *Science* **352**, aac7341 (2016).
5. X. J. Gao *et al.*, *Science* **361**, 1252 (2018).
6. L. B. Andrews *et al.*, *Science* **361**, eaap8987 (2018).
7. S. Toda *et al.*, *Science* **361**, eaat0271 (2018).
8. D. Del Vecchio *et al.*, *Mol. Sys. Biol.* **4**, 161 (2008).
9. L. Morsut *et al.*, *Cell* **164**, 780 (2016).
10. H. K. Chung *et al.*, *Nat. Chem. Biol.* **11**, 713 (2015).
11. N. Roquet *et al.*, *Science* **353**, aad8559 (2016).
12. D. S. Glass, I. H. Riedel-Kruse, *Cell* **174**, 649 (2018).
13. J. Bonnet *et al.*, *Proc. Natl. Acad. Sci. U.S.A.* **109**, 8884 (2012).
14. S. Basu *et al.*, *Nature* **434**, 1130 (2005).
15. E. Cachat *et al.*, *Sci. Rep.* **6**, 20664 (2016).

ACKNOWLEDGMENTS

D.S.G. is a member of the Zuckerman Postdoctoral Scholars Program.

10.1126/science.aav2497

APPLIED OPTICS

Fighting chaos with chaos in lasers

Complex wave interference suppresses nonlinearities that destabilize beams

By **Lan Yang**

For many laser applications, beam stability is critical, but chaotic lasing dynamics can create spatiotemporal instabilities. A long-standing problem in high-power semiconductor lasers (1, 2) is that instabilities can arise from deterministic and random effects that control the complex interactions between the radiation field and matter. The conventional approach to suppress instabilities is to reduce the level of complexity of the system. On page 1225 of this issue, Bittner *et al.* (3) now report a counterintuitive method that introduces an additional layer of complexity, chaotic ray dynamics, to mitigate chaos in lasing dynamics—a strategy similar to “fighting fire with fire.”

This strategy leverages complex wave interference that occurs in deformed cavities (4) or disordered structures (5). Conventional laser resonators feature stable ray trajectories and generally avoid unstable, chaotic ray trajectories. Still, with suitable designs, chaotic waves may aid the development of innovative photonic mechanisms with unconventional properties. For example, chaotic waves may escape from a deformed cavity only into certain angles from specific positions (6, 7), enabling efficient unidirectional laser emission (8, 9). Moreover, an appropriately deformed cavity can support modes localized on both regular and chaotic ray trajectories, between which dynamic tunneling may occur (10). Recently, in a deformed resonator, chaotic photons with time-varying angular momentum were found to help mediate efficient coupling between modes with mismatched momentum via dynamic tunneling (11). Such a mechanism could aid the broadband momentum transformation, thereby opening new avenues for studying broadband physical processes and enabling innovative photonic systems.

Bittner *et al.* demonstrate another important application that relies on the special features of chaotic waves. In their microcavity lasers, two types of chaos result from different mechanisms. One is chaotic wave dynamics (4) introduced by deforming the cavity. The other is chaotic lasing dynamics (12) caused by nonlinear interactions of the light field with the gain medium. These interactions can result in filamentation and unstable filaments leading to overall unstable lasing dynamics. In broad-area semiconductor lasers where many transverse spatial modes coex-

edge-emitting GaAs quantum well broad-area stripe laser (see the figure). The D-shaped laser suppressed filamentation and pulsation, resulting in substantially more stable spatiotemporal dynamics. This approach is also robust against defects and perturbations because additional randomness does not fundamentally change the wave-chaotic nature of the deformed cavity. Full-wave simulations showed that the introduction of structural disorder on a subwavelength scale can suppress lasing instabilities even in effectively one-dimensional semiconductor lasers. Pseudo-random subwavelength-scale fluctuations in lasing mode structures disrupted the coherent nonlinear processes at larger intrinsic length scales.

Deformation and sub-wavelength-scale complexity, which are commonly avoided in photonic structures, can provide additional degrees of freedom to tailor the properties of photonic systems. There are numerous ways to introduce chaotic wave dynamics in microcavities, such as varying the materials, shapes, and geometries. Chaotic photons could further enable unprecedented applications of resonators, includ-

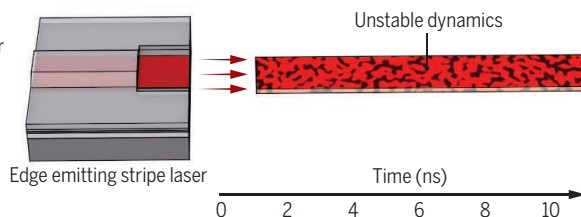
ing optomechanics (13) and frequency combs (14). Moreover, the use of geometry to control nonlinear dynamics demonstrated by Bittner *et al.* may provide alternative solutions to control other complex dynamic systems. ■

Chaos as a remedy for laser stability

The emission from an edge-emitting broad-area stripe laser is compared with that from a laser developed by Bittner *et al.* with a D-shaped microcavity.

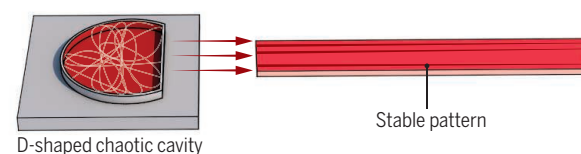
Unstable beam

Coherent nonlinear processes such as filamentation and pulsation create instability.



Stable beam

The microcavity suppresses these processes through random phases of the chaotic waves.



ist, their nonlinear interactions with the gain medium are especially strong (1).

Previous strategies for suppressing unstable laser dynamics in high-power semiconductor lasers tried to reduce the number of spatial modes, for example, by injection locking or with delayed feedback (1, 2). However, as the power grows or the cavity size increases, the number of lasing modes increases, and their nonlinear interactions again cause spatiotemporal instabilities. Instead, Bittner *et al.* used numerous waves propagating with unrelated phases in a deformed microcavity. Thus, complex wave interference successfully disrupts the formation of coherent nonlinear structures on subwavelength scales, such as filaments, that are prone to instabilities. This strategy provides a practical way to stabilize high-power semiconductor lasers even for a large number of lasing modes.

Bittner *et al.* compared a D-shaped, wave-chaotic microcavity laser to a conventional

REFERENCES

1. E. Gehrig, O. Hess, *Spatio-Temporal Dynamics and Quantum Fluctuations in Semiconductor Lasers* (Springer, 2003).
2. J. Ohtsubo, *Semiconductor Lasers: Stability, Instability and Chaos* (Springer, 2017).
3. S. Bittner *et al.*, *Science* **361**, 1225 (2018).
4. J. U. Nöckel, A. D. Stone, *Nature* **385**, 45 (1997).
5. H. Cao *et al.*, *Phys. Rev. Lett.* **82**, 2278 (1999).
6. S. Shinohara *et al.*, *Phys. Rev. Lett.* **104**, 163902 (2010).
7. Q. Song *et al.*, *Phys. Rev. Lett.* **108**, 243902 (2012).
8. J. Wiersig, M. Hentschel, *Phys. Rev. Lett.* **100**, 033901 (2008).
9. X.-F. Jiang *et al.*, *Adv. Mater.* **24**, 0P260 (2012).
10. J. Yang *et al.*, *Phys. Rev. Lett.* **104**, 243601 (2010).
11. X. Jiang *et al.*, *Science* **358**, 344 (2017).
12. L. M. Narducci, N. B. Abraham, *Laser Physics and Laser Instabilities* (World Scientific, 1988).
13. T. J. Kippenberg, K. J. Vahala, *Science* **321**, 1172 (2008).
14. P. Del'Haye *et al.*, *Nature* **450**, 1214 (2007).

Department of Electrical and Systems Engineering,
Washington University, St. Louis, MO 63130, USA. Email:
yang@seas.wustl.edu



Alternating black and yellow stripes adorn the back of juvenile galliform birds.

DEVELOPMENT

A bird's inner stripes

Patterns of stripes on bird plumage are determined from deep under the skin

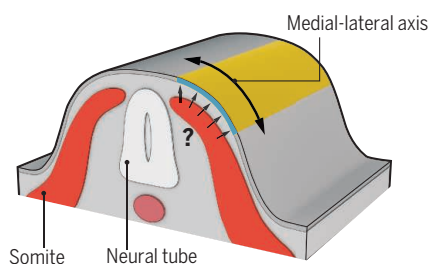
By Benjamin Prud'homme¹ and Nicolas Gompel²

How do the periodic patterns of colored stripes that decorate so many birds and mammals form? These patterns are the object of aesthetic fascination and the focus of endless debate about the mechanisms that generate them or diversify them. Theoreticians show that the most complex of regular patterns can be reproduced in silico using Turing-like reaction-diffusion mechanisms, whereby the concentrations and diffusing properties of an activator and an inhibitor regulate their interactions and thus determine the final periodic pattern (1). By contrast, experimental data indicate that self-organizing processes relying on interactions between skin cells establish striped patterns (2, 3). On page 1216 of this issue, Haupaix *et al.* (4) address this question from a different perspective, by examining the contribution of embryonic structures

that could act as instructive, spatial landmarks to guide the formation of alternating yellow and black stripes on the back of chicks of quails, pheasants, partridges, and their relatives (galliform birds). They show that an early developmental signal from under the skin dictates the position of stripes and therefore periodic patterns. This provides a new framework within which to understand the rich diversity of vertebrate coat decoration.

Feather color patterning in development

An unknown signal from the developing somite (short arrows) triggers the expression of *agouti* (blue) in the developing skin, and thereby determines the position of yellow stripes in chicks.



Juvenile galliform birds are marked with broad stripes running from head to tail. At first glance, they look quite diverse. This is because these stripes vary extensively in shape and width. But Haupaix *et al.* noted that if one ignores this variation, another feature emerges: The stripes, although variable in number, are located at approximately the same positions in all birds. This invariant positioning of the colored stripes suggested that their formation relies on an underlying blueprint of spatial landmarks that are shared by all birds. To track this hypothetical blueprint, the authors examined the process of feather formation and the genetic control of feather coloration during embryonic development.

In all galliform species examined, longitudinal rows of feathers grow in the same sequence in the developing chick skin. The first rows appear close to the middle of the back, and the last row far away from it, just above the wing hinge. Feathers are pigmented as they grow. Some rows consistently produce black pigment throughout their growth, resulting in a solid black stripe. Other rows switch temporarily from black to yellow pigment production as they grow, thereby creating yellow stripes.

In vertebrates, the genetics of pigment production is well studied. One gene, *agouti*, turns off the production of black pigments in growing hairs of mammals. Haupaix *et al.* hypothesized that the bird version of *agouti* may control the switch from black to yellow pigment production in growing feathers where and when it is expressed. They examined the expression of *agouti* in the embryos of different galliform birds and found a striking correlation with the final pattern of yellow stripes in each species. Hence, *agouti* expression prefigures the color pattern of the chicks long before the feathers start to grow. This reinforced the authors' suspicion of a signal that patterns the skin early in development. What could this signal be, and where could it come from?

In sharp contrast to plumage variation, the organization of a bird embryo is invariant among species. In particular, underneath the dorsal skin in the middle of the back lies the neural tube, which is the precursor of neurons and pigmented cells. It is flanked laterally by the somites, which are precursors of muscles and skeletal elements, among other derivatives (see the figure). Haupaix *et al.* reasoned that the stereotyped positions of the color stripes, reflecting the stripes of *agouti* expression, may be dictated by this embryonic architec-

¹Aix Marseille Université, CNRS, Institut de Biologie du Développement de Marseille (IBDM), 13288 Marseille Cedex 9, France. ²Fakultät für Biologie, Ludwig-Maximilians-Universität München, Biozentrum, 82152 Planegg-Martinsried, Germany. Email: benjamin.prudhomme@univ-amu.fr; gompel@biologie.uni-muenchen.de

ture. Indeed, the cells of the skin that eventually give rise to feathers may acquire their identity along the medial-lateral axis, later revealed by their color, by receiving some signals from adjacent embryonic structures. To directly test this idea, the authors used grafting experiments, swapping small pieces of embryonic tissue between species with slightly different patterns of color stripes. Swapping the neural tube between species had no effect on coloration. By contrast, swapping a few somites changed the *agouti* expression pattern, and in turn the local feather coloration, in the chimeric chicks. Hence, skin cells acquire their positional identity from a landmark signal produced by the underlying somites. The pattern variation may in turn result from changes in the strength of this signal, or in how the skin cells interpret it.

The study of Haupaix *et al.* stands out as a direct demonstration that color patterning on the coat of vertebrates relies on spatial patterning information from embryonic structures. Rather than contradicting the idea that local cellular interactions or reaction-diffusion phenomena govern the establishment of color patterns, the existence of an embryonic blueprint provides a new framework within which to consider these processes. Indeed, the embryonic blueprint may guide or bias how skin cells interact. Architects design buildings and decide where structural elements such as walls, windows, pipes, and chimneys are placed. These structural landmarks impose positional constraints for later decoration. Designers have to work within these constraints, but they can still independently create a unique appearance to each building. By analogy, spatial embryonic structures may provide a template that first translates into skin landmarks, which may in turn set specific initial conditions to the local cellular interactions that will define the final coloration pattern.

The work of Haupaix *et al.* opens a new era where self-organizing processes are no longer systematically opposed to embryonic patterning. Yet to reach the integration of these processes and fully understand color pattern formation and color pattern evolution, research is needed to investigate how the early embryonic blueprint and the late cellular interactions are coordinated. Identifying the nature of the somitic signal patterning the skin will be a first step in this direction. ■

REFERENCES

1. S. Kondo, H. Shirota, *Semin. Cell Dev. Biol.* **20**, 82 (2009).
2. M. Inaba *et al.*, *Science* **335**, 677 (2012).
3. A. P. Singh *et al.*, *Nat. Cell Biol.* **16**, 604 (2014).
4. N. Haupaix *et al.*, *Science* **361**, eaar4777 (2018).

10.1126/science.aau5103

NEUROSCIENCE

A gut feeling

Gut-brain signaling involves neurotransmission from gut sensory epithelial cells

By Benjamin U. Hoffman^{1,2} and Ellen A. Lumpkin^{1,3}

The anatomist Friedrich S. Merkel predicted in 1880 that sensory systems are composed of epithelial cells and sensory nerves, which together transform environmental cues into neural signals that trigger our rich sensory experiences (1). We now know that this hypothesis mostly holds true for the canonical senses of vision, hearing, taste, and touch. Perhaps surprisingly, the peripheral outposts of these classical sensory systems (eyes, ears, tongue, and skin) are dwarfed by the human body's largest sensory organ—the gut. Enteroendocrine cells, which are rare epithelial cells that decorate the gut lining, have long been suspected to be sensory receptor cells that inform the brain about ingested nutrients (2). Since their description, these cells were assumed to play a role in metabolism and gut physiology by releasing slow-acting peptide hormones that stimulate neurons through-

“...findings overturn a decades-old dogma that enteroendocrine cells signal exclusively through hormones.”

out the gut and in the brain. On page 1219 of this issue, Kaelberer *et al.* (3) challenge this view by demonstrating that gut enteroendocrine cells locally excite sensory nerves through release of the neurotransmitter glutamate. A recent study of enterochromaffin cells, a subset of enteroendocrine cells, also found that gut signals are transmitted at epithelial-neural synapses through release of the neurotransmitter serotonin (4). Together, these findings overturn a decades-old dogma that enteroendocrine cells signal exclusively through hormones.

Kaelberer *et al.* focused on a subset of mouse enteroendocrine cells marked by

expression of two neuropeptide precursor proteins, cholecystokinin (CCK) and peptide YY (PYY), which are cleaved to produce hormones that control hunger (5, 6). The authors confirmed that these enteroendocrine cells possess anatomical hallmarks of presynaptic cells and that they form direct synaptic connections with vagal and spinal sensory neurons in vivo (3, 7). Moreover, infusing sucrose, or table sugar, into the gut caused vagus nerve activation in an enteroendocrine cell-dependent manner in vivo.

Given the location and relative scarcity of enteroendocrine cells, their function is difficult to study in the intact gut. To overcome this challenge, the authors used an in vitro co-culture model of enteroendocrine cells and sensory neurons. Stimulation of enteroendocrine cells with D-glucose, a component of sucrose, triggered excitatory ionic currents and action potentials in their associated neurons. Further studies revealed that enteroendocrine cells activate sensory neurons within tens to hundreds of milliseconds, a time scale typical of synaptic transmission rather than neuropeptide signaling.

Other epithelial-neuronal synapses, such as inner-ear hair cells and retinal photoreceptors, employ glutamate as a neurotransmitter. Using genetically engineered biosensors, Kaelberer *et al.* demonstrate that D-glucose stimulates glutamate release from enteroendocrine cells. Importantly, blocking glutamate-gated ion channels that mediate synaptic transmission abolished D-glucose-induced currents in vagal neurons in vitro. In vivo studies showed that glutamate-gated ion channels are required for early (<60 s) vagus responses to dietary sugars, whereas neuropeptide receptors are responsible for vagus activity on a longer time scale. Thus, enteroendocrine cells are chemosensory cells that activate vagal sensory neurons via release of glutamate (see the figure). Kaelberer *et al.* hypothesize that synaptic transmission confers precise spatial and temporal information about gut contents. Such sensory feedback could allow neural control of rapid processes that modulate gut physiology, such as muscle contraction, whereas neuropeptides such as CCK are responsible for long-lasting behavioral outputs of gut stimulation, such as satiety (5, 6). A remaining issue is what

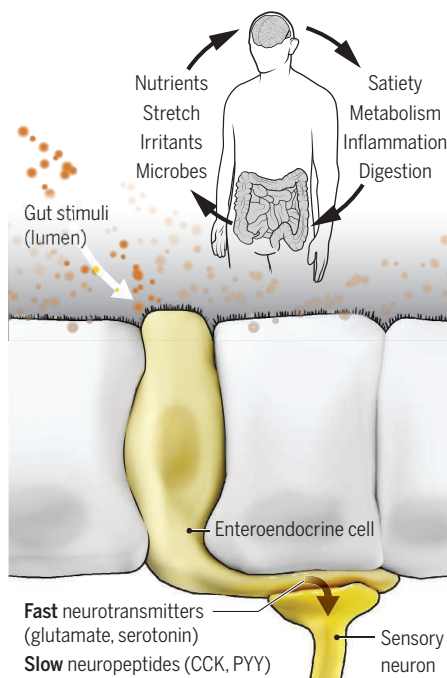
¹Department of Physiology and Cellular Biophysics, Columbia University, New York, NY 10032, USA. ²Medical Scientist Training Program, Columbia University, New York, NY 10032, USA. ³Department of Dermatology, Columbia University, New York, NY 10032, USA. Email: eal2166@columbia.edu

behaviors or physiological processes rely on subsecond neural signaling from the gut.

The finding that gut enteroendocrine cells form glutamatergic synapses identifies a first relay in the neural circuit through which the brain detects gastrointestinal contents, such as nutrients and microbes, to control satiety, metabolism, and digestion. Glutamate is arguably the most ancient excitatory neurotransmitter: Glutamate receptors are encoded in the genomes of primitive nervous systems, such as in ctenophores (marine invertebrates), and of *Trichoplax*, an animal that emerged before nervous systems evolved (8, 9). It is interesting that the mammalian gut has co-opted

Epithelial sensory cells

In addition to secreting neuropeptides, enteroendocrine cells rapidly convey information about nutrients in the gut by releasing neurotransmitters to excite vagal and spinal sensory neurons.



this ancient neurotransmitter to mediate nutrient sensing, which is perhaps the earliest sense to arise during evolution.

Enteroendocrine cells are remarkably heterogeneous, with at least 12 molecularly distinct subtypes that express a multitude of sensory receptor proteins and neurotransmitters (10, 11). Indeed, enterochromaffin cells, which lack expression of CCK and PYY, employ serotonin to convey stimuli such as stretch, irritants, and metabolites to vagal sensory neurons (4, 12). An intriguing possibility is that enteroendocrine cells use discrete neurotransmitter systems to communicate with functionally distinct

subsets of vagal and spinal sensory neurons (13). Such a system could allow detection of different types of ingested nutrients such as sugars, fats, or proteins, or could participate in neural control of the progression of contents through the gastrointestinal tract.

Perhaps most relevant to human health is the possibility that synaptic transmission between gut epithelial cells and sensory neurons provides a signaling node through which microbes interact with our nervous system. The gut provides an array of essential functions for humans including not only nutrient sensing, metabolism, and absorption, but also a barrier to infection from the multiplicity of organisms that compose the gut microbiome. Enteroendocrine cells express toll-like receptors, which detect bacterial products to activate innate immune responses and maintain the epithelial barrier. Activation of these receptors on enteroendocrine cells induces release of neuropeptides, including CCK (14). These data suggest that enteroendocrine cells might not only serve as detectors of gut microbiota, but also participate in proinflammatory and other immune responses.

The findings of Kaelberer *et al.* pose a number of tantalizing open questions. For example, what are the molecular mechanisms of neurotransmitter release in enteroendocrine cells? Which postsynaptic receptors mediate glutamatergic transmission in vagal neurons? Moreover, how do enteroendocrine cells modulate neuronal signals in the presence of environmental irritants or in intestinal disorders? The ability to investigate the first relay station of the gastrointestinal–nervous system circuit in vitro, in conjunction with genetic targeting techniques, provides an exquisite platform to answer these questions. Furthering our understanding of the molecular mechanisms that mediate signaling along the gut–brain axis provides the foundation for the development of future therapeutics to treat gastrointestinal disease. ■

REFERENCES

1. F. S. Merkel, *Über die Endigungen der sensiblen Nerven in der Haut der Wirbeltiere* (H. Schmidt, Rostock, 1880).
2. F. Feyerher, *Über diffuse endokrine epitheliale Organe* (J.A. Barth, Leipzig, 1938).
3. M. M. Kaelberer *et al.*, *Science* **361**, eaat5236 (2018).
4. N. W. Bellono *et al.*, *Cell* **170**, 185 (2017).
5. L. R. Beutler *et al.*, *Neuron* **96**, 461 (2017).
6. Z. Su, A. L. Alhadeff, J. N. Betley, *Cell Rep.* **21**, 2724 (2017).
7. D. V. Bohórquez *et al.*, *J. Clin. Invest.* **125**, 782 (2015).
8. A. Krishnan, H. B. Schiöth, *J. Exp. Biol.* **218**, 562 (2015).
9. L. L. Moroz *et al.*, *Nature* **510**, 109 (2014).
10. A. L. Haber *et al.*, *Nature* **551**, 333 (2017).
11. D. Grün *et al.*, *Nature* **525**, 251 (2015).
12. C. Alcaino *et al.*, *Proc. Natl. Acad. Sci. U.S.A.* **115**, E7632 (2018).
13. E. K. Williams *et al.*, *Cell* **166**, 209 (2016).
14. M. Bogunovic *et al.*, *Am. J. Physiol. Gastrointest. Liver Physiol.* **292**, G1770 (2007).

10.1126/science.aau9973

ARCHAEOLOGY

Bang or whimper?

The evidence for collapse of human civilizations at the start of the recently defined Meghalayan Age is equivocal

By Guy D. Middleton^{1,2}

The International Commission on Stratigraphy recently announced the creation of a new unit in the scale of geological time, the Meghalayan Age, from 4200 years before present, or 2200 BCE, to the present. The Commission explains that this period began with a two-centuries-long megadrought that caused the collapse of civilizations in Egypt, Greece, Syria, Palestine, Mesopotamia, the Indus Valley, and the Yangtze River Valley (1). However, there is little archaeological evidence for such sudden, widespread civilizational collapse.

Since at least 1971, scientists have repeatedly argued that a major drought caused civilizational collapse at numerous locations at this time (2). Some scholars have amassed impressive amounts of data to demonstrate the existence of a megadrought and have linked this causally with civilizational collapse (3). However, detailed archaeological and historical analysis, including recent investigations of chronology and paleoclimate, suggests that rather than simultaneous civilizational collapse, different kinds of changes occurred in different parts of the world at different times, all of them less abrupt than once thought (4–9). The environmental and climatic determinism behind the megadrought-collapse narrative fails to account for specific historical circumstances, the power of human agency to drive substantial change, and the translation of environmental factors into cultural and sociopolitical contexts. Current evidence, therefore, casts doubt on the utility of 2200 BCE as a meaningful beginning to a new age in human terms, whether there was a megadrought or not.

To understand in more detail what happened around 4200 years ago, consider the situation in several of the locations for which collapse has been suggested. In Egypt, there

¹Czech Institute of Egyptology, Charles University, Prague, Czech Republic. ²School of History, Classics and Archaeology, Newcastle University, Newcastle upon Tyne, UK. Email: gdmiddletonphd@gmail.com

is evidence that the centralized power of the pharaoh in the Old Kingdom fragmented slowly into the hands of local potentates in the First Intermediate Period (2181 to 2055 BCE). However, there was no disruption to Egyptian civilization, no dark age, and no mass starvation and death (10). Contemporary tomb inscriptions such as that of the governor Ankhtifi note military exploits, demonstrating that the land could produce enough food to feed armies; non-elite tombs became more common and richer at this time. The Dialogue of Ipuwer, read by some as a factual account of drought, famine, and chaos around 2200 BCE, belongs to a class of later Middle Kingdom "pessimistic" or "lamentation" literature. Written from a rigidly aristocratic perspective, it uses the themes of chaos and disorder—really, social fluidity and mobility—as a counterpoint to an ideology that proclaimed the rightness of centralized pharaonic power and order (11).

Around the same time, the short-lived (about 100 years) Akkadian Empire in Mesopotamia also fell apart, probably due to the desire for independence of the Mesopotamian city-states. Attributing the empire's demise to the megadrought is problematic because the absolute chronology of the empire in Mesopotamia remains debated; it is possible that the empire formed during the period of the megadrought, rather than before it (12). Some sites in northern Mesopotamia were abandoned around 2200 BCE, but urban areas flourished elsewhere in the region, including Carchemish and Ebla, with researchers noting that a climate change explanation does not seem to fit the varied patterns of change over time (5). The collapse of one empire did not imply a general societal collapse of Mesopotamian city-states or Mesopotamian civilization; complex societies continued to exist uninterrupted, and even the Akkadian dynasty continued as rulers of their city.

Urbanism in northern Lebanon continued at this time, though deurbanization is apparent in the south and in the southern Levant (13). This deurbanization was a centuries-long process starting around 2500 BCE, not simultaneous with the end of the Egyptian Old Kingdom or the Akkadian collapse (6). Indus Valley deurbanization was only partial and also a long-term process, with an eastward shift of settlements and cultural continuity (7). In Greece, a land of small-scale, fairly simple societies, changes once thought sudden—the destruction of particular types of high-status houses and



The Stele of Khuivi from the First Intermediate Period in Egypt (2181 to 2055 BCE) is better considered as art and expression from a lively social milieu.

the building of new-style apsidal houses, mainly based on work at Lerna in the 1950s—are now known to have been much more gradual processes (8). In China, researchers note a number of Neolithic collapses, perhaps of chiefdoms, but these happened around 2000 rather than 2200 BCE (9). They also explain that the Henan Longshan culture did not collapse, but rather developed into the complex Erlitou state.

Overall, the archaeological and historical evidence suggests that 2200 BCE was not a threshold date and that there was no sudden, universal civilizational collapse. If there was a megadrought around 2200 BCE and after, it may be more instructive to look at how societies survived—their resilience—rather than suggesting an ancient apocalypse.

What causes the misunderstandings about past collapses? A key issue is communication. Although archaeology and history are interdisciplinary fields, they can seldom be presented in major interdisciplinary scientific journals, because the research does not usually fit into the form of scientific research papers and is difficult to present meaningfully in short articles. Key issues and developments in archaeology are thus less visible to researchers in other fields and in wider academic discourse, with discussion often remaining buried in a vast and disparate archaeological literature. Furthermore, scholars outside archaeology may assume that older or well-known ideas remain valid, but in archaeological discourse, knowledge is often provisional and contested, subject to change and questioning.

Archaeologists are making efforts to address these communication problems through interdisciplinary and outward-

facing projects. For example, the Climate Change and History Research Initiative at Princeton University draws together scholars with a range of specialisms and seeks to communicate more nuanced messages to a wider audience (14). Also, an increasing number of archaeologists combine their expertise with paleoclimatology, leading to more effective and convincing projects (15).

Even if scientists agree that the paleoclimate data indicate substantial and widespread climatic changes around 2200 BCE, accompanied by sudden, severe, and long-lasting aridification, they must be prepared to admit that many people and societies seem to have coped with it and even flourished at this time, as in Egypt. Climate change never inevitably results in societal collapse, though it can pose

serious challenges, as it does today. From an archaeological perspective, the new Late Holocene Meghalayan Age seems to have started with a whimper rather than a bang. ■

REFERENCES AND NOTES

1. The International Commission on Stratigraphy, "Collapse of civilizations worldwide defines youngest unit of the Geologic Time Scale"; stratigraphy.org.
2. B. Bell, *Am. J. Arch.* **75**, 1 (1971).
3. H. Weiss, in *Megadrought and Collapse: From Early Agriculture to Angkor*, H. Weiss, Ed. (Oxford Univ. Press, 2017), pp. 93–159.
4. K. W. Butzer, *Proc. Natl. Acad. Sci. U.S.A.* **109**, 3632 (2012).
5. C. Kuzucuoğlu, C. Marro, in *Sociétés humaines et changement climatique à la fin du troisième millénaire: une crise a-t-elle eu lieu en Haute Mésopotamie?* C. Kuzucuoğlu, C. Marro, Eds. (Institut Français d'Études Anatoliennes-Georges Dumézil, 2007), pp. 583–590.
6. F. Hoffmayer, in *2200 BC – A Climatic Breakdown as a Cause for the Collapse of the Old World?* H. Meller et al., Eds. (Landesmuseum für Vorgeschichte, 2015), pp. 113–130.
7. J. Kenoyer, in *A History of Pakistan*, R. D. Long, Ed. (Oxford Univ. Press, 2015), pp. 1–90.
8. E. Weiberg, in *Social Change in Aegean Prehistory*, C. Wiersma, S. Voutsaki, Eds. (Oxbow, 2017), pp. 32–48.
9. F. Liu, Z. Feng, *Holocene* **22**, 1181 (2012).
10. E. Morris, in *After Collapse: The Regeneration of Complex Societies*, G. M. Schwartz, J. J. Nichols, Eds. (Univ. of Arizona Press, 2006), pp. 58–71.
11. J. Moreno Garcia, in *2200 BC – A Climatic Breakdown as a Cause for the Collapse of the Old World?* H. Meller et al., Eds. (Landesmuseum für Vorgeschichte, 2015), pp. 3–16.
12. W. Sallaberger, in *Sociétés humaines et changement climatique à la fin du troisième millénaire: une crise a-t-elle eu lieu en Haute Mésopotamie?* C. Kuzucuoğlu, C. Marro, Eds. (Institut Français d'Études Anatoliennes-Georges Dumézil, 2007), pp. 417–456.
13. H. Genz, in *2200 BC – A Climatic Breakdown as a Cause for the Collapse of the Old World?* H. Meller et al., Eds. (Landesmuseum für Vorgeschichte, 2015), pp. 97–111.
14. J. Haldon et al., *Proc. Natl. Acad. Sci. U.S.A.* **115**, 3210 (2018).
15. M. Finné et al., *PLOS ONE* **12**, e0189447 (2017).

ACKNOWLEDGMENTS

I thank J. Haldon for commenting on a draft of this paper. This work was supported by the European Regional Development Fund-Project "Creativity and Adaptability as Conditions of the Success of Europe in an Interrelated World" (no. CZ.02.1.01/0.0/0.0/16_019/0000734).

10.1126/science.aau8834

BOOKS *et al.*

Conservationists in Zimbabwe work to save the pangolin, the world's most trafficked mammal.

CONSERVATION

Animal trafficking, unveiled

A nuanced treatise on illegal wildlife trade misses some opportunities to advance the conversation

By **Rosie Cooney**

In a Hanoi restaurant, a cobra lashes its body in a desperate attempt at escape while a waiter expertly slits its belly and extracts its beating heart, sending a stream of blood into a waiting vessel to the delight of the onlooking French diners. This scene hints at one of the factors that drive the illicit trade in wild species. But why is it conducted with such apparent impunity? And why have attempts to address it been so ineffective?

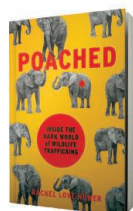
In *Poached*, Rachel Love Nuwer tackles the dynamics of this enormous, murky, and destructive trade. She tracks down wildlife sales and interviews hunters, traders, wildlife breeders, end-users, and conservationists of various stripes. The book focuses heavily on the major wildlife demand centers of Southeast Asia, supplemented by sorties to Kenya, South Africa, and Chad. Traditional Chinese medicine, the Convention on International Trade in Endangered Species of Wild Fauna and Flora (CITES), ivory burns, antipoaching efforts, wildlife farming, organized crime, and pervasive government corruption and

complicity are discussed in a likable and often humorous narrative voice, presenting perspectives and arguments on drivers of the trade and what we should be doing about it.

Poached is nuanced and sensitive. Nuwer largely avoids the simplistic trope of animal-loving Westerners condemning animal exploitation and comes to grips with the cultural attitudes, economic realities, and institutions that shape wildlife consumption. She writes with compassion, for example, of a Vietnamese father who turned to hunting to raise cash for medical treatment for his son, whom he believes is a victim of the Agent Orange bombings of the 1960s.

Poached is chattier and more personal than Vanda Felbab-Brown's recent book on the same topic, which Nuwer cites extensively (1). This makes for a compelling, lively, and highly informative read. From this standpoint, the book is a success. But in terms of elucidating some of the thorny questions underlying the disputes that dog wildlife trade policy, the book has some weaknesses.

Not infrequently, Nuwer presents questions, the answers to which are uncertain, as statements of fact. For example, the contention that allowing legal trade stimulates rather than satiates demand is sometimes presented as a given, despite the evidence on this question being scant, variable, and contested.



Poached

Rachel Love Nuwer
De Capo Press, 2018.
384 pp.

The reviewer is with the International Union for Conservation of Nature's Sustainable Use and Livelihoods Specialist Group, Gland, Switzerland, and the Fenner School of Environment and Society, Australian National University, Canberra, Australia. Email: rosie.cooney@anu.edu.au

Nuwer's discussion of CITES debates over wildlife trade is also rather one-sided. Although the text is peppered with arguments from anti-trade campaigners such as the Environmental Investigation Agency and the International Fund for Animal Welfare, she dismisses the arguments of pro-trade southern African countries and their supporters with short shrift. Given that the latter countries have successful track records of conserving elephants, rhinos, and other wildlife, their positions are worth articulating more clearly. At the heart of their argument lies the observation that legal trade in wildlife can provide tangible benefits to communities and foster broad-based community support for conservation and antipoaching.

Nuwer rightly notes that framing efforts to reduce wildlife trade as a "livelihoods issue" is used to justify unscrupulous hunting and trade. However, abuse of the term does not delegitimize the concern itself, and both legal and illegal trade are critical to poor rural people. Nuwer would have created a richer narrative with more engagement on this issue.

Likewise, the book pays little attention to the unjust political and economic trajectories and exclusionary conservation policies that have made poaching a compelling option. The voices of indigenous and local communities—those who actually live with wildlife and who will largely determine its future—are absent. This unfortunately echoes the dynamics of the global debate on illegal wildlife trade.

Despite these shortcomings, *Poached* is a thoughtful and considered portrayal of the complex illegal wildlife trade, avoiding (most of) the simplifications that pervade many treatments of the subject. ■

REFERENCE

1. V. Felbab-Brown, *The Extinction Market: Wildlife Trafficking and How to Counter It* (Oxford Univ. Press, 2017).

10.1126/science.aau7946

PODCAST

Listening to a pandemic

Stories from the 1918 flu come alive in a new podcast series

By **Heather T. Battles**

Where did the virulent virus that became the 1918 influenza pandemic first emerge and under what conditions? What made it so deadly—especially for young adults? What traces did the disease leave in art and in memory? These and many other questions are the focus of *Going Viral*, a new podcast marking the 100th anniversary of the devastating epidemic.

The program features two expert hosts: Mark Honigsbaum, a historian and Wellcome Trust Research Fellow at Queen Mary University London, and Hannah Mawdsley, a Ph.D. student conducting research on the 1918 influenza at the Imperial War Museum. The first five episodes, each approximately a half hour in duration, were released this past June and July. More are scheduled for this fall. Each episode is densely packed, reflecting the complexity and richness of the topic and the hosts' efforts to represent diverse approaches and perspectives.

The podcast is a wide-ranging, multi-disciplinary examination of the pandemic, spanning molecular research, social history, and current artistic engagements. It features an extensive series of guest appearances by virologists, microbiologists,

historians, writers, and others whose work has shaped our current understanding of the event. These include Laura Spinney, a British science journalist whose book *Pale Rider: The Spanish Flu of 1918 and How It Changed the World* was released last year, and the American virologist Jeffery Taubenberger, who coined the term "mother of all pandemics" and whose team first recovered and analyzed 1918 influenza virus RNA from preserved tissue samples.

The first two episodes detail the work of Taubenberger and others on the genetics of the virus and what made it so virulent. Episodes 3 and 4 are focused primarily on the three competing hypotheses of the geographic origins of the 1918 pandemic and include interviews with proponents for each: French origin, advocated by Queen Mary College virologist John Oxford; Kansas origin, advanced by author John Barry; and Chinese origin, argued for by historian Mark Humphries.

The series's exploration of the three competing hypotheses serves to highlight what they all have in common—namely, the conditions that set the stage for a pandemic. These include (i) a nexus of multiple species with (ii) substantial mobility in (iii) crowded, highly stressful conditions.

Throughout the series, there are fascinating glimpses of the social and cultural impacts of the pandemic. Spinney, for example, describes how the Jewish "black funeral"

ritual tradition was revived during the flu epidemic in Odessa, Ukraine. Indian-born British choreographer Shobana Jeyasingh describes a forthcoming performance inspired by the Spanish flu and explores how the pandemic was experienced outside of the West. In India, for example, the death toll reached between 18 million and 20 million.

The podcast encourages listeners to consider not just the statistics but also how the flu was experienced and subsequently remembered by those who survived it. Early flu deaths, we learn, were often classified as "purulent bronchitis" or "pneumonic plague." Only retrospectively were these cases understood to be the result of the influenza. And although the 1918 flu has been referred to as a "forgotten pandemic," the program reminds us that it was not forgotten everywhere—and certainly not by survivors. In New Zealand, for example, seven publicly accessible commemorative monuments can be found in various parts of the North and South Islands.

What makes this podcast especially compelling is the inclusion of on-location recordings and the dramatized readings from diaries and other first-person accounts. For example, in episode 3, "The Blue Death," the hosts visit the military cemetery at Étaples, the main British base in France during the war and, according to Oxford, the site of the first pandemic flu deaths. Through poignant epitaphs and the story of one soldier in particular—Private Harry Underdown, who died of "bronchitis" in 1917—they convey the deep grief and loss the disease caused. Passages from volunteer nurse Dorthea Crewdson's diary in episode 3 reveal the sense of helplessness among medical personnel at Étaples at the height of the epidemic in the autumn of 1918.

In episode 5, "Global Impacts, Local Traces," the hosts describe inscriptions made in the rock faces at the North Head quarantine station off Sydney, Australia. One records the quarantine of the R.M.S. *Niagara* and includes the ship's name, the date (October 1918), and the word "influenza" etched within the borders of a waving flag. Returning soldiers were confined at North Head for up to 3 months, we learn—a frustrating delay that nevertheless contributed to the comparatively low flu mortality reported in that country.

Ultimately, *Going Viral* succeeds in illustrating the incredible impact of epidemic disease on all facets of human life. By the end of the series, listeners will no doubt find themselves considering the conditions under which the next major pandemic might emerge and hoping for a better outcome. ■

**Going Viral
The Mother
of All Pandemics**
Hannah Mawdsley
and Mark
Honigsbaum
<http://goingviralthehop.libsyn.com>

The reviewer is at the University of Auckland, Auckland, New Zealand. Email: h.battles@auckland.ac.nz



Flu patients are treated in an Army ward in Kansas circa 1918.



LETTERS

Killer whales (*Orcinus orca*) are vulnerable to environmental pollutants.

Edited by Jennifer Sills

Pollution threatens toothed whales

In their Report “Ancient convergent losses of *Paraoxonase 1* yield potential risks for modern marine mammals” (10 August, p. 591), W. K. Meyer *et al.* show that marine mammals are particularly vulnerable to adverse health effects from organophosphorus pesticide pollution because of a functional loss of the primary mammalian metabolic defense mechanism—the *Paraoxonase 1* gene. Unfortunately, this finding is just one example of an evolutionary deficiency that puts marine mammals at increased risk for modern-day pollution.

Toothed whales, which originated in the mid-Eocene from herbivorous artiodactyls (cloven-hooved land mammals) (1), also show a reduced metabolic ability to eliminate persistent environmental pollutants such as biomagnifiable polychlorinated biphenyls (PCBs) compared with carnivorous predators such as polar bears (*Ursus maritimus*), seals and walruses, and humans (2, 3). Because they lack the ability to filter these chemicals, extreme concentrations of PCBs and mercury have been found in high trophic-feeding cetaceans, including killer whales (*Orcinus orca*) (4, 5). Moreover, toothed whales lack the keratinous pollutant sequestration routes, such as hair, that relieve carnivorous marine mammals from their contaminant burden, including mercury (5).

Given the vulnerability of marine mammals, global regulation and remediation

of harmful marine pollutants, including organophosphorus compounds and PCBs, should be urgently prioritized by the United Nations Environment Programme, the Stockholm Convention, and the U.S. Environmental Protection Agency (6, 7). Failing to protect these cetaceans could lead to pollution-mediated population collapses (8, 9) and an irreversible loss of biodiversity and ecosystem services.

Christian Sonne,^{1*} Paul D. Jepson,² Jean-Pierre Desforges,¹ Aage K. O. Alstrup,³ Morten T. Olsen,⁴ Igor Eulaers,¹ Martin Hansen,¹ Robert J. Letcher,⁵ Melissa A. McKinney,⁶ Rune Dietz¹

¹Aarhus University, Roskilde, Denmark. ²Institute of Zoology, Zoological Society of London, London, UK.

³Aarhus University, Aarhus, Denmark. ⁴University of Copenhagen, Copenhagen, Denmark. ⁵Environment and Climate Change Canada, Carleton University, Ottawa, ON, Canada. ⁶McGill University, Ste-Anne-de-Bellevue, QC, Canada.

*Corresponding author. Email: cs@bios.au.dk

REFERENCES

1. J. G. M. Thewissen *et al.*, *Nature* **450**, 20 (2007).
2. M. A. McKinney *et al.*, *Environ. Toxicol. Chem.* **30**, 7 (2011).
3. S. Kim *et al.*, *Genome Biol.* **17**, 211 (2016).
4. R. J. Letcher *et al.*, *Sci. Total Environ.* **408**, 2995 (2010).
5. R. Dietz *et al.*, *Sci. Total Environ.* **443**, 775 (2013).
6. A. M. Milner, I. L. Boyd, *Science* **357**, 1232 (2017).
7. R. J. Law, P. D. Jepson, *Science* **356**, 148 (2017).
8. P. D. Jepson, R. J. Law, *Science* **352**, 1388 (2016).
9. P. D. Jepson *et al.*, *Sci. Rep.* **6**, 18573 (2016).

10.1126/science.aav2403

Good governance for migratory species

In their Policy Forum “Preparing ocean governance for species on the move” (15 June, p. 1189), M. L. Pinsky *et al.* discuss the need to cooperatively govern fisheries affected by climate change. This idea is

not new to Pacific Island states, which supply 30% of the global tuna catch (1). The Parties to the Nauru Agreement (PNA) (2) provide a shining example of how to equitably share the benefits from fishing for skipjack tuna, which move not only among the exclusive economic zones (EEZs) of the island countries but also in response to climate (3). The PNA’s “vessel day scheme” (VDS) (4) was developed explicitly to cooperatively manage these highly migratory tuna species within the combined EEZs of the PNA members.

The cap and trade VDS sets the total annual purse-seine fishing effort at ~45,000 days (i.e., fishing by all vessels must add up to no more than the ~45,000 days mandated for the year) and allocates the days to PNA members based on the past 7 years of catch history. The VDS provides a trading mechanism among PNA members, allowing them to respond to the profound effects of the El Niño Southern Oscillation on the prime fishing grounds for skipjack tuna (3). During La Niña episodes, the best catches are made toward the west of the region (3, 5). During El Niño events, fishing is most efficient up to 4000 km to the east (5). During La Niña events, countries in the west buy days from members in the east to enable fleets to keep fishing in their EEZs. The reverse occurs during El Niño episodes. Thus, regardless of where the fish are caught, all PNA members receive license revenue. The stock for skipjack tuna has remained robust under this cooperative arrangement (6).

The VDS is also designed to govern the fishery as skipjack tuna redistribute to the east due to climate change (7, 8). Over time, PNA members located in the east

will progressively accumulate a greater catch history and receive more days. Cooperative arrangements will need to be more common as climate change drives shifts in species distribution, and the Pacific Islands are leading the way.

Transform Agorau,^{1,2,3} Johann Bell,^{3,4*}

John N. Kittinger^{4,5}

¹ITUNA Intel and Pacific Catalyst, Honiara, Solomon Islands. ²School of Government, Development, and International Affairs, University of the South Pacific, Suva, Fiji. ³Australian National Centre for Ocean Resources and Security, University of Wollongong, Wollongong, NSW 2522, Australia. ⁴Center for Oceans, Conservation International, Honolulu, HI 96825, USA. ⁵Julie Ann Wrigley Global Institute of Sustainability, Center for Biodiversity Outcomes, Arizona State University, Tempe, AZ 85281, USA.

*Corresponding author.

Email: jbell@conservation.org

REFERENCES

1. Pacific Islands Forum Fisheries Agency, "FFA economic and development indicators and statistics 2016" (2016); www.ffa.int/node/1877.
2. PNA Tuna, Nauru Agreement (2010); www.pnatuna.com/content/nauru-agreement.
3. P. Lehodey *et al.*, *Nature* **389**, 715 (1997).
4. PNA Office, Purse Seine Vessel Day Scheme (Majuro, Parties to the Nauru Agreement Office, 2011).
5. P. Lehodey *et al.*, in *Vulnerability of Tropical Pacific Fisheries and Aquaculture to Climate Change*, J. D. Bell *et al.*, Eds. (Secretariat of the Pacific Community, Noumea, New Caledonia, 2011), chap. 8.
6. Pacific Islands Forum Fisheries Agency, "Tuna fishery report card 2017" (2017); www.ffa.int/system/files/Tuna_fishery_report_card_2017.pdf.
7. J. D. Bell *et al.*, *Nat. Clim. Change* **3**, 591 (2013).
8. J. D. Bell *et al.*, in "Impacts of climate change on fisheries and aquaculture," M. Barange *et al.*, Eds. (FAO Fisheries and Aquaculture Technical Paper 627, Rome, 2018), chap. 14; www.fao.org/3/19705EN/19705en.pdf.

10.1126/science.aav2051

TECHNICAL COMMENT ABSTRACTS

Comment on "U-Th dating of carbonate crusts reveals Neandertal origin of Iberian cave art"

Ludovic Slimak, Jan Fietzke, Jean-Michel Geneste, Roberto Ontañón

Hoffmann *et al.* (Reports, 23 February 2018, p. 912) report the discovery of parietal art older than 64,800 years and attributed to Neanderthals, at least 25 millennia before the oldest parietal art ever found. Instead, critical evaluation of their geochronological data seems to provide stronger support for an age of 47,000 years, which is much more consistent with the archaeological background in hand.

Full text: [dx.doi.org/10.1126/science.aau1371](https://doi.org/10.1126/science.aau1371)

ERRATA

Erratum for the Report "Precursors of logical reasoning in preverbal human infants" by N. Cesana-Arlotti *et al.*, *Science* **361, eaav4136 (2018). Published online 21 September 2018; 10.1126/science.aav4136**

OUTSIDE THE TOWER

Science outreach in the Borneo jungle

A group of high school students at a remote school in the Borneo jungle surrounded my outreach team. They asked us to autograph their books, friend them on Facebook, and pose with them for selfies, all smiles and excitement as we set up for a farewell chemistry show 8000 km from our home in New Zealand.

Three days before, we had spent 5 hours on a boat to reach the boarding school at Balleh. The indigenous Iban students and their teachers live at the school during the week and spend only weekends with their families. Our host, a teacher training

Call for submissions

Outside the Tower is an occasional feature highlighting scientists' advocacy experiences. Submit your advocacy story at <http://cts.sciencemag.org>.

college in Kuching, had invited us to forge a partnership with the Balleh school. To make it work, we knew that we would have to overcome language and cultural barriers. Throughout the activities, we encouraged the teachers to participate by asking them to translate important words into Malay and Iban and help us with pronunciation. Although the 200 students were accustomed to book-focused lessons, we used humor and charm to encourage their participation in our hands-on activities. We showed them how to use local flowers and leaves

as pH indicators and practiced measuring skills by finding the density of liquids and preparing acetate stalagmites for a class competition.

As darkness descended on the final day, we began our show. "Oohs" and "aahs" echoed up into the night as we shared some of our favorite chemistry demonstrations. Afterward, the kids went off to bed chattering excitedly, and I sat down with the team, themselves buzzing with creative energy and already discussing plans to return next year.

This successful pilot visit marked the beginning of a 3-year partnership between the institutions. Otago volunteers learned to appreciate a variety of cultures as they worked with schools around Sarawak, the high school students experienced science and scientists in a different light, and their teachers benefited from workshops that helped them develop a new, more engaging, approach to their science teaching.

Dave Warren

Department of Chemistry, University of Otago, Dunedin, Otago 9054, New Zealand. Email: dwarren@chemistry.otago.ac.nz

10.1126/science.aat6367



Students at a boarding school in Borneo conduct hands-on science experiments.

TECHNICAL COMMENT

PALEOANTHROPOLOGY

Comment on “U-Th dating of carbonate crusts reveals Neandertal origin of Iberian cave art”

Ludovic Slimak¹, Jan Fietzke², Jean-Michel Geneste³, Roberto Ontaño⁴

Hoffmann *et al.* (Reports, 23 February 2018, p. 912) report the discovery of parietal art older than 64,800 years and attributed to Neanderthals, at least 25 millennia before the oldest parietal art ever found. Instead, critical evaluation of their geochronological data seems to provide stronger support for an age of 47,000 years, which is much more consistent with the archaeological background in hand.

Hoffmann *et al.* (1) announced the discovery of parietal art older than 64,800 years (64.8 ka). This would represent the first and only concrete evidence for such expressions in Neanderthal society. Previous U-Th dates propose to link parietal art and Neanderthal groups (2) from evidence of a red disc from El Castillo cave covered by calcite aged 40.8 ka. However, in that part of Cantabrian Spain, this date falls within the Aurignacian time scale and so could be associated with anatomically modern humans (AMH) (3, 4). Applying U-Th dating from tiny efflorescences of calcites is a relatively recent development in archaeology (2); the method still has challenges and limitations.

Before the Hoffmann *et al.* paper, the world's oldest parietal art was placed around 36 to 40 ka. Proposing a minimal age of 64.8 ka indicates a very early origin for art. This is in itself not a problem, but the lack of parietal traces for more than 25 subsequent millennia raises questions, given the rich abundance (tens of thousands of recorded examples) of more recent Paleolithic parietal art. Why would parietal art simply become invisible for such a long time, with no plausible anthropological explanation?

The proposition of the discovery of a parietal art at such an age represents a bold claim and so requires careful confirmation of the reliability of the chronology. There is no doubt about the quality of the Hoffmann *et al.* U-Th analyses. The measured isotope ratio data are of state-of-the-art quality, and the corrections applied to the age calculation are within the typical range for these kinds of studies. A question remains, however: Are those corrections sufficient to produce

robust ages, or do we find indications in the data that point toward biases in some of the calculated ages as the method reaches its limits?

The authors deserve credit for devising and applying the sequential sampling technique that tests for preservation of stratigraphic order in essentially every date published from the caves. We take a very conservative approach and cast doubt on a few of the oldest ages, not because there is evidence that they are inaccurate, but because there is not positive proof they are correct. Analyzing the U-Th data presented in that study, we do see strong support for an age of ~47 ka, but less for the ~65 ka age limit stated by the authors.

What is critical to obtain reliable ages for carbonates based on U-Th data?

1) Sample preservation/“closed system”: The carbonate has not been altered in any way after its formation. Such alterations (e.g., diagenesis/recrystallization) have been found to promote a preferential loss of uranium (5, 6), which would make a sample appear older.

2) Correction for nonradiogenic ²³⁰Th: The second point addresses the common problem that not all the ²³⁰Th measured originates from the ²³⁴U decaying since the carbonate formed. This so-called “nonradiogenic” ²³⁰Th is incorporated at the time of formation. If not corrected for, the sample again would appear to be older than it truly is. The two major sources of “non-radiogenic” ²³⁰Th are the detrital fraction and ²³⁰Th in the source water forming the carbonate. For the detrital fraction, the assumption of secular equilibrium of the ²³⁸U decay chain nuclides involved (²³⁸U, ²³⁴U, and ²³⁰Th) is typically made. The amount of detritus is estimated via ²³²Th (not affected by the ²³⁸U decay chain) and a correction factor representing the ²³⁸U/²³²Th ratio in the detrital fraction.

To evaluate the robustness of reported ages, we plot the corrected ages versus the activity ratio ²³²Th/²³⁴U (Fig. 1) of the samples overlying the respective pigment layers (minimum ages in table 1 of Hoffmann *et al.*). Although it is more common to use ²³²Th/²³⁸U, we consider ²³²Th/²³⁴U to be more appropriate in this case because of the differing initial ²³⁴U/²³⁸U ratios and the fact that for the anticipated age range, ²³⁴U (i.e., the immediate parent nuclide of ²³⁰Th) is the better representation. Because the corrections explained are based on ²³²Th, the lower the amount of ²³²Th found in a sample relative to the nuclides of the radiometric clock, the smaller the impact of any ²³²Th-based correction on the age estimate. Conventionally, a value of ~0.005 (based on a ²³⁸U/²³²Th ratio of ~200) is considered to be the upper limit for highly reliable ages. Additionally, a high ²³⁸U/²³²Th ratio supports, but does not guarantee, the assumption of closed-system behavior, as it makes strong uranium loss appear less probable.

In Fig. 1, we find most of the Ardales samples meeting the criterion of low ²³²Th/²³⁴U clustering closely (highlighted by the green ellipse), indicating an upper limit of minimum carbonate formation age of ~47 ka. This age is additionally supported by the lower limit of maximum age

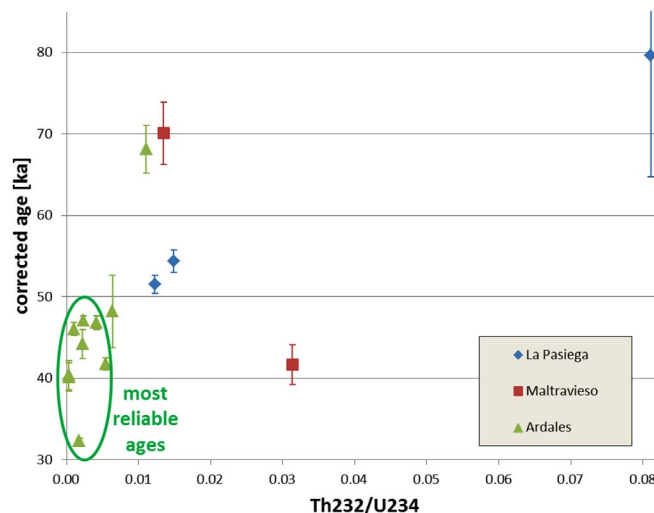


Fig. 1. Minimum U-Th age data from Hoffmann *et al.* (1) versus the activity ratio ²³²Th/²³⁴U, taken as age reliability indicator. Higher ²³²Th/²³⁴U ratios increase the impact of ²³²Th-based corrections on the calculated age. All uncertainties are at 95% confidence level.

¹CNRS UMR 5608 TRACES, Université Toulouse Jean Jaurès, Maison de la Recherche, 31058 Toulouse Cedex 9, France.

²GEOMAR Helmholtz Centre for Ocean Research Kiel, 24148 Kiel, Germany. ³Chauvet Cave Research Group, CNRS UMR 5199 PACEA, La Mouthe Basse, 24620 Les Eyzies, France.

⁴Museum of Prehistory and Archeology of Cantabria, Prehistoric Caves of Cantabria, International Institute of Prehistoric Research of Cantabria, 39009 Santander, Spain.

*Corresponding author. Email: slimak@univ-tlse2.fr

estimated (47.6 ka) from carbonate underneath the pigment layer. The one older-appearing sample (68.1 ka) has a higher $^{232}\text{Th}/^{234}\text{U}$ ratio. It is accompanied by another sample from the exact same site dated at 47.1 ka, which by contrast meets the $^{232}\text{Th}/^{234}\text{U}$ reliability criterion. Thus, we consider a minimum age of ~47 ka very well constrained by dating of multiple samples. For now, any older limit for a minimum age solely depends on the robustness of the one sample dated 68.1 ka. Although it is entirely possible that the sample is providing a correct age estimate, we also need to consider that a single sample standing out from a larger group could indicate problems of this sample's preservation ("open system").

The three La Pasiega PAS34 subsamples have elevated $^{232}\text{Th}/^{234}\text{U}$ relative to the cluster of Ardales samples considered most reliable. Additionally, $^{230}\text{Th}/^{234}\text{U}$, the activity ratio carrying the chronological information, is correlated to $^{232}\text{Th}/^{234}\text{U}$; that is, the subsamples are becoming older with increasing $^{232}\text{Th}/^{234}\text{U}$, indicating possible varying contributions of nonradiogenic ^{230}Th . The authors test different correction factors in their supplementary materials. The age presented in the main text has been obtained using the lowest correction factor (0.8). When applying a slightly higher correction factor (2.0), the age estimate for sample PAS34c is shifted from 79.7 ± 14.9 ka toward 69.9 ± 25.2 ka.

Alternatively, we could consider the whole PAS34 calcite to have been formed in a relatively short period. The trend of $^{230}\text{Th}/^{234}\text{U}$ versus $^{232}\text{Th}/^{234}\text{U}$ could be interpreted as a mixing line between the radiogenic and nonradiogenic

^{230}Th phases. Extrapolating toward the radiogenic endmember ($^{232}\text{Th}/^{234}\text{U} = 0$) results in a combined age of <50 ka for all three subsamples of PAS34, with a nonradiogenic end-member $^{230}\text{Th}/^{232}\text{Th}$ between 2.2 (based on $^{238}\text{U}/^{232}\text{Th}$) and 2.8 (based on $^{234}\text{U}/^{232}\text{Th}$). This correction value is higher than the "bulk earth" value of 0.8 used by the authors, but is still lower than what has been used, e.g., for the Maltravieso samples (3.3 ± 0.2 based on measurements of local sediments). The low $^{238}\text{U}/^{232}\text{Th}$ ratio (3.6) and the strong impact of the applied correction both challenge the age estimated for sample PAS34c. The exact age calculated for PAS34 depends on the correction applied, allowing for a range of approximately 47 to 54 ka.

Like the La Pasiega PAS34 samples, those from Maltravieso also display elevated $^{232}\text{Th}/^{234}\text{U}$ ratios. The range of ages obtained for Maltravieso (supplementary materials of Hoffmann *et al.*), while sampled at close proximity to each other, challenges the reliability of the MAL13A age estimate of ~70 ka. It is a single sample standing out from a larger group of samples providing highly reliable ($^{232}\text{Th}/^{234}\text{U} < 0.005$) and younger ages. Again, we cannot prove that the sample MAL13A has been altered to appear older ("open system"), nor can we clearly rule out such a scenario.

It is noteworthy that Maltravieso and La Pasiega, which appear as the less reliable in terms of U-Th measures, represent the oldest and also archaeologically the only true parietal expressions of graphic categories that have direct comparisons with classic Upper Paleolithic parietal expressions, whereas Ardales concerns

speleothems simply covered with red deposits, with no representation. Closer analyses of these red deposits will be needed to demonstrate their anthropogenic origin. If anthropogenic, these parietal deposits would then represent the strongest and oldest evidence for a parietal "art." At the Ardales chronology, ~47 ka ago, there is no anthropological evidence of AMH in the Iberian Peninsula and more largely in Europe. Only two transitional Paleolithic industries—the Bohunician from Bohunice in central Europe (7) and the Neronian from Mandrin in Mediterranean France, dated ~50 ka (3)—could possibly reveal an earlier AMH presence in Europe, but they have provided for the moment no hominin remains. In that context, Ardales might well indicate that in a more recent period than stated by Hoffmann *et al.*, some late Neanderthal societies may well have produced some parietal traces.

REFERENCES AND NOTES

1. D. L. Hoffmann *et al.*, *Science* **359**, 912–915 (2018).
2. A. W. G. Pike *et al.*, *Science* **336**, 1409–1413 (2012).
3. T. Higham *et al.*, *Nature* **512**, 306–309 (2014).
4. A. B. Marin-Arroyo *et al.*, *PLOS ONE* **13**, e0194708 (2018).
5. J. Osmond, M. Ivanovich, in *Uranium-Series Disequilibrium: Applications to Earth, Marine and Environmental Sciences*, M. Ivanovich, R. S. Harmon, Eds. (Clarendon, 1992), pp. 259–289.
6. D. A. Richards, J. A. Dorale, *Rev. Mineral. Geochem.* **52**, 407–460 (2003).
7. D. Richter, G. Tostevin, P. Skrdla, *J. Hum. Evol.* **55**, 871–885 (2008).

ACKNOWLEDGMENTS

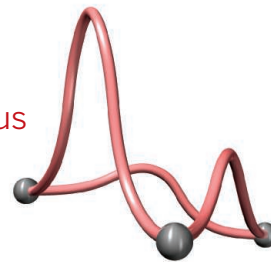
Preparation of this comment benefited from detailed and constructive discussions with W. D. Sharp.

11 May 2018; accepted 28 August 2018
10.1126/science.aau1371

RESEARCH

Building robust porous aromatic molecules

Yamagishi et al., p. 1242



IN SCIENCE JOURNALS

Edited by **Stella Hurtley**

APPLIED ECOLOGY

Using DNA to dissect the ivory trade

The African elephant ivory trade is a multibillion dollar industry linked to the deaths of up to 40,000 elephants each year. Wasser *et al.* used DNA-based tools to identify the major exporters that smuggle ivory out of Africa. They sampled 38 seizures between 2006 and 2015 to distinguish the patterns and occurrences of tusks that came from the same elephant but had been shipped separately. Of the samples, 28 were considered a match, suggesting that tusks from the same elephant are often shipped by the same trafficker in separate shipments. Analysis of the seizure connections revealed three major export networks. Almost all matched seizures passed through a common port within 10 months of one another. —PJB

Sci. Adv. 10.1126/sciadv.aat0625 (2018).



Exploiting tusk DNA to help investigate illegal ivory shipments

PUBLIC HEALTH

Analyzing the drug abuse epidemic

There is a developing drug epidemic in the United States. Jalal *et al.* analyzed nearly 600,000 unintentional drug overdoses over a 38-year period. Although the overall mortality rate closely followed an exponential growth curve, the pattern itself is a composite of several underlying subepidemics of different drugs. Geographic hotspots have

developed over time, as well as drug-specific demographic differences. —BJ

Science, this issue p. 1218

CHEMISTRY

A self-optimizing reactor

Chemists spend a great deal of time tweaking the conditions of known reactions. Small changes to temperature and concentration can have a big influence over product yield. Bédard *et al.* present a flow-based reaction

platform that carries out this laborious task automatically. By using feedback from integrated analytics, the system converges on optimal conditions that can then be applied with high precision afterward. A series of modules with heating, cooling, mixing, and photochemical capabilities could be configured for a broad range of reactions. These include homogeneous and heterogeneous palladium-catalyzed cross-coupling, reductive amination, and the generation of

sensitive intermediates under an inert atmosphere. —JSY

Science, this issue p. 1220

ASTEROSEISMOLOGY

Stellar oscillations show differential rotation

The Sun rotates faster at its equator than at its poles. This process is known as differential rotation and is seen in the motion of sunspots. Helioseismology has shown that

the effect extends into the Sun's interior. It has not been possible to measure whether other stars also experience equivalent differential rotation. Benomar *et al.* used the Kepler spacecraft to monitor stellar oscillations of a group of Sun-like stars. By decomposing the oscillations into separate frequencies, they searched for signs of differential rotation. Several stars do indeed seem to have equators that spin faster than their poles, and none indicated the opposite pattern. —KTS

Science, this issue p. 1231

APPLIED OPTICS

Taming laser instabilities

Broad-area and high-power lasers often suffer from instabilities owing to the chaotic interference of multiple modes within the cavity. Such instabilities can ultimately limit the operation of the laser or damage the cavity. The usual approach to minimizing such instabilities is to limit the number of modes in the cavity. Bittner *et al.* designed a chaotic cavity that disrupts the formation of self-organized structures that lead to instabilities (see the Perspective by Yang). This approach of fighting chaos with chaos by using the boundary condition of the cavity shape may provide a robust route to stabilizing lasers at high operating powers. —ISO

Science, this issue p. 1225;
see also p. 1201

MAMMALIAN EVOLUTION

Early shifts lead to big changes

Mammals represent one of the most morphologically diverse taxonomic groups. One of the unique features underlying this diversity is variability of the spine, which facilitates everything from flexibility for speedy running and support for upright walking. Jones *et al.* studied a group ancestral to modern mammals—nonmammalian synapsids, or mammal-like reptiles. As forelimb function diversified,

the spine developed distinct regions. These regions then differentiated further, leading to the highly varied mammalian forms we see today. —SNV

Science, this issue p. 1249

BIOTECHNOLOGY

Expanding the targeting space of Cas9

CRISPR-Cas9 associates with a guide RNA to target and cleave a specific DNA site next to a protospacer adjacent motif (PAM). *Streptococcus pyogenes* Cas9 (SpCas9), the one most often used for genome editing, only recognizes the NGG sequence (where N is any nucleobase) as the PAM, which restricts regions in the genome that can be targeted. To address this limitation, Nishimasu *et al.* created a SpCas9 variant that recognizes NG rather than NGG. The SpCas9-NG variant increased the targeting range, had a specificity similar to that of the wild-type enzyme, and could be used with a base editor. Thus, SpCas9-NG is a powerful addition to the CRISPR-Cas9 genome engineering toolbox and will be useful in a broad range of applications, from basic research to clinical therapeutics. —SYM

Science, this issue p. 1259

SMART PROSTHETICS

Once more, with feeling

For prosthetics to be as natural and functional as possible, they need to replace lost sensing. Wu *et al.* developed a small, scalable sensor that converts applied pressure into pulses of corresponding frequency, conveying information in a way our brains can understand. Shaped like a tiny, flexible, hollow hockey puck, the sensor measures the change in magnetic impedance when the top of the puck is pressed. The sensor has a low detection limit and high sensitivity and shows stable-frequency pulse generation at a pressure lower than the sensing threshold of human skin. —RLK

Sci. Robot. **3**, eaat0429 (2018).

IN OTHER JOURNALS

Edited by **Sacha Vignieri**
and **Jesse Smith**



MATERIALS SCIENCE

Antibiotic screening via membrane disruption

Some antibiotics destroy harmful bacteria by disrupting their membranes. Pitsalidis *et al.* used a monolayer of lipids as an analog for the membrane in a device designed to measure membrane destruction. The layer is tethered to the surface of an organic electrochemical transducer, where it forms an insulating barrier. The introduction of an antibiotic, such as polymyxin B, disrupts the phospholipids, causing a flux of ions that can be measured as an electrical signal. The authors show that their device can discern molecular-scale differences in the disruption capabilities of two amine-based oligothioetheramide isomers that show a fivefold difference in antibacterial activity. Thus,

their device may find use as a tool to screen for new antibiotics. —MSL

Adv. Mater. 10.1002/adma.201803130
(2018).

KIDNEY DISEASE

A metabolite that reduces kidney injury

Of critically ill patients, 3 to 10% experience acute kidney injury (AKI), a potentially fatal complication caused by severe metabolic stress arising from restricted blood flow to the kidneys. Currently, there is no specific treatment for AKI. By analyzing urinary metabolites from mice and cardiac surgery patients who developed AKI, Poyan Mehr *et al.* showed that nicotinamide adenine dinucleotide (NAD⁺) biogenesis was impaired during AKI. Mice with heterozygous deletion for quinolinate phosphoribosyltransferase,

MAMMALIAN PHYSIOLOGY

Plasticity pow!

Mammals are known for being homeothermic, but by reducing metabolic rate and other activities, mammals that hibernate can greatly decrease their body temperature and still survive. Treat *et al.* found that Malagasy common tenrecs have a remarkable degree of physiological plasticity with respect to body temperature—some individuals hibernate at normal body temperatures, some are active at unusually low body temperatures, and others fall at many points in-between. They further found that oxygen consumption by tenrecs could vary by 25-fold and that their heart rates could decrease by 34% during hibernation with no change in oxygen consumption. Even pregnancy occurs at varying temperatures. Yet, the species is highly susceptible to temperature extremes, suggesting that although such plasticity presents advantages in moderate temperatures, it may be a limiting factor in adaptation to extremes. —SNV
J. Exp. Biol. 10.1242/jeb.185900 (2018).

Tenrecs show remarkable variance in body temperature.

an enzyme involved in NAD⁺ biogenesis, were more susceptible to AKI. In a phase 1 clinical trial, supplementation of the NAD⁺-precursor nicotinamide was safe and reduced incidences of AKI in cardiac surgery patients. NAD⁺ metabolism could be exploited both as a urinary biomarker and as a treatment intervention to reduce incidences of AKI. —MY
Nat. Med. **24**, 1351 (2018).

HOST-GUEST CHEMISTRY
Cagey coordination

Carefully chosen ratios of metal ions and bridging ligands form a wide variety of polyhedral cages in solution. Chemists often have tuned the geometry and polarity of these cages to accommodate particular molecular guests. Rizzuto *et al.* report a pair of larger cages that, in a similar vein, stabilize unusual coordination complexes. An initial cage

with rhodium and cadmium nodes accommodated a cadmium complex coordinated by five pyrazine ligands and a water molecule. An expanded cage assembled from zinc porphyrins accommodated a rotaxane, a macrocycle threaded on an axle coordinated to the cage walls. —JSY
J. Am. Chem. Soc. **140**, 11502 (2018).

GALAXIES

A tidal tussle between M31 and M33

The three largest galaxies in the Local Group are the Andromeda Galaxy (M31), our own Milky Way, and the Triangulum Galaxy (M33). The morphology of M33 has led to suggestions that it recently passed close to M31, but simulations have struggled to reproduce the observed properties. Senczuk *et al.* constructed a simulated

close approach between M33 and M31. They reproduced the number and angle of M33's prominent spiral arms, the warp in its disc, its rotation rate, and more. The model is not uniquely required by the observations but demonstrates that M33's current appearance could plausibly have been generated by tidal interactions with M31. —KTS
Astrophys. J. **864**, 34 (2018).

BACTERIAL IMMUNITY
Anti-CRISPR RNA?

Bacteria use the CRISPR-Cas immune system to fend off viruses; viruses use anti-CRISPR proteins to fight back. Some bacteria have acquired anti-CRISPR proteins in their genomes to avoid self-cutting. Meeske and Marraffini report the intriguing possibility that bacteria might also use RNA to inhibit CRISPR-Cas enzymes. Cas13, the effector of the type VI CRISPR-Cas system, is directed by guide RNA to cleave target RNA in cis, which further unleashes its indiscriminate trans RNA-cutting activity. However, extended complementarity between guide and target RNAs locks Cas13 into an inactive state, which prevents both cis and trans cleavage, suggesting an endogenous RNA-based

mechanism to regulate Cas13. Cas13 is a powerful tool because of its ability to detect and manipulate RNA. The discovery of "anti-CRISPR RNA" has the potential to diversify and expand Cas13's applications. —SYM
Mol. Cell. **71**, 791 (2018).

IMMUNOLOGY
Unlucky devils

Devil facial tumor 1 (DFT1) is a transmissible cancer that has devastated the Tasmanian devil population since it emerged in the 1990s. By losing major histocompatibility class I (MHC I) molecules, DFT1 cells have been able to evade detection as foreign by the host immune system. More recently, a second contagious cancer (DFT2) has emerged, further hampering efforts to preserve this species. Caldwell *et al.* report that DFT2 cells still express MHC I, but the cancer can spread because its most commonly expressed MHC I variants are either nonclassical or shared with host animals. Additionally, heterogenic MHC I expression in DFT2 tumors suggests that expression is not fixed and may gradually be lost, which may have devastating consequences for an already vulnerable population. —STS
eLife **7**, e35314 (2018).



The morphology of the spiral arms of the Triangulum Galaxy, M33, was affected by a close pass with another nearby galaxy, M31.

ALSO IN SCIENCE JOURNALS

Edited by Stella Hurtley

SOLAR CELLS

The road ahead for perovskites

The high power conversion efficiencies of small-area perovskite solar cells (PSCs) have driven interest in the development of commercial devices. Rong *et al.* review recent progress in addressing stability, how to allow mass production, and how to maintain uniformity of large-area films. They note that lifetimes exceeding 10,000 hours under 1 sun (1 kW/m²) illumination have been reported for printable triple mesoscopic PSCs. —PDS

Science, this issue p. 1214

MICROBIOTA

Interspecies competition shapes communities

The gut microbiota of mammals is diverse and dynamic, and gut bacteria respond sensitively to diet and drug intake. Nevertheless, in a healthy adult, microbial community composition remains remarkably stable over time, despite being highly individual. García-Bayona and Comstock review the mechanisms that gut bacterial species use to jostle for space and resources and maintain their populations in the face of intense and varied competition. Bacteria have evolved a range of antibiotics, bacteriocins, toxins, and delivery devices to enable interspecies conflict. These interbacterial weapons possess a spectrum of specificities and range from those that target strains of their own species to broad-acting bacteriocides. This toxic armamentarium provides a valuable resource for potential therapeutic development. —CA

Science, this issue p. 1215

PATTERN FORMATION

How birds change their stripes

From stripes to spots, animals often exhibit periodic coloration. Discrete embryonic domains (prepatterns) precede the periodic feather patterns observed in birds. After documenting natural variation in the striped pattern of galliform birds, Haupaix *et al.* performed long-term skin grafts to transfer the pattern of one species to another (see the Perspective by Prud'homme and Gompel). This approach revealed that periodic stripe formation obeys developmental landmarks upstream of local refining mechanisms. The somitic mesoderm first instructs stripe position through the early expression of the pigmentation gene *agouti*, which then controls stripe width by modulating pigment production in a dose-dependent manner. Thus, during feather patterning, a two-step process is at play. —BAP

Science, this issue p. 1216;

see also p. 1202

SYNTHETIC BIOLOGY

Building smarter synthetic biological circuits

Synthetic genetic and biological regulatory circuits can enable logic functions to form the basis of biological computing; synthetic biology can also be used to control cell behaviors (see the Perspective by Glass and Alon). Andrews *et al.* used mathematical models and computer algorithms to combine standardized components and build programmable genetic sequential logic circuits. Such circuits can perform regulatory functions much like the biological checkpoint circuits of living cells. Circuits composed of interacting proteins could be used to bypass gene regulation, interfacing directly with cellular pathways without genome

modification. Gao *et al.* engineered proteases that regulate one another, respond to diverse inputs that include oncogene activation, process signals, and conditionally activate responses such as those leading to cell death. This platform should facilitate development of "smart" therapeutic circuits for future biomedical applications. —LBR

Science, this issue p. 1217, p. 1252;

see also p. 1199

NEUROSCIENCE

Dissecting the gut-brain axis

It is generally believed that cells in the gut transduce sensory information through the paracrine action of hormones. Kaelberer *et al.* found that, in addition to the well-described classical paracrine transduction, enteroendocrine cells also form fast, excitatory synapses with vagal afferents (see the Perspective by Hoffman and Lumpkin). This more direct circuit for gut-brain signaling uses glutamate as a neurotransmitter. Thus, sensory cues that stimulate the gut could potentially be manipulated to influence specific brain functions and behavior, including those linked to food choices. —PRS

Science, this issue p. 1219;

see also p. 1203

ORGANIC CHEMISTRY

A swift citrusy path to chiral phosphorus

The phosphates in the backbones of DNA and RNA are often drawn like crosses but are in fact tetrahedral. Sulfur is sometimes substituted for one of the phosphate oxygens during development of nucleotide-based drugs. Because of the geometry, this swap can lead to two different isomers. Knouse *et al.* report a pair of phosphorus reagents that conveniently produce either

isomer selectively. This ability depended on the configuration of appended limonene substituents that are subsequently jettisoned. In addition to simplifying the route to sulfur-substituted oligonucleotides, these reagents will enable more precise studies of each isomer's distinct bioactivity. —JSY

Science, this issue p. 1234

QUANTUM ELECTRONICS

Counting the state of a qubit

Operation of a quantum computer will be reliant on the ability to correct errors. This will typically require the fast, high-fidelity quantum nondemolition measurement of a large number of qubits. Opremcak *et al.* describe a method that uses a photon counter to determine the state of a superconducting qubit. Being able to simply read out the qubit state as a photon number removes the need for bulky components and large experimental overhead that characterizes present approaches. —ISO

Science, this issue p. 1239

MICROPOROUS CRYSTALS

Robust assembly of aromatic molecules

Organic materials can exhibit high porosity, but the structures often collapse or decompose at high temperatures. Yamagishi *et al.* synthesized an aromatic molecule that bears a symmetrical outer shell of three dipyritylphenyl wedges and crystallized it from highly dielectric solvents. Porous crystals formed with complex pore-wall structures that resulted from labile C—H...N bonds and van der Waals forces. Despite the weakness of these interactions, the porous structure was stable up to 202°C and could be recovered after collapse by exposure to solvent vapor. —PDS

Science, this issue p. 1242

EARLY ANIMALS**Confirming the identity of early animals**

The first complex organisms emerged during the Ediacaran period, around 600 million years ago. The taxonomic affiliation of many of these organisms has been difficult to discern. Fossils of *Dickinsonia*, bilaterally symmetrical oval organisms, have been particularly difficult to classify. Bobrovskiy *et al.* conducted an analysis using lipid biomarkers obtained from *Dickinsonia* fossils and found that the fossils contained almost exclusively cholesterol, a marker found only in animals (see the Perspective by Summons and Erwin). Thus, *Dickinsonia* were basal animals. This supports the idea that the Ediacaran biota may have been a precursor to the explosion of animal forms later observed in the Cambrian, about 500 million years ago. —SNV

Science, this issue p. 1246;
see also p. 1198

GPCR SIGNALING**Receptor dynamics predict drug effects**

The effect of a drug on a G protein-coupled receptor (GPCR) can be determined by monitoring the downstream effects of that receptor, but not for GPCRs whose signaling pathways are unclear. Yanagawa *et al.* performed single-molecule imaging of different GPCRs in the plasma membrane. They found that the diffusion dynamics correlated with whether the interacting drug activated or inhibited the receptor, resulted in the coupling of GPCRs to G proteins, or induced receptor endocytosis. Thus, analyzing the diffusion of a GPCR provides an estimate for the effect of a candidate drug. —JFF

Sci. Signal. **11**, eaao1917 (2018).

ALZHEIMER'S DISEASE**Getting back to BACE1s**

Drugs that block the β -secretase BACE1 are in clinical trials for treatment of Alzheimer's disease. However, their safety is unclear because mice lacking BACE1 exhibit neurological phenotypes. Ou-Yang *et al.* generated conditional BACE1 knockout mice in which the *Bace1* gene was only ablated in the mature adult animal. Although these conditional adult BACE1 knockout mice largely lacked the phenotypes observed in germline knockout animals, they did exhibit a *Bace1*-null phenotype—disorganization of an axonal pathway in the hippocampus, a brain region critical for memory. Thus, BACE1 inhibitors could potentially disturb hippocampal axonal pathways. —OMS

Sci. Transl. Med. **10**, eaao5620 (2018).

REVIEW SUMMARY

SOLAR CELLS

Challenges for commercializing perovskite solar cells

Yaoguang Rong*, Yue Hu*, Anyi Mei*, Hairen Tan, Makhsud I. Saidaminov, Sang Il Seok†, Michael D. McGehee†, Edward H. Sargent†, Hongwei Han†

BACKGROUND: Perovskite solar cells (PSCs) have attracted intensive attention because of their ever-increasing power conversion efficiency (PCE), low-cost materials constituents, and simple solution fabrication process. Initiated in 2009 with an efficiency of 3.8%, PSCs have now achieved a lab-scale power conversion efficiency of 23.3%, rivaling the performance of commercial multicrystalline silicon solar cells, as well as copper indium gallium selenide (CIGS) and cadmium telluride (CdTe) thin-film solar cells. Thousands of articles related to PSCs have been published each year since 2015, highlighting PSCs as a topic of intense interest in photovoltaics (PV) research. With high efficiencies achieved in lab devices, stability and remaining challenges in upscaling the manufacture of PSCs are two critical concerns that must be addressed on the path to PSC commercialization.

ADVANCES: We review recent progress in PSCs and discuss the remaining challenges along the pathway to their commercialization. Device configurations of PSCs (see the figure) include mesoscopic formal (n-i-p) and inverted (p-i-n) structures, planar formal and inverted structures, and the printable triple mesoscopic structures. PCEs of devices that use these structures

have advanced rapidly in the case of small-area devices ($\sim 0.1 \text{ cm}^2$). PSCs are also attracting attention as top cells for the construction of tandem solar cells with existing mature PV technologies to increase efficiency beyond the Shockley-Queisser limit of single-junction devices.

The stability of PSCs has attracted much well-deserved attention of late, and notable progress has been made in the past few years. PSCs have recently achieved exhibited lifetimes of 10,000 hours under 1 sun (1 kW/m^2) illumination with an ultraviolet filter at a stabilized temperature of 55°C and at short-circuit conditions for a printable triple mesoscopic PSCs. This irradiation is equivalent to the total irradiation of 10 years of outdoor use in most of Europe. However, within the PSC community, standard testing protocols require further development. In addition, transparency in reporting standards on stability tests needs to be improved; this can be achieved by providing both initial photovoltaic performance and normalization parameters.

The upscaling of PSCs has also progressed steadily, leading to PSC mini-modules, standard-sized modules, and power systems. PV companies have set out to manufacture large-area PSC modules (see the figure), and a 110-m^2 perovskite PV system with screen-printed triple

mesoscopic PSC modules was recently debuted. Studies of these increased-area modules and systems will promote the development of PSCs toward commercialization. PSC research is expanding to cover fundamental topics on materials and lab-sized cells, as well as to address issues of industrial-scale manufacturing and deployment.

OUTLOOK: The PV market has been continuously expanding in recent years, bringing opportunities for new PV technologies of which PSCs are promising candidates. It is imperative to achieve a low cost per watt, which means

that both efficiency and lifetime need improvement relative to current parameters. The efficiency gap between lab cells and industrial modules has seen impressive reductions in

ON OUR WEBSITE

Read the full article at <http://dx.doi.org/10.1126/science.aat8235>

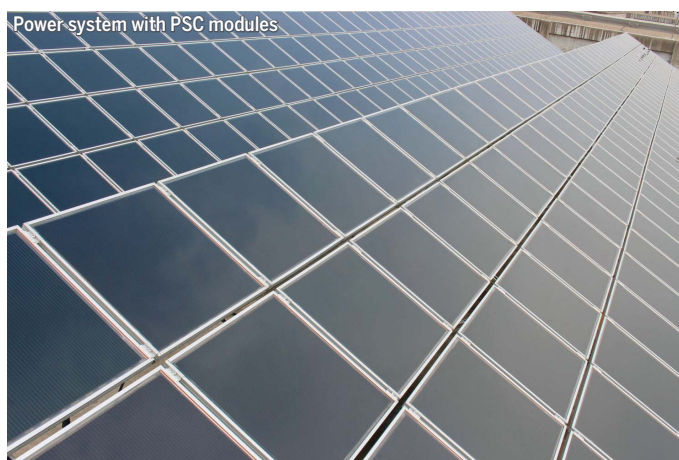
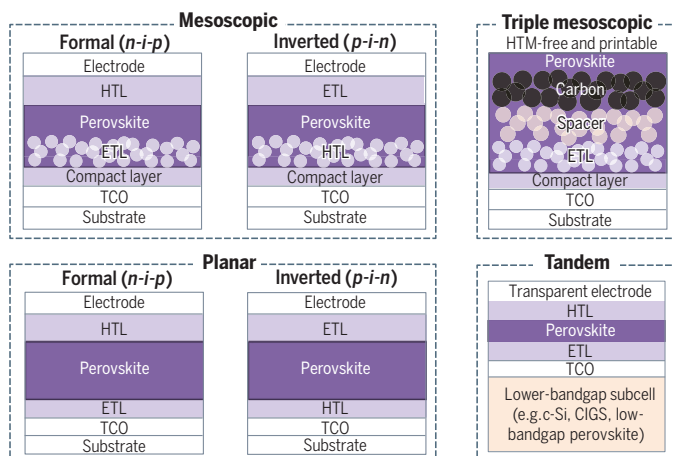
crystalline silicon; PSCs must similarly enlarge module areas to the panel level and need to achieve lifetimes comparable to those of legacy PV technologies. Other improvements will need to include industry-scale electronic-grade films, recycling methods to address concerns regarding lead toxicity, and the adoption of standardized testing protocols to predict the operation lifetime of PSCs. Modules will need to endure light-induced degradation, potential-induced degradation, partial-shade stress, and mechanical shock. The field can benefit from lessons learned during the development of mature PV technologies as it strives to define, and overcome, the hurdles to PSC commercial impact. ■

The list of author affiliations is available in the full article online.

*These authors contributed equally to this work.

†Corresponding author. Email: hongwei.han@mail.hust.edu.cn (H.H.); ted.sargent@utoronto.ca (E.H.S.); michael.mcgehee@colorado.edu (M.D.M.); seoksi@unist.ac.kr (S.I.S.)

Cite this article as Y. Rong et al., *Science* **361**, eaat8235 (2018). DOI: 10.1126/science.aat8235



Configurations and application demonstration of PSCs. PSCs have been developed in various device configurations, including mesoscopic, planar, triple mesoscopic, and tandem structures. Recently, a 110-m^2 perovskite PV system with printable triple mesoscopic PSC modules (3600 cm^2 for each) was launched by WonderSolar in China.

REVIEW

SOLAR CELLS

Challenges for commercializing perovskite solar cells

Yaoguang Rong^{1*}, Yue Hu^{1*}, Anyi Mei^{1,2*}, Hairen Tan^{2,3}, Makhud I. Saidaminov², Sang Il Seok^{4†}, Michael D. McGehee^{5†}, Edward H. Sargent^{2†}, Hongwei Han^{1†}

Perovskite solar cells (PSCs) have witnessed rapidly rising power conversion efficiencies, together with advances in stability and upscaling. Despite these advances, their limited stability and need to prove upscaling remain crucial hurdles on the path to commercialization. We summarize recent advances toward commercially viable PSCs and discuss challenges that remain. We expound the development of standardized protocols to distinguish intrinsic and extrinsic degradation factors in perovskites. We review accelerated aging tests in both cells and modules and discuss the prediction of lifetimes on the basis of degradation kinetics. Mature photovoltaic solutions, which have demonstrated excellent long-term stability in field applications, offer the perovskite community valuable insights into clearing the hurdles to commercialization.

Hybrid organic-inorganic perovskite solar cells (PSCs) have recently emerged as a promising photovoltaic (PV) candidate (1). Perovskites have a general chemical formula of AMX_3 , in which the M metallic cations and X anions form MX_6^{4-} octahedra with A cations occupying the 12-fold coordinated holes within the cavity. These materials exhibit desirable optical-electrical properties for PV devices, such as suitable and tunable bandgap, strong optical absorption, long carrier diffusion length, and high defect tolerance (2). The record-certified power conversion efficiency (PCE) of PSCs has recently risen to 23.3% (3–6) for a small-area device ($\sim 0.09 \text{ cm}^2$) whose active area is well below that of standard commercial crystalline silicon solar cells. Perovskite films are made using solution-based fabrication and are composed of earth-abundant materials (7) (Fig. 1A), but the most efficient devices rely on costly gold and organic hole-transport materials (HTMs) such as 2,2',7,7'-tetrakis(*N,N*-di-*p*-methoxy-phenylamine)-9,9'-spirobifluorene (spiro-OMeTAD).

Although the potential for low-cost PSCs offers a promising prospect for commercializing this PV technology, a complex interplay has unfolded between the pursuit of high efficiency and other commercially viable aspects, such as long-term stability and scale-up manufacturing. This Review aims to provide an overview of recent progress toward the commercialization of PSCs.

Device configurations and performance

PSCs have a layered device structure that includes a transparent conductive oxide (TCO)-coated glass substrate, an n-type semiconductor as the electron-transport layer (ETL), a perovskite absorber layer, a p-type semiconductor as the hole-transport layer (HTL), and a back-contact (metal, TCO, or carbon) (Fig. 1B). In mesoscopic PSCs developed after investigations of dye-sensitized solar cells, the perovskite absorber sensitizes a mesoporous metal oxide layer (e.g., *meso*- TiO_2) used as a scaffold (3, 8). In planar PSCs, the perovskite layer is sandwiched between a planar ETL [e.g., compact TiO_2 (*c*- TiO_2), SnO_2 , or C_{60} and its derivatives] and an HTL [e.g., spiro-OMeTAD, poly(triarylamine) (PTAA), and poly(3,4-ethylenedioxythiophene)-poly(styrenesulfonate) (PEDOT:PSS)] (9–12). Depending on the sequence of depositing the ETL and HTL, the structure can be divided into formal (conventional) versus inverted architectures (13, 14). Notably, the design and fabrication of inverted devices is not a simple reversal from the formal device structure, and the two device structures typically require systematic development of suitable ETLs and HTLs, especially in light of the restrictions in the suitability of processing solvents. In triple mesoscopic PSCs, the perovskite is deposited on a triple-layer scaffold, made of a screen-printed mesoporous TiO_2 layer, a ZrO_2 spacer layer, and a carbon electrode (15, 16). Such devices use carbon electrodes to replace the noble metal back-contacts and do not require a hole-conducting layer.

The prospects of PSCs as a top-cell for constructing tandem solar cells with other PV devices—such as silicon (17), copper indium gallium selenide (CIGS) (18), and low-bandgap perovskites (19)—have been reviewed elsewhere (20). Partnership with existing mature PV technologies not only boosts their efficiency beyond the Shockley-Queisser limit of single-junction devices (21) but also provides access to established market channels (22).

Progress in the efficiency of single-junction PSCs is summarized in Fig. 1C (3–6, 11, 15, 23–35). The perovskite layer and charge-transporting layers are typically deposited by spin coating for small-area ($<1.0 \text{ cm}^2$) lab cells. Enlarging the device area with current techniques to fabricate PSC modules leads to a decrease in PCE of all device structures (8, 9, 36–45). Screen printing, slot-die coating, spray coating, and soft-cover coating methods have been developed to fabricate intermediate-sized PSC modules on the scale of tens of square centimeters (46). Alternative processing strategies must be explored to achieve large-area uniform films and efficient materials utilization.

Ohmic loss due to resistance from the front transparent electrode must also be reduced. The conductivity of FTO films can, in principle, be enhanced by increasing the thickness, but this will decrease its transparency. Depositing conductive grids and/or constructing interconnected unit cells can be used to reduce resistance in large-area modules at some sacrifice to the active area of the modules (47). Geometrical fill factor [(GFF), the ratio between the active area and the total area of a module] can be further enhanced by enlarging the module area, since the ratio of the dead area associated with edges for encapsulation and frames can be reduced.

Stability of PSCs

One challenge in comparing stability among PSCs resides in the use of a range of nonstandard testing protocols within the PSC community (48). For shelf-life stability tests in the dark, PSCs are encapsulated or unencapsulated, and aspects of the ambient environment (e.g., atmosphere, humidity, and temperature) vary (49). Indoor light stability tests use different light sources (50), such as an AM1.5 xenon lamp with or without an ultraviolet (UV) filter, a metal-halide lamp, a sulfur plasma lamp, a halogen lamp, or a UV-free light-emitting diode lamp. Outdoor tests with encapsulated devices (51), thermal stability tests (52), thermal cycling tests (53), and others (54) have also been reported. Transparency in reporting standards on stability tests needs to be improved in the perovskite PV community. Some reports present normalized results without providing initial PV parameters. Such reports risk obscuring the fact that the devices under test for stability are often much less efficient than the devices with the best or even average performance. Thus, it is necessary to present the original PV data and the normalization parameters. We urge the community to develop and then follow standardized protocols to enable accelerated

¹Michael Grätzel Center for Mesoscopic Solar Cells, Wuhan National Laboratory for Optoelectronics, Huazhong University of Science and Technology, Wuhan 430074, Hubei, China.

²Department of Electrical and Computer Engineering, University of Toronto, 35 St. George Street, Toronto, Ontario M5S 1A4, Canada. ³National Laboratory of Solid State Microstructures, Collaborative Innovation Centre of Advanced Microstructures, Jiangsu Key Laboratory of Artificial Functional Materials, College of Engineering and Applied Sciences, Nanjing University, Nanjing 210093, China.

⁴Perovtronics Research Center, School of Natural Science, and School of Energy and Chemical Engineering, Ulsan National Institute of Science and Technology, 50 UNIST-gil, Eonyang-eup, Ulsu-gun, Ulsan 44919, Korea. ⁵Department of Chemical and Biological Engineering, University of Colorado, Boulder, CO 80309, USA.

*These authors contributed equally to this work.

†Corresponding author. Email: hongwei.han@mail.hust.edu.cn (H.H.); ted.sargent@utoronto.ca (E.H.S.); michael.mcgehee@colorado.edu (M.D.M.); seoksi@unist.ac.kr (S.I.S.)

tests and to predict the lifetime of PSCs on the basis of degradation kinetics specific to the cell components (48). The well-established standards [e.g., International Electrotechnical Commission (IEC) 61215 or 61646] in mature crystalline silicon and inorganic thin-film PVs can be deployed by the PSC community, and additional protocols to test the reliability of PSCs can also be advanced.

Here we summarize dominant causes of instability in PSCs on the device level. One source of instability is the chemically active charge-transporting material and interfacial degradation. The TiO_2 -based ETL, which is widely used in high-performing cells, causes photocatalytic degradation under UV illumination. Replacing TiO_2 with other UV-stable materials (e.g., BaSnO_3) (Fig. 2A) (55) or inserting an interfacial modifier (e.g., CsBr, Sb_2S_3 , or Cl atoms) (Fig. 2, B and C) (9, 56, 57) between the ETL and the perovskite absorber can improve stability. Commonly used organic HTMs such as spiro-OMeTAD, poly(3-hexylthiophene) (P3HT), and PTAA encounter thermal or moisture instability in their doped forms. Substituting the organic HTM with inorganic materials (Fig. 2, D and E), inserting

buffer layers between perovskite and HTM, and deploying suitable encapsulation can improve stability (49). Metal electrodes such as Au, Ag, and Al have stability issues as well. Ag and Al electrodes suffer from corrosion by ion migration in perovskite, resulting in an apparent color change and PCE decay (58, 59). Even relatively inert Au diffuses across the organic HTM layer at temperatures exceeding 70°C , leading to an irreversible performance loss (60). Interfacial layers such as Cr, MoO_3 , and reduced graphene oxide have been introduced to prevent metal diffusion and thus improve long-term stability (49, 61). Replacing the metal electrodes with indium tin oxide (ITO) can also improve stability by providing an unreactive electrode and creating a barrier layer that keeps moisture out and retains volatile components of perovskite (17, 53).

Triple mesoscopic PSCs based on $\text{TiO}_2/\text{ZrO}_2$ /carbon/mixed-cation perovskite have passed relatively harsh lifetime testing conditions. With initial efficiencies of 10 to 12%, the PSCs and modules exhibited negligible performance loss after illumination under an unfiltered Xe lamp for 1000 hours (Fig. 2, F and G). The devices also exhibited acceptable stability in thermal stability tests at

85° to 100°C for 2160 hours and in outdoor stability tests in Jeddah, Saudi Arabia, for 168 hours and Wuhan, China, for 720 hours (51, 62, 63). Improved stability in triple mesoscopic PSCs was enabled by removal of unstable components (such as organic HTM and metal electrodes) (64) and incorporation of bulky organic ligand [5-ammoniumvaleric acid (5-AVA)] to form mixed-cation perovskites $(5\text{-AVA})_x(\text{MA})_{1-x}\text{PbI}_3$, where MA is methylammonium (16).

Devices using low-dimensional perovskites in which some or all cations are replaced by large organic ligands exhibited greater stability over long-term operation against moisture and light soaking, as compared with 3D perovskite devices (65–67) (Fig. 3, A and B). However, the large ligands impede charge-transfer transport and sacrifice efficiency (35, 68) (Fig. 3C). Alternatives such as shorter-chain cations (69) and conjugated cations (35) can potentially increase efficiency without sacrificing stability.

Protecting interfaces and grain boundaries—sites where degradation may begin—can slow decomposition. Small-molecule additives such as thiophene, pyridine (70), urea (71), phenyl- C_{60} -butyric acid methyl ester (PC_{60}BM) (72), and quaternary

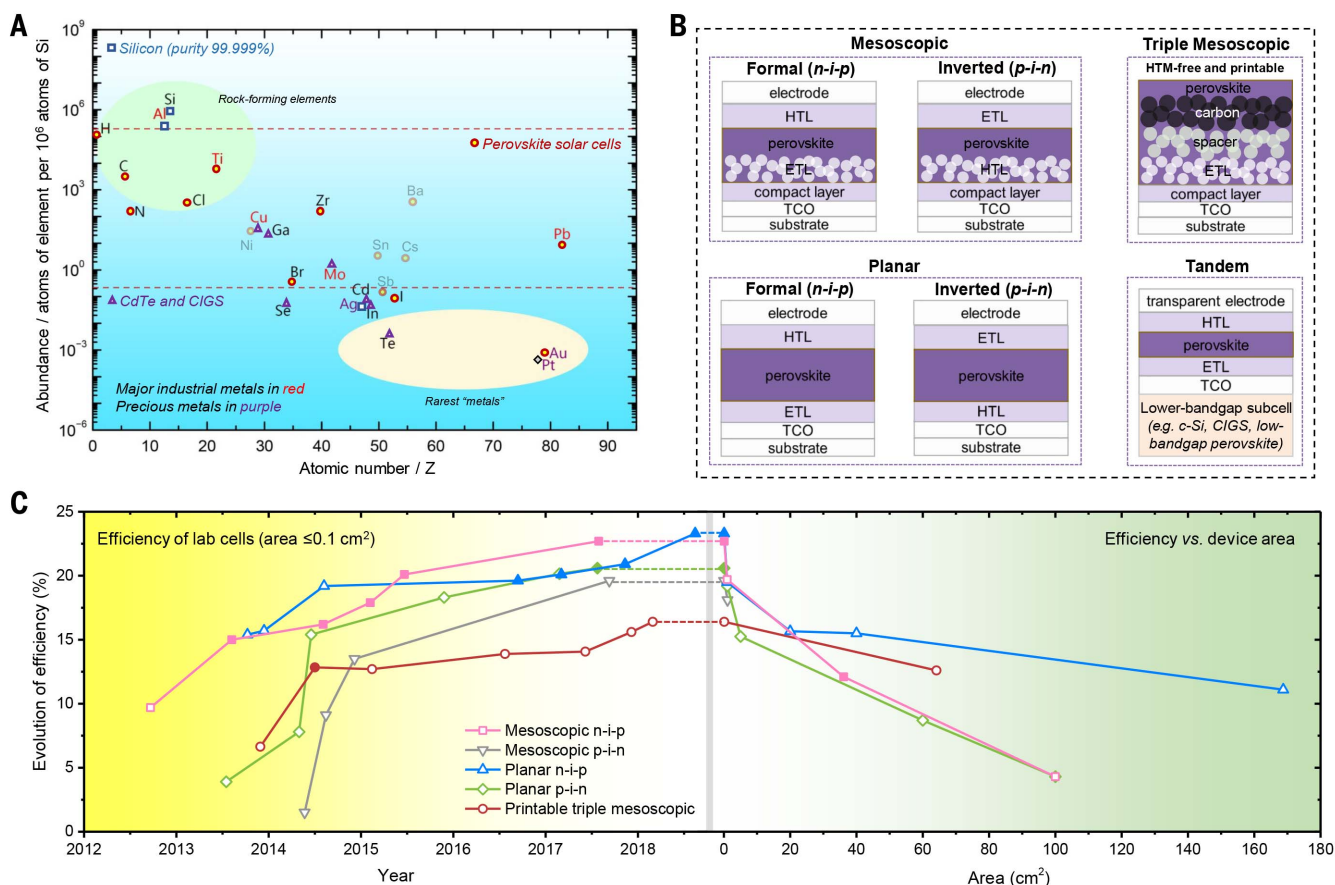


Fig. 1. Chemical elements used in different solar cells, device configurations and efficiencies of PSCs. (A) Atom fraction of elements used for different types of solar cells. The major elements for silicon solar cells are denoted by blue squares, PSCs by red circles, and CdTe and CIGS thin-film solar cells by purple triangles. Ni, Sn, Cs, Ba, and Sb elements are labeled in semitransparent color, as they have been used in PSCs but not in the mainstream architectures.

Major industrial metals and precious metals are categorized according to Goldschmidt classification (7). (B) Four device configurations of PSCs: mesoscopic structure, planar structure, triple mesoscopic structure, and tandem structure with lower-bandgap subcell. (C) Evolution of the best-reported lab-cell ($\leq 0.1 \text{ cm}^2$) efficiencies and large-area ($\geq 1.0 \text{ cm}^2$) device efficiencies. Solid symbols represent certified efficiencies; hollow symbols denote uncertified efficiencies.

ammonium halide (73) have demonstrated improved stability. The hydrophilic side interacts strongly with perovskites, and the hydrophobic side faces outward to protect the surface of perovskites from moisture. In addition, formamidineium (FA^+) or Cs^+ was used to replace the MA^+ cation (74, 75), and Cl^- , Br^- , or SCN^- replaced the I^- anion (76), yielding various perovskites with a series of tolerance factors (77). This result tunes the Pb-I bond and the perovskite crystal systems influencing the formation energy and changes the inherent stability of perovskites.

Upscaling and future applications

Recently, several PV companies have set out to manufacture large-area PSC modules. Microquanta Semiconductor (China) obtained a PCE of 17.4% for a rigid perovskite mini-module with an

active area of 17.8 cm^2 (Fig. 4A). Solliance (the Netherlands) developed 169-cm^2 perovskite modules with a GFF of 90% using laser ablation to define the cells that exhibited a total efficiency of 10% and an active area efficiency of 11.1% (41). The processing steps were carried out at temperatures below 120°C and are compatible with flexible substrates and a roll-to-roll process (Fig. 4B). Saule Technologies (Poland) used inkjet printing to fabricate perovskite solar modules on flexible substrates, which allows the design of free-form patterns (Fig. 4C). Greatcell Solar (previously Dyesol, Australia) has achieved 12% conversion efficiency in 10 cm by 10 cm modules and is committed to full-scale production in 2019 (78). p-OLED (China) and Solaronix (Switzerland) are also engaging in the upscaling of PSCs by providing chemicals and equipment around the world.

Oxford PV (United Kingdom) and Tandem PV (formerly Iris PV, United States) seek to use perovskites to upgrade the performance of silicon solar cells by fabricating high-efficiency perovskite-Si tandem cells. Recently, Oxford PV announced a record-certified PCE of 27.3% for 1-cm^2 perovskite-Si tandem solar cells (79). Huazhong University of Science and Technology (HUST) in China initiated the upscaling of printable triple mesoscopic PSCs and has achieved efficiency $>10\%$ with an area of 100 cm^2 (Fig. 4D). A 7.0-m^2 solar panel was assembled with these cells in early 2015 (51). Recently, a 110-m^2 perovskite PV system with screen-printed triple mesoscopic PSC modules (3600 cm^2 for each) was launched by WonderSolar (Fig. 4E) (80).

Various device architectures and manufacturing processes are the subject of research and

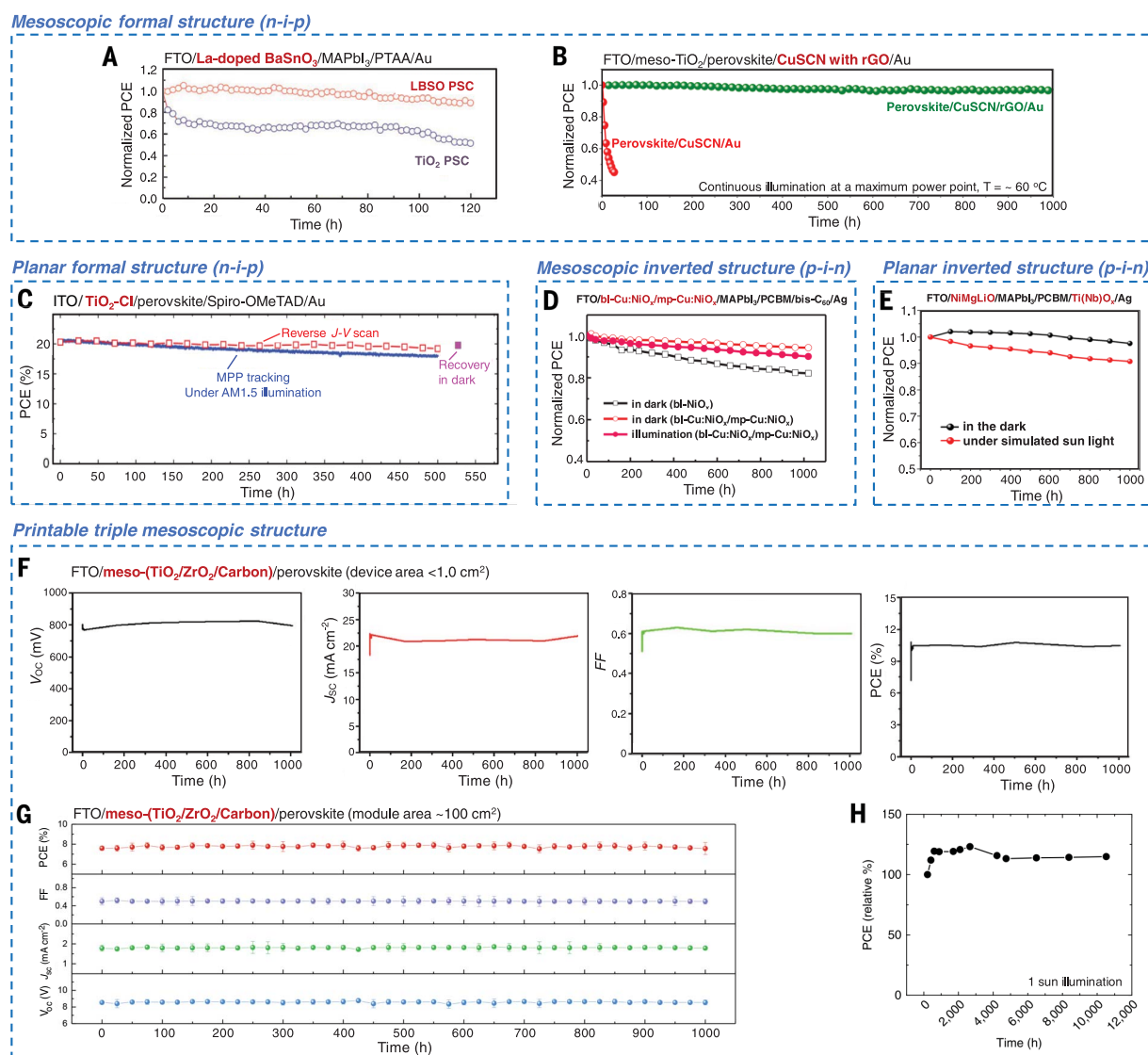


Fig. 2. Summary of operational stability for PSCs with various device architectures. Mesoscopic formal structures (n-i-p) with organic (A) and inorganic (B) HTLs. [Reproduced from (61) with permission] (C) Planar formal structure (n-i-p). MPP, maximum power point; J , current density; V , voltage. (D) Mesoscopic inverted structure (p-i-n). [Reproduced from (8) with permission] (E) Planar inverted structure (p-i-n). [Reproduced from (30) with permission] (F to H) Printable triple mesoscopic structure. Relatively stable devices have been reported for all structures by using appropriate charge-transporting materials, perovskite, and electrodes. OC, open circuit; SC, short circuit; FF, fill factor. [Reproduced from (51, 65) with permission]

with permission] (E) Planar inverted structure (p-i-n). [Reproduced from (30) with permission] (F to H) Printable triple mesoscopic structure. Relatively stable devices have been reported for all structures by using appropriate charge-transporting materials, perovskite, and electrodes. OC, open circuit; SC, short circuit; FF, fill factor. [Reproduced from (51, 65) with permission]

development. As yet, it is unclear which architecture or fabrication method will become dominant. At large scales, it is still challenging to control morphology and obtain uniform perovskite thin films by using either solution- or vacuum-based deposition techniques (81–83). The crystal growth of the perovskite absorber in solvents varies as a result of different evaporation rates at different locations. When the concentration of the precursor solution deposited on a large-area substrate varies, ion migration may occur and may lead to inhomogeneous crystallization. For PSCs in typical mesoscopic or planar structures, the thickness of the perovskite layer is on the order of several hundred nanometers. Pinholes in perovskite films lead to direct contact between the ETL and HTL and cause current leakage and voltage loss for the modules. Al-

though slot-die coating has proved to be an effective method for depositing perovskite thin films on large scales, further optimizations on the compositions of the precursors and crystallization process are required.

The toxicity of the solvents used to prepare perovskite films and other charge-transport layers merits further study and adaptation: Solvent-free deposition methods (37, 82) and solution-based deposition approaches that use reagents with lower toxicity (84) warrant further development. For industrial-scale production, rigorous enclosures that prevent contact between operators and solvents are required, as are recycling and tail-gas-treating units.

In addition to addressing the concerns regarding stability and mass production, a thorough life cycle assessment, including evaluation of mate-

rials, production processes, and environmental impact, should be performed. The lead contained in PSCs has given rise to toxicity concerns. The amount of lead contained in PSCs is below that produced annually by the coal industry when it generates an equivalent amount of electricity (85) and is roughly equivalent to that already contained in a 1-cm-thick layer of natural soil (~0.3 to 1.2 g m⁻²) with the same area (86, 87). Nevertheless, lead in PSCs is more soluble in water and thus can move more readily through the biogeochemical cycle. Therefore, replacing Pb with other nontoxic elements to develop Pb-free PSCs will generate interest if comparable performance can be achieved. It may also be optional to develop additives that immediately convert water-soluble lead compounds into insoluble complexes upon destruction of a large perovskite solar power plant.

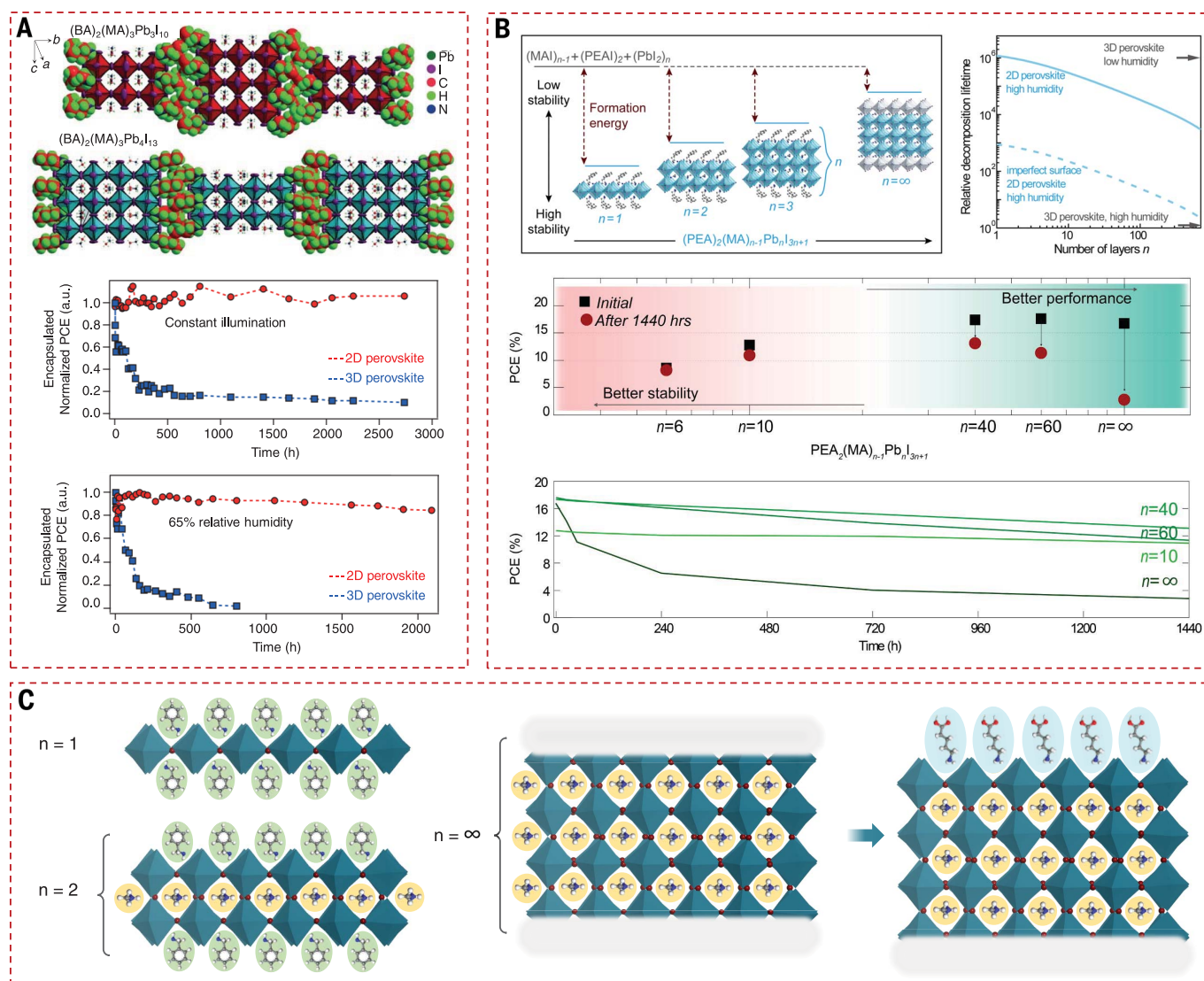


Fig. 3. Strategies to improve the stability of perovskite absorbers.

(A) Encapsulated PSCs based on 2D Ruddlesden-Popper perovskites exhibit much-reduced degradation under constant AM1.5G illumination and high relative humidity. BA, butylammonium; a.u., arbitrary units. [Reproduced from (67) with permission] (B) Improved stability of PSCs by tuning the

dimensionality of the perovskite absorber. [Reproduced from (68) with permission from American Chemical Society] (C) By taking advantage of the hydrophobicity of large cations, the stability of perovskites can be effectively improved by tuning dimensionality. Protecting the interfaces and grain boundaries of perovskites is another way to slow down the degradation.

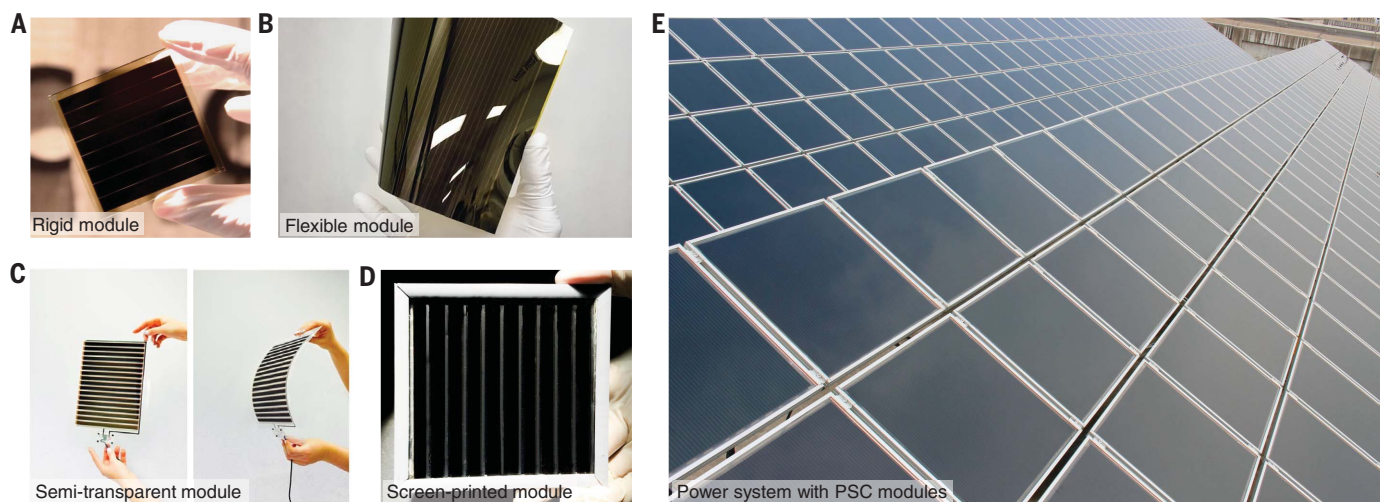


Fig. 4. Perovskite solar modules. (A) Rigid perovskite mini-module. [Courtesy of Microquanta Semiconductor] (B) Roll-to-roll processed flexible module. [Courtesy of Solliance Solar Research] (C) Semitransparent module fabricated via an inkjet printing technique. [Courtesy of Saule

Technologies] (D) Screen-printed module developed by Wuhan National Laboratory for Optoelectronics at HUST. [Reproduced from (51) with permission] (E) Power system with printable triple mesoscopic PSC modules. [Courtesy of WonderSolar]

Life cycle assessment of perovskite tandem solar cells has also raised concerns regarding the environmental impact of gold and spiro-OMeTAD (because of solvent use) (88). Therefore, development of HTL-free and noble-metal-free PSC architectures that do not compromise PCE is a topic of growing interest.

When lead is used in PSCs, the recycling of perovskite modules is required. Experience and lessons from the CdTe PV industry offer hints for the treatment and recycling of lead and cadmium in absorbers. Perovskite solar panels also include frames, glasses, synthetic materials (e.g., HTMs), encapsulation materials [e.g., ethylene vinyl acetate (EVA)], and other materials, that require further development of recycling strategies. One proposed procedure is to remove the layers of PSCs by using adhesive tape and via immersion of the substrate in different organic solvents. PbI_2 can then be recycled from the perovskite solar panel after recrystallization (89). For specific devices such as the printable triple mesoscopic structure, the device scaffold can be reused by washing away the perovskites and reloading them (90). In situ recycling of PSCs through a methylamine gas posttreatment has also been reported (36). For silicon solar cells, recycling efficiency can reach impressive values of 85%, which is important given that up to 78 million tons of waste will be generated by silicon solar panels by 2050 (91). More than 95% of the glass and all-external aluminum frames can be reused. The remaining materials are incinerated to evaporate the encapsulation plastic, and the silicon can be melted again for manufacturing new silicon modules.

Reliability concerns for perovskite solar modules

For commercial PV technologies, international standards such as “Crystalline silicon terrestrial photovoltaic (PV) modules—design qualification and type approval” (IEC 61215) and “Thin-film ter-

restrial photovoltaic (PV) modules—design qualification and type approval” (IEC 61646) have been established and released by the IEC. Specific endurance tests must be passed before the modules are put into field applications. These tests determine the electrical and thermal characteristics of the modules and are needed to show that the modules are capable of withstanding prolonged exposure in climates described in the scope. The actual lifetime expectancy of the modules so qualified still depends on the design, installation, and environment conditions under which they operate.

At present, silicon and inorganic thin-film PV modules have demonstrated exceptionally high levels of reliability in field applications and are able to provide a warranty of 25 years, and the solar panels can maintain a power output $\geq 80\%$ of their initial output after 25 years. Notably, the lifetimes of such PV modules are not only predicated by accelerated aging tests but also have been verified by statistical results obtained with modules under actual outdoor operating conditions (92, 93).

For PSCs, the instability associated with the perovskite absorber and additional instabilities associated with materials interfaces are among the critical hurdles to practical application. The light-soaking test for PSC mini-modules (active area $\sim 50 \text{ cm}^2$) has now been increased to 10,000 hours, but this test has also utilized UV-filtered lamps. The total irradiation is equivalent to the integrated solar irradiation for ~ 10 years in much of Europe. With rigorous device design and proper encapsulation, PSCs (active area $\sim 1 \text{ cm}^2$) have passed the dark damp heat test for 1000 hours, as described in IEC design qualification testing protocol 61215. These results have principally been obtained on small-sized lab devices that are below the area of commercial solar cells. Up to now, there exist no reports of PSCs nor perovskite modules that pass the IEC design qualification-testing protocols for crystalline silicon

and thin-film terrestrial PV modules. Thus, it will be crucial to develop PSCs and modules (with proper encapsulation) that meet IEC standards for reliability.

In addition to heat and irradiation, mechanical shock may also influence the stability of PSCs. Perovskites have a low fracture energy, and their thermal expansion coefficient is more than 10 times that of glass and TCOs—this may lead to delamination during temperature cycling. Cells passed industry-standard tests involving 200 cycles between -40°C and 85°C when encapsulants with a moderate Young’s modulus, such as EVA, were used to help relieve strain in the solar cells. It remains important to ensure that full-sized panels, in which the perovskite layers have been scribed, remain durable during temperature cycling (53).

In practical applications, cells are exposed to high-voltage stress compared to ground since they are connected both in series and in parallel. PSCs should be assessed through the use of potential-induced degradation (PID) testing protocols, and it is noteworthy that other commercial PV technologies (such as inorganic thin-film PVs) have been more prone to PID than is c-Si (94). For silicon solar cells, PID is a reliability concern with varied failure mechanisms, including irreversible ones (such as electrochemical corrosion and sodium ion damage) and reversible ones (due to the accumulation of static charge on the surface of cells). For PSCs, ion migration (95) and charge accumulation (96) are present in cells and lead to the anomalous photocurrent hysteresis effect. Ion migration may lead to severe PID and works against the long-term reliability of modules. It is thus crucial to develop a method to suppress ion migration in PSCs. In future studies, PID testing for PSCs will be required to ensure long-term module reliability.

Partial-shade stress tests remain another topic requiring in-depth studies for perovskite modules:

In PV systems, shaded cells will be under reverse bias, owing to the operation of other cells. IEC 61215 describes partial-shade stress tests to quantify permanent performance loss (97, 98). PSCs have much lower breakdown reverse bias than crystalline silicon and inorganic thin-film solar cells: A reverse-bias breakdown occurs in PSCs between -1 and -4 V (99). In addition, local heating as a result of partial shading may lead to damage or even decomposition of perovskites because organic-inorganic hybrid perovskites are usually not temperature tolerant. It is important for the perovskite community to carry out further studies of partial-shade stress and increase understanding of behavior under reverse bias, as well as to find the means to improve durability under these conditions, possibly by interconnecting bypass diodes within monolithic modules.

Perspective

PSCs can be produced from low-cost materials via a simple fabrication process. PSCs have achieved major advances in efficiency, obtaining high efficiencies in lab cells, and will continue to advance in maturity as stability is enhanced. In general, PSCs feature both a low materials cost and a short energy payback time (<0.22 years) (88, 100).

At present, the major challenge for PSCs is to achieve long-term stability on the module level and to ensure durable outdoor operation. It is necessary for the perovskite PV community to develop a consensus on the stability measurement protocols and release standardized testing protocols within the community. New protocols should be designed to accelerate the aging process under operation conditions and effectively predict the lifetime of PSCs. Although the degradation of the perovskite absorber caused by moisture or oxygen in ambient air can be inhibited by appropriate encapsulations, the performance decay induced by illumination and heat should be addressed through the construction of stable materials and interfaces. Compositional engineering efforts should aim to maximize formation energies and will likely benefit from emerging machine learning algorithms and robotized synthesis.

A loss in efficiency is observed when PSC area increases (87). With continued efforts from the research and industrial communities toward scaling-up of PSCs, we expect that the efficiency gap between lab cells and industrial modules will be minimized and will achieve a level comparable to that of other PV technologies. Cost per kilowatt-hour is dominated by the efficiency and lifetime of solar panels. The abundant low-cost raw materials and simple processing for PSCs indicate pathways to reduce production cost below the level for conventional PV technologies. In the long run, the lower production cost can provide a more sustainable reduction in total module cost, thus making PSCs commercially competitive.

REFERENCES AND NOTES

- M. A. Green, A. Ho-Baillie, H. J. Snaith, The emergence of perovskite solar cells. *Nat. Photonics* **8**, 506–514 (2014). doi: [10.1038/nphoton.2014.134](https://doi.org/10.1038/nphoton.2014.134)
- G. Xing *et al.*, Long-range balanced electron- and hole-transport lengths in organic-inorganic $\text{CH}_3\text{NH}_3\text{PbI}_3$. *Science* **342**, 344–347 (2013). doi: [10.1126/science.1243167](https://doi.org/10.1126/science.1243167); pmid: [24136965](https://pubmed.ncbi.nlm.nih.gov/24136965/)
- H.-S. Kim *et al.*, Lead iodide perovskite sensitized all-solid-state submicron thin film mesoscopic solar cell with efficiency exceeding 9%. *Sci. Rep.* **2**, 591 (2012). doi: [10.1038/srep00591](https://doi.org/10.1038/srep00591); pmid: [22912919](https://pubmed.ncbi.nlm.nih.gov/22912919/)
- N. J. Jeon *et al.*, Solvent engineering for high-performance inorganic-organic hybrid perovskite solar cells. *Nat. Mater.* **13**, 897–903 (2014). doi: [10.1038/nmat4014](https://doi.org/10.1038/nmat4014); pmid: [24997740](https://pubmed.ncbi.nlm.nih.gov/24997740/)
- N. J. Jeon *et al.*, Compositional engineering of perovskite materials for high-performance solar cells. *Nature* **517**, 476–480 (2015). doi: [10.1038/nature14133](https://doi.org/10.1038/nature14133); pmid: [25561177](https://pubmed.ncbi.nlm.nih.gov/25561177/)
- NREL, Best Research-Cell Efficiencies chart; www.nrel.gov/pv/assets/images/efficiency-chart-20180716.jpg.
- V. M. Goldschmidt, The principles of distribution of chemical elements in minerals and rocks. The seventh Hugo Müller Lecture, delivered before the Chemical Society on March 17th, 1937. *J. Chem. Soc.* **0**, 655–673 (1937). doi: [10.1039/JR9370000655](https://doi.org/10.1039/JR9370000655)
- K. Yao *et al.*, A copper-doped nickel oxide bilayer for enhancing efficiency and stability of hysteresis-free inverted mesoporous perovskite solar cells. *Nano Energy* **40**, 155–162 (2017). doi: [10.1016/j.nanoen.2017.08.014](https://doi.org/10.1016/j.nanoen.2017.08.014)
- H. Tan *et al.*, Efficient and stable solution-processed planar perovskite solar cells via contact passivation. *Science* **355**, 722–726 (2017). doi: [10.1126/science.aai9081](https://doi.org/10.1126/science.aai9081); pmid: [28154242](https://pubmed.ncbi.nlm.nih.gov/28154242/)
- Q. Jiang *et al.*, Enhanced electron extraction using SnO_2 for high-efficiency planar-structure $\text{HC}(\text{NH}_2)_2\text{PbI}_3$ -based perovskite solar cells. *Nat. Energy* **2**, 16177 (2016). doi: [10.1038/energy.2016.177](https://doi.org/10.1038/energy.2016.177)
- X. Zheng *et al.*, Defect passivation in hybrid perovskite solar cells using quaternary ammonium halide anions and cations. *Nat. Energy* **2**, 17102 (2017). doi: [10.1038/energy.2017.102](https://doi.org/10.1038/energy.2017.102)
- Y. Bai *et al.*, Enhancing stability and efficiency of perovskite solar cells with crosslinkable silane-functionalized and doped fullerene. *Nat. Commun.* **7**, 12806 (2016). doi: [10.1038/ncomms12806](https://doi.org/10.1038/ncomms12806); pmid: [27703136](https://pubmed.ncbi.nlm.nih.gov/27703136/)
- T. Liu, K. Chen, Q. Hu, R. Zhu, Q. Gong., Inverted Perovskite Solar Cells: Progresses and Perspectives. *Adv. Energy Mater.* **6**, 1600457 (2016). doi: [10.1002/aenm.201600457](https://doi.org/10.1002/aenm.201600457)
- D. Luo *et al.*, Enhanced photovoltage for inverted planar heterojunction perovskite solar cells. *Science* **360**, 1442–1446 (2018). doi: [10.1126/science.aap9282](https://doi.org/10.1126/science.aap9282); pmid: [29954975](https://pubmed.ncbi.nlm.nih.gov/29954975/)
- Z. Ku, Y. Rong, M. Xu, T. Liu, H. Han, Full printable processed mesoscopic $\text{CH}_3\text{NH}_3\text{PbI}_3/\text{TiO}_2$ heterojunction solar cells with carbon counter electrode. *Sci. Rep.* **3**, 3132 (2013). doi: [10.1038/srep03132](https://doi.org/10.1038/srep03132); pmid: [24185501](https://pubmed.ncbi.nlm.nih.gov/24185501/)
- A. Mei *et al.*, A hole-conductor-free, fully printable mesoscopic perovskite solar cell with high stability. *Science* **345**, 295–298 (2014). doi: [10.1126/science.1254763](https://doi.org/10.1126/science.1254763); pmid: [25035487](https://pubmed.ncbi.nlm.nih.gov/25035487/)
- K. A. Bush *et al.*, 23.6%-efficient monolithic perovskite/silicon tandem solar cells with improved stability. *Nat. Energy* **2**, 17009 (2017). doi: [10.1038/energy.2017.9](https://doi.org/10.1038/energy.2017.9)
- C. D. Bailie *et al.*, Semi-transparent perovskite solar cells for tandems with silicon and CIGS. *Energy Environ. Sci.* **8**, 956–963 (2015). doi: [10.1039/C4EE03322A](https://doi.org/10.1039/C4EE03322A)
- G. E. Eperon *et al.*, Perovskite-perovskite tandem photovoltaics with optimized band gaps. *Science* **354**, 861–865 (2016). doi: [10.1126/science.aaf9717](https://doi.org/10.1126/science.aaf9717); pmid: [27856902](https://pubmed.ncbi.nlm.nih.gov/27856902/)
- G. E. Eperon, M. T. Hörantner, H. J. Snaith, Metal halide perovskite tandem and multiple-junction photovoltaics. *Nat. Rev. Chem.* **1**, 0095 (2017). doi: [10.1038/s41570-017-0095](https://doi.org/10.1038/s41570-017-0095)
- W. Shockley, H. J. Queisser, Detailed Balance Limit of Efficiency of p - n Junction Solar Cells. *J. Appl. Phys.* **32**, 510–519 (1961). doi: [10.1063/1.1736034](https://doi.org/10.1063/1.1736034)
- M. A. Green, Commercial progress and challenges for photovoltaics. *Nat. Energy* **1**, 15015 (2016). doi: [10.1038/energy.2015.15](https://doi.org/10.1038/energy.2015.15)
- J. Burschka *et al.*, Sequential deposition as a route to high-performance perovskite-sensitized solar cells. *Nature* **499**, 316–319 (2013). doi: [10.1038/nature12340](https://doi.org/10.1038/nature12340); pmid: [23842493](https://pubmed.ncbi.nlm.nih.gov/23842493/)
- W. S. Yang *et al.*, High-performance photovoltaic perovskite layers fabricated through intramolecular exchange. *Science* **348**, 1234–1237 (2015). doi: [10.1126/science.aaa9272](https://doi.org/10.1126/science.aaa9272); pmid: [25999372](https://pubmed.ncbi.nlm.nih.gov/25999372/)
- H. Tian, B. Xu, H. Chen, E. M. J. Johansson, G. Boschloo, Solid-state perovskite-sensitized p -type mesoporous nickel oxide solar cells. *ChemSusChem* **7**, 2150–2153 (2014). doi: [10.1002/cssc.201402032](https://doi.org/10.1002/cssc.201402032); pmid: [24764196](https://pubmed.ncbi.nlm.nih.gov/24764196/)
- Z. Zhu *et al.*, High-Performance Hole-Extraction Layer of Sol-Gel-Processed NiO Nanocrystals for Inverted Planar Perovskite Solar Cells. *Angew. Chem. Int. Ed.* **53**, 12571–12575 (2014).
- W. Chen *et al.*, Hybrid interfacial layer leads to solid performance improvement of inverted perovskite solar cells. *Energy Environ. Sci.* **8**, 629–640 (2015). doi: [10.1039/C4EE02833C](https://doi.org/10.1039/C4EE02833C)
- J. Y. Jeng *et al.*, $\text{CH}_3\text{NH}_3\text{PbI}_3$ perovskite/fullerene planar-heterojunction hybrid solar cells. *Adv. Mater.* **25**, 3727–3732 (2013). doi: [10.1002/adma.201301327](https://doi.org/10.1002/adma.201301327); pmid: [23775589](https://pubmed.ncbi.nlm.nih.gov/23775589/)
- Z. G. Xiao *et al.*, Efficient, high yield perovskite photovoltaic devices grown by interdiffusion of solution-processed precursor stacking layers. *Energy Environ. Sci.* **7**, 2619–2623 (2014). doi: [10.1039/C4EE01138D](https://doi.org/10.1039/C4EE01138D)
- W. Chen *et al.*, Efficient and stable large-area perovskite solar cells with inorganic charge extraction layers. *Science* **350**, 944–948 (2015). doi: [10.1126/science.aad1015](https://doi.org/10.1126/science.aad1015); pmid: [26516198](https://pubmed.ncbi.nlm.nih.gov/26516198/)
- D. Luo *et al.*, Dual-Source Precursor Approach for Highly Efficient Inverted Planar Heterojunction Perovskite Solar Cells. *Adv. Mater.* **29**, 1604758 (2017). doi: [10.1002/adma.201604758](https://doi.org/10.1002/adma.201604758); pmid: [28295695](https://pubmed.ncbi.nlm.nih.gov/28295695/)
- L. Liu *et al.*, Fully printable mesoscopic perovskite solar cells with organic silane self-assembled monolayer. *J. Am. Chem. Soc.* **137**, 1790–1793 (2015). doi: [10.1021/ja5125594](https://doi.org/10.1021/ja5125594); pmid: [25594109](https://pubmed.ncbi.nlm.nih.gov/25594109/)
- J. Chen *et al.*, Solvent effect on the hole-conductor-free fully printable perovskite solar cells. *Nano Energy* **27**, 130–137 (2016). doi: [10.1016/j.nanoen.2016.06.047](https://doi.org/10.1016/j.nanoen.2016.06.047)
- M. Duan *et al.*, Efficient hole-conductor-free, fully printable mesoscopic perovskite solar cells with carbon electrode based on ultrathin graphite. *Carbon* **120**, 71–76 (2017). doi: [10.1016/j.carbon.2017.05.027](https://doi.org/10.1016/j.carbon.2017.05.027)
- Y. Hu *et al.*, Improved Performance of Printable Perovskite Solar Cells with Bifunctional Conjugated Organic Molecule. *Adv. Mater.* **30**, 1705786 (2018). doi: [10.1002/adma.201705786](https://doi.org/10.1002/adma.201705786); pmid: [29377428](https://pubmed.ncbi.nlm.nih.gov/29377428/)
- W. S. Yang *et al.*, Iodide management in formamidinium-lead-halide-based perovskite layers for efficient solar cells. *Science* **356**, 1376–1379 (2017). doi: [10.1126/science.aan2301](https://doi.org/10.1126/science.aan2301); pmid: [28663498](https://pubmed.ncbi.nlm.nih.gov/28663498/)
- H. Chen *et al.*, A solvent- and vacuum-free route to large-area perovskite films for efficient solar modules. *Nature* **550**, 92–95 (2017). pmid: [28869967](https://pubmed.ncbi.nlm.nih.gov/28869967/)
- S. Razza *et al.*, Perovskite solar cells and large area modules (100 cm^2) based on an air flow-assisted PbI_2 blade coating deposition process. *J. Power Sources* **277**, 286–291 (2015). doi: [10.1016/j.jpowsour.2014.12.008](https://doi.org/10.1016/j.jpowsour.2014.12.008)
- T. Bu *et al.*, A novel quadruple-cation absorber for universal hysteresis elimination for high efficiency and stable perovskite solar cells. *Energy Environ. Sci.* **10**, 2509–2515 (2017).
- J. H. Heo, M. H. Lee, M. H. Jang, S. H. Im, Highly efficient $\text{CH}_3\text{NH}_3\text{PbI}_{3-x}\text{Cl}_x$ mixed halide perovskite solar cells prepared by re-dissolution and crystal grain growth via spray coating. *J. Mater. Chem. A* **4**, 17636–17642 (2016). doi: [10.1039/C6TA06718B](https://doi.org/10.1039/C6TA06718B)
- F. Di Giacomo *et al.*, Up-scalable sheet-to-sheet production of high efficiency perovskite module and solar cells on 6-in. substrate using slot die coating. *Sol. Energy Mater. Sol. Cells* **181**, 53–59 (2017).
- Y. Wu *et al.*, Thermally Stable MAPbI_3 Perovskite Solar Cells with Efficiency of 19.19% and Area over 1 cm^2 achieved by Additive Engineering. *Adv. Mater.* **29**, 1701073 (2017). doi: [10.1002/adma.201701073](https://doi.org/10.1002/adma.201701073)
- C.-Y. Chang, B.-C. Tsai, M.-Z. Lin, Y.-C. Huang, C.-S. Tsao, An integrated approach towards the fabrication of highly efficient and long-term stable perovskite nanowire solar cells. *J. Mater. Chem. A Mater. Energy Sustain.* **5**, 22824–22833 (2017). doi: [10.1039/C7TA07968K](https://doi.org/10.1039/C7TA07968K)
- J. W. Lee, D.-J. Seol, A.-N. Cho, N.-G. Park, High-efficiency perovskite solar cells based on the black polymorph of $\text{HC}(\text{NH}_2)_2\text{PbI}_3$. *Adv. Mater.* **26**, 4991–4998 (2014). doi: [10.1002/adma.201401137](https://doi.org/10.1002/adma.201401137); pmid: [24923708](https://pubmed.ncbi.nlm.nih.gov/24923708/)
- Z. Yang *et al.*, High-Performance Fully Printable Perovskite Solar Cells via Blade-Coating Technique under the Ambient Condition. *Adv. Energy Mater.* **5**, 1500328 (2015). doi: [10.1002/aenm.201500328](https://doi.org/10.1002/aenm.201500328)
- Y. Rong *et al.*, Toward Industrial-Scale Production of Perovskite Solar Cells: Screen Printing, Slot-Die Coating,

- and Emerging Techniques. *J. Phys. Chem. Lett.* **9**, 2707–2713 (2018). doi: [10.1021/acs.jpclett.8b00912](https://doi.org/10.1021/acs.jpclett.8b00912); pmid: [29738259](https://pubmed.ncbi.nlm.nih.gov/29738259/)
47. A. Hinsch *et al.*, Worldwide first fully up-scaled fabrication of $60 \times 100 \text{ cm}^2$ dye solar module prototypes. *Prog. Photovolt. Res. Appl.* **20**, 698–710 (2012). doi: [10.1002/pij.1213](https://doi.org/10.1002/pij.1213)
 48. K. Domanski, E. A. Alharbi, A. Hagfeldt, M. Grätzel, W. Tress, Systematic investigation of the impact of operation conditions on the degradation behaviour of perovskite solar cells. *Nat. Energy* **3**, 61–67 (2018). doi: [10.1038/s41560-017-0060-5](https://doi.org/10.1038/s41560-017-0060-5)
 49. J. You *et al.*, Improved air stability of perovskite solar cells via solution-processed metal oxide transport layers. *Nat. Nanotechnol.* **11**, 75–81 (2016). doi: [10.1038/nnano.2015.230](https://doi.org/10.1038/nnano.2015.230); pmid: [26457966](https://pubmed.ncbi.nlm.nih.gov/26457966/)
 50. M. Saliba *et al.*, Incorporation of rubidium cations into perovskite solar cells improves photovoltaic performance. *Science* **354**, 206–209 (2016). doi: [10.1126/science.aah5557](https://doi.org/10.1126/science.aah5557); pmid: [27708053](https://pubmed.ncbi.nlm.nih.gov/27708053/)
 51. Y. Hu *et al.*, Stable large-area ($10 \times 10 \text{ cm}^2$) printable mesoscopic perovskite module exceeding 10% efficiency. *Solar RRL* **1**, 1600019 (2017).
 52. Y. Lin *et al.*, Enhanced Thermal Stability in Perovskite Solar Cells by Assembling 2D/3D Stacking Structures. *J. Phys. Chem. Lett.* **9**, 654–658 (2018). doi: [10.1021/acs.jpclett.7b02679](https://doi.org/10.1021/acs.jpclett.7b02679); pmid: [29350044](https://pubmed.ncbi.nlm.nih.gov/29350044/)
 53. R. Cheacharon *et al.*, Design and understanding of encapsulated perovskite solar cells to withstand temperature cycling. *Energy Environ. Sci.* **11**, 144–150 (2018). doi: [10.1039/C7EE02564E](https://doi.org/10.1039/C7EE02564E)
 54. K. Domanski *et al.*, Migration of cations induces reversible performance losses over day/night cycling in perovskite solar cells. *Energy Environ. Sci.* **10**, 604–613 (2017). doi: [10.1039/C6EE03352K](https://doi.org/10.1039/C6EE03352K)
 55. S. S. Shin *et al.*, Colloidally prepared La-doped BaSnO_3 electrodes for efficient, photostable perovskite solar cells. *Science* **356**, 167–171 (2017). doi: [10.1126/science.aam6620](https://doi.org/10.1126/science.aam6620); pmid: [28360134](https://pubmed.ncbi.nlm.nih.gov/28360134/)
 56. W. Li *et al.*, Enhanced UV-light stability of planar heterojunction perovskite solar cells with caesium bromide interface modification. *Energy Environ. Sci.* **9**, 490–498 (2016). doi: [10.1039/C5EE03522H](https://doi.org/10.1039/C5EE03522H)
 57. S. Ito, S. Tanaka, K. Manabe, H. Nishino, Effects of Surface Blocking Layer of Sb_2S_3 on Nanocrystalline TiO_2 for $\text{CH}_3\text{NH}_3\text{PbI}_3$ Perovskite Solar Cells. *J. Phys. Chem. C* **118**, 16995–17000 (2014). doi: [10.1021/jp500449z](https://doi.org/10.1021/jp500449z)
 58. Y. Kato *et al.*, Silver Iodide Formation in Methyl Ammonium Lead Iodide Perovskite Solar Cells with Silver Top Electrodes. *Adv. Mater. Interfaces* **2**, 1500195 (2015). doi: [10.1002/admi.201500195](https://doi.org/10.1002/admi.201500195)
 59. H. Back *et al.*, Achieving long-term stable perovskite solar cells via ion neutralization. *Energy Environ. Sci.* **9**, 1258–1263 (2016). doi: [10.1039/C6EE00612D](https://doi.org/10.1039/C6EE00612D)
 60. K. Domanski *et al.*, Not All That Glitters Is Gold: Metal-Migration-Induced Degradation in Perovskite Solar Cells. *ACS Nano* **10**, 6306–6314 (2016). doi: [10.1021/acsnano.6b02613](https://doi.org/10.1021/acsnano.6b02613); pmid: [27187798](https://pubmed.ncbi.nlm.nih.gov/27187798/)
 61. N. Arora *et al.*, Perovskite solar cells with CuSCN hole extraction layers yield stabilized efficiencies greater than 20%. *Science* **358**, 768–771 (2017). doi: [10.1126/science.aam5655](https://doi.org/10.1126/science.aam5655); pmid: [28971968](https://pubmed.ncbi.nlm.nih.gov/28971968/)
 62. X. Li *et al.*, Outdoor Performance and Stability under Elevated Temperatures and Long-Term Light Soaking of Triple-Layer Mesoporous Perovskite Photovoltaics. *Energy Tech.* **3**, 551–555 (2015). doi: [10.1002/ente.201500045](https://doi.org/10.1002/ente.201500045)
 63. A. K. Baranwal *et al.*, 100 °C Thermal Stability of Printable Perovskite Solar Cells Using Porous Carbon Counter Electrodes. *ChemSusChem* **9**, 2604–2608 (2016). doi: [10.1002/cssc.201600933](https://doi.org/10.1002/cssc.201600933); pmid: [27629068](https://pubmed.ncbi.nlm.nih.gov/27629068/)
 64. S. Ito *et al.*, Light stability tests of $\text{CH}_3\text{NH}_3\text{PbI}_3$ perovskite solar cells using porous carbon counter electrodes. *Phys. Chem. Chem. Phys.* **18**, 27102–27108 (2016). doi: [10.1039/C6CP03388A](https://doi.org/10.1039/C6CP03388A); pmid: [27402555](https://pubmed.ncbi.nlm.nih.gov/27402555/)
 65. G. Grancini *et al.*, One-Year stable perovskite solar cells by 2D/3D interface engineering. *Nat. Commun.* **8**, 15684 (2017). doi: [10.1038/ncomms15684](https://doi.org/10.1038/ncomms15684); pmid: [28569749](https://pubmed.ncbi.nlm.nih.gov/28569749/)
 66. D. H. Cao, C. C. Stoumpos, O. K. Farha, J. T. Hupp, M. G. Kanatzidis, 2D Homologous Perovskites as Light-Absorbing Materials for Solar Cell Applications. *J. Am. Chem. Soc.* **137**, 7843–7850 (2015). doi: [10.1021/jacs.5b03796](https://doi.org/10.1021/jacs.5b03796); pmid: [26020457](https://pubmed.ncbi.nlm.nih.gov/26020457/)
 67. H. Tsai *et al.*, High-efficiency two-dimensional Ruddlesden-Popper perovskite solar cells. *Nature* **536**, 312–316 (2016). doi: [10.1038/nature18306](https://doi.org/10.1038/nature18306); pmid: [27383783](https://pubmed.ncbi.nlm.nih.gov/27383783/)
 68. L. N. Quan *et al.*, Ligand-Stabilized Reduced-Dimensionality Perovskites. *J. Am. Chem. Soc.* **138**, 2649–2655 (2016). doi: [10.1021/jacs.5b11740](https://doi.org/10.1021/jacs.5b11740); pmid: [26841130](https://pubmed.ncbi.nlm.nih.gov/26841130/)
 69. Y. Chen *et al.*, Tailoring Organic Cation of 2D Air-Stable Organometal Halide Perovskites for Highly Efficient Planar Solar Cells. *Adv. Energy Mater.* **7**, 1700162 (2017).
 70. N. K. Noel *et al.*, Enhanced photoluminescence and solar cell performance via Lewis base passivation of organic-inorganic lead halide perovskites. *ACS Nano* **8**, 9815–9821 (2014). doi: [10.1021/nn5036476](https://doi.org/10.1021/nn5036476); pmid: [25171692](https://pubmed.ncbi.nlm.nih.gov/25171692/)
 71. J.-W. Lee *et al.*, A Bifunctional Lewis Base Additive for Microscopic Homogeneity in Perovskite Solar Cells. *Chem* **3**, 290–302 (2017). doi: [10.1016/j.chempr.2017.05.020](https://doi.org/10.1016/j.chempr.2017.05.020)
 72. J. Xu *et al.*, Perovskite-fullerene hybrid materials suppress hysteresis in planar diodes. *Nat. Commun.* **6**, 7081 (2015). doi: [10.1038/ncomms8081](https://doi.org/10.1038/ncomms8081)
 73. X. Zheng *et al.*, Boron Doping of Multiwalled Carbon Nanotubes Significantly Enhances Hole Extraction in Carbon-Based Perovskite Solar Cells. *Nano Lett.* **17**, 2496–2505 (2017). doi: [10.1021/acs.nanolett.7b00200](https://doi.org/10.1021/acs.nanolett.7b00200); pmid: [28287749](https://pubmed.ncbi.nlm.nih.gov/28287749/)
 74. Y. C. Kim *et al.*, Beneficial Effects of PbI_2 Incorporated in Organo-Lead Halide Perovskite Solar Cells. *Adv. Energy Mater.* **6**, 1502104 (2016). doi: [10.1002/aenm.201502104](https://doi.org/10.1002/aenm.201502104)
 75. M. Yang *et al.*, Facile fabrication of large-grain $\text{CH}_3\text{NH}_3\text{PbI}_{3-x}\text{Br}_x$ films for high-efficiency solar cells via $\text{CH}_3\text{NH}_3\text{Br}$ -selective Ostwald ripening. *Nat. Commun.* **7**, 12305 (2016). doi: [10.1038/ncomms12305](https://doi.org/10.1038/ncomms12305); pmid: [27477212](https://pubmed.ncbi.nlm.nih.gov/27477212/)
 76. Q. Tai *et al.*, Efficient and stable perovskite solar cells prepared in ambient air irrespective of the humidity. *Nat. Commun.* **7**, 11105 (2016). doi: [10.1038/ncomms11105](https://doi.org/10.1038/ncomms11105); pmid: [27033249](https://pubmed.ncbi.nlm.nih.gov/27033249/)
 77. Q. Chen *et al.*, Under the spotlight: The organic–inorganic hybrid halide perovskite for optoelectronic applications. *Nano Today* **10**, 355–396 (2015). doi: [10.1016/j.nantod.2015.04.009](https://doi.org/10.1016/j.nantod.2015.04.009)
 78. “Quarterly report & appendix 4C, quarter 3 – 2018” (GreatCell Solar, 2018); https://gsiirmau.com/site/PDF/2630_0/March2018QuarterlyReportandAppendix4C
 79. “Oxford PV sets world record for perovskite solar cell” (Oxford PV, 2018); www.oxfordpv.com/news/oxford-pv-sets-world-record-perovskite-solar-cell
 80. WonderSolar; www.wondersolar.cn
 81. Z. Li *et al.*, Scalable fabrication of perovskite solar cells. *Nat. Rev. Mater.* **3**, 18017 (2018). doi: [10.1038/natrevmats.2018.17](https://doi.org/10.1038/natrevmats.2018.17)
 82. J. Ávila, C. Mombolona, P. P. Boix, M. Sessolo, H. J. Bolink, Vapor-Deposited Perovskites: The Route to High-Performance Solar Cell Production? *Joule* **1**, 431–442 (2017). doi: [10.1016/j.joule.2017.07.014](https://doi.org/10.1016/j.joule.2017.07.014)
 83. Y. Deng *et al.*, Surfactant-controlled ink drying enables high-speed deposition of perovskite films for efficient photovoltaic modules. *Nat. Energy* **3**, 560–566 (2018). doi: [10.1038/s41560-018-0153-9](https://doi.org/10.1038/s41560-018-0153-9)
 84. N. K. Noel *et al.*, A low viscosity, low boiling point, clean solvent system for the rapid crystallisation of highly specular perovskite films. *Energy Environ. Sci.* **10**, 145–152 (2017). doi: [10.1039/C6EE02373H](https://doi.org/10.1039/C6EE02373H)
 85. S. D. Stranks, H. J. Snaith, Metal-halide perovskites for photovoltaic and light-emitting devices. *Nat. Nanotechnol.* **10**, 391–402 (2015). doi: [10.1038/nnano.2015.90](https://doi.org/10.1038/nnano.2015.90); pmid: [25947963](https://pubmed.ncbi.nlm.nih.gov/25947963/)
 86. N.-G. Park, M. Grätzel, T. Miyasaka, K. Zhu, K. Emery, Towards stable and commercially available perovskite solar cells. *Nat. Energy* **1**, 16152 (2016). doi: [10.1038/nenergy.2016.152](https://doi.org/10.1038/nenergy.2016.152)
 87. R. A. Wuana, F. E. Okieimen, Heavy Metals in Contaminated Soils: A Review of Sources, Chemistry, Risks and Best Available Strategies for Remediation. *ISRN Ecol.* **2011**, 402647 (2011). doi: [10.5402/2011/402647](https://doi.org/10.5402/2011/402647)
 88. M. Monteiro Lunardi, A. Wing Yi Ho-Baillie, J. P. Alvarez-Gaitan, S. Moore, R. Corkish, A life cycle assessment of perovskite/silicon tandem solar cells. *Prog. Photovolt. Res. Appl.* **25**, 679–695 (2017). doi: [10.1002/pij.2877](https://doi.org/10.1002/pij.2877)
 89. A. Binek *et al.*, Recycling Perovskite Solar Cells To Avoid Lead Waste. *ACS Appl. Mater. Interfaces* **8**, 12881–12886 (2016). doi: [10.1021/acsami.6b03767](https://doi.org/10.1021/acsami.6b03767); pmid: [27149009](https://pubmed.ncbi.nlm.nih.gov/27149009/)
 90. Z. Ku, X. Xia, H. Shen, N. H. Tiep, H. J. Fan, A mesoporous nickel counter electrode for printable and reusable perovskite solar cells. *Nanoscale* **7**, 13363–13368 (2015). doi: [10.1039/C5NR03610K](https://doi.org/10.1039/C5NR03610K); pmid: [26199184](https://pubmed.ncbi.nlm.nih.gov/26199184/)
 91. S. Weckend, A. Wade, G. Heath, “End-of-life management: Solar photovoltaic panels” (IRENA and IEA-PVPS, 2016); http://iea-pvps.org/fileadmin/dam/public/report/technical/IRENA_IEAPVPS_End-of-Life_Solar_PV_Panels_2016.pdf
 92. D. C. Jordan, T. J. Silverman, J. H. Wohlgemuth, S. R. Kurtz, K. T. VanSant, Photovoltaic failure and degradation modes. *Prog. Photovolt. Res. Appl.* **25**, 318–326 (2017). doi: [10.1002/pij.2866](https://doi.org/10.1002/pij.2866)
 93. D. C. Jordan, S. R. Kurtz, Photovoltaic Degradation Rates—an Analytical Review. *Prog. Photovolt. Res. Appl.* **21**, 12–29 (2013). doi: [10.1002/pij.1182](https://doi.org/10.1002/pij.1182)
 94. A. Masuda, Y. Hara, Potential-induced degradation of thin-film Si photovoltaic modules. *Jpn. J. Appl. Phys.* **56**, 04CS04 (2017). doi: [10.7567/JJAP.56.04CS04](https://doi.org/10.7567/JJAP.56.04CS04)
 95. Y. Yuan, J. Huang, Ion Migration in Organometal Trihalide Perovskite and Its Impact on Photovoltaic Efficiency and Stability. *Acc. Chem. Res.* **49**, 286–293 (2016). doi: [10.1021/acs.accounts.5b00420](https://doi.org/10.1021/acs.accounts.5b00420); pmid: [26820627](https://pubmed.ncbi.nlm.nih.gov/26820627/)
 96. P. Lopez-Varo *et al.*, Device Physics of Hybrid Perovskite Solar cells: Theory and Experiment. *Adv. Energy Mater.* **8**, 1702772 (2018). doi: [10.1002/aenm.201702772](https://doi.org/10.1002/aenm.201702772)
 97. B. Jaegel *et al.*, paper presented at the 29th European Photovoltaic Solar Energy Conference and Exhibition, Amsterdam, Netherlands, 22 to 26 September 2014.
 98. T. J. Silverman *et al.*, in *SPIE Optics + Photonics for Sustainable Energy* (SPIE, 2015), vol. 9563. doi: [10.1117/12.2188774](https://doi.org/10.1117/12.2188774)
 99. A. R. Bowring, L. Bertoluzzi, B. C. O'Regan, M. D. McGehee, Reverse Bias Behavior of Halide Perovskite Solar Cells. *Adv. Energy Mater.* **8**, 1702365 (2018). doi: [10.1002/aenm.201702365](https://doi.org/10.1002/aenm.201702365)
 100. J. Gong, S. B. Darling, F. You, Perovskite photovoltaics: Life-cycle assessment of energy and environmental impacts. *Energy Environ. Sci.* **8**, 1953–1968 (2015). doi: [10.1039/C5EE00615E](https://doi.org/10.1039/C5EE00615E)

ACKNOWLEDGMENTS

We thank the reviewers—in particular, one referee who drew our attention to the matter of potential-induced degradation—for constructive feedback. **Funding:** H.H., Y.R., and Y.H. acknowledge financial support from the National Natural Science Foundation of China (91733301, 91433203, 61474049, 51502141, and 21702069), the Ministry of Science and Technology of China (2015AA034601), the Fundamental Research Funds for the Central Universities, the Science and Technology Department of Hubei Province (2017AAA190), and the 111 Project (B07038). E.H.S., H.T., and M.I.S. acknowledge support from the U.S. Office of Naval Research (N00014-17-1-2524). H.T. acknowledges the National 1000 Young Talents Award in China and the Rubicon Grant (680-50-1511) from the Netherlands Organisation for Scientific Research (NWO). M.I.S. acknowledges the support of Banting Postdoctoral Fellowship Program, administered by the Government of Canada. S.I.S. acknowledges the Global Frontier R&D Program (NRF-2011-0031565) and a brand project (1.180043.01) of UNIST. **Competing interests:** H.H. is the chairman of the board and general manager of WonderSolar, and Y.R. is a member of the board and vice general manager of WonderSolar.

10.1126/science.aat8235

REVIEW SUMMARY

MICROBIOTA

Bacterial antagonism in host-associated microbial communities

Leonor García-Bayona and Laurie E. Comstock*

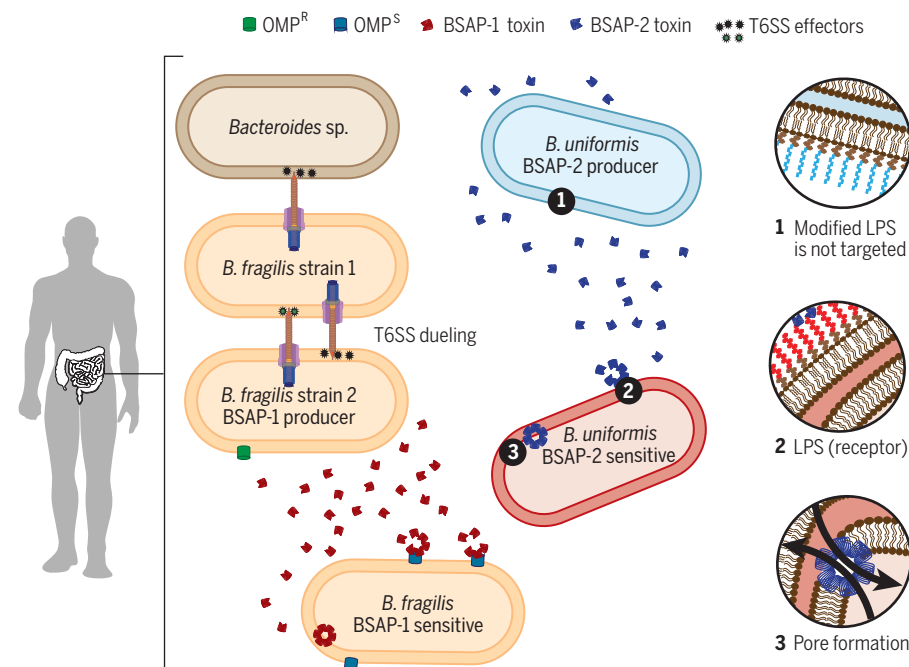
BACKGROUND: Microbial communities are ubiquitous on Earth. The microbiota of different habitats are diverse and have distinct functional traits, but there are common ecological principles that govern their composition. The ability of a microbe to compete with other members of its community for resources is paramount to its success. Competition through the production of molecules that harm other members, known as interference competition, is also important in the assembly and maintenance of microbial communities. As new technologies allow for more in-depth analyses of microbial communities and their genetic content, we are better able to identify new antimicrobial toxins and analyze the effects of their production. Here, we explore the range

of antibacterial protein/peptide toxins and toxin-secretion systems, together with the fitness benefits they confer to the producing organisms. Because human-associated microbial communities have been intensely studied over the past decade, our focus is on the growing body of data regarding bacterial antagonism in these and other host-associated microbial communities.

ADVANCES: Studies continue to reveal the large arsenal of antibacterial peptides and proteins that bacteria produce and the secretion systems that they use to deliver these toxins to competing cells. Bacterially produced antimicrobial peptides and proteins are diverse in terms of their structures, cellular targets, mech-

anisms of action, and spatial range. Their antagonistic range also varies; some are limited to intraspecies killing, whereas others are able to kill across genera, families, and orders. Through a combination of mathematical modeling and experimental model systems, the ecological outcomes of bacterial antagonism are being elucidated. In vivo analyses in host models have shown that some antimicrobial toxins play a role in microbiota-mediated colonization resistance by preventing invasion of pathogens. Some pathogens, however, also use toxins to battle with the resident microbiota to invade an ecosystem and cause disease. Antagonism has also been shown to facilitate genome evolution; the DNA released from killed cells can be taken up and incorporated into the aggressor's genome. In some cases, antagonism has been shown to increase rather than reduce microbial diversity, potentially through promotion of spatial segregation of competing strains, facilitating the exchange of signals and secreted products between related cells (kin). The factors that regulate the production and release of some antibacterial toxins are also becoming better understood. Studies are revealing that toxin producers respond to various environmental signals, including signals that indicate host occupancy, that nutrients are limiting, or that they may be attacked by other bacterial community members.

OUTLOOK: Although bacterial antagonism is an active area of research, we are still in the early stages of understanding the impacts of these interactions in natural community settings and how they influence the overall structure, dynamics, and composition of complex microbial communities. The rapid increase in the number of available metagenomic datasets derived from diverse microbial communities and the expanding capability to culture and genetically modify these organisms is allowing for the identification and characterization of new antibacterial toxins. The protective function of microbiota-produced toxins in warding off pathogens indicates a potential for applications in medical, agricultural, and other industrial settings. In addition, the inclusion of antibacterial toxins in genetically engineered bacteria (live biotherapeutics) may allow for specific targeting of harmful community members, including those involved in therapeutic failures, and may also allow a live biotherapeutic to compete with members of the microbiota to deliver various health-promoting functions. ■

Intra- and interspecies antagonism—the example of *Bacteroides* species in the human gut.

Bacteroides fragilis and *Bacteroides uniformis* use MACPF (membrane attack complex/perforin) toxins—BSAP-1 and BSAP-2, respectively—for intraspecies killing. Producer strains carry a modified receptor [outer membrane protein (OMP) or lipopolysaccharide (LPS) glycan] that confers resistance to its cognate toxin. *B. fragilis* can also kill other *B. fragilis* strains and most gut Bacteroidales species via type VI secretion systems (T6SSs).

Division of Infectious Diseases, Brigham and Women's Hospital, Harvard Medical School, Boston, MA, USA.

*Corresponding author. Email: lcomstock@rics.bwh.harvard.edu
Cite this article as L. García-Bayona and L. E. Comstock, *Science* 361, eaat2456 (2018). DOI: 10.1126/science.aat2456

REVIEW

MICROBIOTA

Bacterial antagonism in host-associated microbial communities

Leonor García-Bayona and Laurie E. Comstock*

Antagonistic interactions are abundant in microbial communities and contribute not only to the composition and relative proportions of their members but also to the longer-term stability of a community. This Review will largely focus on bacterial antagonism mediated by ribosomally synthesized peptides and proteins produced by members of host-associated microbial communities. We discuss recent findings on their diversity, functions, and ecological impacts. These systems play key roles in ecosystem defense, pathogen invasion, spatial segregation, and diversity but also confer indirect gains to the aggressor from products released by killed cells. Investigations into antagonistic bacterial interactions are important for our understanding of how the microbiota establish within hosts, influence health and disease, and offer insights into potential translational applications.

Bacteria commonly live in complex microbial communities and have properties that allow them to survive, replicate, and compete in their ecosystems (1, 2). Central to their survival is the ability to harvest nutrients and scarce resources, to establish a spatial niche, and to withstand specific environmental conditions. In the human gut, colonizing microbes must survive in the face of various host conditions and factors, such as the low pH encountered during transit through the stomach; bile; host-produced immune factors, including antimicrobial peptides; and growth under anoxic conditions (3). Not least among the challenges of life in the gut are the competitive behaviors of other members of the microbial community and the potentially deleterious effects other organisms may have on the local environment, such as production of molecules that modulate host immunity, toxic metabolic end products, and alteration of oxygen levels (3).

The past decade of research has further highlighted the importance of microbial communities for human, animal, and plant health. The mammalian gut is currently one of the most investigated microbial ecosystems. Many studies report rapid changes in gut communities in response to numerous factors—including diet, drugs, and during infection—yet these are often transient, and over the lifetime of a healthy adult, the microbiota remains relatively stable (4, 5). An understanding of the ecological principles that govern this stability and that contribute to ecosystem fluctuations is essential to successfully alter microbial communities for therapeutic and agricultural benefits.

Broadly, ecological competition can be classified as exploitative competition, in which an

organism consumes the resources required by another member, or interference competition, in which a microorganism inhibits the growth of another through the synthesis of harmful products (6). Interference competition can be mediated through the production of different types of molecules, including small-molecule antibiotics, nonribosomally synthesized peptide antimicrobials, metabolites such as hydrogen peroxide, modification of host-produced molecules (7), signal interference, and the production of ribosomally synthesized peptides and protein toxins (6). This Review will largely focus on interference competition among bacteria mediated by diffusible proteinaceous toxins and toxins deployed by contact-dependent systems (Box 1).

Recent studies have provided insights into the benefits of toxin production to organisms within a community, but we still have a limited understanding of the full range of these competitive interactions and their ecological impact. Studies with an ecological slant have ranged from mathematical modeling, experimental systems, and observations of natural microbial communities. In addition, the ever-increasing number of metagenomes of diverse microbial communities is a growing resource for analyzing the numbers and types of toxins produced by a community.

Although the obvious outcome of toxin production is to provide a competitive advantage by killing a competitor, the overall effects to the community can be diverse. Some toxins may allow a competing member to enter an ecosystem (invasion), and some have been shown to function defensively to prevent invasion and to compete with established members. Several studies show that toxin production tends to increase diversity, by promoting spatial segregation, rather than reduce it. When considering the larger ecological consequences of these antagonistic

systems, the specific constraints of each system must also be considered. For example, antagonistic mechanisms that require physical contact cannot kill cells at a distance. Many toxins only target strains of the same species and therefore may not affect other competitors in the community. Further, the synthesis and secretion of these toxins may be physiologically costly and thus affect fitness (8, 9). Toxins whose release requires cell lysis can only be deployed by a fraction of the population and will have different relative fitness costs and dynamics compared with actively secreted toxins. We will examine these themes in more detail in the next sections.

Antagonism between community members

The complex gut microbiota of humans remains relatively stable over time, with many strains persisting for decades (4, 10, 11). The prevalence of diverse antagonistic systems produced by its bacterial members seems counterintuitive considering the overall stability. However, mathematical models of communities with high species diversity predict that communities dominated by antagonistic interactions are more stable than those in which cooperative interactions are more prevalent. Cooperative interactions tend to decrease resilience to perturbations because interspecies dependencies render members especially vulnerable to perturbations to their cooperative partners, whereas more antagonistic communities are predicted to be comparatively resilient (12). Moreover, in structured environments with highly diverse members, mutually antagonistic competitors could be isolated from each other through buffer zones, reducing the extent to which species interact with one another (2). Theoretical work suggests that antagonistic systems may promote diversity in unmixed environments under certain conditions (13, 14), as was shown experimentally for colicin production by *Escherichia coli* (15, 16) and type VI secretion system (T6SS)-mediated antagonism between *Aeromonas hydrophila* and *Vibrio cholerae* (17). Likewise, in natural soil communities, strong interference competition by bidirectionally antagonizing *Myxococcus xanthus* strains depends on the frequency of each strain and contributes to high levels of local diversity by reinforcing barriers to cross-territory invasion (18).

Many bacterial members of the human gut microbiota—including *Lactobacillus* spp., *Bifidobacterium* spp., *E. coli*, *Enterococcus* spp. and *Bacteroides* spp.—produce one or more types of antagonistic toxin systems, ranging from small-peptide bacteriocins, colicins, other secreted proteins, R-type bacteriocins, and toxins delivered by T6SSs (Box 1). The numerous studies of peptide bacteriocins of *Lactobacilli* and *Bifidobacteria* have largely focused on bacteriocin structures, mechanisms of action, therapeutic potential in preventing infection, or their use in the food industry [reviewed in (19, 20)]. By contrast, there is relatively little known about their impacts in their natural ecosystem. One

Division of Infectious Diseases, Brigham and Women's Hospital, Harvard Medical School, Boston, MA, USA.

*Corresponding author. Email: lcomstock@rics.bwh.harvard.edu

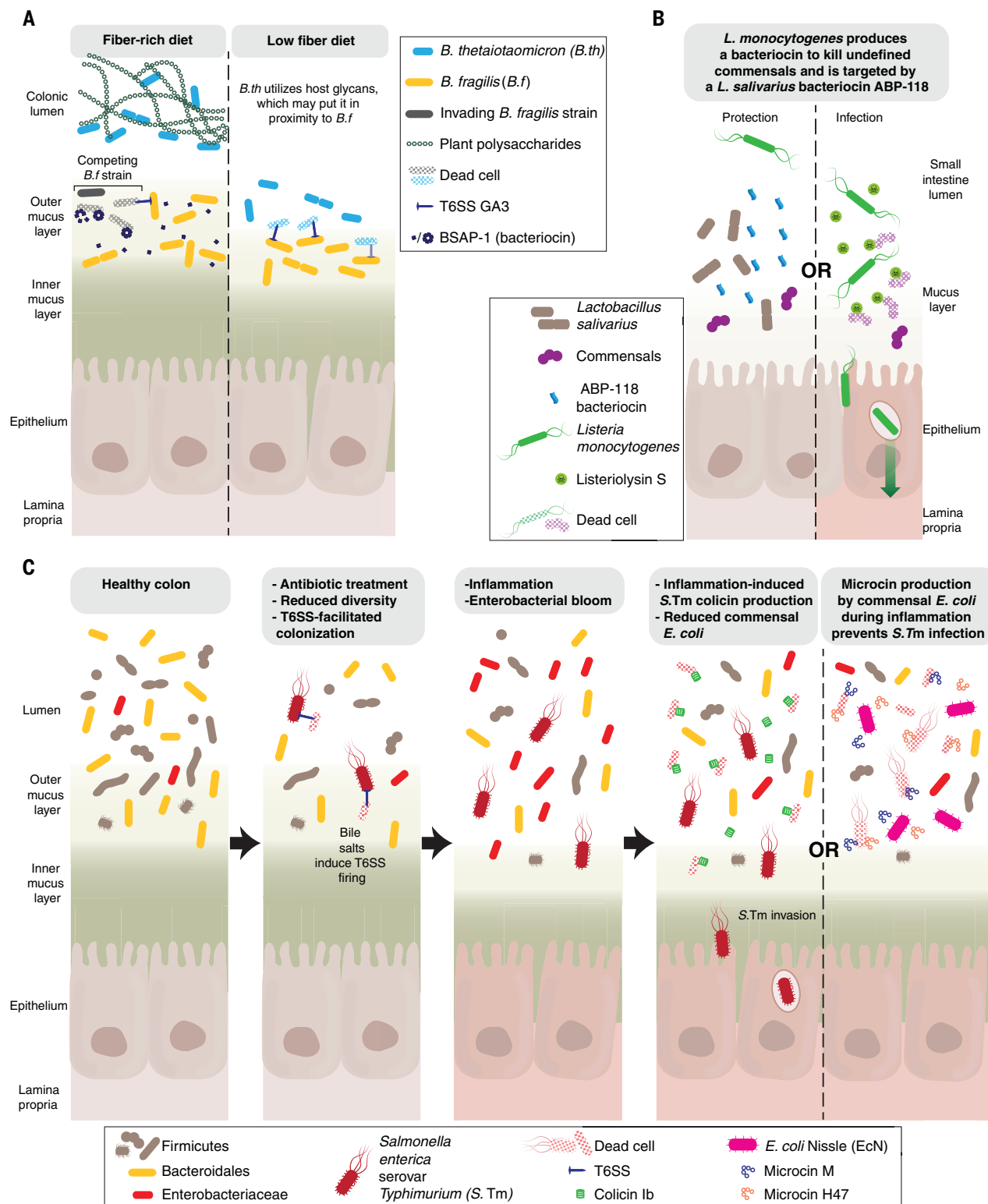


Fig. 1. Examples of interference competition in the gut. (A) *B. fragilis* uses T6SS and bacteriocin-mediated antagonism to compete with other *B. fragilis* strains. It also can use its T6SS to attack other *Bacteroides* species that may localize with *B. fragilis* when dietary polysaccharides are lacking. (B) *L. monocytogenes* colonization of the small intestine is inhibited by the bacteriocin ABP-118 produced by *L. salivarius*. *L. monocytogenes* invasion is facilitated by production of

the bacteriocin listeriolysin S, which targets unknown commensals. (C) Colonization by *S. enterica* serovar *Typhimurium* (*S.Tm*) can occur when antibiotic treatment alters the commensal microbiota, leading to a proteobacterial bloom and *S.Tm*-mediated inflammation. T6SS antagonism and colicin production help *S.Tm* outcompete other commensal enterobacteriaceae and establish infection. Commensal *E. coli* can also produce microcins that prevent *S.Tm* infection.

study analyzed the effect of bacteriocin ABP-118, a broad-spectrum class IIb bacteriocin produced by gut isolates of *Lactobacillus salivarius*. Compositional analyses of the fecal microbiota of mice and pigs indicated only subtle changes in overall community composition due to this bacteriocin (21).

The most abundant and stable members of the gut microbiota, *Bacteroides* spp. produce membrane attack complex/perforin (MACPF) domain pore-forming toxins (22, 23). Two of the best studied of these, BSAP-1 and BSAP-2, have precise intraspecies targets, and nearly all *Bacteroides fragilis* or *Bacteroides uniformis* strains

examined either contain the respective BSAP gene or are sensitive to it (22, 23). The MACPF bacteriocins do not require cognate immunity proteins because the BSAP gene is adjacent to one or more genes encoding a resistant receptor ortholog that likely replaced the native receptor gene (or genes), rendering the BSAP-producing

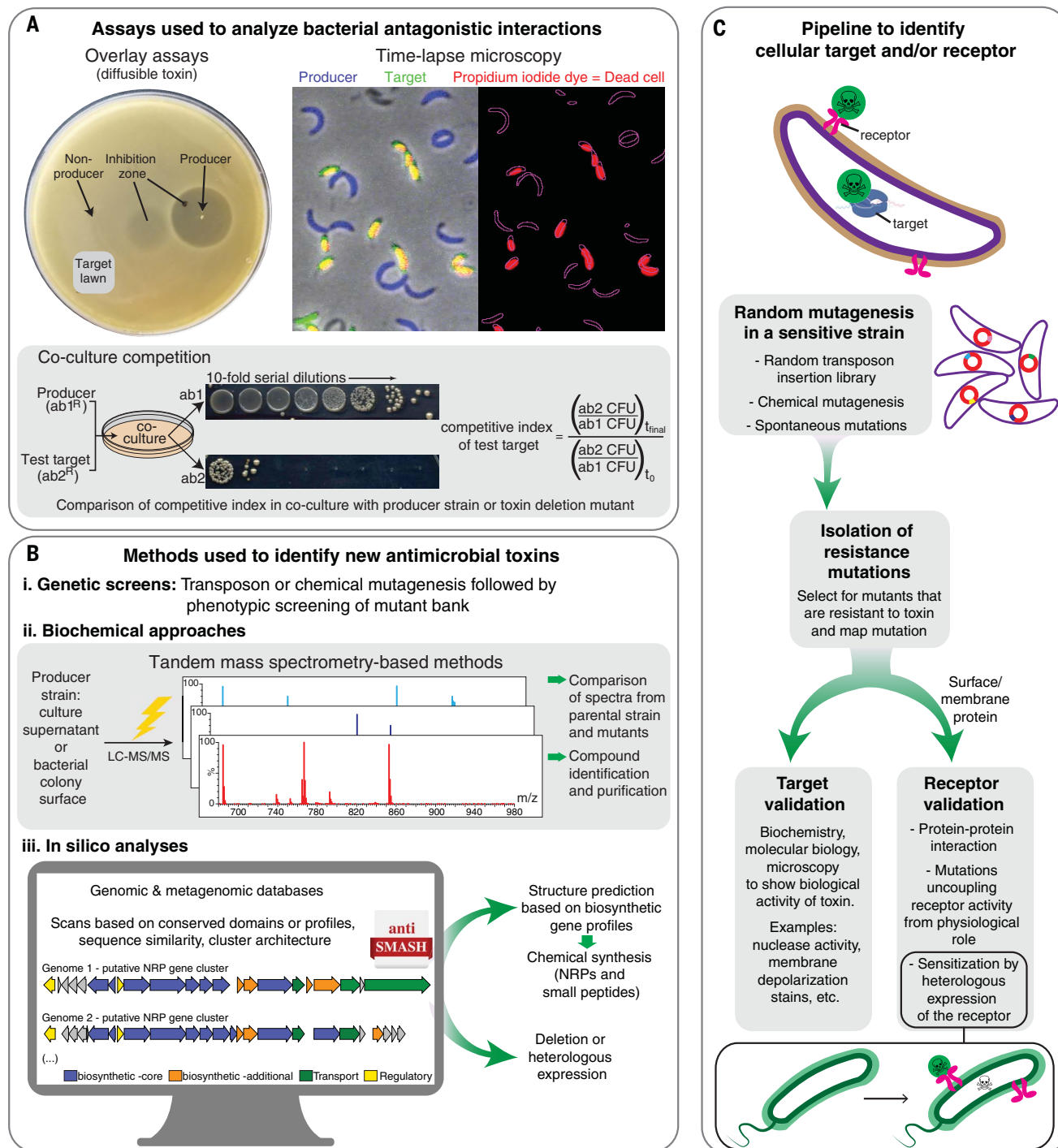


Fig. 2. Experimental approaches to study and characterize new antibacterial toxins. (A) Three phenotypic assays typically used to analyze toxin producer–target cell interactions between two bacteria. ab, antibiotic. (B) Genetic, biochemical, and in silico analyses to identify

new antimicrobial toxins. (C) Identification of surface receptor and cellular target in the sensitive strain can be elucidated by using various methods depending on the strain, its genetic tractability, and whether the receptor is encoded by an essential gene.

strain resistant. BSAP-producing strains have increased fitness in mice when cocolonized with a sensitive isogenic strain, and human gut metagenomic data indicate that coresidence of BSAP-producer and -sensitive strains is rarer than predicted, suggesting that MACPF bacteriocins provide a strong intraspecies competitive advantage to *Bacteroides* in the mammalian gut (23).

Gut Bacteroidales also synthesize T6SSs with many similarities to those of Proteobacterial species (Box 1) (24–26). T6SSs with three distinct genetic architectures are present in diverse gut Bacteroidales species, with genetic architecture 3 (GA3) T6SSs confined to *B. fragilis* (26). In vitro, GA3 T6SSs antagonize nearly all gut Bacteroidales species analyzed (27). By contrast, when analyzing

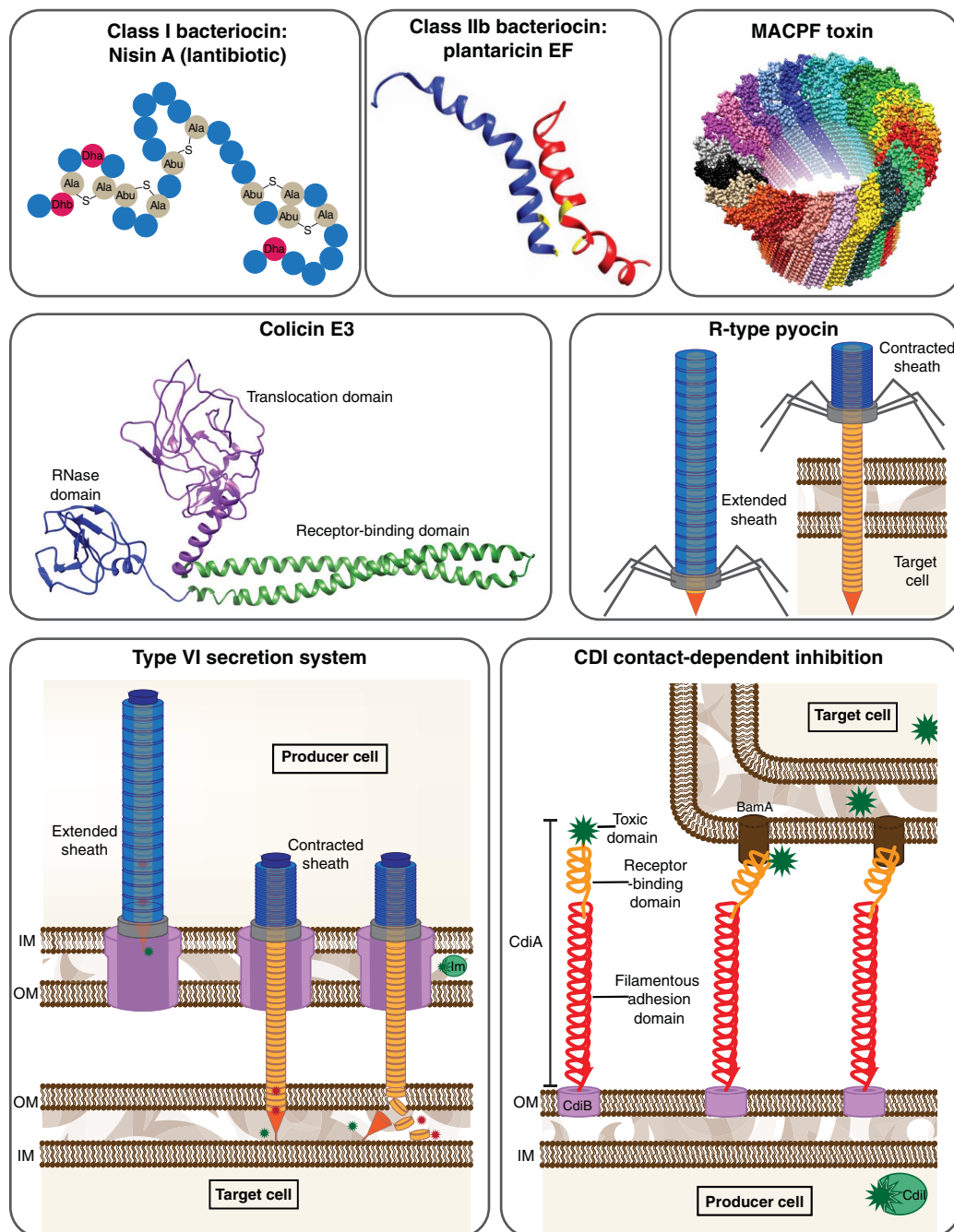
these effects in vivo, GA3 T6SS-sensitive Bacteroidales species are able to colonize the gnotobiotic mouse gut to the same extent when co-inoculated with a wild-type *B. fragilis* strain or its isogenic T6SS mutant (27–29). This effect may be due to the different spatial and nutritional niches of these organisms. *B. fragilis* preferentially consumes host glycans over plant polysaccharides

Table 1. Types and characteristics of antibacterial toxins and toxin secretion systems of bacteria.

	Produced by	Features
Bacteriocins (diffusible toxins)		
Class I	Typically Gram ⁺	Small, 19 to 28 amino acid, <5 kDa Posttranslational modifications, can be cyclical ABC transporter secretion
Class II	Typically Gram ⁺	Small, <10 kDa, typically unmodified Cleaved at GG of leader peptide during secretion Four subclasses (IIa–d), with different structural properties
Microcins	Enterobacteriaceae	Small, <10kDa, linear or knotted peptides Class I <5 kDa, posttranslational modifications Class II 5–10 kDa, modified or unmodified
Colicins and colicin-like bacteriocins	Enterobacteriaceae (colicins), <i>Pseudomonas</i> (S-type)	Require cell lysis for release Three modular domains (Binding, translocation, killing) Colicins A–E, different cellular targets, different cell receptors
F- and R-type bacteriocins (tailocins)	Gram ^{+/–}	Structurally similar to phage tails Rigid and contractile (R) or flexible and noncontractile (F) Require cell lysis for release
Lectin-like bacteriocins	Proteobacteria	High sequence similarity with plant carbohydrate-binding lectins Do not require an immunity protein Lectin domain can be fused to other diverse toxic domains
PT* (also contact-dependent)	Gram ^{+/–}	Diverse toxins with distinct domains and toxin activities Each PT protein typically has three distinct domains Released from the cell using different secretion systems
BSAP	Bacteroidetes	MACPF domains, likely kill by pore formation Mostly intraspecies targeting Do not require immunity protein. Receptor ortholog in producer
Helveticins	Lactobacilli	~ 30 kDa, heat labile, modular Bacteriolytic enzymes (peptidoglycan) Self-export
Cell contact-dependent systems		
T4SS (Antibacterial toxin delivery)	<i>Xanthomonas</i>	Protein complex with a channel that delivers toxic effectors to the periplasm of target cells Likely transfer of diverse toxic effectors Broad range (different orders)
CDI	Proteobacteria	Surface-associated filamentous hemagglutinin domain protein mediates cell-cell adhesion Toxic C-terminal domain cleaved off and imported into target cell Narrow target cell range
T6SS	Gram [–]	A cell-associated retractile phage tail-like apparatus pierces the envelope of the target cell to directly deliver toxic effectors Adenosine 5'-triphosphate (ATP)–dependent process Broad target cell range (often across families)
LXG proteins (Esx type VII secretion)	Gram ⁺	PT domains and immunity proteins toxin likely displayed on producer cell surface
OME	<i>Myxococcus</i>	Outer-membrane lipoprotein toxins exchanged between cells during transient membrane fusion Polymorphic C-terminal toxic domains and cognate immunity protein

*Many PT systems belong to other categories described in this table, such as colicins, pyocins, or CDI.

Fig. 3. Schematic of some bacteriocins and contact-dependent killing systems of bacteria. Class I bacteriocin (Nisin A): small peptides with modified residues (*Dha* dehydroalanine and *Dhb* dehydrobutyrine), and lanthionine (Ala-S-Ala) and β -methylanthionine (Abu-S-Ala) bridges (shown in gray) (100). Class II bacteriocin (Plantaricin EF): small unmodified two-peptide pore-forming bacteriocin that dimerizes and becomes structured in membranes [Protein Data Bank (PDB) 2JUI and 2RLW] (101). MACPF toxin: MACPF-domain toxins produced by *Bacteroides* species are predicted to form multimeric membrane ring pores similar to those adopted by the MACPF domain human immune complement poly-C9 protein shown (PDB 5FMW) (102). Colicin E3: Crystal structure of the modular colicin E3, produced by *E. coli* that cleaves 16S ribosomal RNA in the target cell (PDB 1JCH) (103). R-type bacteriocins: phage tail-like bacteriocins produced by various bacteria that punch holes in the target cell membrane. Type VI secretion system (T6SS): Toxic effectors (depicted as green and red stars) are delivered directly into the target cell via the contractile phage tail-like T6SS. IM, inner membrane; OM, outer membrane; Im, immunity protein. Contact-dependent inhibition (CDI): CdiB mediates export and surface-anchoring of CdiA, which binds a specific surface receptor in the target cell (BamA) and delivers a C-terminal toxic effector. CdiI, immunity protein (104).



(30) and tends to reside near the mucus layer (31). In comparison, *Bacteroides thetaiotaomicron* preferentially consumes plant polysaccharides and uses host mucin glycans when dietary polysaccharides are not available (30). Therefore, when plant polysaccharides are limited and *Bacteroides* species must consume host glycans, they should come into more frequent contact with *B. fragilis* (Fig. 1A). It is possible that GA3 T6SS-mediated antagonism allows *B. fragilis* to carve out a protected niche and thus allows this relative specialist to thrive in the face of competition from more generalists (Fig. 1A).

In silico analyses further support the pervasiveness of antagonism in human microbial communities. Whitney *et al.* showed that the LXG polymorphic toxin (PT) family (Box 1) present in *Streptococcus intermedius* mediates contact-dependent growth inhibition of diverse Firmicutes species in vitro (32). Their analysis of a human gut metagenomic dataset revealed the presence of numerous LXG toxins. Another in silico analysis that probed human metagenomes for biosynthetic clusters uncovered loci predicted to synthesize two nonribosomal peptide antibiotics named humimycins (33). These

heptapeptides were chemically synthesized and shown to have potent activity against *Streptococcus* spp. and *Staphylococcus* spp. Synthetic humimycin A inhibits lipid II flippase and potentiates β -lactam activity against methicillin-resistant *Staphylococcus aureus*. In an *S. aureus* peritonitis-sepsis model, treatment with humimycin A in combination with dicloxacillin increased the survival of mice after 48 hours compared with treatment with either antimicrobial alone (33). Another in silico study also identified a biosynthetic locus for a thiopeptide called lactocillin (34), which is active against

several Gram-positive bacteria. Lactocillin biosynthetic clusters have been found in several human microbiomes. A metatranscriptomics dataset from the human oral microbiota showed that this region is transcribed in vivo, suggesting functional relevance (34).

Data are also suggesting that there may be opportunities to exploit bacteriocins produced by gut bacteria therapeutically. For instance, an *Enterococcus faecalis* strain that produces the bacteriocin bac-21 was shown to displace indigenous enterococci strains, most notably vancomycin-resistant *E. faecalis* V583 in mice (35). Bac-21, like many bacteriocins, has a narrow activity spectrum, making this type of intervention potentially more targeted and less disruptive than the use of antibiotics.

Interference competition in colonization resistance

Host-associated microbial communities often represent a formidable obstacle to invasion by pathogens. This phenomenon, known as colonization resistance, is multifactorial, including competition for nutrients, niche occupation, immune regulation, and modulation of virulence factors (36). The contribution of secreted antimicrobial toxins by the microbiota to prevent invasion by pathogens has only recently been investigated. Many human enteric pathogens—including pathogenic and toxigenic *E. coli*, *Shigella* spp., and *Salmonella* spp.—are Enterobacteriaceae and sometimes fall within the killing spectrum of the toxins of commensal *E. coli*. The human gut symbiont strain *E. coli* Nissle, first isolated in 1917, has been widely used as a probiotic. A recent study demonstrated that *E. coli* Nissle produces microcins that limit the growth of commensal and pathogenic *E. coli*, as well as *Salmonella enterica* serovar Typhimurium during inflammation in a mouse colitis model (Fig. 1C) (37).

Although most diffusible bacteriocins of gut bacteria do not kill across families and orders, there are exceptions. The ABP-118 bacteriocin of *L. salivarius* targets several Gram-positive pathogens, including *Listeria monocytogenes* (Fig. 1B) (38), which is of a distinct order. Most *Staphylococcus* isolates from nasal passages also produce antimicrobial molecules, especially under stress, such as iron limitation (39). Some of these molecules have a very wide spectrum of activity against other nasal microbes, including Actinobacteria, Proteobacteria, and Firmicutes. In an animal colonization model, a nasal *Staphylococcus lugdunensis* strain produced a nonribosomal thiazolidine-containing cyclic peptide antibiotic that prevented nasal colonization by *S. aureus* and correlates with reduced nasal carriage of *S. aureus* in humans (40).

Similar cross-order and phylum-antagonistic interactions have been reported in the vaginal microbiota. The vaginal symbiont *Lactobacillus rhamnosus* produces a bacteriocin called lactocin 160 that antagonizes the vaginal pathogen *Gardnerella vaginalis* (41). Likewise, *Lactobacillus gasseri* EV1461 produces the bacteriocin gassericin E, which inhibits several common agents of bac-

terial vaginosis, including *Atopobium vaginae*, *G. vaginalis*, and *Prevotella bivia* (42).

In addition to human microbial ecosystems, antagonism among plant symbionts are also well studied. *Pseudomonas putida* is a normal soil organism and symbiont of plants and has three distinct T6SSs that allow it to outcompete known plant pathogens in vitro, including *Pseudomonas syringae*, *Xanthomonas campestris*, *Pectobacterium carotovorum*, and *Agrobacterium tumefaciens* (43). In vivo analyses showed that a *P. putida* T6SS limited plant necrosis by the phytopathogen *X. campestris*, and such antagonistic interactions are predicted to be a major factor in this organism's biocontrol properties (43).

There has been an increased interest in engineering gut symbionts to specifically target pathogens without drastically affecting the microbiota, although to date, studies remain at the proof-of-concept stage. For example, the *E. coli* Nissle microcin H47 gene cluster was modified to be induced by tetrathionate, a reactive oxygen species produced during inflammation, increasing the ability of the strain to target *S. enterica* serovar Typhimurium (44). Similarly, *E. coli* was engineered to detect the *P. aeruginosa* quorum-sensing signal and secrete a chimeric bacteriocin designed to target only this pathogen (45). In addition, *Lactococcus lactis* was programmed to detect the sex pheromone of *E. faecalis* from multidrug-resistant strains and express three bacteriocins (46). These studies highlight the potential for arming bacteria with specific antibacterial toxins for clinical and industrial benefit.

Pathogens and invasion of microbial communities

Although we know a great deal about mechanisms that pathogens use to establish infection, only recently has their antagonism of members of the microbiota been shown to be important during infection. Just as members of host-associated microbiota produce toxins to antagonize each other, which can in some cases act to exclude pathogens, pathogens also synthesize toxins that target members of the microbiota. Bacteriocins, contact-dependent growth inhibition (CDI), and T6SSs have all been shown to facilitate pathogen colonization by antagonizing the resident microbiota (Box 1).

Studies have demonstrated a role for *S. enterica* serovar Typhimurium (S.Tm) colicins and bacterially targeted T6SSs in colonization of the mammalian gut. S.Tm mouse infection models often require mice to be treated with antibiotics in order to allow S.Tm colonization, where it then induces inflammation (Fig. 1C). Low iron concentrations in the gut induce expression of colicin Ib by the salmonellae and the siderophore receptor to which it binds. Inflammation allows *Salmonella* and commensal enterobacteria to bloom relative to strict anaerobes (47–49). Under these conditions, S.Tm has a competitive advantage over most commensal *E. coli* because of colicin Ib production (Fig. 1C) (50). A similar

colonization advantage is conferred by one of the T6SSs of S.Tm (SPI-6) because of its antagonism of commensal Enterobacteriaceae (51). A related study showed that a SPI-6 T6SS mutant of *S. enterica* serovar Dublin was attenuated for colonization in birds and mice (52).

The enteric pathogens *Shigella sonnei*, *V. cholerae*, and *L. monocytogenes* also antagonize members of the gut microbiota to establish infection. The T6SS of *S. sonnei* targets commensal *E. coli* in the mouse gut (53) but also targets its congener *Shigella flexneri*. This effect was suggested to possibly explain the increased global prevalence of *S. sonnei* and the decline of *S. flexneri* (53). Similarly, the T6SS of *V. cholerae* antagonizes commensal *E. coli* (54). The resulting *E. coli* cell death was shown to further drive the host innate immune response, enhancing diarrhea and transmission of the organism, demonstrating an additional benefit of antagonism to *V. cholerae* (54). An additional example is the class I bacteriocin of *L. monocytogenes* that alters the gut microbiota to enhance its intestinal colonization (Fig. 1B) (55). It will be interesting to identify what this organism is targeting because the *Listeriaceae* do not have commensal representatives in the gut microbiota.

It is likely that the ability of pathogens to produce antibacterial toxins to bypass colonization resistance by the endogenous microbiota is common in host-associated communities. For example, plant pathogens *A. tumefaciens*, *Xanthomonas citri*, *Xanthomonas fuscans*, and *Erwinia chrysanthemi* use T6SS, T4SS, or CDI to target plant symbionts (56–59), which may facilitate infection and disease.

Antagonism and genome evolution

The dead cells resulting from these lethal interactions provide genetic material that some transformable organisms take up and incorporate into their genomes. Many streptococcal species, including *Streptococcus pneumoniae* and *Streptococcus mutans* coordinately regulate synthesis of the competence machinery and bacteriocin production through quorum sensing (60). In a biofilm model of *S. pneumoniae* mucosal colonization, DNA exchange was enhanced by bacteriocin secretion (61). Therefore, bacteriocin production can inhibit competitors (62), while also increasing access to DNA during competence. Borgeaud *et al.* showed that the T6SS of *V. cholerae* is part of the competence regulon and that DNA released from killed cells could be taken up into toxin producer cells, notably antibiotic resistance genes and pathogenicity islands (63). Thomas *et al.* also showed that variable genes of *V. cholerae* T6SS loci, encoding toxic effectors and immunity proteins (E-I pairs), can be transferred between mutually antagonistic *V. cholerae* strains via transformation (64). Furthermore, newly acquired E-I pairs replace “ancestral” effectors via homologous recombination, yet the recipient strains often retain the ancestral immunity genes, providing immunity to a wider array of toxins, which suggests an ongoing evolutionary arms race between competing strains (65).

Box 1. Types of bacterial toxins/antagonistic systems.

The repertoire of characterized antibacterial toxins and antagonistic systems of bacteria has substantially increased in recent years. Some traditional and newer strategies used in the discovery and characterization of bacterially produced and targeted toxins are summarized in Fig. 2. The arsenal of bacterial antagonistic systems is extremely diverse (Fig. 3 and Table 1). Antimicrobial toxins or systems can be broadly classified into (i) diffusible molecules that are released into the extracellular milieu and (ii) toxins that are delivered directly to the target cell via cell-to-cell contact through a variety of secretion systems.

Bacteriocins

"Bacteriocin" is a broad term used to describe a very heterogeneous group of diffusible bacterially produced peptides or protein antibacterial toxins. These include small peptide toxins that are often posttranslationally modified (PTM), large proteins, and R-type bacteriocins that are multiprotein complexes with similarities to phage (20). Bacteriocins are ubiquitous, with evidence of their production across all major groups of bacteria and many archaea (20, 105). In contrast to antibiotics, bacteriocins typically have a narrow killing spectrum, targeting close relatives of the producing strain (19, 106). This range is most often dictated by the requirement for a specific cell-surface receptor on the target cell that mediates attachment and sometimes import into the cell (107, 108). Bacteriocins use a variety of mechanisms to kill sensitive cells, including pore-formation, inhibition of cell-wall synthesis, degradation of peptidoglycan, inhibition of protein synthesis, nuclease activity, and gyrase inhibition (19, 109, 110).

A distinguishing feature of peptide bacteriocins relative to small-molecule antibiotics and other small-peptide toxins is that bacteriocins are ribosomally synthesized. In general, bacteriocins are encoded within gene clusters that comprise all the products required for synthesis, PTM, and export, along with a gene that encodes an immunity protein that protects the producer cell from its own bacteriocin (107, 111). Often, these bacteriocin biosynthesis regions contain genes involved in regulation, signaling molecules, and other genes of unknown function (111, 112). Peptide bacteriocins are grouped into a few major classes; however, within those classes there is tremendous variety, leading to subclassifications on the basis of structure, PTMs, and conserved cleavage sites.

Bacteria also produce numerous larger-protein bacteriocins, including the well-studied colicins produced exclusively by Enterobacteriaceae [reviewed in (113)]. Colicin secretion is dependent on cell lysis rather than active secretion, so only a subpopulation secretes the toxin. Colicins typically have a common three-domain organization: an N-terminal region involved in membrane translocation, a central receptor binding domain, and a C-terminal variable toxin domain (Fig. 3). Colicins bind specific outer-membrane molecules, which are typically involved in nutrient uptake, and are transported into the recipient cell.

Until recently, nearly all of the studies of bacteriocins of Gram-negative bacteria have been from members of the phylum Proteobacteria. Interest in host-associated micro-

bial communities has resulted in an intense study of gut Bacteroidales species, which are the most abundant Gram-negative bacteria of the human gut microbiota. Studies of these organisms have revealed completely distinct types of diffusible antibacterial toxins. The first class of diffusible toxins identified in *B. fragilis* (BSAP-1) and *B. uniformis* (BSAP-2) have MACPF domains present in host immune molecules that kill bacteria through pore formation (Fig. 3) (22, 23). A second type of diffusible secreted antimicrobial molecule is produced by a subset of *B. fragilis* strains. This molecule is very similar to human ubiquitin and targets a subset of *B. fragilis* strains (114).

In addition to small-peptide and larger-protein toxins, another distinct type of bacterial killing apparatus given the designation bacteriocin is the R-type bacteriocins [reviewed in (115)]. Like the T6SSs discussed below, these structures are similar to phage in that they contain a needlelike structure contained within a contractile sheath (Fig. 3). This complex is coupled to a phage baseplate-like structure and tail fibers that specifically recognize a target molecule on sensitive cells. Unlike T6SSs that are cell-associated and use cellular ATP hydrolysis for sheath contraction, R-type bacteriocins are released extracellularly from the producing cell upon lysis, and their binding to the receptor molecule drives the needle into the target cell. The R-type bacteriocins do not deliver toxic effectors; rather, the pore created by needle penetration of the membrane dissipates the membrane potential, leading to cell death.

Type IV secretion system toxins

Type IV secretion systems (T4SSs) can transfer DNA, proteins, and protein-DNA complexes into neighboring cells in a contact-dependent manner (116). This ATP-dependent multiprotein complex has a translocation channel that spans the whole cell envelope and an extracellular pilus involved in conjugative DNA transfers between bacteria or translocation of effectors largely into eukaryotic cells (116). Recently, a T4SS of the plant pathogen *X. citri* was shown to secrete toxic effectors into bacterial cells and was shown to antagonize two different Proteobacterial species (57). It has been suggested that T4SSs may play a larger role in interbacterial antagonism than currently appreciated (57).

Polymorphic toxins

Polymorphic toxins (PTs) are a diverse group of modular proteins with distinct domains generated through recombination. The N terminus is typically involved in secretion or cell anchoring, the central domain is often involved in receptor

binding, and the C terminus contains the toxin domain. Genomic analyses revealed a tremendous diversity of PTs and found that they are distributed across all major bacterial lineages (117, 118). One abundant family of PT, the recombination hotspot proteins (Rhs), comprises large proteins with a central region of Rhs repeats that adopts a filamentous fold. Other common families of PT include colicins, CDI toxins, and the LXG toxins described below. Some PTs are released in a diffusible form from a producing cell, others are filamentous structures attached to the cell-surface, whereas others are secreted by means of specific secretion systems as well as through outer-membrane exchange (117, 118).

CDI (type V secretion)

The first contact-dependent antagonistic system to be characterized, *cdiBAI*, was discovered in *E. coli*, but similar systems are widespread in Proteobacteria (118–120). CdiA and CdiB are the components of a type V secretion system subclass called two-partner secretion. CdiB is an outer-membrane β -barrel transporter that mediates translocation of CdiA to the cell surface. CdiA is a large, modular filamentous PT similar to a stick with a variable toxin tip (Fig. 3). Toxin delivery into the target cell requires stable cell-to-cell contact and specific surface receptor molecules on the target cell (104). Once contact is established, the toxin moiety is cleaved from the rest of the protein and imported into the cell (121–123). Rhs proteins of Gram-positive bacteria are thought to mediate attachment and toxin delivery through a mechanism similar to CDI (124, 125).

Type VI secretion system

T6SSs are widespread in Proteobacteria (126) and Bacteroidetes (24, 26). The T6SS apparatus allows producer bacteria to inject toxins directly into adjacent bacteria or eukaryotic target cells in a contact-dependent manner (127, 128). The T6SS multiprotein complex shares structural homology to the T4 contractile bacteriophage tail with a portion spanning the cell envelope of the producing cell. The core components are assembled in the cytosol and membrane and are loaded with toxic effectors before firing. A spike-tipped needle (Fig. 3) is surrounded by a contractile sheath, which through a rapid conformational change propels the needle outward, piercing the membrane of the target cell and delivering the cargo, which can include a variety of different toxins, including PTs (118, 129–131). Bacterially targeted T6SSs have only been shown to be produced by and to antagonize Gram-negative bacteria, but the target cells can be of distinct genera and families than the producer.

Box 1. continued**Type VII secretion (Esx pathway)**

The Esx pathway (T7SS) is widespread in Mycobacteria and other Gram-positive bacteria and exports substrates with a variety of biological roles, including antibacterial toxins [reviewed in (132)]. The LXG polymorphic toxins, broadly distributed in Firmicutes, were recently shown to be Esx clients (32, 117). The LXG architecture is analogous to Rhs toxins: a conserved N terminus (LXG domain) necessary for secretion, a middle domain of variable length, and a C-terminal variable toxin domain. In both *S. aureus* and *S. intermedius*, the T7SS was shown to deliver LXG or non-LXG toxins to target cells of diverse Gram-positive species (32, 133).

Other contact-dependent toxin systems

Another contact-dependent toxin system is the surface-associated glycine-zipper toxins (Cdz) recently described in the aquatic oligotrophic α -proteobacterium *Caulobacter crescentus*. Cdz toxins are secreted via a Type I secretion system and form amyloid-like aggregates on the surface of producer cells, which are delivered to target cells upon contact (134). Yet another distinct toxin delivery system is that of OME described in the social bacterium *Myxococcus xanthus*. OME is regulated by a cell-surface receptor, TraA, that is polymorphic between different strains. TraA interactions between cells lead to transient outer-membrane fusion and exchange of lipopolysaccharide, lipid, and lipoprotein (135, 136). The polymorphic SitA lipoprotein toxins are delivered during OME, in which they are serially transferred between cells, killing those lacking the immunity protein (69).

Antagonism as a facilitator of cooperation

The production of a diffusible shared resource (public good) often incurs a fitness cost to the producing cell; therefore, a mechanism to exclude freeloading cheaters is necessary in order to maintain cooperation over evolutionary time (66). Some bacteriocins have been shown to be a mechanism with which to minimize the impact of spontaneous mutant cheaters. For example, in natural populations of *Pseudomonas fluorescens*, strains that produce the siderophore pyoverdine are less susceptible to exploitation by cheaters when they also produce bacteriocins (67). Similarly, in *Burkholderia thailandensis*, a quorum-sensing regulatory circuit controls a T6SS, constraining the proliferation of quorum-sensing mutants that do not synthesize the T6SS immunity genes and would otherwise have a competitive advantage associated with avoiding the metabolic cost of synthesizing and firing the T6SS (68).

Furthermore, in natural communities in which several strains from the same species co-reside, antagonism can discriminate between kin and competitors, therefore assisting in the production of public goods, which are only evolutionarily advantageous if they benefit individuals who share genes for helping. For example, the soil organism *Myxococcus xanthus* displays an array of coordinated behaviors (such as collective swarming, fruiting body formation, and predation) that require division of labor. Myxobacteria exchange large amounts of surface material through contact-dependent outer-membrane exchange (OME) (Box 1), which not only discriminates and supplies resources to kin but also acts as the mechanism by which a PT is delivered (Box 1) (69). Non-kin are killed because they lack the cognate immunity protein, hence limiting cooperation to kin. Cooperation in *Bacillus subtilis* biofilms is similarly coordinated by kin discrimination facilitated by the combinatorial effect of an array of contact-dependent and diffusible antimicrobial toxins, thus facilitating cooperation at different spatial scales (70). Related examples are found in *V. cholerae* biofilms and during multicellular swarming of *Proteus mirabilis*, where T6SS-mediated antagonism between two strains drives spatial segregation, enabling cooperation within each clonal patch (71, 72). Interestingly, the CDI system deployed in biofilm-forming communities of *Burkholderia thailandensis* acts as a "helping greenbeard" to foster cooperation between individuals that express high levels of the same gene, independent of global genetic similarity. In this case, the toxin moiety that kills cells that lack the cognate immunity gene can also act as a signaling molecule among resistant kin to induce expression of cooperative genes (73, 74).

Regulation of antagonism

Competition experiments and mathematical modeling suggest that there are large trade-offs between deploying aggressive phenotypes and investing resources in growth. Therefore, the outcome is strongly dependent on environmental conditions and metabolic cost of each particular antagonism system (2, 75, 76). Interestingly, this cost can be mitigated through tight regulation of arm deployment (77) and recycling of macromolecular complex components (78).

Our current understanding of the *in vivo* regulation of bacteriocin production and contact-dependent systems is limited. In some cases, antimicrobial toxin systems are induced by environmental signals indicating that the bacterium is inside a host—such as gastric fluid (79), bile (51, 80), iron starvation, and hydrogen peroxide (39)—or by other host products such as mucins (80), as well as signals derived from the microbiota (81, 82). Many bacteriocins require a critical cell density of producer cells to achieve toxic environmental concentrations, and therefore, many bacteriocin gene clusters encode quorum-sensing pheromones and their cognate two-component response systems (83). For example, the gene cluster involved in production of

gassericin E by the vaginal symbiont *L. gasseri* EV1461 encodes an autoinducer peptide, a histidine kinase, and a response regulator, ensuring production only at high cell densities (42).

Regulation of bacterial antagonism systems through different general stress responses can be broadly classified as "competition sensing," in which toxin production is triggered in response to biotic damage or stress caused by competitors, such as starvation, envelope stress, or DNA damage (83). By contrast, abiotic stress responses, such as heat shock or osmotic stress, tend not to induce expression of antimicrobials (83). Many colicins are part of the LexA regulon (LexA is the master regulator of the SOS response to DNA damage). *Pseudomonas aeruginosa* and *Serratia marcescens* fire their T6SS in response to attack by a T6SS-mediated attack from other species (77, 84, 85). Some antimicrobial systems are regulated by specific signals, such as the absence of a nutrient, and others use a Trojan horse strategy (by modifying the toxin to look like a nutrient) to target competitors that consume a specific resource. For example, microcin MccE492 from *Klebsiella pneumoniae* and MccH47 from *E. coli* have a siderophore moiety attached to the toxic peptide. These bacteriocins are produced during iron starvation and taken up by target cells via their siderophore receptor, leading to death of cells that lack the immunity protein (86–88).

Moreover, bacteria can survey their environment for incoming threats by detecting specific exogenous molecules, such as volatile organic compounds and diffusible secondary metabolites, in a manner akin to pathogen-associated molecular pattern recognition by the mammalian immune system (89, 90). This type of "danger sensing" allows the cell to respond by anticipating attacks, therefore minimizing damage or eliminating the source of the threat. Many diffusible bacteriocins and contact-dependent systems may be regulated in this manner (89). For example, debris from lysed *P. aeruginosa* acts as a danger signal that triggers deployment of its T6SS in nearby unharmed cells (91). Some bacteria, including *L. gasseri* EV1461, can "eavesdrop" on the quorum-sensing signals of competing species and respond by expressing broad-spectrum antibiotics, as well as by generating antimicrobial resistance strategies (42, 89, 92, 93). Notably, the *bfp* quorum-sensing system that regulates bacteriocin production in *S. pneumoniae* is highly polymorphic, and instances of cross-talk and eavesdropping between strains are common (9). Simulations using four strains with varying ability to sense neighbor's quorum-sensing signals show that eavesdropping can confer a fitness advantage with a negative frequency dependence (a strain present at low frequency can induce bacteriocin production to invade a more abundant population). Westhoff *et al.* postulated recently that bacterial responses to danger may be fine-tuned to the proximity of the perceived threat, indicating that more distant threats may be countered by diffusible antimicrobial products, whereas response to contact-dependent

antagonism may be an immediate counter-attack (90).

Perspectives

Antibacterial toxin production is ubiquitous in microbial communities. Bacteria synthesize a diverse array of antimicrobial toxins and systems for their secretion. In agreement with the principle of "habitat-filtering," phylogenetically related species tend to reside in similar environments and compete for resources; therefore, narrow range antagonism systems are common (2, 94). Yet many organisms are armed with multiple antibacterial toxins, some that kill strains of the same species and others that kill across species, genera, families, and orders. Furthermore, a single-secretion apparatus (such as T6SS) can be used to simultaneously deploy an array of toxic effectors that target different cellular processes, giving these producer cells an upper hand in an evolutionary arms race and increasing the range of possible competitors that can be targeted (65, 95). There are also numerous examples in which reciprocal fighting should occur, such as the battles between armed pathogens and armed members of the microbiota or between two natural members of a microbial community. The outcome of such reciprocal antagonism likely depends on density (strain frequency) (18), species range, and its local distribution (diffusible versus contact dependent) and mechanism of toxicity.

The studies highlighted in this Review demonstrate numerous fitness benefits to toxin producers in microbial communities. The most obvious benefit is the killing of competitors that may use the same nutrients and scarce resources, but there are distinct ecological outcomes to these interactions. Antagonism can prevent organisms from invading ecosystems but can also assist invasion. Killed cells release DNA that can be taken up by the killer, leading to genome evolution. Material released from dead cells can also modulate host responses, increasing transmission of a pathogenic aggressor (54). Antagonism can also maintain microbial diversity, promote spatial segregation of different genotypes, and facilitate cooperation between kin cells.

Despite numerous advances in this field, there is still limited knowledge of the ecological effects of antagonism owing to an incomplete understanding of the spatial architecture of many natural communities, regulatory factors governing toxin synthesis and secretion, diffusion capabilities of various toxins in these natural communities, and the combinatorial effects of the deployment of multiple toxins. Analyses to further probe these interactions will benefit from a combination of mechanistic analyses, experimental model studies, and mathematical modeling as well as analyses of metagenomic and metatranscriptomic datasets of natural microbial communities. This combination of analyses is key to understanding how antagonistic interactions allow an organism to establish and compete in a community and, therefore, influence its overall structure and composition.

Continued analyses of these ecological effects will help to facilitate the translation of these antimicrobial toxins into clinical, agricultural, and industrial applications. Such toxins could potentially allow a genetically engineered beneficial organism to get a foothold in an ecosystem to deliver a therapeutic property or to prevent invasion of pathogens into host-associated communities. Antimicrobial toxins could also be used to selectively remove strains with pathogenic potential such as *Clostridium difficile*, strains carrying resistance genes to clinically relevant antibiotics, and organisms associated with various drug failures such as to the cardiac drug digoxin (96) and cancer immunotherapies (97–99). The next decade is likely to usher in an era of selective microbiota engineering in which antimicrobial toxins may play an important role.

REFERENCES AND NOTES

- M. E. Hibbing, C. Fuqua, M. R. Parsek, S. B. Peterson, Bacterial competition: Surviving and thriving in the microbial jungle. *Nat. Rev. Microbiol.* **8**, 15–25 (2010). doi: [10.1038/nrmicro2259](#); pmid: [19946288](#)
- M. Ghoul, S. Mitri, The ecology and evolution of microbial competition. *Trends Microbiol.* **24**, 833–845 (2016). doi: [10.1016/j.tim.2016.06.011](#); pmid: [27546832](#)
- A. J. Bäuml, V. Sperandio, Interactions between the microbiota and pathogenic bacteria in the gut. *Nature* **535**, 85–93 (2016). doi: [10.1038/nature18849](#); pmid: [27383983](#)
- J. J. Faith et al., The long-term stability of the human gut microbiota. *Science* **341**, 1237439 (2013). doi: [10.1126/science.1237439](#); pmid: [23828941](#)
- A. Moya, M. Ferrer, Functional redundancy-induced stability of gut microbiota subjected to disturbance. *Trends Microbiol.* **24**, 402–413 (2016). doi: [10.1016/j.tim.2016.02.002](#); pmid: [26996765](#)
- A. E. F. Little, C. J. Robinson, S. B. Peterson, K. F. Raffa, J. Handelsman, Rules of engagement: Interspecies interactions that regulate microbial communities. *Annu. Rev. Microbiol.* **62**, 375–401 (2008). doi: [10.1146/annurev.micro.030608.101423](#); pmid: [18544040](#)
- C. G. Buffie et al., Precision microbiome reconstitution restores bile acid mediated resistance to *Clostridium difficile*. *Nature* **517**, 205–208 (2015). doi: [10.1038/nature13828](#); pmid: [25337874](#)
- B. S. Weber, P. M. Ly, J. N. Irwin, S. Pukatzki, M. F. Feldman, A multidrug resistance plasmid contains the molecular switch for type VI secretion in *Acinetobacter baumannii*. *Proc. Natl. Acad. Sci. U.S.A.* **112**, 9442–9447 (2015). doi: [10.1073/pnas.1502966112](#); pmid: [26170289](#)
- E. L. Miller et al., Eavesdropping and crosstalk between secreted quorum sensing peptide signals that regulate bacteriocin production in *Streptococcus pneumoniae*. *ISME J.* (2018). doi: [10.1038/s41396-018-0178-x](#); pmid: [29899510](#)
- R. S. Mehta et al., Stability of the human faecal microbiome in a cohort of adult men. *Nat. Microbiol.* **3**, 347–355 (2018). doi: [10.1038/s41564-017-0096-0](#); pmid: [29335554](#)
- T. N. Jayasinghe et al., Long-term stability in the gut microbiome over 46 years in the life of Billy Apple. *Hum. Microbiome J.* **5**, 6–7 (2017). doi: [10.1016/j.jhumic.2017.09.001](#)
- K. Z. Coyte, J. Schluter, K. R. Foster, The ecology of the microbiome: Networks, competition, and stability. *Science* **350**, 663–666 (2015). doi: [10.1126/science.1262602](#); pmid: [26542567](#)
- M. I. Abrudan, S. Brown, D. E. Rozen, Killing as means of promoting biodiversity. *Biochem. Soc. Trans.* **40**, 1512–1516 (2012). doi: [10.1042/BST20120196](#); pmid: [23176508](#)
- P. Szabó, T. Czárán, G. Szabó, Competing associations in bacterial warfare with two toxins. *J. Theor. Biol.* **248**, 736–744 (2007). doi: [10.1016/j.jtbi.2007.06.022](#); pmid: [17686495](#)
- B. Kerr, M. A. Riley, M. W. Feldman, B. J. M. Bohannan, Local dispersal promotes biodiversity in a real-life game of rock-paper-scissors. *Nature* **418**, 171–174 (2002). doi: [10.1038/nature00823](#); pmid: [12110887](#)
- B. C. Kirkup, M. A. Riley, Antibiotic-mediated antagonism leads to a bacterial game of rock-paper-scissors in vivo.

- Nature* **428**, 412–414 (2004). doi: [10.1038/nature02429](#); pmid: [15042087](#)
- M. Wong et al., Microbial herd protection mediated by antagonistic interaction in polymicrobial communities. *Appl. Environ. Microbiol.* **82**, 6881–6888 (2016). doi: [10.1128/AEM.02210-16](#); pmid: [27637882](#)
- O. Rendueles, M. Amherd, G. J. Velicer, Positively frequency-dependent interference competition maintains diversity and pervades a natural population of cooperative microbes. *Curr. Biol.* **25**, 1673–1681 (2015). doi: [10.1016/j.cub.2015.04.057](#); pmid: [26051889](#)
- P. D. Cotter, R. P. Ross, C. Hill, Bacteriocins—A viable alternative to antibiotics? *Nat. Rev. Microbiol.* **11**, 95–105 (2013). doi: [10.1038/nrmicro2937](#); pmid: [23268227](#)
- M. A. Riley, in *Encyclopedia of Microbiology* (Elsevier, 2009), pp. 32–44.
- E. Riboulet-Bisson et al., Effect of *Lactobacillus salivarius* bacteriocin Abp118 on the mouse and pig intestinal microbiota. *PLOS ONE* **7**, e31113 (2012). doi: [10.1371/journal.pone.0031113](#); pmid: [22363561](#)
- M. Chatzidakis-Livanis, M. J. Coyne, L. E. Comstock, An antimicrobial protein of the gut symbiont *Bacteroides fragilis* with a MACPF domain of host immune proteins. *Mol. Microbiol.* **94**, 1361–1374 (2014). doi: [10.1111/mmi.12839](#); pmid: [25339613](#)
- K. G. Roelofs, M. J. Coyne, R. R. Gentyala, M. Chatzidakis-Livanis, L. E. Comstock, *Bacteroides* secreted antimicrobial proteins target surface molecules necessary for gut colonization and mediate competition in vivo. *MBio* **7**, e01055-e16 (2016). doi: [10.1128/mBio.01055-16](#); pmid: [27555379](#)
- A. B. Russell et al., A type VI secretion-related pathway in *Bacteroidetes* mediates interbacterial antagonism. *Cell Host Microbe* **16**, 227–236 (2014). doi: [10.1016/j.chom.2014.07.007](#); pmid: [25070807](#)
- M. J. Coyne, N. L. Zitomersky, A. M. McGuire, A. M. Earl, L. E. Comstock, Evidence of extensive DNA transfer between bacteroidales species within the human gut. *MBio* **5**, e01305–e01314 (2014). doi: [10.1128/mBio.01305-14](#); pmid: [24939888](#)
- M. J. Coyne, K. G. Roelofs, L. E. Comstock, Type VI secretion systems of human gut *Bacteroidales* segregate into three genetic architectures, two of which are contained on mobile genetic elements. *BMC Genomics* **17**, 58 (2016). doi: [10.1186/s12864-016-2377-z](#); pmid: [26768901](#)
- M. Chatzidakis-Livanis, N. Geva-Zatorsky, L. E. Comstock, *Bacteroides fragilis* type VI secretion systems use novel effector and immunity proteins to antagonize human gut *Bacteroidales* species. *Proc. Natl. Acad. Sci. U.S.A.* **113**, 3627–3632 (2016). doi: [10.1073/pnas.1522510113](#); pmid: [26951680](#)
- A. L. Hecht et al., Strain competition restricts colonization of an enteric pathogen and prevents colitis. *EMBO Rep.* **17**, 1281–1291 (2016). doi: [10.15252/embr.201642282](#); pmid: [27432285](#)
- A. G. Wexler et al., Human symbionts inject and neutralize antibacterial toxins to persist in the gut. *Proc. Natl. Acad. Sci. U.S.A.* **113**, 3639–3644 (2016). doi: [10.1073/pnas.1525637113](#); pmid: [26957597](#)
- N. A. Pudlo et al., Symbiotic human gut bacteria with variable metabolic priorities for host mucosal glycans. *MBio* **6**, e01282–e15 (2015). doi: [10.1128/mBio.01282-15](#); pmid: [26556271](#)
- S. M. Lee et al., Bacterial colonization factors control specificity and stability of the gut microbiota. *Nature* **501**, 426–429 (2013). doi: [10.1038/nature12447](#); pmid: [23955152](#)
- J. C. Whitney et al., A broadly distributed toxin family mediates contact-dependent antagonism between gram-positive bacteria. *eLife* **6**, e26938 (2017). doi: [10.7554/eLife.26938](#); pmid: [28696203](#)
- J. Chu et al., Discovery of MRSA active antibiotics using primary sequence from the human microbiome. *Nat. Chem. Biol.* **12**, 1004–1006 (2016). doi: [10.1038/nchembio.2207](#); pmid: [27748750](#)
- M. S. Donia et al., A systematic analysis of biosynthetic gene clusters in the human microbiome reveals a common family of antibiotics. *Cell* **158**, 1402–1414 (2014). doi: [10.1016/j.cell.2014.08.032](#); pmid: [25215495](#)
- S. Kommineni et al., Bacteriocin production augments niche competition by enterococci in the mammalian gastrointestinal tract. *Nature* **526**, 719–722 (2015). doi: [10.1038/nature15524](#); pmid: [26479034](#)
- K. J. Rangan, H. C. Hang, Biochemical mechanisms of pathogen restriction by intestinal bacteria. *Trends Biochem. Sci.*

- 42, 887–898 (2017). doi: [10.1016/j.tibs.2017.08.005](https://doi.org/10.1016/j.tibs.2017.08.005); pmid: 28927699
37. M. Sassone-Corsi *et al.*, Microcins mediate competition among Enterobacteriaceae in the inflamed gut. *Nature* **540**, 280–283 (2016). doi: [10.1038/nature20557](https://doi.org/10.1038/nature20557); pmid: 27798599
38. S. C. Corr *et al.*, Bacteriocin production as a mechanism for the anti-infective activity of *Lactobacillus salivarius* UCC118. *Proc. Natl. Acad. Sci. U.S.A.* **104**, 7617–7621 (2007). doi: [10.1073/pnas.0700440104](https://doi.org/10.1073/pnas.0700440104); pmid: 17456596
39. D. Janek, A. Zipperer, A. Kulik, B. Krismer, A. Peschel, High frequency and diversity of antimicrobial activities produced by nasal *Staphylococcus* strains against bacterial competitors. *PLOS Pathog.* **12**, e1005812 (2016). doi: [10.1371/journal.ppat.1005812](https://doi.org/10.1371/journal.ppat.1005812); pmid: 27460492
40. A. Zipperer *et al.*, Human commensals producing a novel antibiotic impair pathogen colonization. *Nature* **535**, 511–516 (2016). doi: [10.1038/nature18634](https://doi.org/10.1038/nature18634); pmid: 27466123
41. Y. Turovskiy, R. D. Ludescher, A. A. Aroutcheva, S. Faro, M. L. Chikindas, Lactocin 160, a bacteriocin produced by vaginal *Lactobacillus rhamnosus*, targets cytoplasmic membranes of the vaginal pathogen, *Gardnerella vaginalis*. *Probiotics Antimicrob. Proteins* **1**, 67–74 (2009). doi: [10.1007/s12602-008-9003-6](https://doi.org/10.1007/s12602-008-9003-6); pmid: 20445810
42. A. Maldonado-Barragán, B. Caballero-Guerrero, V. Martín, J. L. Ruiz-Barba, J. M. Rodríguez, Purification and genetic characterization of gassericin E, a novel co-culture inducible bacteriocin from *Lactobacillus gasserii* EV1461 isolated from the vagina of a healthy woman. *BMC Microbiol.* **16**, 37 (2016). doi: [10.1186/s12866-016-0663-1](https://doi.org/10.1186/s12866-016-0663-1); pmid: 26969428
43. P. Bernal, L. P. Allsopp, A. Filloux, M. A. Llamas, The *Pseudomonas putida* T6SS is a plant weapon against phytopathogens. *ISME J.* **11**, 972–987 (2017). doi: [10.1038/ismej.2016.169](https://doi.org/10.1038/ismej.2016.169); pmid: 28045455
44. J. D. Palmer *et al.*, Engineered probiotic for the inhibition of *Salmonella* via tetrathionate-induced production of microcin H47. *ACS Infect. Dis.* **4**, 39–45 (2018). doi: [10.1021/acsinfecdis.7b00114](https://doi.org/10.1021/acsinfecdis.7b00114); pmid: 28918634
45. S. Gupta, E. E. Bram, R. Weiss, Genetically programmable pathogen sense and destroy. *ACS Synth. Biol.* **2**, 715–723 (2013). doi: [10.1021/sb4000417](https://doi.org/10.1021/sb4000417); pmid: 23763381
46. J. Borrero, Y. Chen, G. M. Dunny, Y. N. Kaznessis, Modified lactic acid bacteria detect and inhibit multidrug-resistant enterococci. *ACS Synth. Biol.* **4**, 299–306 (2015). doi: [10.1021/sb500090b](https://doi.org/10.1021/sb500090b); pmid: 24896372
47. S. E. Winter *et al.*, Host-derived nitrate boosts growth of *E. coli* in the inflamed gut. *Science* **339**, 708–711 (2013). doi: [10.1126/science.1232467](https://doi.org/10.1126/science.1232467); pmid: 23932266
48. S. E. Winter *et al.*, Gut inflammation provides a respiratory electron acceptor for *Salmonella*. *Nature* **467**, 426–429 (2010). doi: [10.1038/nature09415](https://doi.org/10.1038/nature09415); pmid: 20864996
49. M. X. Byndloss, A. J. Bäuml, The germ-organ theory of non-communicable diseases. *Nat. Rev. Microbiol.* **16**, 103–110 (2018). doi: [10.1038/nrmicro.2017.158](https://doi.org/10.1038/nrmicro.2017.158); pmid: 29307890
50. L. P. Nedialkova *et al.*, Inflammation fuels colicin Ib-dependent competition of *Salmonella* serovar Typhimurium and *E. coli* in enterobacterial blooms. *PLOS Pathog.* **10**, e1003844 (2014). doi: [10.1371/journal.ppat.1003844](https://doi.org/10.1371/journal.ppat.1003844); pmid: 24391500
51. T. G. Sana *et al.*, *Salmonella* Typhimurium utilizes a T6SS-mediated antibacterial weapon to establish in the host gut. *Proc. Natl. Acad. Sci. U.S.A.* **113**, E5044–E5051 (2016). doi: [10.1073/pnas.1608858113](https://doi.org/10.1073/pnas.1608858113); pmid: 27503894
52. D. Pezosa *et al.*, Only one of the two type VI secretion systems encoded in the *Salmonella enterica* serotype Dublin genome is involved in colonization of the avian and murine hosts. *Vet. Res.* **45**, 2 (2014). doi: [10.1186/1297-9716-45-2](https://doi.org/10.1186/1297-9716-45-2); pmid: 24405577
53. M. C. Anderson, P. Vonaesch, A. Saffarian, B. S. Marteyn, P. J. Sansonetti, Shigella sonnei encodes a functional T6SS used for interbacterial competition and niche occupancy. *Cell Host Microbe* **21**, 769–776.e3 (2017). doi: [10.1016/j.chom.2017.05.004](https://doi.org/10.1016/j.chom.2017.05.004); pmid: 28618272
54. W. Zhao, F. Caro, W. Robins, J. J. Mekalanos, Antagonism toward the intestinal microbiota and its effect on *Vibrio cholerae* virulence. *Science* **359**, 210–213 (2018). doi: [10.1126/science.aap8775](https://doi.org/10.1126/science.aap8775); pmid: 29326272
55. J. J. Quereda *et al.*, Bacteriocin from epidemic *Listeria* strains alters the host intestinal microbiota to favor infection. *Proc. Natl. Acad. Sci. U.S.A.* **113**, 5706–5711 (2016). doi: [10.1073/pnas.1523899113](https://doi.org/10.1073/pnas.1523899113); pmid: 27140611
56. L.-S. Ma, A. Hachani, J.-S. Lin, A. Filloux, E.-M. Lai, Agrobacterium tumefaciens deploys a superfamily of type VI secretion DNase effectors as weapons for interbacterial competition in planta. *Cell Host Microbe* **16**, 94–104 (2014). doi: [10.1016/j.chom.2014.06.002](https://doi.org/10.1016/j.chom.2014.06.002); pmid: 24981331
57. D. P. Souza *et al.*, Bacterial killing via a type IV secretion system. *Nat. Commun.* **6**, 6453 (2015). doi: [10.1038/ncomms7453](https://doi.org/10.1038/ncomms7453); pmid: 25743609
58. A. Darsonval *et al.*, Adhesion and fitness in the bean phyllosphere and transmission to seed of *Xanthomonas fuscans* subsp. *fuscans*. *Mol. Plant Microbe Interact.* **22**, 747–757 (2009). doi: [10.1094/MPMI-22-6-0747](https://doi.org/10.1094/MPMI-22-6-0747); pmid: 19445599
59. C. M. Rojas, J. H. Ham, W.-L. Deng, J. J. Doyle, A. Collmer, HecA, a member of a class of adhesins produced by diverse pathogenic bacteria, contributes to the attachment, aggregation, epidermal cell killing, and virulence phenotypes of *Erwinia chrysanthemi* EC16 on *Nicotiana glauca* seedlings. *Proc. Natl. Acad. Sci. U.S.A.* **99**, 13142–13147 (2002). doi: [10.1073/pnas.202586999](https://doi.org/10.1073/pnas.202586999); pmid: 12271135
60. E. Shanker, M. J. Federle, Quorum sensing regulation of competence and bacteriocins in *Streptococcus pneumoniae* and *mutans*. *Genes (Basel)* **8**, 15 (2017). doi: [10.3390/genes810015](https://doi.org/10.3390/genes810015); pmid: 28067778
61. W.-Y. Wholey, T. J. Kochan, D. N. Storck, S. Dawid, Coordinated bacteriocin expression and competence in *Streptococcus pneumoniae* contributes to genetic adaptation through neighbor predation. *PLOS Pathog.* **12**, e1005413 (2016). doi: [10.1371/journal.ppat.1005413](https://doi.org/10.1371/journal.ppat.1005413); pmid: 26840124
62. C. Y. Wang, S. Dawid, Mobilization of Bacteriocins during competence in *Streptococci*. *Trends Microbiol.* **26**, 389–391 (2018). doi: [10.1016/j.tim.2018.03.002](https://doi.org/10.1016/j.tim.2018.03.002); pmid: 29588109
63. S. Borgeaud, L. C. Metzger, T. Scrinari, M. Blokesch, The type VI secretion system of *Vibrio cholerae* fosters horizontal gene transfer. *Science* **347**, 63–67 (2015). doi: [10.1126/science.1260064](https://doi.org/10.1126/science.1260064); pmid: 25554784
64. J. Thomas, S. S. Watve, W. C. Ratcliff, B. K. Hammer, Horizontal gene transfer of functional type VI killing genes by natural transformation. *MBio* **8**, e00654-17 (2017). doi: [10.1128/mbio.00654-17](https://doi.org/10.1128/mbio.00654-17); pmid: 28743812
65. P. C. Kirchberger, D. Unterwiesing, P. Provenzano, S. Pukatzki, Y. Boucher, Sequential displacement of Type VI Secretion System effector genes leads to evolution of diverse immunity gene arrays in *Vibrio cholerae*. *Sci. Rep.* **7**, 45133 (2017). doi: [10.1038/srep45133](https://doi.org/10.1038/srep45133); pmid: 28327641
66. D. Wall, Kin recognition in bacteria. *Annu. Rev. Microbiol.* **70**, 143–160 (2016). doi: [10.1146/annurev-micro-102215-095325](https://doi.org/10.1146/annurev-micro-102215-095325); pmid: 27359217
67. J. B. Bruce, G. A. Cooper, H. Chabas, S. A. West, A. S. Griffin, Cheating and resistance to cheating in natural populations of the bacterium *Pseudomonas fluorescens*. *Evolution* **71**, 2484–2495 (2017). doi: [10.1111/evo.13328](https://doi.org/10.1111/evo.13328); pmid: 28833073
68. C. Majerczyk, E. Schneider, E. P. Greenberg, Quorum sensing control of Type VI secretion factors restricts the proliferation of quorum-sensing mutants. *eLife* **5**, e14712 (2016). doi: [10.7554/eLife.14712](https://doi.org/10.7554/eLife.14712); pmid: 27183270
69. C. N. Vassallo *et al.*, Infectious polymorphic toxins delivered by outer membrane exchange discriminate kin in myxobacteria. *eLife* **6**, e29397 (2017). doi: [10.7554/eLife.29397](https://doi.org/10.7554/eLife.29397); pmid: 28820387
70. N. A. Lyons, B. Kragh, P. Stefanic, I. Mandic-Mulec, R. Kolter, A combinatorial kin discrimination system in *Bacillus subtilis*. *Curr. Biol.* **26**, 733–742 (2016). doi: [10.1016/j.cub.2016.01.032](https://doi.org/10.1016/j.cub.2016.01.032); pmid: 26923784
71. L. McNally *et al.*, Killing by Type VI secretion drives genetic phase separation and correlates with increased cooperation. *Nat. Commun.* **8**, 14371 (2017). doi: [10.1038/ncomms14371](https://doi.org/10.1038/ncomms14371); pmid: 28165005
72. C. J. Alteri *et al.*, Multicellular bacteria deploy the type VI secretion system to preemptively strike neighboring cells. *PLOS Pathog.* **9**, e1003608 (2013). doi: [10.1371/journal.ppat.1003608](https://doi.org/10.1371/journal.ppat.1003608); pmid: 23828598
73. E. C. Garcia, Contact-dependent interbacterial toxins deliver a message. *Curr. Opin. Microbiol.* **42**, 40–46 (2018). doi: [10.1016/j.mib.2017.09.011](https://doi.org/10.1016/j.mib.2017.09.011); pmid: 29078204
74. E. S. Danka, E. C. Garcia, P. A. Cotter, Are CDI systems multicolored, facultative, helping greenbeards? *Trends Microbiol.* **25**, 391–401 (2017). doi: [10.1016/j.tim.2017.02.008](https://doi.org/10.1016/j.tim.2017.02.008); pmid: 28285908
75. D. B. Borenstein, P. Ringel, M. Basler, N. S. Wingreen, Established microbial colonies can survive Type VI secretion assault. *PLOS Comput. Biol.* **11**, e1004520 (2015). doi: [10.1371/journal.pcbi.1004520](https://doi.org/10.1371/journal.pcbi.1004520); pmid: 26485125
76. P. L. Conlin, J. R. Chandler, B. Kerr, Games of life and death: Antibiotic resistance and production through the lens of evolutionary game theory. *Curr. Opin. Microbiol.* **21**, 35–44 (2014). doi: [10.1016/j.mib.2014.09.004](https://doi.org/10.1016/j.mib.2014.09.004); pmid: 25271120
77. M. Lazzaro, M. F. Feldman, E. García Vescovi, A transcriptional regulatory mechanism finely tunes the firing of Type VI secretion system in response to bacterial enemies. *MBio* **8**, e00559-17 (2017). doi: [10.1128/mbio.00559-17](https://doi.org/10.1128/mbio.00559-17); pmid: 28830939
78. M. Basler, M. Pilhofer, G. P. Henderson, G. J. Jensen, J. J. Mekalanos, Type VI secretion requires a dynamic contractile phage tail-like structure. *Nature* **483**, 182–186 (2012). doi: [10.1038/nature10846](https://doi.org/10.1038/nature10846); pmid: 22367545
79. C. M. Guinane *et al.*, Impact of environmental factors on bacteriocin promoter activity in gut-derived *Lactobacillus salivarius*. *Appl. Environ. Microbiol.* **81**, 7851–7859 (2015). doi: [10.1128/AEM.02339-15](https://doi.org/10.1128/AEM.02339-15); pmid: 26341205
80. V. Bachmann *et al.*, Bile salts modulate the mucin-activated type VI secretion system of pandemic *Vibrio cholerae*. *PLOS Negl. Trop. Dis.* **9**, e0004031 (2015). doi: [10.1371/journal.pntd.0004031](https://doi.org/10.1371/journal.pntd.0004031); pmid: 26317760
81. A. K. Korgaonkar, M. Whiteley, *Pseudomonas aeruginosa* enhances production of an antimicrobial in response to N-acetylglucosamine and peptidoglycan. *J. Bacteriol.* **193**, 909–917 (2011). doi: [10.1128/JB.01175-10](https://doi.org/10.1128/JB.01175-10); pmid: 21169497
82. A. Venkataraman, M. A. Rosenbaum, J. J. Werner, S. C. Winans, L. T. Angenent, Metabolite transfer with the fermentation product 2,3-butanediol enhances virulence by *Pseudomonas aeruginosa*. *ISME J.* **8**, 1210–1220 (2014). doi: [10.1038/ismej.2013.232](https://doi.org/10.1038/ismej.2013.232); pmid: 24401856
83. D. M. Cornforth, K. R. Foster, Competition sensing: The social side of bacterial stress responses. *Nat. Rev. Microbiol.* **11**, 285–293 (2013). doi: [10.1038/nrmicro2977](https://doi.org/10.1038/nrmicro2977); pmid: 23456045
84. M. Basler, B. T. Ho, J. J. Mekalanos, Tit-for-tat: Type VI secretion system counterattack during bacterial cell-cell interactions. *Cell* **152**, 884–894 (2013). doi: [10.1016/j.cell.2013.01.042](https://doi.org/10.1016/j.cell.2013.01.042); pmid: 23415234
85. M. LeRoux *et al.*, Quantitative single-cell characterization of bacterial interactions reveals type VI secretion is a double-edged sword. *Proc. Natl. Acad. Sci. U.S.A.* **109**, 19804–19809 (2012). doi: [10.1073/pnas.1213963109](https://doi.org/10.1073/pnas.1213963109); pmid: 23150540
86. S. Rebuffat, Microcins in action: Amazing defence strategies of Enterobacteria. *Biochem. Soc. Trans.* **40**, 1456–1462 (2012). doi: [10.1042/BST20120183](https://doi.org/10.1042/BST20120183); pmid: 23176498
87. G. Vassiliadis, D. Destoumieux-Garzón, C. Lombard, S. Rebuffat, J. Peduzzi, Isolation and characterization of two members of the siderophore-microcin family, microcins M and H47. *Antimicrob. Agents Chemother.* **54**, 288–297 (2010). doi: [10.1128/AAC.00744-09](https://doi.org/10.1128/AAC.00744-09); pmid: 19884380
88. X. Thomas *et al.*, Siderophore peptide, a new type of post-translationally modified antibacterial peptide with potent activity. *J. Biol. Chem.* **279**, 28233–28242 (2004). doi: [10.1074/jbc.M400228200](https://doi.org/10.1074/jbc.M400228200); pmid: 15102848
89. M. LeRoux, S. B. Peterson, J. D. Mougous, Bacterial danger sensing. *J. Mol. Biol.* **427**, 3744–3753 (2015). doi: [10.1016/j.jmb.2015.09.018](https://doi.org/10.1016/j.jmb.2015.09.018); pmid: 26434507
90. S. Westhoff, G. P. van Wezel, D. E. Rozen, Distance-dependent danger responses in bacteria. *Curr. Opin. Microbiol.* **36**, 95–101 (2017). doi: [10.1016/j.mib.2017.02.002](https://doi.org/10.1016/j.mib.2017.02.002); pmid: 28258981
91. M. LeRoux *et al.*, Kin cell lysis is a danger signal that activates antibacterial pathways of *Pseudomonas aeruginosa*. *eLife* **4**, e05701 (2015). doi: [10.7554/eLife.05701](https://doi.org/10.7554/eLife.05701); pmid: 25643398
92. J. R. Chandler, S. Heilmann, J. E. Mittler, E. P. Greenberg, Acyl-homoserine lactone-dependent eavesdropping promotes competition in a laboratory co-culture model. *ISME J.* **6**, 2219–2228 (2012). doi: [10.1038/ismej.2012.69](https://doi.org/10.1038/ismej.2012.69); pmid: 22763647
93. R. P. Ryan *et al.*, Interspecies signalling via the *Stenotrophomonas maltophilia* diffusible signal factor influences biofilm formation and polymyxin tolerance in *Pseudomonas aeruginosa*. *Mol. Microbiol.* **68**, 75–86 (2008). doi: [10.1111/j.1365-2958.2008.06132.x](https://doi.org/10.1111/j.1365-2958.2008.06132.x); pmid: 18312265
94. R. Levy, E. Borenstein, Metabolic modeling of species interaction in the human microbiome elucidates community-level assembly rules. *Proc. Natl. Acad. Sci. U.S.A.* **110**, 12804–12809 (2013). doi: [10.1073/pnas.1300926110](https://doi.org/10.1073/pnas.1300926110); pmid: 23858463
95. P. D. Ringel, D. Hu, M. Basler, The role of type VI secretion system effectors in target cell lysis and subsequent horizontal gene transfer. *Cell Reports* **21**, 3927–3940 (2017). doi: [10.1016/j.celrep.2017.12.020](https://doi.org/10.1016/j.celrep.2017.12.020); pmid: 29281838
96. H. J. Haider *et al.*, Predicting and manipulating cardiac drug inactivation by the human gut bacterium *Enterobacter*. *Science* **341**, 295–298 (2013). doi: [10.1126/science.1235872](https://doi.org/10.1126/science.1235872); pmid: 23869020
97. V. Gopalakrishnan *et al.*, Gut microbiome modulates response to anti-PD-1 immunotherapy in melanoma patients.

- Science **359**, 97–103 (2018). doi: [10.1126/science.aan4236](https://doi.org/10.1126/science.aan4236); pmid: [29097493](https://pubmed.ncbi.nlm.nih.gov/29097493/)
98. B. Routy *et al.*, Gut microbiome influences efficacy of PD-1-based immunotherapy against epithelial tumors. *Science* **359**, 91–97 (2018). doi: [10.1126/science.aan3706](https://doi.org/10.1126/science.aan3706); pmid: [29097494](https://pubmed.ncbi.nlm.nih.gov/29097494/)
 99. V. Matson *et al.*, The commensal microbiome is associated with anti-PD-1 efficacy in metastatic melanoma patients. *Science* **359**, 104–108 (2018). doi: [10.1126/science.aao3290](https://doi.org/10.1126/science.aao3290); pmid: [29302014](https://pubmed.ncbi.nlm.nih.gov/29302014/)
 100. E. Breukink, B. de Kruijff, The lantibiotic nisin, a special case or not? *Biochim. Biophys. Acta* **1462**, 223–234 (1999). doi: [10.1016/S0005-2736\(99\)00208-4](https://doi.org/10.1016/S0005-2736(99)00208-4); pmid: [10590310](https://pubmed.ncbi.nlm.nih.gov/10590310/)
 101. N. Firmland, P. Rogne, G. Firmland, J. Nissen-Meyer, P. E. Kristiansen, Three-dimensional structure of the two peptides that constitute the two-peptide bacteriocin plantaricin EF. *Biochim. Biophys. Acta* **1784**, 1711–1719 (2008). doi: [10.1016/j.bbapap.2008.05.003](https://doi.org/10.1016/j.bbapap.2008.05.003); pmid: [18555030](https://pubmed.ncbi.nlm.nih.gov/18555030/)
 102. N. V. Dudkina *et al.*, Structure of the poly-C9 component of the complement membrane attack complex. *Nat. Commun.* **7**, 10588 (2016). doi: [10.1038/ncomms10588](https://doi.org/10.1038/ncomms10588); pmid: [26841934](https://pubmed.ncbi.nlm.nih.gov/26841934/)
 103. S. Soelaiman, K. Jakes, N. Wu, C. Li, M. Shoham, Crystal structure of colicin E3: Implications for cell entry and ribosome inactivation. *Mol. Cell* **8**, 1053–1062 (2001). doi: [10.1016/S1097-2765\(01\)00396-3](https://doi.org/10.1016/S1097-2765(01)00396-3); pmid: [11741540](https://pubmed.ncbi.nlm.nih.gov/11741540/)
 104. Z. C. Ruhe *et al.*, CdiA effectors use modular receptor-binding domains to recognize target bacteria. *MBio* **8**, e00290-17 (2017). doi: [10.1128/mBio.00290-17](https://doi.org/10.1128/mBio.00290-17); pmid: [28351921](https://pubmed.ncbi.nlm.nih.gov/28351921/)
 105. A. Besse, J. Peduzzi, S. Rebuffat, A. Carré-Mlouka, Antimicrobial peptides and proteins in the face of extremes: Lessons from archaeocins. *Biochimie* **118**, 344–355 (2015). doi: [10.1016/j.biochi.2015.06.004](https://doi.org/10.1016/j.biochi.2015.06.004); pmid: [26092421](https://pubmed.ncbi.nlm.nih.gov/26092421/)
 106. M. A. Riley, in *Prokaryotic Antimicrobial Peptides*, D. Drider, S. Rebuffat, Eds. (Springer New York, 2011), pp. 13–26.
 107. S. Rebuffat, in *Prokaryotic Antimicrobial Peptides*, D. Drider, S. Rebuffat, Eds. (Springer New York, 2011), pp. 55–72.
 108. I. F. Nes, in *Prokaryotic Antimicrobial Peptides*, D. Drider, S. Rebuffat, Eds. (Springer New York, 2011), pp. 3–12.
 109. D. M. Gordon, E. Oliver, J. Littlefield-Wyer, in *Bacteriocins*, M. A. Riley, M. A. Chavan, Eds. (Springer Berlin Heidelberg, 2007), pp. 5–18.
 110. N. C. K. Heng, P. A. Wescombe, J. P. Burton, R. W. Jack, J. R. Tagg, in *Bacteriocins*, M. A. Riley, M. A. Chavan, Eds. (Springer Berlin Heidelberg, 2007), pp. 45–92.
 111. M. C. Rea, R. P. Ross, P. D. Cotter, C. Hill, in *Prokaryotic Antimicrobial Peptides*, D. Drider, S. Rebuffat, Eds. (Springer New York, 2011), pp. 29–53.
 112. J. T. Morton, S. D. Freed, S. W. Lee, I. Friedberg, A large scale prediction of bacteriocin gene blocks suggests a wide functional spectrum for bacteriocins. *BMC Bioinformatics* **16**, 381 (2015). doi: [10.1186/s12859-015-0792-9](https://doi.org/10.1186/s12859-015-0792-9); pmid: [26558535](https://pubmed.ncbi.nlm.nih.gov/26558535/)
 113. E. Cascales *et al.*, Colicin biology. *Microbiol. Mol. Biol. Rev.* **71**, 158–229 (2007). doi: [10.1128/MMBR.00036-06](https://doi.org/10.1128/MMBR.00036-06); pmid: [17347522](https://pubmed.ncbi.nlm.nih.gov/17347522/)
 114. M. Chatzidaki-Livanis *et al.*, Gut symbiont *Bacteroides fragilis* secretes a eukaryotic-like ubiquitin protein that mediates intraspecies antagonism. *MBio* **8**, e01902-17 (2017). doi: [10.1128/mBio.01902-17](https://doi.org/10.1128/mBio.01902-17); pmid: [29184019](https://pubmed.ncbi.nlm.nih.gov/29184019/)
 115. D. Scholl, Phage tail-like bacteriocins. *Annu. Rev. Virol.* **4**, 453–467 (2017). doi: [10.1146/annurev-virology-101416-041632](https://doi.org/10.1146/annurev-virology-101416-041632); pmid: [28961412](https://pubmed.ncbi.nlm.nih.gov/28961412/)
 116. E. Grohmann, P. J. Christie, G. Waksman, S. Backert, Type IV secretion in Gram-negative and Gram-positive bacteria. *Mol. Microbiol.* **107**, 455–471 (2018). doi: [10.1111/mmi.13896](https://doi.org/10.1111/mmi.13896); pmid: [29235173](https://pubmed.ncbi.nlm.nih.gov/29235173/)
 117. D. Zhang, R. F. de Souza, V. Anantharaman, L. M. Iyer, L. Aravind, Polymorphic toxin systems: Comprehensive characterization of trafficking modes, processing, mechanisms of action, immunity and ecology using comparative genomics. *Biol. Direct* **7**, 18 (2012). doi: [10.1186/1745-6150-7-18](https://doi.org/10.1186/1745-6150-7-18); pmid: [22731697](https://pubmed.ncbi.nlm.nih.gov/22731697/)
 118. A. Jamet, X. Nassif, New players in the toxin field: Polymorphic toxin systems in bacteria. *MBio* **6**, e00285–e15 (2015). doi: [10.1128/mBio.00285-15](https://doi.org/10.1128/mBio.00285-15); pmid: [25944858](https://pubmed.ncbi.nlm.nih.gov/25944858/)
 119. S. K. Aoki *et al.*, Contact-dependent inhibition of growth in *Escherichia coli*. *Science* **309**, 1245–1248 (2005). doi: [10.1126/science.1115109](https://doi.org/10.1126/science.1115109); pmid: [16109881](https://pubmed.ncbi.nlm.nih.gov/16109881/)
 120. S. K. Aoki *et al.*, A widespread family of polymorphic contact-dependent toxin delivery systems in bacteria. *Nature* **468**, 439–442 (2010). doi: [10.1038/nature09490](https://doi.org/10.1038/nature09490); pmid: [21085179](https://pubmed.ncbi.nlm.nih.gov/21085179/)
 121. J. S. Webb *et al.*, Delivery of CdiA nuclease toxins into target cells during contact-dependent growth inhibition. *PLOS ONE* **8**, e57609 (2013). doi: [10.1371/journal.pone.0057609](https://doi.org/10.1371/journal.pone.0057609); pmid: [23469034](https://pubmed.ncbi.nlm.nih.gov/23469034/)
 122. Z. C. Ruhe, J. Y. Nguyen, C. M. Beck, D. A. Low, C. S. Hayes, The proton-motive force is required for translocation of CDI toxins across the inner membrane of target bacteria. *Mol. Microbiol.* **94**, 466–481 (2014). doi: [10.1111/mmi.12779](https://doi.org/10.1111/mmi.12779); pmid: [25174572](https://pubmed.ncbi.nlm.nih.gov/25174572/)
 123. J. L. E. Willett, G. C. Gucinski, J. P. Fatherree, D. A. Low, C. S. Hayes, Contact-dependent growth inhibition toxins exploit multiple independent cell-entry pathways. *Proc. Natl. Acad. Sci. U.S.A.* **112**, 11341–11346 (2015). doi: [10.1073/pnas.1512124112](https://doi.org/10.1073/pnas.1512124112); pmid: [26305955](https://pubmed.ncbi.nlm.nih.gov/26305955/)
 124. S. Koskiniemi *et al.*, Rhs proteins from diverse bacteria mediate intercellular competition. *Proc. Natl. Acad. Sci. U.S.A.* **110**, 7032–7037 (2013). doi: [10.1073/pnas.1300627110](https://doi.org/10.1073/pnas.1300627110); pmid: [23572593](https://pubmed.ncbi.nlm.nih.gov/23572593/)
 125. S. J. Foster, Molecular analysis of three major wall-associated proteins of *Bacillus subtilis* 168: Evidence for processing of the product of a gene encoding a 258 kDa precursor two-domain ligand-binding protein. *Mol. Microbiol.* **8**, 299–310 (1993). doi: [10.1111/j.1365-2958.1993.tb01574.x](https://doi.org/10.1111/j.1365-2958.1993.tb01574.x); pmid: [8316082](https://pubmed.ncbi.nlm.nih.gov/8316082/)
 126. F. Boyer, G. Fichant, J. Berthod, Y. Vandenbrouck, I. Attree, Dissecting the bacterial type VI secretion system by a genome wide in silico analysis: What can be learned from available microbial genomic resources? *BMC Genomics* **10**, 104 (2009). doi: [10.1186/1471-2164-10-104](https://doi.org/10.1186/1471-2164-10-104); pmid: [19284603](https://pubmed.ncbi.nlm.nih.gov/19284603/)
 127. R. D. Hood *et al.*, A type VI secretion system of *Pseudomonas aeruginosa* targets a toxin to bacteria. *Cell Host Microbe* **7**, 25–37 (2010). doi: [10.1016/j.chom.2009.12.007](https://doi.org/10.1016/j.chom.2009.12.007); pmid: [20114026](https://pubmed.ncbi.nlm.nih.gov/20114026/)
 128. A. B. Russell *et al.*, Type VI secretion delivers bacteriolytic effectors to target cells. *Nature* **475**, 343–347 (2011). doi: [10.1038/nature10244](https://doi.org/10.1038/nature10244); pmid: [21776080](https://pubmed.ncbi.nlm.nih.gov/21776080/)
 129. J. C. Whitney *et al.*, An interbacterial NAD(P)(+) glycohydrolase toxin requires elongation factor Tu for delivery to target cells. *Cell* **163**, 607–619 (2015). doi: [10.1016/j.cell.2015.09.027](https://doi.org/10.1016/j.cell.2015.09.027); pmid: [26456113](https://pubmed.ncbi.nlm.nih.gov/26456113/)
 130. A. B. Russell, S. B. Peterson, J. D. Mougous, Type VI secretion system effectors: Poisons with a purpose. *Nat. Rev. Microbiol.* **12**, 137–148 (2014). doi: [10.1038/nrmicro3185](https://doi.org/10.1038/nrmicro3185); pmid: [24384601](https://pubmed.ncbi.nlm.nih.gov/24384601/)
 131. J. Ma *et al.*, PAAR-Rhs proteins harbor various C-terminal toxins to diversify the antibacterial pathways of type VI secretion systems. *Environ. Microbiol.* **19**, 345–360 (2017). doi: [10.1111/1462-2920.13621](https://doi.org/10.1111/1462-2920.13621); pmid: [27871130](https://pubmed.ncbi.nlm.nih.gov/27871130/)
 132. M. Unnikrishnan, C. Constantinidou, T. Palmer, M. J. Pallen, The enigmatic Exs proteins: Looking beyond mycobacteria. *Trends Microbiol.* **25**, 192–204 (2017). doi: [10.1016/j.tim.2016.11.004](https://doi.org/10.1016/j.tim.2016.11.004); pmid: [27894646](https://pubmed.ncbi.nlm.nih.gov/27894646/)
 133. Z. Cao, M. G. Casabona, H. Kneuper, J. D. Chalmers, T. Palmer, The type VII secretion system of *Staphylococcus aureus* secretes a nuclease toxin that targets competitor bacteria. *Nat. Microbiol.* **2**, 16183 (2016). doi: [10.1038/nmicrobiol.2016.183](https://doi.org/10.1038/nmicrobiol.2016.183); pmid: [27723728](https://pubmed.ncbi.nlm.nih.gov/27723728/)
 134. L. García-Bayona, M. S. Guo, M. T. Laub, Contact-dependent killing by *Caulobacter crescentus* via cell surface-associated, glycine zipper proteins. *eLife* **6**, e24869 (2017). doi: [10.7554/eLife.24869](https://doi.org/10.7554/eLife.24869); pmid: [28323618](https://pubmed.ncbi.nlm.nih.gov/28323618/)
 135. E. Nudleman, D. Wall, D. Kaiser, Cell-to-cell transfer of bacterial outer membrane lipoproteins. *Science* **309**, 125–127 (2005). doi: [10.1126/science.1112440](https://doi.org/10.1126/science.1112440); pmid: [15994555](https://pubmed.ncbi.nlm.nih.gov/15994555/)
 136. D. T. Pathak *et al.*, Cell contact-dependent outer membrane exchange in myxobacteria: Genetic determinants and mechanism. *PLOS Genet.* **8**, e1002626 (2012). doi: [10.1371/journal.pgen.1002626](https://doi.org/10.1371/journal.pgen.1002626); pmid: [22511878](https://pubmed.ncbi.nlm.nih.gov/22511878/)

ACKNOWLEDGMENTS

We thank M. J. Coyne, G. L. Lozano, K. Coyte, and T. Zhang for helpful discussions. **Funding:** The Comstock laboratory is funded by Public Health Service grants R01AI120633 and R01AI093771 from the NIH/National Institute of Allergy and Infectious Diseases.

10.1126/science.aat2456

RESEARCH ARTICLE SUMMARY

PATTERN FORMATION

The periodic coloration in birds forms through a prepattern of somite origin

Nicolas Haupaix, Camille Curantz, Richard Bailleul, Samantha Beck, Annie Robic, Marie Manceau*

INTRODUCTION: In animals, coat color is often arranged in periodic motifs that vary widely, from striped to spotted patterns. These intricate designs have long fascinated developmental biologists and mathematicians alike. What are the mechanisms underlying the formation of periodic patterns and shaping their diversity? Spatial organization in the developing skin involves prepatterns that precede the color pattern. Self-organizing events have long been thought to act upstream of prepatterns (e.g., through molecular diffusion or pigment cell interaction). Changes in both of these molecular and cellular events may contribute to periodic pattern variation. However, periodic patterns are highly reproducible within species and display specific orientation and periodicity, which suggests that they also rely on preexisting spatial reference.

RATIONALE: Documenting phenotype diversity constitutes a promising framework for the prediction of such spatial landmarks, comparable to mathematical modeling strategies. We surveyed variation in the transient periodic pattern visible in juvenile birds of the galliform group, in which longitudinal stripes are organized in a black-yellow-black sequence in the dorsal region.

RESULTS: By comparing the striped pattern for 10 galliform bird species, we showed that the width of each stripe varied and that their number increased with dorsum size. In contrast, their absolute positions were comparable. We analyzed pigment appearance in the embryonic skin of five representative species and showed that the periodic striped pattern results from the timely production of yellow coloration at specific

locations. This yellow-production pulse was not triggered by a certain stage of feather growth or by dynamics of feather follicle production across the dorsum. However, it was linked to the early expression of *agouti*. This well-known pigmentation gene displayed a composite expression pattern in



The striped pattern of a Japanese quail embryo. Galliform birds display a longitudinal pattern of colored stripes already visible a few days before hatching (here in a Japanese quail, *Coturnix japonica*). Stripes form through differential deposition of black and yellow pigments along growing feathers in the dorsum. Our work shows that this pattern is controlled by a prepattern instructed by the somitic mesoderm.

longitudinal bands whose width and position correlated with that of yellow stripes in each species. To test *agouti*'s role, we used a functional approach by exploiting mutant strains of quails: The increase (in the Fawn strain) or decrease (in the recessive black strain) of *agouti* expression levels respectively led to wider or narrower yellow stripes. Comparing pigment distribution across feathers between these gain- or loss-of-function mutants and

ON OUR WEBSITE

Read the full article at <http://dx.doi.org/10.1126/science.aar4777>

wild-type quails showed that *agouti* controls stripe width by adjusting the duration of the yellow-production pulse in a dose-dependent manner. Both the position of *agouti*-expressing bands and that of yellow stripes did not change in mutant quails.

To identify the origin of signals controlling localized *agouti* expression and setting the position of yellow stripes, we performed hetero-specific grafting experiments: Embryonic tissues from donor quails were transplanted into pheasant hosts. We found that after transplanting somites (from which dermal cells originate), chimeras locally displayed quail-like expression of *agouti* in the developing skin. Long-term experiments showed that hosts displayed a striped color pattern typical of the donor at the level of the graft. Such changes were not observed when the neural tube (from which pigment-producing cells originate) was grafted. These results showed that the somitic mesoderm autonomously instructs *agouti* expression and consequently the position of yellow stripes.

CONCLUSION: We conclude from this work that the galliform striped pattern is achieved in a two-step mechanism. The somite provides positional information to the developing dermis; this controls the position of *agouti* expression in a prepattern that foreshadows yellow stripes. Their width is then refined by *agouti*, which locally controls yellow production in a dose-dependent manner. This sequential organization of space, combining early landmarks and local mechanisms, may govern the formation (and thus constrain the evolution) of many periodic patterns. ■

The list of author affiliations is available in the full article online.

*Corresponding author. Email: marie.manceau@college-de-france.fr
Cite this article as N. Haupaix et al., *Science* **361**, eaar4777 (2018). DOI: [10.1126/science.aar4777](https://doi.org/10.1126/science.aar4777)

RESEARCH ARTICLE

PATTERN FORMATION

The periodic coloration in birds forms through a prepatter of somite origin

Nicolas Haupaix¹, Camille Curantz¹, Richard Bailleul¹, Samantha Beck¹, Annie Robic², Marie Manceau^{1*}

The periodic stripes and spots that often adorn animals' coats have been largely viewed as self-organizing patterns, forming through dynamics such as Turing's reaction-diffusion within the developing skin. Whether preexisting positional information also contributes to the periodicity and orientation of these patterns has, however, remained unclear. We used natural variation in colored stripes of juvenile galliform birds to show that stripes form in a two-step process. Autonomous signaling from the somite sets stripe position by forming a composite prepatter marked by the expression profile of *agouti*. Subsequently, *agouti* regulates stripe width through dose-dependent control of local pigment production. These results reveal that early developmental landmarks can shape periodic patterns upstream of late local dynamics, and thus constrain their evolution.

Many vertebrates display intricate color patterns characterized by a periodic arrangement of pigments in stripes or spots (1). This spatial organization was recently shown to involve genes whose embryonic expression profile forms a prepatter preceding the adult pattern [e.g., the developmental expression of the pigmentation genes *edn3b* and *alx3* foreshadows striped patterns in the fur of cats and African striped mice, respectively (2, 3)]. A long-standing challenge has been to uncover the em-

bryonic pattern-forming events acting upstream of prepatterns to create discrete compartments in the developing skin. Computer simulations of stochastic dynamics such as Turing's reaction-diffusion, which involves the interaction of at least one self-activating factor and its inhibitor diffusing at long range, reproduce periodic motifs that resemble those observed in the wild; this finding suggests that color self-organizes in the skin tissue [see (4) for a review]. This hypothesis is supported by a handful of empirical studies. In

zebrafish, longitudinal stripes form through interaction [depolarization-repulsion (5)] of pigment cells sequentially aggregating locally, forming interstripes, then expanding and compacting within stripe regions (6, 7). In striped cats, the aminopeptidase taqpep creates periodicity by establishing an *edn3b*-expressing prepatter (2). Changes in cell behaviors or in the biological parameters of molecular players (e.g., clearance rate, which reflects the rate of molecule elimination; diffusivity) may contribute to natural variation in periodic patterns, consistent with theoretical predictions: Modifying the corresponding parameters of simulations gives rise to a vast array of patterns (4). Most periodic color patterns, however, display specific orientation or periodicity and are highly reproducible within species, which suggests that their formation does not entirely rely on stochastic events. Here, we investigated whether early developmental landmarks provide pre-existing spatial reference to periodic patterns.

Stripes vary in number and width but have comparable positions relative to the dorsal midline

To predict potential spatial landmarks, we surveyed phenotypic variation in the transient striped pattern visible along the dorsum of juvenile birds of the galliform group (8, 9). In flat-skin specimens for 10 species chosen for their representative varying patterns (table S1), we compared feather types according to pigmentation along barbs (i.e., primary branches). We distinguished two main types:

¹Center for Interdisciplinary Research in Biology, CNRS 7241, INSERM U1042, Collège de France, Paris, France.

²GenPhySE, Toulouse University, INRA, INPT ENVT 31326, Castanet-Tolosan, France.

*Corresponding author. Email: marie.manceau@college-de-france.fr



Fig. 1. Stripes vary in width and shape, but not position, in galliforms.

(A) Flat-skin preparations of dorsal skin regions (white rectangle) in juvenile individuals of 10 galliform bird species ($n = 2$ to 5 per species, see table S1) show their alternating yellow and black stripes, labeled as cy (central yellow), cb (central black), ly (lateral yellow), lb (lateral black), and ly2 (additional lateral yellow) stripes. This pattern is symmetrical over the dorsal midline (dm, in red) and was thus used as a landmark reference. Scale bars, 1 cm. (B) Measures of absolute distances from the dorsal midline to the boundary between each stripe at wing and leg levels [indicated by Wi and Le in (A) and (C)] demonstrate interspecies variation in stripe width. We also observed changes in the number of lateral stripes despite differences in dorsum size (species are shown in size order,

with smallest at top). Conversely, cb and ly stripes have comparable positions. Green lines represent cb distance from the dorsal midline (2 to 4 mm at wing level, 2 to 3 mm at leg level); blue lines represent ly distance from the dorsal midline (3 to 9 mm at wing level, 3 to 6 mm at leg level). C.j, *Coturnix japonica*; O.p, *Oreortyx picta*; P.p, *Perdix perdix*; A.r, *Alectoris rufa*; N.m, *Numida meleagris*; C.am, *Chrysolophus amherstiae*; S.r, *Syrnaticus reevesii*; P.c, *Phasianus colchicus*; C.au, *Chrosioptylon auritus*; M.g, *Meleagris gallopavo*. Error bars indicate SD. (C) Feathers of the dorsal tract organize in feather rows (fr; shown in orange in *C. japonica*). Their spatial arrangement varies between species. Plotting feather types at each position of the tract produces precise spatial representations of the color pattern.

black (*b*; entirely eumelaninic) and yellow (*y*; with a pheomelanin band and black base and tip) (fig. S1). This allowed us to identify a common stripe sequence, symmetrical over the dorsal midline and extending from the wing to the tail: The most central stripe is black (*cb*)—sometimes containing a few central yellow feathers (*cy*)—and is flanked by two lateral yellow stripes (*ly*) (Fig. 1A). We observed that the number of stripes often increased with dorsum size, hence variation in color pattern does not result solely from scaling. The position of each stripe relative to dorsum size varied between species (fig. S2). In comparison, absolute distances between the dorsal midline and the center of the stripes closest to the median (i.e., *cb* and *ly*) were comparable; this suggests that these stripes are positioned early, prior to dorsal skin expansion (Fig. 1B). The width of each stripe also varied between species. To detail this variation, we compared stripe boundaries relative to feather tracts, which are feather-covered skin areas separated by near-glabrous regions. Within tracts, feathers form longitudinal rows whose number, spacing, and length along the anteroposterior axis is typical to each species (10, 11) (fig. S3). We plotted feather types at each position of the dorsal tract and found that color boundaries are highly reproducible within species' tracts (e.g., in *Coturnix japonica*, the *cb-ly* boundary is characterized by the consistent production of *b/y* split feather types). However, these color boundaries vary between species relative to feather row number (i.e., stripe width) and along the anteroposterior axis (i.e., stripe shape; Fig. 1C). This suggests that variation in stripe width or shape results from differences in local mechanisms occurring during feather tract formation.

Interspecies differences in *agouti* expression correlate with stripe pattern variation

We took advantage of both the absence of variation in stripe position and the presence of differences in stripe width or shape to link the juvenile color pattern to (i) pigment production and (ii) tract formation during embryogenesis (in contrast to phenotypic surveys classically limited to observations of adult patterns). We used five species representative of variation in the width or shape of stripes, the presence or absence of *cy/lb* stripes, and the organization of the dorsal tract (namely *C. japonica*, *Alectoris rufa*, *Perdix perdix*, *Phasianus colchicus*, and *Syrnaticus reevesii*). We first compared the appearance of pigments in these species. We found that pigment production starts a few days before hatching (when all feather follicles of the dorsal tract are visible; fig. S4) and occurs in a medial-to-lateral wave: Eumelanin pigments are first produced in the most central feathers, forming one (*P. colchicus*, *S. reevesii*) or two (*C. japonica*, *A. rufa*, *P. perdix*) longitudinal black bands, and then progressively appearing laterally. This forms the *cb* stripe. Eumelanin production is transiently

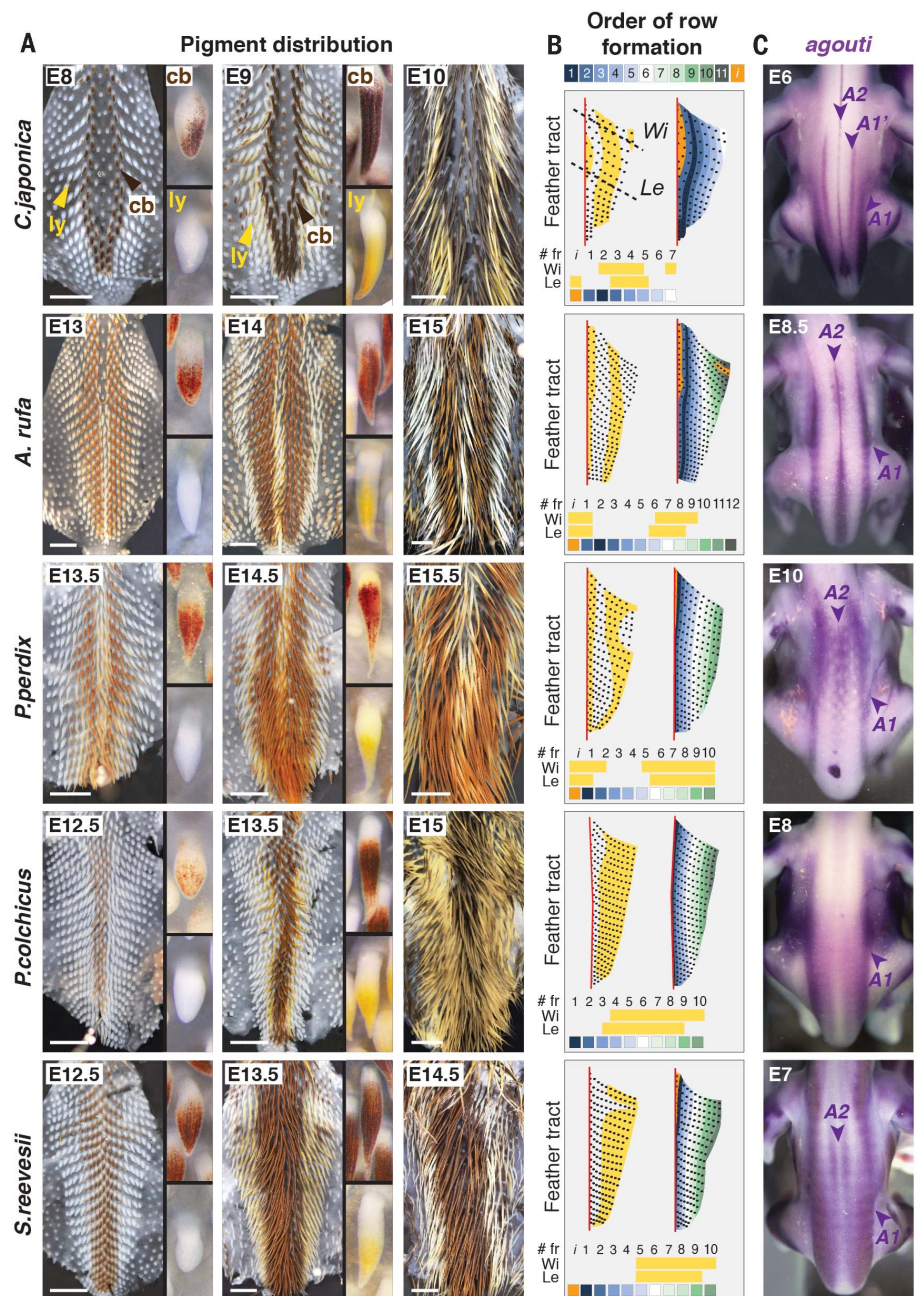


Fig. 2. Stripes form through yellow pulses independent of tract differentiation. (A) Flat-skin preparations of dorsal embryonic skins in five species (left) and high-magnification views of developing feathers in *cb* (upper right) and *ly* (bottom right) stripes allow visualization of the sequential production of pigments. Scale bars, 0.25 cm. (B) Color pattern diagrams (left) and color-coded representations of each feather (#fr) at wing (Wi) and leg (Le) levels show the positions of *cy* and *ly* stripes (which sometimes differ between Wi and Le; *C. japonica* has an additional *ly*2 stripe). A blue-to-green color code on diagrams (right) and for each feather (squares) shows the order of formation of feather rows (1 to 11, depending on species). Intercalate feathers (*i*, in orange) may form after tract formation. We observed no correlation between the order of formation of feather rows and their position in the tract (i.e., #fr), nor with the position of *cy* and *ly* stripes. (C) In situ hybridizations for *agouti* (in purple) reveal the two most lateral expressing bands present in all species (A1), two intermediary bands visible only in *C. japonica* (A1'), and one A2 band visible in *C. japonica*, *A. rufa*, *P. perdix*, and to a lesser extent, *S. reevesii*. (A1') A1 and A2 (purple arrowheads) foreshadow *ly* and *cy* stripes [compare with (B)]. E, embryonic day of development.

replaced in lateral feather rows by pheomelanin, forming the banded pattern in feathers of *ly* stripes. The most lateral feathers produce only eumelanin (forming *lb* stripes), and the most central feathers transiently produce pheomelanin (forming the *cy* stripe; Fig. 2A). Thus, the striped pattern results from localized "pulses" of yellow pigment production (*cy* and *ly* stripes) in an otherwise black-producing tissue.

To test whether yellow pulses occur at certain stages of tract differentiation, we reconstructed the sequence resulting in the spatial arrangement of follicles across the dorsal tract in all species and compared it with the position of the yellow-producing domains. Developing follicles stained with the β -catenin marker (12) first correspond to one (*P. colchicus*, *S. reevesii*) or two (*C. japonica*, *A. rufa*, *P. perdix*) longitudinal bands; rows of follicles are then added in a wave traveling ventrally [consistent with previous observations in the chick (13)], and lastly in the most central area, completing the dorsal tract (fig. S5). Tracing back *cy* and *ly* feather rows to their order of for-

mation showed that this order differs between species (Fig. 2B). Thus, the position of *cy* and *ly* stripes is not set by a mechanism taking place at given stages of tract formation.

We next tested whether yellow pulses are triggered by feather growth: We compared, in the *ly* stripe, (i) stages at which feathers switch to pheomelanin or back to eumelanin production, and (ii) the size and proximodistal position of the pheomelanin band in fully grown *y* feathers (as a readout for the onset and duration of the pulse). We found no correlation between these and the timing of yellow production (fig. S6). Thus, yellow pulses are not temporally linked to stages of feather growth. Because yellow-producing domains have shared positions and varying widths that do not correlate with dynamics of tract formation, we predicted that they rely on prepatterns established before skin differentiation. The signaling peptide Agouti controls the production of pheomelanin pigments in a timely fashion in the hair (14) and marks pre-patterns of light color domains in the embryonic

skin (3, 15) and along individual feathers (16). We found that prior to follicle formation in the five bird species, two *agouti*-expressing bands (*A1*) form in the dermis on both sides of the neural tube. In *C. japonica*, *A. rufa*, *P. perdix*, and weakly in *S. reevesii*, a thinner central band of *agouti* (*A2*) also appears a few hours after *A1*, and in *C. japonica* only, additional thin bands (*A1'*) intercalate between the *A1* and *A2* bands, a few hours after *A2* appearance (Fig. 2C and fig. S7). Thus, *agouti* expression is composite in space and time. In all species, the pattern of *agouti*-expressing bands resembled that of yellow stripes.

Agouti foreshadows yellow stripes and controls their width in a dose-dependent manner

To confirm this spatial correlation, we linked the position of each band to presumptive feather rows using double in situ hybridization for *agouti* and β -catenin in *C. japonica*. We found that the *A1'* *agouti* band is expressed in the presumptive domain of the second feather row, consisting of

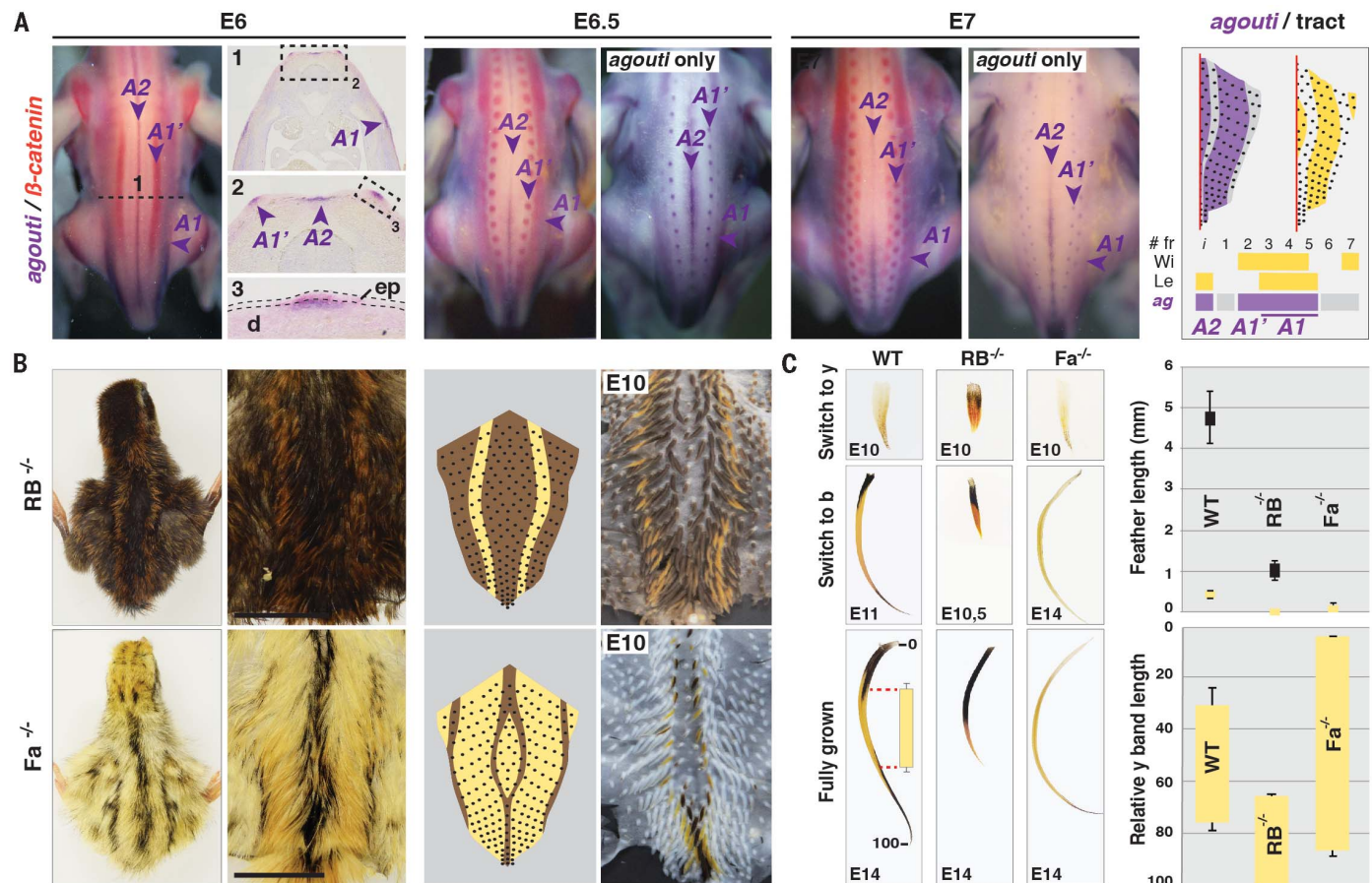


Fig. 3. *agouti* marks a striped prepattern and controls stripe width.

(A) Double in situ stains for *agouti* (purple) and β -catenin (red) at E6, E6.5, and E7 show (in whole-mount embryos and sections) that *A1'* corresponds to fr#2, *A1* corresponds to fr#3 to 5, and *A2* corresponds to fr#1 (putative domains correspond to interlimb level on an E16 dorsal tract map). ep, epidermis; d, dermis. (B) Juvenile flat skins, pattern maps, and embryonic flat skins of mutant strains of *C. japonica* show a reduction (RB^{-/-}; upper panels, *n* = 5) or extension (Fa^{-/-}; lower panels, *n* = 5) of *cy* and *ly* stripe

width. (C) Observations and quantifications of *y* feather length (as detailed in fig. S6; upper graph) when they first switch to yellow production (yellow dot plots) or back to black production (black dot plots) show that the yellow pulse occurs earlier in RB^{-/-} than in wild-type individuals. Measures of the size of the yellow band relative to the length of fully grown feathers (fig. S6 and see scheme in *C. japonica*; lower graph) show that the yellow pulse occurs for a longer duration in Fa^{-/-} than in wild-type individuals. Error bars indicate SD.

the first *b/y* feather of the *ly* stripe, whereas *A1* corresponds to the third through fifth rows, forming the rest of the *ly* stripe, and *A2* covers the central rows that form the *cy* stripe. In this species, *agouti* is later restricted to feather follicles of these stripes (Fig. 3A). Thus, the composite expression of the (*A1'*)*A1* and *A2* *agouti* bands reveals a prepattern that foreshadows the position of *ly* and *cy* yellow stripes, respectively. To understand how *agouti* expression affects stripe patterning, we used a functional quantitative approach and assessed the striped phenotype in mutant *C. japonica* strains. In recessive-black quails (*RB*^{-/-}), *agouti*'s spatial pattern is maintained with no change in the position or width/shape of the *A1*, *A1'*, and *A2* bands (fig. S8), but a frame-shift mutation in *agouti*'s coding sequence results in a marked decrease in transcript expression levels (17). We found that these birds display overall shorter feathers organized in thinner *ly* stripes (i.e., only feather rows 3 and 4 produce yellow, versus rows 2 and 5 in wild-type individuals), and no visible *cy* stripe (Fig. 3B). These changes in *ly* stripe width result from a decrease in the duration of the yellow pulse: Relative to

wild-type quails, feathers of *RB*^{-/-} quails switch back to eumelanin production earlier (consequently producing fewer *y* feathers containing smaller yellow bands; Fig. 3C). Conversely, quails of the Fawn mutant strain (*Fa*^{-/-}) are homozygous for a duplication at *agouti* responsible for an increase in its expression levels (17, 18). In *Fa*^{-/-} birds, the spatial pattern of *agouti* remains unchanged (fig. S8) but the *ly* (rows 1 or 2 through row 6) and *cy* stripes are wider, with *y* feathers displaying longer yellow bands because of a delayed switch to eumelanin production (i.e., increase in the duration of the yellow pulse; Fig. 3, B and C). These loss- or gain-of-function experiments show a role for *agouti*: At given positions (i.e., expressing bands), this gene regulates stripe width through a dose-dependent control of the duration of the yellow pulse. *Agouti* is a peptide diffusing in a paracrine manner; its localized expression may thus create a signaling gradient to which dermal cells respond according to their position: Certain thresholds of *agouti* levels trigger yellow production to locally fine-tune the border of yellow stripes and modulate the length of the yellow band (consistent with the latter being increased in

feathers at the center of *ly* stripes relative to those at the edge; fig. S1). This raises the appealing possibility that striped pattern evolution is governed by differential regulation of *agouti* expression levels.

The somitic mesoderm controls localized *agouti* expression and yellow stripe position

Contrary to stripe width, the position of stripes is conserved between species; this suggests that early developmental landmarks establish *agouti*'s composite prepattern. We studied the earliest visible expression of *agouti* in the embryonic skin in all five species and found it comparably located in the dermis above the neural tube (A2; fig. S9) and the dorsomedial part of differentiating somites (A1; Fig. 4A). Previous quail-chick grafting experiments showed that both the neural tube and somites contribute to the skin lineage. Feather follicle cells originate from the somite dermomyotome, and their spatial distribution is mesoderm-dependent (13, 19). Conversely, pigment-producing cells (melanocytes) derive from the neural crest (20, 21), but despite evidence

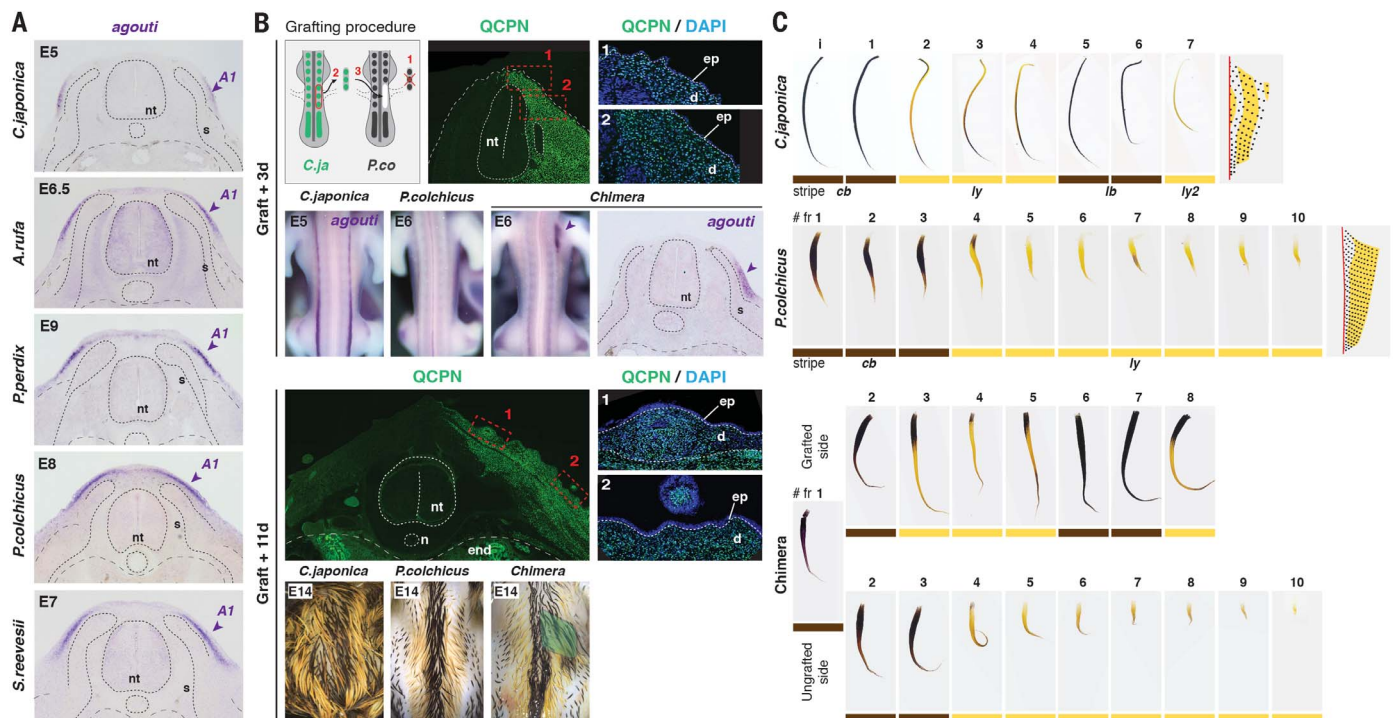


Fig. 4. Stripe color pattern has a somitic origin. (A) Sections of in situ hybridization for *agouti* (in purple) show that in all species, *A1* bands (purple arrowheads) locate in the embryonic dermal area above the developing somite. nt, neural tube; s, somite. (B) *C. japonica*'s three last formed somites at HH13 (i.e., immediately posterior to the wing bud) were grafted in place of those of *P. colchicus*; 3 days after grafting, immunohistochemistry for QCPN (in green) revealed that *C. japonica*'s cells invaded the host tissues ($n = 8$). High-magnification views with DAPI stains (in blue) show that QCPN⁺ cells locate in the developing dermis but not in the epidermis in regions corresponding to *A1/A1'* (red square 2) and *A2* (red square 1). At that stage, grafted regions in chimeras strongly express *agouti* in position of the *A1* band (purple arrowhead,

$n = 7$), similar to *C. japonica* but contrary to *P. colchicus* embryos. Eleven days after grafting, QCPN⁺ cells also locate in the dermis, including the papillae of feather follicles, but not in the epidermis. Relative to *C. japonica* and *P. colchicus* controls (left panels, $n = 3$ per species), feathers of the chimera at the same stage (right panels, $n = 4$) resemble those of the host except in the grafted area (in green). (C) The chimera's grafted side (third series from top) has the same stripe and feather pattern (see #fr) as *C. japonica* (first series and color pattern diagram); conversely, its ungrafted side (fourth series) has the same stripe and feather pattern as *P. colchicus* (second series and color pattern diagram). In chimeras, the first feather (#fr1) is common to the grafted and ungrafted sides. n, notochord; end, endoderm.

that their differentiation responds to cues from the feather papillae (22), the means by which they govern color patterning remained unclear, as grafted strains were homogeneously colored (and quail melanocytes produced black pigments in the host). We thus performed somite and neural tube transplantations from *C. japonica* donors into *P. colchicus* hosts (because both species display a typical striped pattern; Fig. 4B). Three days after transplanting the right half of the *C. japonica* neural tube (prior to major migration of the neural crest) in place of that of *P. colchicus* at the equivalent stage, no expression of *agouti* (normally visible in *C. japonica* but not *P. colchicus* embryos at that stage; fig. S7) was detected in the dermis of chimeras. *C. japonica* cells (stained with the specific QCPN marker) were observed in the developing neural tube, dermis, and epidermis. The same was true 11 days after grafting [i.e., embryonic day 14 (E14), when coloration is visible in lateral stripes]; at that stage, some QCPN⁺ cells coexpressed the melanocyte marker Trp1 (fig. S10). In these chimeras, the grafted and ungrafted parts of the skin displayed similar color (and feather) patterns (fig. S11). This demonstrates that the neural tube, despite generating melanocytes producing black pigments by default (20, 21), does not spatially control the expression of *agouti* expression or the activity of melanocytes (and thus the position of yellow-producing domains). Conversely, 3 days after replacing the undifferentiated somites of *P. colchicus* located below wing level by those of *C. japonica*, QCPN⁺ cells invaded the whole dermal compartment and we observed strong expression of *agouti* in the grafted dermis in the position of the *A1* band (Fig. 4B). Eleven days after transplantation, QCPN⁺ cells did not express Trp1 (fig. S12). Growing feathers of the grafted side were longer than those of the ungrafted side, spatially organized according to *C. japonica*'s dorsal tract [fig. S11 and consistent with previous work (13)], and displayed the color pattern seen below wing level in *C. japonica* (note that it differs from leg level; see Fig. 2B). Specifically, *lb* feathers were present in the lateral part of the tract and yellow pigments were produced in feather rows 2 to 4, thereby reducing the width of the *ly* stripe in the grafted side relative to the ungrafted side (Fig. 4C). Thus, the localized expression of *agouti* and production of yellow pigments (and therefore, the striped coloration pattern) are autonomously instructed by the somitic mesoderm.

Discussion

Results from this study show that the striped pattern is achieved in a two-step mechanism. The somite procures positional information, creating specific compartments in the dermis at precise locations (controlling the position of *agouti*-expressing bands and consequently yellow stripes). This prepattern is then refined according to expression levels of *agouti* (temporally controlling pigment-type production and consequently the width of each stripe). These results raise the possibility that most natural patterns, including periodic designs, rely on (and are constrained by) a

stepwise organization of space that combines late, local events producing periodicity and early positional sources ensuring reproducibility, which is the key to fitness and proper directionality (in this case, longitudinal stripes depend on information from axial structures). Our work thus opens new avenues following from current theoretical models: Simulations of Turing's reaction-diffusion (and other self-organizing systems) can be framed using initial conditions corresponding to developmental landmarks. Extending empirical work on other natural patterns will better define such initial conditions and thus shed light on developmental constraints to color pattern evolution.

Materials and methods

Specimen sampling

Previously euthanized specimens of 1- to 3-day-old hatchlings (for 10 species of galliform birds; table S1) and fertilized eggs (for *C. japonica*, *A. rufa*, *P. perdix*, *P. colchicus*, and *S. reevesii*) were obtained from authorized local breeders (Ferme de Chanteloup, Carina, Mr. Bouly de Lesdain, Les Bois de Vaux) and stored at -20°C prior to processing. After egg incubation in Brinsea ova-easy 190 incubators, embryos at various stages of development were dissected in PBS and fixed in 4% formaldehyde.

Stripe pattern analyses

Flat skin specimens were prepared from frozen carcasses through an incision of the skin along the ventral midline and cautious separation of the scalp from body muscles. Dissected skins were stretched flat, left to dry for 1 week, and imaged. Measures of distances between stripe boundaries were performed from the dorsal midline to the wings and legs (Fig. 1A) using a Vernier caliper (*C. japonica* and *A. rufa*, *n* = 5; *Oreortyx picta* and *Chrosioptylon auritum*, *n* = 2; all other species, *n* = 3). Within the measured area, all species displayed *cb*, *ly*, *lb* (*Chrysolophus amherstiae*, and *S. reevesii* only at leg level), and *ly2* (except *S. reevesii*) stripes. Only *C. japonica*, *A. rufa*, *P. perdix*, and *Meleagris gallopavo* had *cy* stripes. Spatial reference maps of dorsal tracts were obtained by (i) plucking out all feathers (using forceps), which revealed their respective positions along longitudinal rows (i.e., feather rows) from the neck to the tail, and (ii) recording color at each position (coded yellow when feathers displayed pheomelanin and black when they only contained eumelanin).

Pigments, tracts, and feather spacing analyses

Embryonic flat-skin specimens were obtained by performing longitudinal openings from neck to tail in embryos of *C. japonica*, *A. rufa*, *P. perdix*, *P. colchicus*, and *S. reevesii* and separating the developing skin tissue from the body (using microscissors and forceps). Dissected skins were fixed in 4% formaldehyde and stored in 80% glycerol. Developing feathers were plucked, mounted on glass slides in fluoromount (Southern Biotech), imaged, and measured using Fiji software (23).

The "switch to *y*" measure corresponds to the distance (in mm) from the tip of the feather to the distal limit of the yellow band (*C. japonica*, E10, *n* = 12; *A. rufa*, E13.5, *n* = 12; *P. perdix*, E13.5, *n* = 12; *P. colchicus*, E14, *n* = 21; *S. reevesii*, E14, *n* = 23; RB^{-/-}, E10, *n* = 22; Fa^{-/-}, E10, *n* = 18). The "switch to *b*" measure corresponds to the distance (in mm) from the tip of the feather to the distal limit of the black base (*C. japonica*, E11, *n* = 32; *A. rufa*, E15, *n* = 32; *P. perdix*, E15, *n* = 7; *P. colchicus*, E15, *n* = 38; *S. reevesii*, E14.5, *n* = 24; RB^{-/-}, E10.5, *n* = 14; Fa^{-/-}, *n* = 0, in this strain no eumelanin was seen before hatching). The "relative *y* band length" measure (in %) corresponds to the length of the yellow band normalized to the length of the whole, fully grown *y* feather from its base (0) to its tip (100); see schemes in Fig. 3 and fig. S6 (*C. japonica*, E13, *n* = 24; *A. rufa*, E22, *n* = 8; *P. perdix*, E22, *n* = 6; *P. colchicus*, E22, *n* = 19; *S. reevesii*, E22, *n* = 8; RB^{-/-}, E14, *n* = 6; Fa^{-/-}, E14, *n* = 6).

Distance ratios were calculated between #fr1-2, fr2-3... to fr5-6 for three series along the feather row (see scheme in fig. S11).

Expression analyses

In situ hybridization experiments were performed as described (24) using antisense riboprobes synthesized from vectors containing a 269-bp fragment of *C. japonica*, *A. rufa*, or *S. reevesii*'s coding sequences for *agouti*, or an 881-bp fragment of *C. japonica*'s coding sequence for *β-catenin*. For double in situ hybridizations, riboprobes were labeled with digoxigenin or fluorescein and sequentially revealed with anti-digoxigenin-AP or anti-fluorescein-AP antibodies (both 1:2000, Roche) and NBT/BCIP (Promega) or fast-red (Abcam) substrates.

Primers: *agouti*-F: TGCTCTGCTACAGTTTGCTCAG; *agouti*-R: TGGTTTGCAGGTTTGTAA; *β-catenin*-F: AGCTGACTTGATGGAGTTGGA; *β-catenin*-R: TCGTGATGGCCAAGAATTTC).

Heterospecific grafting

Quail-pheasant grafting procedures were adapted from previous quail-chick grafting experiments (25): At HH13 in *C. japonica*, the three last formed somites (just posterior to the wing bud), or the right half of the neural tube alongside these somites, were ablated using glass microneedles and cleaned of potential additional neighboring tissue in PBS. Transplants were immediately transferred into HH13 *P. colchicus* hosts in which equivalent tissues had been previously removed (see schemes in Fig. 4 and fig. S10). Grafted eggs were kept humid by adding ampicillin-containing PBS solution on the yolk surface, closed with tape, and re-incubated (37°C, 50% humidity) for 3 or 11 days (i.e., a stage corresponding to E14 in *P. colchicus*). Chimeras were dissected (feathers were rapidly removed for analysis) and fixed in 4% formaldehyde. The extent of the graft was determined by screening chimeras for the presence of (i) pigments in the dermis and epidermis, which are normally absent in *P. colchicus* but visible in *C. japonica* individuals at that stage (fig. S11), and (ii) QCPN⁺ cells on transverse sections.

Immunohistochemistry

Control and grafted embryonic specimens were embedded in gelatin/sucrose, sectioned using a CM 3050S cryostat (Leica), mounted in fluoro-mount, and immunostained using primary antibodies directed against QCPN (DSHB; 1:10) and Trp1 (Bruce Morgan laboratory; 1:20), and Alexa-conjugated secondary antibodies (Molecular Probes; 1:500). Cell nuclei were revealed using 4',6-diamidino-2-phenylindole (DAPI; Southern Biotech).

Imaging

Whole-mount flat skins and stained/grafted embryos were imaged using an AF-S Micro NIKKOR 60-mm f/2.8G ED macro-lens equipped with a D5300 camera (Nikon) and a MZ FLIII stereomicroscope (Leica) equipped with a DFC 450C camera (Leica). Tissue sections were imaged using a BX53 fluorescence microscope (Olympus; for in situ hybridization or fluorescent stains) or a CSU-W1 spinning-disk confocal microscope (Zeiss) equipped with a CMOS flash 4 camera (Hamamatsu; for Trp1/QCPN fluorescent stains).

REFERENCES AND NOTES

1. H. B. Cott, *Adaptive Coloration in Animals* (Methuen, 1940).
2. C. B. Kaelin *et al.*, Specifying and sustaining pigmentation patterns in domestic and wild cats. *Science* **337**, 1536–1541 (2012). doi: [10.1126/science.1220893](https://doi.org/10.1126/science.1220893); pmid: [22997338](https://pubmed.ncbi.nlm.nih.gov/22997338/)
3. R. Mallarino *et al.*, Developmental mechanisms of stripe patterns in rodents. *Nature* **539**, 518–523 (2016). doi: [10.1038/nature20109](https://doi.org/10.1038/nature20109); pmid: [27806375](https://pubmed.ncbi.nlm.nih.gov/27806375/)
4. S. Kondo, T. Miura, Reaction-diffusion model as a framework for understanding biological pattern formation. *Science* **329**, 1616–1620 (2010). doi: [10.1126/science.1179047](https://doi.org/10.1126/science.1179047); pmid: [20929839](https://pubmed.ncbi.nlm.nih.gov/20929839/)
5. M. Inaba, H. Yamanaka, S. Kondo, Pigment pattern formation by contact-dependent depolarization. *Science* **335**, 677 (2012). doi: [10.1126/science.1212821](https://doi.org/10.1126/science.1212821); pmid: [22323812](https://pubmed.ncbi.nlm.nih.gov/22323812/)
6. A. P. Singh, U. Schach, C. Nüsslein-Volhard, Proliferation, dispersal and patterned aggregation of iridophores in the skin prefigure striped colouration of zebrafish. *Nat. Cell Biol.* **16**, 604–611 (2014). doi: [10.1038/ncb2955](https://doi.org/10.1038/ncb2955); pmid: [24776884](https://pubmed.ncbi.nlm.nih.gov/24776884/)
7. P. Mahalwar, B. Walderich, A. P. Singh, C. Nüsslein-Volhard, Local reorganization of xanthophores fine-tunes and colors the striped pattern of zebrafish. *Science* **345**, 1362–1364 (2014). doi: [10.1126/science.1254837](https://doi.org/10.1126/science.1254837); pmid: [25214630](https://pubmed.ncbi.nlm.nih.gov/25214630/)
8. T. Price, M. Pavelka, Evolution of a colour pattern: History, development, and selection. *J. Evol. Biol.* **9**, 451–470 (1996). doi: [10.1046/j.1420-9101.1996.9040451.x](https://doi.org/10.1046/j.1420-9101.1996.9040451.x)
9. T. W. Hiscock, S. G. Megason, Mathematically guided approaches to distinguish models of periodic patterning. *Development* **142**, 409–419 (2015). doi: [10.1242/dev.107441](https://doi.org/10.1242/dev.107441); pmid: [25605777](https://pubmed.ncbi.nlm.nih.gov/25605777/)
10. C. L. Nitzsch, *Pterylography* (Ray Society, 1867).
11. M. H. Clench, Variability in Body Pterylosis, with Special Reference to the Genus *Passer*. *Auk* **87**, 650–691 (1970). doi: [10.2307/4083702](https://doi.org/10.2307/4083702)
12. S. Noramly, A. Freeman, B. A. Morgan, β -catenin signaling can initiate feather bud development. *Development* **126**, 3509–3521 (1999). pmid: [10409498](https://pubmed.ncbi.nlm.nih.gov/10409498/)
13. P. Sengel, *Morphogenesis of Skin* (Cambridge Univ. Press, 1976).
14. G. S. Barsh, The genetics of pigmentation: From fancy genes to complex traits. *Trends Genet.* **12**, 299–305 (1996). doi: [10.1016/0168-9525\(96\)10031-7](https://doi.org/10.1016/0168-9525(96)10031-7); pmid: [8783939](https://pubmed.ncbi.nlm.nih.gov/8783939/)
15. M. Manceau, V. S. Domingues, R. Mallarino, H. E. Hoekstra, The developmental role of Agouti in color pattern evolution. *Science* **331**, 1062–1065 (2011). doi: [10.1126/science.1200684](https://doi.org/10.1126/science.1200684); pmid: [21350176](https://pubmed.ncbi.nlm.nih.gov/21350176/)
16. S. J. Lin *et al.*, Topology of feather melanocyte progenitor niche allows complex pigment patterns to emerge. *Science* **340**, 1442–1445 (2013). doi: [10.1126/science.1230374](https://doi.org/10.1126/science.1230374); pmid: [23618762](https://pubmed.ncbi.nlm.nih.gov/23618762/)
17. T. Hiragaki *et al.*, Recessive black is allelic to the yellow plumage locus in Japanese quail and associated with a frameshift deletion in the ASIP gene. *Genetics* **178**, 771–775 (2008). doi: [10.1534/genetics.107.077040](https://doi.org/10.1534/genetics.107.077040); pmid: [18287406](https://pubmed.ncbi.nlm.nih.gov/18287406/)
18. F. Minvielle, D. Gourichon, J.-L. Monvoisin, Effects of two-locus combinations, using the roux, lavender, and beige mutations, on plumage color of Japanese quail. *J. Hered.* **94**, 517–522 (2003). doi: [10.1093/jhered/esg091](https://doi.org/10.1093/jhered/esg091); pmid: [14691319](https://pubmed.ncbi.nlm.nih.gov/14691319/)
19. C. Hornik, K. Krishan, F. Yusuf, M. Scaal, B. Brand-Saberi, cDermo-1 misexpression induces dense dermis, feathers, and scales. *Dev. Biol.* **277**, 42–50 (2005). doi: [10.1016/j.ydbio.2004.08.050](https://doi.org/10.1016/j.ydbio.2004.08.050); pmid: [15572138](https://pubmed.ncbi.nlm.nih.gov/15572138/)
20. C. S. Le Lièvre, N. M. Le Douarin, Mesenchymal derivatives of the neural crest: Analysis of chimaeric quail and chick embryos. *J. Embryol. Exp. Morphol.* **34**, 125–154 (1975). pmid: [1185098](https://pubmed.ncbi.nlm.nih.gov/1185098/)
21. M. A. Selleck, M. Bronner-Fraser, Origins of the avian neural crest: The role of neural plate-epidermal interactions. *Development* **121**, 525–538 (1995). pmid: [7768190](https://pubmed.ncbi.nlm.nih.gov/7768190/)
22. M. K. Richardson, A. Hornbruch, L. Wolpert, Pigment patterns in neural crest chimeras constructed from quail and guinea fowl embryos. *Dev. Biol.* **143**, 309–319 (1991). doi: [10.1016/0012-1606\(91\)90082-E](https://doi.org/10.1016/0012-1606(91)90082-E); pmid: [1991554](https://pubmed.ncbi.nlm.nih.gov/1991554/)

ACKNOWLEDGMENTS

We thank J. P. Lavandier, J. M. Bouly de Lesdain, the Ferme de Chanteloup, the Collège de France administrative and imaging platform staff, and N. Quenech'du for help with specimen sampling and imaging; D. Gourichon for help with quail mutant strains; and F. Schmitt, J. Gros, B. Prud'homme, T. Lecuit, and M. Hidalgo for helpful comments on the manuscript. **Funding:** Supported by a Paris Science et Lettres Young Investigator Grant and ERC Starting Grant 639060. **Author contributions:** N.H. collected samples for all species and performed all expression and functional analyses; N.H. and S.B. prepared and analyzed adult and embryonic flat-skin specimens; N.H. and C.C. performed and analyzed grafting experiments; C.C. performed all fluorescent imaging; R.B. performed in situ hybridization experiments for β -catenin; A.R. produced quail mutant strains; M.M. conceived and designed analyses; and M.M., C.C., and N.H. wrote the manuscript. **Competing interests:** The authors declare no competing interests. **Data and materials availability:** All data are available in the manuscript or the supplementary materials.

SUPPLEMENTARY MATERIALS

www.sciencemag.org/content/361/6408/aar4777/suppl/DC1
Figs. S1 to S12

Table S1

References (23–25)

21 December 2017; accepted 27 July 2018
[10.1126/science.aar4777](https://doi.org/10.1126/science.aar4777)

RESEARCH ARTICLE SUMMARY

SYNTHETIC BIOLOGY

Cellular checkpoint control using programmable sequential logic

Lauren B. Andrews, Alec A. K. Nielsen, Christopher A. Voigt*

INTRODUCTION: Modern computing is based on sequential logic, in which the state of a circuit depends both on the present inputs as well as the input history (memory). Implementing sequential logic inside a living cell would enable it to be programmed to progress through discrete states. For example, cells could be designed to differentiate into a multicellular structure or order the multistep construction of a material. A key challenge is that sequential logic requires the implementation of regulatory feedback, which has proven difficult to design and scale.

RATIONALE: We present a quantitative method to design regulatory circuits that encode sequential logic. Our approach uses NOT gates as the core unit of regulation, in which an input promoter drives the expression of a repres-

sor protein that turns off an output promoter. Each gate is characterized by measuring its response function, in other words, how changing the input affects the output at steady state. Mathematically, the response functions are treated as nullclines, and tools from nonlinear dynamics (phase plane and bifurcation analyses) are applied to predict how combining gates leads to multiple steady states and dynamics. The circuits can be connected to genetic sensors that respond to environmental information. This is used to implement checkpoint control, in which the cell waits for the right signals before continuing to the next state. Circuits are built that instruct *Escherichia coli* to proceed through a linear or cyclical sequence of states.

RESULTS: First, pairs of repressors are combined to build the simplest unit of sequential

logic: a set-reset (SR) latch, which records a digital bit of information. The SR latches can be easily connected to each other and to sensors because they are designed such that the inputs and outputs are both promoters. Each latch requires two repressors that inhibit each other's expression. A total of 11 SR latches were designed by using a phase plane analysis. The computation accurately predicts the existence of multiple steady states by using only the empirical NOT gate response functions. A set of 43 circuits was constructed that connects these latches to different combinations of sensors that respond to small molecules in the media. These circuits are shown to reliably hold their state for >48 hours over many cell divisions, only switching states in response to the sensors that connect to the set and reset inputs of the latch.

ON OUR WEBSITE

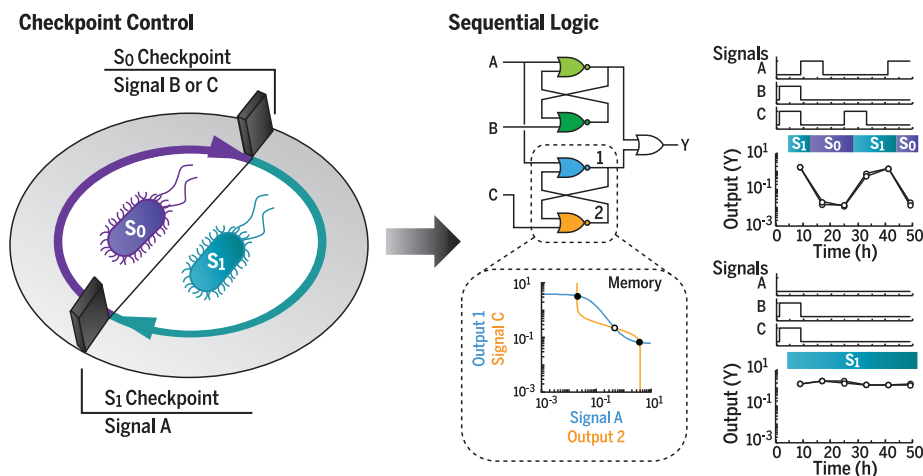
Read the full article at <http://dx.doi.org/10.1126/science.aap8987>

Larger circuits are constructed by combining multiple SR latches and additional feedback loops. A gated data (D) latch, common in electronic integrated circuits, is constructed where one input sets the state of the circuit and the second input locks this state. Up to three SR latches (based on six repressors) are combined in a single cell, thus allowing three bits to be reversibly stored. The performances of these circuits closely match those predicted by the responses of the component gates and a bifurcation analysis.

Circuits are designed to implement checkpoint control, in which cells wait indefinitely in a state until the correct signals are received to progress to the next state. The progression can be designed to be cyclical, analogous to cell cycle phases, during which cells progress through a series of states until returning to the starting state. The length of time in each state is indefinite, which is confirmed by demonstrating stability for days when the checkpoint conditions are not met.

Circuits are designed to implement checkpoint control, in which cells wait indefinitely in a state until the correct signals are received to progress to the next state. The progression can be designed to be cyclical, analogous to cell cycle phases, during which cells progress through a series of states until returning to the starting state. The length of time in each state is indefinite, which is confirmed by demonstrating stability for days when the checkpoint conditions are not met.

CONCLUSION: This work demonstrates the implementation of sequential logic circuits in cells by combining reliable units of regulation according to simple rules. This approach is conducive to design automation software, which can use these rules to combine gates to build larger circuits. This provides a designable path to building regulatory networks with feedback loops, critical to many cellular functions and ubiquitous in natural networks. This represents a critical step toward performing advanced computation inside of cells. ■



Quantitative design of sequential logic in living cells. Cells can be genetically programmed to respond to temporal stimuli by using complex sequential logic circuits. (Left) Checkpoint control is one such example in which the circuit state (s_0 and s_1) transitions when the specified input signals are presented. (Middle) Sequential logic circuits can be designed from simple steady-state response functions measured in relative promoter units by using principles of nonlinear dynamics. Bistable latches are used as rewritable memory. The colored symbols represent gates. (Right) The circuit output (Y) was measured for cells that were grown in inputs that were varied over time. The square waveforms indicate the presence or absence of the input signals. Over multiple days, the cells can be cycled through the circuit states or held waiting for the next checkpoint.

The list of author affiliations is available in the full article online.

*Corresponding author. Email: cavoigt@gmail.com

Cite this article as L. B. Andrews et al., *Science* **361**, eaap8987 (2018). DOI: [10.1126/science.aap8987](https://doi.org/10.1126/science.aap8987)

RESEARCH ARTICLE

SYNTHETIC BIOLOGY

Cellular checkpoint control using programmable sequential logic

Lauren B. Andrews^{1,2*}, Alec A. K. Nielsen², Christopher A. Voigt^{1,2†}

Biological processes that require orderly progression, such as growth and differentiation, proceed via regulatory checkpoints where the cell waits for signals before continuing to the next state. Implementing such control would allow genetic engineers to divide complex tasks into stages. We present genetic circuits that encode sequential logic to instruct *Escherichia coli* to proceed through a linear or cyclical sequence of states. These are built with 11 set-reset latches, designed with repressor-based NOR gates, which can connect to each other and sensors. The performance of circuits with up to three latches and four sensors, including a gated D latch, closely match predictions made by using nonlinear dynamics. Checkpoint control is demonstrated by switching cells between multiple circuit states in response to external signals over days.

The most complex processes in biology use checkpoint control to synchronize cells in the face of noisy and asynchronous conditions (1). Checkpoints are implemented between stages of a cascade via a gene regulatory network that integrates environmental and cellular information before triggering a switch instructing the cell to proceed. Checkpoints are ubiquitous across eukaryotic and prokaryotic processes, such as the cell cycle (2–4), cell development pathways (5, 6), inflammation (7), stress response (8–11), pathogenesis (12), and the assembly of molecular machines (13). From the perspective of cellular engineering, a generalizable method for implementing checkpoint control would allow the division of complex tasks into stages from which cells only proceed when the proper conditions are met (nutrient or precursor availability, cell-cell signaling, environmental niche recognition, etc.).

A progression of events can be implemented via a cascade in which one transcription factor regulates the next. Cycles are formed when the last transcription factor regulates the first in the cascade. To study these regulatory features in isolation, synthetic cascades and cycles have been constructed with heterologous transcription factors (14–18). Once initiated, the cascades and cycles progress continuously through each transcription factor in series, either concluding at the end of a cascade or oscillating via a stable limit cycle.

By contrast, checkpoints use bistable switches to control the transitions between discrete stages. This allows the cell to stop and wait until signals

that regulate progression cross a threshold. When multiple environmental and cellular signals are required, they can be integrated by regulation encoding Boolean logic operations (AND, OR, etc.) (19). A bistable switch introduces hysteresis into the transition, which stops the cells from reversing to the prior state when the stimuli are removed, and it waits for the necessary signals to progress forward (20–22). Checkpoint control leads to variability in the time spent in each stage but synchronizes the requirements for progression across cells and buffers against fluctuations (1). The switch acts as a form of memory to keep track of the cell state during this period.

In electronics, circuits containing logic and rewritable memory are referred to as “sequential logic.” Nearly universal across microprocessors, sequential logic is necessary to control the timing and order of processing steps within algorithms (23). Information is stored regarding the past state of the circuit, and this is integrated with input signals to determine the circuit’s next state transition. The input signals are integrated by “combinational logic,” whose output is only a function of the inputs. Latches are analogous to bistable switches and have two stable states that are used to store one digital bit of information. The simplest is a set-reset (SR) latch, composed of cross-coupled NOR gates that integrate two inputs to switch the latch between two states, which are read by two outputs. This architecture suffers from having a forbidden state (both inputs on), which can lead to instabilities in the circuit due to timing effects. More complex latches store a bit of information without having a forbidden combination of inputs. A common example is the data (D) latch used in microprocessors for temporary data storage and to synchronize asynchronous signals (24, 25).

Synthetic genetic circuits have been built that encode the core functions required for sequential logic. Combinational logic has been implemented

inside cells through a variety of biochemical mechanisms (26–32). Here we focus on logic gates that are implemented on the level of transcription, in which the inputs and outputs of the gates are promoters regulated by transcription factors. This defines RNA polymerase (RNAP) flux as the common signal carrier, which facilitates the implementation of more complex circuits by layering simpler gates (33). It also simplifies the connection of genetic sensors to the circuit when the sensor responds to a stimulus by activating a promoter. Following this paradigm, we have shown that a library of repressor-based NOR gates can be rationally connected in different permutations to apply arbitrary combinational logic operations to up to four sensors (34). Central to this approach are the empirical gate response functions (how the output changes as a function of input at steady state) that are used to computationally identify those gates that can be functionally connected.

Rewritable memory has also been implemented as a transcriptional circuit (35–39). One implementation is a “genetic toggle switch” that consists of a pair of repressors that regulate each other’s promoter (40–44). The resulting cross-repression leads to the bistability required for an SR latch. The inputs of the original implementation (40) are the small molecule inducers of the repressors, which complicates the connection of latches to each other, to combinational logic, or to sensors. The toggle switch has been connected to a single sensor by having the output promoter drive the expression of one repressor, and this has been used to remember transient exposure to a sugar, quorum signal, or an antibiotic (45–47). SR latches with two promoter inputs have been built based on DNA-inverting enzymes and sigma: anti-sigma factor sequestration, but we avoided these architectures because of toxicity, a dearth of orthogonal variants, or the absence of hysteresis (35, 48, 49). No more than a single SR latch has been shown to operate in a cell. More complex switches, such as the D latch, have been proposed and studied computationally but have not been implemented (50–53).

Here we present a theory-guided approach to building complex sequential logic circuits. Repressor-based NOR gates are connected to each other and sensors by signal matching their response functions. Latches are designed by recognizing that these empirical functions can serve as nullclines to identify gate combinations that will exhibit bistability (54). Further, the latch quality can be predicted quantitatively by the separation of the stable and unstable steady states. This is used to design 11 SR latches, a D latch, and circuits with up to three latches in a single cell. We demonstrate sequential logic that encodes a series of circuit states, separated by checkpoints, where progression is controlled by up to four sensors responding to different signals.

Design of SR latches

Bistability is a necessary criterion for building an SR latch. This is achieved by arranging two repressors to regulate each other’s expression. For

¹Broad Institute of MIT and Harvard, Cambridge, MA 02142, USA. ²Synthetic Biology Center, Department of Biological Engineering, Massachusetts Institute of Technology, Cambridge, MA 02139, USA.

*Present address: Department of Chemical Engineering, University of Massachusetts, Amherst, MA 01003, USA.

†Corresponding author. Email: cvoigt@gmail.com

the latch to be extensible, it must have two promoter inputs and two promoter outputs. If these are characterized with the same units, the information can be used to connect the latch to genetic sensors (Fig. 1A), other circuits, and cellular responses. Previously, we characterized insulated NOR gates that have two input promoters in series driving the expression of a repressor that

turns the output promoter off (55, 56). Because the promoters are arranged in series, their activity is summed, and the gate response function is treated as a single-input NOT gate (Fig. 1B). Our latch design uses this gate type, in which one of the NOR inputs is the set input promoter (S) to the latch and the other is a promoter regulated by a second NOR gate (Fig. 1C). In turn, the two

inputs to the second NOR gate are the reset input promoter (R) to the latch and a promoter repressed by the first gate.

The response function of a NOT gate captures how the gate's output changes as a function of its input at steady state. Because the input and output promoter activities of the gates are measured in relative promoter units (RPUs) (see

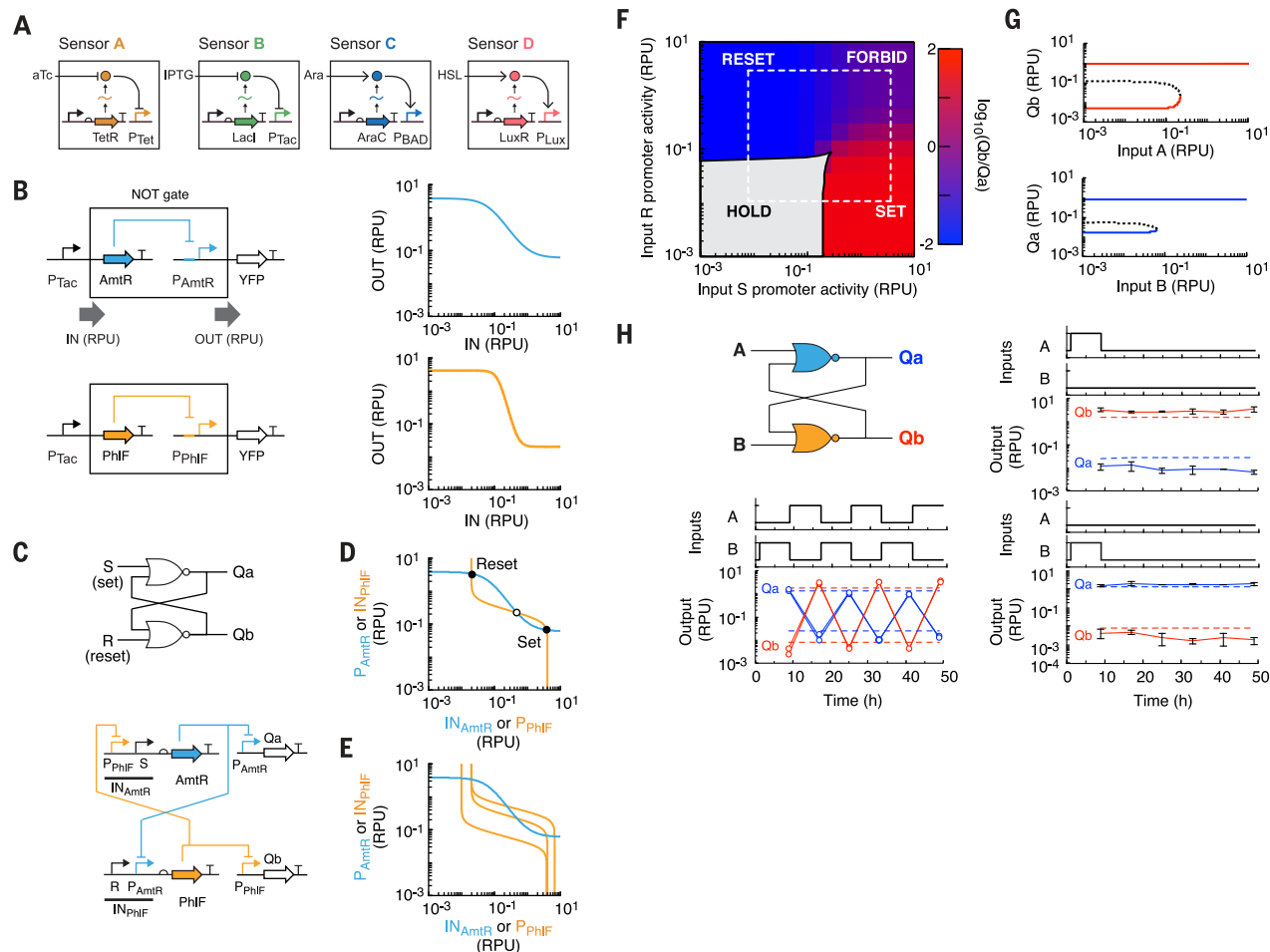


Fig. 1. Design of a bistable SR latch. (A) The genetic sensors (A, B, C, and D) used in this work are shown. The one-letter abbreviations are used consistently in the circuit diagrams shown in the figures. The sensor output promoters serve as the inputs to the circuits. P, promoter; Ara, arabinose; HSL, *N*-(3-oxohexanoyl)-L-homoserine lactone. (B) Two repressor-based NOT gates and their corresponding empirical response functions are shown (table S1) (34). The promoter activities, measured in RPU, are used as indirect measures of the RNAP flux (gray arrow) into and out of the gates. (C) The wiring diagram (top) and genetic implementation (bottom) of an SR latch is shown. IN_{AmrR} and IN_{PhIF} are the total (summed) input promoter activities into each gate. The output promoter activities (Qa and Qb) are measured with yellow fluorescent protein (white gene arrows) and two reporter plasmids. (D) A phase plane analysis is performed by plotting the response functions from (B) as nullclines (supplementary materials). The intersections are stable and unstable steady states, shown as open and solid circles, respectively. (E) The orange lines represent the nullclines for three strengths of RBSs controlling the expression of the PhIF repressor that alter the threshold of the response function and the number of intersections (multistability). (F) A bifurcation analysis is shown for the AmrR-PhIF SR latch. This was computed using an ODE model based on the NOT gate response

functions and AUTO software (supplementary methods). The bistable region (gray) indicates memory by holding the latch state (HOLD). The SET, RESET, and FORBIDDEN states are contained in the monostable regions (color). The dashed lines correspond to the OFF and ON outputs of sensors A and B (input S and input R, respectively) at the inducer concentrations used in the experiments. The model is provided in Systems Biology Markup Language (SBML) (supplementary file) (89). (G) Hysteresis plots are shown for the transitions between HOLD and SET (top) or HOLD and RESET (bottom). Stable and unstable steady states are indicated as solid and dashed lines, respectively. The transitions correspond to the white dashed lines in (F). (H) Experiments validating the AmrR-PhIF SR latch are shown. The blue and yellow symbols are gates. The methods are described in the text and supplementary materials. The input waveforms correspond to no inducer when low and either 2 ng/ml aTc (sensor A) or 1 mM IPTG (sensor B) when high. The model-predicted outputs are shown as dashed lines. Data points and error bars for the graphs on the right are shown as the average and standard deviation of three replicates performed on different days. The switching experiments to the left show two trajectories performed on different days. Additional experiments with additional input waveforms are provided in fig. S3.

methods), the two NOT functions can be plotted as nullclines on the same phase plane (Fig. 1D) (see the supplementary materials for the biophysical model) (54). The circuit is monostable when the nullclines only intersect once, meaning it does not exhibit the bistability necessary for a latch. When there are three intersections, the latch has two stable states separated by an unstable steady state. An exemplar is shown in Fig. 1C, where gates based on two repressors (AmtR and PhlF) are combined to design an SR latch. These gates use repressors that are Tet repressor (TetR) homologs and orthogonal; in other words, they do not bind to each other's operators (34, 55). The ribosome binding site (RBS) that controls repressor expression can be used to change the threshold of a gate. Thus, by changing the RBS, the response function can be shifted in relation to the second gate in the latch until bistability is achieved (Fig. 1E) (57).

A full bifurcation analysis was performed for the AmtR-PhlF SR latch from an ordinary differential equation (ODE) model (methods and supplementary files). This demarcates the boundaries of the SET, RESET, and HOLD regions within phase space (Fig. 1F). Note that there is also a FORBIDDEN region corresponding to the simultaneous activation of both inputs where the output signals degrade to an intermediate value. This bifurcation graph fully characterizes the SR latch and can be used to quantitatively predict the response obtained from connecting any two sensors, provided that their dynamic range is known in RPU. Each sensor performs the SET and RESET functions and alternating their activity switches the latch repeatedly between the two stable states. Once in either state, the reduction of the input (e.g., input A when in the SET state) is not able to switch the latch state without turning on the other input. Thus, this acts as memory, where the state is held indefinitely (Fig. 1G) (58, 59).

The AmtR-PhlF SR latch design was constructed by using a two-plasmid system, one carrying the circuit and the other carrying an output promoter fused to yellow fluorescent protein (YFP) (fig. S1). The sensors that respond to anhydrotetracycline hydrochloride (aTc) (sensor A) and isopropyl- β -D-1-thiogalactopyranoside (IPTG) (sensor B) were used as inputs (Fig. 1A). Two output plasmids were constructed that independently report the Qa and Qb outputs (separate strains and experiments). Cells containing the circuit and one output plasmid were initialized by growing them to exponential phase in the absence of inducer and then diluting them into fresh media with either 2 ng/ml aTc or 1 mM IPTG (methods). Every 8 hours, the samples were analyzed by flow cytometry to measure YFP, and an aliquot was diluted into fresh media containing the same or different inducers. Figure 1H shows the response of the outputs of the circuit to changes in the activity of the sensors, shown as the square waveform. By alternating between inducers, the circuit can be switched back and forth repeatedly for 2 days and more than 60 generations without breaking. When one inducer is pulsed, the circuits

hold their state over this period. Notably, the model quantitatively predicts the level of both outputs (dashed lines in Fig. 1H), including when the circuit is in an intermediate FORBIDDEN state and the steady state that is reached after the inducers are removed (fig. S4).

A library of SR latches was then designed by combining gates based on 10 orthogonal repressors from the TetR repressor family that cooperatively bind their respective operator DNA sequence (34, 55). Each gate has a different response function that, when combined in a phase plane analysis, can be analyzed for bistability (Fig. 2A). Forming a bistable switch requires that nullclines intersect at three points. Of the 45 combinations, 23 are predicted to exhibit bistability (blue boxes in Fig. 2A); however, not all are expected to behave equally. In some cases, the distance between the stable and unstable steady states (d_1 and d_2 in Fig. 2B), referred to as the equilibria separation, is small (60). Another measure is transversality or, in other words, the degree to which the nullclines do not overlap. Switches with short equilibria separation and poor transversality are sensitive to fluctuations, which can drive the switch into the opposite state (fig. S5). As expected, cooperative gates with steeper thresholds are more likely to lead to bistable switches; for example, the PhlF gate (Hill coefficient $n = 4.2$) is predicted to form a bistable switch with all other repressors. The cooperativity of each repressor was measured empirically in the context of the gate. Cooperativity could arise from the formation of multimers and/or the binding to multiple sites in a promoter.

We built the 15 SR latches that were predicted to be bistable, including some with short separation and poor transversality (Fig. 2C). These were constructed and evaluated, as described above (methods). Each latch was initialized in the first state (SET or RESET) by growing cells with the appropriate inducer. To test the latch's memory, the cells were then grown in the absence of inducer (HOLD), and, after 8 hours, the outputs were assayed by flow cytometry. The measurements are compared to the predicted outputs in Fig. 2D. Eleven of the SR latches exhibited at least a 10-fold dynamic range and held both latch states. Four had one state that spontaneously flipped during the memory assay (red arrows in fig. S5), which could be predicted from the equilibrium separation (Fig. 2E). Intriguingly, the cutoff separation corresponds to the standard deviation of the cytometry population when converted to RPU (fig. S2). For functional SR latches, the average dynamic range is 162-fold repression.

An additional 26 SR latch circuits were constructed by permuting the sensors connected to the latches and RBS variants of the component gates. Because the sensors are measured in standardized units, in theory, it can easily be determined whether they can be functionally connected to a particular latch (Fig. 1F). For the AmtR-HlyIIR SR latch, six permutations of sensors were tested, and all were able to functionally connect as predicted (Fig. 2F). This was repeated for different permutations of sensors connected to latches com-

prised of different pairs of repressors (fig. S5). Out of this set of 26 SR latches, 19 latches were functional, and the measured outputs agreed with the predictions (fig. S6A). The latches that did not hold both states correlated with poor predicted equilibria separation (fig. S6B).

Genetic D latch and memory registers

We sought to construct larger circuits containing multiple latches and feedback using the principles of signal matching and nonlinear dynamics (54). First, we designed a gated D latch, which has two inputs corresponding to the set (S) and lock (L) inputs (Fig. 3A). The latch state is determined by whether S is low or high when the lock is off. When locked, the state of the latch is stored irrespective of the input S. In contrast to the SR latch, this architecture has no FORBIDDEN state and associated instabilities. As such, it is commonly used in electronics to synchronize multiple latches to record at the same time through a shared clock signal that serves as the L input.

The D latch contains four NOR gates, two of which are cross-coupled to introduce positive feedback that results in cross-repression (Fig. 3A). The other two gates provide the upstream logic to control locking and unlocking of the latch and relaying the input S. Signal matching was performed to assign repressors to each gate by using a modified version of the Cello software (34) that used a hill-climbing algorithm to identify an assignment with the designed response by simulating all state transitions and applying a circuit score cutoff of at least 10-fold for valid assignments (methods). After selecting the repressors for each gate, a bifurcation analysis was performed by using the corresponding model to determine how the latch switches between states (Fig. 3B) (supplementary materials). The activation of the S input switches between the outputs (Qa and Qb) that are active. When the lock is off, the transition between the two is bistable. The bistable region expands as the lock signal increases, until it encompasses the entire range of S, thus storing the bit of memory. It is noteworthy that the bifurcation diagram differs substantially from that of the SR latch (Fig. 1F), and this complex behavior can be predicted by using the simple gate response functions.

The design for the D latch was constructed with the aTc-inducible sensor A serving as the S signal and the arabinose-inducible sensor C serving as the lock L (Fig. 3C). The circuit was constructed by using the same two-plasmid system as before, with two versions of the output plasmid to measure Qa and Qb by using separate strains. The D latch was evaluated by the same protocol as the SR latches, except no inducer was used during the initialization step (methods). The transitions between all combinations of states were evaluated, and they closely matched the predicted outputs (Fig. 3, D and E, and fig. S9). The D latch switched states over six cycles, correctly recorded in response to the lock signal, and maintained the memory states for longer than 2 days.

Multibit rewritable memory registers were then constructed by combining multiple parallel

SR latches in a circuit (Fig. 3F). To operate together in a cell, each latch requires two repressors orthogonal to the others in the circuit. From the set of 11 functional SR latches (Fig. 2C), up to three are fully orthogonal to each other. Based on this set, we constructed five circuits containing different combinations of two latches (figs. S10 and S11) and one containing three

latches (Fig. 3F). The quantitative response of all the outputs to changes in the activity of the three sensors was predicted by extending the approach used for individual SR latches. A phase plane analysis was performed on the basis of an ODE model parameterized by the response functions of the repressor-based gates (supplementary materials).

Three sensors for IPTG, aTc, and arabinose serve as the inputs to multiple latches, following an architecture similar to memory-register design in electronics. The construction of the circuit is based on the same two-plasmid system as before, except that there are six possible output plasmids so that the circuit outputs (Qa, Qb, Qc, Qd, Qe, and Qf) can be measured by using separate strains

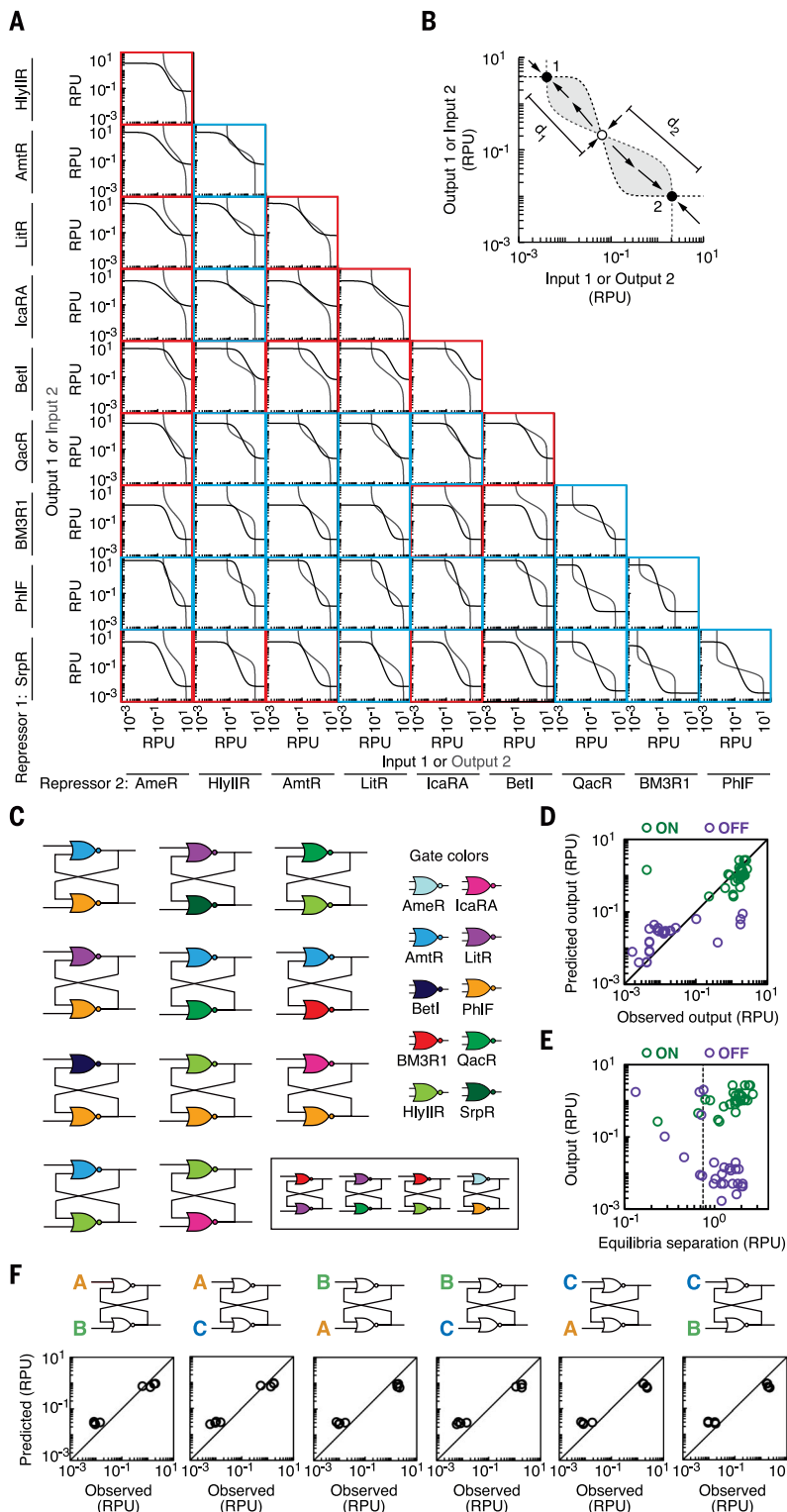


Fig. 2. Connecting gates to build SR latches. (A) Phase planes for all combinations of 10 repressors are shown. The nullclines are the empirical response functions measured previously (34). Repressor pairs predicted to be monostable or bistable are boxed in red or blue, respectively. For some gates, multiple RBS variants are available. In these cases, we show the pair of gates that produce the greatest transversality, calculated as the area between the nullclines. (B) The phase plane analysis is shown for the SrpR and PhlF repressors. The equilibria separation is given by the distance in phase space of the stable state from the unstable state (d_1 and d_2), and the transversality is shaded in gray. (C) The wiring diagrams are shown for the set of 11 SR latches that were constructed and validated experimentally. The box surrounds four additional combinations found to be nonfunctional. Sensors A and B were used in these experiments to assay the SR latch library. Colors correspond to the repressor of each gate. (D) Quantitative comparison of the predicted and measured output (both Qa and Qb) for the set of 15 latches, as determined by phase plane analysis. The black line is $x = y$. For each SR latch, both outputs for each latch state are plotted after holding the state (absence of either input). Experimental measurements were performed in duplicate, and the mean observed value is plotted (fig. S5). Each output promoter was measured in the ON (green) and OFF (purple) state. The four SR latches that spontaneously switched are marked with red arrows in fig. S5, and sensor permutations were also tested for these SR latches. (E) The observed outputs in the ON (green) and OFF (purple) states are plotted against the corresponding equilibria separation for the state [d_1 or d_2 in (B)] for the SR latch library in (C). The dashed line is the mean standard deviation of the cytometry distributions when the output is ON (fig. S2). (F) Six permutations of sensors A, B, and C were connected to the AmtR-HlyIIR SR latch. The dynamic range of the sensors in the presence and absence of inducer was used to compute the ON and OFF states of the latch, and these states were compared to those determined experimentally. The observed output data points are the average of duplicate experiments. The black lines are $x = y$.

(Fig. 3G). Growth and induction were performed as before. All six outputs were found to be quantitatively correct for input pulses of each sensor (Fig. 3F). Different patterns of square waveforms for each input were tested over 2 days, and the circuit performed quantitatively as predicted, except for one trajectory after 2 days (Fig. 3H). After a single pulse, the memory could be held over a day, after which at least one output became un-

stable (fig. S11). We also tested five simpler circuits containing different combinations of two SR latches and sensors, and these were found to function quantitatively as predicted (figs. S10 and S11).

Designing checkpoint control

Sequential logic circuits were designed to implement checkpoint control. This requires that ge-

netic circuits remain in their current state until they receive the necessary sensory inputs to transition to the next state. In computer science, this is referred to as a finite-state machine, which is defined as being able to exist in one of a finite number of circuit states at a given time and where external inputs control state transitions. In this context, a state diagram is used to enumerate the states (s_0, s_1, \dots, s_i), and allowed transitions are

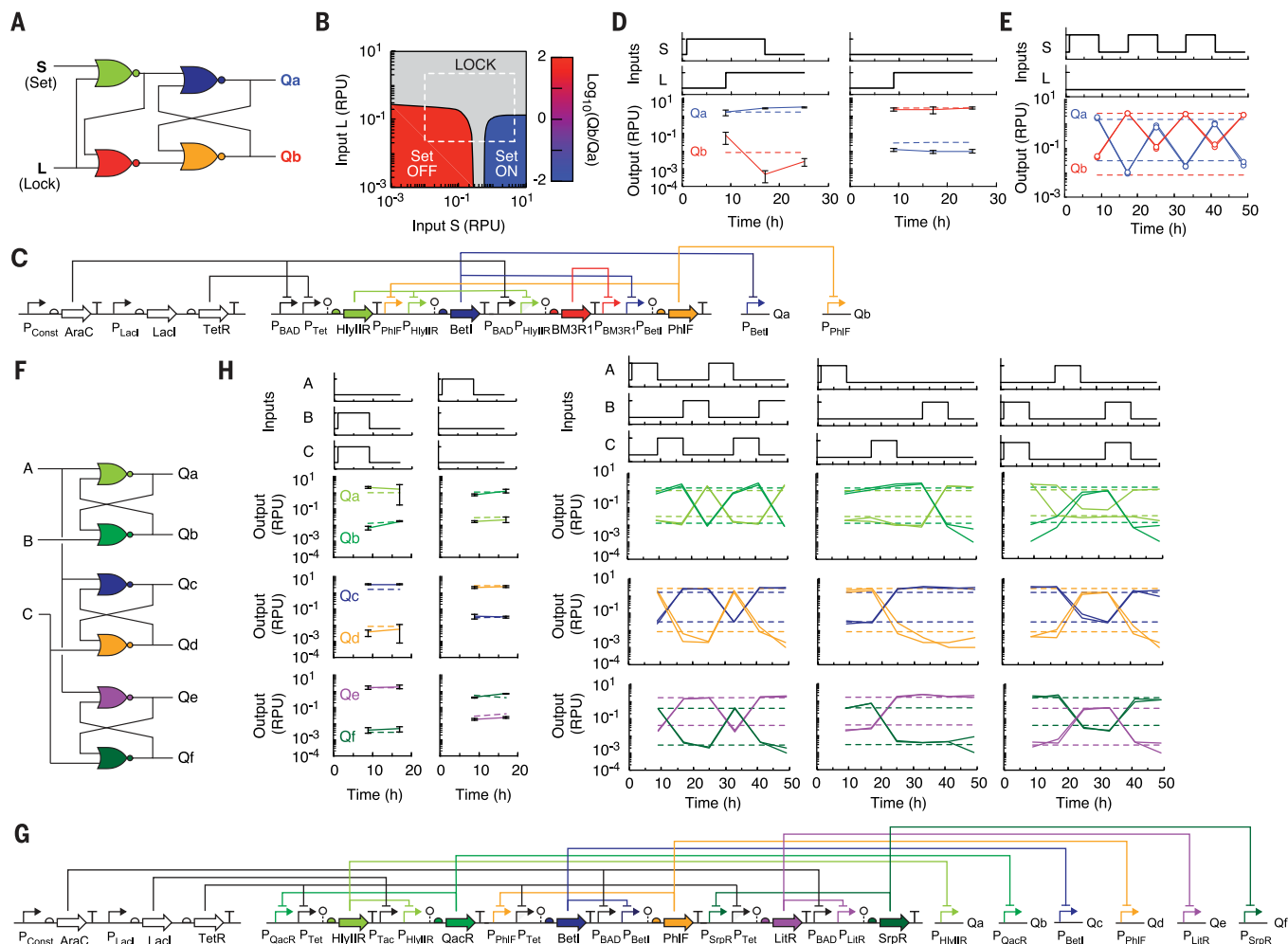


Fig. 3. Circuits comprising multiple latches. (A) The D latch circuit wiring diagram. Colors correspond to the repressor assigned to each gate (see Fig. 2C). (B) Bifurcation analysis of the D latch from an ODE model (supplementary materials). Bistable regions are shown in gray, and the monostable regions are colored according to the ratio of the two outputs (Q_b/Q_a). The white dashed lines mark the ON and OFF inputs used in the experiments, and sensors A and C are connected to the S and L inputs, respectively. Corresponding phase plane analysis and hysteresis curves are provided in fig. S8. (C) Genetic diagram of the D latch, including sensors, gates, and outputs. The two output promoters (Q_a and Q_b) were fused to *yfp* and carried on a separate plasmid. (D) Experiments verifying the performance of the D latch. The waveforms correspond to the presence and absence of inducers for the two sensors (sensor A is 2 ng/ml aTc, and sensor C is 5 mM L-arabinose). The dashed lines show the predicted outputs from a steady-state model. The data points were calculated from three replicates performed on different days, and the error bars are the standard deviation. (E) Cells were repeatedly switched between states by adding and removing the set signal (aTc) over 2 days. No arabinose was added to the media, keeping the lock in the OFF

state. Two trajectories are shown, which were performed on different days. The responses to additional waveforms are shown in fig. S9. (F) A memory register was constructed from three SR latches connected to sensors A, B, and C. Colors correspond to the repressor assigned to each gate (see Fig. 2C). (G) Genetic diagram for the three-latch memory register. Six output plasmids were constructed to measure the Q_a , Q_b , Q_c , Q_d , Q_e , and Q_f outputs in separate experiments. (H) The responses of the three-latch memory register to different input waveforms are shown. The sensor inputs A, B, and C were 2 ng/ml aTc, 1 mM IPTG, and 5 mM L-arabinose, respectively. The dashed lines are the steady-state levels predicted by the model (supplementary materials). (Left graphs) The ability to hold a state (memory) is shown for combinations of inputs. Each point represents an average and standard deviation calculated from three experiments performed on different days. (Right graphs) The ability to hold and switch states over 2 days is shown. The lines show the trajectories for two experiments performed on different days, and the colors indicate the output (Q_a to Q_f) and corresponding output promoter and repressor. Additional experiments showing the circuit response to other waveforms are shown in fig. S11.

indicated by arrows that are labeled by the status of the inputs required (sensors A, B, C, and D) and the state of the output (Y) during the transition, assuming an instantaneous response (Fig. 4). The current state is maintained until signals are received to transition to a different state.

Three circuits were designed to have two, three, and four states, respectively. They are all based on a core circuit containing two SR latches whose outputs are integrated by a final gate that implements OR, NOR, or three-input NOR logic. The two-latch register can exist in four possible states (2^2); however, the state diagram can be simplified by collapsing equivalent states that have the same output and transitions. For each circuit, repressors were assigned to the gates via signal matching, and the DNA sequence was designed and constructed as before (methods).

The circuit shown in Fig. 4A has two states (s_0 and s_1). The checkpoint for the $s_1 \rightarrow s_0$ transition is controlled by sensor A (aTc). The checkpoint for the $s_0 \rightarrow s_1$ transition is controlled by the logic B OR C (the presence of either IPTG or arabinose). Pulses of the inducer(s) switch the cells between states (Fig. 4A) (methods). The cells can be made to oscillate between the circuit states by adding the appropriate inducers back and forth between states. However, unlike a limit cycle oscillator, the cells remain in the current state in the absence of the checkpoint signals or when inputs are pulsed that do not participate in the checkpoint (see Fig. 4A and fig. S12 for additional trajectories). We demonstrate that the states can be held stably for days.

The addition of a NOR gate to the circuit expands the number of states to three (s_0 , s_1 , and s_2) (Fig. 4B). This can be viewed as a cycle in which the transitions between states are controlled by checkpoints: $s_0 \rightarrow s_1$ (arabinose), $s_1 \rightarrow s_2$ (IPTG), and $s_2 \rightarrow s_0$ (aTc). The cycle cannot proceed in the reverse direction because there is no transition from s_2 returning to s_1 . All state transitions showed the predicted circuit output for all experiments, including repeatable switching and stable memory propagation (Fig. 4B and fig. S13).

To increase the number of circuit states to four, an additional sensor (sensor D) that responds to acyl-homoserine lactone and a three-input NOR gate were added (Fig. 4C). The three-input NOR gate was constructed by placing a third input promoter upstream of a NOR gate (fig. S15). The resulting state diagram is complex and cannot be reduced to a simple cycle. The SR latches act to store the past history of three inputs (A, B, and C), and A serves as the shared reset signal for the register. The circuit was tested with pulses of each input, and the output response behaved as expected over 2 days (Fig. 4C and fig. S14).

Discussion

Natural regulatory networks are rife with complex interconnected feedback loops that implement multistable switches and dynamical behaviors (67). For engineering purposes, it would be valuable to be able to recreate these functions (62). To be designable, the approach must be based on reliable units of regulation that can be combined

by following simple rules. Here we demonstrate the core functions of sequential logic that are central to computation and representative of the simplest units of feedback control. Surprisingly, we can predict how to build complex multilatch circuits with feedback using only the steady-state response functions of the underlying NOT gates. These functions are simple to measure and report in standard promoter activity units. Circuit-design software can use these functions to automate the combination of gates to build user-defined sequential logic. Now, this is specified by using structural Verilog to define the desired circuit (supplementary files). However, this work provides the groundwork for implementing higher-level tools that will allow a user to specify the desired sequential logic or finite-state machine behavior with a state table or state diagram (63–65).

This designability is not intrinsic to biology, but rather comes from intense prior engineering efforts to design gates that are modular and insulated, such that the underlying function is context independent (34, 56, 66). These gates need to have cooperative thresholds to build circuits that exhibit multistability and complex dynamics. Our gates are based on TetR homologs that exhibit cooperativity, and we have found that having at least one gate with a Hill coefficient $n \geq 2.4$ is required to consistently build a robust bistable switch. By contrast, other means of repression, including transcription activator-like (TAL) effector proteins and CRISPR interference (CRISPRi), offer the possibility of many orthogonal gates but are noncooperative ($n \approx 1$) (67–69). Incorporating positive feedback into the latch design is a means by which the bistable region could be expanded (43, 70–72), but this would complicate design automation.

There are many potential applications for programmable sequential logic that can be modularly connected to sensors. The sensors in this work respond to small molecules, but others could respond to diverse signals, such as dissolved gases, light or color, environmental stresses, and temperature (73). The outputs of the circuits are also modular and can be used to control metabolic pathways (74), regulate host gene expression using CRISPRi (68), or implement permanent memory to irreversibly record the state (75). This work demonstrates the programmable ability to implement checkpoint control as a state machine. Importantly, this is not an irreversible progression for a sequence of signals; the cycle of states can be repeated in a single cell and its progeny. This enables the design of cycles and developmental networks for engineering applications that require that cells exist in a particular state for an unspecified amount of time. For example, therapeutic cells could be built to sense transient stimuli, such as throughout the gastrointestinal tract, and switch to a new state when the next signal is encountered. There are similar applications for diagnostic cells (48, 76–81), pathways to complex chemicals and materials that require cycles of ordered operations (82), and sentinel plants and microbes with responsive traits (31, 83, 84).

Materials and methods

Strains, media, and inducers

E. coli NEB 10-beta [Δ (ara-leu) 7697 *araD139 fhuA* Δ lacX74 *galK16 galE15 e14- ϕ 80dlacZAM15 recA1 relA1 endA1 nupG rpsL* (Str^R) *rph spoT1* (Δ (*mrr-hsdRMS-mcrBC*))], which is a derivative of *E. coli* DH10B (85), was used for experimentally measuring circuits. *E. coli* was cultured in LB Miller medium (Sigma-Aldrich, L3152) for routine cloning and propagation of plasmids. Genetic circuits were assayed in M9 minimal media (Sigma-Aldrich, M6030; 6.78 g/liter Na_2HPO_4 , 3 g/liter KH_2PO_4 , 1 g/liter NH_4Cl , 0.5 g/liter NaCl final concentration) with 0.34 g/liter thiamine hydrochloride (Sigma-Aldrich, T4625), 0.2% Casamino acids (Acros, AC61204), 2 mM MgSO_4 (Sigma-Aldrich, 230391), 0.1 mM CaCl_2 (Sigma-Aldrich, 449709), and 0.4% D-glucose (Sigma-Aldrich, G8270). Antibiotics used to select for circuit plasmids were 100 $\mu\text{g/ml}$ carbenicillin (Corning, 46-100), 50 $\mu\text{g/ml}$ kanamycin (Sigma-Aldrich, K4000), and 50 $\mu\text{g/ml}$ spectinomycin (Sigma-Aldrich, S9007). The inputs used for the sensor promoters were isopropyl β -D-1-thiogalactopyranoside (IPTG; Sigma-Aldrich, 16758), anhydrotetracycline hydrochloride (aTc; Sigma-Aldrich, 37919), L-arabinose (L-ara; Sigma-Aldrich, A3256), and *N*-(3-oxohexanoyl)-L-homoserine lactone (3OC6-HSL; Sigma-Aldrich, K3007).

Genetic circuit assembly

Genetic circuits were built using the repressor gates, three-input circuit backbone, and output plasmid as in the EcoICIGT1 UCF file (34). Genetic circuits were constructed by hierarchical Type IIS assembly in two sequential assembly reactions (fig. S1B). In the first assembly reaction, transcriptional unit constructs were assembled by joining the input promoter fragment(s) to the fragment containing the insulated repressor (ribozyme, RBS, repressor gene, terminator). A BsaI Type IIS Assembly reaction was performed for this step. The promoter and repressor fragments were supplied to the reaction as purified plasmid DNA, and the destination vector was supplied as a purified PCR product. These Type IIS assembly reactions were performed in 5 μl total volume containing 20 fmol of each purified part plasmid, 10 fmol of the purified destination vector PCR product, 5 U BsaI enzyme (New England Biolabs, R0535), and 2.5 U T4 DNA ligase (20 U/ μl HC; Promega, M1794) in 1X T4 DNA Ligase Buffer (Promega). The reaction mixture was incubated in a thermal cycler (Bio-Rad C1000 thermal cycler, 80°C lid) with the protocol: 37°C for 5 hours, followed by 50°C for 30 min, and inactivated at 80°C for 10 min. Then, 1 μl of the assembly reaction was transformed into 5 μl chemically competent cells (*E. coli* NEB 5-alpha, New England Biolabs, C2988J). After recovery in SOC, the cells were plated on LB agar containing carbenicillin. Colonies were grown, and the constructed transcriptional unit plasmids were sequenced by Sanger sequencing. In the second assembly reaction, these transcriptional unit constructs were assembled together into the circuit backbone containing the sensors to generate the

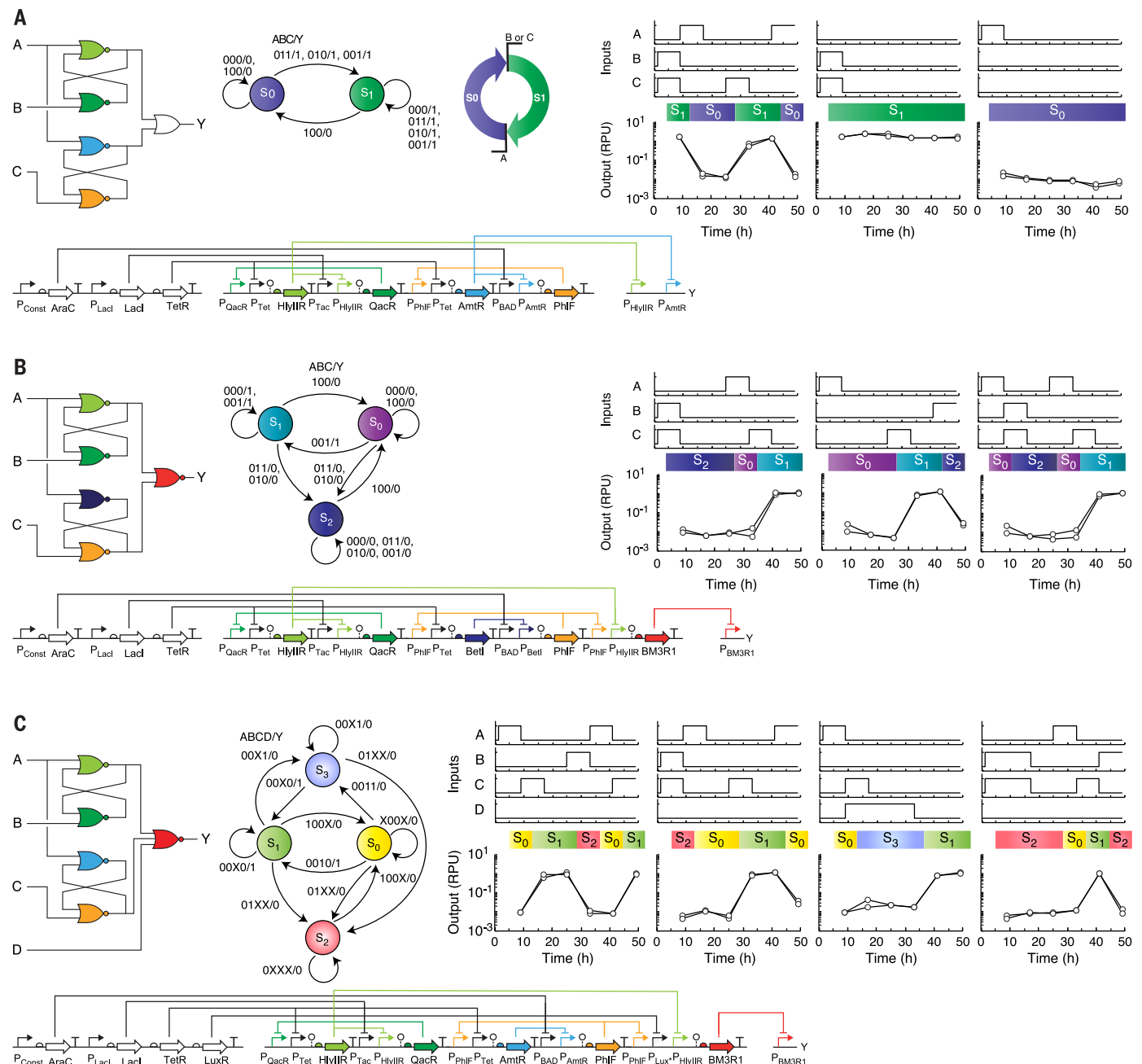


Fig. 4. Implementing checkpoint control by using sequential logic.

Circuit-wiring diagrams are shown with the gate colors indicating the assigned repressors (colors as in Fig. 2C); the uncolored gate in (A) is an OR gate. Sensors A, B, C, and D serve as the inputs, and Y is the circuit output promoter. The standard graphical description is shown for each finite-state machine generated by the circuits. The circuit states s_i are shown in circles, and the arrows mark state transitions, where the input causing the transition and the resulting output response are labeled (ABC/Y in binary digits 0 or 1, corresponding to OFF or ON, respectively). (A) A circuit designed to have two nonredundant states. A simplified "checkpoint" diagram is shown, in which the colored arrows represent the states and the bent lines show the sensors and corresponding logic required to progress to the next state. Experiments were performed for

different input waveforms, showing the ability to switch between states (left) and hold states (right) as memory in the absence of the correct sensory inputs. The output Y is shown, as measured with YFP and cytometry (methods). The color bars in the graph show the predicted state for that set of inputs. (B) A circuit designed to have three nonredundant states is shown, following the same format as in (A). (C) A circuit designed to have four nonredundant states is shown. The X in the state diagram indicates that the input can be either 0 or 1 for the state transition. Plasmids for the four-input circuit are shown in figs. S16 and S17. For sequential circuits in all panels, two experimental trajectories are shown, performed on different days. Additional waveforms were evaluated for all the circuits (figs. S12 to S14). The inducer concentrations used were 2 ng/ml aTc, 1 mM IPTG, 5 mM L-arabinose, and 10 μ M 3OC6-HSL.

final circuit plasmid constructs. For these Type IIS assemblies, the 5- μ l reaction volume contained 20 fmol of each purified transcriptional unit plasmid (one plasmid for each gate in the circuit design), 10 fmol of the purified circuit backbone plasmid (three-input or four-input backbone, fig. S19), 5 U BbsI enzyme (New England Biolabs, R0535), and 2.5 U T4 DNA ligase (20 U/ μ l HC; Promega, M1794) in 1X T4 DNA Ligase Buffer (Promega). The reaction mixture was incubated in a thermal cycler for 6 hours at 37°C, followed by 30 min at 50°C, and then 10 min at 80°C. Then, 2 μ l of the assembly reaction was transformed into 8 μ l chemically competent cells (*E. coli* NEB 10-beta, New England Biolabs, C3019I). After recovery in SOC, the cells were plated on LB agar containing kanamycin and X-gal. Plasmid DNA was purified from clonal cultures, and the constructed circuits plasmids were sequenced by Sanger sequencing.

Part plasmids (86) and destination vectors were assembled by Type IIS restriction-ligation (also referred to as Golden Gate assembly) using the SapI, BsaI, or BbsI restriction enzymes or constructed by PCR site-directed mutagenesis (also referred to as inverse PCR or round-the-horn PCR) using Q5 polymerase (New England Biolabs, M0493). Repressor part plasmids were constructed by Type IIS assembly. Promoter part plasmids and destination vectors were prepared by inverse PCR. For Type IIS assembly of part plasmids, fragments were PCR amplified with Q5 polymerase, digested with DpnI (New England Biolabs, R0176), purified (Qiagen QIAquick column or Agencourt AMPure XP beads), and assembled in a 5- μ l reaction containing 10 fmol each purified fragment, 5 U Type IIS enzyme, and 2.5 U T4 DNA ligase (20 U/ μ l HC; Promega, M1794) in 1X T4 DNA Ligase Buffer (Promega) with the protocol: 37°C for 6 hours, 50°C for 20 min, and 80°C for 15 min (Bio-Rad C1000 thermal cycler, 80°C lid). Type IIS enzymes used were BsaI (New England Biolabs, R0535), BbsI (New England Biolabs, R0539), and SapI (New England Biolabs, R0569). PCR site-directed mutagenesis was used to construct small parts \leq 80 bp (e.g., promoters, terminators, and spacers) with half of the part to be inserted added to the 5' end of the forward and reverse primer. PCR was performed with Q5 polymerase according to manufacturer's recommended protocol using NEB Tm Calculator, followed by DpnI digestion, purification, and simultaneous phosphorylation and ligation with T4 polynucleotide kinase (New England Biolabs, M0201) and T4 DNA ligase (New England Biolabs, M0202) in 1X ligase buffer at room temperature for 1 hour and inactivation 65°C for 10 min before chemical transformation. Part plasmids contained the ColE1 high-copy origin of replication and a standard antibiotic resistance cassette (Kan^R or Amp^R). Parts were flanked by BsaI cut sites and the 4-bp linker sequences GGAG, TACG, AATG, AGGT, GCTT, or CTGA. Plasmids and assembly reactions were chemically transformed cells, clonally amplified, and sequence verified by Sanger sequencing. All part sequences are listed in table S2 and provided in the supplementary SBOL file.

Circuit induction assays

Circuit plasmids were cotransformed with an output plasmid containing YFP expressed by the circuit output promoter (fig. S19D: pPAmeR-YFP, pPAmtR-YFP, pPBetI-YFP, pPBM3R1-YFP, pPHlyIIR-YFP, pPICaRA-YFP, pPLitR-YFP, pPPhIF-YFP, pPQacR-YFP, pPSrpR-YFP, or pPAmtR-PHlyIIR-YFP). When a circuit contains multiple output promoters, these were measured independently in multiple strains, where each strain contains a reporter for one output. To cotransform the circuit and output plasmids, 0.5 μ l of the purified circuit plasmid and 0.5 μ l of the purified output plasmid were transformed into 5 μ l chemically competent cells (*E. coli* NEB 10-beta, New England Biolabs, C3019I) and plated on LB agar containing kanamycin and spectinomycin. One colony was inoculated into 200 μ l M9 minimal media with appropriate antibiotics in a V-bottom 96-well microtiter plate (ThermoFisher Scientific, 249952) sealed with a breathable seal (WorldWide Medical Products Inc., 41061023) and incubated for 16 hours (overnight) at 37°C with shaking (1000 rpm) in an Elmi DTS-4 Digital Thermostatic Microplate Shaker (Elmi Ltd., Riga, Latvia). After overnight incubation, cells were diluted with two serial dilutions of 15 μ l culture into 185 μ l M9 minimal media with antibiotics (178-fold total dilution) and incubated for 3 hours at 37°C with shaking (1000 rpm) in a V-bottom plate (ThermoFisher Scientific, 249952). Then cells were diluted by two serial dilutions (resulting in 658-fold dilution), the first with 15 μ l culture into 185 μ l M9 minimal media with antibiotics, and then 15 μ l diluted culture into 145 μ l M9 minimal media with antibiotics and inducers. The inducer concentrations used for the sensors were 2 ng/ml aTc, 1 mM IPTG, 5 mM L-arabinose, and 10 μ M 3OC6-HSL. The cells were incubated for 8 hours at 37°C with shaking (1000 rpm) in a V-bottom plate with a breathable seal. To measure cell fluorescence, a 5- μ l aliquot of the cell culture was diluted into 195 μ l phosphate buffered saline (PBS, pH 7.4) with 2 mg/ml kanamycin and incubated for 1 hour at room temperature before flow cytometry analysis.

To change the inducers or continue growing the cells, the cells were diluted (658-fold total) by two serial dilutions: (i) 15 μ l culture into 185 μ l M9 minimal media with antibiotics, then (ii) 15 μ l diluted culture into 145 μ l M9 minimal media with antibiotics and inducer inputs as needed. For media containing 3OC6-HSL, the cells were washed by pelleting and resuspending in fresh media before carrying out the two dilutions. The diluted cells were then incubated for 8 hours at 37°C with shaking (1000 rpm) in a V-bottom plate with a breathable seal. Then to measure cell fluorescence, an aliquot of cells was diluted into phosphate buffered saline (PBS, pH 7.4) with 2 mg/ml kanamycin and incubated at room temperature for 1 hour before flow cytometry analysis.

Flow cytometry analysis

Fluorescence was measured using an LSRII Fortessa flow cytometer (BD Biosciences, San Jose, CA) and the BD FACSDiva software. The settings

used were: 437-V FSC voltage, 289-V SSC voltage, and 425-V green laser (488 nm) voltage. For each culture, fluorescence was measured on the FITC channel, and the data for all events were collected with a cutoff of 20,000 gated events. A flow rate of approximately 1000 events/s or less was used for analysis. The cells were gated with a rectangular gate for cell-sized particles using the FlowJo software (TreeStar Inc., Ashland, OR). The median cell fluorescence was calculated in FlowJo using the geometric median statistical tool.

Conversion of fluorescence AU to RPU

The arbitrary units of fluorescence from the cytometry measurements were converted to relative promoter units, as described previously (34, 87). The conversion follows: $RPU = (\langle YFP \rangle - \langle YFP_0 \rangle) / (\langle YFP_{RPU} \rangle - \langle YFP_0 \rangle)$, where $\langle YFP \rangle$ is the median fluorescence of the promoter, $\langle YFP_0 \rangle$ is the median fluorescence of white cells (*E. coli* NEB 10-beta lacking plasmids), and $\langle YFP_{RPU} \rangle$ is the median fluorescence of the standard promoter. The standard plasmid that we use for RPU measurements is pJSBS_RPU_standard in fig. S19. In this manuscript, we used either pAN1717 or pAN1730, depending on whether the circuit contained 2 or \geq 3 sensors to measure the standard fluorescence (because of a concern over the potential impact of the burden of expressing additional regulators). In theory, we could convert the fluorescence values to that of the standard plasmid, pJSBS_RPU_standard. However, in our hands, all three plasmids produced statistically indistinguishable fluorescence measurements, so the conversion factor is unity.

Construction and characterization of four-input circuit backbone

The circuit shown in Fig. 4C required that four sensors be carried on a single plasmid backbone. Therefore, we constructed four-input circuit backbones by adding the LuxR regulator to the three-input circuit backbone (pAN871). Permutations of the sensor operons were constructed (fig. S16). For each circuit backbone, the sensors were characterized, and the toxicity of the backbone was tested by measuring the growth (OD600) in a plate reader (Biotek H1 Synergy Hybrid Multi-Mode Reader) with shaking at 37°C (fig. S16). Sensor characterization was performed to determine the dynamic range of each sensor on the circuit backbone (34). The ON and OFF activity of each sensor input promoter (P_{Tet} , P_{Tac} , P_{BAD} , or P_{Lux}) was measured in RPU by growing the cells with and without the appropriate inducer (2 ng/ml aTc, 1 mM IPTG, 5 mM L-arabinose, or 10 μ M 3OC6-HSL) (fig. S16). Cells containing each sensor characterization plasmid were grown as described above for the circuit assays and measured by flow cytometry. The pLW555 plasmid was selected as the best four-input circuit backbone. The plasmid map is shown in fig. S16. The sensor response functions for pLW555 were measured by testing additional inducer concentrations (fig. S17). The sensor input promoter values for the three-input circuit backbone pAN871 were P_{Tet} (ON = 3.66 RPU, OFF = 0.0078 RPU),

P_{Tac} (ON = 2.96 RPU, OFF = 0.011 RPU), and P_{BAD} (ON = 2.25 RPU, OFF = 0.022 RPU). The measured sensor input promoters for the four-input circuit backbone pLW555 were P_{Tet} (ON = 3.16 RPU, OFF = 0.0097 RPU), P_{Tac} (ON = 1.61 RPU, OFF = 0.0072 RPU), P_{BAD} (ON = 1.48 RPU, OFF = 0.020 RPU), and P_{Lux} (ON = 1.32 RPU, OFF = 0.0056 RPU).

Computational analysis of circuits

The ODE models for the SR latch, D latch and three-latch memory register are provided as supplementary files in the .ode input file format that was used. Numerical analysis of the ODE models was performed using the XPP AUTO software (XPPAUT 8.0 version) with the Runge-Kutta numerical method for the phase plane analyses and bifurcation analyses (88). The numeric parameters were set as follows: step size $dt = 0.001$, nullcline grid size = 40, output storage integration steps $n = 1$, and total time = 500. To simulate state transitions, the initial conditions were set to the previous state's steady-state output values, and the sensor input values were updated corresponding to the inducer inputs present. The measured sensor input promoter values from the sensor characterization were used for the inputs to the model. The previously measured gate response functions were used (34). The bifurcation analyses were performed using the AUTO interface and starting at a steady-state point. The AUTO numeric parameters were the default values, except: the maximum number of steps = 1000, the initial step size = 0.01 (sign was changed to represent increasing or decreasing inducer input), minimum step size = 0.001, and maximum step size = 0.01. To account for the experimentally measured copy-number difference between the circuit backbone and the output plasmid, the XPPAUT predictions were multiplied by a scaling factor $\epsilon = 0.25$. The equilibria separation was calculated as the distance d between the x - y coordinates of the unstable equilibrium U and a stable equilibrium (S1 or S2) in log-log scale on the phase plane plot as:

$$d_1 = \sqrt{(x_{S1} - x_U)^2 + (y_{S1} - y_U)^2}$$

and

$$d_2 = \sqrt{(x_{S2} - x_U)^2 + (y_{S2} - y_U)^2}$$

Transversality was calculated as the area between the nullcline curves between the three intersecting points in log-log coordinate space using trapezoidal numerical integration in Matlab. A modified version of the Cello software (34) was used to assign gates to the D latch. The Cello software and code is available open source (<https://github.com/CIDARLAB/cello>). In this version, the hill-climbing assignment algorithm was selected for the gate assignment. To specify the sequential logic, we split the D latch's state table into a time series of truth tables that sampled all state transitions. We used structural Verilog to specify how the NOR gates are wired together (supplementary files). Cello was run locally using the Cello API, and the growth score cutoff was

changed to 0.10. The input UCF file was the EcoICI_GITL_UCF.json file (34) with the LmrA and PsrA gates removed. The Cello code is written in Java (version 1.8.0_31) and uses the Apache Maven (version 3.2.1) software project management.

REFERENCES AND NOTES

- H. H. McAdams, A. Arkin, It's a noisy business! Genetic regulation at the nanomolar scale. *Trends Genet.* **15**, 65–69 (1999). doi: [10.1016/S0168-9525\(98\)01659-X](https://doi.org/10.1016/S0168-9525(98)01659-X); pmid: [10098409](https://pubmed.ncbi.nlm.nih.gov/10098409/)
- L. H. Hartwell, T. A. Weinert, Checkpoints: Controls that ensure the order of cell cycle events. *Science* **246**, 629–634 (1989). doi: [10.1126/science.2683079](https://doi.org/10.1126/science.2683079); pmid: [2683079](https://pubmed.ncbi.nlm.nih.gov/2683079/)
- A. Verdugo, P. K. Vinod, J. J. Tyson, B. Novak, Molecular mechanisms creating bistable switches at cell cycle transitions. *Open Biol.* **3**, 120179 (2013). doi: [10.1098/rsob.120179](https://doi.org/10.1098/rsob.120179); pmid: [23486222](https://pubmed.ncbi.nlm.nih.gov/23486222/)
- G. Yao, T. J. Lee, S. Mori, J. R. Nevins, L. You, A bistable Rb-E2F switch underlies the restriction point. *Nat. Cell Biol.* **10**, 476–482 (2008). doi: [10.1038/ncb1711](https://doi.org/10.1038/ncb1711); pmid: [18364697](https://pubmed.ncbi.nlm.nih.gov/18364697/)
- A. Ciliberto, J. J. Tyson, Mathematical model for early development of the sea urchin embryo. *Bull. Math. Biol.* **62**, 37–59 (2000). doi: [10.1006/bulm.1999.0129](https://doi.org/10.1006/bulm.1999.0129); pmid: [10824420](https://pubmed.ncbi.nlm.nih.gov/10824420/)
- J. E. Ferrell Jr. et al., Simple, realistic models of complex biological processes: Positive feedback and bistability in a cell fate switch and a cell cycle oscillator. *FEBS Lett.* **583**, 3999–4005 (2009). doi: [10.1016/j.febslet.2009.10.068](https://doi.org/10.1016/j.febslet.2009.10.068); pmid: [19878681](https://pubmed.ncbi.nlm.nih.gov/19878681/)
- C. Nathan, Points of control in inflammation. *Nature* **420**, 846–852 (2002). doi: [10.1038/nature01320](https://doi.org/10.1038/nature01320); pmid: [12490957](https://pubmed.ncbi.nlm.nih.gov/12490957/)
- H. Maamar, D. Dubnau, Bistability in the *Bacillus subtilis* K-state (competence) system requires a positive feedback loop. *Mol. Microbiol.* **56**, 615–624 (2005). doi: [10.1111/j.1365-2958.2005.04592.x](https://doi.org/10.1111/j.1365-2958.2005.04592.x); pmid: [15819619](https://pubmed.ncbi.nlm.nih.gov/15819619/)
- C. A. Voigt, D. M. Wolf, A. P. Arkin, The *Bacillus subtilis* sin operon: An evolvable network motif. *Genetics* **169**, 1187–1202 (2005). doi: [10.1534/genetics.104.031955](https://doi.org/10.1534/genetics.104.031955); pmid: [15466432](https://pubmed.ncbi.nlm.nih.gov/15466432/)
- B. B. Zhou, S. J. Elledge, The DNA damage response: Putting checkpoints in perspective. *Nature* **408**, 433–439 (2000). doi: [10.1038/35044005](https://doi.org/10.1038/35044005); pmid: [11100718](https://pubmed.ncbi.nlm.nih.gov/11100718/)
- A. Tiwari, J. C. Ray, J. Narula, O. A. Igoshin, Bistable responses in bacterial genetic networks: Designs and dynamical consequences. *Math. Biosci.* **231**, 76–89 (2011). doi: [10.1016/j.mbs.2011.03.004](https://doi.org/10.1016/j.mbs.2011.03.004); pmid: [21385588](https://pubmed.ncbi.nlm.nih.gov/21385588/)
- S. Koirala et al., A nutrient-tunable bistable switch controls motility in *Salmonella enterica* serovar Typhimurium. *mBio* **5**, e01611–e01614 (2014). doi: [10.1128/mBio.01611-14](https://doi.org/10.1128/mBio.01611-14); pmid: [25161191](https://pubmed.ncbi.nlm.nih.gov/25161191/)
- P. Aldridge, K. T. Hughes, Regulation of flagellar assembly. *Curr. Opin. Microbiol.* **5**, 160–165 (2002). doi: [10.1016/S1369-5274\(02\)00302-8](https://doi.org/10.1016/S1369-5274(02)00302-8); pmid: [11934612](https://pubmed.ncbi.nlm.nih.gov/11934612/)
- M. B. Elowitz, S. Leibler, A synthetic oscillatory network of transcriptional regulators. *Nature* **403**, 335–338 (2000). doi: [10.1038/35002125](https://doi.org/10.1038/35002125); pmid: [10659856](https://pubmed.ncbi.nlm.nih.gov/10659856/)
- J. Stricker et al., A fast, robust and tunable synthetic gene oscillator. *Nature* **456**, 516–519 (2008). doi: [10.1038/nature07389](https://doi.org/10.1038/nature07389); pmid: [18971928](https://pubmed.ncbi.nlm.nih.gov/18971928/)
- S. Hooshanghi, W. E. Bentley, From unicellular properties to multicellular behavior: Bacteria quorum sensing circuitry and applications. *Curr. Opin. Biotechnol.* **19**, 550–555 (2008). doi: [10.1016/j.copbio.2008.10.007](https://doi.org/10.1016/j.copbio.2008.10.007); pmid: [18977301](https://pubmed.ncbi.nlm.nih.gov/18977301/)
- N. Rosenfeld, J. W. Young, U. Alon, P. S. Swain, M. B. Elowitz, Gene regulation at the single-cell level. *Science* **307**, 1962–1965 (2005). doi: [10.1126/science.1106914](https://doi.org/10.1126/science.1106914); pmid: [15790856](https://pubmed.ncbi.nlm.nih.gov/15790856/)
- J. Müller, C. Kuttler, B. A. Hense, M. Rothballer, A. Hartmann, Cell-cell communication by quorum sensing and dimension-reduction. *J. Math. Biol.* **53**, 672–702 (2006). doi: [10.1007/s00285-006-0024-z](https://doi.org/10.1007/s00285-006-0024-z); pmid: [16897015](https://pubmed.ncbi.nlm.nih.gov/16897015/)
- H. Bolouri, E. H. Davidson, Modeling transcriptional regulatory networks. *BioEssays* **24**, 1118–1129 (2002). doi: [10.1002/bies.10189](https://doi.org/10.1002/bies.10189); pmid: [12447977](https://pubmed.ncbi.nlm.nih.gov/12447977/)
- C. D. Thron, Bistable biochemical switching and the control of the events of the cell cycle. *Oncogene* **15**, 317–325 (1997). doi: [10.1038/sj.onc.1201190](https://doi.org/10.1038/sj.onc.1201190); pmid: [9233766](https://pubmed.ncbi.nlm.nih.gov/9233766/)
- J. J. Tyson, Models of cell cycle control in eukaryotes. *J. Biotechnol.* **71**, 239–244 (1999). doi: [10.1016/S0168-1656\(99\)00027-9](https://doi.org/10.1016/S0168-1656(99)00027-9); pmid: [10483109](https://pubmed.ncbi.nlm.nih.gov/10483109/)
- M. Laurent, N. Kellershohn, Multistability: A major means of differentiation and evolution in biological systems. *Trends Biochem. Sci.* **24**, 418–422 (1999). doi: [10.1016/S0968-0004\(99\)01473-5](https://doi.org/10.1016/S0968-0004(99)01473-5); pmid: [10542403](https://pubmed.ncbi.nlm.nih.gov/10542403/)
- A. P. Chandrakasan, W. J. Bowhill, F. Fox, Eds., *Design of High-Performance Microprocessor Circuits* (Wiley-IEEE Press, 2001).
- S. Hauck, S. Burns, G. Borriello, C. Ebeling, An FPGA for implementing asynchronous circuits. *IEEE Des. Test Comput.* **11**, 60–69 (1994). doi: [10.1109/MDT.1994.303848](https://doi.org/10.1109/MDT.1994.303848)
- S. W. Moore, G. S. Taylor, P. A. Cunningham, R. D. Mullins, P. Robinson, "Self calibrating clocks for globally asynchronous locally synchronous systems," in *Proceedings 2000 International Conference on Computer Design* (IEEE Computer Society, 2000), pp. 73–78.
- R. Weiss, G. E. Homsy, T. F. Knight, "Toward in vivo digital circuits," in *Evolution as Computation*, L. F. Landweber, E. Winfree, Eds. (Natural Computing Series, Springer, 2002), pp. 275–295.
- N. E. Buchler, U. Gerland, T. Hwa, On schemes of combinatorial transcription logic. *Proc. Natl. Acad. Sci. U.S.A.* **100**, 5136–5141 (2003). doi: [10.1073/pnas.0930314100](https://doi.org/10.1073/pnas.0930314100); pmid: [12702751](https://pubmed.ncbi.nlm.nih.gov/12702751/)
- R. S. Cox 3rd, M. G. Surette, M. B. Elowitz, Programming gene expression with combinatorial promoters. *Mol. Syst. Biol.* **3**, 145 (2007). doi: [10.1038/msb4100187](https://doi.org/10.1038/msb4100187); pmid: [18004278](https://pubmed.ncbi.nlm.nih.gov/18004278/)
- W. A. Lim, Designing customized cell signalling circuits. *Nat. Rev. Mol. Cell Biol.* **11**, 393–403 (2010). doi: [10.1038/nrm2904](https://doi.org/10.1038/nrm2904); pmid: [20485291](https://pubmed.ncbi.nlm.nih.gov/20485291/)
- B. Wang, M. Buck, Customizing cell signaling using engineered genetic logic circuits. *Trends Microbiol.* **20**, 376–384 (2012). doi: [10.1016/j.tim.2012.05.001](https://doi.org/10.1016/j.tim.2012.05.001); pmid: [22682075](https://pubmed.ncbi.nlm.nih.gov/22682075/)
- J. A. Brophy, C. A. Voigt, Principles of genetic circuit design. *Nat. Methods* **11**, 508–520 (2014). doi: [10.1038/nmeth.2926](https://doi.org/10.1038/nmeth.2926); pmid: [24781324](https://pubmed.ncbi.nlm.nih.gov/24781324/)
- J. Chappell, K. E. Watters, M. K. Takahashi, J. B. Lucks, A renaissance in RNA synthetic biology: New mechanisms, applications and tools for the future. *Curr. Opin. Chem. Biol.* **28**, 47–56 (2015). doi: [10.1016/j.cbpa.2015.05.018](https://doi.org/10.1016/j.cbpa.2015.05.018); pmid: [26093826](https://pubmed.ncbi.nlm.nih.gov/26093826/)
- B. Cantón, A. Labno, D. Endy, Refinement and standardization of synthetic biological parts and devices. *Nat. Biotechnol.* **26**, 787–793 (2008). doi: [10.1038/nbt1413](https://doi.org/10.1038/nbt1413); pmid: [18612302](https://pubmed.ncbi.nlm.nih.gov/18612302/)
- A. A. K. Nielsen et al., Genetic circuit design automation. *Science* **352**, aac7341 (2016). doi: [10.1126/science.aac7341](https://doi.org/10.1126/science.aac7341); pmid: [27034378](https://pubmed.ncbi.nlm.nih.gov/27034378/)
- J. Bonnet, P. Subsoontorn, D. Endy, Rewritable digital data storage in live cells via engineered control of recombination directionality. *Proc. Natl. Acad. Sci. U.S.A.* **109**, 8884–8889 (2012). doi: [10.1073/pnas.1202344109](https://doi.org/10.1073/pnas.1202344109); pmid: [22615351](https://pubmed.ncbi.nlm.nih.gov/22615351/)
- C. M. Ajo-Franklin et al., Rational design of memory in eukaryotic cells. *Genes Dev.* **21**, 2271–2276 (2007). doi: [10.1101/gad.1586107](https://doi.org/10.1101/gad.1586107); pmid: [17875664](https://pubmed.ncbi.nlm.nih.gov/17875664/)
- D. R. Burrill, P. A. Silver, Making cellular memories. *Cell* **140**, 13–18 (2010). doi: [10.1016/j.cell.2009.12.034](https://doi.org/10.1016/j.cell.2009.12.034); pmid: [20085698](https://pubmed.ncbi.nlm.nih.gov/20085698/)
- D. R. Burrill, M. C. Inniss, P. M. Boyle, P. A. Silver, Synthetic memory circuits for tracking human cell fate. *Genes Dev.* **26**, 1486–1497 (2012). doi: [10.1101/gad.189035.112](https://doi.org/10.1101/gad.189035.112); pmid: [22751502](https://pubmed.ncbi.nlm.nih.gov/22751502/)
- T. Shopera et al., Robust, tunable genetic memory from protein sequestration combined with positive feedback. *Nucleic Acids Res.* **43**, 9086–9094 (2015). doi: [10.1093/nar/gkv936](https://doi.org/10.1093/nar/gkv936); pmid: [26384562](https://pubmed.ncbi.nlm.nih.gov/26384562/)
- T. S. Gardner, C. R. Cantor, J. J. Collins, Construction of a genetic toggle switch in *Escherichia coli*. *Nature* **403**, 339–342 (2000). doi: [10.1038/35002131](https://doi.org/10.1038/35002131); pmid: [10659857](https://pubmed.ncbi.nlm.nih.gov/10659857/)
- W. Chen, J. E. Bailey, Communication to the editor. Application of the cross-regulation system as a metabolic switch. *Biotechnol. Bioeng.* **43**, 1190–1193 (1994). doi: [10.1002/bit.260431124](https://doi.org/10.1002/bit.260431124); pmid: [18615532](https://pubmed.ncbi.nlm.nih.gov/18615532/)
- T. Ellis, X. Wang, J. J. Collins, Diversity-based, model-guided construction of synthetic gene networks with predicted functions. *Nat. Biotechnol.* **27**, 465–471 (2009). doi: [10.1038/nbt.1536](https://doi.org/10.1038/nbt.1536); pmid: [19377462](https://pubmed.ncbi.nlm.nih.gov/19377462/)
- T. Lebar et al., A bistable genetic switch based on designable DNA-binding domains. *Nat. Commun.* **5**, 5007 (2014). doi: [10.1038/ncomms6007](https://doi.org/10.1038/ncomms6007); pmid: [25264186](https://pubmed.ncbi.nlm.nih.gov/25264186/)
- J. W. Lee et al., Creating single-copy genetic circuits. *Mol. Cell* **63**, 329–336 (2016). doi: [10.1016/j.molcel.2016.06.006](https://doi.org/10.1016/j.molcel.2016.06.006); pmid: [27425413](https://pubmed.ncbi.nlm.nih.gov/27425413/)
- H. Kobayashi et al., Programmable cells: Interfacing natural and engineered gene networks. *Proc. Natl. Acad. Sci. U.S.A.* **101**, 8414–8419 (2004). doi: [10.1073/pnas.0402940101](https://doi.org/10.1073/pnas.0402940101); pmid: [15159530](https://pubmed.ncbi.nlm.nih.gov/15159530/)
- C. Lou et al., Synthesizing a novel genetic sequential logic circuit: A push-on push-off switch. *Mol. Syst. Biol.* **6**, 350 (2010). doi: [10.1038/msb.2010.2](https://doi.org/10.1038/msb.2010.2); pmid: [20212522](https://pubmed.ncbi.nlm.nih.gov/20212522/)
- J. W. Kotula et al., Programmable bacteria detect and record an environmental signal in the mammalian gut. *Proc. Natl.*

- Acad. Sci. U.S.A.* **111**, 4838–4843 (2014). doi: [10.1073/pnas.1321321111](#); pmid: [24639514](#)
48. D. Chen, A. P. Arkin, Sequestration-based bistability enables tuning of the switching boundaries and design of a latch. *Mol. Syst. Biol.* **8**, 620 (2012). doi: [10.1038/msb.2012.52](#); pmid: [23089683](#)
 49. J. Fernandez-Rodriguez, L. Yang, T. E. Gorochowski, D. B. Gordon, C. A. Voigt, Memory and combinatorial logic based on DNA inversions: Dynamics and evolutionary stability. *ACS Synth. Biol.* **4**, 1361–1372 (2015). doi: [10.1021/acssynbio.5b00170](#); pmid: [26548807](#)
 50. G. Rodrigo, A. Jaramillo, Computational design of digital and memory biological devices. *Syst. Synth. Biol.* **1**, 183–195 (2007). doi: [10.1007/s11693-008-9017-0](#); pmid: [19003443](#)
 51. G. Fritz, N. E. Buchler, T. Hwa, U. Gerland, Designing sequential transcription logic: A simple genetic circuit for conditional memory. *Syst. Synth. Biol.* **1**, 89–98 (2007). doi: [10.1007/s11693-007-9006-8](#); pmid: [19003438](#)
 52. P. Hillenbrand, G. Fritz, U. Gerland, Biological signal processing with a genetic toggle switch. *PLOS ONE* **8**, e68345 (2013). doi: [10.1371/journal.pone.0068345](#); pmid: [23874595](#)
 53. C. H. Chuang, C. L. Lin, Synthesizing genetic sequential logic circuit with clock pulse generator. *BMC Syst. Biol.* **8**, 63 (2014). doi: [10.1186/1752-0509-8-63](#); pmid: [24884665](#)
 54. S. H. Strogatz, *Nonlinear Dynamics and Chaos: With Applications to Physics, Biology, Chemistry, and Engineering* (Addison-Wesley, 1994).
 55. B. C. Stanton *et al.*, Genomic mining of prokaryotic repressors for orthogonal logic gates. *Nat. Chem. Biol.* **10**, 99–105 (2014). doi: [10.1038/nchembio.1411](#); pmid: [24316737](#)
 56. A. Tamsir, J. J. Tabor, C. A. Voigt, Robust multicellular computing using genetically encoded NOR gates and chemical 'wires'. *Nature* **469**, 212–215 (2011). doi: [10.1038/nature09565](#); pmid: [21150903](#)
 57. S. Chen *et al.*, Automated design of genetic toggle switches with predetermined bistability. *ACS Synth. Biol.* **1**, 284–290 (2012). doi: [10.1021/sb300027y](#); pmid: [23651251](#)
 58. G. M. Guidi, A. Goldbeter, Bistability without hysteresis in chemical reaction systems: A theoretical analysis of irreversible transitions between multiple steady states. *J. Phys. Chem. A* **101**, 9367–9376 (1997). doi: [10.1021/jp972244k](#)
 59. J. E. Ferrell, W. Xiong, Bistability in cell signaling: How to make continuous processes discontinuous, and reversible processes irreversible. *Chaos* **11**, 227–236 (2001). doi: [10.1063/1.1349894](#); pmid: [12779456](#)
 60. J. L. Cherry, F. R. Adler, How to make a biological switch. *J. Theor. Biol.* **203**, 117–133 (2000). doi: [10.1006/jtbi.2000.1006](#); pmid: [10704297](#)
 61. J. E. Ferrell Jr., Self-perpetuating states in signal transduction: Positive feedback, double-negative feedback and bistability. *Curr. Opin. Cell Biol.* **14**, 140–148 (2002). doi: [10.1016/S0955-0674\(02\)00314-9](#); pmid: [11891111](#)
 62. T. Afroz, C. L. Beisel, Understanding and exploiting feedback in synthetic biology. *Chem. Eng. Sci.* **103**, 79–90 (2013). doi: [10.1016/j.ces.2013.02.017](#)
 63. V. A. Pedroni, *Circuit Design and Simulation with VHDL* (MIT Press, ed. 2, 2010).
 64. A. T. Abdel-Hamid, M. Zaki, S. Tahar, in *Canadian Conference on Electrical and Computer Engineering 2004* (IEEE Canada, 2004), vol. 4, pp. 1907–1910.
 65. P. Coussy, A. Morawiec, *High-Level Synthesis: From Algorithm to Digital Circuit* (Springer, 2008).
 66. C. Lou, B. Stanton, Y. J. Chen, B. Munsy, C. A. Voigt, Ribozyme-based insulator parts buffer synthetic circuits from genetic context. *Nat. Biotechnol.* **30**, 1137–1142 (2012). doi: [10.1038/nbt.2401](#); pmid: [23034349](#)
 67. A. Garg, J. J. Lohmueller, P. A. Silver, T. Z. Armel, Engineering synthetic TAL effectors with orthogonal target sites. *Nucleic Acids Res.* **40**, 7584–7595 (2012). doi: [10.1093/nar/gks404](#); pmid: [22581776](#)
 68. L. S. Qi *et al.*, Repurposing CRISPR as an RNA-guided platform for sequence-specific control of gene expression. *Cell* **152**, 1173–1183 (2013). doi: [10.1016/j.cell.2013.02.022](#); pmid: [23452860](#)
 69. A. A. Nielsen, C. A. Voigt, Multi-input CRISPR/Cas genetic circuits that interface host regulatory networks. *Mol. Syst. Biol.* **10**, 763 (2014). doi: [10.15252/msb.20145735](#); pmid: [25422271](#)
 70. B. Huang *et al.*, Interrogating the topological robustness of gene regulatory circuits by randomization. *PLOS Comput. Biol.* **13**, e1005456 (2017). doi: [10.1371/journal.pcbi.1005456](#); pmid: [28362798](#)
 71. M. Lu, J. Onuchic, E. Ben-Jacob, Construction of an effective landscape for multistate genetic switches. *Phys. Rev. Lett.* **113**, 078102 (2014). doi: [10.1103/PhysRevLett.113.078102](#); pmid: [25170733](#)
 72. A. H. Chau, J. M. Walter, J. Gerardin, C. Tang, W. A. Lim, Designing synthetic regulatory networks capable of self-organizing cell polarization. *Cell* **151**, 320–332 (2012). doi: [10.1016/j.cell.2012.08.040](#); pmid: [23039994](#)
 73. F. Zhang, J. Keasling, Biosensors and their applications in microbial metabolic engineering. *Trends Microbiol.* **19**, 323–329 (2011). doi: [10.1016/j.tim.2011.05.003](#); pmid: [21664818](#)
 74. K. Temme, R. Hill, T. H. Segall-Shapiro, F. Moser, C. A. Voigt, Modular control of multiple pathways using engineered orthogonal T7 polymerases. *Nucleic Acids Res.* **40**, 8773–8781 (2012). doi: [10.1093/nar/gks597](#); pmid: [22743271](#)
 75. L. Yang *et al.*, Permanent genetic memory with >1-byte capacity. *Nat. Methods* **11**, 1261–1266 (2014). doi: [10.1038/nmeth.3147](#); pmid: [25344638](#)
 76. J. C. Anderson, E. J. Clarke, A. P. Arkin, C. A. Voigt, Environmentally controlled invasion of cancer cells by engineered bacteria. *J. Mol. Biol.* **355**, 619–627 (2006). doi: [10.1016/j.jmb.2005.10.076](#); pmid: [16330045](#)
 77. E. J. Archer, A. B. Robinson, G. M. Süel, Engineered *E. coli* that detect and respond to gut inflammation through nitric oxide sensing. *ACS Synth. Biol.* **1**, 451–457 (2012). doi: [10.1021/sb3000595](#); pmid: [23656184](#)
 78. K. A. Haynes, F. Ceroni, D. Flicker, A. Younger, P. A. Silver, A sensitive switch for visualizing natural gene silencing in single cells. *ACS Synth. Biol.* **1**, 99–106 (2012). doi: [10.1021/sb3000035](#); pmid: [22530199](#)
 79. A. Courbet, D. Endy, E. Renard, F. Molina, J. Bonnet, Detection of pathological biomarkers in human clinical samples via amplifying genetic switches and logic gates. *Sci. Transl. Med.* **7**, 289ra83 (2015). doi: [10.1126/scitranslmed.aaa3601](#); pmid: [26019219](#)
 80. S. Slomovic, K. Pardee, J. J. Collins, Synthetic biology devices for in vitro and in vivo diagnostics. *Proc. Natl. Acad. Sci. U.S.A.* **112**, 14429–14435 (2015). doi: [10.1073/pnas.1508521112](#); pmid: [26598662](#)
 81. L. Morsut *et al.*, Engineering customized cell sensing and response behaviors using synthetic notch receptors. *Cell* **164**, 780–791 (2016). doi: [10.1016/j.cell.2016.01.012](#); pmid: [26830878](#)
 82. M. J. Smanski *et al.*, Synthetic biology to access and expand nature's chemical diversity. *Nat. Rev. Microbiol.* **14**, 135–149 (2016). doi: [10.1038/nrmicro.2015.24](#); pmid: [26876034](#)
 83. M. S. Antunes *et al.*, A synthetic de-greening gene circuit provides a reporting system that is remotely detectable and has a re-set capacity. *Plant Biotechnol. J.* **4**, 605–622 (2006). doi: [10.1111/j.1467-7652.2006.00205.x](#); pmid: [17309732](#)
 84. M. S. Antunes *et al.*, Programmable ligand detection system in plants through a synthetic signal transduction pathway. *PLOS ONE* **6**, e16292 (2011). doi: [10.1371/journal.pone.0016292](#); pmid: [21283542](#)
 85. T. Dufree *et al.*, The complete genome sequence of *Escherichia coli* DH10B: Insights into the biology of a laboratory workhorse. *J. Bacteriol.* **190**, 2597–2606 (2008). doi: [10.1128/JB.01695-07](#); pmid: [18245285](#)
 86. L. B. A. Woodruff *et al.*, Registry in a tube: Multiplexed pools of retrievable parts for genetic design space exploration. *Nucleic Acids Res.* **45**, 1553–1565 (2017). pmid: [28007941](#)
 87. J. R. Kelly *et al.*, Measuring the activity of BioBrick promoters using an in vivo reference standard. *J. Biol. Eng.* **3**, 4 (2009). doi: [10.1186/1754-1611-3-4](#); pmid: [19298678](#)
 88. B. Ermentrout, *Simulating, Analyzing, and Animating Dynamical Systems: A Guide to XPPAUT for Researchers and Students* (Software, Environments, and Tools Series, Society for Industrial and Applied Mathematics, Philadelphia, 2002).
 89. N. Roehner, Z. Zhang, T. Nguyen, C. J. Myers, Generating systems biology markup language models from the synthetic biology open language. *ACS Synth. Biol.* **4**, 873–879 (2015). doi: [10.1021/sb5003289](#); pmid: [25822671](#)

ACKNOWLEDGMENTS

We thank N. Roehner for help with converting the models to SBML.

Funding: This work was supported by funding from the Defense Advanced Research Projects Agency (DARPA) Living Foundries program (awards HR0011-13-1-0001 and HR0011-15-C-0084). C.A.V. and A.A.K.N. were supported by the Office of Naval Research Multidisciplinary University Research Initiative grant N00014-13-1-0074.

Author contributions: L.B.A. and C.A.V. conceived of the study, designed experiments, and wrote the manuscript. L.B.A. and A.A.K.N. developed the computational analysis. L.B.A. performed the experiments. **Competing interests:** C.A.V. and A.A.K.N. are founders of Asimov, Inc., a company related to this work. **Data and materials availability:** All data are available in the manuscript or the supplementary materials.

SUPPLEMENTARY MATERIALS

www.sciencemag.org/content/361/6408/eaap8987/suppl/DC1

Supplementary Text

Figs. S1 to S19

Tables S1 to S3

References (90–97)

Data Files S1 to S8

8 September 2017; accepted 3 August 2018

10.1126/science.aap8987

RESEARCH ARTICLE SUMMARY

PUBLIC HEALTH

Changing dynamics of the drug overdose epidemic in the United States from 1979 through 2016

Hawre Jalal, Jeanine M. Buchanich, Mark S. Roberts, Lauren C. Balmert, Kun Zhang, Donald S. Burke*

INTRODUCTION: The epidemic of substance use disorders and drug overdose deaths is a growing public health crisis in the United States. Every day, 174 people die from drug overdoses. Currently, opioids (including prescription opioids, heroin, and synthetic opioids such as fentanyl and its chemical analogs) are the leading cause of overdose deaths. The overdose mortality data can reveal the complex and evolving dynamics of drug use in the United States.

RATIONALE: Reports on the U.S. drug overdose epidemic tend to focus on changes in yearly statistics. Improved understanding of the long-term dynamics of the overdose epidemic may aid in the development of more effective epidemic prevention and control strategies. At present, there are no reliable methods to forecast the likely future course of the epidemic. We focused on deaths from overdoses as a relatively reliable metric of the epidemic because all deaths are required to be reported in all U.S. states and territories using the standardized International

Classification of Diseases. In an effort to understand the epidemic dynamics and perhaps predict its future course, we analyzed records of 599,255 deaths from 1979 through 2016 from the National Vital Statistics System where unintentional drug poisoning was identified as the main cause of death. We examined the time course of the overall number of deaths; the contributions of individual drugs (prescription opioids, heroin, synthetic opioids like fentanyl, methadone, cocaine, methamphetamine) to the overall curve; changes in the populations most affected by each drug as measured by demographic factors of age, sex, race, and urbanicity; and changes in the geographic distribution of deaths due to each drug as measured by the county of residence of each decedent.

RESULTS: The overall mortality rate for unintentional drug poisonings in the United States grew exponentially from 1979 through 2016. This exponentially increasing mortality rate has tracked along a remarkably smooth trajectory (log linear $R^2 = 0.99$) for at least 38 years

(left panel). By contrast, the trajectories of mortality rates from individual drugs have not tracked along exponential trajectories. Cocaine was a leading cause in 2005–2006, which was overtaken successively by prescription opioids, then heroin, and then synthetic opioids such as fentanyl. The demographic patterns of deaths due to each drug have also shown substantial

ON OUR WEBSITE

Read the full article at <http://dx.doi.org/10.1126/science.aau1184>

variability over time. Until 2010, most deaths were in 40- to 50-year-old persons, from cocaine and increasingly from prescription drugs. Deaths from heroin and then fentanyl have subsequently predominated, affecting younger persons, ages 20 to 40 (middle panel). Mortality rates for males have exceeded those for females for all drugs. Rates for whites exceeded those for blacks for all opioids, but rates were much greater among blacks for cocaine. Death rates for prescription drugs were greater for rural than urban populations. The geographic patterns of deaths also vary by drug. Prescription opioid deaths are widespread across the United States (right panel), whereas heroin and fentanyl deaths are predominantly located in the northeastern United States and methamphetamine deaths in the southwestern United States. Cocaine deaths tend to be associated with urban centers. The online manuscript provides many details of the patterns of mortality in these data.

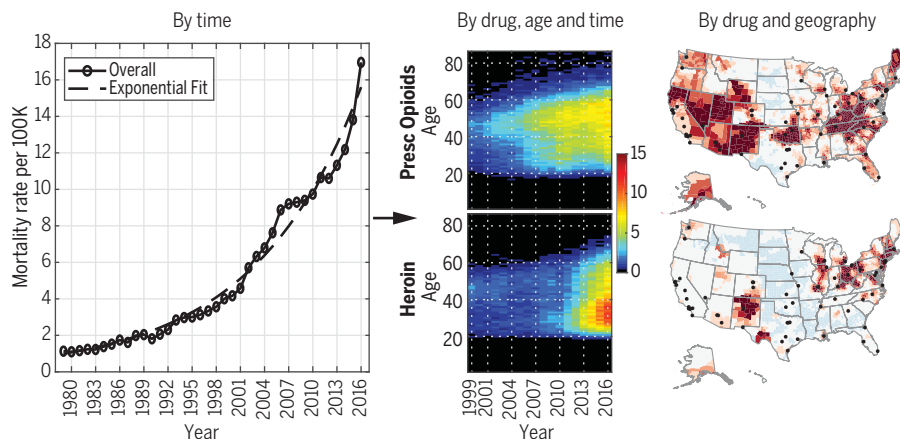
CONCLUSION: The U.S. drug overdose epidemic has been inexorably tracking along an exponential growth curve since at least 1979. Although there have been transient periods of minor acceleration or deceleration, the overall drug overdose mortality rate has regularly returned to the exponential growth curve. This historical pattern of predictable growth for at least 38 years suggests that the current opioid epidemic may be a more recent manifestation of an ongoing longer-term process. This process may continue along this path for several more years into the future. Paradoxically, there has been substantial variability with which specific drugs have become dominant in varying populations and geographic locales. This variability all but negates the possibility of confident predictions about the future role of specific drugs. Indeed, it is possible that a future overdose epidemic may be driven by a new or obscure drug that is not among the leading causes of drug overdose death today. Understanding the forces that are holding multiple subepidemics together onto a smooth exponential trajectory may be important in revealing, and effectively dealing with, the root causes of the epidemic. ■

The list of author affiliations is available in the full article online.

*Corresponding author. Email: donburke@pitt.edu

Cite this article as H. Jalal et al., *Science* 361, eaau1184 (2018). DOI: 10.1126/science.aau1184

Overdose Mortality Rate



Exponential growth in overdose deaths. The smooth overall U.S. overdose mortality curve (left panel) is a composite of multiple subepidemics, as revealed by changing patterns of overdose deaths by age distribution (middle panel; color indicates deaths per 100,000 persons), and by geography (right panel; color shows hotspots), for prescription opioids (upper) and heroin (lower). Subepidemic patterns for other drugs are shown in the full manuscript.

RESEARCH ARTICLE

PUBLIC HEALTH

Changing dynamics of the drug overdose epidemic in the United States from 1979 through 2016

Hawre Jalal¹, Jeanine M. Buchanich², Mark S. Roberts¹, Lauren C. Balmert^{2,4}, Kun Zhang⁵, Donald S. Burke^{3*}

Better understanding of the dynamics of the current U.S. overdose epidemic may aid in the development of more effective prevention and control strategies. We analyzed records of 599,255 deaths from 1979 through 2016 from the National Vital Statistics System in which accidental drug poisoning was identified as the main cause of death. By examining all available data on accidental poisoning deaths back to 1979 and showing that the overall 38-year curve is exponential, we provide evidence that the current wave of opioid overdose deaths (due to prescription opioids, heroin, and fentanyl) may just be the latest manifestation of a more fundamental longer-term process. The 38+ year smooth exponential curve of total U.S. annual accidental drug poisoning deaths is a composite of multiple distinctive subepidemics of different drugs (primarily prescription opioids, heroin, methadone, synthetic opioids, cocaine, and methamphetamine), each with its own specific demographic and geographic characteristics.

The epidemic of substance use disorders and drug overdose deaths in the United States is a growing public health crisis. Every day, 174 people in the United States die from drug overdoses (1). Currently, opioids (including prescription opioids, heroin, and synthetic opioids such as fentanyl and its chemical analogs) are the main causes of overdose deaths in the United States, leading the U.S. government to declare the opioid crisis to be a public health emergency (2).

Knowledge of the opioid epidemic has been mostly limited to scattered statistics that only reveal selected aspects of the epidemic, such as specific geographic regions, specific time periods, and/or specific drugs. For example, a recent National Center for Health Statistics (NCHS) data brief shows that the Appalachian region and southwest region have overdose death rates statistically higher than the national rate (3). Similarly, a recent study has identified geospatial clusters of heroin-related overdose deaths in Southern California in 2000, and emerging later in New England, the Mid-Atlantic, and the Great Lakes region between 2013 and 2014 (4).

We lack a detailed analysis of the opioid epidemic in the context of the larger drug epidemic that reveals the complex and evolving dynamics of drug use in the United States (5). This manuscript examines mortality patterns of all accidental (unintentional) drug poisonings as reported through the U.S. National Vital Statistics

System from 1979 through 2016. We describe the overall pattern of drug overdose deaths in the United States and reveal specific aspects of these deaths by drug, demography, and geography; we refer to these patterns as subepidemics.

The overdose epidemic is a composite of multiple subepidemics

Annual mortality rates attributed to prescription opioids, heroin, methadone, synthetic opioids other than methadone, cocaine, methamphetamine, unspecified narcotics, and unspecified drugs are shown in Fig. 1. Drug classes are defined in the supplementary materials and table S1, which sorts the drugs by their International Classification of Diseases (ICD) codes. Accidental drug poisoning trend analyses begin in 1979 with the ninth revision (ICD-9), owing to comparability issues with the cause of death in earlier revisions. Similarly, analyses by drug and drug class begin in 1999 (with ICD-10) because those classifications are not comparable with ICD-9.

Since 2010, the mortality curves for all drug types have been increasing, except for methadone and for unspecified drugs and narcotics. Each drug's mortality curve shows some variability. For example, the mortality rate from prescription opioids decreased slightly in 2012, whereas the mortality rates from heroin and synthetic opioids have been increasing rapidly. These trends may be related because several epidemic interventions may have reduced the impact of prescription opioids around 2010, including the reformulation of OxyContin in 2010 (6), implementation of pain clinic laws and mandatory checking of Prescription Drug Monitoring Program data by prescribers (7), the reduction in

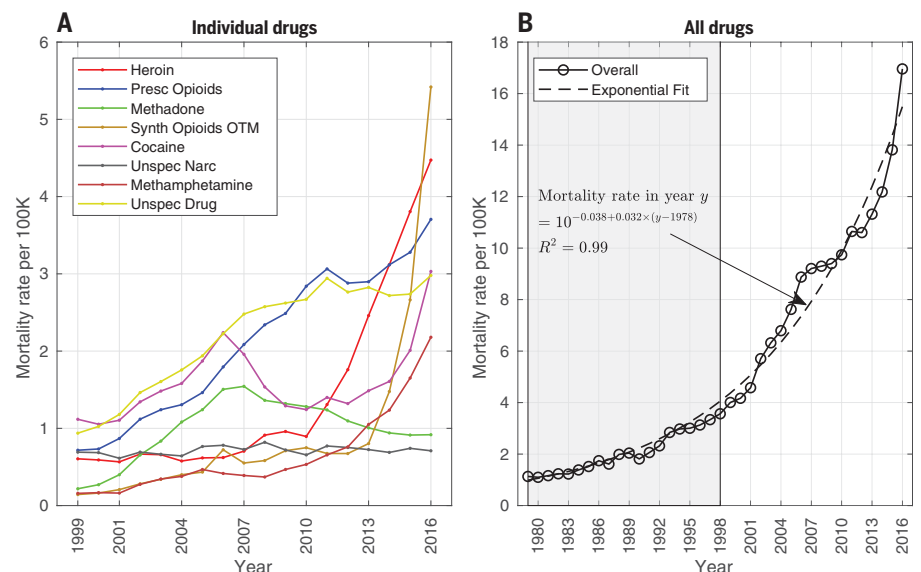


Fig. 1. Mortality rates from unintentional drug overdoses. (A and B) Mortality rates for (A) individual drugs and (B) all drugs. Detailed data for individual drugs are only available from 1999 to 2016, although additional data for all drugs are available since 1979 (this area is grayed out). The exponential equation and fit are shown for all drugs. (Synth Opioids OTM: synthetic opioids other than methadone. This category includes fentanyl and its analogs.)

¹Department of Health Policy and Management, Graduate School of Public Health, University of Pittsburgh, Pittsburgh, PA, USA. ²Department of Biostatistics, Graduate School of Public Health, University of Pittsburgh, Pittsburgh, PA, USA. ³Department of Epidemiology, Graduate School of Public Health, University of Pittsburgh, Pittsburgh, PA, USA. ⁴Department of Preventive Medicine (Biostatistics), Feinberg School of Medicine, Northwestern University, Chicago, IL, USA. ⁵Division of Unintentional Injury Prevention, Centers for Disease Control and Prevention, Atlanta, GA, USA.

*Corresponding author. Email: donburke@pitt.edu

the amount of opioids prescribed (8), and the rescheduling of hydrocodone compounds in 2014 (9). Although these changes may have reduced the overdose deaths from prescription opioids, it is possible that they may have led some

opioid-dependent persons to switch to illicit opioids, such as heroin and fentanyl (10–12). Economic factors may also have contributed to the transition from prescription opioids to heroin; heroin is increasingly more available, easier to

use through non-oral routes, and becoming purer and less expensive than prescription opioids (13). In addition, the subsequent sharp increase in fentanyl overdose deaths after 2013 is consistent with law enforcement data showing

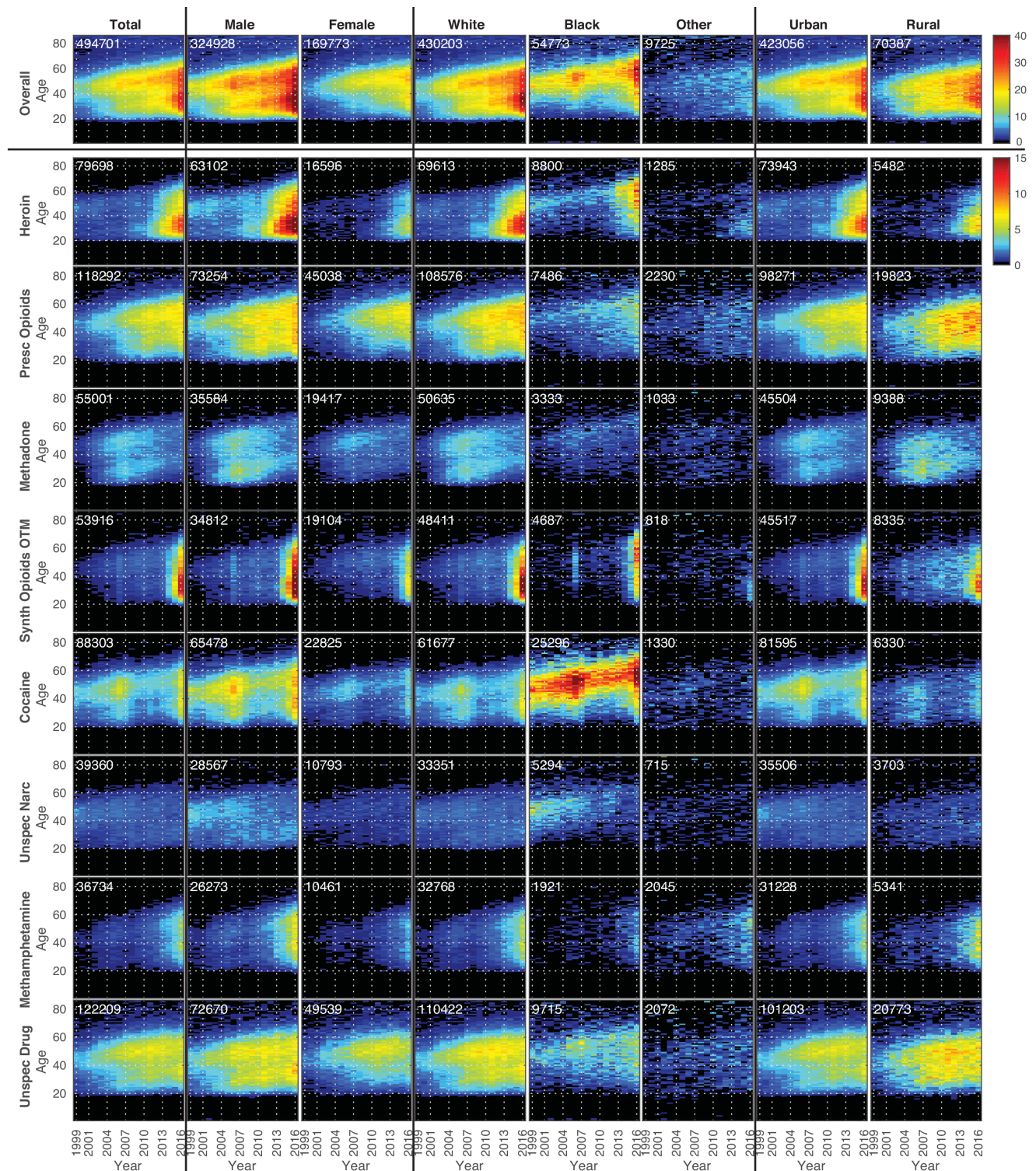


Fig. 2. Heatmaps showing the subepidemics by demography and urbanicity. Total number of deaths in each category from 1999 through 2016 are shown in the upper left corner of each plot. The colors indicate age-adjusted mortality rates per 100,000 people. (Synth Opioids OTM: synthetic opioids other than methadone. This category includes fentanyl and its analogs.)

increased seizures of illicitly manufactured fentanyl (14, 15).

Several other fluctuations observed in the drug-specific mortality curves may also, in retrospect, be explainable. For example, in 2006, a spike in overdose deaths in the United States associated with fentanyl was traced to a production laboratory in Mexico (16). Similarly, the decline in methadone deaths after 2007 may be attributed to the removal of methadone from the preferred drug list by state Medicaid programs, which used to be major sources of methadone prescriptions for pain management (17). The rise and fall of cocaine-related overdose deaths in the United States appears to be linked to production and supply in Colombia, which in turn have reflected diplomatic turns of events in a decades-long civil war (18). Although opioids are the major offenders, drugs other than opioids, such as cocaine and methamphetamine, now also contribute substantially to the rising counts of overdose deaths in the United States (19).

We also examined the mortality rates for deaths reported as being due to unspecified narcotics and unspecified drugs. Mortality rates from the unspecified narcotics have remained stable during the study period, but unspecified drugs closely follow prescription opioid mortality rates until 2008 and start to diverge after 2013, possibly indicating improvements in vital statistics reporting by some states.

Mortality curves from individual drugs do not show regular or predictable growth patterns. Nonetheless, we observed that the annual sum of all drug overdose mortality rates follows a remarkably smooth mathematical trajectory. Figure 1B plots changes in the total accidental poisoning mortality rate, from all drugs. Note that the total mortality rate per year is less than the sum of the mortality rates reported for individual drugs, owing to listing of more than one drug on the death certificate in many individual cases (see fig. S2). The total accidental poisoning mortality rate closely tracks along an exponential growth curve defined as annual overall mortality rate in year (y) = $10^{(a + b*(y - 1978))}$, where $a = -0.038$ [confidence interval (CI) = (-0.104, 0.027)] and $b = 0.032$ [CI = (0.030, 0.034)]. With this exponential growth, the doubling time is approximately 9 years. Of particular interest is the observation that the first half of this long-term smooth exponential growth curve predates the current opioid epidemic.

The drug-specific subepidemics differ significantly with respect to their time course, geographic spread, and demographic groups affected

Next, we examined death record data available from 1999 to 2016 to determine if there were any patterns in the demography or geography of mortality by drug that might explain how these variable individual drug curves might meld into a single smooth exponential process. To reveal patterns in these data, we use visualization techniques consisting of heat-

maps (Fig. 2) and geospatial hotspot analyses (Fig. 3).

Figure 2 is a matrix of 72 individual age distribution heatmaps depicting how the age of overdose decedents has historically changed over time, as analyzed by drugs, gender, race, and urbanicity. Age has been recognized as an important predictor in transitions from non-use or asymptomatic use to problematic drug use (20, 21) of illicit drugs, and the middle-aged have had higher rates of prescription opioid deaths than other age groups (3, 22–24). In addition, significant increases in heroin overdose-related hospitalizations among the age groups of 20 to 29 and 50 to 59 have recently been identified, suggesting potential new cohorts of heroin users among these age groups (25, 26).

These age distribution heatmaps reveal some distinct patterns. One pattern is a clear bimodal distribution of unintentional drug overdoses: a younger group (age 20 to 40 years) and an older group (age 40 to 60 years). The relative amplitudes of these groupings vary according to drug, gender, race, and urbanicity. The younger age group predominates among deaths due to heroin and synthetic opioids, and especially among males, whites, and in urban counties. Mortality rates from prescription opioids and unspecified drugs were higher among the older age group, especially among females, among whites, and in rural counties.

Recent studies have examined the unspecified drug overdose death category and attributed some deaths in this category to prescription opioids because many states have drastically under-reported prescription opioid-related overdose deaths, owing to lack of toxicology testing for drug specificity in overdose deaths (27). From 1999 to 2016, there were 112,480 drug overdose deaths in which unspecified drugs were identified as the contributory cause of death, as compared to 106,193 deaths in which prescription opioids were a contributory cause of death. The patterns of overdose mortality rates for which the drug was unspecified closely resemble the patterns for prescription opioids across age, gender, race, and urbanicity. The heatmaps clearly present these similarities.

Mortality differences between male and female rate are associated with age and type of drug. Prior reports of prescription opioid mortality rates have shown nearly four times higher rates in younger males than younger females, in contrast to only 1.3-fold higher rates in older males relative to older females (28). The heatmaps reveal that these differences can be mostly explained by the type of drug. The higher risk among young males relative to young females is mostly attributable to heroin and synthetic drugs, whereas the risk of death among older females is mostly attributable to prescription opioids and unspecified drugs. These differences by age, sex, and type of drug have generally become more apparent in recent years.

The description of the association between drug overdose deaths and race in the literature has been mostly limited to the reports that show

increased mortality rates, especially for opioids among whites (22–24, 29–31). In addition to the increased overdose deaths among whites, the heatmaps reveal that the age showing the peak mortality rate for cocaine among blacks has increased with each year, indicating a cohort aging effect. This pattern is especially noticeable among men and in urban counties. Among whites, the younger age group is at greatest risk for heroin and synthetic opioid deaths, whereas among blacks, the older age group is at greater risk.

The increase in drug poisoning mortality in 2016 is due to increased mortality from multiple drug-specific subepidemics: synthetic opioids (most likely fentanyl) among males, whites, and those in urban counties; heroin among young adults; prescription opioids among the middle-aged and blacks; and cocaine and methamphetamine among a wider age range, males, and whites.

To reveal geographic hotspots of each of the drugs over time, we also performed geospatial hotspot analyses of deaths due to each drug, broken into historical time intervals. Figure 3 shows the geographic distribution of eight drug classes at each of four periods. Taken together, these maps provide a synoptic view of changing landscape of drug mortality hotspots. [See the supplementary materials for a detailed description of the methodology.]

From 1999 to 2016, the epidemic intensity, as well as the spatial distribution of deaths attributed to prescription drugs, heroin, synthetic opioids other than methadone, cocaine, and methamphetamine, have all increased. Only for methadone has the epidemic intensity and spatial distribution peaked and then declined. Although the overall national epidemic may be smooth and continuous, each drug has shown a specific geospatial pattern of spread during this 18-year period. Heroin hotspots have changed from being closely clustered around large cities to being distributed more widely, especially in the Northeast and the Southwest. Prescription opioid hotspots initially were prominent in the southwestern United States and Appalachia but subsequently spread to involve much of the western United States, Oklahoma, Florida, and New England. Fentanyl and fentanyl analog hotspots have centered in opioid hotspots, especially in the Appalachian and Northeast regions. Cocaine hotspots have also centered around large cities but have diffused more broadly in recent years. Methamphetamine deaths have increased most dramatically in the western and southwestern United States. Almost every region in the country is a hotspot for mortality from one or more drugs. The only large region that appears to have been relatively spared (a relative “cold spot” for all drugs) is composed of the north central states.

These detailed demographic and geographic analyses do not suggest obvious mechanisms as to how multiple drug-specific subepidemics have merged into a single smooth exponential 38+ year process. Indeed, these findings add to the paradox by revealing how disparate the individual drug epidemics are.

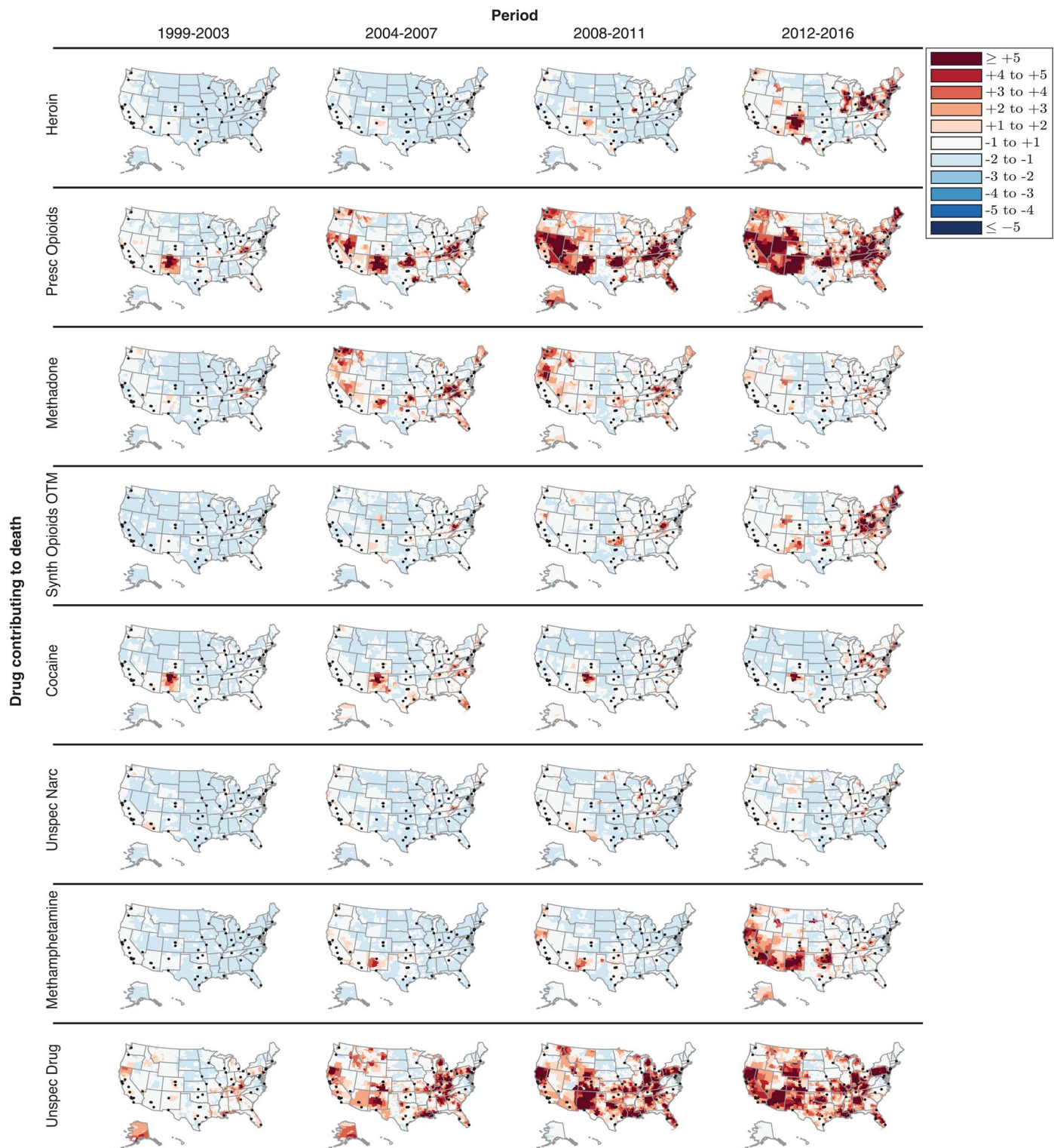


Fig. 3. Geospatial hotspot analysis by drug and period. The G_i^* statistics are standardized using pooled statistics across all drugs and periods. The various shades of red and blue indicate pooled standard deviations above and below the pooled mean, respectively, as shown in the legend. The small black

circles indicate major cities with populations greater than 300,000 people. None of the regions were less than 2 pooled standard deviations below the pooled average. (Synth Opioids OTM: synthetic opioids other than methadone. This category includes fentanyl and its analogs.)

Effective public health responses will be crucial to address the USA drug crisis. Understanding the demographic and geographic characteristics of the subepidemics as reflected by overdose death patterns may be valuable in designing and strengthening “upstream” public health surveillance systems for substance abuse and non-fatal overdoses among living persons (32), and elucidation of the underlying complexity of the drug-specific subepidemics may facilitate development of more effective, locally tailored primary, secondary, and tertiary prevention strategies (33, 34). For the large existing population of persons with substance use disorder or addiction (35), availability of and access to treatments and harm reduction services that are subepidemic specific may be valuable in preventing more overdose deaths. Lastly, better understanding of local drug death patterns may lead to innovative collaborations between public health and law enforcement, which could include data sharing (36), partnership at the local and community level on harm reduction, and linking people with addiction to treatment (37).

Caveats

Our findings should be interpreted with caution. First, there is substantial variation in the level of specificity of drug reporting for vital statistics across states and/or counties. A recent analysis found that in 2015, the percentage of overdose deaths with the drug unspecified ranged from 0% in the District of Columbia to just over 50% in Pennsylvania (38). The geographic distribution of these deaths not attributed to specified drugs can be seen in Fig. 3. This analysis and others (39) have found that states with centralized medico-legal systems have more complete drug reporting than states with decentralized systems. Figure S1 reproduces Fig. 2 with data only from states that produce good-quality data [as defined by the U.S. Centers for Disease Control and Prevention (CDC)] with fewer unspecified drug overdose diagnoses, and the results are almost identical, supporting the validity of the national-level data analyses.

Second, our categories of specific drug mortality rates are not mutually exclusive; therefore, overdose deaths that involve multiple drugs could be counted more than once. Multidrug abuse and overdose are increasing, and it is not always clear which drug or drugs are responsible for the overdose. Figure S2 shows how the relationships among various drugs have changed over time. In this figure, we show that the percentage of death certificates listing synthetic opioids OTM (other than methadone), cocaine, and methamphetamine as a secondary drug has increased dramatically in recent years, regardless of the index drug. While, the percentage of deaths attributed to heroin in addition to another drug is showing early signs of decline, this decline is, of course, only relative to the rapid rise in deaths due to the index drug. Additionally, the 10th revision of the International Classification of Diseases (ICD-10) only has a set number of codes for drug classes. Overdoses are

now being attributed to new drugs, such as fentanyl analogs, but the drug class codes have not changed (e.g., acyl fentanyl would be coded as T40.4), meaning that even with complete drug reporting, death certificates lose some drug specificity during the coding process. Additionally, coroners and medical examiners may not be able to identify newer psychoactive substances, indicating that these drugs will not be recorded on the death certificate. Such ambiguities in diagnostics do not affect our main finding of an exponential increase in the rate for overall drug overdose, as each overdose death is counted once.

Third, the intent of an overdose death is not always easy to determine by a medical examiner or coroner. Our study only focused on unintentional or accidental drug overdoses, which constitute roughly 85% of all drug overdoses every year; however, we recognize that the practice or capacity of determining intent varies by states.

Lastly, the dynamics of the substance use epidemic are not fully captured in drug overdose mortality data alone. A more complete analysis would also describe the initiation, natural history, treatment, and progression of drug use.

The opioid crisis may be part of a larger, longer-term process

The epidemic of drug overdoses in the United States has been inexorably tracking along an exponential growth curve since at least 1979, well before the surge in opioid prescribing in the mid-1990s. Although there have been transient periods of minor acceleration or deceleration, the overall drug overdose mortality rate has regularly returned to the exponential growth curve. This historical pattern of predictable growth for at least 38 years strongly suggests that the epidemic will continue along this path for several more years. By contrast, the recent historical variability with which some specific drugs have waxed and waned makes predictions about the future role of specific drugs far more uncertain. Indeed, it is possible that in the future, the drug overdose epidemic may be driven by a new or heretofore obscure psychoactive substance.

Understanding the forces that are holding multiple subepidemics together into a smooth exponential trajectory may be important in revealing the root causes of the epidemic, and this understanding may be crucial to implementation of prevention and intervention strategies. Economic and technological “push” factors may be at work to increase supply, such as improved communications and supply chains, efficiencies in drug manufacturing, and expanding drug markets, leading to lower prices and higher drug purities (40, 41). Sociological and psychological “pull” forces may be operative to accelerate demand, such as despair, loss of purpose, and dissolution of communities (42, 43). Elucidation of the dynamics of the “deep” drivers of the overdose epidemic may provide valuable new insights.

Materials and methods

This section provides a summary of the materials and methods. A more detailed explanation

can be found in the supplementary materials. Death information was obtained from the Mortality Multiple Cause Micro-data Files from 1979 to 2016. These data use ICD-9, enabling us to identify accidental drug poisoning deaths since 1979. In addition, we can identify specific drugs as contributory causes of accidental overdose deaths since 1999, because the use of ICD-10 starts from this time. For example, the ICD-10 code for heroin is T40.1, and for natural and semi-synthetic opioids (including prescription opioids), the code is T40.2.

To illustrate the changing dynamics of the drug-overdose deaths on multiple levels, we examined overdose mortality rates at three levels of detail: (i) national level, by drug, over time; (ii) national level, by drug, over time, with detailed analysis by demographic groups of age, sex, race, and urbanicity; and (iii) county-level cluster analysis, by drug, over time (hotspot analysis).

For national-level analyses, we computed mortality rates for individuals by drug codes and by age, sex, race, and urbanicity. For each computation, we used the appropriate denominator from the U.S. census population estimates from 1999 through 2016. To distinguish rural from urban counties, we used the 2013 Rural-Urban Continuum Codes (RUCC). RUCC codes 1–3 were considered urban, and RUCC codes 4–9 were classified as rural.

In the county-level analysis, we used the Getis-Ord G_i^* statistic to show geospatial clustering of hot (high) and cold (low) spots of mortality rates. The G_i^* statistic identifies these hot and cold spots on the basis of contiguous counties. The G_i^* statistic is essentially a Z-score standardized by a mean and standard deviation of mortality rates in all the counties. Typically, the G_i^* statistic can display geospatial information on one dimension such as mortality rates. To add additional dimensions and compare mortality rates by drug and time, we restandardized the G_i^* statistics by using the pooled mean and standard deviations of the G_i^* statistics across all drugs and over time. This restandardization allowed us to produce a set of comparable maps across time and drugs.

REFERENCES AND NOTES

1. P. Seth, L. Scholl, R. A. Rudd, S. Bacon, Overdose Deaths Involving Opioids, Cocaine, and Psychostimulants - United States, 2015–2016. *MMWR Morb. Mortal. Wkly. Rep.* **67**, 349–358 (2018). doi: [10.15585/mmwr.mm6712a1](https://doi.org/10.15585/mmwr.mm6712a1); pmid: [29596405](https://pubmed.ncbi.nlm.nih.gov/29596405/)
2. HHS Acting Secretary Declares Public Health Emergency to Address National Opioid Crisis (2017); <https://www.hhs.gov/about/news/2017/10/26/hhs-acting-secretary-declares-public-health-emergency-address-national-opioid-crisis.html>.
3. H. Hedegaard, M. Warner, A. M. Miniño, Drug Overdose Deaths in the United States, 1999–2015. NCHS Data Brief, US Department of Health and Human Services no. 273 (2017).
4. K. Stewart, Y. Cao, M. H. Hsu, E. Artigiani, E. Wish, Geospatial Analysis of Drug Poisoning Deaths Involving Heroin in the USA, 2000–2014. *J. Urban Health* **94**, 572–586 (2017). doi: [10.1007/s11524-017-0177-7](https://doi.org/10.1007/s11524-017-0177-7); pmid: [28639058](https://pubmed.ncbi.nlm.nih.gov/28639058/)
5. D. S. Burke, Forecasting the opioid epidemic. *Science* **354**, 529 (2016). doi: [10.1126/science.aal2943](https://doi.org/10.1126/science.aal2943); pmid: [27811241](https://pubmed.ncbi.nlm.nih.gov/27811241/)
6. T. J. Cicero, M. S. Ellis, Abuse-Deterrent Formulations and the Prescription Opioid Abuse Epidemic in the United States: Lessons Learned From OxyContin. *JAMA Psychiatry* **72**.

- 424–430 (2015). doi: [10.1001/jamapsychiatry.2014.3043](https://doi.org/10.1001/jamapsychiatry.2014.3043); pmid: [25760692](https://pubmed.ncbi.nlm.nih.gov/25760692/)
7. D. Dowell, K. Zhang, R. K. Noonan, J. M. Hockenberry, Mandatory Provider Review And Pain Clinic Laws Reduce The Amounts Of Opioids Prescribed And Overdose Death Rates, Mandatory Provider Review And Pain Clinic Laws Reduce The Amounts Of Opioids Prescribed And Overdose Death Rates. *Health Aff. (Millwood)* **35**, 1876–1883 (2016). doi: [10.1377/hlthaff.2016.0448](https://doi.org/10.1377/hlthaff.2016.0448); pmid: [27702962](https://pubmed.ncbi.nlm.nih.gov/27702962/)
 8. G. P. Guy Jr. et al., Vital Signs: Changes in Opioid Prescribing in the United States, 2006–2015. *MMWR Morb. Mortal. Wkly. Rep.* **66**, 697–704 (2017). doi: [10.15585/mmwr.mm6626a4](https://doi.org/10.15585/mmwr.mm6626a4); pmid: [28683056](https://pubmed.ncbi.nlm.nih.gov/28683056/)
 9. C. M. Jones, P. G. Lurie, D. C. Throckmorton, Effect of US Drug Enforcement Administration's Rescheduling of Hydrocodone Combination Analgesic Products on Opioid Analgesic Prescribing. *JAMA Intern. Med.* **176**, 399–402 (2016). doi: [10.1001/jamainternmed.2015.7799](https://doi.org/10.1001/jamainternmed.2015.7799); pmid: [26809459](https://pubmed.ncbi.nlm.nih.gov/26809459/)
 10. A. Alpert, D. Powell, R. L. Pacula, "Supply-Side Drug Policy in the Presence of Substitutes: Evidence from the Introduction of Abuse-Deterrent Opioids" (National Bureau of Economic Research, 2017).
 11. T. J. Cicero, M. S. Ellis, H. L. Surratt, Effect of abuse-deterrent formulation of OxyContin. *N. Engl. J. Med.* **367**, 187–189 (2012). doi: [10.1056/NEJMc1204141](https://doi.org/10.1056/NEJMc1204141); pmid: [22784140](https://pubmed.ncbi.nlm.nih.gov/22784140/)
 12. W. C. Becker, L. E. Sullivan, J. M. Tetrault, R. A. Desai, D. A. Fiellin, Non-medical use, abuse and dependence on prescription opioids among U.S. adults: Psychiatric, medical and substance use correlates. *Drug Alcohol Depend.* **94**, 38–47 (2008). doi: [10.1016/j.drugalcdep.2007.09.018](https://doi.org/10.1016/j.drugalcdep.2007.09.018); pmid: [18063321](https://pubmed.ncbi.nlm.nih.gov/18063321/)
 13. National drug control strategy: Data supplement 2016. (Office of National Drug Control Policy Executive, Office of the President of the United States Washington, DC, 2016).
 14. R. M. Gladden, P. Martinez, P. Seth, Fentanyl Law Enforcement Submissions and Increases in Synthetic Opioid-Involved Overdose Deaths - 27 States, 2013–2014. *MMWR Morb. Mortal. Wkly. Rep.* **65**, 837–843 (2016). doi: [10.15585/mmwr.mm6533a2](https://doi.org/10.15585/mmwr.mm6533a2); pmid: [27560775](https://pubmed.ncbi.nlm.nih.gov/27560775/)
 15. A. B. Peterson et al., Increases in Fentanyl-Related Overdose Deaths - Florida and Ohio, 2013–2015. *MMWR Morb. Mortal. Wkly. Rep.* **65**, 844–849 (2016). doi: [10.15585/mmwr.mm6533a3](https://doi.org/10.15585/mmwr.mm6533a3); pmid: [27560948](https://pubmed.ncbi.nlm.nih.gov/27560948/)
 16. Public Health Advisory: Methadone Use for Pain Control May Result in Death and Life-Threatening Changes in Breathing and Heart Beat (2006 www.fda.gov/ForConsumers/ConsumerUpdates/ucm124346.htm).
 17. M. Faul, M. Bohm, C. Alexander, Methadone Prescribing and Overdose and the Association with Medicaid Preferred Drug List Policies - United States, 2007–2014. *MMWR Morb. Mortal. Wkly. Rep.* **66**, 320–323 (2017). doi: [10.15585/mmwr.mm6612a2](https://doi.org/10.15585/mmwr.mm6612a2); pmid: [28358791](https://pubmed.ncbi.nlm.nih.gov/28358791/)
 18. N. Miroff, "A side effect of peace in Colombia? A cocaine boom in the U.S." *The Washington Post*, 8 May 2017.
 19. C. McCall Jones, G. T. Baldwin, W. M. Compton, Recent Increases in Cocaine-Related Overdose Deaths and the Role of Opioids. *Am. J. Public Health* **107**, 430–432 (2017). doi: [10.2105/AJPH.2016.303627](https://doi.org/10.2105/AJPH.2016.303627); pmid: [28177817](https://pubmed.ncbi.nlm.nih.gov/28177817/)
 20. W. M. Compton, C. M. Jones, G. T. Baldwin, Relationship between Nonmedical Prescription-Opioid Use and Heroin Use. *N. Engl. J. Med.* **374**, 154–163 (2016). doi: [10.1056/NEJMra1508490](https://doi.org/10.1056/NEJMra1508490); pmid: [26760086](https://pubmed.ncbi.nlm.nih.gov/26760086/)
 21. W. M. Compton, D. A. Dawson, K. P. Conway, M. Brodsky, B. F. Grant, Transitions in illicit drug use status over 3 years: A prospective analysis of a general population sample. *Am. J. Psychiatry* **170**, 660–670 (2013). doi: [10.1176/appi.ajp.2012.12060737](https://doi.org/10.1176/appi.ajp.2012.12060737); pmid: [23511653](https://pubmed.ncbi.nlm.nih.gov/23511653/)
 22. J. M. Buchanich et al., Patterns and trends in accidental poisoning death rates in the US, 1979–2014. *Prev. Med.* **89**, 317–323 (2016). doi: [10.1016/j.ypmed.2016.04.007](https://doi.org/10.1016/j.ypmed.2016.04.007); pmid: [27085991](https://pubmed.ncbi.nlm.nih.gov/27085991/)
 23. L. H. Chen, H. Hedegaard, M. Warner, Drug-poisoning deaths involving opioid analgesics: United States, 1999–2011. NCHS data brief, No. 166 (National Center for Health Statistics, Hyattsville, MD, 2014).
 24. L. J. Paulozzi, C. M. Jones, K. A. Mack, R. A. Rudd; Centers for Disease Control and Prevention (CDC). Vital signs: Overdoses of prescription opioid pain relievers—United States, 1999–2008. *MMWR Morb. Mortal. Wkly. Rep.* **60**, 1487–1492 (2011). pmid: [22048730](https://pubmed.ncbi.nlm.nih.gov/22048730/)
 25. D. Tedesco et al., Opioid Abuse And Poisoning: Trends In Inpatient And Emergency Department Discharges. *Health Aff. (Millwood)* **36**, 1748–1753 (2017). doi: [10.1377/hlthaff.2017.0260](https://doi.org/10.1377/hlthaff.2017.0260); pmid: [28971919](https://pubmed.ncbi.nlm.nih.gov/28971919/)
 26. G. P. Guy Jr., E. Pasalic, K. Zhang, Emergency Department Visits Involving Opioid Overdoses, U.S., 2010–2014. *Am. J. Prev. Med.* **54**, e37–e39 (2018). doi: [10.1016/j.amepre.2017.09.003](https://doi.org/10.1016/j.amepre.2017.09.003); pmid: [29132953](https://pubmed.ncbi.nlm.nih.gov/29132953/)
 27. C. J. Ruhm, Geographic Variation in Opioid and Heroin Involved Drug Poisoning Mortality Rates. *Am. J. Prev. Med.* **53**, 745–753 (2017). pmid: [28797652](https://pubmed.ncbi.nlm.nih.gov/28797652/)
 28. S. Calcaterra, J. Glanz, I. A. Binswanger, National trends in pharmaceutical opioid related overdose deaths compared to other substance related overdose deaths: 1999–2009. *Drug Alcohol Depend.* **131**, 263–270 (2013). doi: [10.1016/j.drugalcdep.2012.11.018](https://doi.org/10.1016/j.drugalcdep.2012.11.018); pmid: [23294765](https://pubmed.ncbi.nlm.nih.gov/23294765/)
 29. L. C. Balmert et al., Patterns and Trends in Accidental Poisoning Deaths: Pennsylvania's Experience 1979–2014. *PLOS ONE* **11**, e0151655 (2016). doi: [10.1371/journal.pone.0151655](https://doi.org/10.1371/journal.pone.0151655); pmid: [26963396](https://pubmed.ncbi.nlm.nih.gov/26963396/)
 30. M. Warner, L. H. Chen, D. M. Makuc, Increase in fatal poisonings involving opioid analgesics in the United States, 1999–2006. *NCHS Data Brief*, 1–8 (2009). pmid: [19796521](https://pubmed.ncbi.nlm.nih.gov/19796521/)
 31. L. Paulozzi, J. Annet; Centers for Disease Control and Prevention (CDC). Unintentional poisoning deaths—United States, 1999–2004. *MMWR Morb. Mortal. Wkly. Rep.* **56**, 93–96 (2007). pmid: [17287712](https://pubmed.ncbi.nlm.nih.gov/17287712/)
 32. A. M. Vivolo-Kantor et al., Vital Signs: Trends in Emergency Department Visits for Suspected Opioid Overdoses - United States, July 2016–September 2017. *MMWR Morb. Mortal. Wkly. Rep.* **67**, 279–285 (2018). doi: [10.15585/mmwr.mm6709e1](https://doi.org/10.15585/mmwr.mm6709e1); pmid: [29518069](https://pubmed.ncbi.nlm.nih.gov/29518069/)
 33. A. Kolodny et al., The prescription opioid and heroin crisis: A public health approach to an epidemic of addiction. *Annu. Rev. Public Health* **36**, 559–574 (2015). doi: [10.1146/annurev-publhealth-031914-122957](https://doi.org/10.1146/annurev-publhealth-031914-122957); pmid: [25581144](https://pubmed.ncbi.nlm.nih.gov/25581144/)
 34. Epidemic: Responding to America's Prescription Drug Abuse Crisis (Office of National Drug Control Policy, Executive Office of the President of the United States, Washington, DC, 2011).
 35. 2016 National Survey on Drug Use and Health: Detailed Tables (Center for Behavioral Health Statistics and Quality, Substance Abuse and Mental Health Services Administration, Rockville, MD, 2017).
 36. While Greater Attention Given to Combating Synthetic Opioids, Agencies Need to Better Assess Their Efforts (United States Government Accountability Office, Washington, DC, 2018).
 37. The Unprecedented Opioid Epidemic (Police Executive Research Forum, Washington, DC, 2017).
 38. J. M. Buchanich, L. C. Balmert, K. E. Williams, D. S. Burke, The Effect of Incomplete Death Certificates on Estimates of Unintentional Opioid-Related Overdose Deaths in the United States, 1999–2015. *Public Health Rep.* **133**, 423–431 (2018). pmid: [29945473](https://pubmed.ncbi.nlm.nih.gov/29945473/)
 39. M. Warner, L. J. Paulozzi, K. B. Nolte, G. G. Davis, L. S. Nelson, State Variation in Certifying Manner of Death and Drugs Involved in Drug Intoxication Deaths. *Acad. Forensic Pathol.* **3**, 231–237 (2013). doi: [10.23907/2013.029](https://doi.org/10.23907/2013.029)
 40. S. G. Mars et al., Heroin-related overdose: The unexplored influences of markets, marketing and source-types in the United States. *Soc. Sci. Med.* **140**, 44–53 (2015). doi: [10.1016/j.socscimed.2015.06.032](https://doi.org/10.1016/j.socscimed.2015.06.032); pmid: [26202771](https://pubmed.ncbi.nlm.nih.gov/26202771/)
 41. G. Unick, D. Rosenblum, S. Mars, D. Ciccarone, The relationship between US heroin market dynamics and heroin-related overdose, 1992–2008. *Addiction* **109**, 1889–1898 (2014). doi: [10.1111/add.12664](https://doi.org/10.1111/add.12664); pmid: [24938727](https://pubmed.ncbi.nlm.nih.gov/24938727/)
 42. A. Case, A. Deaton, Mortality and morbidity in the 21st century. *Brookings Pap. Econ. Act.* **2017**, 397–476 (2017). doi: [10.1353/eca.2017.0005](https://doi.org/10.1353/eca.2017.0005); pmid: [29033460](https://pubmed.ncbi.nlm.nih.gov/29033460/)
 43. E. M. Stein, K. P. Gennuso, D. C. Ugboaja, P. L. Remington, The Epidemic of Despair Among White Americans: Trends in the Leading Causes of Premature Death, 1999–2015. *Am. J. Public Health* **107**, 1541–1547 (2017). doi: [10.2105/AJPH.2017.303941](https://doi.org/10.2105/AJPH.2017.303941); pmid: [28817333](https://pubmed.ncbi.nlm.nih.gov/28817333/)

ACKNOWLEDGMENTS

We thank reviewers from the National Center for Injury Prevention and Control and the National Centers for Health Statistics for improvements to the manuscript. **Funding:** This study was supported in part by CDC grant 1PA1605230 and NIH/NCATS grant 1KL2TR0001856 (H.J.) and by Robert Wood Johnson Foundation grant 72858 (J.M.B. and D.S.B.). **Author contributions:** D.S.B. conceived the study, H.J. and J.M.B. conducted the data analyses, and all authors contributed to the interpretation of results and writing of the manuscript. **Competing interests:** The authors declare no competing interests. **Data and materials availability:** (i) Multiple Cause of Death Data from the Center of Disease Control and Prevention available by request at <https://wonder.cdc.gov/mcd.html>. (ii) Population demographics from the U.S. Census available at www.census.gov/ces/dataproducts/demographicdata.html. strategies. Disclaimer: The findings and conclusions in this report are those of the authors and do not necessarily represent the official position of the Centers for Disease Control and Prevention.

SUPPLEMENTARY MATERIALS

www.sciencemag.org/content/361/6408/eaau1184/suppl/DC1
Materials and Methods
Figs. S1 and S2
Table S1
References (44–49)

8 May 2018; accepted 9 August 2018
[10.1126/science.aau1184](https://doi.org/10.1126/science.aau1184)

RESEARCH ARTICLE SUMMARY

NEUROSCIENCE

A gut-brain neural circuit for nutrient sensory transduction

Melanie Maya Kaelberer, Kelly L. Buchanan, Marguerita E. Klein, Bradley B. Barth, Marcia M. Montoya, Xiling Shen, Diego V. Bohórquez*

INTRODUCTION: In 1853, Sydney Whiting wrote in his classic *Memoirs of a Stomach*, "...and between myself and that individual Mr. Brain, there was established a double set of electrical wires, by which means I could, with the greatest ease and rapidity, tell him all the occurrences of the day as they arrived, and he also could impart to me his own feelings and impressions." Historically, it is known that the gut must communicate with the brain, but the underlying neural circuits and transmitters mediating gut-brain sensory transduction still remain unknown. In the gut, there is a single layer of epithelial cells separating the lumen from the underlying tissue. Dispersed within this layer reside electrically excitable cells termed enteroendocrine cells, which sense ingested nutrients and microbial metabolites. Like taste or olfactory receptor cells, enteroendocrine cells fire action potentials in the presence of stimuli. However, unlike other sensory epithelial cells, no synaptic link between

enteroendocrine cells and a cranial nerve has been described. The cells are thought to act on nerves only indirectly through the slow endocrine action of hormones, like cholecystokinin. Despite its role in satiety, circulating concentrations of cholecystokinin peak only several minutes after food is ingested and often after the meal has ended. Such a discrepancy suggests that the brain perceives gut sensory cues through faster neuronal signaling. Using a mouse model, we sought to identify the underpinnings of this neural circuit that transduces a sense from gut to brain.

RATIONALE: Our understanding of brain neural circuits is being propelled forward by the emergence of molecular tools that have high topographical and temporal precision. We adapted them for use in the gut. Single-cell quantitative real-time polymerase chain reaction and single-cell Western blot enabled the assessment of synaptic proteins. A mono-

synaptic rabies virus revealed the neural circuit's synapse. The neural circuit was recapitulated in vitro by using nodose neurons cocultured with either minigut organoids or purified enteroendocrine cells. This system, coupled to optogenetics and whole-cell patch-clamp recording, served to determine the speed of transduction. Whole-nerve electrophysiology, along with optical excitation and silencing, helped to uncover the neurotransmission properties of the circuit in vivo. The underlying neurotransmitter was revealed by using receptor pharmacology and a fluorescent reporter called iGluSnFR.

RESULTS: Single-cell analyses showed that a subset of enteroendocrine cells contains presynaptic adhesion proteins, including some necessary for synaptic adhesion. Mono-

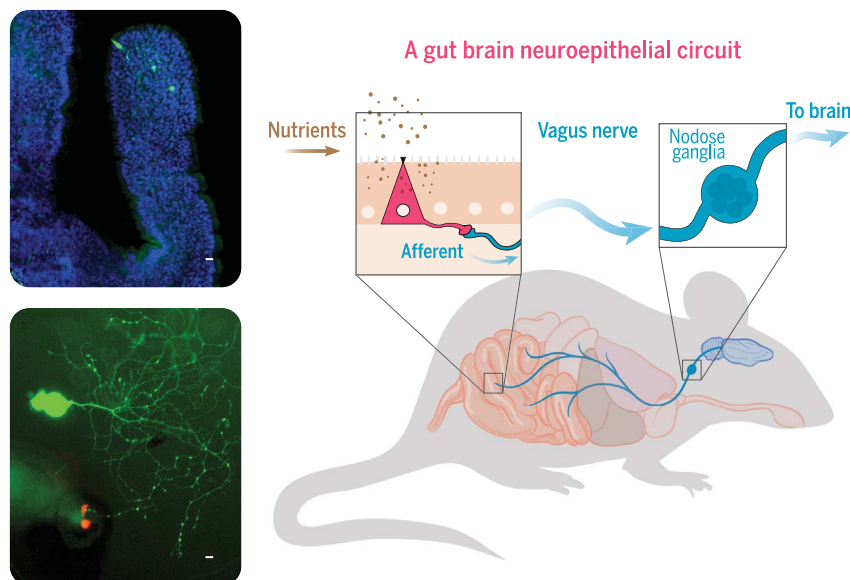
ON OUR WEBSITE

Read the full article at <http://dx.doi.org/10.1126/science.aat5236>

synaptic rabies tracing revealed that enteroendocrine cells synapse with vagal nodose neurons. This neuroepithelial circuit connects the intestinal lumen with the

brainstem in one synapse. In coculture, this connection was sufficient to transduce a sugar stimulus from enteroendocrine cells to vagal neurons. Optogenetic activation of enteroendocrine cells elicited excitatory postsynaptic potentials in connected nodose neurons within milliseconds. In vivo recordings showed that enteroendocrine cells are indeed necessary and sufficient to transduce a sugar stimulus to the vagus. By using iGluSnFR, we found that enteroendocrine cells synthesize the neurotransmitter glutamate, and pharmacological inactivation of cholecystokinin and glutamate receptors revealed that these cells use glutamate as a neurotransmitter to transduce fast, sensory signals to vagal neurons.

CONCLUSION: We identified a type of gut sensory epithelial cell that synapses with vagal neurons. This cell has been referred to as the gut endocrine cell, but its ability to form a neuroepithelial circuit calls for a new name. We term this gut epithelial cell that forms synapses the neuropod cell. By synapsing with the vagus nerve, neuropod cells connect the gut lumen to the brainstem. Neuropod cells transduce sensory stimuli from sugars in milliseconds by using glutamate as a neurotransmitter. The neural circuit they form gives the gut the rapidity to tell the brain of all the occurrences of the day, so that he, too, can make sense of what we eat. ■



The neuropod cells. (Top left) Neuropod cells synapse with sensory neurons in the small intestine, as shown in a confocal microscopy image. Blue indicates all cells in villus; green indicates green fluorescent protein (GFP) in neuropod cell and sensory neurons. (Bottom left) This neural circuit is recapitulated in a coculture system between organoids and vagal neurons. Green indicates GFP in vagal neuron; red indicates tdTomato red fluorescence in neuropod cell. (Right) Neuropod cells transduce fast sensory signals from gut to brain. Scale bars, 10 μ m.

The list of author affiliations is available in the full article online.

*Corresponding author. Email: diego.bohorquez@duke.edu
Cite this article as M. M. Kaelberer et al., *Science* 361, eaat5236 (2018). DOI: 10.1126/science.aat5236

RESEARCH ARTICLE

NEUROSCIENCE

A gut-brain neural circuit for nutrient sensory transduction

Melanie Maya Kaelberer¹, Kelly L. Buchanan², Marguerita E. Klein¹, Bradley B. Barth³, Marcia M. Montoya³, Xiling Shen³, Diego V. Bohórquez^{1,4,5*}

The brain is thought to sense gut stimuli only via the passive release of hormones. This is because no connection has been described between the vagus and the putative gut epithelial sensor cell—the enteroendocrine cell. However, these electrically excitable cells contain several features of epithelial transducers. Using a mouse model, we found that enteroendocrine cells synapse with vagal neurons to transduce gut luminal signals in milliseconds by using glutamate as a neurotransmitter. These synaptically connected enteroendocrine cells are referred to henceforth as neuropod cells. The neuroepithelial circuit they form connects the intestinal lumen to the brainstem in one synapse, opening a physical conduit for the brain to sense gut stimuli with the temporal precision and topographical resolution of a synapse.

Whereas touch, sight, sound, scent, and taste are transduced to the brain by innervated epithelial sensor cells (1), perception of gut stimuli is thought to occur only indirectly, through the slow action of hormones (2). The putative gut epithelial sen-

sor cells—enteroendocrine cells—are assumed to lack synapses with the cranial nerve that innervates the viscera—the vagus (3).

Coined in the 1930s (4), the term enteroendocrine is rooted in the notion that nutrients stimulate the release of hormones. These neuropeptides

either enter the bloodstream or act on nearby nerves minutes to hours after ingesting a meal (5). But enteroendocrine cells have several features of epithelial transducers: They have mechanical (6), olfactory (7), and taste (8) receptors; their membranes contain voltage-gated ion channels that render them electrically excitable (9); and they are capable of forming synapses (10). Almost two-thirds of enteroendocrine cells synapse with adjacent nerves in the intestinal and colonic mucosa (10). Similar features have been confirmed in a subset of colonic enteroendocrine cells known as enterochromaffin (11). Therefore, we hypothesized that enteroendocrine cells synapse with the vagus to transduce a sense from gut to brain.

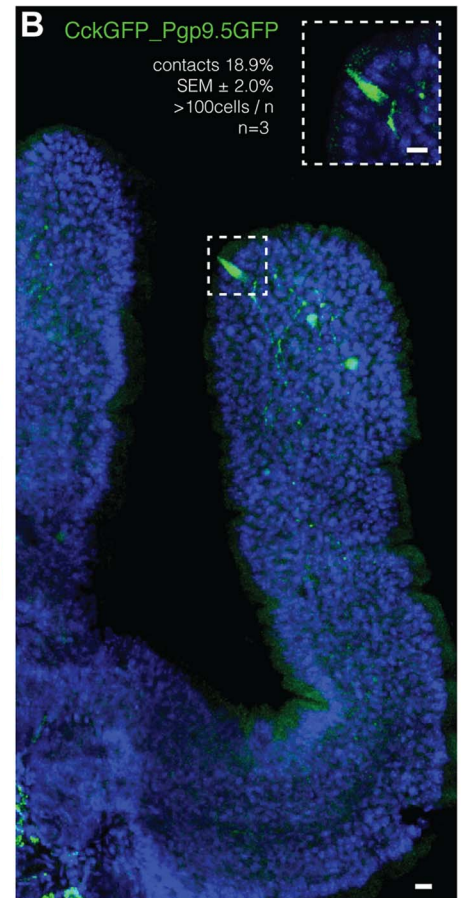
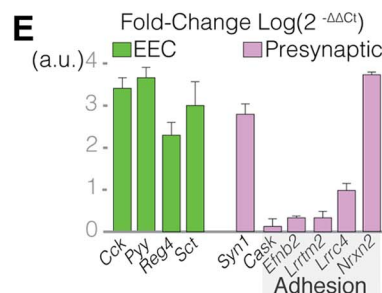
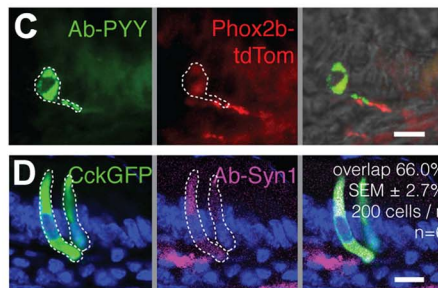
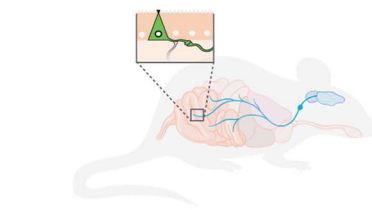
Innervated epithelial sensors in the gut

Using mass spectroscopy (see methods and table S1), we confirmed that enteroendocrine cells express multiple neuropeptides (12, 13), including both cholecystokinin (CCK) and peptide YY (PYY). Thus, we identified these cells using CCK and

Fig. 1. Enteroendocrine cells contact sensory nerve fibers.

(A) CckGFP_Pgp9.5GFP mice express GFP in CCK-enteroendocrine cells and Pgp9.5 sensory nerve fibers. The two cell types are shown in the enlarged view, with the CCK-enteroendocrine cell represented by a triangle. (B) Confocal microscopy image of proximal small intestine villus showing a GFP-labeled CCK-enteroendocrine cell and GFP-labeled Pgp9.5 nerve fibers; 18.9 ± 2.0% SEM of CckGFP cells contact Pgp9.5 fibers (*n* = 3 mice, >100 cells per mouse). (C) PYY-stained enteroendocrine cells (left, green) in the colon contact Phox2b vagal nerve fibers (center, red) in a Phox2bCRE_tdTomato mouse; merged image is shown on the right. (D) Two-thirds of CckGFP (green) enteroendocrine cells colocalize with the presynaptic marker synapsin-1 (purple) (*n* = 6 mice, 200 cells per mouse). (E) Real-time quantitative polymerase chain reaction (qPCR) expression levels of presynaptic transcripts, including genes encoding for synaptic adhesion proteins (*n* = 3 mice, >10,000 cells per cell type per mouse; error bars indicate mean ± SEM; a.u., arbitrary units; EEC, enteroendocrine cell). All scale bars, 10 μm.

A CckGFP_Pgp9.5GFP



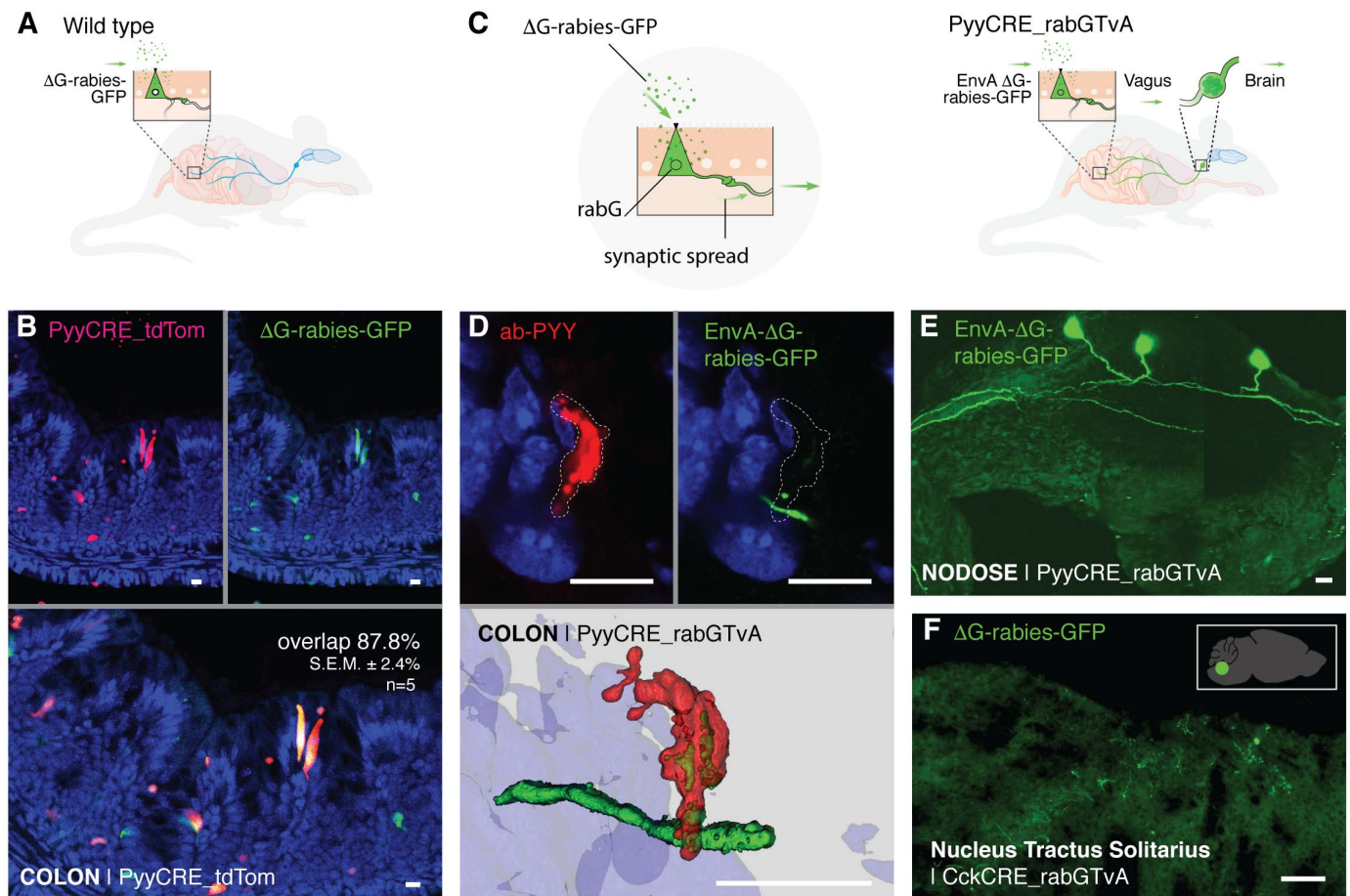


Fig. 2. Enterοendoϋrine cells of the colon and small intestine synapse with vagal nodose neurons. (A) Model of ΔG-rabies-GFP enema delivery. (B) PYY cells expressing tdTomato (top left, red) are infected by ΔG-rabies-GFP (top right, green). Overlay (bottom) shows overlap of $87.8 \pm 2.4\%$ SEM ($n = 5$ mice). In the absence of G glycoprotein (ΔG), ΔG-rabies-GFP does not spread beyond the infected PYY cell. (C) EnvA-ΔG-rabies-GFP virus enters cells via the TvA receptor and spreads by using the rabG protein within specific cells. (D) EnvA-ΔG-rabies-GFP (top right, green) infects PYY cells (top left, red) and spreads

synaptically to underlying colon nerve fibers. Three-dimensional reconstruction (bottom) shows EnvA-ΔG-rabies-GFP-infected PYY cell and mono-synaptically labeled nerve fiber. (E) EnvA-ΔG-rabies-GFP enema infects colonic enterοendoϋrine cells and spreads onto vagal neurons in the nodose ganglion (green). (F) In additional experiments, ΔG-rabies-GFP delivered by oral gavage spreads in the intestinal lumen of CckCRE_rabG-TvA mice to label the nucleus tractus solitarius (green). This neuroepithelial circuit links the intestinal lumen with the brainstem. The inset shows the location of the nucleus tractus solitarius in the mouse brain. All scale bars, 10 μ m.

PYY. In the mouse small intestine and colon, enterοendoϋrine cells contacted sensory nerve fibers (Fig. 1, A to C). About one in five CCK-expressing enterοendoϋrine (CCK-enterοendoϋrine) cells contacted Pgp9.5 sensory nerve fibers that express green fluorescent protein (Pgp9.5GFP nerve fibers) ($18.9 \pm 2.0\%$ SEM, >100 cells per mouse, $n = 3$ mice) (Fig. 1B). CCK-enterοendoϋrine cells immunoreact with an antibody against the presynaptic protein synapsin-1 (Fig. 1D), showing that these connections have synaptic features. Furthermore, using single-cell Western blot, we found that 83% of enterοendoϋrine cells contain synapsin-1 (164 of 198 CckGFP cells analyzed) (fig. S1). Compared with other intestinal epithelial cells, purified CCK-enterοendoϋrine cells express the synaptic adhesion genes *Efnb2*, *Lrrtm2*, *Lrrc4*, and *Nrxn2* (Fig. 1E), showing that these epithelial sensors have the machinery to form synapses.

From gut lumen to brainstem in one synapse

To determine the source of neurons synapsing with enterοendoϋrine cells, we used a modified rabies virus (ΔG-rabies-GFP) (10). This rabies virus infects neurons but lacks the G glycoprotein necessary for transsynaptic spread (Fig. 2A) (14). In intestinal organoids, rabies prefers to infect enterοendoϋrine cells over other epithelial cells (fig. S2A). In the mouse, when introduced into the lumen of the colon by enema, almost 9 out of 10 infected cells are PYY-enterοendoϋrine cells ($87.8 \pm 2.4\%$ SEM, $n = 5$ mice) (Fig. 2B) (10). The lack of fluorescence in the underlying mucosa shows that, in the absence of its G glycoprotein, the rabies virus does not spread beyond infected enterοendoϋrine cells.

To trace the neural circuit, we bred a mouse (strain PyyCRE_rabG-TvA) in which enterοendoϋrine cells express the G glycoprotein (rabG) (Fig.

2C). In these mice, rabies delivered by enema infects enterοendoϋrine cells and spreads through synapses onto nerves. Some of the nerve fibers can be traced to vagal nodose neurons (control group: 0 positive out of 3 PyyCRE_tdTomato mice; experimental group: 4 positive out of 5 PyyCRE_rabG-TvA mice). Furthermore, an enema of the chemical tracer dye Fast Blue labeled both nodose ganglia, confirming that the vagus indeed innervates the distal colon (15). In control experiments in which the right cervical vagus was severed, the Fast Blue enema labeled the left (intact) but not the right (vagotomized) nodose (fig. S3).

Because ΔG-rabies-GFP can infect any neuronal cell it contacts, we restricted its entrance to enterοendoϋrine cells only by using an EnvA-coated rabies (EnvA-ΔG-rabies-GFP) (Fig. 2C). EnvA is an envelope glycoprotein of the avian sarcoma leukosis virus that binds to the avian

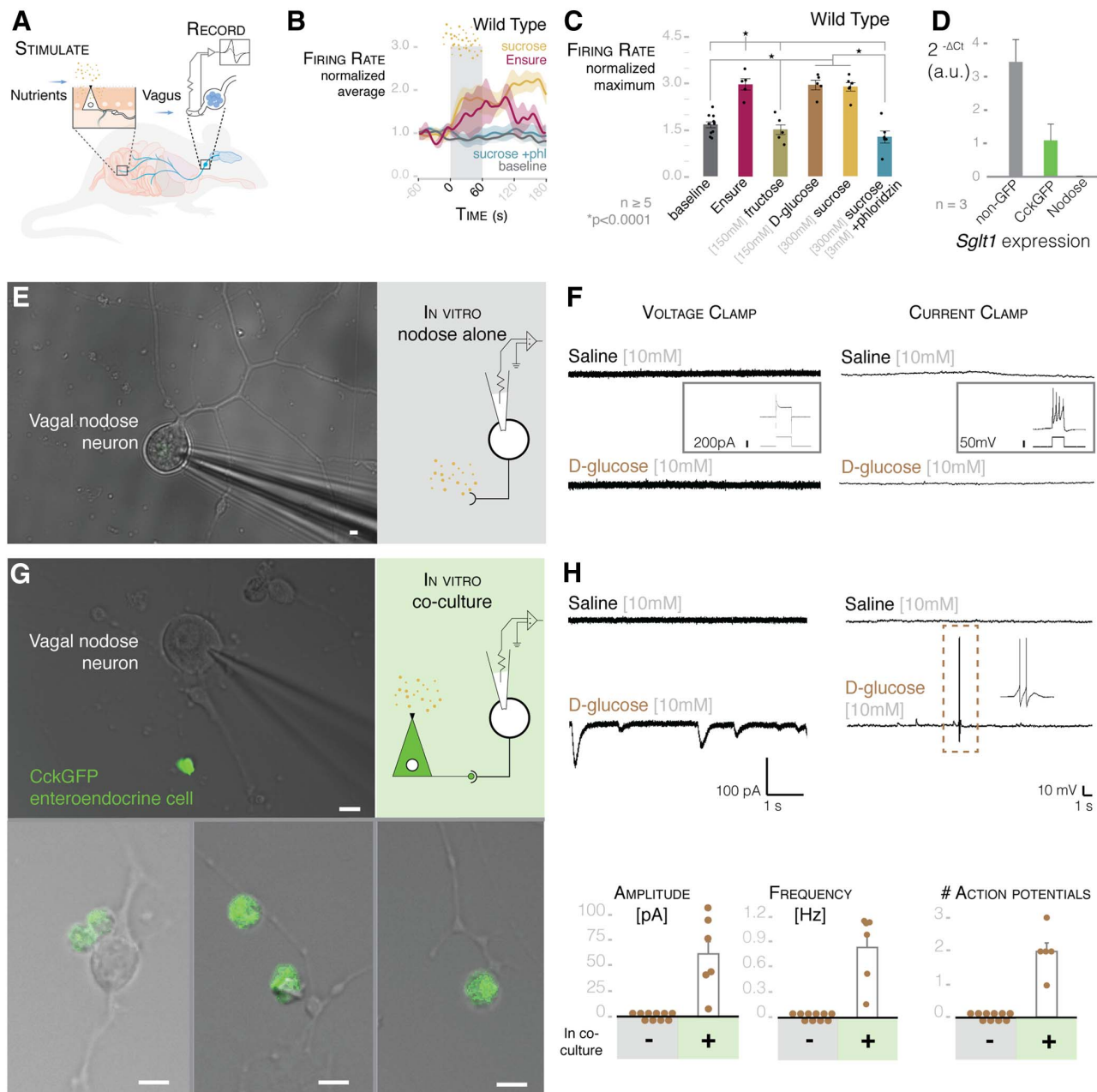


Fig. 3. Enteroendocrine cells transduce glucose stimuli onto vagal neurons. (A) Model of intestinal intraluminal perfusion and vagal nerve electrophysiology. (B) Normalized traces for baseline, Ensure, 300 mM sucrose, and 300 mM sucrose with 3 mM phloridzin (phl) in wild-type mice. Gray bar indicates treatment period; shading indicates SEM. (C) Ensure, 300 mM sucrose, and 150 mM D-glucose stimulate vagal firing rate, which is abolished by SGLT1-blocker phloridzin [$n \geq 5$ mice; $*P < 0.0001$, analysis of variance (ANOVA) with post hoc Tukey's HSD test; error bars indicate SEM]. (D) Intestinal epithelial cells express *Sglt1*, but nodose neurons do not ($n = 3$ mice, $>10,000$ cells per cell type per mouse; data are presented as mean \pm SEM). (E) Nodose neurons cultured alone for electrophysiology (widefield microscopy image on left, model on right). (F) Nodose neurons do not respond to 10 mM

glucose in voltage-clamp (left trace) or current-clamp (right trace) mode. Insets show that neurons respond to voltage or current pulse, indicating viability. (G) Nodose neurons cocultured with GFP-positive enteroendocrine cells for electrophysiology (image on left, model on right). Innervated enteroendocrine cells are shown at the bottom. (H) In coculture, glucose evoked EPSCs (top left) and action potentials (top right) in connected neurons (scale of current or voltage and time are shown below the traces). Dashed-line box indicates action potentials expanded in right inset. Quantification of EPSC amplitude and frequency (bottom left and center; $n = 21$ neurons alone; $n = 6$ neurons connected to enteroendocrine cells) and action potentials (bottom right; $n = 21$ alone; $n = 5$ neurons connected to enteroendocrine cells) in GFP-negative (-) and -positive (+) cells. All scale bars, 10 μ m.

TvA receptor. Therefore, EnvA- Δ G-rabies-GFP only infects cells that express the TvA receptor. In the PyyCRE_{rabG}-TvA mouse, PYY-enteroendocrine cells express the TvA receptor, and an enema of EnvA- Δ G-rabies-GFP infects

enteroendocrine cells exclusively. Then, it spreads to synaptically connected neurons. Of a total of nine mice, five had visible infection of nerve fibers in the colon (Fig. 2D), and two of those five had visible infection in the vagal nodose (Fig. 2E and

movie S1; confirmed in vitro in fig. S4). Labeled fibers were also observed in the dorsal root ganglia of four out of the five infected mice (fig. S5). No infection of nerves was observed in littermate controls that lack CRE recombinase ($n = 5$ mice).

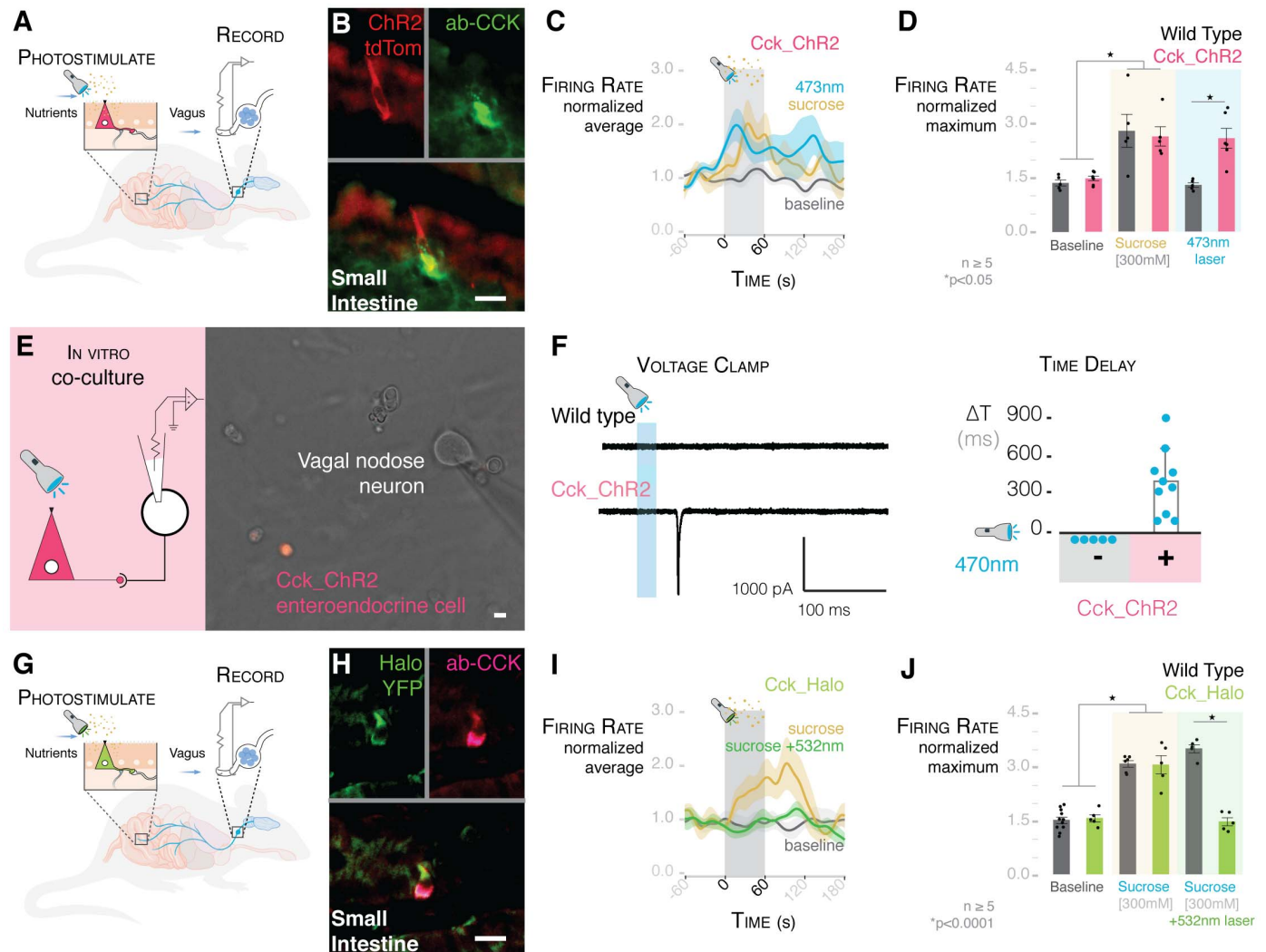


Fig. 4. Millisecond transduction from enteroendocrine cells to vagal neurons. (A) Model of intraluminal photostimulation and vagal electrophysiology. (B) In CckCRE_ChR2-tdTomato mice, intestinal enteroendocrine cells express ChR2. (C) Normalized traces for 473-nm intraluminal laser, 300 mM sucrose, and baseline in CckCRE_ChR2 mice. Shading indicates SEM. (D) 473-nm intraluminal laser stimulates vagal firing rate in CckCRE_ChR2, but not wild-type, mice ($n \geq 5$ mice; $*P < 0.05$, ANOVA with post hoc Tukey's HSD test; error bars indicate SEM). (E) Patch-clamp electrophysiology of neurons (model on left) in coculture with CckCRE_ChR2 cells (image on right). (F) In coculture, 473-nm photostimulation evoked EPSCs (trace on left) in connected nodose neurons (quantification on right)

($n = 9$ neurons connected to enteroendocrine cells; –, neurons alone; +, neurons cocultured with enteroendocrine cells; ΔT , time between stimulus and onset of EPSCs). Scale of current and time is shown below the trace. (G) Model of intraluminal photoinhibition and vagal electrophysiology. (H) In CckCRE_Halo-YFP mice, intestinal enteroendocrine cells express halorhodopsin (eNpHR3.0). (I) Normalized traces for baseline, 300 mM sucrose, and 300 mM sucrose with 532-nm intraluminal laser. Shading indicates SEM. (J) In CckCRE_Halo, but not wild-type, mice, a 532-nm intraluminal laser abolishes the effect of sucrose on vagal firing rate ($n \geq 5$ mice per group; $*P < 0.0001$, ANOVA with post hoc Tukey's HSD test; error bars indicate SEM). All scale bars, 10 μm .

Delivering the virus by oral gavage into CckCRE_rabG-TvA mice yielded similar results (fig. S5). In these mice, labeled vagal nodose neurons projected upstream into the nucleus tractus solitarius of the brainstem (Fig. 2F). Monosynaptic rabies tracing shows a neural circuit linking the small intestine or colon lumen to the brainstem in one synapse.

A gut-brain neural circuit in a dish

In coculture, vagal nodose neurons clearly extended axons to enteroendocrine cells of intestinal organoids (fig. S4A and movie S2). We traced this

neural circuit in vitro using EnvA- ΔG -rabies-GFP to confirm that synapses are formed. To ensure that only infected neurons spread EnvA- ΔG -rabies-GFP, nodose neurons were incubated with virus before coculture with organoids. In control experiments, EnvA- ΔG -rabies-GFP did not infect wild-type nodose neurons (fig. S4B). However, EnvA- ΔG -rabies-GFP infected vagal nodose neurons that express the TvA receptor (Phox2bCRE_rabG-TvA). Forty-eight to 72 hours after coculture, the virus spread onto enteroendocrine cells in intestinal organoids, demonstrating synaptic connection in vitro (fig. S4C).

Transduction of a sense from gut to brain

We tested the function of this neuroepithelial circuit using luminal stimuli and whole-nerve electrophysiology. The initial stimulus used was Ensure—a whole-nutrient solution. Luminal Ensure stimulated an increase in vagal firing rate (Fig. 3, A to C). Next, we focused on a distinctive nutrient, sugar. When ingested, sugar is sensed in the duodenum, but it is unclear whether this stimulus is sensed by the vagus directly or transduced via enteroendocrine cells (16). In wild-type mice, perfusing the sugar sucrose (100 to 300 mM) significantly increased vagal firing rate

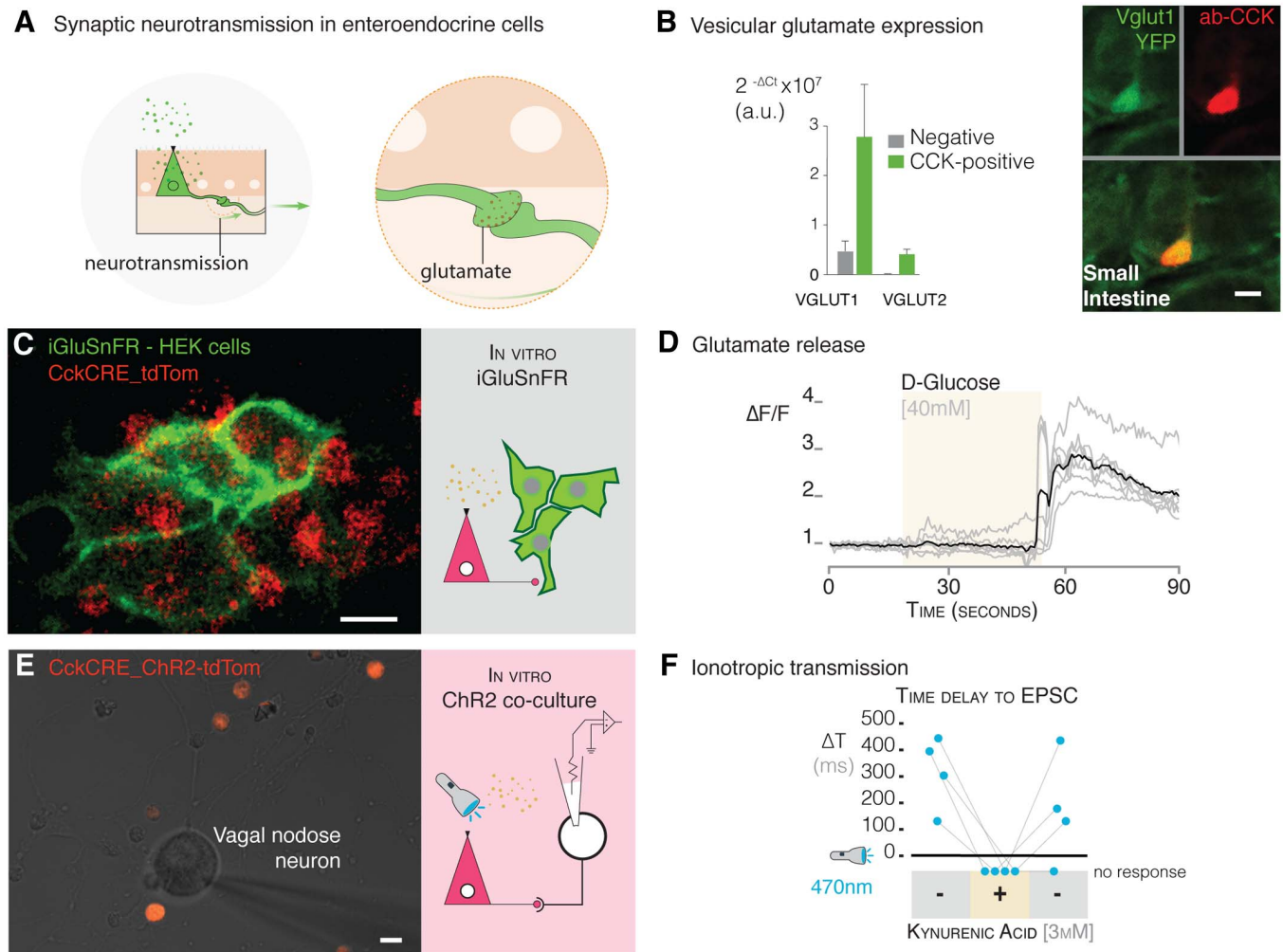


Fig. 5. Glutamate is used as a neurotransmitter between enteroendocrine cells and neurons. (A) Model of synaptic neurotransmission in enteroendocrine cells. (B) Enteroendocrine cells express the vesicular glutamate genes encoding VGLUT1 and 2 (*Slc17a7* and *Slc17a6*) (quantification by qPCR on left, confocal microscopy images on right). (C) CckCRE_tdTomato enteroendocrine cells were cocultured with HEK cells that express the glutamate sniffer protein, iGluSnFR (multiphoton microscopy image on left, model on right). (D) A stimulus of 40 mM D-glucose administered during the time period indicated by the beige shading elicits a response in iGluSnFR-HEK cells ($n = 3$ cultures; individual cell, gray trace;

average of all cells, black trace). $\Delta F/F$, difference in fluorescence intensity between resting state and after stimulus. (E) Coculture with neurons and CckCRE_ChR2 cells (multiphoton microscopy image on left) for electrophysiology of neurons and microperfusion of the glutamate-receptor blocker kynurenic acid (model on right). (F) In coculture, 473-nm photo-stimulation evoked EPSCs in connected nodose neurons, these currents were abolished, and no response was observed with the addition (+) of 3 mM kynurenic acid. The response was recovered after the drug was washed off (indicated by second “–” condition on right) ($n = 4$ neurons connected to enteroendocrine cells). All scale bars, 10 μm .

over baseline (Fig. 3, B and C, and fig. S6). D-Glucose (150 mM), but not fructose (150 mM), had the same effect. No effect was observed when the vagus was severed (fig. S7), when hyperosmolar phosphate-buffered saline was perfused (700 mosmol), or when sucrose was applied intraperitoneally (300 mM) (fig. S8). The vagal response was abolished when sucrose was perfused with phloridzin, a blocker of the electrogenic glucose transporter SGLT1 (17) (Fig. 3, B and C). A transcription profile showed that, unlike vagal nodose neurons, CCK-enteroendocrine cells express *Sglt1*, suggesting that the stimulus is transduced by the epithelial cells (Fig. 3D).

Evidence gathered on dissociated colonic enteroendocrine cells, and the enteroendocrine-like

cell line STC1, has shown that enteroendocrine cells sense glucose (18). We therefore packaged a rabies virus to carry the calcium reporter GCaMP6s ($\Delta\text{G-rabies-GCaMP6s}$) and used it to infect enteroendocrine cells in intestinal organoids. When presented with D-glucose (10 mM), calcium transients were elicited in CCK-enteroendocrine cells ($56.0 \pm 20.0\%$ of the KCl control response; $n = 3$ cells) (fig. S2, B to D). One previous report found that rat nodose neurons respond to glucose (19). However, in contrast with enteroendocrine cells, vagal neurons are unlikely to face steep changes in glucose concentrations because they do not contact the intestinal lumen (20). We therefore measured calcium transients in dissociated nodose neurons and found that

D-glucose (10 mM) did not elicit a response (fig. S9, A and B) ($n = 246$ cells pooled from three mice).

To discard the possibility that only nodose neurons innervating the intestine may sense glucose, we retrotraced them by injecting Fast Blue dye into the duodenum (fig. S9C). In Fast Blue-labeled vagal neurons, no calcium response was observed in the presence of D-glucose (20 mM) (fig. S9C). Furthermore, neither excitatory currents nor action potentials were observed in the presence of a D-glucose (10 to 20 mM) stimulus using patch-clamp electrophysiology (Fig. 3, E and F). Current injection demonstrated that these cultured nodose neurons were functionally viable (inset of Fig. 3F).

We then cocultured vagal nodose neurons with intestinal enteroendocrine cells (10). After 48 to 72 hours, there were visible connections between neurons and enteroendocrine cells (Fig. 3G). Coculturing did not alter the resting membrane potential, the current, or the spike threshold of the vagal nodose neurons. However, a D-glucose (10 mM) stimulus now evoked excitatory postsynaptic currents (EPSCs) and action potentials in those neurons connected to enteroendocrine cells (Fig. 3H). In voltage-clamp mode, the average current of the EPSCs was 61.65 ± 15.21 pA, and the average frequency was 0.86 ± 0.17 Hz ($n = 6$ neurons connected to enteroendocrine cells). In current-clamp mode, this in vitro connection was sufficient to elicit action potentials in the connected neurons (average of 2 ± 0.32 action potentials, $n = 5$ neurons connected to enteroendocrine cells).

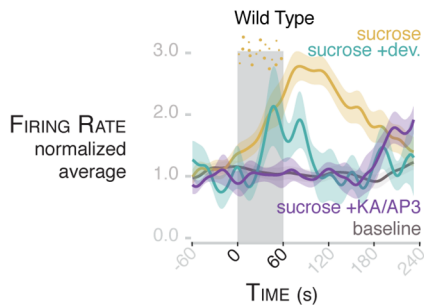
Synaptic speed and specificity

Two recent reports have shown that hypothalamic neurons controlling food intake are inhibited by nutrients within seconds of the nutrients entering the duodenum (21, 22). Therefore, it is likely that enteroendocrine cells transduce sensory signals from nutrients at a much faster rate than previously thought possible. To test the speed of transduction, we bred a mouse (strain CckCRE_ChR2-tdTomato) in which enteroendocrine cells express channelrhodopsin 2 (ChR2)—an excitatory light-gated ion channel activated by 473-nm light (Fig. 4, A and B). A 473-nm stimulus applied to these cells elicited excitatory currents and significantly reduced food intake by the mice, showing functional expression of the channel (fig. S10) (see methods).

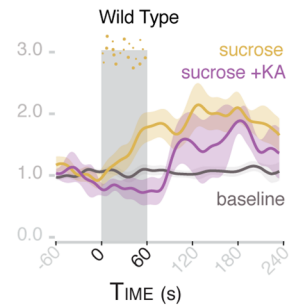
Vagal firing rate is significantly increased when a 473-nm laser stimulus is applied to the duodenal lumen of CckCRE_ChR2 mice. No response was observed in wild-type controls (Fig. 4, C and D; for laser-activation controls, see fig. S11). The firing rate increased rapidly after laser stimulation, reaching its peak, on average, in 72.7 ± 20.9 s (fig. S12). In vitro, vagal nodose neurons cultured alone did not respond to photostimulation. To determine the precise transduction speed, we cocultured them with CckCRE_ChR2 enteroendocrine cells (Fig. 4E). In vagal nodose neurons connected to enteroendocrine cells, a 470-nm photostimulus elicited EPSCs within 60 to 800 ms ($n = 9$ pairs) (Fig. 4F).

To test the specificity of transduction, we bred a mouse (CckCRE_Halo-YFP) in which intestinal enteroendocrine cells express the light-inhibitory channel eNpHR3.0 (halorhodopsin)—an inhibitory light-gated ion channel activated by 532-nm light (Fig. 4, G and H)—and yellow fluorescent protein (YFP). In these mice, luminal sucrose (300 mM) elicited a vagal response; however, when a 532-nm laser stimulus was presented along with the sucrose, vagal activity was abolished (Fig. 4, I and J; for laser activation controls, see fig. S13). In control wild-type mice, a 532-nm laser stimulus failed to attenuate the sucrose response. These data revealed that enteroendocrine cells are necessary and sufficient to

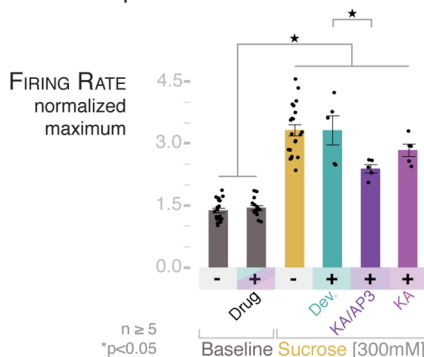
A CCK vs. glutamate



B Ionotropic blocker



C Peak response



D Time to peak



Fig. 6. The rapid vagal response to sucrose is dependent on glutamate, whereas CCK contributes to the prolonged response. (A) Normalized traces for baseline, 300 mM sucrose, 300 mM sucrose after treatment with 2 mg/kg devazepide, and 300 mM sucrose after treatment with glutamate inhibitor cocktail KA/AP3 [150 μ g/kg kynurenic acid (KA) with 1 mg/kg DL-2-amino-3-phosphonopropionic acid (AP-3)] in wild-type mice. Shading indicates SEM. (B) Normalized traces for baseline, 300 mM sucrose, and 300 mM sucrose after treatment with 150 μ g/kg KA in wild-type mice. Shading indicates SEM. (C) KA/AP3 attenuates the maximum normalized vagal firing rate in response to sucrose, whereas devazepide and KA alone do not. (D) KA/AP3 and KA alone prolong the time to peak from an average of 92.8 s to 198 and 179 s, respectively.

Devazepide (2 mg/kg) does not significantly change the time to peak (mean = 67.1 s). For (C) and (D), $n \geq 5$ mice per group; * $P < 0.05$, ANOVA with post hoc Tukey's HSD test; error bars indicate SEM.

transduce a glucose stimulus onto vagal neurons within milliseconds.

The neurotransmitter

The possibility exists that innervated enteroendocrine cells could use a classic neurotransmitter to transduce the above-described sensory signals. Other sensory epithelial transducers—including photoreceptors (23), auditory hair cells (24), Merkel cells (25), and olfactory receptor cells (26)—use vesicular glutamate as a neurotransmitter. Thus, we hypothesized that enteroendocrine cells use glutamate as a neurotransmitter as well. We found that intestinal enteroendocrine cells express significant quantities of the transcript for the vesicular glutamate transporter 1 protein (VGLUT1) (Fig. 5, A and B). In a transgenic Vglut1CRE_YFP mouse, fluorescence was observed in distinct intestinal epithelial cells that resemble enteroendocrine cells, and almost 4 in 10 of those fluorescent cells contained for CCK ($38.80 \pm 2.53\%$ SEM, 100 cells per mouse, $n =$

3 mice). Moreover, vagal nodose neurons express at least eight glutamate receptors (fig. S14).

To test whether enteroendocrine cells release glutamate, we used the sniffer protein iGluSnFR. This membrane-bound protein fluoresces green in the presence of glutamate (27). Transfected iGluSnFR-HEK (human embryonic kidney) cells did not respond to a D-glucose (40 mM) stimulus but did respond to glutamate (100 μ M) (fig. S15). We then cocultured iGluSnFR-HEK cells with Tomato-expressing enteroendocrine cells (CckCRE_tdTomato) (Fig. 5C). This time, when presented with a D-glucose stimulus (40 mM), iGluSnFR-HEK cells fluoresced green ($n = 3$ cultures; Fig. 5D), indicating that enteroendocrine cells release glutamate. Then, we cocultured CckCRE_ChR2 enteroendocrine cells with vagal neurons to determine if glutamate serves as a neurotransmitter in this synapse. In connected neurons, a 470-nm stimulus elicited EPSCs that were abolished by adding kynurenic acid (3 mM), an ionotropic glutamate-receptor

blocker (Fig. 5, E and F). The response was recovered once the blocker was washed away ($n = 4$ neurons connected to enteroendocrine cells) (Fig. 5F).

Hormone versus neurotransmitter

In a transgenic mouse in which VGLUT1-enteroendocrine cells express ChR2 (Vglut1CRE₊ChR2-YFP), a luminal laser stimulus of 473-nm significantly increased vagal firing rate (fig. S16). The amplitude and timing of the peak response was comparable to the CckCRE₊ChR2 experiments (figs. S12 and S16). The same laser stimulus applied to the subdiaphragmatic or cervical vagus did not alter firing rate (fig. S17). However, the response was abolished when the 473-nm laser was presented along with a cocktail of glutamate-receptor blockers [metabotropic blocker AP-3 (1 mg per kg of body weight) with ionotropic blocker kynurenic acid (150 μ g/kg)] (fig. S16). These data revealed a type of enteroendocrine cell that uses glutamate to drive vagal firing.

Next, we compared the respective contributions of CCK and glutamate to vagal firing. The peak vagal firing rate elicited by a sucrose stimulus was not affected when the CCK-A receptor was blocked with devazepide (2 mg/kg) (Fig. 6, A and C). In control experiments, the same dose of devazepide fully blocked the vagal response to luminal CCK (fig. S18). Although the peak response and time to peak were not altered by devazepide, the length of the response was attenuated after 120 s (Fig. 6, A, C, and D; and figs. S18 and S19), suggesting that it takes minutes for released CCK to stimulate vagal firing. By contrast, blocking both ionotropic and metabotropic glutamate receptors attenuated the speed, peak, and magnitude of the vagal response to sucrose (Fig. 6, C and D, and fig. S19). Indeed, the first 60 s of the vagal response to sucrose was suppressed by the ionotropic blocker kynurenic acid alone (Fig. 6B and fig. S20), delaying the time to peak to around 180 s (Fig. 6D and fig. S18C). These data revealed that synaptic glutamate is used by an epithelial sensor cell in the gut to rapidly transduce luminal stimuli to the central nervous system.

The neuropod cells

In recent years, enteroendocrine cells have emerged as sensors of mechanical, chemical, and bacterial signals in the gastrointestinal tract (2, 3). However, their transducer properties have been obscured by their name. By synapsing with the vagus, these sensor cells provide a neuroepithelial circuit for fast sensory transduction. As such, we see the need for a new name to refer to gut sensory epithelial cells that synapse with nerves. We refer to these cells as neuropod cells. We hypothesize that the gut-brain neural circuit formed by neuropod cells and vagal nodose neurons could lead to the following possibilities: (i) rapid computation of stimuli to distinguish their physical (e.g., volume) versus chemical (e.g., calorie) properties; (ii) precise sensory representation of specific gastrointestinal regions; (iii) localized

plasticity encoded within the neural circuit; and (iv) timely vagal efferent feedback to modulate gastrointestinal sensory function. Like other sensory transducers, neuropod cells use synaptic signals to help the brain make sense of the food we eat.

Materials and methods summary

Animals

Mouse care and experiments were carried out in accordance with protocols approved by the Institutional Animal Care and Use Committee at Duke University Medical Center under the protocol A009-16-01. Mice were housed in the Duke University animal facilities, where they were kept on a 12-hour light-dark cycle. They received food and water ad libitum. The specific strains can be found in the supplemental methods.

Rabies production and tracing

G-deleted rabies virus production was performed in house as described in Wickersham *et al.* (28). For colon monosynaptic tracing, P1 mice were given an enema of EnvA- Δ G-rabies-GFP (5.9×10^9 ffu/ml). For small intestine monosynaptic tracing, P1 mice were given a gavage of Δ G-rabies-GFP (9.8×10^8 ffu/ml). Mice were sacrificed 7 days after exposure at P8. Harvested tissue was fixed in 4% PFA then treated with serial sucrose solutions. Ganglia were whole-mount imaged with a multiphoton microscopy system (Bruker Ultima IV with a Chameleon Vision II tunable laser). All other tissue was frozen in OCT blocks and sectioned for immunohistochemistry.

Organoid culture

Organoids were cultured using a protocol adapted from Sato *et al.* 2009 (29). Isolated crypts were resuspended in Matrigel (Corning #356231) and plated 50 μ l per well in a 24-well plate in organoid media. Organoid media contains 1x Glutamax, 10 mM HEPES, 200 U/ml Penicillin-Streptomycin, 1x N2 supplement, 1x B27 supplement, 0.25 ng/ml EGF, 50 ng/ml Noggin, and 100 ng/ml r-Spondin in Advanced DMEM/f12.

Enteroendocrine cell and nodose neuron coculture

Enteroendocrine cells of CckGFP and CckCRE₊ChR2-tdTomato small intestines were isolated as previously described in Bohórquez *et al.* (10). Enteroendocrine cells were sorted into organoid culture media (listed above) plus 10 ng/ml NGF. Sorted cells were plated on 1% Matrigel coated 12-mm coverslips at a concentration of ~5000 to 10,000 enteroendocrine cells per coverslip. Nodose neurons were dissected and incubated with Liberase (Roche) digestion enzyme. Neurons in media were plated evenly on up to eight coverslips with enteroendocrine cells. Patch-clamp electrophysiology was performed 2 to 5 days after plating.

Immunohistochemistry

Immunohistochemistry was performed as previously described in Bohórquez *et al.* (10). Pri-

mary antibodies: Rb-Anti-PYY [DVB3] (1:1000); Rb-Anti-CCK (1:1000; courtesy of Rodger Liddle or Phoenix Pharmaceuticals H-069-04); Gt-Anti-PSD95 (1:500; Santa Cruz Biotechnology: sc-6926); Rb-Anti-Syn1 (1:500; Cell Signaling Technology: 5297S); Ck-Anti-GFP (1:500; Abcam: ab13970). Secondary antibodies from Jackson ImmunoResearch: Dk-Anti-Rb-488 (1:250); Dk-Anti-Rb-Cy3 (1:250); Dk-Anti-Gt-Cy5 (1:250); and Dk-Anti-Ck-488 (1:250). Imaging was done on a Zeiss 880 Airyscan inverted confocal microscope. Data are presented as the mean percentage \pm SEM.

Real-time quantitative PCR

RNA from CckGFP-positive and -negative epithelial cells was extracted based on the manufacturer's protocol using the RNeasy Micro Plus Kit (Qiagen #74034). Then cDNA was produced per manufacturer's protocol using the High Capacity cDNA Reverse Transcription Kit (Applied Biosystems #4368814). TaqMan probes used are listed in supplemental materials. Real-time qPCR was run on a StepOnePlus System (Thermo Fischer), using TaqMan Fast Universal PCR Master Mix (Applied Biosystems #4352042) according to the manufacturer's protocol. Transcription rate was determined as $2^{-\Delta\Delta C_t}$, or compared as fold-change over GFP negative epithelial cells using $2^{-\Delta\Delta C_t}$. All values are reported as mean \pm SEM.

Electrophysiology

Enteroendocrine cells and nodose neurons were cocultured as described above. Recordings were carried out at room temperature using a Multi-Clamp 700B amplifier (Axon Instruments), digitized using a Digidata 1550A (Axon Instruments) interface, and pClamp software (Axon Instruments) for data acquisition. Recordings were made using borosilicate glass pipettes pulled to ~3.5 M Ω resistance. Extracellular solution contained (in mM): 140 NaCl, 5 KCl, 2 CaCl₂, 2 MgCl₂, 10 HEPES, pH 7.4 (300 to 305 mosmol). For voltage-clamp recordings, intracellular solution contained (in mM): 140 CsF, 10 NaCl, 0.1 CaCl₂, 2 MgCl₂, 1.1 EGTA, 10 HEPES, 10 sucrose (pH 7.25, 290 to 295 mosmol). For current-clamp recordings, intracellular solution contained (in mM): 140 KCl, 0.5 EGTA, 5 HEPES, 3 Mg-ATP, 10 sucrose (pH 7.25, 290 to 295 mosmol). Data are presented as the mean \pm SEM, and significance was determined using a two-tailed Student's *t* test.

iGluSnFR-HEK cell and enteroendocrine cell coculture and imaging

CckCRE₊tdTomato enteroendocrine cells were isolated as described above. Isolated cells were mixed with iGluSnFR-HEK cells at a ratio of 10:1, then plated on 1% Matrigel coated coverslips. Control iGluSnFR-HEK cells were plated alone. Cells were incubated for 12 to 18 hours before imaging. Coverslips were imaged using a multiphoton microscopy system (Bruker Ultima IV with a Chameleon Vision II tunable laser). Imaging series were analyzed using Fiji (it's just ImageJ), and cell traces were plotted with Excel.

Vagus nerve recording

Wild-type control ($n = 5$ to 9), CckCRE_ChR2-tdTomato ($n = 6$), CckCRE_Halo-YFP ($n = 5$), and Vglut1CRE_ChR2-YFP ($n = 6$) mice were used for vagal recordings. The cervical vagus was exposed in anesthetized mice and two platinum iridium wires (Medwire by Sigmund Cohn Corp) were looped around the vagus nerve for recording. A 20-gauge gavage needle was surgically inserted through the stomach wall and into the duodenum. Saline and stimulant tubes were connected to the gavage needle. For optogenetic experiments, a fiber optic cable (FT020, ThorLabs) was threaded through the gavage needle into the lumen of the duodenum. A perfusion exit incision was made 10 cm distal to the pyloric sphincter. During each recording, PBS was constantly perfused through the duodenum using a peristaltic pump (Cole-Parmer) at the lowest setting for a flow rate of ~400 μ l PBS per minute. For stimulus delivery, see extended methods in supplemental materials. Data acquisition: A differential amplifier and bandpass filter (1000 \times gain, 300-Hz to 5-kHz bandpass filter; A-M Systems LLC) was used and the signal was processed using a data acquisition board and software (20-kHz sampling rate; Signal Express, National Instruments Corp). The raw data was analyzed using a spike sorting algorithm (MATLAB by MathWorks). Spikes were detected using simple threshold detection based on RMS noise. The firing rate was calculated using a Gaussian kernel smoothing algorithm (200-ms time scale). Statistical Methods: Stimulation response was quantified as the maximum firing rate after stimulation (stimulant conditions) or during recording (baseline). Time to peak was calculated as time from start of stimulus to maximum firing rate. Area under the curve was calculated as area under the curve for the entire 6-min recording. Maximum firing rate, time to peak, and area under curve are analyzed across genotype, stimulation condition, and their interaction term by ANOVA, followed by Tukey HSD post hoc testing (JMP by SAS Institute).

REFERENCES AND NOTES

1. B. Alberts, D. Bray, J. Lewis, M. Raff, K. Roberts, J. D. Watson, *Molecular Biology of the Cell* (Garland, ed. 3, 1994), pp. 907–982.
2. A. Psichas, F. Reimann, F. M. Gribble, Gut chemosensing mechanisms. *J. Clin. Invest.* **125**, 908–917 (2015). doi: [10.1172/JCI76309](https://doi.org/10.1172/JCI76309); pmid: [25664852](https://pubmed.ncbi.nlm.nih.gov/25664852/)
3. J. B. Furness, L. R. Rivera, H. J. Cho, D. M. Bravo, B. Callaghan, The gut as a sensory organ. *Nat. Rev. Gastroenterol. Hepatol.* **10**, 729–740 (2013). doi: [10.1038/nrgastro.2013.180](https://doi.org/10.1038/nrgastro.2013.180); pmid: [24061204](https://pubmed.ncbi.nlm.nih.gov/24061204/)
4. F. Feyrter, *Über diffuse endokrine epitheliale Organe* (J. A. Barth, Leipzig, Germany, 1938).

5. J. F. Rehfeld, The new biology of gastrointestinal hormones. *Physiol. Rev.* **78**, 1087–1108 (1998). doi: [10.1152/physrev.1998.78.4.1087](https://doi.org/10.1152/physrev.1998.78.4.1087); pmid: [9790570](https://pubmed.ncbi.nlm.nih.gov/9790570/)
6. D. Castaneda *et al.*, Mechanosensitive ION channel Piezo2 distribution in mouse small bowel and colon enterochromaffin cells. *Gastroenterology* **152**, S180 (2017). doi: [10.1016/S0016-5085\(17\)30916-2](https://doi.org/10.1016/S0016-5085(17)30916-2)
7. T. Braun, P. Volland, L. Kunz, C. Prinz, M. Gatzl, Enterochromaffin cells of the human gut: Sensors for spices and odorants. *Gastroenterology* **132**, 1890–1901 (2007). doi: [10.1053/j.gastro.2007.02.036](https://doi.org/10.1053/j.gastro.2007.02.036); pmid: [17484882](https://pubmed.ncbi.nlm.nih.gov/17484882/)
8. H. J. Jang *et al.*, Gut-expressed gustducin and taste receptors regulate secretion of glucagon-like peptide-1. *Proc. Natl. Acad. Sci. U.S.A.* **104**, 15069–15074 (2007). doi: [10.1073/pnas.0706890104](https://doi.org/10.1073/pnas.0706890104); pmid: [17724330](https://pubmed.ncbi.nlm.nih.gov/17724330/)
9. G. J. Rogers *et al.*, Electrical activity-triggered glucagon-like peptide-1 secretion from primary murine L-cells. *J. Physiol.* **589**, 1081–1093 (2011). doi: [10.1113/jphysiol.2010.198069](https://doi.org/10.1113/jphysiol.2010.198069); pmid: [21224236](https://pubmed.ncbi.nlm.nih.gov/21224236/)
10. D. V. Bohórquez *et al.*, Neuroepithelial circuit formed by innervation of sensory enteroendocrine cells. *J. Clin. Invest.* **125**, 782–786 (2015). doi: [10.1172/JCI78361](https://doi.org/10.1172/JCI78361); pmid: [25555217](https://pubmed.ncbi.nlm.nih.gov/25555217/)
11. N. W. Bellono *et al.*, Enterochromaffin cells are gut chemosensors that couple to sensory neural pathways. *Cell* **170**, 185–198.e16 (2017). doi: [10.1016/j.cell.2017.05.034](https://doi.org/10.1016/j.cell.2017.05.034); pmid: [28648659](https://pubmed.ncbi.nlm.nih.gov/28648659/)
12. A. L. Haber *et al.*, A single-cell survey of the small intestinal epithelium. *Nature* **551**, 333–339 (2017). doi: [10.1038/nature24489](https://doi.org/10.1038/nature24489); pmid: [29144463](https://pubmed.ncbi.nlm.nih.gov/29144463/)
13. L. L. Glass *et al.*, Single-cell RNA-sequencing reveals a distinct population of proglucagon-expressing cells specific to the mouse upper small intestine. *Mol. Metab.* **6**, 1296–1303 (2017). doi: [10.1016/j.molmet.2017.07.014](https://doi.org/10.1016/j.molmet.2017.07.014); pmid: [29031728](https://pubmed.ncbi.nlm.nih.gov/29031728/)
14. N. R. Wall, I. R. Wickersham, A. Cetin, M. De La Parra, E. M. Callaway, Monosynaptic circuit tracing in vivo through Cre-dependent targeting and complementation of modified rabies virus. *Proc. Natl. Acad. Sci. U.S.A.* **107**, 21848–21853 (2010). doi: [10.1073/pnas.1011756107](https://doi.org/10.1073/pnas.1011756107); pmid: [21115815](https://pubmed.ncbi.nlm.nih.gov/21115815/)
15. S. M. Altschuler, J. Escardo, R. B. Lynn, R. R. Miselis, The central organization of the vagus nerve innervating the colon of the rat. *Gastroenterology* **104**, 502–509 (1993). doi: [10.1016/0016-5085\(93\)90419-D](https://doi.org/10.1016/0016-5085(93)90419-D); pmid: [8425692](https://pubmed.ncbi.nlm.nih.gov/8425692/)
16. E. K. Williams *et al.*, Sensory neurons that detect stretch and nutrients in the digestive system. *Cell* **166**, 209–221 (2016). doi: [10.1016/j.cell.2016.05.011](https://doi.org/10.1016/j.cell.2016.05.011); pmid: [27238020](https://pubmed.ncbi.nlm.nih.gov/27238020/)
17. A. Scalfani, H. Koepsell, K. Ackroff, SGLT1 sugar transporter/sensor is required for post-oral glucose appetite. *Am. J. Physiol. Regul. Integr. Comp. Physiol.* **310**, R631–R639 (2016). doi: [10.1152/ajpregu.00432.2015](https://doi.org/10.1152/ajpregu.00432.2015); pmid: [26791832](https://pubmed.ncbi.nlm.nih.gov/26791832/)
18. F. Reimann *et al.*, Glucose sensing in L cells: A primary cell study. *Cell Metab.* **8**, 532–539 (2008). doi: [10.1016/j.cmet.2008.11.002](https://doi.org/10.1016/j.cmet.2008.11.002); pmid: [19041768](https://pubmed.ncbi.nlm.nih.gov/19041768/)
19. G. Grabauskas, I. Song, S. Zhou, C. Owyang, Electrophysiological identification of glucose-sensing neurons in rat nodose ganglia. *J. Physiol.* **588**, 617–632 (2010). doi: [10.1113/jphysiol.2009.182147](https://doi.org/10.1113/jphysiol.2009.182147); pmid: [20008464](https://pubmed.ncbi.nlm.nih.gov/20008464/)
20. H. R. Berthoud, M. Kressel, H. E. Raybould, W. L. Neuhuber, Vagal sensors in the rat duodenal mucosa: Distribution and structure as revealed by in vivo Dil-tracing. *Anat. Embryol. (Berl.)* **191**, 203–212 (1995). doi: [10.1007/BF00187819](https://doi.org/10.1007/BF00187819); pmid: [7771683](https://pubmed.ncbi.nlm.nih.gov/7771683/)
21. L. R. Beutler *et al.*, Dynamics of gut-brain communication underlying hunger. *Neuron* **96**, 461–475.e5 (2017). doi: [10.1016/j.neuron.2017.09.043](https://doi.org/10.1016/j.neuron.2017.09.043); pmid: [29024666](https://pubmed.ncbi.nlm.nih.gov/29024666/)
22. Z. Su, A. L. Alhadeff, J. N. Betley, Nutritive, post-ingestive signals are the primary regulators of AgRP neuron activity. *Cell Reports* **21**, 2724–2736 (2017). doi: [10.1016/j.celrep.2017.11.036](https://doi.org/10.1016/j.celrep.2017.11.036); pmid: [29212021](https://pubmed.ncbi.nlm.nih.gov/29212021/)
23. C. Brandon, D. M. Lam, L-glutamic acid: A neurotransmitter candidate for cone photoreceptors in human and rat retinas. *Proc. Natl. Acad. Sci. U.S.A.* **80**, 5117–5121 (1983). doi: [10.1073/pnas.80.16.5117](https://doi.org/10.1073/pnas.80.16.5117); pmid: [6136039](https://pubmed.ncbi.nlm.nih.gov/6136039/)
24. O. P. Ottersen *et al.*, Molecular organization of a type of peripheral glutamate synapse: The afferent synapses of hair cells in the inner ear. *Prog. Neurobiol.* **54**, 127–148 (1998). doi: [10.1016/S0301-0082\(97\)00054-3](https://doi.org/10.1016/S0301-0082(97)00054-3); pmid: [9481795](https://pubmed.ncbi.nlm.nih.gov/9481795/)
25. H. Haeberle *et al.*, Molecular profiling reveals synaptic release machinery in Merkel cells. *Proc. Natl. Acad. Sci. U.S.A.* **101**, 14503–14508 (2004). doi: [10.1073/pnas.0406308101](https://doi.org/10.1073/pnas.0406308101); pmid: [15448211](https://pubmed.ncbi.nlm.nih.gov/15448211/)
26. D. A. Berkowicz, P. Q. Trombley, G. M. Shepherd, Evidence for glutamate as the olfactory receptor cell neurotransmitter. *J. Neurophysiol.* **71**, 2557–2561 (1994). doi: [10.1152/jn.1994.71.6.2557](https://doi.org/10.1152/jn.1994.71.6.2557); pmid: [7931535](https://pubmed.ncbi.nlm.nih.gov/7931535/)
27. J. S. Marvin *et al.*, An optimized fluorescent probe for visualizing glutamate neurotransmission. *Nat. Methods* **10**, 162–170 (2013). doi: [10.1038/nmeth.2333](https://doi.org/10.1038/nmeth.2333); pmid: [23314171](https://pubmed.ncbi.nlm.nih.gov/23314171/)
28. I. R. Wickersham *et al.*, Monosynaptic restriction of transsynaptic tracing from single, genetically targeted neurons. *Neuron* **53**, 639–647 (2007). doi: [10.1016/j.neuron.2007.01.033](https://doi.org/10.1016/j.neuron.2007.01.033); pmid: [17329205](https://pubmed.ncbi.nlm.nih.gov/17329205/)
29. T. Sato *et al.*, Single Lgr5 stem cells build crypt-villus structures in vitro without a mesenchymal niche. *Nature* **459**, 262–265 (2009). doi: [10.1038/nature07935](https://doi.org/10.1038/nature07935); pmid: [19329995](https://pubmed.ncbi.nlm.nih.gov/19329995/)

ACKNOWLEDGMENTS

The authors wish to thank Y. H. Kim, A. Chamesian, M. Park, S. Swain, M. Foster, C. Chen, W. Liu, and G. Wen for their contributions. We also thank A. Pereda, R. Liddle, S. Lisberger, E. Bohórquez, and the Grass Laboratory and Grass Fellows classes of '14, '16, and '17 for their constructive feedback. We thank L. Looger for his gracious donation of the iGluSnFR plasmid. Our sincere appreciation is expressed to the staff of the Duke Light Microscopy and Flow Cytometry Core Facilities. The laboratory mailing address is MSRB-1, room 221A, 203 Research Drive, Durham, NC 27710, USA. **Funding:** NIH K01 DK-103832 (PI, D.V.B.), NIH R03 DK114500-01 (PI, D.V.B.), AGA-Elsevier Pilot Research Award (PI, D.V.B.), NIH P30 DK034987 UNC-CGIBD Pilot Research Award (PI, D.V.B.), DARPA-ElectRx N2002850300 (PI, X.S.; Co-I, D.V.B.), NIH 10T2OD023849-01 (PI, X.S.; Co-I, D.V.B.), The Hartwell Foundation (PI, D.V.B.), The Dana Foundation (PI, D.V.B.), and The Grass Foundation (PI, D.V.B.). K.L.B. is a Howard Hughes Medical Institute Medical Research Fellow.

Author contributions: M.M.K. planned animal breedings and qPCR experiments and performed monosynaptic rabies tracing, electrophysiology experiments, calcium imaging recordings, immunohistochemistry, and data analysis. M.M.K., K.L.B., and B.B.B. optimized vagal cuff protocol and initial data analysis. K.L.B. performed all vagal cuff recordings, immunohistochemistry, and data analysis. M.E.K. manufactured monosynaptic rabies strains, culture organoids, rabies infection of enteroendocrine cells in organoids, organoid-nodose monosynaptic tracing, and data analysis. M.M.M. performed all animal breeding, mouse colony management, genotyping, and quality control. X.S. advised with biomedical implants, including abdominal window, as well as data analysis. M.M.K. and D.V.B. planned experiments and composed figures. D.V.B. conceptualized, acquired funding for, and supervised the project, as well as wrote the final manuscript. **Competing interests:** Some of the findings in this manuscript have been used to file a provisional patent application. No other competing interests are declared. **Data and materials availability:** All data are available in the manuscript or the supplementary materials.

SUPPLEMENTARY MATERIALS

www.sciencemag.org/content/361/6408/eaat5236/suppl/DC1
Materials and Methods
Figs. S1 to 20
Table S1
References (30–37)
Movies S1 and S2
Data S1

12 March 2018; accepted 2 August 2018
10.1126/science.aat5236

RESEARCH ARTICLE

CHEMISTRY

Reconfigurable system for automated optimization of diverse chemical reactions

Anne-Catherine Bédard^{1*}, Andrea Adamo^{2*}, Kosi C. Aroh², M. Grace Russell¹, Aaron A. Bedermann¹, Jeremy Torosian², Brian Yue², Klavs F. Jensen^{2†}, Timothy F. Jamison^{1†}

Chemical synthesis generally requires labor-intensive, sometimes tedious trial-and-error optimization of reaction conditions. Here, we describe a plug-and-play, continuous-flow chemical synthesis system that mitigates this challenge with an integrated combination of hardware, software, and analytics. The system software controls the user-selected reagents and unit operations (reactors and separators), processes reaction analytics (high-performance liquid chromatography, mass spectrometry, vibrational spectroscopy), and conducts automated optimizations. The capabilities of this system are demonstrated in high-yielding implementations of C-C and C-N cross-coupling, olefination, reductive amination, nucleophilic aromatic substitution (S_NAr), photoredox catalysis, and a multistep sequence. The graphical user interface enables users to initiate optimizations, monitor progress remotely, and analyze results. Subsequent users of an optimized procedure need only download an electronic file, comparable to a smartphone application, to implement the protocol on their own apparatus.

Chemists invest substantial time in repetitive experimental tasks, such as reaction monitoring and iterative optimization. These activities limit the effort they would otherwise direct toward innovation and creativity and, in turn, inhibit the pace of discovery and development in fields that depend upon molecular synthesis (1–3). Here, we describe an integrated, automated approach to mitigate these challenges.

Critical in our investigations was the use of continuous-flow synthesis (4). The standard for commodity chemical manufacturing, this approach has received substantial attention in the past decade for its implementation in the synthesis of many classes of complex organic molecules, including pharmaceuticals (1, 5–8). Four years ago, the end-to-end, fully integrated continuous manufacturing of a formulated pharmaceutical (aliskiren) was accomplished in a bespoke system designed for a single specific purpose. Subsequently, several technological and chemical advances enabled the creation of a compact (1.26 m³) reconfigurable system for the end-to-end synthesis, purification, and formulation of four different pharmaceuticals. Interchanging the system

among the pharmaceuticals involved designing and developing a synthetic route, selecting the appropriate types and sizes of reactors, reassembling the hardware, and optimizing the overall process (9, 10). Recently, a team from Eli Lilly described a continuous manufacturing process to support phase 1 and 2 clinical trials of an active pharmaceutical ingredient (11).

The opportunities offered by flow synthesis in earlier stages of chemical discovery and development also have attracted major attention (2, 3). Automated peptide and oligonucleotide synthesis revolutionized protein chemistry and molecular biology by providing scientists rapid access to complex biomolecules (12, 13). More recently, Burke and co-workers developed an approach that uses a cross-coupling reaction to produce milligram quantities of organic molecules by an iterative, deprotection-coupling-purification sequence (14). A modular Vaportec-based approach by Seeberger streamlined the divergent multistep syntheses of five active pharmaceutical ingredients (15), and systems developed by Ley feature monitoring and control of multistep syntheses of several specific molecular targets (16, 17). Multiple studies of automated optimization (18–22) have demonstrated the utility of continuous-flow and droplet systems in identifying optimal reaction conditions and catalysts for selected reactions. Advances in high-throughput experimentation (HTE) have shown that collections of molecules can be accessed in reduced time (23, 24). For example, researchers at Eli Lilly demonstrated that automation of batch processes

can enhance the efficacy of HTE and accelerate assaying of a library of potential biological modulators (25). Very recently, researchers at Pfizer reported a continuous-flow droplet platform capable of screening >1500 reagent combinations for a particular reaction as exemplified by a Suzuki-Miyaura coupling (26).

All of the above important advances are tailored to specific chemical reactions and/or targets. That is, the systems were not conceived with the flexibility to perform a varied array of reactions without some measure of redesign or reoptimization. Therefore, we aspired to create a compact, fully integrated, easily reconfigurable, benchtop system that enables automated optimization of a wide range of chemical transformations. During the initial investigations of such a system, we recognized that several challenges would need to be addressed. These include the chemical compatibility of components and pumping mechanisms; development of a unified, modular system for truly plug-and-play operation; appropriate software for system control and real-time monitoring (using established analytical methods) for automated feedback optimization; and ultimately, integration into a single, small-footprint platform that requires little user expertise with flow chemistry. Presented herein is the realization of these goals in a lab-scale, automated, and reconfigurable continuous-flow synthesis platform, demonstrated in single-step and multistep sequences encompassing several of the most widely used reactions in organic chemistry.

System concept and design

The system (Fig. 1) was designed to simplify labor-intensive chemical experimentation, in a manner similar to the way gas chromatography and high-performance liquid chromatography (HPLC) allow rapid automated analysis of samples with minimal technical training. To do so, we targeted the development and integration of three capabilities: hardware components that perform the syntheses and purifications, in-line analytical technologies that monitor reaction progress, and a user interface that provides software control and monitoring. The resulting system would thus be reconfigurable and perform a wide range of chemical reactions. Users would select the appropriate analytical instrument for a given optimization, and user-friendly software based in MATLAB and LabVIEW would provide control of both the system and the analytical instrument. This design would additionally offer the user a trio of modes to operate the system: (i) automated optimization of a specific reaction or sequence of reactions; (ii) synthesis of a range of substrates under user-selected conditions, for example, to investigate the scope of the transformation under conditions obtained from an optimization; (iii) or scale-up of a selected synthesis under conditions obtained from a previous optimization.

We aimed for chemically compatible plug-and-play reaction components that would enable rapid realization of different chemical transformations on a general platform providing the

¹Department of Chemistry, Massachusetts Institute of Technology, Cambridge, MA 02139, USA. ²Department of Chemical Engineering, Massachusetts Institute of Technology, Cambridge, MA 02139, USA.

*These authors contributed equally to this work.

†Corresponding author. Email: tfj@mit.edu (T.F.J.); kfjensen@mit.edu (K.F.J.)

necessary fluid and temperature control and having an intuitive graphical user interface with robust optimization algorithms. Realization of the goal of plug-and-play use of the system presented, perhaps, the greatest challenge. In principle, one could combine commercial technologies (pumps, reactor tubes, in-line separators, among others) for a particular optimization, but this approach would offer only a minimal enhancement in ease of use, and would require a large footprint. Rather, we desired a system wherein only reactor modules and separators would be attached by the user in a matter of seconds, without the need to reconfigure pumps, tubes, or other flow components. This versatility was achieved by the development of a universal bay (Fig. 1B), a standardized and flexible interface that can host any type of reaction module necessary for the particular chemistry being performed. The present system comprises five such bays, and six different modules have been developed thus far: a heated reactor (up to 120°C), a cooled reactor (to -20°C), a light-emitting diode (LED)-based photo-

chemistry reactor, a packed-bed reactor (for solid supported reagents and catalysts, as well as passive mixing), a membrane-based liquid-liquid separator (purification via extraction), and a bypass (for reagent addition in a minimal volume, mixing, or unused bay). The volume of each reactor ranges between 215 and 860 μL , depending on the internal diameter of the disposable PFA tubing used. Each bay is fed by a M6 Vici pump, with the exception of bay 1, which is connected to two pumps (Fig. 1B). In total, up to six different solutions containing reagents and/or solvents can be delivered into the system. The complete platform is contained within a small footprint and a total volume of 0.22 m^3 [0.61 m (width) \times 0.86 m (length) \times 0.41 m (height)].

To augment the versatility and enable intuitive use of the system by those with only minimal expertise, we designed a simple graphical interface (Fig. 1D, details of the user interface and automation scheme provided in figs. S8 and S10, and accompanying text). Automated optimization is enabled by integrating continuous reac-

tion monitoring and precise control of the key reaction parameters using two pressure sensors, two flow meters, one phase sensor, five infrared (IR)-based temperature sensors, and two cameras for web-based remote monitoring. Several in-line analytical methods can be used with the system to enable reaction monitoring and subsequent autonomous optimization. Although HPLC provides the best balance of generality and instrument cost, IR spectroscopy (Mettler Toledo ReactIR), Raman spectroscopy (Marqmetrix Raman BallProbe), and mass spectrometry (Advion MS with electrospray ionization) are also compatible (27, 28). The control software behind the user interface continuously analyzes and records the data received from these devices.

Many optimization algorithms may be used with the system, but we have found that the stable noisy optimization by branch and fit [SNOBFIT (29)] algorithm provides a convenient means for global optimization of single- or multi-step processes without the need for a theoretical model. This agnostic, "black-box" approach

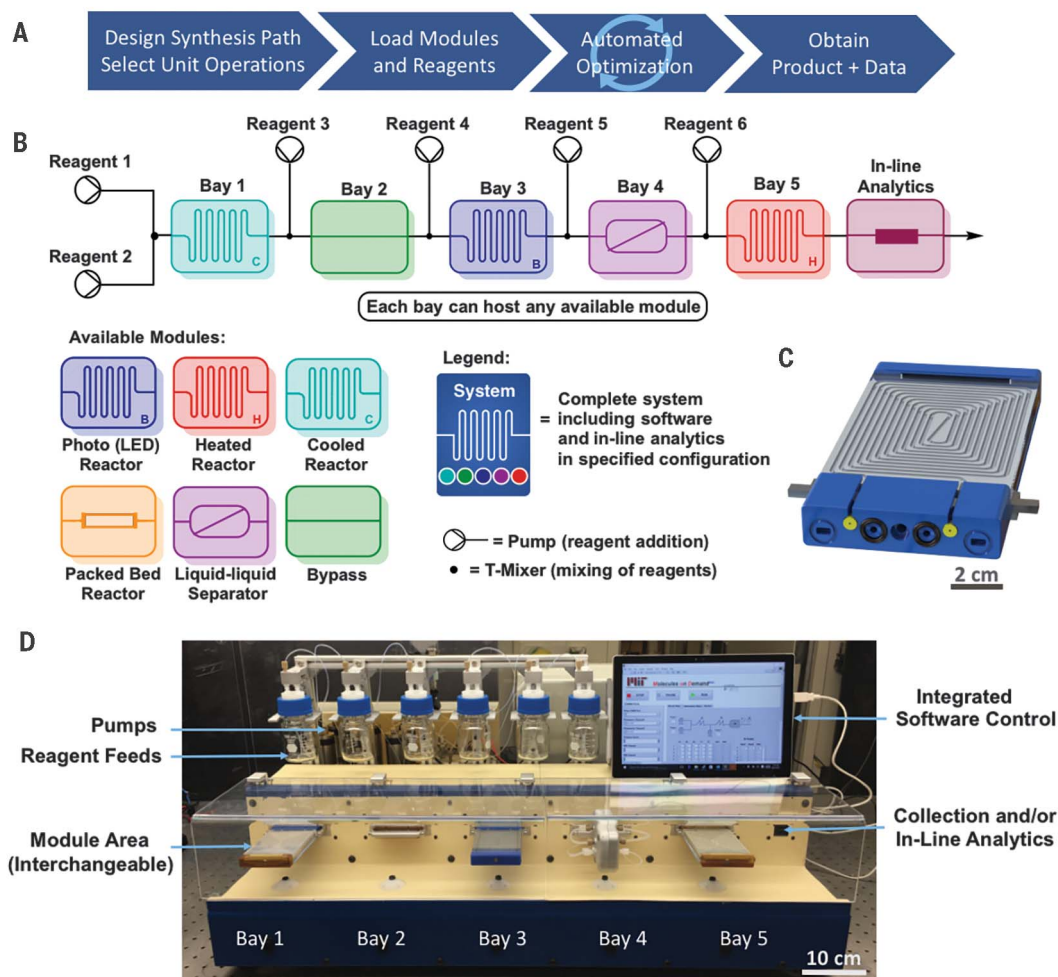


Fig. 1. Plug-and-play, reconfigurable, continuous-flow chemical synthesis system. (A) General four-step protocol for using the system. (B) Representative configuration of the components in the system. (C) CAD (computer-aided design) representation of the LED

reactor; shown is a view of the end that attaches to a universal bay on the system. See figs. S2, S4, and S5 for details of the fluidic and electrical connections in the universal bay. (D) Schematic representation of the configuration shown in (B) and available modules.

provides generality and flexibility to the system (30, 31) by performing local optimizations around the best conditions while continuously searching other, more distant regions to ensure that a global (rather than local) optimum is found. Alternatively, faster optimization procedures could be implemented, but with a trade-off in requiring prior knowledge of the system and an attendant loss of generality (31).

Automated optimization of chemical transformations

We began our tests of the system with a Paal-Knorr pyrrole synthesis. In addition to being a classic method for assembling important heterocycles, it provided us the twofold opportunity to compare the performance of the system with others we had investigated (28) and also to validate a suite of analytical methods (HPLC, MS, IR, and Raman; see the supplementary materials for details). Subsequently, these activities also enabled us to evaluate the portability of the platform by performing the same automated optimization in two different laboratories. To this end, after optimization of a Paal-Knorr pyrrole synthesis (see supplementary materials) in one laboratory (Jensen), the system was transferred to another (Jamison), wherein the optimization converged independently on the same reaction conditions. In this exercise, only the platform and the software were transferred between the groups; two different HPLCs were used, providing additional validation of the flexibility and generality of the system.

We next evaluated the generality and ease of use of the system described above. As thousands

(5⁶) of configurations of reactor modules are possible, we reasoned that the system should have the intrinsic capacity to perform automated optimization of a large range of chemical transformations and multistep syntheses. We selected six important and widely used reactions to exemplify this point: Buchwald-Hartwig amination, Horner-Wadsworth-Emmons olefination, reductive amination, Suzuki-Miyaura cross-coupling, nucleophilic aromatic substitution (S_NAr), and a visible light photoredox reaction. We also selected a two-step process that would inform us about the amenability of the system toward multistep reaction optimization, which is especially useful in cases wherein the product of the first reaction is of limited stability (for example, ketene generation followed by alkene cycloaddition).

For these investigations, we used a general four-step protocol (Fig. 1A) in each optimization: (i) design of the reaction sequence (selecting the reagents, solvents, and catalysts); (ii) attachment of the appropriate module to each bay and loading of the reagents and solvent feeds; (iii) selection of the parameter boundaries (time, temperature, catalyst loading) within which the system will perform the optimization; and (iv) execution of the automated optimization. We also found that remote operation and monitoring of the system during an optimization are possible with any smartphone, tablet, or computer that has internet access.

The Buchwald-Hartwig amination is central to many areas of chemical research, including the discovery and development of pharmaceuticals, agricultural chemicals, and organic light-emitting diodes (32). The palladium-catalyzed

coupling of 1-bromo-4-methoxybenzene (**1**) with 4-methoxyaniline (**2**) under basic conditions was investigated using the recently reported (33) BrettPhosPdG₃ pre-catalyst (**3**). Figure 2A shows the platform setup for the reaction optimization. Bays 1 and 2 were used for reagent addition and mixing, and the amination itself was performed in bay 3 using a heated reactor. Introduction of toluene and water in bay 4 then enabled a continuous liquid-liquid separation in bay 5. A 60-nl sample of the organic layer was analyzed directly by an in-line HPLC system, with the conversion of aniline **2** assayed relative to an internal standard. The complete results of the automated optimization sequence may be found in fig. S17 and tables S1 and S2. The desired secondary amine **7** was obtained in a 72% yield after the in-line purification. The reproducibility of the system that we observed also merits comment. The 72% yield obtained after the automated optimization of the Buchwald-Hartwig amination was replicated (72% yield) by another user operating the system under the same conditions, i.e., without reoptimization.

With the optimum conditions in hand, we next used the system to investigate the substrate scope under identical conditions (Fig. 2C), thereby providing the opportunity to study valuable structure-reactivity relationships in an exceptionally controlled manner. If desired, the user may also optimize each individual case using this automated system. The palladium-catalyzed reactions of the anilines and arylbromides examined proceeded with overall chemical yields of 72 to 99% and with material throughput rates of 430 to 816 mg/hour.

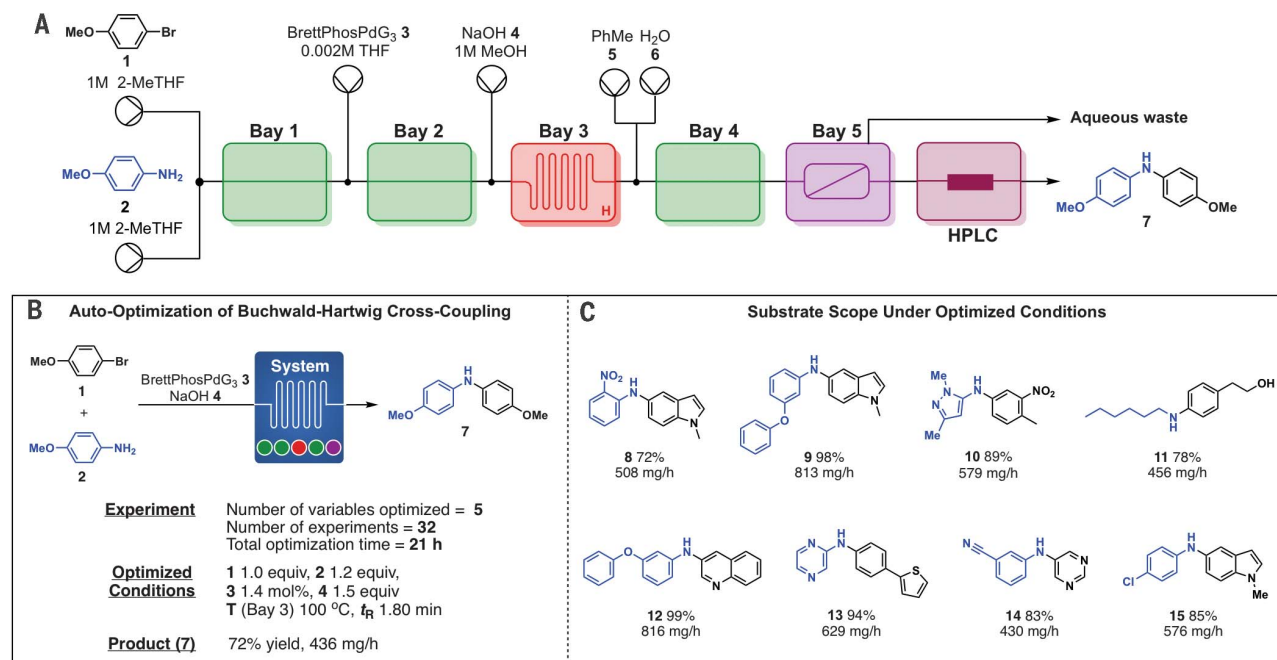


Fig. 2. Buchwald-Hartwig cross-coupling automated optimization and examples. (A) The system setup for the optimization of the Buchwald-Hartwig cross-coupling using a heated reactor in bay 3 and a liquid-liquid separator in bay 5. (B) Summary of the optimal conditions

found for the Buchwald-Hartwig amination (details in fig. S17 and tables S1 and S2). (C) Substrate scope evaluated using optimized conditions determined in (B). Isolated yield after column chromatography. T, temperature; t_R, residence time.

Optimization of six additional reactions and sequences allowed us to test the generality of the system. Each of the following employed a unique array of modules in the five universal bays: Horner-Wadsworth-Emmons (HWE) olefination, reductive amination, Suzuki-Miyaura cross-coupling, S_NAr , the generation of an iminium electrophile via photoredox catalysis, and ketene generation with subsequent alkene cycloaddition (Figs. 3 and 4; complete details in supplementary materials). The HWE, for example, is a two-step process (phosphonium ylide generation and alkene formation), and optimization in the system used heated reactors in bays 1 and 2. As shown in Fig. 3B,

after the automated optimization of the model reaction (32 reaction conditions examined in a continuous 10-hour period), a range of olefins were obtained under the same conditions in high yield with throughput up to 3.1 g/hour. Although the structures of the aldehyde, ketone, and phosphonate reagents were varied, all those examined underwent efficient HWE transformations under the optimized conditions.

In a similar manner, but with another system configuration, a two-step reductive amination sequence was optimized (33 experiments in 14 hours, Fig. 3C). The system discovered that a total residence time of 2.05 min was sufficient for the

synthesis of amine **33**. The stereochemical integrity of chiral amines and aldehydes was preserved in the two cases that the system examined (**38** and **40**). The more hindered amine **36** provided a lower yield when subjected to the previously optimized reaction condition; incomplete imine formation (bay 1) followed by direct reduction of the aldehyde (bay 2) afforded appreciable amounts of an alcohol byproduct (details in supplementary materials). Nevertheless, highlighting another feature of the system, a rapid reoptimization of the imine formation step provided **36** in 97% yield. The Suzuki-Miyaura cross-coupling optimization (Fig. 3E) was performed using a packed-bed

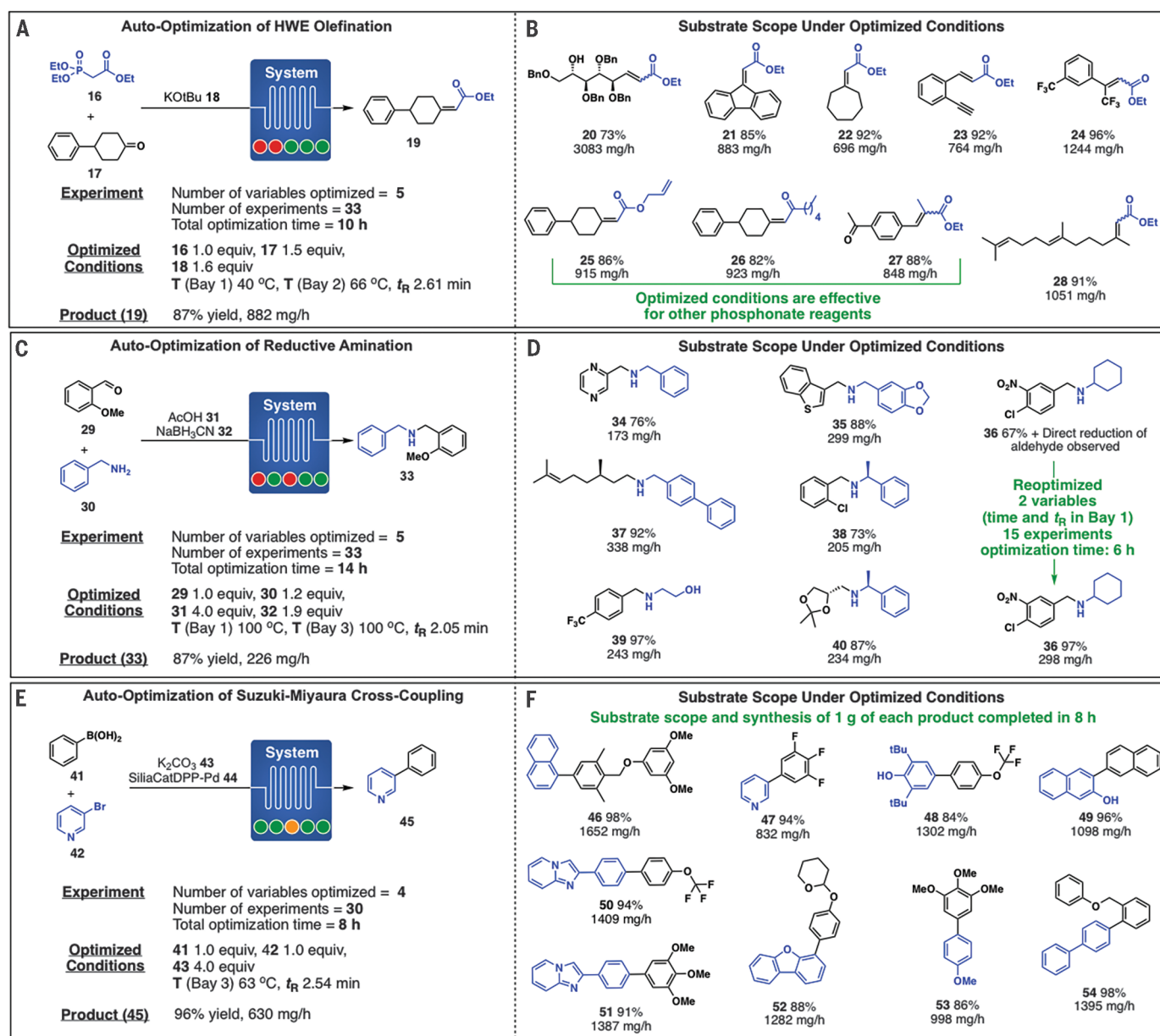


Fig. 3. Three different transformations optimized and demonstrated in the system. (A) HWE auto-optimization (details in fig. S17 and tables S1 and S3). (B) Substrate scope evaluation under optimized conditions in (A). (C) Reductive amination auto-optimization (details in fig. S18 and tables S1 and S4).

(D) Substrate scope evaluation under optimized conditions in (C). (E) Suzuki-Miyaura cross-coupling auto-optimization (details in figs. S19 and S20 and tables S1 and S5). (F) Substrate scope evaluation under optimized conditions in (E). Isolated yield after column chromatography. T, temperature; t_R , residence time.

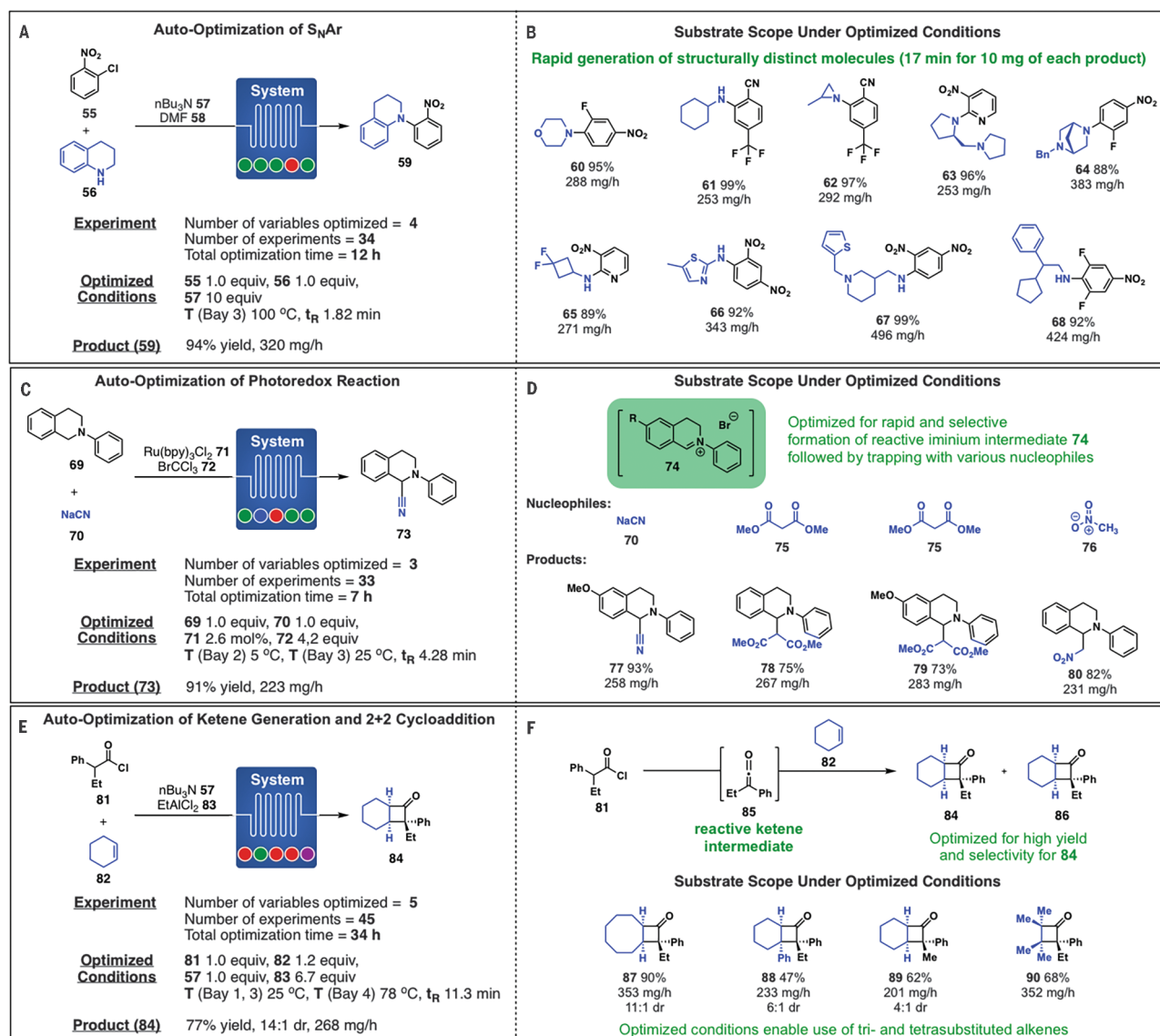


Fig. 4. Automated optimization of substitution and photochemical reactions using the platform. (A) Summary of the optimal conditions found for the S_NAr (details in fig. S21 and tables S1 and S6). (B) Substrate scope evaluated using optimized conditions established in (A). (C) Summary of the optimal conditions found for the photoredox reaction (details in figs. S22 and S23 and tables S1 and S7). (D) Substrate scope evaluated

using optimized conditions determined in (C). Isolated yield after column chromatography. (E) Auto-optimization of ketene generation and [2 + 2] cycloaddition (details in fig. S24 and tables S1 and S8). (F) Multistep reaction sequence in (E) and substrate scope evaluation under optimized conditions in (E). Isolated yield after column chromatography. T, temperature; t_R , residence time.

reactor containing the solid-supported catalyst siliaCat DPP-Pd (**34**). Automated experimentation (30 experiments in 8 hours) provided conditions that afforded **45** in 96% yield and were transposed to a wide variety of other cross-coupling partners (Fig. 3F, **46** to **54**). Because the reagent feed can be exchanged rapidly, only 8 hours were required to provide 1 g of each of nine desired products, demonstrating the ability of the system to generate synthetically useful quantities of desired materials in a short period of time.

We next explored an S_NAr reaction. Automated optimization of the model reaction (Fig. 4A) required 12 hours and afforded tertiary amine **59** in 94% yield. Using the optimized conditions, we

obtained several distinct structures (**60** to **68**) in high yields (88 to 99%). The rapid generation of a library of nine compounds (10 mg scale) was achieved in a total time of only 20 min, demonstrating the potential of this system for use in discovery efforts in, for example, the pharmaceutical industry. Furthermore, because the system operates at steady state using continuous-flow chemistry, scaling up of a reaction occurs readily and rapidly (**4**). For example, 10 mg of **59** was obtained in 5 min, corresponding to 7.7 g of amine **59** per day. The LED photoreactor, which includes active cooling for temperature control, was then applied to an automated optimization of a photoredox reaction (Fig. 4C) that proceeds

by way of a reactive intermediate, iminium ion **74** (Fig. 4D). In this optimization, the boundary parameters were selected based on batch precedents from the Stephenson (**35**) and Rueping (**36–38**) groups. Under the optimized conditions, reactions were complete within 3 min, whereas previous reports indicate that a 3-hour reaction time was generally required in batch (**4**, **39**, **40**).

To investigate the ability of the system to optimize multistep sequences, we targeted a ketene generation and Lewis acid-promoted alkene cycloaddition to form cyclobutanones, inspired by a precedent from Brown (**41**). The first reaction produces the reactive ketene intermediate **85** from the acyl chloride **81**, and cycloaddition of

cyclohexene **82** affords cyclobutanone **84**. In-line quench and separation prior to analysis and product collection purifies the reaction mixtures. As the entire system may be operated under an inert atmosphere (N₂, for example), it provides a means for the safe handling of the pyrophoric Lewis acid ethylaluminum dichloride **83** by minimizing direct manipulation of this reagent by the user. Also noteworthy was that the objective function used in the optimization included terms for both product yield and selectivity for **84**, highlighting the flexibility of the optimization approach. The desired cyclobutanone **84** was produced in 77% yield and 14:1 diastereomeric ratio, comparable in both efficiency and selectivity to the Brown precedent, but at much higher temperature (78°C versus <23°C). This approach also expanded the scope of this valuable transformation; under the optimized conditions, cyclobutanones from tri- and tetrasubstituted alkenes, not possible in the originally reported conditions (47), may now be synthesized.

Outlook

In conclusion, we have developed a fully integrated, versatile system and demonstrated the automated optimization of a diverse array of chemical reactions. The examination of the substrate scope in each of the seven reactions and multistep sequences afforded greater than 50 compounds in high yield. This reconfigurable system has changed the way we approach experimentation and optimization in several ways. It accelerates the synthesis of lab-scale quantities of molecules and allows investigators to direct more of their efforts toward the creative aspects of research. The system's generality and ease of use obviates the need for expertise in flow chemistry to realize its benefits. The system also provides a means to optimize and evaluate the scope of a reaction in a matter of hours or days and do so under identical reaction conditions for each substrate of interest, if desired. Transfer of experimental results is now direct, electronic, and seamless; the time-consuming exercise of reopti-

mizing literature procedures should thus diminish in its frequency. Moreover, the data obtained in each optimization and evaluation may build a foundation of knowledge useful in machine learning pursuits.

REFERENCES AND NOTES

1. T. N. Glasnov, C. O. Kappe, *Chemistry* **17**, 11956–11968 (2011).
2. S. V. Ley, D. E. Fitzpatrick, R. M. Myers, C. Battilocchio, R. J. Ingham, *Angew. Chem. Int. Ed.* **54**, 10122–10136 (2015).
3. S. V. Ley, D. E. Fitzpatrick, R. J. Ingham, R. M. Myers, *Angew. Chem. Int. Ed.* **54**, 3449–3464 (2015).
4. M. B. Plutschack, B. Pieber, K. Gilmore, P. H. Seeberger, *Chem. Rev.* **117**, 11796–11893 (2017).
5. B. Gutmann, D. Cantillo, C. O. Kappe, *Angew. Chem. Int. Ed.* **54**, 6688–6728 (2015).
6. C. Wiles, P. Watts, *Green Chem.* **14**, 38–54 (2012).
7. C. Wiles, P. Watts, *Future Med. Chem.* **1**, 1593–1612 (2009).
8. L. Vaccaro, D. Lanari, A. Marrocchi, G. Strappaveccia, *Green Chem.* **16**, 3680–3704 (2014).
9. A. Adamo *et al.*, *Science* **352**, 61–67 (2016).
10. P. L. Heider *et al.*, *Org. Process Res. Dev.* **18**, 402–409 (2014).
11. K. P. Cole *et al.*, *Science* **356**, 1144–1150 (2017).
12. A. El-Faham, F. Albericio, *Chem. Rev.* **111**, 6557–6602 (2011).
13. C. A. G. N. Montalbetti, V. Falque, *Tetrahedron* **61**, 10827–10852 (2005).
14. J. Li *et al.*, *Science* **347**, 1221–1226 (2015).
15. D. Ghislieri, K. Gilmore, P. H. Seeberger, *Angew. Chem. Int. Ed.* **54**, 678–682 (2015).
16. R. J. Ingham *et al.*, *Angew. Chem. Int. Ed.* **54**, 144–148 (2015).
17. R. J. Ingham, C. Battilocchio, J. M. Hawkins, S. V. Ley, *Beilstein J. Org. Chem.* **10**, 641–652 (2014).
18. D. Cortés-Borda *et al.*, *Org. Process Res. Dev.* **20**, 1979–1987 (2016).
19. B. J. Reizman, Y.-M. Wang, S. L. Buchwald, K. F. Jensen, *React. Chem. Eng.* **1**, 658–666 (2016).
20. B. J. Reizman, K. F. Jensen, *Chem. Commun. (Camb.)* **51**, 13290–13293 (2015).
21. J. P. McMullen, K. F. Jensen, *Org. Process Res. Dev.* **14**, 1169–1176 (2010).
22. D. E. Fitzpatrick, C. Battilocchio, S. V. Ley, *Org. Process Res. Dev.* **20**, 386–394 (2016).
23. A. Buitrago Santanilla *et al.*, *Science* **347**, 49–53 (2015).
24. K. H. Bleicher, H.-J. Böhm, K. Müller, A. I. Alanine, *Nat. Rev. Drug Discov.* **2**, 369–378 (2003).
25. A. G. Godfrey, T. Masquelin, H. Hemmerle, *Drug Discov. Today* **18**, 795–802 (2013).
26. D. Perera *et al.*, *Science* **359**, 429–434 (2018).
27. D. L. Browne *et al.*, *Rapid Commun. Mass Spectrom.* **26**, 1999–2010 (2012).
28. J. S. Moore, K. F. Jensen, *Org. Process Res. Dev.* **16**, 1409–1415 (2012).
29. W. Huyer, A. Neumaier, *ACM Trans. Math. Softw.* **35**, 9:1–9:25 (2008).
30. V. Sans, L. Cronin, *Chem. Soc. Rev.* **45**, 2032–2043 (2016).
31. B. J. Reizman, K. F. Jensen, *Acc. Chem. Res.* **49**, 1786–1796 (2016).
32. P. Ruiz-Castillo, S. L. Buchwald, *Chem. Rev.* **116**, 12564–12649 (2016).

33. N. C. Bruno, M. T. Tudge, S. L. Buchwald, *Chem. Sci. (Camb.)* **4**, 916–920 (2013).
34. V. Pandarus, G. Gingras, F. Bédard, R. Ciriminna, M. Pagliaro, *Org. Process Res. Dev.* **18**, 1550–1555 (2014).
35. D. B. Freeman, L. Furst, A. G. Condie, C. R. J. Stephenson, *Org. Lett.* **14**, 94–97 (2012).
36. M. Rueping, S. Zhu, R. M. Koenigs, *Chem. Commun. (Camb.)* **47**, 12709–12711 (2011).
37. M. Rueping, S. Zhu, R. M. Koenigs, *Chem. Commun. (Camb.)* **47**, 8679–8681 (2011).
38. M. Rueping, C. Vila, R. M. Koenigs, K. Poschorny, D. C. Fabry, *Chem. Commun. (Camb.)* **47**, 2360–2362 (2011).
39. C. K. Prier, D. A. Rankic, D. W. C. MacMillan, *Chem. Rev.* **113**, 5322–5363 (2013).
40. N. A. Romero, D. A. Nicewicz, *Chem. Rev.* **116**, 10075–10166 (2016).
41. C. M. Rasik, M. K. Brown, *J. Am. Chem. Soc.* **135**, 1673–1676 (2013).

ACKNOWLEDGMENTS

Funding: This project was supported by the Army Research Office (ARO) under contract W911NF-15-1-0183. **Author contributions:** All authors participated in writing and revising the manuscript. A.-C.B. developed chemistry, designed and executed optimizations, analyzed optimization results, and refined the system; A.A. designed, built, and refined the system hardware; K.C.A. developed the user interface and optimization algorithms, refined the system, designed and executed optimizations, and analyzed optimization results; M.G.R. developed chemistry, designed and executed optimizations, and analyzed optimization results; A.A.B. developed chemistry and designed the system; J.T. and B.Y. contributed to parts design, testing, and building the system; K.F.J. and T.F.J. designed the system, analyzed optimization results, provided oversight for the project, and secured funding for the project. **Competing interests:** A.A. is the founder of Zaiport Flow Technologies. T.F.J. is a cofounder of Snapdragon Chemistry, Inc., and a scientific adviser for Zaiport Flow Technologies, Continuous Pharmaceuticals, Paraza Pharmaceuticals, and Asymchem. A.A., K.C.A., A.A.B., K.F.J., and T.F.J. are inventors on patent application PCT/US2017/030649 (International Patent Application WO2017/192595 A1) submitted by the Massachusetts Institute of Technology that covers the system described in the manuscript. **Data and materials availability:** The data from the optimizations, the MATLAB code, and the LabView code are available at https://github.com/kosiaroh/Reconfigurable_System_for_Automated_Optimization_of_Diverse_Chemical_Reactions. The other data reported in this paper are available in the article or in the supplementary materials.

SUPPLEMENTARY MATERIALS

www.sciencemag.org/content/361/6408/1220/suppl/DC1
Materials and Methods
Figs. S1 to S81
Tables S1 to S8

22 January 2018; accepted 25 July 2018
10.1126/science.aat0650

APPLIED OPTICS

Suppressing spatiotemporal lasing instabilities with wave-chaotic microcavities

Stefan Bittner¹, Stefano Guazzotti², Yongquan Zeng³, Xiaonan Hu³, Hasan Yilmaz¹, Kyungduk Kim¹, Sang Soon Oh^{2,4}, Qi Jie Wang³, Ortwin Hess^{2*}, Hui Cao^{1,*}

Spatiotemporal instabilities are widespread phenomena resulting from complexity and nonlinearity. In broad-area edge-emitting semiconductor lasers, the nonlinear interactions of multiple spatial modes with the active medium can result in filamentation and spatiotemporal chaos. These instabilities degrade the laser performance and are extremely challenging to control. We demonstrate a powerful approach to suppress spatiotemporal instabilities using wave-chaotic or disordered cavities. The interference of many propagating waves with random phases in such cavities disrupts the formation of self-organized structures such as filaments, resulting in stable lasing dynamics. Our method provides a general and robust scheme to prevent the formation and growth of nonlinear instabilities for a large variety of high-power lasers.

Systems with complex spatiotemporal dynamics can exhibit instabilities and even chaotic dynamics, as seen for example in weather patterns, turbulent flow, population dynamics (1), or chemical reactions (2). Beyond natural occurrences, spatiotemporal instabilities also appear in sophisticated technological systems such as fusion reactors exhibiting plasma instabilities (3) or type II superconductors with complex vortex dynamics (4). Lasers

are another important class of systems exhibiting inherent spatiotemporal instabilities and deterministic chaos due to the nonlinear interaction of the light field with the active medium (5–7). The underlying nonlinearities are particularly pronounced for high-power lasers, which have a large transverse area and operate on many spatial (transverse) modes. Nonlinear modal interactions entail spatiotemporal instabilities, such as irregular pulsation and filamentation [e.g., in

broad-area edge-emitting semiconductor lasers (8–14)], that degrade the spatial, spectral, and temporal properties of the emission.

Because high-power lasers have widespread applications in materials processing, large-scale displays, laser surgery, and pumping sources, much effort has been invested in suppressing lasing instabilities. Most proposed strategies seek to reduce the level of complexity by reducing the number of lasing modes. For broad-area semiconductor lasers, this can be achieved by external control [e.g., through injection of a coherent signal (15, 16) or delayed optical feedback (17–19)] or schemes based on parity-time symmetry (20, 21). These approaches, although successful with moderate powers, quickly become less effective when increasing the cavity size in order to harness more power. An external control signal applied via injection or feedback through the cavity boundary has a diminished effect deep inside a large cavity, and thus it fails to control the dynamics over the whole cavity. Furthermore, these approaches are typically sensitive to external perturbations and require a careful adjustment of parameters to reach stabilization.

¹Department of Applied Physics, Yale University, New Haven, CT 06520, USA. ²Blackett Laboratory, Department of Physics, Imperial College London, London SW7 2AZ, UK.

³Center for OptoElectronics and Biophotonics, School of Electrical and Electronic Engineering and Photonics Institute, Nanyang Technological University, 639798 Singapore.

⁴School of Physics and Astronomy, Cardiff University, Cardiff CF24 3AA, UK.

*Corresponding author. Email: hui.cao@yale.edu (H.C.); o.hess@imperial.ac.uk (O.H.)

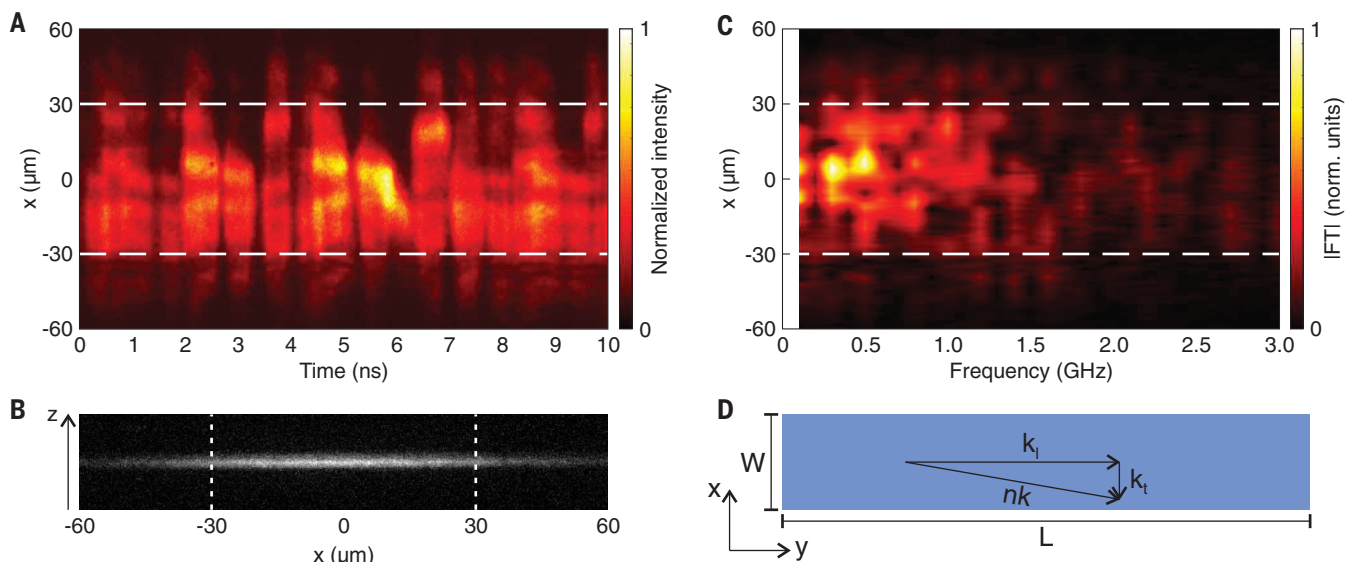


Fig. 1. Spatiotemporal instabilities of an electrically pumped edge-emitting semiconductor laser. The top metal contact is 60 μm wide and 0.98 mm long. **(A)** Spatiotemporal image of the emission intensity $I(x, t)$ at one of the cleaved facets. The stripe laser was injected with an electric current of 400 mA and 2- μs pulses; the lasing threshold current was $I_{\text{th}} = 230$ mA. The image was taken 0.37 μs after the start of the pump pulse, well beyond any turn-on transient. Part of the emission stems from outside the region of the top contact (marked by white dashed lines) as a result of

lateral spread of the injected current in the GaAs. **(B)** Image of electroluminescence from the end facet for a pump current of 100 mA (below threshold) and a pulse length of $t_p = 20$ μs . The emission is spatially homogeneous without any visible defects. **(C)** Temporal Fourier transform of $I(x, t)$ in (A). **(D)** Sketch of a rectangular Fabry-Perot cavity of length L and width W where $L \gg W$. The wave vector can be separated into longitudinal and transverse components k_l and k_t , respectively. Because $k_l \gg k_t$, the lasing modes propagate predominantly in the longitudinal (y) direction.

Our approach aims to eliminate spatiotemporal instabilities in broad-area edge-emitting semiconductor lasers without reducing the number of lasing modes and is thus applicable to high-power operation. Instead of suppressing the filaments via external signals, we disrupt the coherent nonlinear processes that lead to their formation by using cavities with complex spatial structure to create many propagating waves with random phases. The complex interference of these waves prevents the formation of self-organized structures such as filaments that are prone to modulational instabilities. We demonstrate the generality and robustness of this approach through experiments and numerical simulations with two different systems: (i) two-dimensional (2D) microcavities featuring chaotic ray dynamics and (ii) 1D cavities with random fluctuations of the refractive index. The chaotic ray dynamics and the structural disorder, respectively, are responsible for the creation of multiwave interference effects.

Conventional broad-area edge-emitting lasers

We first show the complex spatiotemporal dynamics of GaAs quantum well lasers in the widely used stripe geometry. The reflections from two cleaved facets in the longitudinal direction (parallel to the stripe axis) and gain guiding in the transverse direction (perpendicular to the stripe axis) provide optical confinement (22). Spatiotemporal traces of the lasing emission intensity at one end facet were measured by a streak camera with picosecond resolution (22). As shown in Fig. 1A, the lasing emission is spatially concentrated at multiple locations—so-called filaments—that sometimes move in the transverse direction (8–10). Emission patterns (Fig. S5) measured during the same pulse as in Fig. 1 demonstrate that the lasing emission can change suddenly from a nearly uniform distribution to concentration in small regions or filaments. Such diverse emission profiles illustrate that the formation of filaments is an inherent feature of the lasing dynamics and is not due to inhomogeneities of the cavity. This is confirmed by an electroluminescence image taken below lasing threshold (Fig. 1B) displaying a homogeneous intensity distribution across the facet. Furthermore, the lasing emission oscillates rapidly and irregularly in time (Fig. 1A). The spatially resolved temporal Fourier transform of the emission intensity $I(x, t)$ (Fig. 1C) reveals a number of frequency components up to about 1.5 GHz, which accounts for the irregular oscillations on a nanosecond time scale.

The filaments are formed through spatiotemporal nonlinear processes including spatial hole burning, carrier-induced index variation, and self-focusing (8–14). The stripe laser cavity is of Fabry-Perot (FP) type, and the light field propagates predominantly in the longitudinal direction. The wave vector component in the longitudinal direction, k_z , is much larger than that in the transverse direction, k_t . Consequently, the transverse wavelength $\lambda_t = 2\pi/k_t$ is typically

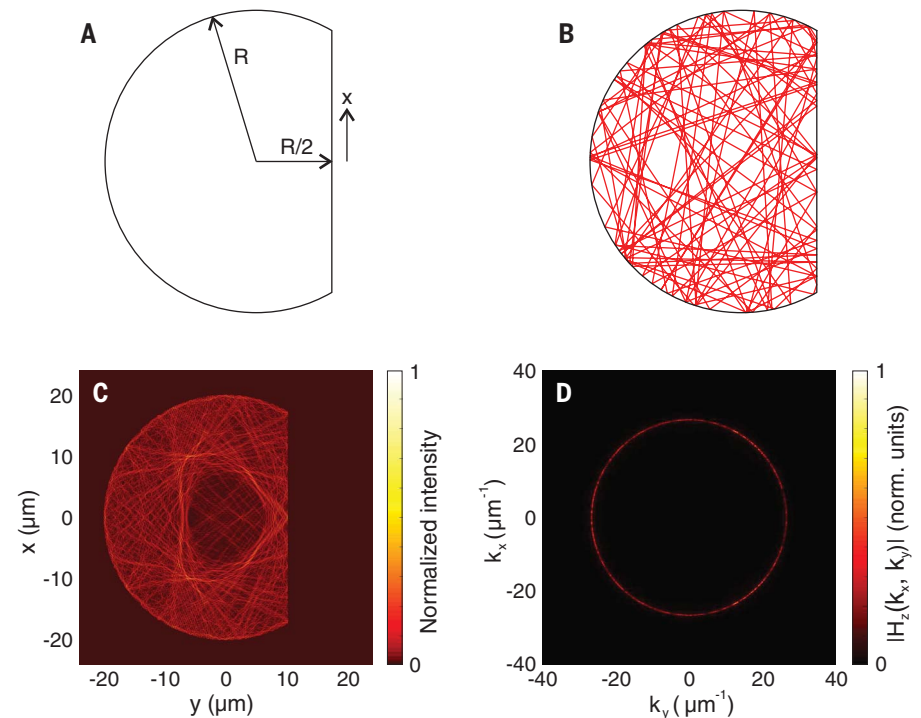


Fig. 2. D-cavity with chaotic ray dynamics. (A) Geometry of the D-cavity. A section is removed from a circle with radius R along a straight cut $R/2$ away from the center. The coordinate along this segment of the boundary is denoted by x . (B) A typical ray trajectory in a closed D-cavity covers the entire cavity and propagates in all directions. (C) Intensity distribution of a typical high-Q mode ($\lambda = 800.4$ nm, $Q = 3443$) in a dielectric D-cavity with radius $R = 20$ μm and refractive index $n = 3.37$. (D) The wave vector distribution of the same mode is isotropic, indicating that there is no dominant direction of propagation.

on the order of a few micrometers, and much longer than the longitudinal wavelength $\lambda_l = 2\pi/k_l$. A variation of the field intensity in the transverse direction on the scale of λ_t can result in filamentation due to carrier-induced index changes: A region of increased intensity depletes the gain, thus raising the refractive index locally and forming a lens. The lens will focus light and further enhance local intensity. This self-focusing process generates a filament with a typical width of several micrometers, comparable to the transverse wavelength. Because the optical gain is less depleted outside the filament, the filament tends to migrate transversely to the neighboring region of higher gain. Meanwhile, additional filaments may form at locations of less carrier depletion. These filaments will interact nonlinearly via the semiconductor quantum well. As a result of dynamic gain and nonlinear interaction, the filaments vary in space and time, leading to complex spatiotemporal dynamics and instabilities (9). The resulting degradation and temporal fluctuations of the output profile limit the laser applications.

Wave-chaotic microcavity lasers

Microcavities with chaotic ray dynamics (23–25) have been studied in the context of wave-dynamical chaos (26). The resonant modes of the passive cavities are determined by a linear wave equation and do not exhibit chaos in the

sense of an exponential sensitivity to the initial conditions. However, the chaotic ray dynamics manifests in the spatial and spectral properties of the cavity resonances; for example, the spatial field distributions feature a pseudo-random, speckle-like structure. Such wave-chaotic microcavities have been used to tailor steady-state lasing properties such as output directionality, lasing threshold, and lasing spectrum (23–25, 27, 28). Here, we investigate the temporal dynamics of such lasers.

As an example, we consider a D-shaped cavity (Fig. 2A), which has fully chaotic ray dynamics. A single trajectory (Fig. 2B) generally covers the entire cavity and propagates in all possible directions. The classical ray dynamics manifests in the spatial structure of the resonant modes (Fig. 2C). The intensity distribution features an irregular, pseudo-random structure, reminiscent of a speckle pattern with an average grain size of $\lambda/(2n)$, where n is the refractive index. The characteristic length scale is isotropic, in contrast to the FP-cavity modes that feature a larger transverse wavelength than longitudinal wavelength. The wave vector distribution (Fig. 2D) reveals that the D-cavity mode is a superposition of numerous plane waves in all possible directions.

These features of the chaotic cavity modes directly affect the lasing dynamics: Because the spatial structure of the modes is so fine-grained

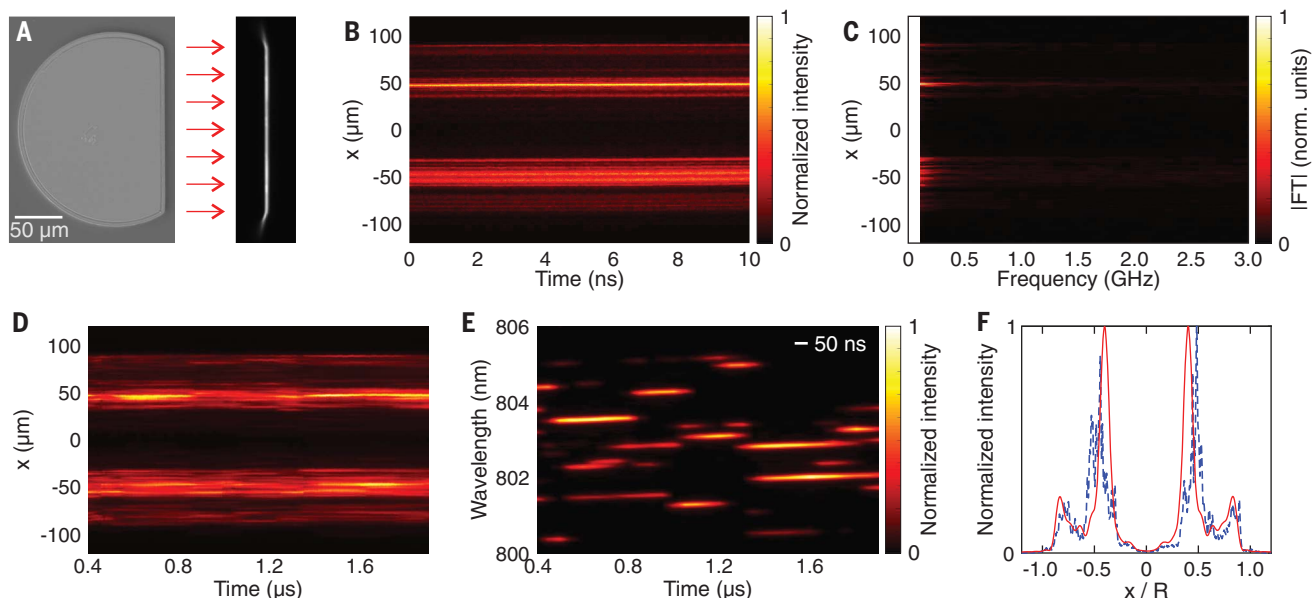


Fig. 3. Lasing dynamics in a D-cavity with radius of 100 μm fabricated by reactive ion etching. (A) Top-view SEM image (left) and optical image of the electroluminescence on the straight boundary segment (right). The pump current for the electroluminescence image was 3 mA, well below the lasing threshold of $I_{\text{th}} = 150$ mA. The intensity profile is homogeneous. (B) Spatiotemporal image of the emission intensity, $I(x, t)$, at the straight segment for a pump current of 500 mA during a 10-ns interval at 1.4 μs after the start of a 2- μs pump pulse. (C) Temporal Fourier

transform of $I(x, t)$ in (B), demonstrating the absence of nanosecond-scale oscillations. (D) Spatiotemporal image of the emission intensity during the interval 0.4 to 1.9 μs . (E) Spectrotemporal image for the same pump conditions as in (D), measured with temporal resolution of 50 ns. (F) Lasing emission intensity distribution at the straight segment for a pump current of 500 mA, measured with the CCD camera and integrated over a 2- μs pulse (blue dashed line). Also shown is the numerically calculated emission profile of high-Q modes (red solid line).

in all directions, the spatial extent of field intensity variations is too small to create a lensing effect, and additionally there are no dominant propagation directions that light could be focused toward. These qualitative differences of the mode structure and the associated length scales relative to FP cavities result from complex multi-wave interference and can prevent the formation of coherent spatiotemporal structures such as filaments.

We fabricated D-cavity lasers by photolithography and wet or dry (reactive ion) etching (22). Figure 3A shows a scanning electron microscopy (SEM) image of a cavity fabricated by reactive ion etching. Figure 3B is the spatiotemporal trace of the lasing emission intensity $I(x, t)$ at the straight segment of the boundary of the D-cavity. Relative to the emission trace in a 10-ns interval for the stripe laser (Fig. 1A), the D-cavity laser emission has nearly constant intensity and does not exhibit rapid pulsations. The temporal Fourier transform of $I(x, t)$ in Fig. 3C confirms the absence of gigahertz frequency oscillations, in contrast to Fig. 1C. The spatiotemporal trace of the D-cavity laser (Fig. 3D) over a time interval of 1.5 μs reveals temporal fluctuation of the emission intensity on a much longer scale of ~ 100 ns.

The temporal fluctuations of the emission spectrum were measured by a spectrometer equipped with an intensified charge-coupled device (ICCD) camera (fig. S2) (22). The time-resolved emission spectrum (Fig. 3E) consists of multiple lasing peaks at any given time. Each

peak persists for tens or even hundreds of nanoseconds, and is then replaced by new peaks at different wavelengths.

To quantify the time scales of the spatiotemporal and spectrotemporal dynamics, we calculated the autocorrelation functions of the spatio- and spectrotemporal data and determined the corresponding correlation times (fig. S4) (22). The correlation times are $\tau_{\text{corr}}^{(\lambda)} = 94$ ns and $\tau_{\text{corr}}^{(x)} = 83$ ns, respectively, for the measurements shown in Fig. 3. Therefore, the spatio- and spectrotemporal dynamics of the D-cavity laser feature the same characteristic time scales. They are about two orders of magnitude slower than those of the stripe laser (≤ 1 ns). These results were further confirmed by measurements of other D-cavity lasers with different size.

As seen in Fig. 3, B and D, the lasing emission from the straight segment of the D-cavity is spatially inhomogeneous. This inhomogeneity is not caused by defects on the sidewall, as confirmed by the smooth electroluminescence profile in Fig. 3A. When the pump current increases, a spatially inhomogeneous emission pattern gradually develops (see fig. S7). The intensity profile for 500 mA (Fig. 3F, dashed blue line) exhibits two distinct length scales. The coarse scale, on the order of several tens of micrometers, represents the size of the dark region in the middle and the bright regions of strong emission around it. The fine scale, on the order of a few micrometers, is the width of the narrow peaks inside the bright regions. Experimentally, the coarse scale is proportional to the cavity size (see

fig. S7), whereas the fine scale is limited by the spatial resolution of the imaging optics. According to numerical simulations (22), the coarse-scale emission profile reflects the sum of the intensity distributions of the passive D-cavity modes with high quality (Q) factors. Those high- Q modes within the gain spectrum correspond to the lasing modes because of their low thresholds, and their intensity distributions determine the total emission profile. The calculated emission intensity profile shown as red solid line in Fig. 3F (also see fig. S9) (22) agrees well with the coarse structure of the measured emission profile. While the coarse structure is maintained throughout the pulse, the fine-scale peaks appear or disappear over the course of the pulse as different lasing modes turn on or off.

Next, we show that the remaining fluctuations of the laser emission from wave-chaotic cavities result from thermal effects. The current injection causes sample heating, which modifies the refractive index of the cavity and the gain spectrum of the quantum well. Consequently, the lasing modes may change, leading to dynamic variations of the emission spectra as well as the spatial emission intensity distributions. To investigate the thermal effects, we increased the pump pulse length t_p to 200 μs . After the turn-on of the pump current, the sample temperature first rose quickly, then gradually stabilized. If heating effects were relevant, the lasing dynamics would slow down over time.

Figure 4A presents the spectrotemporal data for a D-cavity laser with $R = 200$ μm . Over a time

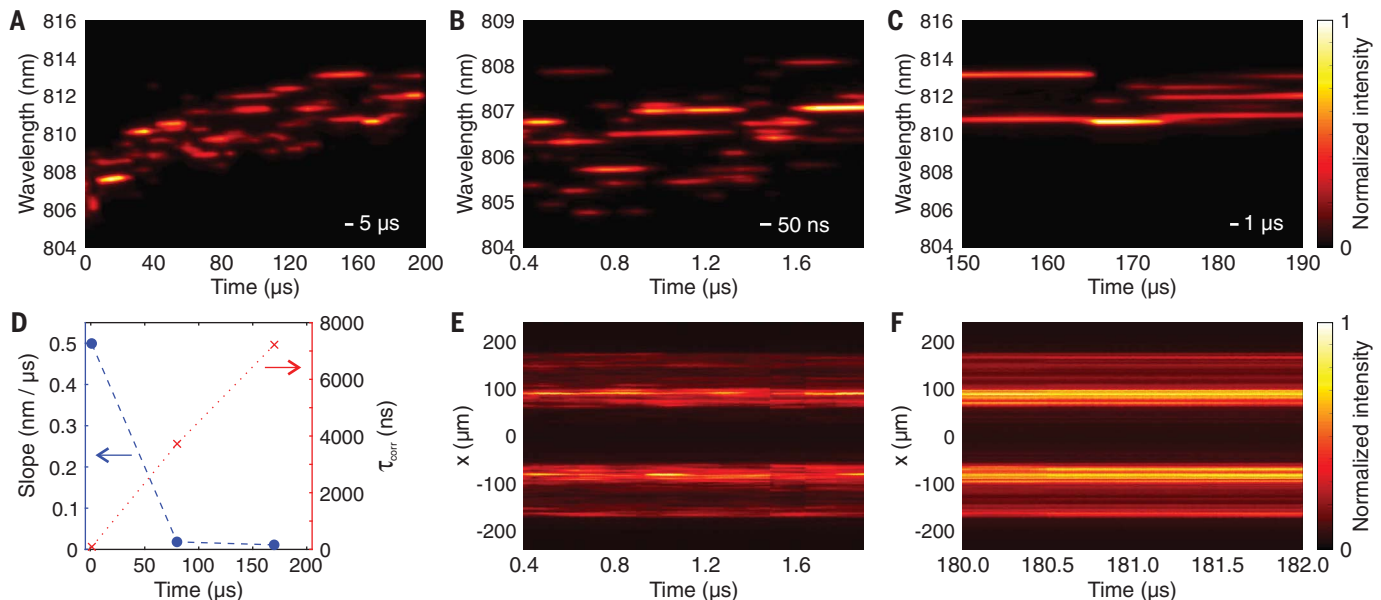


Fig. 4. Thermal effect on the lasing dynamics. A D-cavity laser fabricated by reactive ion etching with radius $R = 200 \mu\text{m}$ was pumped by a pulse $t_p = 200 \mu\text{s}$ long. The pump current was 800 mA; the lasing threshold was $I_{\text{th}} = 300 \text{ mA}$. (A) Spectrochronogram of the lasing emission for 0 to 200 μs measured with temporal resolution of 5 μs . The spectral shift to longer wavelengths is caused by an increase of the sample temperature. (B) Spectrochronogram for 0.4 to 1.9 μs measured with temporal resolution of 50 ns. (C) Spectrochronogram for 150 to 190 μs measured with

temporal resolution of 1 μs . (D) Rate of the red shift of the center of mass of the emission spectra (blue circles) and the spectral correlation times $\tau_{\text{corr}}^{(\lambda)}$ (red crosses) at different times during the 200- μs pulse. The red-shift slope decreases by almost two orders of magnitude as the sample temperature stabilizes, and conversely the spectral correlation time increases by two orders of magnitude. (E and F) Spatiotemporal image of the lasing emission during 0.4 to 1.9 μs (E) and during 180 to 182 μs (F), showing that the spatiotemporal dynamics becomes more stable with time.

interval of $t_p = 200 \mu\text{s}$, the lasing spectrum exhibits a continuous shift to longer wavelengths due to the increase of the sample temperature. However, the red shift of the lasing spectrum notably slows down during the later part of the pump pulse, and individual peaks last longer in time. We computed the center of mass (COM) for the time-resolved spectrum $\lambda_{\text{COM}}(t)$ and found that it is fitted well by an exponential function, $\lambda_{\text{COM}}^{(\text{fit})}(t) = \lambda_0 - \lambda_1 \exp(-t/\tau_{\text{th}})$, with a decay time $\tau_{\text{th}} = 174 \mu\text{s}$ (22). The slope $d\lambda_{\text{COM}}^{(\text{fit})}(t)/dt$ gives the rate of the spectral shift. The sample temperature gradually stabilizes during the pulse, as indicated by the decreasing slope of $\lambda_{\text{COM}}(t)$ from 0.5 nm/ μs during the first two microseconds to 0.01 nm/ μs at 170 μs (Fig. 4D).

To characterize the change of the time scale of the emission fluctuations, we measured the time-resolved spectra at different times during the 200- μs pulse with better temporal resolution. The spectral correlation time for a D-cavity laser increases from $\tau_{\text{corr}}^{(\lambda)} = 90 \text{ ns}$ during the first 2 μs (Fig. 4B) to 7.2 μs during the interval 150 to 190 μs (Fig. 4C). Figure 4D shows the correlation times and slope of λ_{COM} at different times during the pulse, illustrating how the emission fluctuations slow down as the temperature stabilizes. Spatiotemporal measurements also confirmed that the lasing dynamics become more stable with time (Fig. 4, E and F).

These results illustrate the effect of the temperature change on the lasing dynamics, and indicate that better thermal management can

lead to a further stabilization of the temporal dynamics of wave-chaotic lasers. This is in stark contrast to the wide-stripe lasers, which did not exhibit a stable dynamics at all. Fast oscillations and pulsations on a nanosecond time scale persisted until 200 μs , even though the emission spectra indicated that the sample had reached a thermal equilibrium after $\sim 50 \mu\text{s}$ (fig. S6) (22).

We also tested the D-cavity lasers fabricated by wet chemical etching. Although the cavity side-walls are not vertical and are rougher than for fabrication by reactive ion etching, the spatiotemporal and spectrotemporal dynamics of the lasing emission are very similar (fig. S11) (22). These results demonstrate the robustness of the stable lasing dynamics against fabrication imperfections in a wave-chaotic cavity. However, the spatial emission profile differs from that of a dry-etched cavity. This is attributed to the modification of the mode structures by the rough boundary, and was confirmed by numerical simulations (fig. S12) (22). Even in the presence of boundary roughness, the complex wave interference persists in the wave-chaotic cavities and suppresses the formation of filamentation and spatiotemporal instabilities. Consequently, the lasing emission profile is dictated by the passive cavity mode structure.

Lasing dynamics in disordered cavities

Although wave-chaotic cavities can efficiently suppress lasing instabilities, they lack emission directionality because of the absence of a pre-

dominant propagation direction. Therefore, the question arises whether we can suppress lasing instabilities via complex wave interference while obtaining directional emission.

We consider a simple 1D dielectric slab cavity with random fluctuations of the refractive index (Fig. 5B). The index fluctuations generate multiple reflected waves that interfere subsequently. Thus, the resonant modes no longer have a constant frequency spacing, and their spatial profiles become irregular with varying spatial scales (Fig. 5B and fig. S13), reminiscent of the modes in a 2D wave-chaotic cavity (fig. S8).

To simulate their lasing dynamics, we solved the semiconductor Maxwell-Bloch equations in the time domain. Our full-wave model goes beyond the slowly varying envelope/rotating wave (in time) and paraxial (in space) approximations, fully resolving the spatiotemporal dynamics on suboptical cycle and subwavelength scales (22). The population inversion-dependent optical gain has an asymmetric spectrum, which closely reproduces that of a semiconductor quantum well. Taking into account the dynamical coupling between the light field and the carrier system, we include all spatiotemporal and nonlinear effects such as spatial hole burning and multiwave mixing mediated by the carriers (29, 30).

We compare the simulated lasing dynamics of a disordered cavity to that of a homogeneous cavity with regular mode structure in Fig. 5A. The disordered cavity features stable lasing dynamics over a wide range of pump currents,

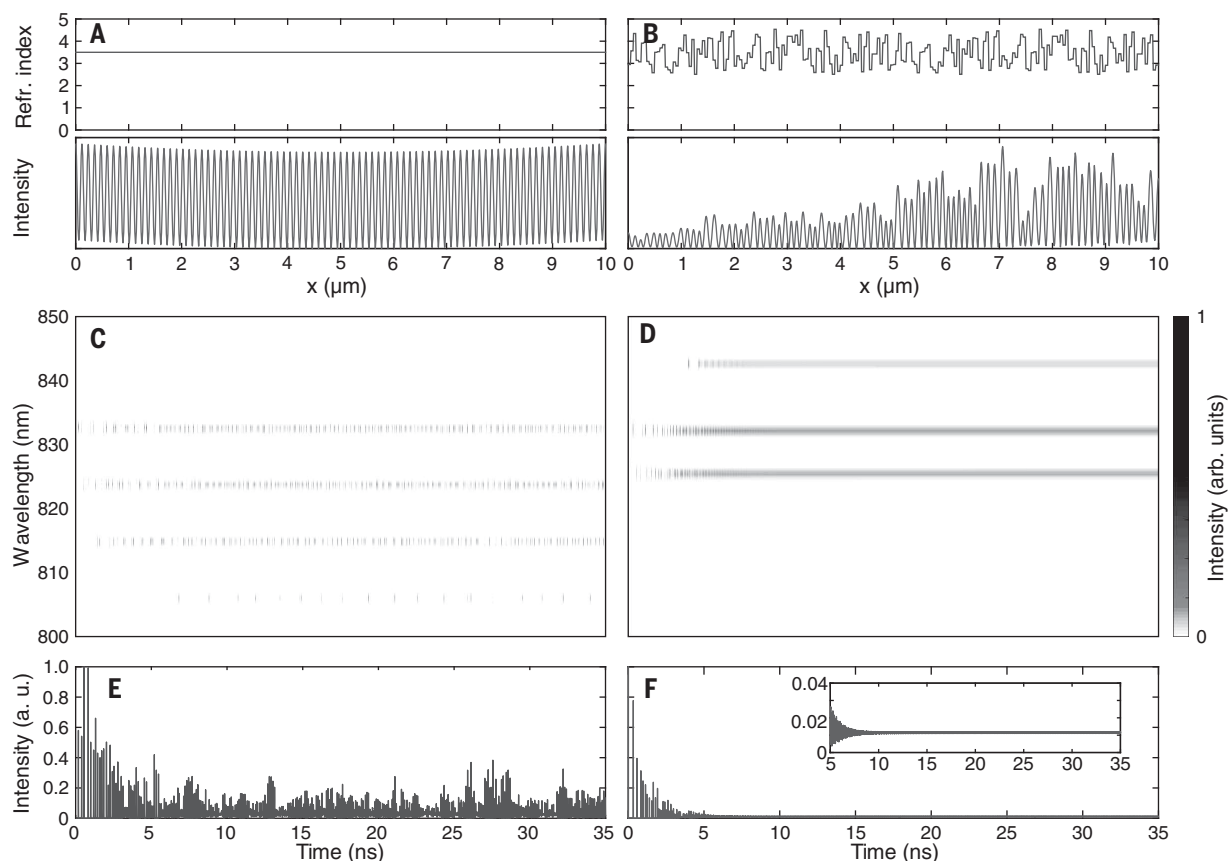


Fig. 5. Simulation of the lasing dynamics in one-dimensional cavities with homogeneous refractive index profile and spatially varying index profile, respectively, at the same pump current density $J = 500 \text{ A cm}^{-2}$. (A and B) Spatial distribution of the refractive index (top panels) and the field intensity (bottom panels) for a mode at $\lambda = 833.3 \text{ nm}$ in the homogeneous

cavity (A) and for a mode at $\lambda = 833.8 \text{ nm}$ in the disordered cavity (B). (C and D) Spectrochromogram of the emission intensity from the homogeneous cavity (C) and from the disordered cavity (D). (E and F) Total output intensity for the homogeneous cavity (E) and for the disordered cavity (F). The inset in (F) shows a magnification of the output intensity after 5 ns.

whereas lasing in the homogeneous cavity is stable only just above threshold and becomes unstable with increasing pump current (figs. S14 and S15) (22). For example, when the pump current is about five times the threshold value ($J_{\text{th}} = 104 \text{ A cm}^{-2}$), four longitudinal modes lase in the homogeneous cavity, and all modes pulsate irregularly on a subnanosecond time scale (Fig. 5C). The total emission intensity in Fig. 5E fluctuates in time and does not approach a constant value even well beyond the transient dynamics. These instabilities are caused by the nonlinear interactions between the lasing modes and the gain medium through processes such as spatial hole burning and multiwave mixing (37).

The disordered cavity, with a lasing threshold ($J_{\text{th}} = 96 \text{ A cm}^{-2}$) almost identical to that of the homogeneous cavity, has three modes lasing at the same pump current density. After some initial pulsations, each lasing mode reaches a steady state (Fig. 5D). The total output intensity also approaches a constant value beyond the transient period (Fig. 5F). The stable state of multimode lasing is reached more quickly at higher pump current (fig. S15) (22).

Therefore, even in a 1D cavity, the interference of multiple scattered waves with random phases

can lead to stable lasing dynamics, and the stabilization is complete in the absence of thermal effects. These results confirm the generic nature of our scheme to suppress spatiotemporal instabilities by increasing the spatial complexity of the lasing modes.

Discussion and conclusion

Our approach for obtaining a stable state of multimode lasing in broad-area edge-emitting semiconductor lasers is fundamentally different from previous ones in several respects. Most previous approaches aim at suppressing the spatiotemporal instabilities and the formation of self-organized structures such as filaments by minimizing the number of lasing modes. Our approach maintains multimode lasing while achieving stable temporal dynamics by using cavities with chaotic ray dynamics or with random refractive index fluctuations to tailor the spatial properties of the lasing modes. Although the mechanisms causing lasing instabilities in 1D and 2D cavities are different, both are disrupted by complex wave interference. Because this process is present across the whole cavity, we attain global suppression of the instabilities, in contrast to schemes such as injection and

feedback that can influence the dynamics only locally.

Note that our scheme of achieving stable multimode operation is very robust with respect to perturbations such as boundary roughness, because such perturbations do not qualitatively change the already pseudo-random structure of the lasing modes. Although small modifications of the cavity geometry of broad-area edge-emitting semiconductor lasers were considered previously (32–35), a dominant propagation direction and thus well-defined wave fronts were maintained, and the spatial scales of the modes were not substantially modified, in stark contrast to the wave-chaotic and disordered cavities presented here.

Although the multimode operation of D-cavity lasers produces emission with relatively low spatial coherence (36), which prevents tight focusing, the temporal stability of the lasing power and the emission profile, as shown in this work, is essential to produce stable beam profiles necessary for many high-power applications. For example, laser processing of materials and devices requires diverse beam shapes such as circular flat-top, square, rectangle, or line profiles, and various beam-shaping techniques have

been developed in recent years (37). Low spatial coherence of the laser beams prevents coherent artifacts and enables smooth intensity profiles; for example, the D-cavity laser emission may be coupled to a multimode fiber to produce a stable flat-top beam free of speckle. Another potential application is pumping high-power multimode fiber lasers and amplifiers.

In previous studies, broad-area vertical-cavity surface-emitting lasers (VCSELs) with pulsed pumping have demonstrated nonmodal emission with low spatial coherence, when the interplay between a rapid thermal chirp and the build-up of a thermal lens breaks up the global cavity modes (38). As the VCSEL becomes thermally stable with time, the multimode operation resumes and fast temporal dynamics appears. This is fundamentally different from wave-chaotic cavities in which the stable state of lasing is maintained in multimode operation. It should be mentioned that random fiber lasers can also exhibit temporal fluctuations (39), which disappear for stronger pumping. Both the mechanism inducing the instabilities [interplay between stimulated Brillouin scattering (SBS) and Rayleigh scattering] and that quenching the instabilities (suppression of SBS) are distinct from those for the 1D disordered semiconductor lasers we simulated (22).

We therefore propose the demonstrated suppression of lasing instabilities by means of complex multiwave interference as a new paradigm for manipulating the temporal dynamics of multimode lasers. We believe it is generally applicable to other high-power lasers exhibiting instabilities, such as broad-area VCSELs and solid-state lasers, as well as multimode fiber lasers and amplifiers. By deforming the cavity or fiber cross section or introducing random refractive index fluctuations, the spatial mode structure becomes speckled, preventing lens formation and self-focusing instabilities. On a more general level, this work opens a new direction of research combining concepts from both wave-dynamical chaos and deterministic chaos. This combination and its

implications have been barely investigated so far in lasers or other nonlinear wave-dynamical systems. We expect that the idea of manipulating nonlinear temporal dynamics by disrupting the formation of self-organized structures not only will have an impact on laser physics but also will find applications in other systems with complex spatiotemporal dynamics.

REFERENCES AND NOTES

- M. P. Hassell, H. N. Comins, R. M. Mayt, *Nature* **353**, 255–258 (1991).
- I. R. Epstein, K. Showalter, *J. Phys. Chem.* **100**, 13132–13147 (1996).
- J. P. Graves *et al.*, *Nat. Commun.* **3**, 624 (2012).
- E. Altshuler, T. H. Johansen, *Rev. Mod. Phys.* **76**, 471–487 (2004).
- N. B. Abraham, L. A. Lugiato, L. M. Narducci, *J. Opt. Soc. Am. B* **2**, 7 (1985).
- G. Huyet, M. C. Martinoni, J. R. Tredicce, S. Rica, *Phys. Rev. Lett.* **75**, 4027–4030 (1995).
- J. Ohtsubo, *Semiconductor Lasers: Stability, Instability and Chaos* (Springer, 2013).
- I. Fischer, O. Hess, W. Elsässer, E. Göbel, *Europhys. Lett.* **35**, 579–584 (1996).
- O. Hess, *Chaos Solitons Fractals* **4**, 1597–1618 (1994).
- O. Hess, T. Kuhn, *Phys. Rev. A* **54**, 3360–3368 (1996).
- J. Marcianite, G. Agrawal, *IEEE J. Quantum Electron.* **33**, 1174–1179 (1997).
- J. R. Marcianite, G. P. Agrawal, *IEEE Photonics Technol. Lett.* **10**, 54–56 (1998).
- D. Scholz *et al.*, *Opt. Express* **16**, 6846–6859 (2008).
- M. Arahata, A. Uchida, *IEEE J. Sel. Top. Quantum Electron.* **21**, 1800609 (2015).
- T. Pawletko, M. Houssin, M. Knoop, M. Vedel, F. Vedel, *Opt. Commun.* **174**, 223–229 (2000).
- S. Takimoto, T. Tachikawa, R. Shogenji, J. Ohtsubo, *IEEE Photonics Technol. Lett.* **21**, 1051–1053 (2009).
- J. Martín-Regalado, G. H. M. van Tartwijk, S. Balle, M. S. Miguel, *Phys. Rev. A* **54**, 5386–5393 (1996).
- S. K. Mandre, I. Fischer, W. Elsässer, *Opt. Commun.* **244**, 355–365 (2005).
- C. Zink, M. Niebuhr, A. Jechow, A. Heuer, R. Menzel, *Opt. Express* **22**, 14108–14113 (2014).
- H. Hodaie, M.-A. Miri, M. Heinrich, D. N. Christodoulides, M. Khajavikhan, *Science* **346**, 975–978 (2014).
- W. Liu *et al.*, *Nat. Commun.* **8**, 15389 (2017).
- See supplementary materials.
- H. E. Türeci, G. L. Schwefel, P. Jacquod, A. D. Stone, *Prog. Opt.* **47**, 75–137 (2005).
- T. Harayama, S. Shinohara, *Laser Photonics Rev.* **5**, 247–271 (2010).
- H. Cao, J. Wiersig, *Rev. Mod. Phys.* **87**, 61–111 (2015).
- H.-J. Stöckmann, *Quantum Chaos: An Introduction* (Cambridge Univ. Press, 2000).
- Y.-F. Xiao *et al.*, *Front. Optoelectron. China* **3**, 109–124 (2010).
- X. Jiang *et al.*, *Science* **358**, 344–347 (2017).
- S. Guazzotti, A. Pusch, D. E. Reiter, O. Hess, *Phys. Rev. B* **94**, 115303 (2016).
- K. Böhringer, O. Hess, *Prog. Quantum Electron.* **32**, 159–246 (2008).
- L. Furfaro *et al.*, *IEEE J. Quantum Electron.* **40**, 1365–1376 (2004).
- H. Adachi, O. Hess, E. Abraham, P. Ru, J. V. Moloney, *J. Opt. Soc. Am. B* **10**, 658 (1993).
- G. Levy, A. Hardy, *IEEE J. Quantum Electron.* **33**, 26–32 (1997).
- C. Simmendinger, D. Preiß, O. Hess, *Opt. Express* **5**, 48–54 (1999).
- A. Büttner, U. D. Zeitner, R. Kowarschik, *J. Opt. Soc. Am. B* **22**, 796 (2005).
- B. Redding *et al.*, *Proc. Natl. Acad. Sci. U.S.A.* **112**, 1304–1309 (2015).
- K. Fuse, *Laser Tech. J.* **12**, 19–22 (2015).
- S. K. Mandre, W. Elsässer, I. Fischer, M. Peeters, G. Verschaffelt, *Opt. Express* **16**, 4452–4464 (2008).
- S. K. Turitsyn *et al.*, *Nat. Photonics* **4**, 231–235 (2010).

ACKNOWLEDGMENTS

H.C. and S.B. thank A. D. Stone, H. Türeci, L. Ge, J. Andreasen, and C. Vanneste for fruitful discussions. **Funding:** The work conducted at Yale University is supported partly by the Office of Naval Research (ONR) with MURI grant N00014-13-1-0649, and by the Air Force Office of Scientific Research (AFOSR) under grant FA9550-16-1-0416. The research at Imperial College London is partly supported by the Engineering and Physical Sciences Research Council (EPSRC) UK through projects EP/L024926/1 and EP/L027151/1, by AFOSR under grant FA9550-14-1-0181, and with funding by the European Regional Development Fund through the Welsh Government. For the work at Nanyang Technological University, funding support is acknowledged from the Singapore Ministry of Education Tier 2 Program (MOE 2016-T2-1-128) and the Singapore National Research Foundation Competitive Research Program (NRF-CRP18-2017-02). **Author contributions:** S.B. conducted experimental characterization and data analysis, and prepared the manuscript; H.Y., Y.Z., X.H., and Q.J.W. did sample fabrications; K.K. calculated the resonant modes in D-cavities; S.G. and S.S.O. modeled the semiconductor laser dynamics; O.H. guided the theory of complex semiconductor laser dynamics and edited the paper; and H.C. proposed the idea, initiated the research, and edited the paper. **Competing interests:** The authors declare no competing financial interests. **Data and materials availability:** All data needed to evaluate the conclusions in the paper are present in the paper or the supplementary materials.

SUPPLEMENTARY MATERIALS

www.sciencemag.org/content/361/6408/1225/suppl/DC1
Materials and Methods
Supplementary Text
Figs. S1 to S15
Table S1
References (40–42)

5 February 2018; accepted 1 August 2018
Published online 16 August 2018
10.1126/science.aas9437

REPORT

ASTEROSEISMOLOGY

Asteroseismic detection of latitudinal differential rotation in 13 Sun-like stars

O. Benomar^{1,*}, M. Bazot¹, M. B. Nielsen¹, L. Gizon^{1,2,3}, T. Sekii⁴, M. Takata⁵, H. Hotta⁶, S. Hanasoge^{1,7}, K. R. Sreenivasan^{1,8}, J. Christensen-Dalsgaard⁹

The differentially rotating outer layers of stars are thought to play a role in driving their magnetic activity, but the underlying mechanisms that generate and sustain differential rotation are poorly understood. We report the measurement using asteroseismology of latitudinal differential rotation in the convection zones of 40 Sun-like stars. For the most significant detections, the stars' equators rotate approximately twice as fast as their midlatitudes. The latitudinal shear inferred from asteroseismology is much larger than predictions from numerical simulations.

Analysis of acoustic oscillations visible on the Sun's surface by using helioseismology has been critical for constraining its rotation profile. Helioseismology has revealed that the rotation rate of the Sun's convection zone decreases with latitude (*1, 2*). This latitudinal differential rotation has a magnitude of 11% of the average rate from equator to midlatitudes ($\approx 45^\circ$ latitude) and 30% between equator and the poles. At the base of the convection zone, the Sun transitions to solid-body rotation. How such a rotation profile is established and maintained is still poorly understood. However, it is likely that differential rotation plays a role in sustain-

ing the solar magnetic field through a dynamo mechanism (*3–5*).

So far, little is known about the latitudinal differential rotation in other stars, and classical methods for investigating it are primarily sensitive to the near-surface layers. Most studies rely on photometric variability from starspots at different latitudes (*6*) or use Doppler imaging to track magnetic features at the surface and their migration in latitude (*7, 8*). Another approach involves studying the Fourier transform of the spectroscopic line profiles (*9, 10*).

Asteroseismology provides an opportunity to probe rotation inside stars, including Sun-like

pulsators (*11–13*), because it studies the resonant frequencies of waves within the body of the star. Among these are acoustic waves that travel at various depths and have a varying sensitivity to rotation with latitude. These acoustic waves can be used to infer the star's internal rotation both in radius and latitude (*14–17*).

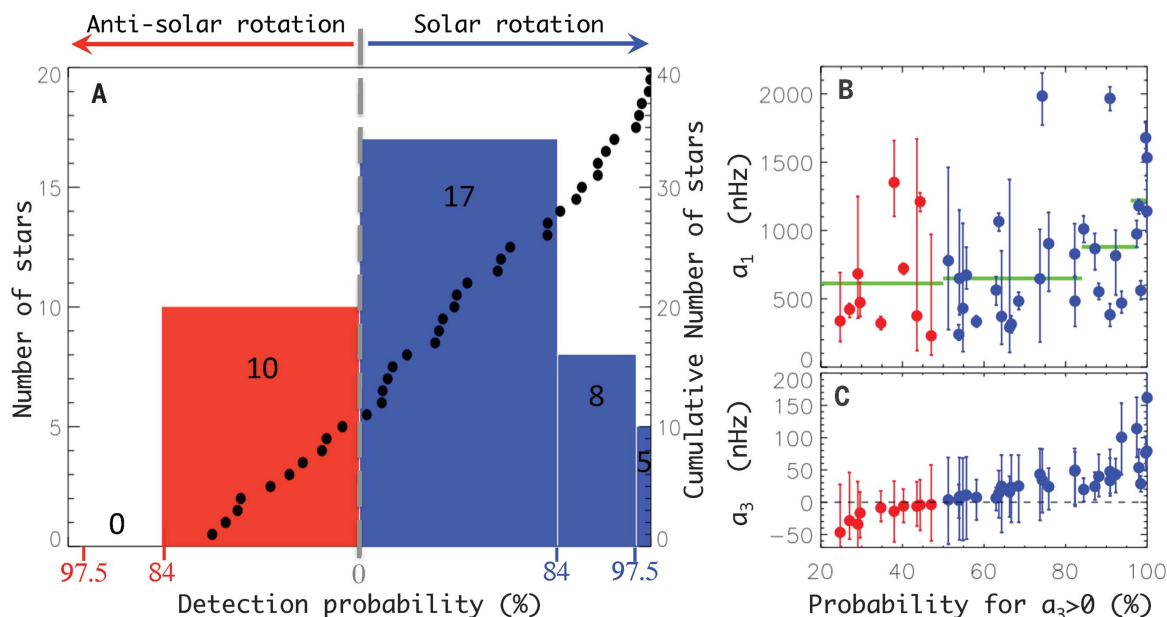
The NASA *Kepler* spacecraft has provided high-precision, long-duration photometric time series for many stars, which is necessary for the study of the differential rotation of Sun-like stars with asteroseismology.

Oscillations of Sun-like stars are driven by the stochastic convective motion of material in the outer envelope of the stars. Each mode of oscillation is identified by the overtone number *n* and spherical harmonic functions of angular degree *l* and azimuthal order *m*. Modes with the same *n* and *l* but different *m* appear as multiplets of $2l + 1$ components. The splitting of modes in a multiplet provides information about the rotation profile and on the physical processes acting within the star (such as flows, internal structure, and tidal forces).

An efficient means for quantifying the impact of rotation on the split frequencies of acoustic

Fig. 1. Detection of solar rotation and antisolar rotation.

(A) Histogram of the detection significance for solarlike versus antisolar rotation by using *Kepler* asteroseismic light curves (colored bars). The cumulative distribution is also shown (black dots). All stars with conclusive detections of $a_3 \neq 0$ ($>84\%$ significance) have solarlike rotation ($a_3 > 0$). (B) Average internal rotation as measured with a_1 . Stars with high detection significance rotate faster than those with low significance. (C) The latitudinal differential rotation coefficient a_3 .



waves is through the use of Clebsch-Gordan a -coefficients a_1, a_2, a_3, \dots (18). This decomposition has been used extensively in helioseismology but not in the analysis of other stars. For stars other than the Sun, only low-degree modes ($l \leq 3$) can be observed, and so only the coefficients a_1, a_2 , and a_3 can be determined. The coefficient a_1 is an average of the rotation rate. The a_2 coefficient is related to the asphericity (19), and a_3 is a measure of the latitudinal differential rotation (16). The coefficient a_3 is positive when the pole rotates slower than the equator—that is, if the star exhibits a solarlike rotation profile (fig. S1). Conversely, a_3 is negative for antisolar rotation profiles. Simulations tend to show that fast rotation causes solarlike rotation, whereas slower rotation rates lead to antisolar rotation (20–22), although simulations found an antisolar rotation at solar rotation rates (21, 22). This is evidently incompatible with solar observations, and constraints from other stars are necessary to resolve this issue.

Pulsations appear as Lorentzian profiles in a power spectrum of the star's photometric time series (23). The analysis of the pulsations is performed by fitting a model to the power spectrum by using a Markov chain Monte Carlo (MCMC) sampling technique (11). The contribution of a_1 to mode frequencies is easily measured, but the absolute value of a_3 is approximately two orders of magnitude smaller than a_1 , so it is only possible to measure it by using multiyear observations from space instruments such as *Kepler*.

We performed a combined measurement of the a_1 and a_3 coefficients for 40 stars of mass between 0.9 and 1.5 M_\odot (where M_\odot is the mass of the Sun), observed as part of the *Kepler* LEGACY sample (24, 25). By integrating the probability density functions of a_3 determined by fitting the power spectra, we computed the detection significance for either solar or antisolar latitudinal differential rotation (Fig. 1 and table S1). Applying a detection threshold at a probability of 84% (excluding $a_3 = 0$ with a detection significance $>1\sigma$ for a Gaussian), we found that none of the stars unambiguously show antisolar rotation, whereas 32% (13 stars) show significant solarlike rotation. Five stars have a detection probability of more than 97.5% (or a significance $>2\sigma$). The excess of solarlike rotators may be due to an observational limitation. Antisolar differential rotation is theoretically expected (20, 26) for slow rotators, in which a_1 and a_3 are difficult to measure. Our sample consists predominantly of fast rotators, so we may only be sensitive to stars with solarlike rotation profiles. Our most statistically significant detections have relatively high rotation rates compared with those below the detection threshold.

The Rossby number is an indicator of the influence of rotation on a fluid compared with convective motion. Current theory (20) predicts that solarlike rotators should have a Rossby number less than unity. For the majority of our significant detections, we found a Rossby number less than 0.8 (fig. S2).

We next sought to estimate the rotational shear between the equator and higher latitudes. For

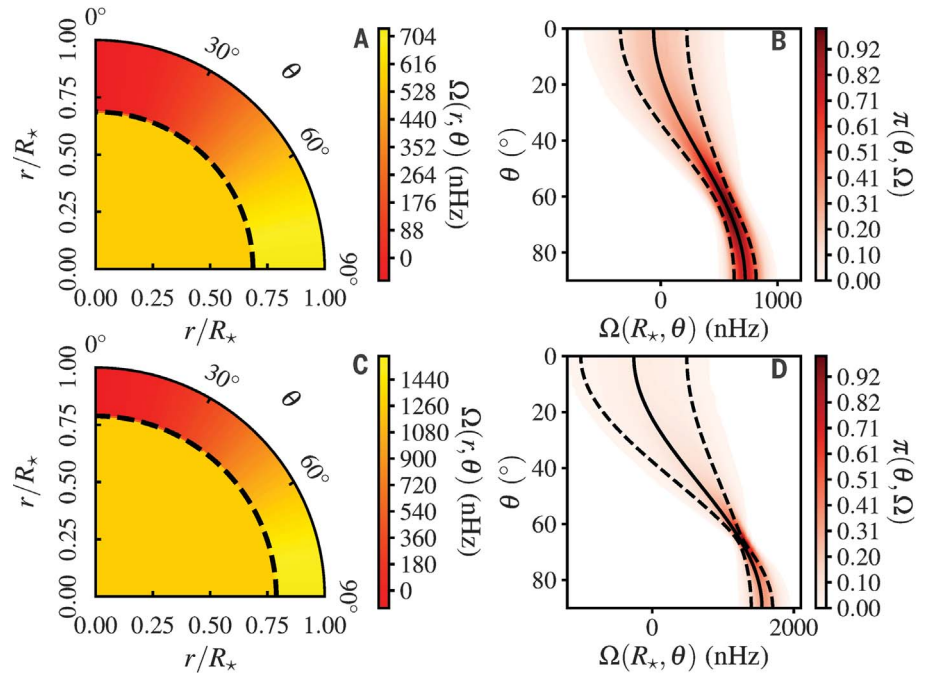


Fig. 2. Rotation profiles from inversion for HD 173701 and HD 187160. (A and B) HD 173701. (C and D) HD 187160. (A) and (C) display the most likely rotation profile (colors) and the interface between radiative and convective zone (dashed lines). (B) and (D) show the probability density, $\pi(\theta, \Omega)$, at each latitude of the rotation profile in the convection zone (red-shaded region). The 1σ confidence interval is highlighted with dashed lines. The latitudinal differential rotation is well constrained for colatitudes $\theta > 45^\circ$.

this, we selected two representative stars (HD 173701 and HD 187160) in terms of a_1, a_3 , and internal structure (thickness of convection zone). Their power spectra are shown in figs. S3 and S4 with the best-fitting model. HD 173701 is a cool dwarf of spectral type G8 (the Sun is of spectral type G2), with a mass $0.974 \pm 0.029 M_\odot$ and age 4.69 ± 0.44 billion years (24). It is known to be very active (27), with irregular variability on time scales that range from 8 to 40 days, likely caused by starspots. The probability density function deduced from the fit indicates that $a_1 = 574.6 \pm 82.0$ nHz and $a_3 = 28.4 \pm 12.5$ nHz (fig. S5). HD 187160 is of spectral type F9 and has a mass and age of $1.09 \pm 0.03 M_\odot$ and 3.28 ± 0.16 billion years. Thus, HD 187160 is similar to a younger version of the Sun. It has a visible magnitude of 7.4 and a faint, cool spectroscopic binary companion of magnitude 8.7 (28). The average internal rotation period is ~ 9 days ($a_1 = 1185.0 \pm 51.7$ nHz). The light curve of HD 187160 shows variability at two distinct time scales, one at ~ 9.4 days and another at ~ 17.5 days. We attribute this variability to starspots on the surfaces of HD 187160 and its fainter noninteracting companion, respectively. We measured $a_3 = 53.7 \pm 25.0$ nHz (fig. S6).

We have evaluated the potential systematic errors associated with the mode-fitting methodology using simulated power spectra for HD 173701 and HD 187160 (23). These systematic errors are small, meaning that a_3 in both cases is positive, with a probability higher than 97.5%.

This confirms that these stars have poles that rotate slower than the equator.

To obtain a latitudinal rotation profile, we used an inversion of the a -coefficients (16). Because we only measured a_1 and a_3 , we were restricted to a two-parameter rotation model for this. We assumed a solarlike rotation profile $\Omega(\theta) = \Omega_0 + 3\Omega_1(5\cos^2\theta - 1)/2$ in the convection zone, where θ is the colatitude (complementary angle of the latitude so that $\theta = 0$ is the pole and $\theta = 90^\circ$ is the equator). The average internal rotation rate is given by Ω_0 , and the term in $\Omega_1 \propto \Omega_{\text{pole}} - \Omega_{\text{eq}}$ measures the contrast in rotation (latitudinal shear) from the equator to the pole in the convection zone. In the equation, Ω_{pole} and Ω_{eq} are the pole and equator rotation rates, respectively. The convection zone extends from the surface down to $0.687R_\star$ for HD 173701 and to $0.785R_\star$ for HD 187160, where R_\star is the stellar radius. Because of its relatively fast rotation, HD 187160 was investigated for possible variations of a_1 with the overtone n (fig. S7). We did not find evidence of significant variation. Studies of radial differential rotation of low-mass main-sequence stars indicate that variation in a_1 should not exceed 30% (29), and we therefore do not expect this to have an effect on the inversion.

The fundamental properties of the stellar models assumed for the inversion and the results of the inversion are provided in tables S2 and S3, respectively. The two-dimensional rotation profiles and the probability density of the rotation rate are shown in Fig. 2 at different latitudes for

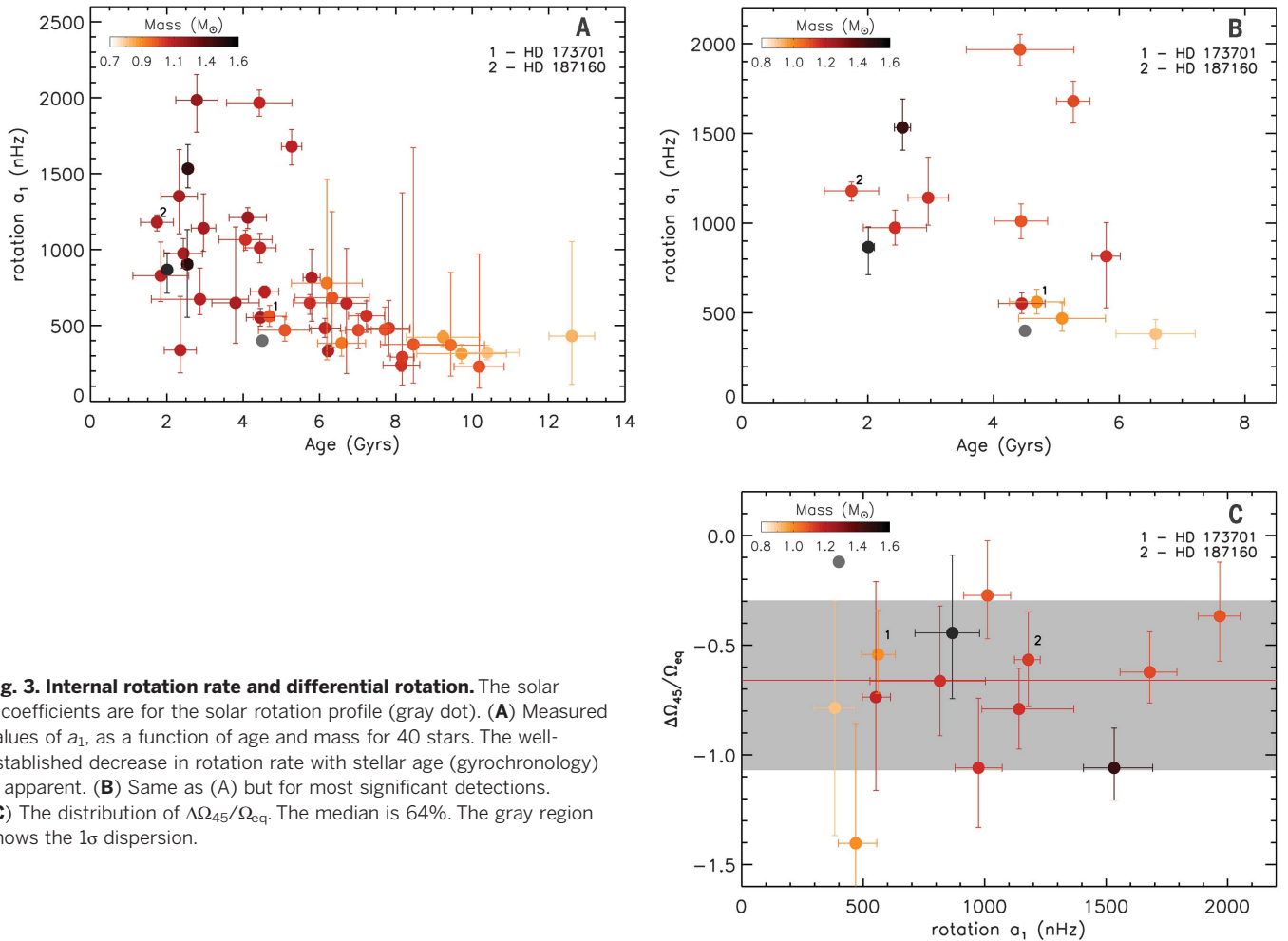


Fig. 3. Internal rotation rate and differential rotation. The solar a -coefficients are for the solar rotation profile (gray dot). (A) Measured values of a_1 , as a function of age and mass for 40 stars. The well-established decrease in rotation rate with stellar age (gyrochronology) is apparent. (B) Same as (A) but for most significant detections. (C) The distribution of $\Delta\Omega_{45}/\Omega_{eq}$. The median is 64%. The gray region shows the 1σ dispersion.

both stars. By construction, the profile is symmetric around the equator and around the rotation axis, so only one quadrant is shown. The rotation rate in the interior matches that of the envelope at a latitude of 26.5° ($\theta = 63.5^\circ$) because of the structure of the two-zone rotation profile. As is shown by the probability density of the rotation profile, the uncertainty on the rotation rate increases substantially toward the poles, beyond a value of $\sim 45^\circ$ latitude. At high latitudes, the modes become much less sensitive to rotation, thus yielding less information. This limit is imposed by the lack of visible modes with an angular degree higher than $l = 2$ in the spectrum. We found that both HD 173701 and HD 187160 exhibit a latitudinal shear from equator to 45° latitude $\Delta\Omega_{45}/\Omega_{eq}$ which is approximately five times greater than that of the Sun.

As suggested by numerical simulations, the fast rotation of HD 187160 means that the functional form of its rotation profile may not be solarlike (23). We have considered this possibility for HD 187160 (fig. S8) and found that alternative rotation profiles have larger latitudinal shear than the solarlike rotation profile. However, computation of the Bayesian evidence (necessary to de-

termine the goodness of the fit) shows that the solarlike profile is the most likely model.

Because of loss of angular momentum, such as from magnetic braking, a star's rotation is expected to slow with its age (t). This age-rotation relation is apparent in our data: Fig. 3, A and B, shows a_1 as a function of the age given by stellar models (25).

As shown in Fig. 3C, the latitudinal shear between the equator and midlatitude for the subset of 13 stars with significant detections is $\sim 60\%$, albeit with a large scatter. HD 173701 and HD 187160 are representative of this ensemble, with a differential rotation of $\sim 50\%$. The Sun has a significantly lower shear factor than that of the considered ensemble. The difference is of more than 1σ from the dispersion of the ensemble.

This unexpectedly large shear poses a challenge to theoretical models. The balance between angular momentum transport (owing to anisotropy in the turbulent flow) and small-scale flows, which act as enhanced turbulent viscosity, plays a dominant role in regulating latitudinal shear (30). The large shear we found indicates a correspondingly large anisotropy in the turbulence, leading to efficient angular momentum transport and suppression of turbulent viscosity. In a

typical stellar convection zone, turbulent anisotropy, driven by rotation, substantially affects large-scale flows. Thus, enhanced angular momentum transport and diminished turbulent viscosity amplify large-scale flows and suppress small-scale flows. This could be caused by a very efficient small-scale dynamo, in which small-scale flows are suppressed (31). In addition, large-scale magnetic fields tend to reduce shear through the Lorentz force (32). However, our results indicate that Lorentz-force feedback is ineffective in the stars we investigated. Thus, the large-scale magnetic field is likely transported efficiently into the deeper regions of the star in which rigid rotation is expected. For this, magnetic pumping is a candidate mechanism (33).

REFERENCES AND NOTES

1. M. J. Thompson, J. Christensen-Dalsgaard, M. S. Miesch, J. Toomre, *Annu. Rev. Astron. Astrophys.* **41**, 599–643 (2003).
2. J. Schou et al., *Astrophys. J.* **505**, 390–417 (1998).
3. P. Charbonneau, *Living Rev. Sol. Phys.* **7**, 3 (2010).
4. M. Ossendrijver, *Astron. Astrophys. Rev.* **11**, 287–367 (2003).
5. E. N. Parker, *Astrophys. J.* **122**, 293 (1955).
6. K. Oláh et al., *Astron. Astrophys.* **501**, 703–713 (2009).
7. J. R. Barnes et al., *Mon. Not. R. Astron. Soc.* **357**, L1–L5 (2005).
8. J.-F. Donati, A. Collier Cameron, *Mon. Not. R. Astron. Soc.* **291**, 1–19 (1997).

9. A. Reiners, J. H. M. M. Schmitt, M. Kürster, *Astron. Astrophys.* **376**, L13–L16 (2001).
10. D. F. Gray, *Astrophys. J.* **211**, 198 (1977).
11. O. Benomar, M. Takata, H. Shibahashi, T. Ceillier, R. A. García, *Mon. Not. R. Astron. Soc.* **452**, 2654–2674 (2015).
12. L. Gizon *et al.*, *Proc. Natl. Acad. Sci. U.S.A.* **110**, 13267–13271 (2013).
13. T. Appourchaux *et al.*, *Astron. Astrophys.* **488**, 705–714 (2008).
14. M. N. Lund *et al.*, *Astron. Astrophys.* **570**, A54 (2014).
15. C. Aerts, J. Christensen-Dalsgaard, D. Kurtz, *Asteroseismology* (Springer Science, ed. 1, 2010).
16. L. Gizon, S. K. Solanki, *Sol. Phys.* **220**, 169–184 (2004).
17. L. Gizon, S. K. Solanki, *Astrophys. J.* **589**, 1009–1019 (2003).
18. J. Schou, J. Christensen-Dalsgaard, M. J. Thompson, *Astrophys. J.* **433**, 389 (1994).
19. L. Gizon *et al.*, *Sci. Adv.* **2**, e1601777 (2016).
20. T. Gastine, J. Wicht, J. M. Aurnou, *Icarus* **225**, 156–172 (2013).
21. H. Hotta, M. Rempel, T. Yokoyama, *Astrophys. J.* **798**, 51 (2015).
22. Y. Fan, F. Fang, *Astrophys. J.* **789**, 35 (2014).
23. Materials and methods are available as supplementary materials.
24. M. N. Lund *et al.*, *Astrophys. J.* **835**, 172 (2017).
25. V. Silva Aguirre *et al.*, *Astrophys. J.* **835**, 173 (2017).
26. N. A. Featherstone, M. S. Miesch, *Astrophys. J.* **804**, 67 (2015).
27. R. Kiefer, A. Schad, G. Davies, M. Roth, *Astron. Astrophys.* **598**, A77 (2017).
28. B. D. Mason, G. L. Wycoff, W. I. Hartkopf, G. G. Douglass, C. E. Worley, *Astron. J.* **122**, 3466–3471 (2001).
29. M. B. Nielsen, H. Schunker, L. Gizon, J. Schou, W. H. Ball, *Astron. Astrophys.* **603**, A6 (2017).
30. H. Hotta, M. Rempel, T. Yokoyama, *Science* **351**, 1427–1430 (2016).
31. M. Rempel, *Astrophys. J.* **789**, 132 (2014).
32. B. B. Karak *et al.*, *Astron. Astrophys.* **576**, A26 (2015).
33. N. H. Brummell, T. L. Clune, J. Toomre, *Astrophys. J.* **570**, 825–854 (2002).

ACKNOWLEDGMENTS

The authors thank T. R. White and S. Kamiaka for their helpful discussions. **Funding:** This work is supported by NYUAD institute grant G1502. Research funding from the German Aerospace Center (Grant 50001501) and the Max Planck Society (PLATO Science) is acknowledged. Funding for the Stellar Astrophysics Centre is provided by The Danish National Research Foundation (grant DNR106). The research was supported by the ASTERISK project (ASTERoseismic Investigations with SONG and *Kepler*) funded by the European Research

Council (grant agreement 267864). Funding for the *Kepler* mission is provided by the NASA Science Mission directorate. **Author contributions:** O.B., M.B., and L.G. designed the research. O.B. performed seismic analyses and lead in writing the manuscript. M.B. performed seismic inversion. M.B.N. analyzed the light curves variability. All authors discussed the results and contributed to sections of the manuscript. **Competing interests:** None declared. **Data and materials availability:** This paper includes data collected by the *Kepler* mission, provided by the Kepler Asteroseismic Science Operations Center (KASOC) and available at <https://doi.org/10.7910/DVN/8SK6OL>. Further details on the data used are listed in table S4. The TAMCMC analysis code is available at <https://github.com/OthmanB/TAMCMC-C>.

SUPPLEMENTARY MATERIALS

www.sciencemag.org/content/361/6408/1231/suppl/DC1
Materials and Methods
Figs. S1 to S8
Tables S1 to S4
References (34–75)

24 August 2017; accepted 25 July 2018
10.1126/science.aao6571

ORGANIC CHEMISTRY

Unlocking P(V): Reagents for chiral phosphorothioate synthesis

Kyle W. Knouse^{1*}, Justine N. deGruyter^{1*}, Michael A. Schmidt^{2†}, Bin Zheng², Julien C. Vantourout¹, Cian Kingston¹, Stephen E. Mercer³, Ivar M. McDonald³, Richard E. Olson³, Ye Zhu², Chao Hang², Jason Zhu², Changxia Yuan², Qinggang Wang², Peter Park⁴, Martin D. Eastgate^{2†}, Phil S. Baran^{1†}

Phosphorothioate nucleotides have emerged as powerful pharmacological substitutes of their native phosphodiester analogs with important translational applications in antisense oligonucleotide (ASO) therapeutics and cyclic dinucleotide (CDN) synthesis. Stereocontrolled installation of this chiral motif has long been hampered by the systemic use of phosphorus(III) [P(III)]-based reagent systems as the sole practical means of oligonucleotide assembly. A fundamentally different approach is described herein: the invention of a P(V)-based reagent platform for programmable, traceless, diastereoselective phosphorus-sulfur incorporation. The power of this reagent system is demonstrated through the robust and stereocontrolled synthesis of various nucleotidic architectures, including ASOs and CDNs, via an efficient, inexpensive, and operationally simple protocol.

Molecular-based gene therapy is rapidly emerging as one of the most promising modes of disease amelioration, as evidenced by the swell of clinical trials employing microRNA, small interfering RNA, and antisense oligonucleotides (ASOs) (1). In a recent example, the ASO nusinersen (trade name Spinraza) (Fig. 1A) was approved by the U.S. Food and Drug Administration (FDA) as the sole available treatment of spinal muscular atrophy, the leading genetic cause of infant mortality (2). This breakthrough therapy comprises 18 nucleosides bound by phosphorothioate (PS) linkages (i.e., those in which one of the nonbridging oxygen atoms has been substituted with a sulfur). Compared with the native phosphodiester linkage, this simple modification confers a higher degree of metabolic stability and improved cellular uptake through an observation known as the thio effect (3–6). In fact, most FDA-approved ASOs incorporate this moiety, with numerous candidates under clinical evaluation (7). Although the PS alteration enhances the pharmacological profile of these systems, it comes at the expense of substantially increased structural complexity—each phosphorus atom is now an uncontrolled stereogenic center (8). Thus, in the case of Spinraza, patients receive a mixture of more than 100,000 discrete diastereoisomers that, in principle, may bear distinct three-dimensional structures and pharmaceutical properties (9, 10). Despite recent

studies suggesting that stereodefined systems may improve therapeutic efficacy, readily scalable preparation methods often disregard the stereochemistry at phosphorus, whereas most of the methods that enable stereocontrol are impractical for large-scale manufacturing (10–24). As outlined in Fig. 1B, three coupling paradigms have traditionally been employed to facilitate P–O bond formation, each relying on cumbersome P(III)-based reagent strategies. The first (Fig. 1B, i), which produces stereorandom PS ASOs, commences with a classic phosphoramidite loading step to append the first nucleoside, followed by deprotection, coupling to a second nucleoside, and then oxidative sulfurization of the resulting P(III) species to the P(V) state (11, 12). The second strategy (Fig. 1B, ii), capable of accessing stereo-defined PS linkages, uses a phosphoramidate containing a P(III)-centered chiral auxiliary to control the phosphorous stereochemistry but is otherwise identical to the first. The most mature manifestation of this method stems from work developed by Wada and co-workers (further refined by WAVE Life Sciences) and requires a total of seven steps for the preparation of the chiral auxiliary (10, 13–15). Finally, an approach pioneered by Stec and co-workers (Fig. 1B, iii) relies on a similar strategy that begins with a P(III)-oxathiaphospholane loading reaction, followed (again) by oxidative sulfurization to furnish a chiral P(V)-oxathiaphospholane (OTP) sulfide auxiliary; this stable OTP can then be coupled to form the requisite internucleotide linkage using a simple amine activator [typically 1,8-diazabicyclo [5.4.0]undec-7-ene (DBU)] (16–18). However, by Stec's own admission, this strategy is scale limited, suffers poor coupling efficiency, requires resolution of stereorandom OTPs, and is extremely labor intensive (19). Taken together, the deficiencies of current methods point to an overreliance on low-valent P–O bond forming chemistry, as P(III) has historically been viewed as the sole gateway

for loading (and primary access for coupling) reactions. Reported herein is a major departure from that dogma: the invention of simple, P(V)-based reagents for phosphorus-sulfur incorporation (PSI, stylized hereafter as Ψ) (1) via reactions characterized by marked rapidity and scalability and complete stereocontrol at phosphorus.

Challenging the lore of the field, we opted for an inventive approach with the mission of bypassing P(III) entirely; the reaction sequence should rely exclusively on a P(V)-based platform to forge all key P–heteroatom bonds. This would require the development of a readily accessible reagent with programmable stereochemistry, capable of achieving both loading and coupling steps with robust precision. The realization of this design required a systematic investigation of three key components: (i) an inexpensive chiral backbone to predictably impart stereocontrol, (ii) a safe source of P(V) to eliminate the previously unavoidable oxidative sulfurization step, and (iii) a reactive yet stable leaving group to enable a facile loading reaction. Ideally, a traceless approach would join the parent species in a direct and asymmetric fashion while liberating a single P(S)O unit with no evidence of the chemical method of installation remaining. These disparate attributes should harmoniously assemble in such a way as to appeal to both process and discovery chemists—traits such as scalability, stability, crystallinity, and rapid reaction times were deemed critical to success. A matrix of candidate backbones, PS sources, and leaving groups was systematically investigated, as summarized in Fig. 1C. The tactical combination of these three constituents proved essential in achievement of the goals set forth above, leading to invention of the Ψ reagent system (1; Fig. 1D). Featuring a rigid, limonene-derived backbone anchored to an OTP sulfide core and a stable perfluorinated thiophenol leaving group, this platform embodies an impressive balance of stability and reactivity. The Ψ reagents enable the rapid construction of stereopure nucleotide systems and boast an operational simplicity akin to iterative peptide assembly.

Both (R)-PS- and (S)-PS-linked oligonucleotides can be readily accessed through selection of the desired Ψ reagent enantiomer, (+)- Ψ and (–)- Ψ , respectively (Fig. 2A). Derived from limonene, an inexpensive chiral pool terpene and common food additive, these OTP sulfide reagents are produced after epoxidation and ring opening. In the figure, the loading step refers to the appendage of the first nucleoside to the Ψ reagent to deliver a stable OTP-adduct, whereas the coupling forms the chiral internucleotide linkage. A variety of nucleosides (4 to 7) can be loaded in excellent yield (76 to 96%; Fig. 2B) onto Ψ with complete stereocontrol, accompanied by loss of pentafluorothiophenol. When using Ψ in excess, no competitive displacement of the OTP-sulfur is observed, despite the fact that this entity is primed for a subsequent coupling step. The 30-min reaction is air and moisture tolerant, occurs at ambient temperature, and requires only DBU as an activator. Notably, the next nucleoside in the sequence can

¹Department of Chemistry, The Scripps Research Institute, 10550 North Torrey Pines Road, La Jolla, CA 92037, USA.

²Chemical and Synthetic Development, Bristol-Myers Squibb, One Squibb Drive, New Brunswick, NJ 08903, USA.

³Department of Discovery Chemistry, Bristol-Myers Squibb Research and Development, 5 Research Parkway, Wallingford, CT 06492, USA. ⁴Department of Discovery Chemistry, Bristol-Myers Squibb, P.O. Box 5400, Princeton, NJ 08543, USA.

*These authors contributed equally to this work.

†Corresponding author. Email: michael.schmidt@bms.com (M.A.S.); martin.eastgate@bms.com (M.D.E.); pbaran@scripps.edu (P.S.B.)

be coupled under identical conditions to deliver the dinucleotide as a single diastereoisomer, again in exceptional yield (70 to 91%). The intermediate loaded OTP nucleosides are generally crystalline, bench-stable species.

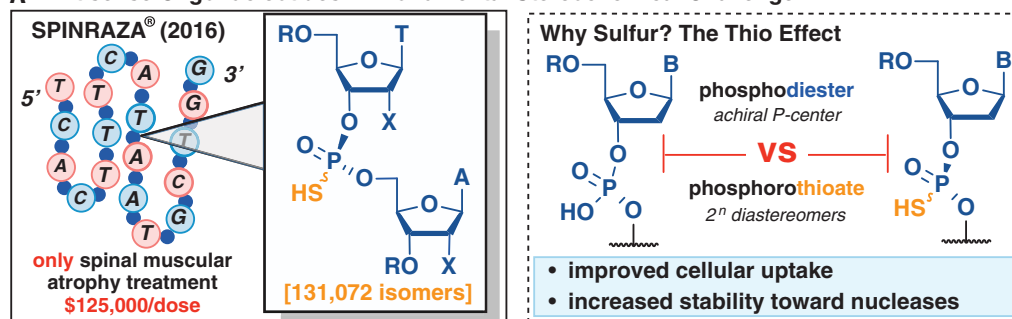
Dimeric combinations of the four native deoxynucleosides (A, T, G, and C) were prepared in high yields with complete stereocontrol; no differences in reaction performance were observed, regardless of base identity (Fig. 2C; **8** to **17**). In a testament to the power of these transformations, both enantiomers of the Ψ reagents were made on a multigram scale, as were all loaded and coupled compounds. Further, these reactions operate under complete reagent control, as evidenced by the stereochemical outcome in every case: (+)- Ψ leads to (*S*)-loaded and (*R*)-coupled products, whereas (–)- Ψ reactions are predictably reversed. In a feature distinct to these systems, one can simply invert the coupling sequence order to obtain the opposite P-stereochemistry using the same isomer of Ψ reagent (see supplementary materials for a graphical discussion).

Cyclic dinucleotides (CDNs) are macrocyclic natural products endowed with noteworthy biological activities and a storied history (25). Ample research indicates that these compounds play a number of prominent biological roles, most notably as secondary messengers in both the mammalian immune system and bacterial communication (26–31). Their role as agonists of innate immune response via binding and activation of the stimulator of interferon genes (STING) protein has led to a surge of interest across the pharmaceutical industry (26, 27, 32). As a consequence, numerous industrial and academic groups have targeted CDN constructs for evaluation as potential therapeutic agents. Just as the PS modification facilitates a marked improvement in ASO properties, a similar effect has been observed in CDNs, adding a layer of complexity to an already challenging class of natural products (8, 33–40). To be sure, the current impediment to rapid clinical progression of these compounds lies in the chemical synthesis. The modular strategies of traditional medicinal chemistry programs are stymied by both the poorly soluble nature of CDNs and the litany of engineered protecting-group schemes required to shield the array of heteroatoms found in the nucleobase, sugar core, and P(III)-based starting materials. As shown

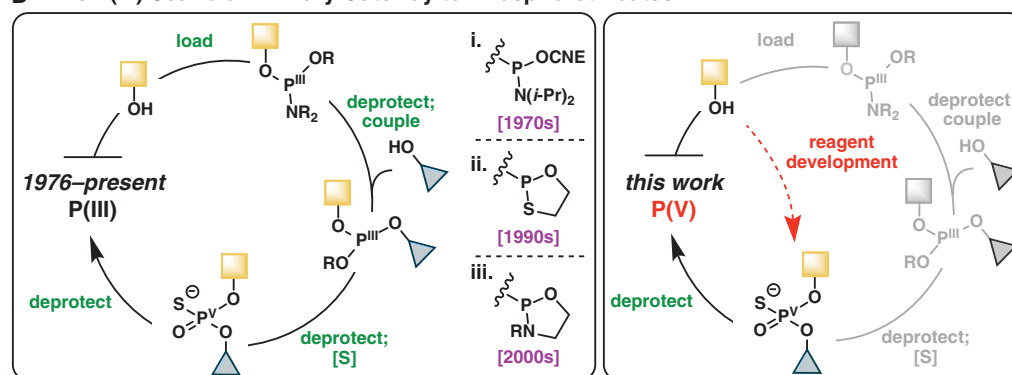
in Fig. 3A, nine steps are generally required from the parent nucleoside to prepare a single CDN as a mixture of all four possible diastereoisomers, with an observed ratio that appears to be substrate dependent (33–40). Of this arduous sequence, only four steps can be considered construction reactions, or those that contribute directly to P–O bond formation. The remainder account for various synthetic concessions, including

protecting-group manipulations and P(III)-to-P(V) oxidations. As compared with PS linkage integration in ASOs, the challenge of incorporating chiral PS linkages into CDNs becomes far more profound, as one is at the mercy of substrate bias to obtain diastereoselectivity at phosphorus. Modular, stereocontrolled CDN synthesis has so far proven elusive (Fig. 3A). In contrast, Ψ reagents enable a marked divergence from the

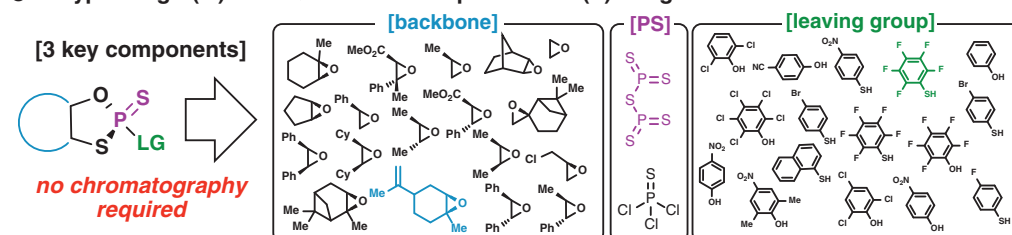
A Antisense Oligonucleotides: A Monumental Stereochemical Challenge



B The P(III) Scaffold: Primary Gateway to Phosphorothioates



C Bypassing P(III): The Quest to Develop an Ideal P(V) Reagent



D PSI Reagent: A Simple, Redox-Economic Alternative

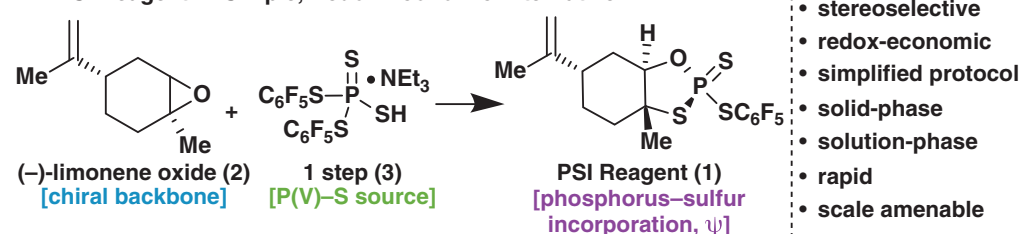
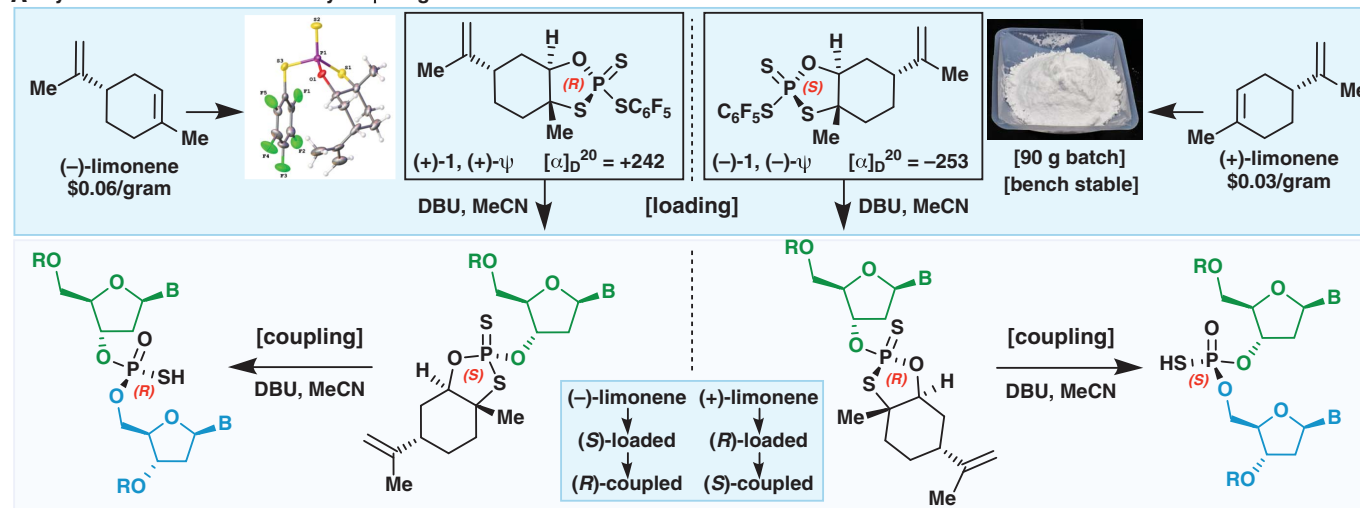
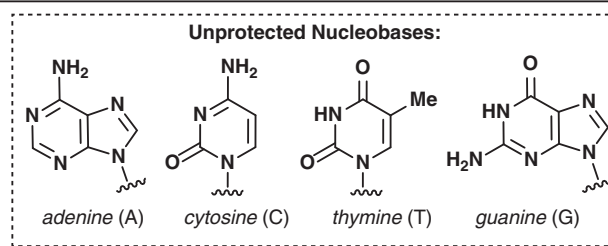
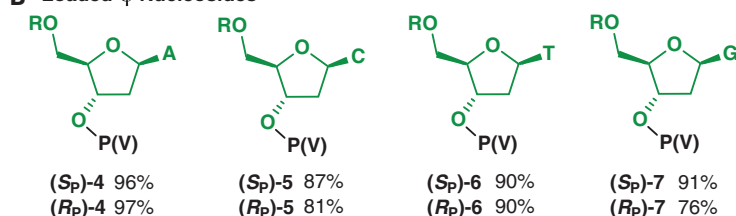
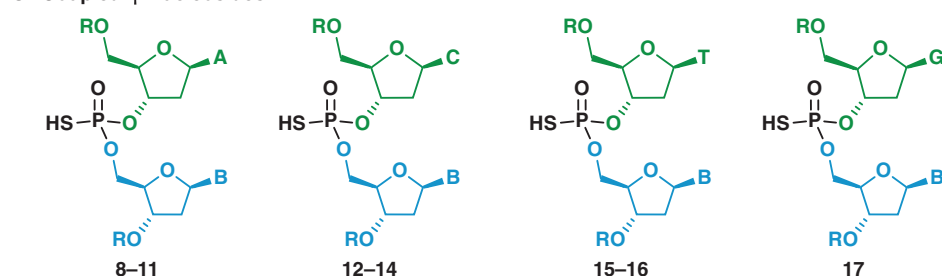


Fig. 1. Background and development. (A) Inspiration, (B) historical context, (C) development, and (D) invention of the Ψ reagent platform. *i*-Pr, iso-propyl; Me, methyl; Ph, phenyl; Cy, cyclohexyl; Et, ethyl; LG, leaving group.

A Synthesis and stereochemistry of Ψ reagentsB Loaded Ψ NucleosidesC Coupled Ψ Nucleosides

dinucleotide	yield (d.r.)
8, dA-dA (<i>R_p</i>)	65% (>99:1)
9, dA-dC (<i>S_p</i>)	91% (>99:1)
10, dA-dT (<i>S_p</i>)	61% (>99:1)
11, dA-dG (<i>S_p</i>)	79% (>99:1)
12, dC-dC (<i>R_p</i>)	73% (>99:1)
13, dC-dT (<i>S_p</i>)	76% (>99:1)
14, dC-dG (<i>R_p</i>)	82% (>99:1)
15, dT-dT (<i>S_p</i>)	72% (>99:1)
16, dT-dG (<i>S_p</i>)	67% (>99:1)
17, dG-dG (<i>R_p</i>)	86% (>99:1)

Fig. 2. Formalisms for the use of Ψ reagents in dinucleotide synthesis. (A) Stereochemical assignments. (B) Loading of nucleoside monomers. (C) Coupling to produce stereopure PS dinucleotides. R, TBDPS (*tert*-butyldiphenylsilyl). Loading:

nucleoside [1 equivalent (equiv.)], Ψ reagent (1.3 equiv.), DBU (1.3 equiv.), MeCN, 25°C, 30 min. Coupling: nucleoside-P(V) (1.0 equiv.), coupling partner (2.0 equiv.), DBU (3.0 equiv.), MeCN, 25°C, 30 min.

traditional P(III) approach, requiring only four or five steps from a starting nucleoside to arrive at a stereopure CDN. Two general protocols for CDN synthesis have been devised, as outlined in Fig. 3B. The stepwise approach ensures complete transfer of stereochemical information from the Ψ reagent by forging the CDN macrocycle one P–O bond at a time. To this point, CDN **21** was constructed as a single diastereoisomer in 14% overall yield via an operationally simple sequence: First, the desired Ψ reagent was loaded onto a nucleoside at either the 3' or 5' position and was then coupled to a resin-bound nucleoside (itself anchored to the solid support). The dinucleotide was then cleaved from the solid support to reveal the remaining free alcohol with no purification required. The final coupling reaction was achieved within 10 minutes to afford the desired

CDN target. Conversely, the concerted protocol accomplishes macrocyclization directly from the linear dinucleotide diol, as in **20**. Notably, CDN **21**, procured in stereopure form via the stepwise approach, was accessed in 44% yield via the concerted method, albeit with a 3:1 diastereomeric ratio (d.r.), a result of the aforementioned competitive 3' versus 5' Ψ loading in the penultimate bond formation (Fig. 3C, path A versus path B). Though step-economic, the concerted sequence effects high d.r. only when the reactivity of the 3' and 5' alcohols is sufficiently differentiated to enable selective reactivity with the Ψ reagent. As with the synthesis of linear dinucleotides (Fig. 2C), the order of assembly can be used to program the resulting phosphorus stereochemistry; thus, **18** was synthesized as three distinct stereoisomers, each with perfect stereocontrol,

whereas CDN **19** was obtained in 24% overall yield as a single diastereoisomer. Both approaches can be conducted with similar facility in solution and as well as in solid phase.

Beyond dimeric nucleotides, fascination surrounding P(III) in the context of general solid-phase oligonucleotide construction persists. This intrigue has resulted in a staggering number of publications and an entire industry of specialized equipment built to accommodate the complex reactivity and sensitivity of P(III)-derived systems. Perhaps unsurprisingly, reports of P(V) approaches to solid-phase oligonucleotide synthesis (SPOS) of PS-analogs remain conspicuously absent. To this end, an unoptimized automated load-deprotect-couple P(V) cycle (Fig. 4) was employed, using equipment designed for P(III) chemistry, to furnish the homo-dT pentamer (**23**) as a single

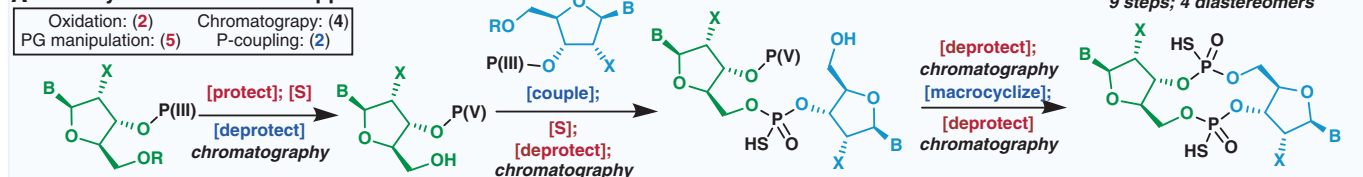
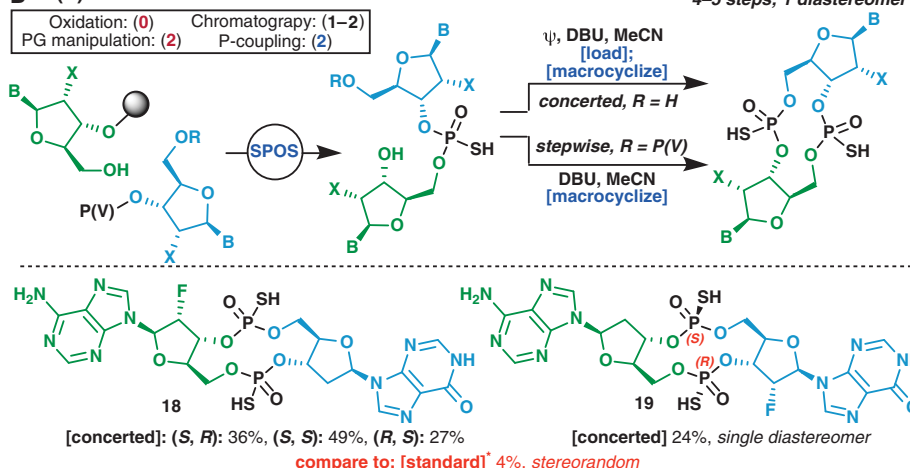
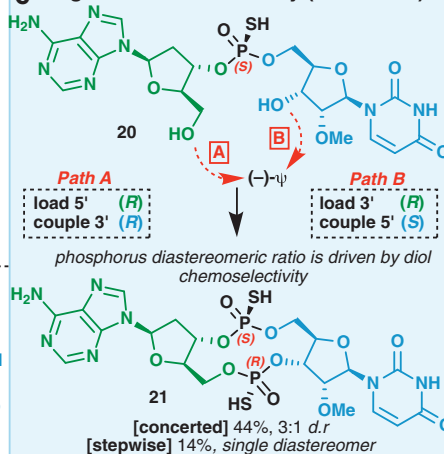
A CDN Synthesis: Standard Approach**B P(V) Protocol****C Origin of Stereoselectivity (Concerted)**

Fig. 3. Applications of the ψ reagent platform to the simplified synthesis of CDNs. (A) Prior approach. **(B)** Stepwise and concerted macrocyclization using ψ . *See (40) for the literature method. **(C)** Origin of observed stereochemistry in concerted protocol. PG, protecting group.

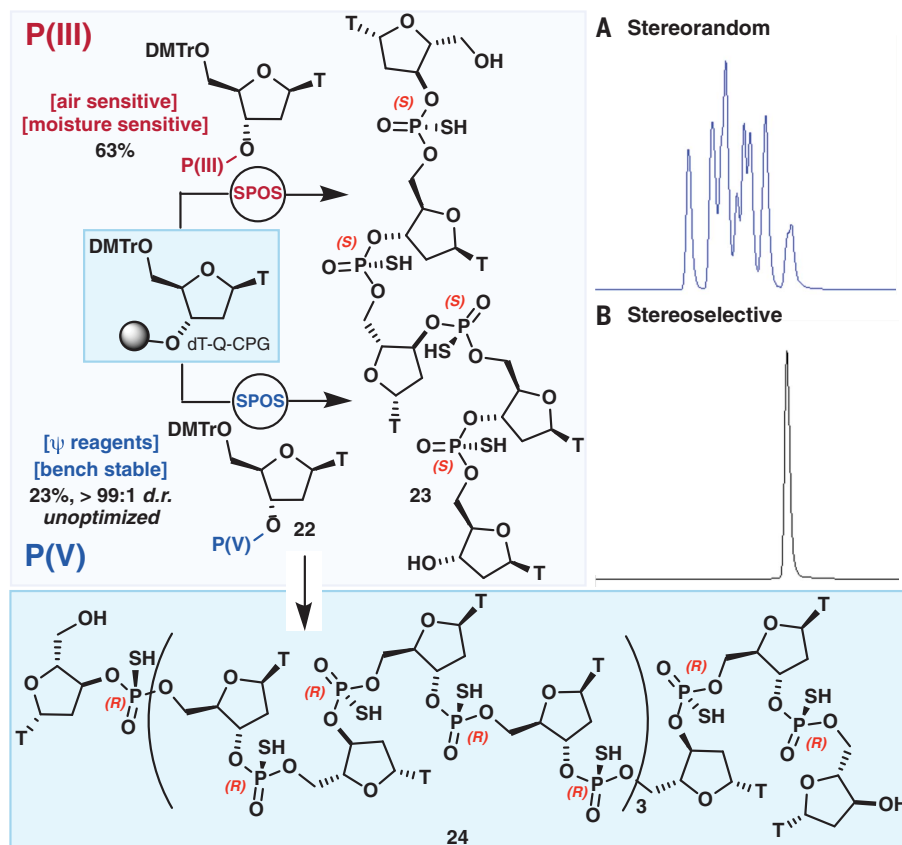


Fig. 4. Automated synthesis of PS oligonucleotides. (A) Crude HPLC trace of pentamer **23** (16 diastereoisomers) synthesized under standard P(III) automated conditions. **(B)** Crude HPLC trace of pentamer **23** (1 diastereoisomer) synthesized under unoptimized ψ automated conditions. DMTr, dimethoxytrityl.

diastereoisomer in 23% yield. Notably, **23** was constructed without rigorous exclusion of air and moisture, in stark contrast to the operational constraints of traditional P(III) SPOS. Under traditional automated phosphoramidite conditions, the same oligonucleotide was obtained as a mixture of 16 diastereoisomers in 63% yield. In a promising demonstration, the 16-nucleotide oligomer **24** was successfully constructed via the unoptimized ψ approach, though with an expected drop in crude purity (see supplementary materials for details). Indeed, the introduction of ψ reagents engenders an advantageous approach to oligonucleotide synthesis enabled by a simple, reagent-based strategy capable of similarly effective solution- and solid-phase chemistry.

REFERENCES AND NOTES

- C. E. Dunbar et al., *Science* **359**, eaan4672 (2018).
- E. W. Ottesen, *Transl. Neurosci.* **8**, 1–6 (2017).
- H. P. Vosberg, F. Eckstein, *J. Biol. Chem.* **257**, 6595–6599 (1982).
- S. T. Cooke, *Antisense Research and Applications* (Springer, ed. 1, 1998).
- E. Wickstrom, *J. Biochem. Biophys. Methods* **13**, 97–102 (1986).
- J. Purcell, A. C. Hengge, *J. Org. Chem.* **70**, 8437–8442 (2005).
- C. A. Stein, D. Castanotto, *Mol. Ther.* **25**, 1069–1075 (2017).
- J. Li, M. D. Eastgate, *Org. Biomol. Chem.* **13**, 7164–7176 (2015).
- H. G. Bohr et al., *Mol. Ther. Nucleic Acids* **8**, 428–441 (2017).
- N. Iwamoto et al., *Nat. Biotechnol.* **35**, 845–851 (2017).
- S. L. Beaucage, M. H. Caruthers, *Tetrahedron Lett.* **22**, 1859–1862 (1981).
- M. H. Caruthers, in *Synthesis and Applications of DNA and RNA*, S. A. Narang, Ed. (Academic Press, 1987), pp. 47–94.
- N. Oka, M. Yamamoto, T. Sato, T. Wada, *J. Am. Chem. Soc.* **130**, 16031–16037 (2008).
- Y. Nukaga, K. Yamada, T. Ogata, N. Oka, T. Wada, *J. Org. Chem.* **77**, 7913–7922 (2012).

15. N. Oka, T. Kondo, S. Fujiwara, Y. Maizuru, T. Wada, *Org. Lett.* **11**, 967–970 (2009).
 16. W. J. Stec, A. Grajkowski, M. Koziolkiewicz, B. Uznanski, *Nucleic Acids Res.* **19**, 5883–5888 (1991).
 17. W. J. Stec *et al.*, *J. Am. Chem. Soc.* **117**, 12019–12029 (1995).
 18. W. J. Stec *et al.*, *J. Am. Chem. Soc.* **120**, 7156–7167 (1998).
 19. P. Guga, W. J. Stec, *Curr. Protoc. Nucleic Acid Chem.* **14**, 4.17.1–4.17.28 (2003).
 20. N. Iwamoto, N. Oka, T. Sato, T. Wada, *Angew. Chem. Int. Ed.* **48**, 496–499 (2009).
 21. R. P. Iyer, D. Yu, N.-H. Ho, W. Tan, S. Agrawal, *Tetrahedron Asymmetry* **6**, 1051–1054 (1995).
 22. M. Guo, D. Yu, R. P. Iyer, S. Agrawal, *Bioorg. Med. Chem. Lett.* **8**, 2539–2544 (1998).
 23. A. Wilk, A. Grajkowski, L. R. Phillips, S. L. Beaucage, *J. Am. Chem. Soc.* **122**, 2149–2156 (2000).
 24. M. Li *et al.*, *Chem. Commun.* **53**, 541–544 (2017).
 25. P. Clivio, S. Coantic-Castex, D. Guillaume, *Chem. Rev.* **113**, 7354–7401 (2013).
 26. D. L. Burdette *et al.*, *Nature* **478**, 515–518 (2011).
 27. L. Sun, J. Wu, F. Du, X. Chen, Z. J. Chen, *Science* **339**, 786–791 (2013).
 28. M. Gomelsky, *Mol. Microbiol.* **79**, 562–565 (2011).
 29. P. Ross *et al.*, *FEBS Lett.* **186**, 191–196 (1985).
 30. P. Ross *et al.*, *Carbohydr. Res.* **149**, 101–117 (1986).
 31. P. Ross *et al.*, *Nature* **325**, 279–281 (1987).
 32. R. Cross, *Chem. Eng. News* **96**, 24–26 (2018).
 33. C. Battistini, S. Fustinoni, M. G. Brasca, D. Borghi, *Tetrahedron* **49**, 1115–1132 (1993).
 34. P. Guga *et al.*, *Tetrahedron* **62**, 2698–2704 (2006).
 35. H. Yan, A. L. Aguilar, *Nucleosides Nucleotides Nucleic Acids* **26**, 189–204 (2007).
 36. H. Yan, X. Wang, R. KuoLee, W. Chen, *Bioorg. Med. Chem. Lett.* **18**, 5631–5634 (2008).
 37. J. Zhao, E. Veliath, S. Kim, B. L. Gaffney, R. A. Jones, *Nucleosides Nucleotides Nucleic Acids* **28**, 352–378 (2009).
 38. B. L. Gaffney, E. Veliath, J. Zhao, R. A. Jones, *Org. Lett.* **12**, 3269–3271 (2010).
 39. N. Fei *et al.*, *Chem. Commun.* **50**, 8499–8502 (2014).
 40. T. Lioux *et al.*, *J. Med. Chem.* **59**, 10253–10267 (2016).
- ACKNOWLEDGMENTS**
- We thank B. Fink and A. Cernijenko for insightful discussions; J. Chen (TSRI) for assistance with analysis; D.-H. Huang and L. Pasternack (TSRI) for assistance with nuclear magnetic resonance spectroscopy; and A. L. Rheingold, C. E. Moore, and M. Gembicky (UCSD) for x-ray analysis. **Funding:** Financial support for this work was provided by NIH (grant GM-118176), Bristol-Myers Squibb, and NSF GRFP (J.N.D.). **Author contributions:** K.W.K., J.N.D., M.A.S., M.D.E., and P.S.B. conceived of the work. K.W.K., J.N.D., M.A.S., B.Z., J.C.V., C.K., S.E.M., I.M.M., Y.Z., C.H., J.Z., C.Y., and Q.W. designed and executed all experiments and performed all data analysis. R.E.O. and P.P. provided specific insight and direction for the ASO and CDN studies, respectively. K.W.K., J.N.D., and P.S.B. wrote the manuscript. M.A.S., M.D.E., R.E.O., and I.M.M. assisted with editing. **Competing interests:** A provisional U.S. patent application on this work has been filed (application number 62657551), with K.W.K., J.N.D., M.A.S., B.Z., M.D.E., I.M.M., R.E.O., and P.S.B. listed as inventors. P.S.B. is a paid consultant for Bristol-Myers Squibb. **Data and materials availability:** Crystallographic data are available free of charge from the Cambridge Crystallographic Data Centre under reference numbers CCDC 1840250, 1849772, and 1849773. Experimental procedures, frequently asked questions, extensive optimization data, ¹H nuclear magnetic resonance (NMR) spectra, ¹³C NMR spectra, ³¹P NMR spectra, analytical high-performance liquid chromatography (HPLC) traces, and mass spectrometry data are available in the supplementary materials.
- SUPPLEMENTARY MATERIALS**
- www.sciencemag.org/content/361/6408/1234/suppl/DC1
Materials and Methods
Supplementary Text
Figs. S1 to S4
Tables S1 to S5
References (41–48)
NMR Spectra
- 4 June 2018; accepted 12 July 2018
Published online 2 August 2018
10.1126/science.aau3369

QUANTUM ELECTRONICS

Measurement of a superconducting qubit with a microwave photon counter

A. Opremcak^{1*}, I. V. Pechenezhskiy^{1*†}, C. Howington², B. G. Christensen¹, M. A. Beck¹, E. Leonard Jr.¹, J. Suttle¹, C. Wilen¹, K. N. Nesterov¹, G. J. Ribeill^{1‡}, T. Thorbeck^{1§}, F. Schlenker¹, M. G. Vavilov¹, B. L. T. Plourde², R. McDermott^{1||}

Fast, high-fidelity measurement is a key ingredient for quantum error correction. Conventional approaches to the measurement of superconducting qubits, involving linear amplification of a microwave probe tone followed by heterodyne detection at room temperature, do not scale well to large system sizes. We introduce an approach to measurement based on a microwave photon counter demonstrating raw single-shot measurement fidelity of 92%. Moreover, the intrinsic damping of the photon counter is used to extract the energy released by the measurement process, allowing repeated high-fidelity quantum nondemolition measurements. Our scheme provides access to the classical outcome of projective quantum measurement at the millikelvin stage and could form the basis for a scalable quantum-to-classical interface.

To harness the tremendous potential of quantum computers, it is necessary to implement robust error correction to combat decoherence of the fragile quantum states. Error correction relies on high-fidelity, repeated measurements of an appreciable fraction of the quantum array throughout the run time of the algorithm (1). In the context of superconducting qubits, measurement is performed by heterodyne detection of a weak microwave probe tone transmitted across or reflected from a linear cavity that is dispersively coupled to the qubit (2–8). This approach relies on bulky, magnetic nonreciprocal circuit components to isolate the qubit from noisy amplification stages (5, 9–11); moreover, the measurement result is only accessible after room-temperature heterodyne detection and thresholding, complicating efforts to implement low-latency feedback conditioned on the measurement result (12, 13). The physical footprint, wiring heat load, and latency associated with conventional amplifier-based qubit measurement stand as major impediments to scaling superconducting qubit technology.

An alternative approach involves entanglement of the qubit with the linear resonator to create cavity pointer states characterized by large differential photon occupation, followed by subsequent photodetection (14). In our experiments (Fig. 1A), microwave drive at one of the two dressed cavity frequencies maps the qubit state onto “bright” and “dark” cavity pointer states. Discrimination of the states is performed directly

at the millikelvin stage by the Josephson photo-multiplier (JPM), a microwave photon counter; we use no nonreciprocal components between the qubit and JPM. The JPM is based on a single Josephson junction in a radiofrequency superconducting quantum interference device (SQUID) loop that is biased close to the critical flux where a phase slip occurs. The circuit parameters are chosen to yield a potential energy landscape with one or two local minima, depending on flux bias; the distinct local minima correspond to classically distinguishable flux states in the device [see (15), section S1]. Once the JPM is properly biased, the presence of resonant microwaves induces a rapid tunneling event between the two classically distinguishable states of the detector (Fig. 1B). In the absence of microwave input, transitions

occur at an exponentially suppressed dark rate (Fig. 1C). Thus, the absorption of resonant microwaves creates a readily measured “click” (16).

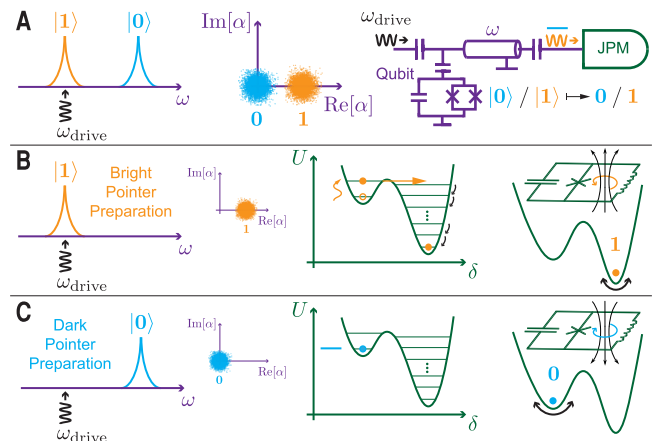
The qubit and the JPM are fabricated on different silicon substrates and housed in separate aluminum enclosures connected via a coaxial transmission line with characteristic impedance $Z_0 = 50 \, \Omega$ and length $L_0 = 14 \, \text{cm}$ [see (15), sections S2 and S3]. The qubit chip (purple circuit in Fig. 2A) incorporates an asymmetric transmon (Fig. 2B) that is capacitively coupled to a half-wave coplanar waveguide (CPW) resonator, the qubit cavity, with frequency $\omega_J/2\pi = 5.020 \, \text{GHz}$ and qubit-cavity coupling strength $g_J/2\pi = 110 \, \text{MHz}$ (17–19). The qubit is operated at a fixed frequency $\omega_q/2\pi = 4.433 \, \text{GHz}$ and has an anharmonicity $\alpha/2\pi = -250 \, \text{MHz}$.

The JPM (green circuit in Fig. 2A) is based on the capacitively shunted flux-biased phase qubit (20). The JPM is capacitively coupled to a local auxiliary CPW resonator, the capture cavity, with bare frequency $\omega_2/2\pi = 5.028 \, \text{GHz}$ and coupling strength $g_2/2\pi = 40 \, \text{MHz}$. A micrograph of the JPM is shown in Fig. 2C. The circuit involves a single Al-AlO_x-Al Josephson junction with critical current $I_0 = 1 \, \mu\text{A}$ embedded in a 3+3 turn gradiometric loop with inductance $L_g = 1.1 \, \text{nH}$. The junction is shunted by an external parallel-plate capacitor $C_s = 3.3 \, \text{pF}$. The plasma frequency of the JPM is tunable with external flux from 5.9 to 4.4 GHz (Fig. 2, D and E), allowing for both resonant and dispersive interactions between the JPM and capture cavity.

The qubit and capture cavities are capacitively coupled to the mediating transmission line [see also (15), section S4 and tables S1 to S3]. After pointer state preparation, microwave energy leaks out of the qubit cavity, and a fraction of that energy is transferred to the capture cavity (21). Without an intervening isolator or circulator to damp unwanted reflections, the finite length L_0 of the transmission line admits a standing wave structure with an approximate mode spacing of

Fig. 1. Qubit state measurement using the JPM. (A) Measurement overview. Microwave drive at the dressed cavity

resonance corresponding to the qubit $|1\rangle$ state creates bright and dark cavity pointer states with large differential photon occupation. These pointer states are detected using the JPM, which stores the measurement result as a classical bit at the millikelvin stage. (B) Bright pointer detection. Microwaves resonant with the JPM promote the circuit from the ground state of a metastable local minimum (here, left potential well) to an excited state. The detector subsequently undergoes a rapid tunneling transition that allows relaxation to the global minimum of the potential (here, right potential well). (C) Dark pointer detection. Energy contained in the dark pointer state is insufficient to induce a tunneling event. The presence (B) or absence (C) of an interwell tunneling transition results in classically distinguishable flux (oscillation) states in the detector.



¹Department of Physics, University of Wisconsin–Madison, Madison, WI 53706, USA. ²Department of Physics, Syracuse University, Syracuse, NY 13244, USA.

*These authors contributed equally to this work. †Present address: University of Maryland, College Park, MD 20742, USA. ‡Present address: Raytheon BBN Technologies, Cambridge, MA 02138, USA. §Present address: IBM T. J. Watson Research Center, Yorktown Heights, NY 10598, USA.

||Corresponding author. Email: rfmcdmott@wisc.edu

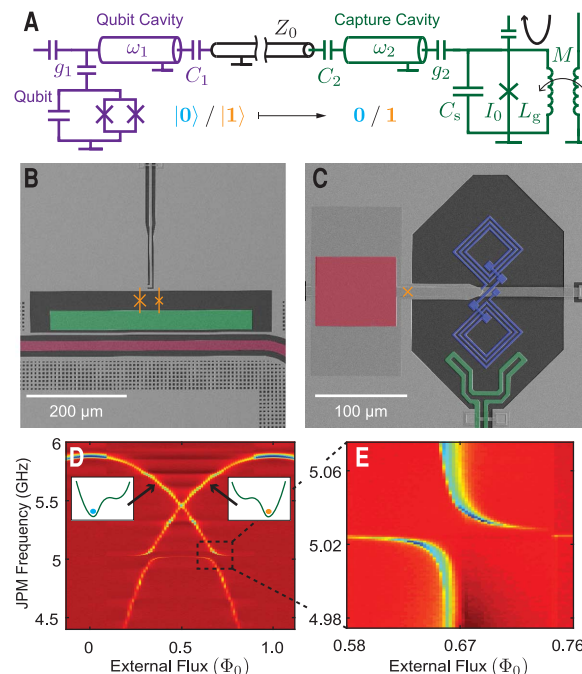
$v_p/2L_0$, where v_p is the phase velocity of propagation in the cable. With these complications in mind, L_0 was chosen to avoid destructive interference in the vicinity of ω_1 and ω_2 , which can substantially degrade photon transfer efficiency [see (15), section S5].

In the timing diagram of the measurement (Fig. 3A), the cartoon insets depict the dynamics of the JPM phase particle at critical points throughout the measurement sequence. We begin with a deterministic reset of the JPM, which is accomplished by biasing the JPM potential into a single-well configuration [see (15), section S1]. A depletion interaction between the JPM and capture cavity mode immediately follows in order to dissipate spurious microwave excitations generated during reset. Additional details of this depletion process are described below and in Fig. 4, A and B. Next, we use mode repulsion between the JPM and capture cavity to tune ω_2 in order to maximize photon transfer efficiency. The response of the capture cavity to an applied drive tone at four distinct JPM-capture cavity detunings, and thus four different values of ω_2 , is shown in Fig. 3B; the detuning is chosen such that $\omega_1 = \omega_2$. At the beginning of the tune and capture stage, a qubit X-gate (I-gate) is performed and a subsequent qubit cavity drive tone is applied to prepare the bright (dark) pointer state [see (15), section S6]. The cavities are held on resonance for 750 ns to allow the pointer states to leak from the qubit cavity to the capture cavity; this time was determined by maximizing measurement fidelity with respect to the drive pulse duration. The bright pointer state corresponds to a mean qubit cavity photon occupation $\bar{n}_1 \sim 10$, calibrated using the ac Stark effect (Fig. 3E) [see (15), section S8] (22, 23). After pointer state transfer, the JPM is biased into resonance with the capture cavity, and occupation of that mode induces intrawell excitations of the phase particle on a time scale $\pi/2g_2 \sim 6$ ns (Fig. 3C) (24). Finally, a short (~ 10 ns) bias pulse is applied to the JPM to induce interwell tunneling of excited states (25); the amplitude of the bias pulse is adjusted to maximize tunneling contrast between qubit excited and ground states (Fig. 3D). At this point, the measurement is complete: The measurement result is stored in the classical flux state of the JPM. To retrieve the result of qubit measurement for subsequent analysis at room temperature, we use a weak microwave probe tone to interrogate the plasma resonance of the JPM after measurement. The JPM bias is adjusted so that the plasma frequencies associated with the two local minima in the potential are slightly different; reflection from the JPM can distinguish the flux state of the detector with $>99.9\%$ fidelity in <500 ns [see (15), section S4].

Each measurement cycle yields a binary result—"0" or "1"—the classical result of projective quantum measurement. To access qubit state occupation probabilities, the measurement is repeated 10,000 times. The JPM switching probabilities represent raw measurement outcomes, uncorrected for state preparation, relaxation, or gate errors. In Fig. 3, F and G, we display the raw

Fig. 2. Experimental setup.

(A) Circuit schematic. The qubit circuit (purple) is connected to the JPM circuit (green) via a coaxial transmission line (black) [see (15), tables S1 to S3]. (B) Micrograph of the transmon circuit with superconducting island (green), qubit cavity (maroon), and Josephson junctions (orange). (C) Micrograph of the JPM circuit (capture cavity not shown) with its 3+3 turn gradiometric loop inductance L_g (blue), single Josephson junction with critical current I_0 (orange), parallel-plate capacitor C_s (red), and on-chip flux bias line with mutual inductance M (green). (D) JPM spectroscopy versus external flux. Insets show cartoons of a phase particle bound to the left and right wells. (E) Enlargement of the avoided level crossing between the JPM and capture cavity.



measurement outcomes for qubit Ramsey and Rabi experiments, respectively. The JPM measurements achieve a raw fidelity of 92%. The bulk of our fidelity loss is due to qubit energy relaxation during pointer state preparation and dark counts, which contribute infidelity of 5% and 2%, respectively. In our setup, dark counts stem from both excess $|1\rangle$ population of the qubit and spurious microwave energy contained in our dark pointer state. We attribute the remaining infidelity to imperfect gating and photon loss during pointer state transfer. The qubit T_1 of 6.6 μ s measured in these experiments is consistent with separate measurements of the same device using conventional heterodyne readout techniques; we see no evidence of JPM-induced degradation of qubit T_1 .

As noted earlier, JPM switching events release a large energy on the order of 100 photons as the JPM relaxes from a metastable minimum to the global minimum of its potential (26). It is critical to understand the backaction of JPM switching events on the qubit state. The JPM tunneling transient has a broad spectral content, and Fourier components of this transient that are resonant with the capture and qubit cavities will induce a spurious population in these modes that will lead to photon shot noise dephasing of the qubit (27, 28). In Fig. 4A, we show the results of qubit Ramsey scans performed with (orange) and without (blue) a forced JPM tunneling event before the experiment. In the absence of any mitigation of the classical backaction, qubit Ramsey fringes show strongly suppressed coherence and a frequency shift indicating spurious photon occupation in the qubit cavity (29). However, we can use the intrinsic damping of the JPM mode itself to controllably dissipate the energy in the linear cavities and fully suppress photon shot noise dephasing. Immediately after JPM reset, the

JPM is biased to a point where the levels in the shallow minimum are resonant with the linear cavity modes. Energy from the capture cavity leaks back to the JPM, inducing intrawell transitions; at the selected bias point, the interwell transition probability is negligible. The JPM mode is strongly damped, with quality factor $Q \sim 300$, set by the loss tangent of the SiO_2 dielectric used in the JPM shunt capacitor (30). As a result, the energy coupled to the JPM is rapidly dissipated. With this deterministic reset of the cavities, fully coherent qubit Ramsey fringes that correspond to the absence of a JPM switching event are recovered for depletion times ≥ 40 ns, as shown in Fig. 4B. We reiterate that no nonreciprocal components are used in these experiments to isolate the qubit chip from the classical backaction of the JPM.

In Fig. 4C we explore the quantum nondemolition (QND) character of our measurement protocol (31). We prepare the qubit in the superposition state $(|0\rangle - i|1\rangle)/\sqrt{2}$ aligned along the $-y$ axis of the Bloch sphere. We verify the state by performing an overdetermined tomography (20). Here the direction θ and length t of a tomographic pulse are swept continuously over the equatorial plane of the Bloch sphere before measurement. For control pulses applied along the x axis, the qubit undergoes the usual Rabi oscillations; for control applied along y , the qubit state vector is unaffected. After an initial JPM-based measurement (including an additional 1.4 μ s of delay for qubit cavity ringdown), we perform a tomographic reconstruction of the qubit state by applying a prerotation and a final JPM-based measurement. In the right-hand panel of Fig. 4C, we display tomograms corresponding to the classical measurement results "0" (top) and "1" (bottom). When the measurement result "0" is returned, we find a tomogram that

Fig. 3. JPM-based qubit measurement. (A) We begin by resetting the JPM into a well-defined flux state. A subsequent depletion interaction removes spurious microwave excitations generated during reset (see Fig. 4, A and B, for more details). (B) Next, we tune the capture cavity frequency to maximize transfer efficiency from the qubit cavity. The response of the capture cavity to an applied drive at four distinct JPM-capture cavity detunings is shown; the detuning is chosen such that $\omega_2 = \omega_1$. During the tune and capture interval, a qubit X-gate (I-gate) is applied, and microwave drive at the dressed $|1\rangle$ cavity resonance is used to prepare the bright (dark) pointer state. As we drive the qubit cavity, a fraction of the microwave energy is transferred to the capture cavity during this capture step. (C) The JPM is then tuned into resonance with the capture cavity for photodetection. Photons present in the capture cavity induce intrawell transitions of the JPM to higher excited states. (D) Finally, a brief bias pulse is applied to induce tunneling of excited JPM states. The arrows on the bottom axes in (B) to (D) indicate optimal bias parameters. At this point, the measurement is complete, and the result is encoded in the classical flux state of the JPM. Microwave reflectometry is subsequently used to interrogate the JPM. (E) Stark spectroscopy used to calibrate qubit cavity photon occupation. JPM-detected Ramsey fringes and Rabi oscillations versus qubit drive detuning are shown in (F) and (G), respectively.

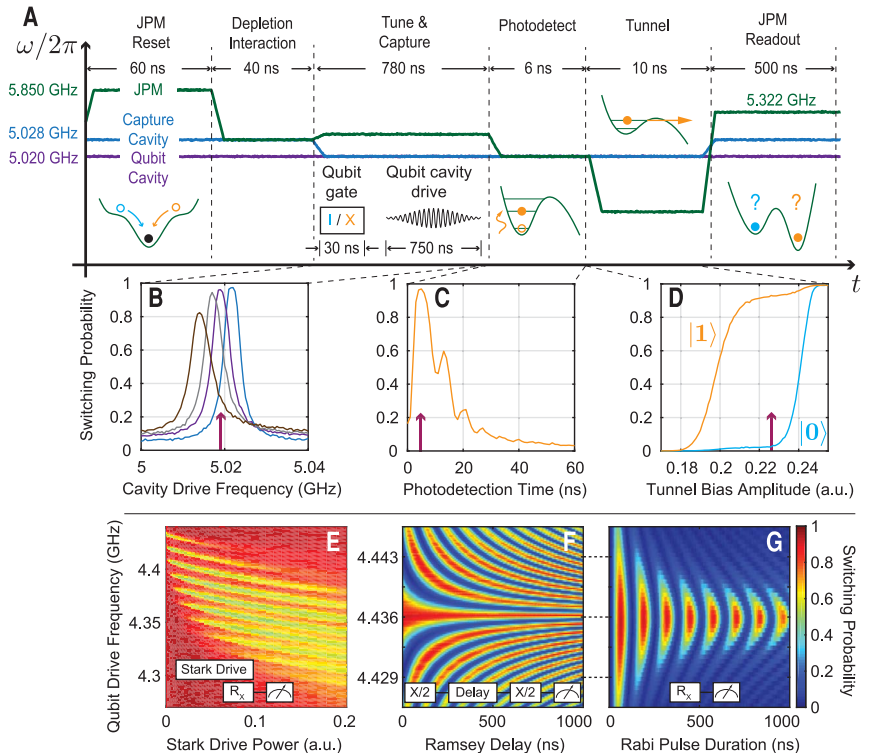
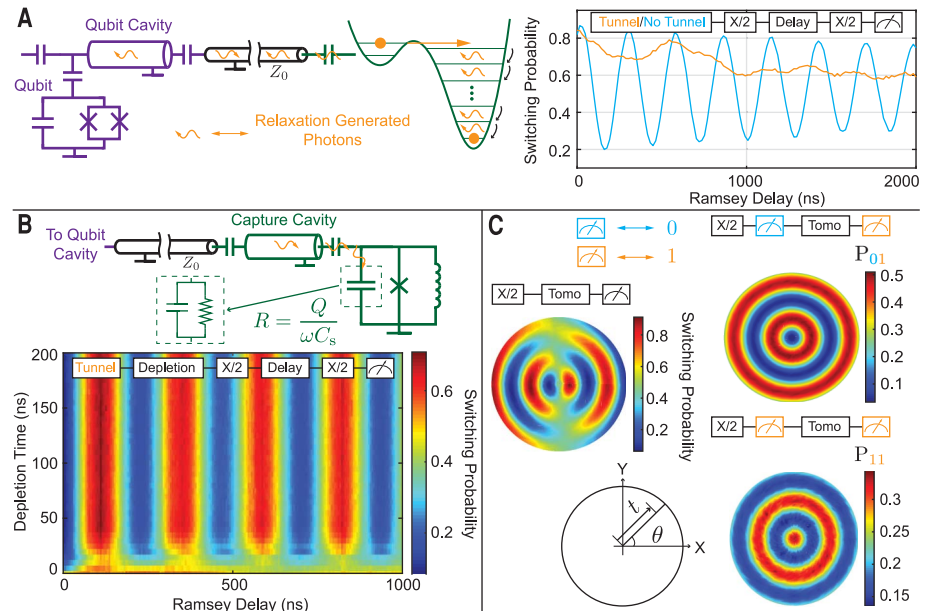


Fig. 4. Mitigating backaction and preserving QND properties. (A) The JPM switching event releases energy on the order of 100 photons, inducing spurious population of the capture and qubit cavities. The right-hand panel shows baseline qubit Ramsey fringes (blue) and Ramsey fringes measured after a forced tunneling event by the JPM (orange). (B) After the fast flux pulse that induces JPM tunneling, we adjust JPM bias so that energy deposited in the cavities is dissipated in the JPM, yielding a deterministic reset of the cavities. The color plot shows qubit Ramsey fringes versus duration of the depletion interaction between the JPM and the capture cavity. (C) Qubit tomography after JPM-based measurement. We prepare the superposition state $(|0\rangle - i|1\rangle)/\sqrt{2}$ and verify the state with overdetermined qubit tomography (left panel). To characterize the qubit state after JPM-based measurement, we prepare the same superposition state, measure with the JPM, and then perform qubit tomography on the resulting state. Qubit tomography conditioned on the JPM measurement shows high overlap with target states $|0\rangle$ (top right) and $|1\rangle$ (bottom right).



overlaps with the ideal $|0\rangle$ state with fidelity 91% [see (15), section S9]. When the result “1” is returned, the measured tomogram corresponds to overlap fidelity of 69% with the $|1\rangle$ state. The loss in fidelity for the qubit $|1\rangle$ state is consistent with the measured qubit T_1 time of $6.6\ \mu\text{s}$ and the $2.8\ \mu\text{s}$ between successive measurement drive tones. We conclude that our JPM-based measurement is highly QND.

Our high-fidelity, fast photon counter-based qubit measurement approach provides access to the binary result of projective quantum measurement at the millikelvin stage without the need for nonreciprocal components between the qubit and counter. In a future system, JPM-based readout could form the basis of the measurement side of a robust, scalable interface between a quantum array and a proximal classical controller, for

example, by encoding the flux state of the JPM onto classical single-flux quantum (SFQ) voltage pulses (32, 33) for subsequent postprocessing via SFQ-based digital logic (34).

REFERENCES AND NOTES

1. A. G. Fowler, M. Mariantoni, J. M. Martinis, A. N. Cleland, *Phys. Rev. A* **86**, 032324 (2012).
2. A. Blais, R.-S. Huang, A. Wallraff, S. M. Girvin, R. J. Schoelkopf, *Phys. Rev. A* **69**, 062320 (2004).

3. I. Siddiqi *et al.*, *Phys. Rev. Lett.* **93**, 207002 (2004).
4. F. Mallet *et al.*, *Nat. Phys.* **5**, 791–795 (2009).
5. E. Jeffrey *et al.*, *Phys. Rev. Lett.* **112**, 190504 (2014).
6. J. Kelly *et al.*, *Nature* **519**, 66–69 (2015).
7. J. M. Martinis, *npj Quantum Inf.* **1**, 15005 (2015).
8. D. Sank *et al.*, *Phys. Rev. Lett.* **117**, 190503 (2016).
9. J. E. Johnson *et al.*, *Phys. Rev. Lett.* **109**, 050506 (2012).
10. C. Macklin *et al.*, *Science* **350**, 307–310 (2015).
11. T. Walter *et al.*, *Phys. Rev. Appl.* **7**, 054020 (2017).
12. D. Ristè, J. G. van Leeuwen, H.-S. Ku, K. W. Lehnert, L. DiCarlo, *Phys. Rev. Lett.* **109**, 050507 (2012).
13. D. Ristè *et al.*, *Nature* **502**, 350–354 (2013).
14. L. C. G. Govia *et al.*, *Phys. Rev. A* **90**, 062307 (2014).
15. See supplementary materials.
16. Y.-F. Chen *et al.*, *Phys. Rev. Lett.* **107**, 217401 (2011).
17. J. Koch *et al.*, *Phys. Rev. A* **76**, 042319 (2007).
18. R. Barends *et al.*, *Phys. Rev. Lett.* **111**, 080502 (2013).
19. M. D. Hutchings *et al.*, *Phys. Rev. Appl.* **8**, 044003 (2017).
20. M. Steffen *et al.*, *Phys. Rev. Lett.* **97**, 050502 (2006).
21. J. Wenner *et al.*, *Phys. Rev. Lett.* **112**, 210501 (2014).
22. D. I. Schuster *et al.*, *Phys. Rev. Lett.* **94**, 123602 (2005).
23. D. I. Schuster *et al.*, *Nature* **445**, 515–518 (2007).
24. M. Hofheinz *et al.*, *Nature* **454**, 310–314 (2008).
25. K. B. Cooper *et al.*, *Phys. Rev. Lett.* **93**, 180401 (2004).
26. R. McDermott *et al.*, *Science* **307**, 1299–1302 (2005).
27. A. P. Sears *et al.*, *Phys. Rev. B* **86**, 180504 (2012).
28. F. Yan *et al.*, *Nat. Commun.* **7**, 12964 (2016).
29. D. T. McClure *et al.*, *Phys. Rev. Appl.* **5**, 011001 (2016).
30. J. M. Martinis *et al.*, *Phys. Rev. Lett.* **95**, 210503 (2005).
31. A. Lupaşcu, C. J. M. Verwijs, R. N. Schouten, C. J. P. M. Harmans, J. E. Mooij, *Phys. Rev. Lett.* **93**, 177006 (2004).
32. A. Herr (Kidiyarova-Shevchenko), A. Fedorov, A. Shnirman, E. Il'ichev, G. Schön, *Supercond. Sci. Technol.* **20**, S450–S454 (2007).
33. K. G. Fedorov, A. V. Shcherbakova, M. J. Wolf, D. Beckmann, A. V. Ustinov, *Phys. Rev. Lett.* **112**, 160502 (2014).
34. R. McDermott *et al.*, *Quantum Sci. and Technol.* **3**, 024004 (2018).

ACKNOWLEDGMENTS

We acknowledge stimulating discussions with M. Vinje, L. B. Ioffe, and M. Saffman. Portions of this work were performed in the Wisconsin Center for Applied Microelectronics, a research core facility managed by the College of Engineering and supported by the University of Wisconsin–Madison. Other portions were performed at the Cornell NanoScale Facility, a member of the National Nanotechnology Coordinated Infrastructure (NNCI), which is supported by the National Science Foundation under grant no. ECCS-1542081. R.M., B.L.T.P., and M.G.V. are inventors on patent number US 9,692,423 B2 held by Wisconsin Alumni Research Foundation, Syracuse University, and Universität des

Saarlandes that covers a system and method for circuit quantum electrodynamics measurement. **Funding:** This work was supported by the U.S. Government under ARO grants W911NF-14-1-0080 and W911NF-15-1-0248. **Author contributions:** R.M. and B.L.T.P. designed and oversaw the experiment. A.O. and C.H. designed and fabricated the samples. A.O., I.V.P., and B.G.C. performed the experiment and analyzed the data. B.G.C., M.G.V., and K.N.N. provided theoretical assistance. A.O., I.V.P., C.H., B.G.C., M.G.V., B.L.T.P., and R.M. co-wrote the manuscript. All remaining authors contributed to the experimental setup, software infrastructure, or fabrication recipes used in these experiments. **Competing interests:** The authors declare no competing financial interests.

Data and materials availability: All data, materials, and unique computer codes necessary to understand and assess the conclusions of this paper are available in the supplementary materials.

SUPPLEMENTARY MATERIALS

www.sciencemag.org/content/361/6408/1239/suppl/DC1
Materials and Methods
Figs. S1 to S6
Tables S1 to S3
References (35, 36)

28 February 2018; accepted 17 July 2018
10.1126/science.aat4625

MICROPOROUS CRYSTALS

Self-assembly of lattices with high structural complexity from a geometrically simple molecule

Hiroshi Yamagishi^{1*†}, Hiroshi Sato¹, Akihiro Hori², Yohei Sato³, Ryotaro Matsuda², Kenichi Kato⁴, Takuzo Aida^{1,5†}

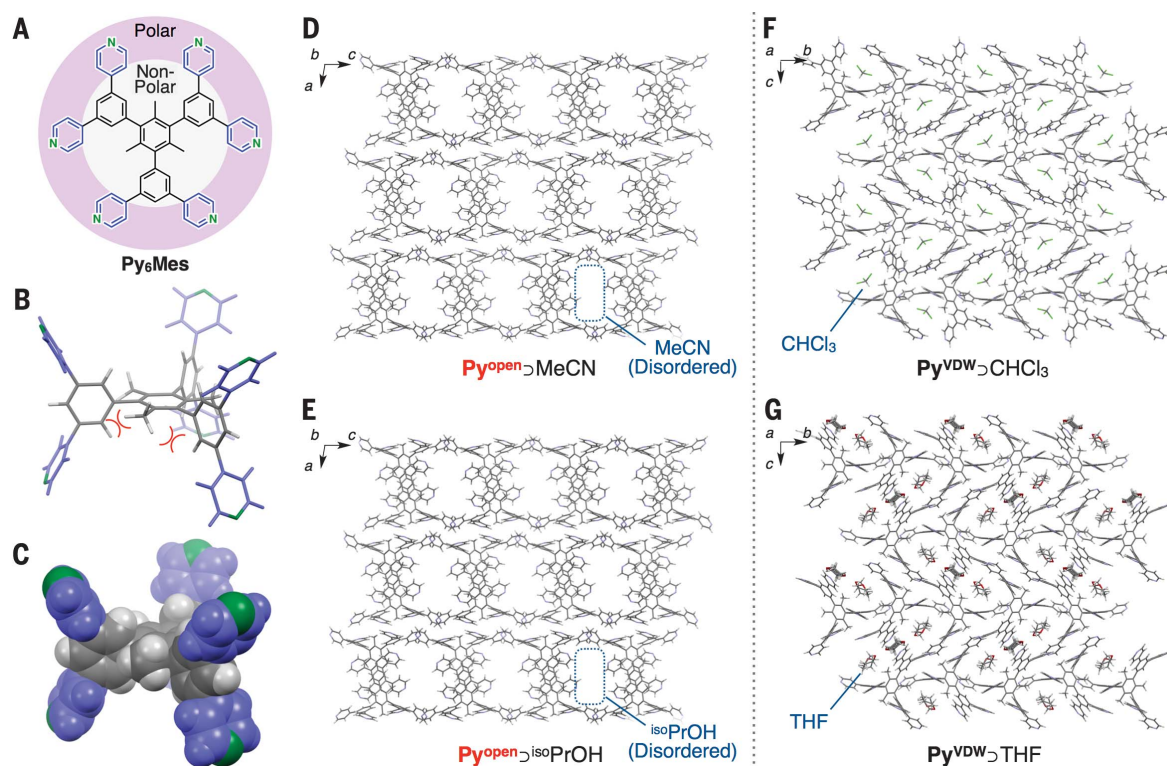
Here we report an anomalous porous molecular crystal built of C–H...N-bonded double-layered roof-floor components and wall components of a segregatively interdigitated architecture. This complicated porous structure consists of only one type of fully aromatic multijoint molecule carrying three identical dipyridylphenyl wedges. Despite its high symmetry, this molecule accomplishes difficult tasks by using two of its three wedges for roof-floor formation and using its other wedge for wall formation. Although a C–H...N bond is extremely labile, the porous crystal maintains its porosity until thermal breakdown of the C–H...N bonds at 202°C occurs, affording a nonporous polymorph. Though this nonporous crystal survives even at 325°C, it can retrieve the parent porosity under acetonitrile vapor. These findings show how one can translate simplicity into ultrahigh complexity.

The research field of crystal engineering was initiated by Desiraju and co-workers, who established its basic concept in the late 1980s by using small organic molecules of geometrical simplicity (1). Since then, organic molecules of further structural complexity have begun to be used for crystal engineering in conjunction with coordinating metal ions to obtain more-complex crystals that have tailored functions (2–4). During our curiosity-driven study on the solution behaviors of hyperbranched, multi-

joint, fully aromatic molecules, we made a serendipitous finding that may be antithetic to the current trend. Like dendrimers (5–7), such aromatic molecules are characterized by their nonplanar morphology and conformational flexibility, so that they are noncrystalline in the solid state, except for a few examples (8, 9). Py₆Mes is a newly designed *D*_{3h}-symmetric molecule that consists exclusively of aromatic rings that are connected via single bonds (Fig. 1A). The nonplanarity of this multijoint aromatic molecule stems from a

large steric repulsion between the methyl groups of the mesitylene (Mes) core and connected phenylene rings (Fig. 1B). Py₆Mes has a propeller shape with a symmetry group of *D*_{3h}, which carries a polar outer shell composed of six pyridyl (Py) units for sterically protecting the nonpolar aromatic core (Fig. 1, A to C). We were curious about whether Py₆Mes, which has a nonpolar solvophobic core, is soluble in highly dielectric media as a discrete spherical amphiphile because of its solvophilic shell. However, despite this characteristic, Py₆Mes readily precipitated in acetonitrile (MeCN) and 2-propanol (*iso*PrOH), affording the porous crystal Py^{open}, which included crystallographically disordered solvent molecules in its nanopores (Fig. 1D). Although Py^{open} comprises only one type of geometrically simple molecule, it accomplishes very complicated tasks (Fig. 2B). As shown in Figs. 1D and 2D, Py₆Mes uses two of its three dipyridylphenyl wedges for the construction of C–H...N-bonded double-layered roof-floor components, adopting a cofacial orientation. In

Fig. 1. Molecular structures of Py₆Mes and crystal packing diagrams of Py^{open} MeCN, Py^{open} *iso*PrOH, Py^{VDW} CHCl₃, and Py^{VDW} THF. (A to C) Molecular structure (A), wireframe (B), and CPK (C) representations of Py₆Mes. The pyridyl rings are colored in blue and green, whereas the mesitylenyl and phenyl rings are colored in black and white. (D to G) Wireframe representations of the crystal-packing diagrams of Py^{open} MeCN (D), Py^{open} *iso*PrOH (E), Py^{VDW} CHCl₃ (F), and Py^{VDW} THF (G).



¹Department of Chemistry and Biotechnology, School of Engineering, The University of Tokyo, 7-3-1 Hongo, Bunkyo-ku, Tokyo 113-8656, Japan. ²Department of Applied Chemistry, Graduate School of Engineering, Nagoya University, Furo-cho, Chikusa-ku, Nagoya 464-8603, Japan. ³Institute for Integrated Cell-Material Sciences (WPI-iCeMS), Kyoto University, Yoshida, Sakyo-ku, Kyoto 606-8501, Japan. ⁴RIKEN SPring-8 Center, 1-1-1 Kouto, Sayo-cho, Sayo-gun, Hyogo 679-5148, Japan. ⁵RIKEN Center for Emergent Matter Science, 2-1 Hirosawa, Wako, Saitama 351-0198, Japan.

*Present address: Division of Materials Science, Faculty of Pure and Applied Sciences, University of Tsukuba, 1-1-1 Tennodai, Tsukuba, Ibaraki 305-8571, Japan.

†Corresponding author. Email: aida@macro.t.u-tokyo.ac.jp (T.A.); yamagishi@macro.t.u-tokyo.ac.jp (H.Y.)

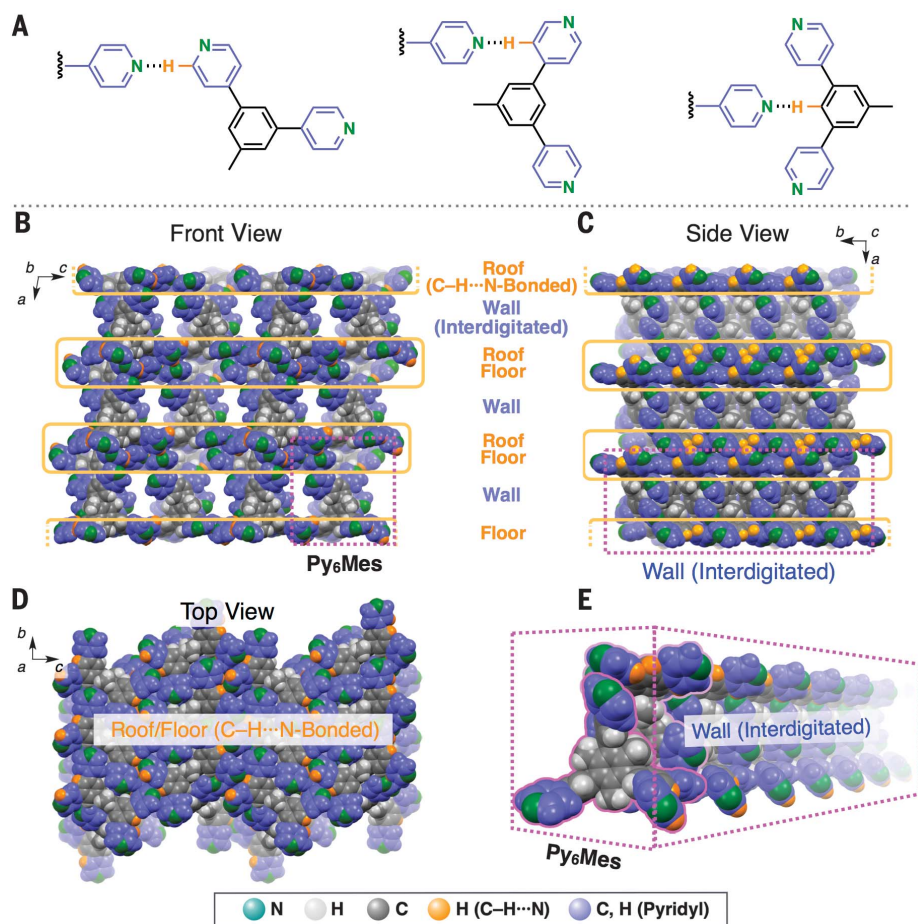


Fig. 2. Modes of C-H...N bonds in Py^{open}>MeCN and crystal-packing diagrams of Py^{open}>MeCN.

(A) Drawings representing the modes of C-H...N bonds in Py^{open}>MeCN. (B to E) CPK representations of the crystal-packing diagrams of Py^{open}>MeCN. Orange outlines indicate the C-H...N-bonded roofs and floors in Py^{open}>MeCN [(B) and (C)], and dashed purple outlines indicate the wall connected to the roof and floor [(B), (C), and (E)].

an orthogonal direction to the roof-floor components, Py₆Mes uses its residual one dipyridyl-phenyl wedge together with the mesitylenyl core for the construction of wall components formed by a solvophobically interdigitated architecture (Fig. 2E). Such difficult tasks, as accomplished by Py₆Mes, illustrate how ultrahigh structural complexity can be achieved through self-assembly of a single molecule of ultrahigh symmetry. Furthermore, even though Py^{open} has C-H...N-bonded parts, it has an exceptionally high thermal stability (Fig. 3B) and, at the same time, has an excellent self-healing ability (Fig. 3C). These findings also allow us to tackle a current issue in materials science: how thermally robust materials are made to self-heal (10–15).

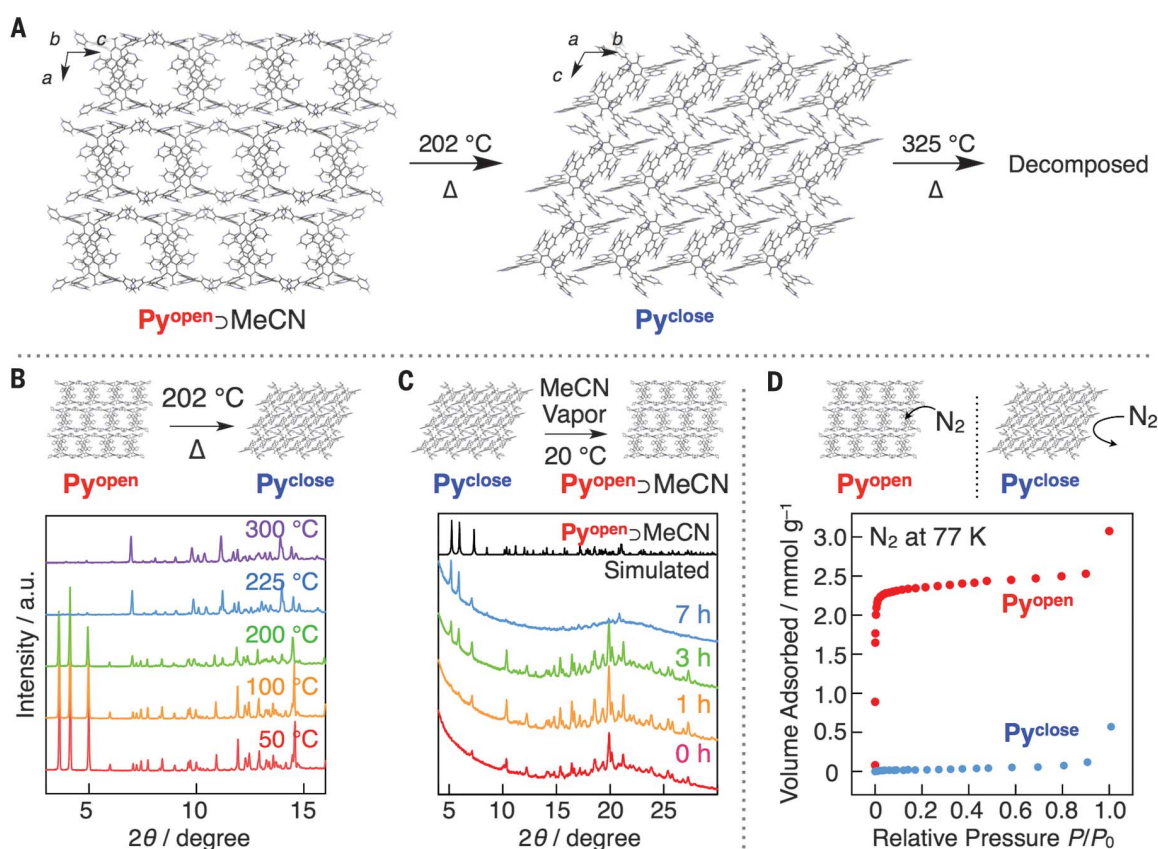
C-H...N bonds are far more labile than conventional hydrogen bonds (16–20). However, in contrast to hydrogen bonds, C-H...N bonds can survive even in highly dielectric media because their attraction force is given essentially by a dispersion force (21–23). To the best of our knowledge, Py^{open} reported herein is the most thermostable porous crystal among those comprising non-classical C-H...X bonds (24–26) and among all healable porous organic and metal-organic crystals reported thus far (10–12). Py₆Mes, the component of Py^{open}, carries three dipyridylphenyl wedges at its mesitylene core (Fig. 1A; details for the synthesis of Py₆Mes are available in the sup-

plementary materials). In MeCN that has an exceptionally high relative permittivity ($\epsilon_r = 37.5$), Py₆Mes self-assembles into single crystals that are suitable for x-ray crystallography. The as-received crystal adopts a space group of $P2_1/c$ and includes crystallographically disordered MeCN molecules in its zigzag-shaped one-dimensional (1D) nanopores, which have diameters of 6 Å (Py^{open}>MeCN; Fig. 1D and fig. S13). As expected, each dipyridyl-phenyl wedge tilts almost perpendicularly to the connected mesitylenyl core, adopting a dihedral angle in the range of 70 to 90°, but none of the three dipyridylphenyl wedges are crystallographically identical. Despite a large number of aromatic rings, only one pair of pyridyl rings that contain N3 atoms likely forms a cofacial π -stack with an interplanar distance of 3.36 Å (fig. S14B). Among the five pairs of geometrically close H and C atoms, only two pairs (H8A...C18 and H18...C13; fig. S14A and table S1) form a C-H... π bond. Five out of the six pyridyl rings in Py₆Mes are involved in the formation of the C-H...N bonds (Fig. 2, A to D, and table S1). Overall, the back-to-back connected double-layered roof-floor components, supported by C-H...N bonds, are formed along the crystallographic bc plane (Fig. 2, B to D), whereas the wall components that are formed by the interdigitation of the dipyridylphenylmesitylenyl parts are constructed along the crystallographic b axis

(Fig. 2E). Thermogravimetric analysis (TGA) of Py^{open}>MeCN showed that the included MeCN molecules began to be released from the nanopores even at room temperature, affording guest-free Py^{open} at 50°C, which is a much lower temperature than the boiling point (82°C) of MeCN (black curve in fig. S7). These observations indicate that the guest MeCN molecules are only weakly trapped in the nanopores of Py^{open}. As expected, the powdery sample of guest-free Py^{open} displayed a typical type I sorption isotherm for N₂, with a steep slope in the low relative pressure (P/P_0) region and a Brunauer-Emmett-Teller (BET) surface area of 219 m² g⁻¹ (red circles in Fig. 3D). The pore size distribution, as estimated by micropore analysis (27), was unimodal with a maximum peak at 0.6 nm (fig. S8), which is in excellent agreement with the diameter of the 1D nanopore observed in Fig. 1D.

As has been discussed for porous crystals in the literature (28), the relative permittivity of the crystallization solvent largely affects the mode of solute-solvent interactions and therefore affects the crystal structures. When Py₆Mes was allowed to assemble in highly dielectric ^{iso}PrOH ($\epsilon_r = 18.3$), the formation of solvent-including porous crystal Py^{open}>^{iso}PrOH (Fig. 1E) occurred, which is isomorphic to Py^{open}>MeCN (Fig. 1D), and its nanopores, again, included crystallographically disordered ^{iso}PrOH molecules. Considering also that the TGA profile of Py^{open}>^{iso}PrOH with respect

Fig. 3. Transformations among $\text{Py}^{\text{open}}\text{MeCN}$, Py^{open} , and Py^{close} , and their N_2 adsorption isotherms. (A) Wire-frame representations of the crystal-packing diagrams of $\text{Py}^{\text{open}}\text{MeCN}$ and Py^{close} . **(B)** PXRD profiles of Py^{open} measured at different temperatures upon heating [wavelength (λ) = 1.07965 Å]. θ , angle of scattering. **(C)** Time-dependent PXRD profiles of Py^{close} incubated in a cuvette filled with MeCN vapor (λ = 1.54 Å). The black line represents a PXRD profile simulated from the single-crystal structure of $\text{Py}^{\text{open}}\text{MeCN}$. **(D)** N_2 adsorption isotherms of Py^{open} (red circles) and Py^{close} (blue circles) at 77 K.



to the release of isoPrOH (red curve in fig. S7) is analogous to that observed for $\text{Py}^{\text{open}}\text{MeCN}$, we conclude that Py^{open} weakly traps isoPrOH , similarly to when MeCN is used, in its nanopores. In sharp contrast to the above cases in highly dielectric media, when Py_6Mes was allowed to assemble in moderately dielectric media such as chloroform (CHCl_3 , $\epsilon_r = 4.8$) and tetrahydrofuran (THF, $\epsilon_r = 7.6$), classical van der Waals inclusion crystals denoted as $\text{Py}^{\text{VDW}}\text{CHCl}_3$ and $\text{Py}^{\text{VDW}}\text{THF}$ formed, respectively (Fig. 1, F and G; for their crystal structures, see the supplementary materials). As summarized in table S2, we observed a clear correlation between the relative permittivities of the crystallization solvents and space groups of the resulting polymorphs (29). Inclusion crystals $\text{Py}^{\text{VDW}}\text{CHCl}_3$ (Fig. 1F) and $\text{Py}^{\text{VDW}}\text{THF}$ (Fig. 1G) are isomorphous to each other and have a space group of $P2_1/n$, but they are geometrically different from $\text{Py}^{\text{open}}\text{MeCN}$ (Fig. 1D) and $\text{Py}^{\text{open}}\text{isoPrOH}$ (Fig. 1E), both of which adopt a space group of $P2_1/c$. It is likely that Py_6Mes is no longer amphiphilic in moderately dielectric CHCl_3 and THF; that is, these solvents are affiliative toward both the shell and core parts of Py_6Mes . Consequently, Py_6Mes does not form a solvophobically interdigitated structure, as observed for the wall components in $\text{Py}^{\text{open}}\text{MeCN}$ and $\text{Py}^{\text{open}}\text{isoPrOH}$ (Fig. 1, D and E). In $\text{Py}^{\text{VDW}}\text{CHCl}_3$ (Fig. 1F) and $\text{Py}^{\text{VDW}}\text{THF}$ (Fig. 1G), the included solvent molecules are essential constituents for supporting the crystal structures. Hence, as confirmed by TGA (fig. S7) and x-ray diffraction

(XRD) (fig. S10), the crystals were easily demolished after heating at 100°C for 3 hours to remove the included solvent molecules.

Porous crystals, particularly when guest-free, are intrinsically unstable unless they use metal coordination bonds or dynamic covalent bonds. In the literature (24–26), none of the reported porous crystals that are composed of nonclassical C–H...X bonds can survive above 130°C. As described earlier, Py^{open} turned out to be far more thermally robust than the reported examples. In a differential scanning calorimetry (DSC) profile over a wide temperature range from 40° to 300°C, guest-free Py^{open} in the first heating process displayed a single exothermic peak at 202°C due to a crystalline phase transition (red curve in fig. S5). Upon subsequent cooling, neither an exothermic peak nor an endothermic peak appeared (blue curve in fig. S5), indicating that the phase transition at 202°C is irreversible. Accordingly, its powder XRD (PXRD) profiles did not change up to 202°C (red, yellow, and green curves in Fig. 3B) and remained essentially identical to that simulated from the single-crystal structure of $\text{Py}^{\text{open}}\text{MeCN}$ (fig. S12). Upon further heating to induce the phase transition, the PXRD profile changed abruptly (blue and purple curves in Fig. 3B) and irreversibly (fig. S11), affording a new crystalline phase. Although the crystals thus formed were heavily cracked and no longer eligible for single-crystal x-ray structural analysis, we successfully identified the crystalline structure by means of Rietveld analysis for the PXRD profile measured

at 50°C (see supplementary materials). In contrast to Py^{open} , the product, denoted nonporous Py^{close} adopting a space group of $P\bar{1}$, has no solvent-accessible 1D channels (Fig. 3A and fig. S15, A to D). Consistently, Py^{close} showed a higher density (1.192 g cm^{−3}) than porous Py^{open} (1.022 g cm^{−3}) and barely adsorbed N_2 (blue circles in Fig. 3D). The Rietveld analysis indicated that none of the C–H...N bonding pairs that were originally present in Py^{open} were shorter than sum of the van der Waals radii of the H and N atoms (table S3), suggesting that the crystalline phase transition at 202°C was triggered by thermal breakdown of the C–H...N bonds in the double-layered roof-floor components (fig. S15, A to D).

Although self-healing is one of the attractive features in materials science, an essential challenge, in the case of solid materials, is to address the general issue that high thermal robustness and excellent healing ability are mutually exclusive (13–15). Py^{close} is thermally more robust than Py^{open} and can survive even at 325°C (Fig. 3A). Nevertheless, under MeCN vapor, Py^{close} self-healed to retrieve its parent porosity at ambient temperatures. Typically, crystalline Py^{close} was put in a glass vial that was filled with MeCN vapor and incubated at 20°C. As shown in Fig. 3C, a set of new PXRD peaks assignable to $\text{Py}^{\text{open}}\text{MeCN}$ gradually emerged at the expense of the original diffractions due to Py^{close} , where the complete recovery of the original diffractions required 7 hours (Fig. 3C). The total volume of MeCN vapor eventually adsorbed by Py^{close} on its recovery was

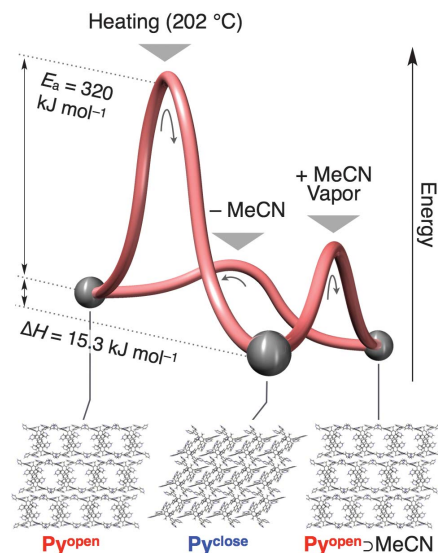


Fig. 4. An energy diagram for the consecutive transformation cycle involving $\text{Py}^{\text{open}} \rightarrow \text{Py}^{\text{open}} \rightarrow \text{MeCN}$, Py^{open} , and Py^{close} . Energy levels of $\text{Py}^{\text{open}} \rightarrow \text{MeCN}$, Py^{open} , and Py^{close} were estimated on the basis of the DSC and TGA profiles. The arrows indicate the direction of the crystal transformations. E_a , activation energy.

nearly equal to the original pore volume of Py^{open} (fig. S17). Guest-free Py^{open} obtained from $\text{Py}^{\text{open}} \rightarrow \text{MeCN}$ thus recovered again showed a N_2 adsorption behavior characteristic of microporous materials (fig. S16). The observed recovery is not the consequence of a trivial process involving partial dissolution of Py^{close} in MeCN followed by recrystallization of Py_6Mes , because a finely ground amorphous powder sample of Py^{open} , when likewise treated under MeCN vapor at 20°C, did not transform back into Py^{open} but gradually exerted a totally different XRD pattern (fig. S9) and MeCN adsorption profile (fig. S18). Namely, the reversible transformation occurs only between $\text{Py}^{\text{open}} \rightarrow \text{MeCN}$ and Py^{close} .

Here we demonstrate that $\text{Py}^{\text{open}} \rightarrow \text{MeCN}$ consecutively transforms into guest-free Py^{open} and then nonporous Py^{close} , which transforms back into $\text{Py}^{\text{open}} \rightarrow \text{MeCN}$ under MeCN vapor. Figure 4 shows a possible energy diagram for the overall crystalline transformation based on the DSC and TGA profiles. As described above, the release of guest MeCN molecules from $\text{Py}^{\text{open}} \rightarrow \text{MeCN}$ to afford Py^{open} likely requires only a negligibly small activation energy, as evidenced by the TGA profile of $\text{Py}^{\text{open}} \rightarrow \text{MeCN}$ (fig. S7). By contrast, the trans-

formation of Py^{open} into Py^{close} requires considerable heating and features a single exothermic peak in DSC at 202°C (fig. S5), for which the change in enthalpy (ΔH) value was evaluated to be 15.3 kJ mol⁻¹. By means of the Kissinger method (30), the activation energy for this process was evaluated to be as high as 320 kJ mol⁻¹ (fig. S6). On the other hand, the regeneration of $\text{Py}^{\text{open}} \rightarrow \text{MeCN}$ from Py^{close} under MeCN vapor occurs autonomously (Fig. 3C), suggesting that this transformation is energetically downhill and has a small activation energy to overcome, even at ambient temperatures. As is apparent in Fig. 3A, this process requires only a moderate reorientation of the interdigitating dipyriddyphenylmesitylenyl units to effectively cancel their dipoles. We suppose that MeCN vapor would play an intermediate role in this reorientation event.

As exemplified by the formation of Py^{VDW} in moderately dielectric media (Fig. 1, F and G), assembled structures usually reflect the symmetry of constituent molecules. In this sense, it may be difficult to imagine that high-symmetry Py_6Mes is the sole constituent for porous Py^{open} , whose roof-floor components are structurally and orientationally different from its wall component (Fig. 1, D and E). Apart from the exciting physical properties of Py^{open} that may change the preconception of healable solid materials (Fig. 4), the most intriguing result presented here is that Py_6Mes , in highly dielectric media for constructing Py^{open} , uses its three equivalent wedges for totally different tasks (Fig. 2B). This example demonstrates that even a single molecule of geometrical simplicity could assemble into a highly complicated exotic material of low symmetry.

REFERENCES AND NOTES

- G. R. Desiraju, *Angew. Chem. Int. Ed. Engl.* **34**, 2311–2327 (1995).
- M. Irie, T. Fukaminato, K. Matsuda, S. Kobatake, *Chem. Rev.* **114**, 12174–12277 (2014).
- H. Furukawa, K. E. Cordova, M. O’Keeffe, O. M. Yaghi, *Science* **341**, 1230444 (2013).
- S. Horike, S. Shimomura, S. Kitagawa, *Nat. Chem.* **1**, 695–704 (2009).
- D. A. Tomalia *et al.*, *Polym. J.* **17**, 117–132 (1985).
- S. M. Grayson, J. M. J. Fréchet, *Chem. Rev.* **101**, 3819–3868 (2001).
- C. J. Hawker, J. M. J. Fréchet, *J. Am. Chem. Soc.* **112**, 7638–7647 (1990).
- R. E. Bauer, V. Enkelmann, U. M. Wiesler, A. J. Berresheim, K. Müllen, *Chem. Eur. J.* **8**, 3858–3864 (2002).
- S. Nakajima *et al.*, *Chem. Commun. (Camb.)* **54**, 2534–2537 (2018).
- Y. Sakata *et al.*, *Science* **339**, 193–196 (2013).
- Y.-G. Huang *et al.*, *Nat. Commun.* **7**, 11564 (2016).
- J. Tian, P. Thallapally, J. Liu, G. J. Exarhos, J. L. Atwood, *Chem. Commun. (Camb.)* **47**, 701–703 (2011).
- P. Cordier, F. Tournilhac, C. Soulié-Ziakovic, L. Leibler, *Nature* **451**, 977–980 (2008).
- Y. Chen, A. M. Kushner, G. A. Williams, Z. Guan, *Nat. Chem.* **4**, 467–472 (2012).
- Y. Yanagisawa, Y. Nan, K. Okuro, T. Aida, *Science* **359**, 72–76 (2018).
- U. Samanta, P. Chakrabarti, J. Chandrasekhar, *J. Phys. Chem. A* **102**, 8964–8969 (1998).
- F. A. Cotton, L. M. Daniels, G. T. Jordan IV, C. A. Murillo, *Chem. Commun. (Camb.)* **0**, 1673–1674 (1997).
- M. Mascal, *Chem. Commun. (Camb.)* **0**, 303–304 (1998).
- V. R. Thalladi, A. Gehrke, R. Boese, *New J. Chem.* **24**, 463–470 (2000).
- E. Arunan *et al.*, *Pure Appl. Chem.* **83**, 1619–1636 (2011).
- G. R. Desiraju, T. Steiner, *The Weak Hydrogen Bond in Structural Chemistry and Biology* (Oxford Univ. Press, 1999).
- M. Nishio, Y. Umezawa, K. Honda, S. Tsuboyama, H. Suezawa, *CrystEngComm* **11**, 1757–1788 (2009).
- G. R. Desiraju, *Acc. Chem. Res.* **35**, 565–573 (2002).
- P. Sozzani, S. Bracco, A. Comotti, L. Ferretti, R. Simonutti, *Angew. Chem. Int. Ed.* **44**, 1816–1820 (2005).
- K. J. Msayib *et al.*, *Angew. Chem. Int. Ed.* **48**, 3273–3277 (2009).
- C. G. Bezzu, M. Helliwell, J. E. Warren, D. R. Allan, N. B. McKeown, *Science* **327**, 1627–1630 (2010).
- R. S. Mikhail, S. Brunauer, E. E. Bodor, *J. Colloid Interface Sci.* **26**, 45–53 (1968).
- N. B. McKeown, *J. Mater. Chem.* **20**, 10588–10597 (2010).
- I. M. Smallwood, *Handbook of Organic Solvent Properties* (Butterworth-Heinemann, Oxford, 2012).
- H. E. Kissinger, *Anal. Chem.* **29**, 1702–1706 (1957).

ACKNOWLEDGMENTS

H.Y. thanks A. I. Cooper and M. A. Little in the Department of Chemistry and Materials Innovation Factory, University of Liverpool, for x-ray diffraction measurements. Synchrotron radiation experiments were performed at BL44B2 in Spring-8 with the approval of the RIKEN Spring-8 Center (proposal 20160024).

Funding: This work was supported by the Japan Society for the Promotion of Science (JSPS) through its Grant-in-Aid for Scientific Research (S) (18H05260) on “Innovative functional materials based on multi-scale interfacial molecular science.” H.Y. thanks the JSPS for a Young Scientist Fellowship and Leading Graduate Schools (MERIT) and the Leverhulme Trust (Leverhulme Research Centre for Functional Materials Design) for providing funding during a research placement at the University of Liverpool. **Author contributions:** H.Y. performed and interpreted all the experiments associated with molecular synthesis, crystal growth, and structural characterization. H.S. performed the sorption experiments. K.K. conducted synchrotron x-ray studies. A.H., Y.S., and R.M. carried out crystallographic studies. All authors contributed to the writing and editing of the manuscript. H.Y. and T.A. conceived the project, designed experiments, and directed the research. **Competing interests:** None declared. **Data and materials availability:** Crystallographic data reported in this paper are listed in the supplementary materials and archived at the Cambridge Crystallographic Data Centre under reference numbers CCDC 1857527 to 1857531. All other data needed to evaluate the conclusions in the paper are present in the paper or the supplementary materials.

SUPPLEMENTARY MATERIALS

www.sciencemag.org/content/361/6408/1242/suppl/DC1
Materials and Methods
Figs. S1 to S18
Tables S1 to S3
References (31–38)

20 March 2018; accepted 23 July 2018
10.1126/science.aat6394

EARLY ANIMALS

Ancient steroids establish the Ediacaran fossil *Dickinsonia* as one of the earliest animals

Ilya Bobrovskiy^{1*}, Janet M. Hope¹, Andrey Ivantsov², Benjamin J. Nettersheim³, Christian Hallmann^{3,4}, Jochen J. Brocks^{1*}

The enigmatic Ediacara biota (571 million to 541 million years ago) represents the first macroscopic complex organisms in the geological record and may hold the key to our understanding of the origin of animals. Ediacaran macrofossils are as “strange as life on another planet” and have evaded taxonomic classification, with interpretations ranging from marine animals or giant single-celled protists to terrestrial lichens. Here, we show that lipid biomarkers extracted from organically preserved Ediacaran macrofossils unambiguously clarify their phylogeny. *Dickinsonia* and its relatives solely produced cholesteroloids, a hallmark of animals. Our results make these iconic members of the Ediacara biota the oldest confirmed macroscopic animals in the rock record, indicating that the appearance of the Ediacara biota was indeed a prelude to the Cambrian explosion of animal life.

The Ediacara biota remains one of the greatest mysteries in paleontology. Members of this assemblage were initially described as animals (1, 2); however, as collections grew, it became apparent that Ediacaran fossils and their body plans are difficult to compare with modern phyla (3, 4). A major complication for the study of Ediacaran organisms is their soft-bodied nature and particular mode of preservation, rarely found in younger fossils. Thus, the interpretation of various members of the Ediacara biota has crossed several Kingdoms and Domains, ranging from bacterial colonies (5), marine fungi (6), lichens (7), and giant protists (8, 9) to stem-group animals and crown-group Eumetazoa (4, 10, 11). The recent general consensus is that these fossils are polyphyletic (12, 13): At least some members of the Ediacara biota are almost unanimously interpreted as bilaterian animals (*Kimberella*) (14, 15), whereas others are confidently ascribed to giant protozoa (*Palaeopascichmus*) (16). *Beltanelliformis*—although previously interpreted as bacteria, benthic and planktonic algae, as well as different animals—is now recognized as a spherical colony of cyanobacteria on the basis of their biomarker content (17). The affinity of most other Ediacarans, however, remains controversial, even at the Kingdom level (4). Most recently, arguments surrounding these fossils have centered on lichens, giant protists, and stem- or crown-group Metazoa.

Whereas the lichen hypothesis (7) requires an implausible reinterpretation of the habitat of the Ediacara biota from a marine to a conti-

mental depositional environment (18), for many Ediacaran fossils, including dickinsoniids, it currently seems impossible to distinguish between giant protist and metazoan origins (4, 19). Some Ediacaran fossils, such as *Palaeopascichmus*, were likely giant unicellular eukaryotes (protists) (16), which means that in contrast to modern ecosystems, these organisms were present and sometimes extremely abundant in shallow-water Ediacaran habitats (20). Features of dickinsoniids such as “quilting” patterns, the inferred absence of dorso-ventral differentiation, and putative external digestion mode were found to be compatible with modern giant protists and hard to reconcile with metazoans (8, 20). Some modern giant protists can be up to 25 cm in size (21). In the absence of metazoan competition, they may have become even larger, possibly providing an explanation for the size range of Ediacaran protistan fossils (8). Some giant protists even have a motile lifestyle, compatible with Ediacaran trace fossils (22) and dickinsoniid “footprints” (15). For dickinsoniids, the absence of evidence for a mouth and gut, perceived absence of bilateral symmetry, and possible external digestion are all consistent with a protistan origin. However, all of the above characteristics are also compatible with basal Metazoa such as the Placozoa that are situated at the very base of Eumetazoa (23), whereas rejection of an external digestion mode and acceptance of supposed cephalization (15) may place dickinsoniids even higher on the metazoan tree. The nature of dickinsoniids, and most other Ediacaran fossils, thus remains unresolved.

We applied a new approach (17) to test the lichen, protist, and animal hypotheses by studying biomarkers extracted from organically preserved dickinsoniids. Hydrocarbon biomarkers are the molecular fossils of lipids and other biological compounds. Encased in sedimentary rock, biomarkers may retain information about their biological origins for hundreds of millions of

years. For instance, hopanes are the hydrocarbon remains of bacterial hopanepolyols, whereas saturated steranes and aromatic steroids are diagenetic products of eukaryotic sterols. The most common sterols of Eukarya possess a cholesteroloid, ergosteroid, or stigmateroid skeleton with 27, 28, or 29 carbon atoms, respectively. These C₂₇ to C₂₉ sterols, distinguished by the alkylation pattern at position C-24 in the sterol side chain, function as membrane modifiers and are widely distributed across extant Eukarya, but their relative abundances can give clues about the source organisms (24).

Apart from *Dickinsonia* (Fig. 1B), which is one of the most recognizable Ediacaran fossils, dickinsoniids include *Andiva* (Fig. 1C and fig. S1), *Vendia*, *Yorgia*, and other flattened Ediacaran organisms with segmented metameric bodies and a median line along the body axes, separating the “segments.” The specimens for this study were collected from two surfaces in the Lyamtsa (*Dickinsonia*) and Zimmie Gory (*Andiva*) localities of the Ediacara biota in the White Sea region (Russia). Both *Dickinsonia* and *Andiva* are preserved in negative hyporelief on the sole of sandstones with microbial mat impressions and consist of a thin (up to ~3 μm) film of organic matter. The organic matter was detached from the rock surface (fig. S1) and extracted for hydrocarbon biomarkers under strict exclusion of contamination (materials and methods). Much thinner organic films covering the surfaces around *Andiva* fossils from the Zimmie Gory locality were extracted as well, providing a background signal coming from associated microbial mats. Investigation of biomarker composition of surrounding surfaces and enclosing sedimentary rocks allowed us not only to subtract the background signal but also to make sure that the biomarker signal from the fossils is not contaminated (supplementary text). We analyzed biomarkers using gas chromatography-mass spectrometry (materials and methods).

The deposits immediately above and below *Dickinsonia* are characterized by a monoaromatic steroid distribution of 10.6 to 11.9% cholesteroloids, 13.4 to 16.8% ergosteroids, and 71.3 to 76.0% stigmateroids, which is consistent with the general steroid distribution of sediments at the Lyamtsa locality (Fig. 1). The strong stigmateroid predominance is typical for the Ediacaran period and presumably related to green algae (Chlorophyta) inhabiting benthic mats or the water column (25). In these and all other Ediacaran sediment samples from the White Sea region, the carbon-number distribution of saturated steranes is nearly identical to the distribution of monoaromatic steroid homologs and always dominated by green algal stigmateroids (Table 1). By contrast, biomarkers extracted from the isolated organic matter of the largest *Dickinsonia* specimen had a monoaromatic steroid distribution of 93% cholesteroloids, 1.8% ergosteroids, and 5.2% stigmateroids (Fig. 1A and Table 1). A general trend of increasing monoaromatic cholesteroloid abundance from 84.8 to 93.0% from the smaller to the larger *Dickinsonia* specimens

¹Research School of Earth Sciences, Australian National University, Canberra ACT 2601, Australia. ²Borissiak Paleontological Institute, Russian Academy of Sciences, Moscow 117997, Russia. ³Max Planck Institute for Biogeochemistry, Jena 07745, Germany. ⁴MARUM—Center for Marine Environmental Sciences, University of Bremen, Bremen 28359, Germany. *Corresponding author. Email: ilya.bobrovskiy@anu.edu.au (I.B.); jochen.brocks@anu.edu.au (J.J.B.)

Fig. 1. Biomarkers from organically preserved *Dickinsonia*.

(A) Mass/charge ratio 253 selected ion recording chromatogram showing the distribution of monoaromatic steroids (MAS) of the solvent extract of a large *Dickinsonia* specimen (*Dickinsonia*-2; 5.5 cm width). (B) Organically preserved *Dickinsonia* from the Lyamtsa locality (*Dickinsonia*-2). (C) Metastable reaction monitoring chromatogram showing the sum of C_{27-29} sterane traces of *Dickinsonia*-2. $\alpha\beta = 5\alpha(H)$, $14\beta(H)$, $17\beta(H)$ (and correspondingly for $\alpha\alpha$ and $\beta\alpha$); S and R indicate isomerization at position C-20. (D) Relationship between the MAS $C_{27}/MAS C_{29}$ ratio and the Animal Decomposition Index (ADI) = $(C_{27} 5\beta/5\alpha)/(C_{29} 5\beta/5\alpha)$ in *Dickinsonia* ($n = 6$ samples), *Andiva* ($n = 2$ samples), and bulk rock extracts from the Lyamtsa and Zimmie Gory localities ($n = 32$ samples). Only samples with detectable MAS were used in the plot. ADI is a measure of the quantity of sterols that decomposed in the anaerobic microenvironment of an animal carcass relative to normal sterol decomposition within the background sediment. ADI ≈ 1 indicates that cholesterol and stigmateroids underwent alteration in the same diagenetic environment consistent with the absence of animal tissue. ADI > 1 indicates contribution of animal sterols to the biomarker signal. (E) Relationship between the $5\beta/5\alpha$ sterane isomer ratio for cholestane (C_{27}) and stigmastane (C_{29}) in *Dickinsonia* ($n = 8$ samples), *Andiva* ($n = 2$ samples), and bulk rock extracts from the Lyamtsa and Zimmie Gory localities ($n = 54$ samples). $5\beta/5\alpha = (\beta\alpha\alpha 20R + \alpha\alpha\alpha 20S)/\alpha\alpha\alpha 20R$. MAS structures: I = $5\beta(H)10\beta(CH_3)$, II = $5\alpha(H)10\beta(CH_3)$, V = $5\beta(CH_3)10\beta(H)$, and VII = $5\alpha(CH_3)10\alpha(H)$.

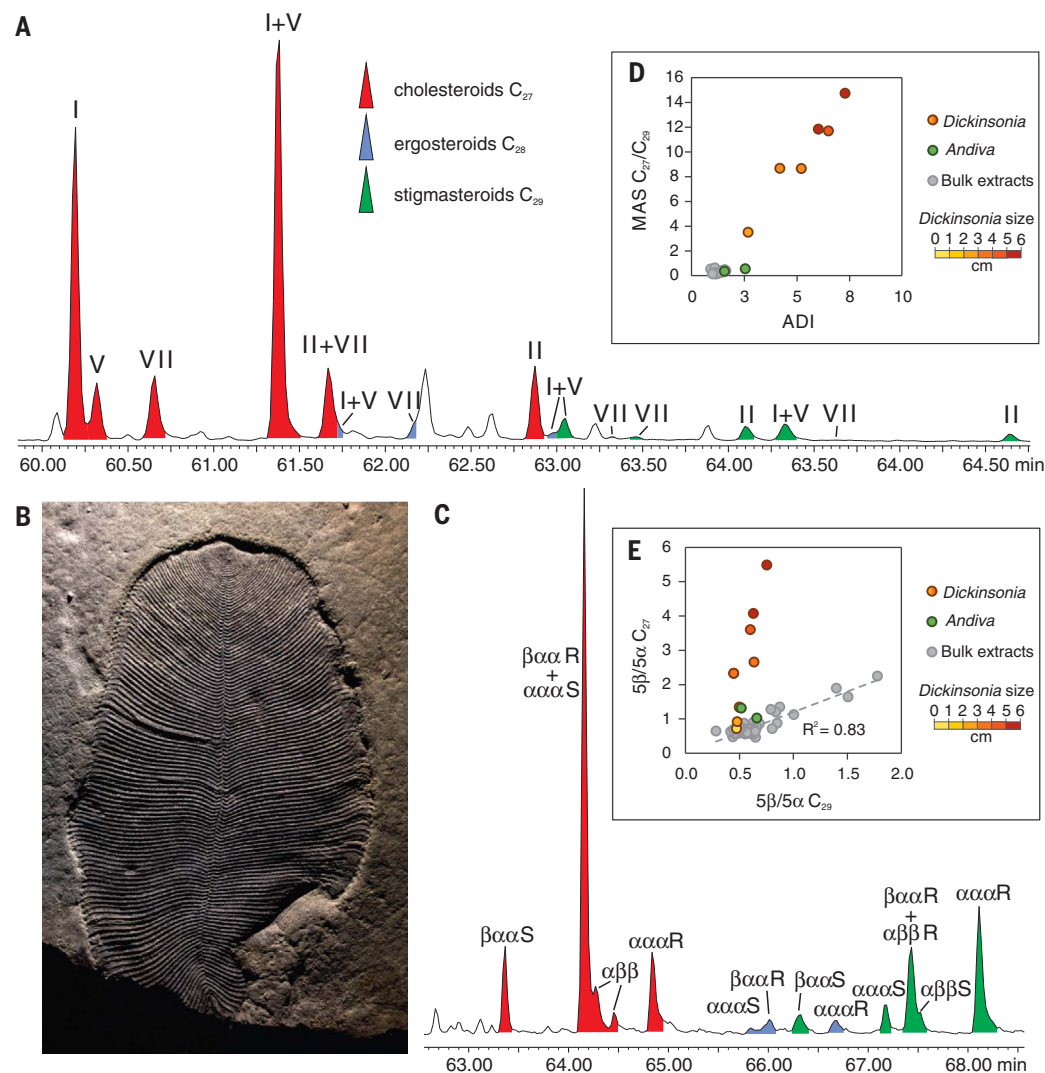


(Fig. 1D) reflects decreasing contribution of the green algal background signal (fig. S2).

The striking abundance of cholesterol in *Dickinsonia* is corroborated by an unusual sterane isomer distribution. In sediments surrounding the fossils in Lyamtsa and Zimmie Gory localities, the ratio of 5β over 5α stereoisomers for all steranes is generally near the equilibrium diagnostic for abiological isomerization (average $5\beta/5\alpha = 0.65 \pm 0.26$, $n = 54$ samples) (Fig. 1, D and E). By contrast, in the fossils, $5\beta/5\alpha$ of cholestane is markedly elevated—up to 5.5 in *Dickinsonia* (Table 1 and Fig. 1, C, D, and E)—values that are generated through strictly anaerobic microbial activity (26, 27), such as during the decay of carcasses. Although the gut flora of some mammals is known to produce 5β -stanols (precursors of 5β -steranes) (28), high relative abundances of these molecules in some background sediments (Fig. 1E) and macroalgae (17) from the White Sea contests the otherwise exciting possibil-

ity that 5β -steranes originated from *Dickinsonia*'s gut microbiota (supplementary text). 5β ergosteranes and stigmateranes in the *Dickinsonia* extracts are not elevated (Table 1), demonstrating that they are ultimately not derived from dickinsoniids but from the underlying microbial mat or surrounding sediment (fig. S2). On the basis of these steroid homolog and isomer patterns, we compute that the sterols of living *Dickinsonia* consisted of at least 99.7% cholesterol (supplementary text). Within analytical precision, it is impossible to exclude that *Dickinsonia* produced traces of ergosteroids (up to 0.23%) or stigmateroids (up to 0.07%). Such sterols, if present, may be derived from the organism itself but could also represent dietary uptake or contributions from symbionts.

Biomarker signatures of *Andiva* specimens from the Zimmie Gory locality are less well differentiated from the microbial mat background signal and do not display a clear elevation of

cholesteroids relative to the background (Table 1). Yet even in these fossils, $5\beta/5\alpha$ ratios for cholestanes are much higher ($5\beta/5\alpha = 1.02$ to 1.31) when compared with ergosteranes and stigmateranes from the fossil extract ($5\beta/5\alpha = 0.52$ to 0.66) and the surrounding mat ($5\beta/5\alpha = 0.65$ to 0.81) (Table 1). On the basis of these values, we can compute a conservative minimum C_{27} sterol content of 88.1% for *Andiva* (supplementary text).

Using the remarkable steroid patterns of the fossils, it is possible to test the position of dickinsoniids on the phylogenetic tree. Lichen-forming fungi only produce ergosteroids, and even in those that host symbiotic algae, ergosteroids remain the major sterols (29, 30). *Dickinsonia* contained no or a maximum of only 0.23% ergosteroids, conclusively refuting the lichen hypothesis (7). The groups of rhizarian protists that include gigantic representatives (Gromiidae, Xenophyophorea, and other Foraminifera) and their retarian relatives all produce a complex

Table 1. Steroid distributions in *Dickinsonia* and *Andiva* extracts. C₃₀ steranes are only represented by 24-isopropylcholestanes. 5 β /5 α = ($\beta\alpha\alpha$ 20R + $\alpha\alpha\alpha$ 20S)/ $\alpha\alpha\alpha$ 20R. ADI = (C₂₇ 5 β /5 α)/(C₂₉ 5 β /5 α) (Fig. 1). Only the I and V monoaromatic steroid isomers (nomenclature provided in Fig. 1) were used for all computations because they display the least coelution with other peaks on the chromatogram. Numbers in parentheses are standard deviation values, and numbers in brackets next to zero values represent the detection limit (the maximum of a given compound that may be present when not detected). n/a, not applicable; dashes indicate not measurable.

Sample	Locality	Size (width, cm)	Saturated steranes							Monoaromatic steroids				
			C ₂₇ (%)	C ₂₈ (%)	C ₂₉ (%)	C ₃₀	C ₂₇ 5 β /5 α	C ₂₈ 5 β /5 α	C ₂₉ 5 β /5 α	ADI	C ₂₇ (%)	C ₂₈ (%)	C ₂₉ (%)	C ₂₇ /C ₂₉
<i>Dickinsonia</i> -1	Lyamtsa	6.0	48.1 (1.3)	5.7 (0.2)	45.8 (1.2)	0.4 (0.04)	3.61 (0.21)	0.52 (0.34)	0.60 (0.06)	6.01 (0.67)	92.4 (2.5)	2.1 (0.1)	5.5 (0.3)	11.84 (0.93)
<i>Dickinsonia</i> -2	Lyamtsa	5.5	63.2 (1.5)	4.9 (0.2)	31.9 (0.8)	0 {0.05}	5.49 (0.28)	0.65 (0.34)	0.75 (0.06)	7.28 (0.65)	93.0 (2.3)	1.8 (0.1)	5.2 (0.3)	14.75 (0.91)
<i>Dickinsonia</i> -3	Lyamtsa	4.5	47.9 (1.5)	6.1 (0.3)	46.0 (1.4)	0 {0.03}	4.08 (0.29)	0.75 (0.34)	0.63 (0.04)	6.50 (0.64)	92.5 (3.2)	2.7 (0.2)	4.8 (0.3)	11.71 (1.41)
<i>Dickinsonia</i> -4	Lyamtsa	4.0	33.4 (2.2)	8.0 (0.7)	58.5 (3.5)	0 {0.08}	2.66 (0.41)	0.97 (0.34)	0.64 (0.08)	4.18 (0.83)	87.9 (6.4)	4.8 (0.7)	7.3 (0.9)	8.67 (1.59)
<i>Dickinsonia</i> -5	Lyamtsa	4.0	44.8 (0.9)	7.6 (0.4)	47.6 (1.0)	0 {0.01}	2.33 (0.10)	0.81 (0.34)	0.45 (0.02)	5.21 (0.32)	91.3 (4.5)	3.6 (0.4)	5.1 (0.5)	8.66 (1.81)
<i>Dickinsonia</i> -6	Lyamtsa	3.5	27.5 (0.7)	9.9 (0.5)	62.6 (1.3)	0 {0.04}	1.34 (0.07)	0.79 (0.34)	0.50 (0.02)	2.67 (0.18)	84.8 (5.7)	3.4 (0.5)	11.8 (1.2)	3.51 (0.80)
<i>Dickinsonia</i> -7	Lyamtsa	1.0	17.2 (1.2)	6.9 (1.2)	75.9 (3.6)	0 {0.18}	0.71 (0.10)	0.22 (0.34)	0.47 (0.05)	1.49 (0.26)	—	—	—	—
<i>Dickinsonia</i> -8	Lyamtsa	2.5	20.5 (1.3)	6.7 (1.2)	72.7 (3.6)	0 {0.10}	0.91 (0.13)	0.26 (0.34)	0.48 (0.05)	1.89 (0.32)	—	—	—	—
<i>Dickinsonia</i> - Sandstone	Lyamtsa	n/a	11.6 (0.3)	8.9 (0.2)	78.9 (1.2)	0.6 (0.04)	0.64 (0.04)	0.85 (0.34)	0.52 (0.02)	1.23 (0.08)	11.9 (1.0)	16.8 (1.5)	71.3 (4.4)	0.17 (0.01)
<i>Dickinsonia</i> - Clay	Lyamtsa	n/a	9.7 (0.3)	7.8 (0.2)	82.0 (1.3)	0.5 (0.03)	0.61 (0.03)	0.71 (0.34)	0.59 (0.02)	1.03 (0.07)	10.6 (0.7)	13.4 (0.9)	76.0 (3.3)	0.2 (0.01)
<i>Andiva</i> -1	Zimnie Gory	8.0	24 (0.4)	10.3 (0.3)	64.3 (0.9)	1.3 (0.1)	1.07 (0.04)	0.76 (0.34)	0.68 (0.02)	1.55 (0.07)	21.5 (0.8)	17.5 (0.7)	61.0 (1.9)	0.36 (0.01)
<i>Andiva</i> -2	Zimnie Gory	4.0	24.9 (1.2)	12.2 (1.2)	61.8 (2.7)	1.0 (0.2)	1.31 (0.15)	0.81 (0.34)	0.52 (0.04)	2.54 (0.36)	29.3 (2.6)	12.6 (1.4)	58.1 (4.5)	0.55 (0.05)
<i>Andiva</i> Mat	Zimnie Gory	n/a	25.8 (1.0)	15.8 (1.0)	57.4 (1.9)	1.0 (0.1)	0.80 (0.07)	0.96 (0.34)	0.65 (0.04)	1.24 (0.13)	18.7 (1.4)	21.4 (1.6)	59.8 (3.5)	0.35 (0.02)
<i>Andiva</i> - Sandstone	Zimnie Gory	n/a	37.5 (1.0)	10.5 (0.3)	51.6 (1.3)	0.5 (0.04)	0.65 (0.04)	0.91 (0.34)	0.61 (0.03)	1.08 (0.08)	25.6 (1.7)	15.7 (1.2)	58.7 (3.4)	0.43 (0.03)
<i>Andiva</i> -Clay	Zimnie Gory	n/a	23.1 (0.5)	9.5 (0.3)	65.9 (1.3)	1.5 (0.02)	0.86 (0.04)	0.84 (0.34)	0.68 (0.02)	1.26 (0.07)	19.4 (1.6)	11.2 (1.2)	69.4 (4.7)	0.28 (0.02)

mixture of sterols, with cholesteroloids comprising 10.3 to 78.2% of the mixture, ergosteroids 4.9 to 43.0%, and stigmateroids 7.2 to 60.1% (table S4). Moreover, rhizarian protists may produce C₃₀ sterols (24-*n*-propylcholesteroids) that can form a notable (up to ~20%) proportion of their total sterol content (37). By contrast, in most *Dickinsonia* and *Andiva* extracts, C₃₀ sterols were below detection limits. Thus, the steroid composition of dickinsoniids is markedly distinct from steroid distributions observed in Rhizaria, rendering a protozoan affinity of these fossils extremely unlikely. All animals—with rare exceptions, such as some demosponges and bivalve molluscs—are characterized by exclusive production of C₂₇ sterols (32, 33). The closest relatives of metazoans, *Choanoflagellata* and *Filasterea*, produce 90 to 100% and 84 to 100% of cholesterol, respectively, and contain up to 16% ergosteroids (34–36). Although the sterol composition of some choanoflagellates and filastereans falls within the range observed for *Dickinsonia* and

Andiva, they are unlikely precursor candidates because these groups are only ever represented by microscopic organisms, leaving a stem- or crown-group metazoan affinity as the only plausible phylogenetic position for *Dickinsonia* and its morphological relatives.

Molecular fossils firmly place dickinsoniids within the animal kingdom, establishing *Dickinsonia* as the oldest confirmed macroscopic animals in the fossil record (558 million years ago) next to marginally younger *Kimberella* from Zimnie Gory (555 million years ago) (37). However alien they looked, the presence of large dickinsoniid animals, reaching 1.4 m in size (38), reveals that the appearance of the Ediacara biota in the fossil record is not an independent experiment in large body size but indeed a prelude to the Cambrian explosion of animal life.

REFERENCES AND NOTES

1. R. C. Sprigg, *Trans. R. Soc. S. Aust.* **71**, 212–224 (1947).
2. M. F. Glaessner, *The Dawn of Animal Life: A Biohistorical Study* (Cambridge Univ. Press, UK, 1984).

3. G. M. Narbonne, *Science* **305**, 1141–1144 (2004).
4. S. Xiao, M. Laflamme, *Trends Ecol. Evol.* **24**, 31–40 (2009).
5. M. Steiner, J. Reitner, *Geology* **29**, 1119–1122 (2001).
6. K. J. Peterson, B. Waggoner, J. W. Hagadorn, *Integr. Comp. Biol.* **43**, 127–136 (2003).
7. G. J. Retallack, *Nature* **493**, 89–92 (2013).
8. A. Seilacher, *Geol. Soc. London Spec. Publ.* **286**, 387–397 (2007).
9. A. Y. Zhuravlev, *Neues Jahrb. Geol. Palaontol. Abh.* **190**, 299–314 (1993).
10. G. M. Narbonne, *Annu. Rev. Earth Planet. Sci.* **33**, 421–442 (2005).
11. S. D. Evans, M. L. Droser, J. G. Gehling, *PLOS ONE* **12**, e0176874 (2017).
12. D. Grazhdankin, in *Encyclopedia of Geobiology*, J. Reitner, V. Thiel, Eds. (Springer, 2011), pp. 342–348.
13. D. H. Erwin *et al.*, *Science* **334**, 1091–1097 (2011).
14. M. A. Fedonkin, B. M. Waggoner, *Nature* **388**, 868–871 (1997).
15. A. Y. Ivantsov, *Stratigr. Geol. Correl.* **21**, 252–264 (2013).
16. J. B. Antcliffe, A. J. Gooday, M. D. Brasier, *Palaentology* **54**, 1157–1175 (2011).
17. I. Bobrovskiy, J. M. Hope, A. Krasnova, A. Ivantsov, J. J. Brooks, Molecular fossils from organically preserved Ediacara biota reveal cyanobacterial origin for *Beltanelliformis*. *Nat. Ecol. Evol.* **2**, 437–440 (2018).
18. S. Xiao *et al.*, *Geology* **41**, 1095–1098 (2013).

19. M. L. Droser, J. G. Gehling, . *Proc. Natl. Acad. Sci. U.S.A.* **112**, 4865–4870 (2015).
20. D. Grazhdankin, *J. Paleontol.* **88**, 269–283 (2014).
21. A. J. Gooday *et al.*, *Biol. Conserv.* **207**, 106–116 (2017).
22. M. V. Matz, T. M. Frank, N. J. Marshall, E. A. Widder, S. Johnsen, *Curr. Biol.* **18**, 1849–1854 (2008).
23. E. A. Sperling, J. Vinther, *Evol. Dev.* **12**, 201–209 (2010).
24. J. K. Volkman, *Org. Geochem.* **36**, 139–159 (2005).
25. R. B. Kodner, A. Pearson, R. E. Summons, A. H. Knoll, *Geobiology* **6**, 411–420 (2008).
26. T. M. Peakman, J. W. De Leeuw, W. I. C. Rijpstra, *Geochim. Cosmochim. Acta* **56**, 1223–1230 (1992).
27. S. J. Gaskell, G. Eglinton, *Geochim. Cosmochim. Acta* **40**, 1221–1228 (1976).
28. I. D. Bull, M. J. Lockheart, M. M. Elhmmali, D. J. Roberts, R. P. Evershed, *Environ. Int.* **27**, 647–654 (2002).
29. J. D. Weete, M. Abril, M. Blackwell, *PLOS ONE* **5**, e10899 (2010).
30. S. Safe, L. M. Safe, W. S. G. Maass, *Phytochemistry* **14**, 1821–1823 (1975).
31. J. Grabenstatter *et al.*, *Org. Geochem.* **63**, 145–151 (2013).
32. A. Kanazawa, *Fish. Sci.* **67**, 997–1007 (2001).
33. G. D. Love *et al.*, *Nature* **457**, 718–721 (2009).
34. R. B. Kodner, R. E. Summons, A. Pearson, N. King, A. H. Knoll, *Proc. Natl. Acad. Sci. U.S.A.* **105**, 9897–9902 (2008).
35. D. A. Gold *et al.*, *Proc. Natl. Acad. Sci. U.S.A.* **113**, 2684–2689 (2016).
36. S. R. Najje, M. C. Molina, I. Ruiz-Trillo, A. D. Uttaro, *Open Biol.* **6**, 160029 (2016).
37. D. Grazhdankin, *Paleobiology* **30**, 203–221 (2004).
38. R. Jenkins, in *Natural History of the Flinders Ranges*, M. Davies, C. R. Twidale, M. J. Tyler, Eds. (Royal Society of South Australia, 1996), vol. 7, pp. 33–45.

ACKNOWLEDGMENTS

We thank E. Luzhnaya, A. Krasnova, A. Nagovitsyn, P. Rychkov, V. Rychkov, and S. Rychkov for their help with collecting Ediacaran fossils; E. Golubkova with organizing one of the field trips; P. Pringle and R. Taroza for laboratory support; and F. Not, C. Schmidt, R. Schiebel, P. De Deckker, S. Eggins, J. Pawlowski, S. S. Bowser, and M. Stühr for rhizarian specimens. **Funding:** The study is funded by Australian Research Council grants DP160100607 and DP170100556 (to J.J.B.), Russian Foundation for Basic Research project 17-05-02212A (A.I. and I.B.), and the Max-Planck-Society (C.H.). I.B. gratefully acknowledges an

Australian Government Research Training Program stipend scholarship, and B.J.N. acknowledges a Geobiology fellowship of the Agouron Institute. **Author contributions:** I.B. designed the study and analyzed biomarkers from Ediacaran fossils; J.M.H. helped with biomarker analysis; I.B. and A.I. collected fossils; B.J.N., C.H., J.M.H., and J.J.B. analyzed modern Rhizaria; and I.B. and J.J.B. interpreted data and wrote the manuscript, with contributions from all authors. **Competing interests:** Authors declare no competing interests. **Data and materials availability:** All data required to understand and assess the conclusions of this research are available in the main text and supplementary materials.

SUPPLEMENTARY MATERIALS

www.sciencemag.org/content/361/6408/1246/suppl/DC1
Materials and Methods
Supplementary Text
Figs. S1 to S6
Tables S1 to S4
References (39–55)

2 April 2018; accepted 6 August 2018
10.1126/science.aat7228

MAMMALIAN EVOLUTION

Fossils reveal the complex evolutionary history of the mammalian regionalized spine

K. E. Jones^{1*}, K. D. Angielczyk², P. D. Polly³, J. J. Head⁴, V. Fernandez⁵, J. K. Lungmus⁶, S. Tulga⁷, S. E. Pierce^{1*}

A unique characteristic of mammals is a vertebral column with anatomically distinct regions, but when and how this trait evolved remains unknown. We reconstructed vertebral regions and their morphological disparity in the extinct forerunners of mammals, the nonmammalian synapsids, to elucidate the evolution of mammalian axial differentiation. Mapping patterns of regionalization and disparity (heterogeneity) across amniotes reveals that both traits increased during synapsid evolution. However, the onset of regionalization predates increased heterogeneity. On the basis of inferred homology patterns, we propose a “pectoral-first” hypothesis for region acquisition, whereby evolutionary shifts in forelimb function in nonmammalian therapsids drove increasing vertebral modularity prior to differentiation of the vertebral column for specialized functions in mammals.

The evolution of the mammalian body plan from the ancestral amniote condition is one of the most iconic macroevolutionary transitions in the vertebrate fossil record (1, 2). A unique feature of mammals is their specialized vertebral column, which displays constrained vertebral counts but highly disparate morphologies (2–4). In therian mammals, the presacral vertebral column is traditionally divided into cervical, rib-bearing thoracic, and ribless lumbar regions (Fig. 1A). In contrast, the presacral vertebrae of basal amniotes are comparatively uniform and show little differentiation (Fig. 1B). The transition from an “unregionalized” to a “regionalized” presacral column is an important step in mammalian evolution and has been linked to the origin of specialized gaits and respiratory function (1, 2, 5, 6).

Recent quantitative work has detected subtle presacral regionalization in extant snakes and limbed lizards, superficially unregionalized taxa (7). It was hypothesized that the ancestral amniote condition is “cryptic regionalization,” in which regions are present but are only subtly expressed. The global-patterning *Homeobox* (*Hox*) genes were implicated as underlying these conserved regionalization patterns. Under this model, the degree of regionalization—the number of regions present—has remained constant through

mammalian evolution, whereas the amount of morphological disparity between regions (here termed heterogeneity) has increased. But this evolutionary scenario is based solely on data from extant species.

The two amniote clades—Synapsida (mammals and their relatives) and Sauropsida (reptiles, birds, and their relatives)—diverged more than 320 million years ago and have independently undergone substantial morphological transformations. Therefore, to document the evolution of the mammalian vertebral column, we must examine mammals’ extinct forerunners, the nonmammalian synapsids. Here, we examined the presacral vertebral columns of 16 exceptionally preserved nonmammalian synapsids (including “pelycosaurs,” basal therapsids, and cynodonts), one extinct amniote outgroup, and a broad range of extant salamanders, reptiles, and mammals. Using morphometric data, we quantified patterns of region-

alization and heterogeneity and compared their evolution to elucidate when and how synapsid presacral differentiation occurred.

Using a likelihood-based segmented regression approach, we calculated a regionalization score for each taxon [an Akaike information criterion (AIC)-weighted average of the relative fit of one- to six-region hypotheses], producing a continuous variable that reflects the estimated number of vertebral regions (fig. S2). Similar to prior work (7), most reptiles and some extant mammals (e.g., monotremes) have regionalization scores indicating the presence of four regions (Fig. 2A), whereas therians (marsupials and placentals) most frequently display five regions. Therian regionalization scores are also more variable, probably reflecting high ecomorphological diversification of their axial system (4). Thus, data from extant amniotes alone support the null hypothesis of conserved regionalization. However, both salamanders and basal synapsids have lower regionalization scores than extant amniotes (Fig. 2A, cool colors), which demonstrates that regionalization increased independently in the sauropsid and synapsid lineages. Accordingly, we reject the hypothesis of conserved regionalization patterns in amniotes, and instead propose the hypothesis of increasing regionalization in synapsid evolution.

Heterogeneity, expressed as the logarithm of the mean variance of the morphological measures for each column, also increased during synapsid evolution (Fig. 2B). Lepidosaurs and salamanders have low heterogeneity, denoting relative uniformity of the axial column; therians have much higher values, reflecting their extreme disparity; and crocodilians have intermediate levels. Most nonmammalian synapsids also have intermediate levels of heterogeneity. The outgroup *Diadectes* and the ophiacodontids display particularly low values, reinforcing previous assertions of homoplastic increases in mammals and archosaurs from a homogeneous ancestral condition (7). The cynodont *Kayentatherium* has more heterogeneous morphologies than the

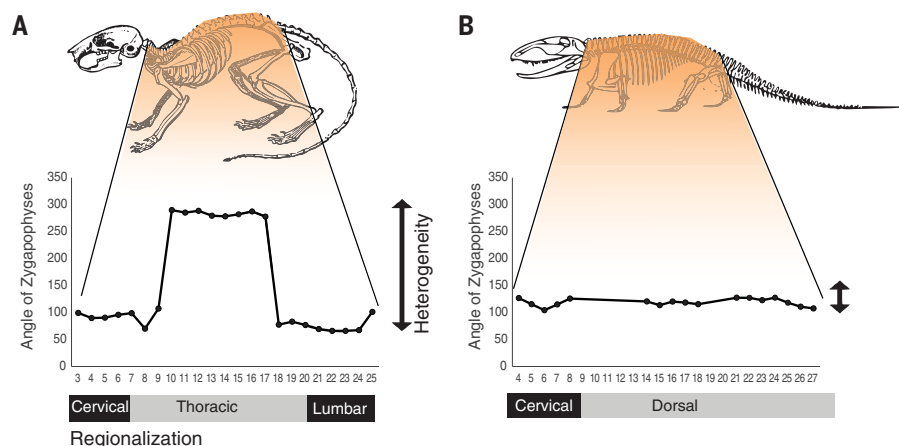


Fig. 1. Regionalization and heterogeneity. (A) The therian presacral column is highly regionalized and morphologically differentiated (*Mus musculus*). (B) Basal synapsids display a homogeneous dorsal region with little differentiation (*Ophiacodon*).

¹Museum of Comparative Zoology and Department of Organismic and Evolutionary Biology, Harvard University, Cambridge, MA 02138, USA. ²Integrative Research Center, Field Museum of Natural History, Chicago, IL 60605, USA. ³Department of Earth and Atmospheric Sciences, Indiana University, Bloomington, IN 47405, USA. ⁴Department of Zoology and University Museum of Zoology, University of Cambridge, Cambridge CB2 3EJ, UK. ⁵European Synchrotron Radiation Facility, 38000 Grenoble, France. ⁶Department of Organismal Biology and Anatomy, University of Chicago, Chicago, IL 60637, USA. ⁷Department of Geophysical Sciences, University of Chicago, Chicago, IL 60637, USA. *Corresponding author. Email: katrinajones@fas.harvard.edu (K.E.J.); spierce@oeb.harvard.edu (S.E.P.)

other fossil taxa, reflecting its position close to the mammal radiation. Given the association between heterogeneity and functional specialization of the axial skeleton in therians, the more homogeneous morphologies of most non-mammalian synapsids point toward functional conservatism.

Although regionalization and heterogeneity increased during synapsid evolution, they are not significantly related (fig. S7 and table S6, $P = 0.73$), meaning that simple linear change is insufficient to explain these patterns. Instead, quantitative trait modeling supports evolution toward shifting adaptive optima (multiple optimum Ornstein-Uhlenbeck models) for these data (table S7). On the basis of AIC fitting, we reconstructed two major adaptive shifts in each trait during synapsid evolution (Fig. 3 and fig. S8). The adaptive optimum for regionalization increases from around three regions in “pelycosaurs” to around four regions at the base of Therapsida, with a later shift to five regions occurring in Theria. The adaptive optimum for heterogeneity increases first at Cynodontia and subsequently within therians. Taken together, our data reveal that vertebral regionalization increased before heterogeneity increased, hence these two measures of axial differentiation evolved independently.

To understand how vertebral regionalization increased in synapsids, we reconstructed region boundaries recovered in the best-fit segmented regression models (Fig. 4A). Region boundaries were then cross-referenced with developmental data, anatomical landmarks, and variation in extant species to identify homologies (Fig. 4B). In extant tetrapods, the cervicothoracic transition is correlated with *Hox6* expression, rib morphology, and the position of the forelimb and brachial plexus (8). Therefore, the cervicothoracic boundary was identified by (i) the position of the posterior branch of the brachial plexus, and (ii) the location of the anterior sternal articulation or first long rib. Functional studies in *Mus* also show that *Hox9* patterns the transition from sternal to nonarticulating ribs and that *Hox10* controls the suppression of ribs altogether in the lumbar region (Fig. 4B) (9, 10). In keeping with this association, dorsal regions were defined relative to their proximity to long ribs (anterior dorsal), short ribs (posterior dorsal), or absent ribs (lumbar).

Using these criteria, region homology hypotheses were constructed in key taxa for which rib or neural anatomy are known (Fig. 4B). In salamanders (and the stem amniote *Diadectes*; see supplementary text), three regions are recovered. The anterior break correlates with the posterior branch of the brachial plexus in *Ambystoma*, implying homology with the cervical region despite the lack of a true “neck” (Fig. 4B, red region). Although salamanders have poorly developed ribs, the position of the posterior break in the mid-trunk is consistent with the anterior-posterior dorsal transition in other taxa (Fig. 4, yellow and pale blue regions). This ancestral three-region pattern is retained in the most basal synapsids. In “pelycosaurs,” the first break corresponds

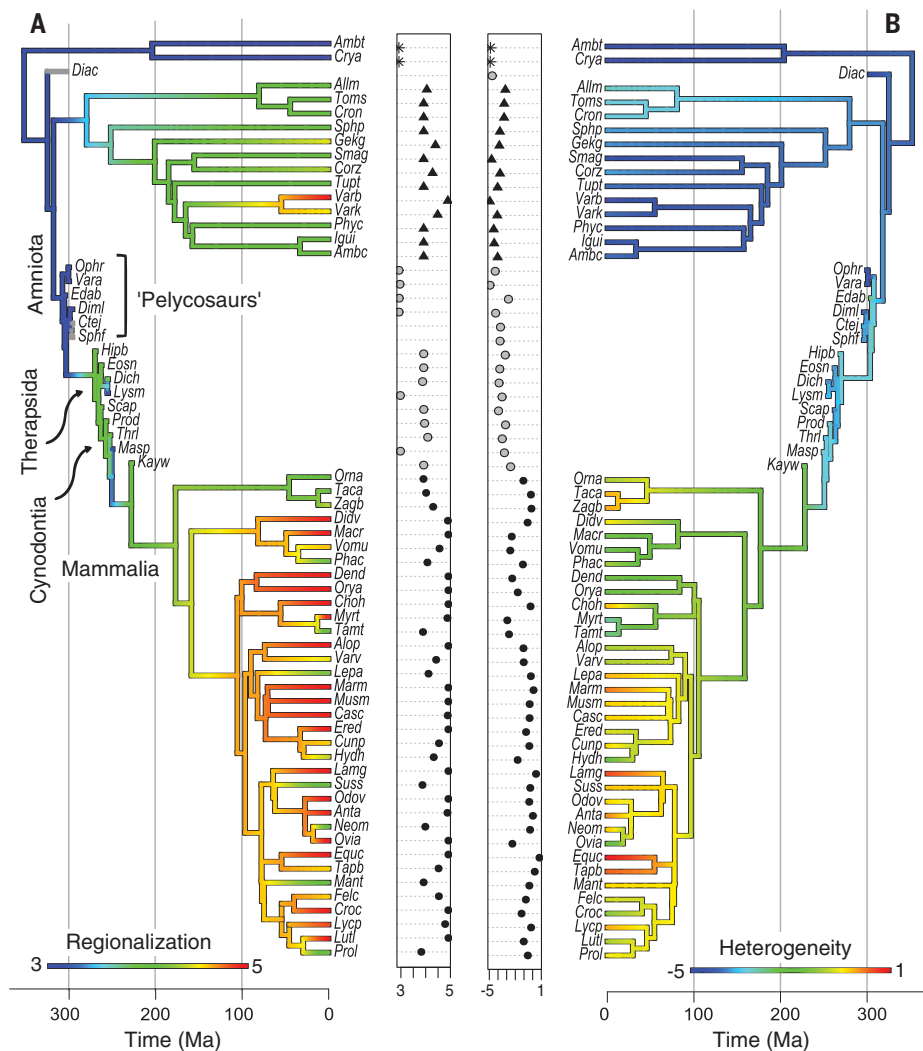


Fig. 2. Evolution of presacral differentiation in amniotes. (A) Regionalization score. (B) Heterogeneity [log(mean variance)]. Warmer colors reflect more regions and greater morphological heterogeneity, respectively. Black circles, mammals; gray circles, fossil taxa; triangles, reptiles; stars, amphibians; grayed tips in (A), fossil taxa excluded because of <0.75 r^2 of regionalization model. See table S5 for full taxonomic names. Ma, millions of years.

to the inferred cervicothoracic transition based on rib length and forelimb position (e.g., v5 in *Edaphosaurus*, v7 in *Dimetrodon*), whereas the second break corresponds to the gradual transition from longer to shorter dorsal ribs, signifying cervical, anterior dorsal, and posterior dorsal homologies (*Edaphosaurus*; Fig. 4B).

Our data point to the convergent addition of a fourth region in distinct locations in sauropsids and synapsids. In sauropsids, a fourth region is detected anterior to the brachial plexus, suggesting a novel cranial region within the neck (*Iguana*; Fig. 4B, purple region). Sauropsids exhibit more variation in cervical count than do synapsids (11), providing a potential connection between neck plasticity and cervical modularity in this lineage. Conversely, in basal therapsids and cynodonts, a fourth region is detected posterior to the cervicothoracic transition (*Thrinaxodon*; Fig. 4B, orange region). In *Thrinaxodon*, the first break

corresponds to the cervicothoracic transition and first full-length rib (v7–8), the second break lies in the middle of the long rib series (v12–13), and the anterior-posterior dorsal boundary falls at the transition from long to short ribs (v19–20). These regions conform to the ancestral cervical region (red), a novel pectoral region (orange), and the ancestral anterior dorsal (yellow) and posterior dorsal (pale blue) regions. Therian mammals display an additional break within the posterior dorsal region that differentiates the ribless lumbar region (*Mus*; Fig. 4B, blue region).

Considering the pattern of region acquisition, we propose a “pectoral-first” hypothesis for the evolution of mammalian presacral regionalization (Fig. 4). Under this hypothesis, “pelycosaurs” retained the three-region ancestral amniote condition. In basal therapsids, addition of a fourth “pectoral module” accompanied the reorganization of the pectoral girdle and forelimb. Unlike

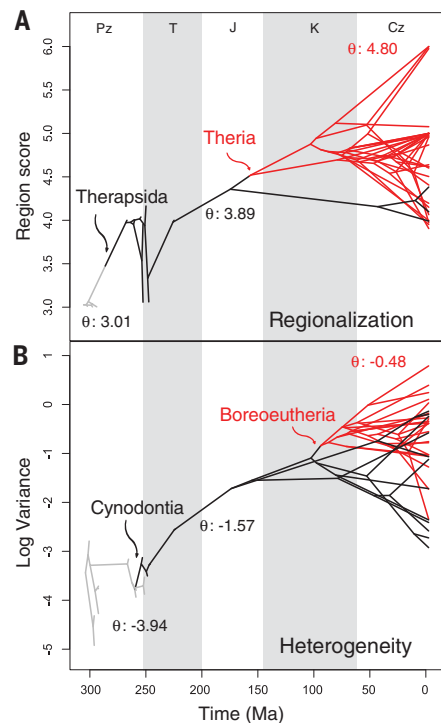


Fig. 3. Adaptive regime shifts in vertebral evolution. (A) Regionalization. (B) Heterogeneity. Theta denotes adaptive optima of each regime. Pz, Paleozoic; T, Triassic; J, Jurassic; K, Cretaceous; Cz, Cenozoic.

“pelycosaurs,” therapsids are characterized by reduction of the pectoral girdle dermal bones and increased shoulder mobility (1, 12). Medial extrinsic shoulder muscles (e.g., levator scapulae, serratus ventralis) originating on the scapula are thought to have expanded their axial insertions during synapsid evolution (12). As these vital body-support muscles attach directly onto the underlying vertebrae and ribs, shifts in pectoral morphology and function likely drove divergent neck- and shoulder-selective regimes in the axial skeleton, providing impetus for increased regionalization (1, 12, 13). Further, the vertebrae, medial extrinsic shoulder muscles, and dorsal border of the scapula all develop directly from somitic mesoderm (primaxial), signifying strong developmental ties between these structures (14).

It has been proposed that the muscular diaphragm evolved from an unmuscularized septum or “proto-diaphragm” via co-option of shoulder muscle precursor cells that were later canalized into a distinct cell population by repatterning of the posterior neck (15). Reorganization of the anterior column and pectoral girdle in therapsids may have facilitated this transition by increasing cervicothoracic modularity and remodeling shoulder musculature. Subsequent fixation of the cervical count at seven in nonmammalian cynodonts is hypothesized to represent the appearance of the mammalian-style muscular dia-

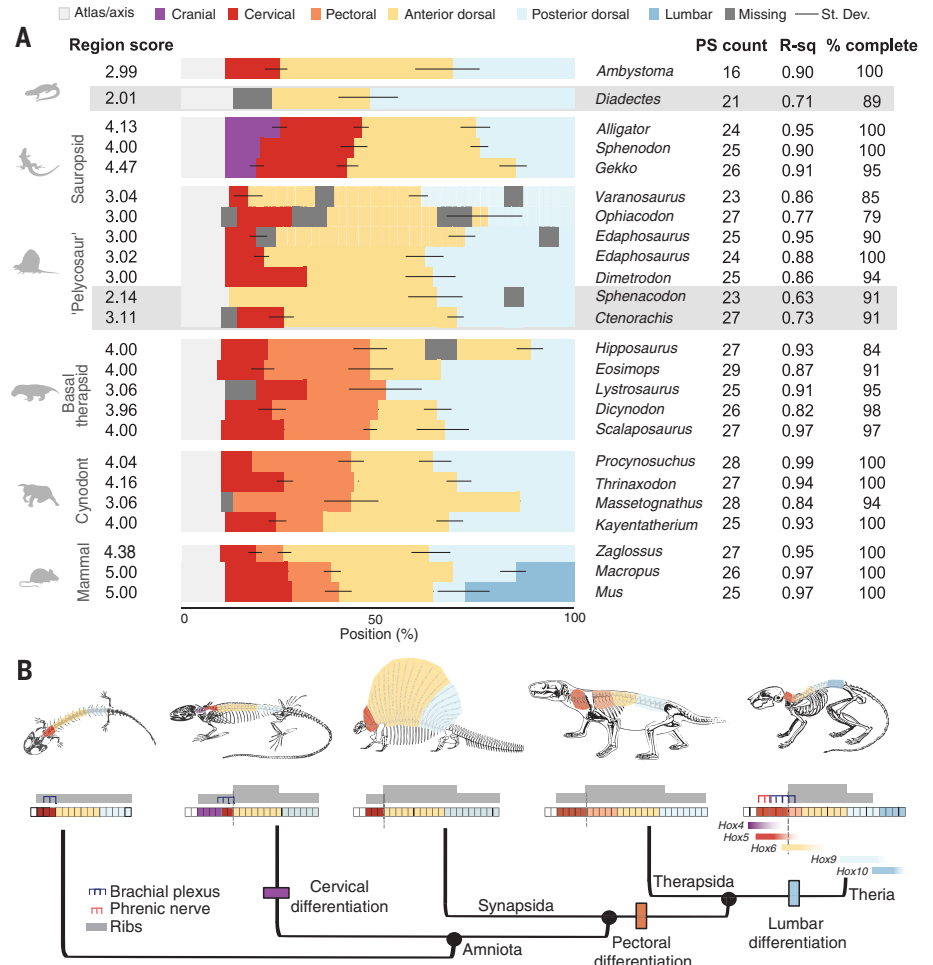


Fig. 4. Best-fit region models, region homologies, and evolutionary hypothesis. (A) Best-fit region models for select taxa. Colors represent inferred region homologies; St. Dev., standard deviation of break locations; PS count, presacral count; R-sq, adjusted r^2 ; % complete, total completeness; shaded region models reflect taxa with $<0.75 r^2$ fit (excluded from evolutionary reconstructions). **(B)** “Pectoral-first” hypothesis for the evolution of synapsid presacral regionalization. Taxa (left to right): *Ambystoma*, *Iguana*, *Edaphosaurus* [redrawn from (17)], *Thrinaxodon* [redrawn from (2)], *Mus*. Width of gray bars reflects relative rib lengths and/or connection to sternum; vertical dashed lines denote cervicothoracic transition. For *Mus*, Hox bands correspond to vertebrae affected by functional gene manipulation (18).

phragm (6). Thus, anterior regionalization that had initially been associated with shoulder evolution in early therapsids was likely later exapted in cynodonts in response to selection for increased ventilatory efficiency (5, 15).

A “lumbar module” evolved later in therian mammals. Evolution of the lumbar region in mammals is associated with *Hox10*, which functions to repress rib formation and patterns lumbar identity in *Mus* (10) (Fig. 4B). Convergent loss or gain of lumbar ribs in multiple fossil theriiform clades suggests high plasticity of this character early in therian evolution (16). Within therians, lumbar count and morphology vary, and this is reflected by translocation of the (morphometrically defined) region boundary in our sample. Because the lumbar region plays a critical role in mammalian locomotion, it is predicted that region variability is related to ecological

specialization caused by clade-specific functional overprinting.

Regional differentiation is “the major structural difference between reptilian and mammalian vertebral columns” (13), yet its evolution has never been quantitatively examined. Our findings show that regionalization and heterogeneity—the two aspects of vertebral differentiation—evolved independently. Forelimb reorganization in therapsids drove initial increases in regionalization as a result of developmental and functional connections between the pectoral girdle and underlying vertebrae. High heterogeneity and presumed functional diversity did not appear until crown mammals. The combination of a regionalized axial skeleton with heterogeneous vertebral morphologies ultimately enabled mammals to become specialized for a remarkable diversity of ecologies and behaviors.

REFERENCES AND NOTES

1. T. S. Kemp, *The Origin and Evolution of Mammals* (Oxford Univ. Press, 2005).
2. F. A. Jenkins Jr., *Evolution* **24**, 230–252 (1970).
3. N. Schilling, *Front. Zool.* **8**, 4–23 (2011).
4. E. J. Slijper, *Verh. K. Ned. Akad. Wet. Afd. Natuurkd. Tweede Reeks* **42**, 1–128 (1946).
5. D. R. Carrier, *Paleobiology* **13**, 326–341 (1987).
6. E. A. Buchholz et al., *Evol. Dev.* **14**, 399–411 (2012).
7. J. J. Head, P. D. Polly, *Nature* **520**, 86–89 (2015).
8. A. C. Burke, C. E. Nelson, B. A. Morgan, C. Tabin, *Development* **121**, 333–346 (1995).
9. D. C. McIntyre et al., *Development* **134**, 2981–2989 (2007).
10. D. M. Wellik, M. R. Capecchi, *Science* **301**, 363–367 (2003).
11. J. Müller et al., *Proc. Natl. Acad. Sci. U.S.A.* **107**, 2118–2123 (2010).
12. A. S. Romer, *Bull. Am. Mus. Nat. Hist.* **46**, 10 (1922).
13. A. Crompton, F. A. Jenkins Jr., *Annu. Rev. Earth Planet. Sci.* **1**, 131–155 (1973).
14. P. Valasek et al., *J. Anat.* **216**, 482–488 (2010).
15. T. Hirasawa, S. Kuratani, *J. Anat.* **222**, 504–517 (2013).
16. Z. X. Luo, P. Chen, G. Li, M. Chen, *Nature* **446**, 288–293 (2007).
17. H.-D. Sues, R. R. Reisz, *Trends Ecol. Evol.* **13**, 141–145 (1998).
18. D. M. Wellik, *Dev. Dyn.* **236**, 2454–2463 (2007).

ACKNOWLEDGMENTS

We thank R. Asher, B. Brainerd, D. Brinkman, T. Capellini, C. Capobianco, J. Chupasko, J. Cundiff, K. Jakata, T. Kemp, C. Mehling, A. Millhouse, M. Omura, A. Resetar, J. Rosado, B. Rubidge, R. Smith, K. Smithson, C. Tabin, R. Tykoski, I. Werneburg, and B. Zipfel. **Funding:** Supported by NSF grants EAR-1524523 (S.E.P.) and EAR-1524938 (K.D.A.) and by an AAA Postdoctoral Fellowship (K.E.J.). **Author contributions:** Study design, K.E.J.,

K.D.A., and S.E.P.; methods, K.E.J., P.D.P., and S.E.P.; data collection, K.E.J., K.D.A., S.E.P., J.J.H., V.F., J.K.L., and S.T.; data analysis, K.E.J.; manuscript preparation, K.E.J., K.D.A., and S.E.P. **Competing interests:** The authors have no competing interests. **Data and materials availability:** Data are available in table S5 and Dryad (doi:10.5061/dryad.jm820mg). Code is available via github (<https://github.com/katrinajones/regions>).

SUPPLEMENTARY MATERIALS

www.sciencemag.org/content/361/6408/1249/suppl/DC1
Materials and Methods
Supplementary Text
Figs. S1 to S8
Tables S1 to S7
References (19–49)

30 October 2017; resubmitted 27 April 2018
Accepted 25 July 2018
10.1126/science.aar3126

SYNTHETIC BIOLOGY

Programmable protein circuits in living cells

Xiaojing J. Gao*, Lucy S. Chong*, Matthew S. Kim, Michael B. Elowitz†

Synthetic protein-level circuits could enable engineering of powerful new cellular behaviors. Rational protein circuit design would be facilitated by a composable protein-protein regulation system in which individual protein components can regulate one another to create a variety of different circuit architectures. In this study, we show that engineered viral proteases can function as composable protein components, which can together implement a broad variety of circuit-level functions in mammalian cells. In this system, termed CHOMP (circuits of hacked orthogonal modular proteases), input proteases dock with and cleave target proteases to inhibit their function. These components can be connected to generate regulatory cascades, binary logic gates, and dynamic analog signal-processing functions. To demonstrate the utility of this system, we rationally designed a circuit that induces cell death in response to upstream activators of the Ras oncogene. Because CHOMP circuits can perform complex functions yet be encoded as single transcripts and delivered without genomic integration, they offer a scalable platform to facilitate protein circuit engineering for biotechnological applications.

Synthetic biology seeks to enable rational design of circuits that confer new functions in living cells. Most efforts thus far have centered on gene regulation because of the relative ease with which transcription factors and other nucleic acid-interacting proteins can be configured to regulate one another's expression (1–10). However, many natural cellular functions are implemented by protein-level circuits, in which proteins specifically modify each other's activity, localization, or stability. For example, caspase-mediated programmed cell death is regulated by a circuit of proteases that activate one another through cleavage (11). Synthetic protein circuits could provide advantages over gene regulation circuits, including faster operation, direct coupling to endogenous pathways, single-transcript delivery, and function without genomic integration (Fig. 1A).

The key challenge is designing composable protein components whose inputs and outputs are of the same type, so that they can form a wide variety of protein circuits (12), much as a few electronic components can be wired to produce a variety of electronic circuits (Fig. 1A). Although natural protein domains have been combined to generate proteins with hybrid functions or to rewire cellular pathways for research (13–18) and biomedical applications (17, 19), the lack of composability has limited our ability to design protein-level function in living cells.

Viral proteases provide a promising basis for such a system (20, 21). Many of them exhibit strong specificity for short cognate target sites, which can be recognized and cleaved in various protein contexts (22–24). Natural viral diversity provides multiple proteases with distinct spe-

cificities (25). Viral proteases can be used with degrons to control protein stability (26–29). They can also activate transcription factors (30–32), synthetic intein zymogens (33), and other proteases in a purified protein system (20, 21).

We first focused on the well-characterized tobacco etch virus protease (TEVP) (34). To quantify TEVP activity, we designed a reporter in which a cognate cleavage site (tevs) is inserted between a citrine fluorescent protein and a dihydrofolate reductase (DHFR) degron, which can be inhibited by trimethoprim (TMP) as a positive control (35) (Fig. 1B). We transfected human embryonic kidney (HEK) 293 cells with plasmids expressing different combinations of TEVP, the reporter, and an mCherry cotransfection marker, and we analyzed cells by flow cytometry. We used the mCherry signal to select highly transfected cells, which showed the largest separation of basal reporter fluorescence from cellular autofluorescence to maximize the observable dynamic range of the reporter (materials and methods, Fig. 1B, and fig. S1A). Treating cells with TEVP strongly increased reporter abundance to levels similar to those obtained by TMP inhibition of the degron (Fig. 1B and fig. S1B, left). We also designed a complementary repressible reporter in which TEVP cleavage exposes a destabilizing N-terminal tyrosine residue (26, 36) (Fig. 1C and fig. S1B, right). These designs generalized in a straightforward manner to the related tobacco vein mottling virus protease (TVMVP) (37) and, with some modifications, to the unrelated hepatitis C virus protease (HCVP) (24, 38) (fig. S1, C and D, and supplementary text). Furthermore, measuring activation of each reporter in response to each protease revealed limited cross-activation (Fig. 1D). Thus, three viral proteases can be used to orthogonally increase or decrease cognate reporters.

To enable the design of complex circuits, we next sought to achieve protease-protease regulation. The degron strategy used for the reporters

failed to produce strong regulation, possibly because proteases can cleave degrons within the same protease molecule with relaxed specificity (28). Instead, we designed a scheme that regulates protease activity rather than abundance. We incorporated antiparallel heterodimerizing leucine zipper domains (39) to each half of a split TEVP (40) to reconstitute its activity (Fig. 1E, left). We also inserted HCVP cleavage sites between the leucine zippers and TEVP to allow HCVP to inhibit TEVP. Finally, we fused a leucine zipper (complementary to one of the zippers on split TEVP) to HCVP, thus enhancing its ability to dock with and inhibit its TEVP target (fig. S1E, left). This design successfully produced repression of TEVP by HCVP (Fig. 1E, left).

To generalize this design, we engineered a similar TEVP variant repressed by TVMVP (fig. S1E, right). On the basis of its sequence similarity to TEVP (fig. S1F), we also engineered TVMVP variants repressed by either HCVP (Fig. 1E, right) or TEVP (fig. S1G). To make these designs more compact, we linked the two halves of each regulated protease with a single leucine zipper flanked by cleavage sites for the input protease, creating single-chain repressible proteases (Fig. 1F and fig. S1, H and I). Similar approaches enabled us to engineer protease regulation of the unrelated protease HCVP by using a different split strategy (supplementary text). In these constructs, cleavage by either TEVP or TVMVP strongly reduced HCVP activity, enabling signal propagation through three-stage protease cascades (Fig. 1G and fig. S1J). Together, this strategy established a composable protease regulation system.

Using this system, we designed core circuit functions, starting with Boolean logic. We identified three design principles that together would be sufficient to enable all eight two-input gates: First, incorporation of a consecutive pair of distinct cleavage sites between a degron and a target protein can implement OR logic, because cleavage of either site is sufficient to stabilize the protein (Fig. 2 and fig. S2A, OR). Second, to implement AND logic, we flanked the target protein with FKBP (41) and DHFR degrons on the N and C termini, respectively, each removable with a distinct cleavage site. On the N terminus, a leucine zipper was necessary to facilitate input protease docking. In this design, removal of both degrons was necessary to stabilize the protein (Fig. 2 and fig. S2A, AND). Third, to implement negation, we either used the N-end degron strategy (Fig. 1C) or propagated signals through an intermediate protease repression step (Fig. 1E). Cotransfection of each basic gate (OR, AND, and NOR as a specific case of negation) with varying concentrations of its inputs revealed the expected logic functions (Fig. 2 and fig. S2B). Further, varying the concentration of the reporter plasmid enabled tuning of output levels without disrupting the logical computation, facilitating matching of input and output levels in more complex circuits (fig. S2C). Finally, by utilizing the HCVP inhibitor asunaprevir (28) and a rapamycin-induced TEVP (40, 42), we found that these gates could also be controlled by small-molecule inputs (fig. S3A).

Howard Hughes Medical Institute, Division of Biology and Biological Engineering, Broad Center, California Institute of Technology, 1200 East California Boulevard, Pasadena, CA 91125, USA.

*These authors contributed equally to this work.

†Corresponding author. Email: melowitz@caltech.edu

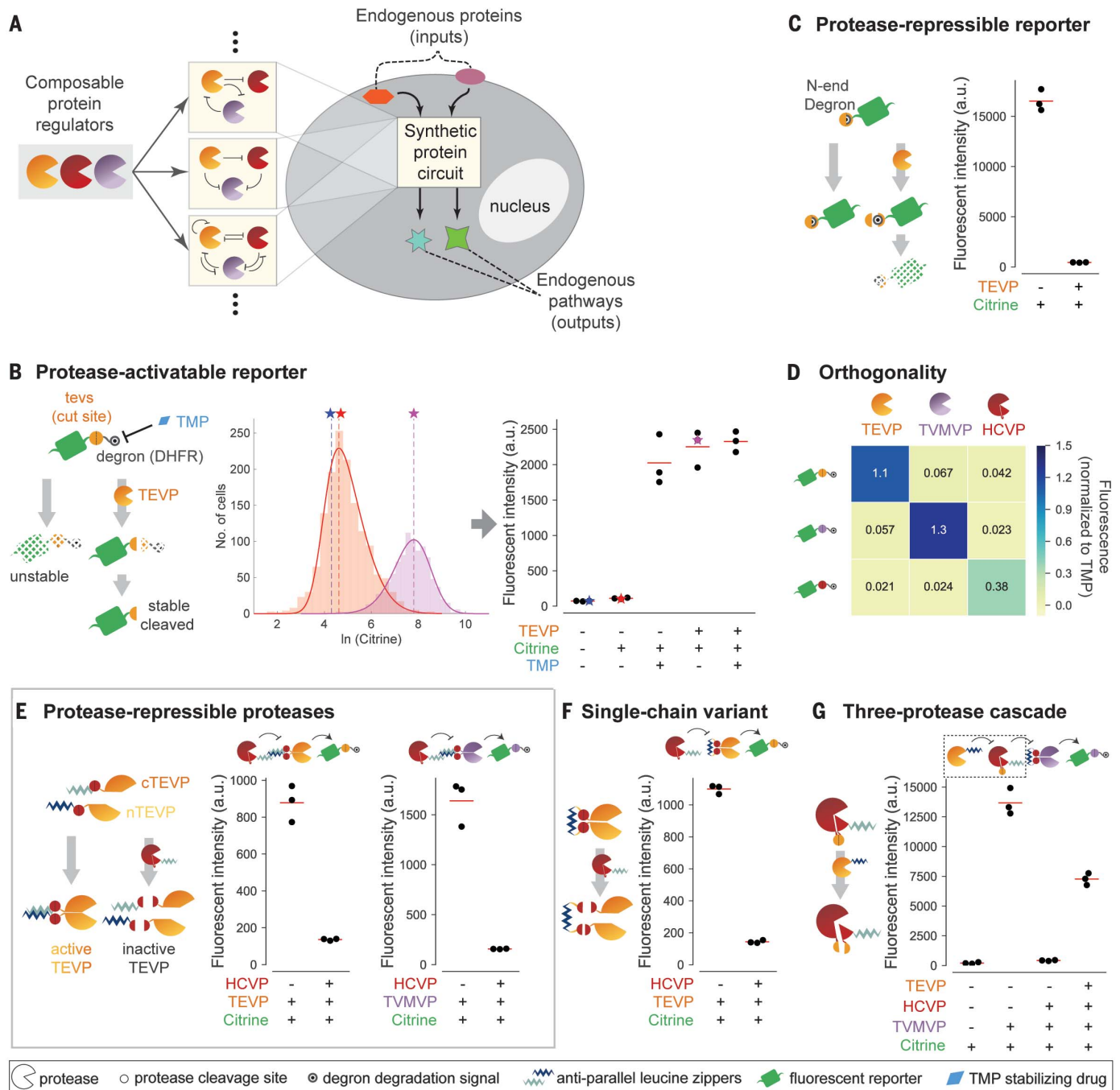


Fig. 1. Design of composable protein circuit components. (A) Composable protein units (partial circles, left) can regulate one another in arbitrary configurations with diverse functions (middle). Protein-level circuits can interface directly with endogenous protein pathways and operate without modifying the genome or entering the nucleus (right). (B) The protease-activatable reporter (green) is stabilized by removal of a DHFR degron (black target) through protease (partial circle) cleavage of a corresponding target site (yellow circle). TMP (blue diamond) inhibits the degron and thus stabilizes the reporter. (Middle) Flow cytometry distributions of reporter fluorescence with (purple) or without (orange) TEVP. Distributions are limited to the gated area in fig. S1A. Solid curves indicate skew Gaussian fits. Vertical dashed lines and stars indicate distribution modes, which are plotted in subsequent figure panels. (Right) Analysis of reporter response to TMP and/or TEVP. Each dot represents one replicate. Stars indicate data from the middle panel. a.u., arbitrary units. (C) In the protease-repressible reporter, protease

cleavage exposes an N-end degron (covered target) to destabilize the reporter. (D) Three proteases (columns) exhibit orthogonal regulation of three reporters (rows). Mean fluorescence intensity of three independent measurements is normalized to the TMP-stabilized value of the corresponding reporter. (E) Design for protease-repressible proteases. TEVP is split as indicated and then reconstituted through dimerizing leucine zippers (light and dark blue zig-zags). A leucine zipper-tagged HCVP (red partial circle) can dock with the target TEVP and cleave it to remove leucine zippers, effectively repressing TEVP. TVMVP (purple partial circle) can be regulated using the same design. (F) A single-chain variant of the HCV-repressible TEVP allows docking of and repressive cleavage by HCVP. (G) Protease regulation can propagate through a three-stage cascade. Repressible HCVP uses a variant design, in which TEVP cleavage separates core HCVP from its docking leucine zipper and activity-enhancing copeptide (small pie slice). In all panels, red lines indicate triplicate mean.

These results thus show that three core gates exhibit robust and tunable operation across multiple input methods.

Next, we combined these principles to design and validate the other two-input gates (Fig. 2 and fig. S2A). Furthermore, to test whether output from one gate could be directly used as input to a subsequent gate, we constructed a more complex nested NOR function by using additional orthogonal proteases from soybean mosaic virus (SMVP) (43) and herpes simplex virus (HSVP) (44) (fig. S3B). The output from this system was consistent with that expected from the logical function $\text{NOR}[\text{TEVP}, \text{NOR}(\text{SMVP}, \text{HSVP})]$ (fig. S3B).

Beyond Boolean logic, analog signal filtering can enable many cellular functions, such as the ability to selectively respond to specific input concentration ranges (45, 46). The incoherent feed-forward loop (IFFL) motif, in which an input both activates and inhibits the same target, provides a simple implementation for this function (47, 48). Inspired by the IFFL, we combined an activating arm, in which TEVP removes a C-terminal degron, with a repressing arm, in which TVMVP reveals a destabilizing N-end tyrosine (Fig. 3A). To tune the position and sharpness of the bandpass, we also introduced a positive-feedback loop based on re-

ciprocal inhibition between HCVP and TVMVP on the repression arm, such that the amount of HCVP expression sets a threshold for TVMVP activity (Fig. 3A).

To characterize this bandpass circuit, we considered the abundance of TEVP and TVMVP as input and varied it through the concentration of transfected DNA, which correlated linearly with protein abundance (fig. S4A). The individual activating and repressing arms of the circuit generated increasing and decreasing responses, respectively, to increasing amounts of TEVP and TVMVP (Fig. 3, B and C). Addition of HCVP increased both the threshold and the sharpness of the response to TVMVP titration (Fig. 3C). Combining the two arms into a single circuit generated the anticipated bandpass behavior when we covaried TEVP and TVMVP expression through either different amounts of plasmid (Fig. 3D) or 4-epitetracycline induction (fig. S4B). Finally, varying the abundance of HCVP tuned the position and amplitude of the bandpass response (Fig. 3D and fig. S4B). These results demonstrate rational engineering of tunable analog bandpass filters.

Temporal signal processing, such as adaptation to a change in input, has a critical role in diverse biological systems (49) and has been demonstra-

ted synthetically in bacteria at the gene regulation level (50). To engineer adaptation with the CHOMP (circuits of hacked orthogonal modular proteases) system, we designed an IFFL containing the three-step cascade (Fig. 1G) to introduce a delay in the repressing arm relative to the activating arm (Fig. 3E). To enable sudden induction, we adopted the rapamycin-induced TEVP used for the logic gates (figs. S3A and S4C). To facilitate dynamic readout of circuit output in individual cells, we used a far-red (infrared) fluorescent protein (IFP) that is synthesized in a nonfluorescent state but can be posttranslationally switched on by TEVP (51) (fig. S4D, left). We also added a conditional N-end degron to enable repression by TVMVP (Fig. 3E).

We encoded the entire pulse-generation circuit as a single open reading frame, with interleaved 2A self-cleaving peptides (52) to separate distinct protein components (Fig. 3F). This gene (encoding the single reading frame) was then stably incorporated in the genome (materials and methods). We used flow cytometry to analyze the response of the reporter in a single clone over time after rapamycin addition. Cells exhibited the expected adaptive dynamics, with a rise in fluorescence on a time scale of hours and a subsequent decay to baseline over ~1 day (fig. S4D, right). To

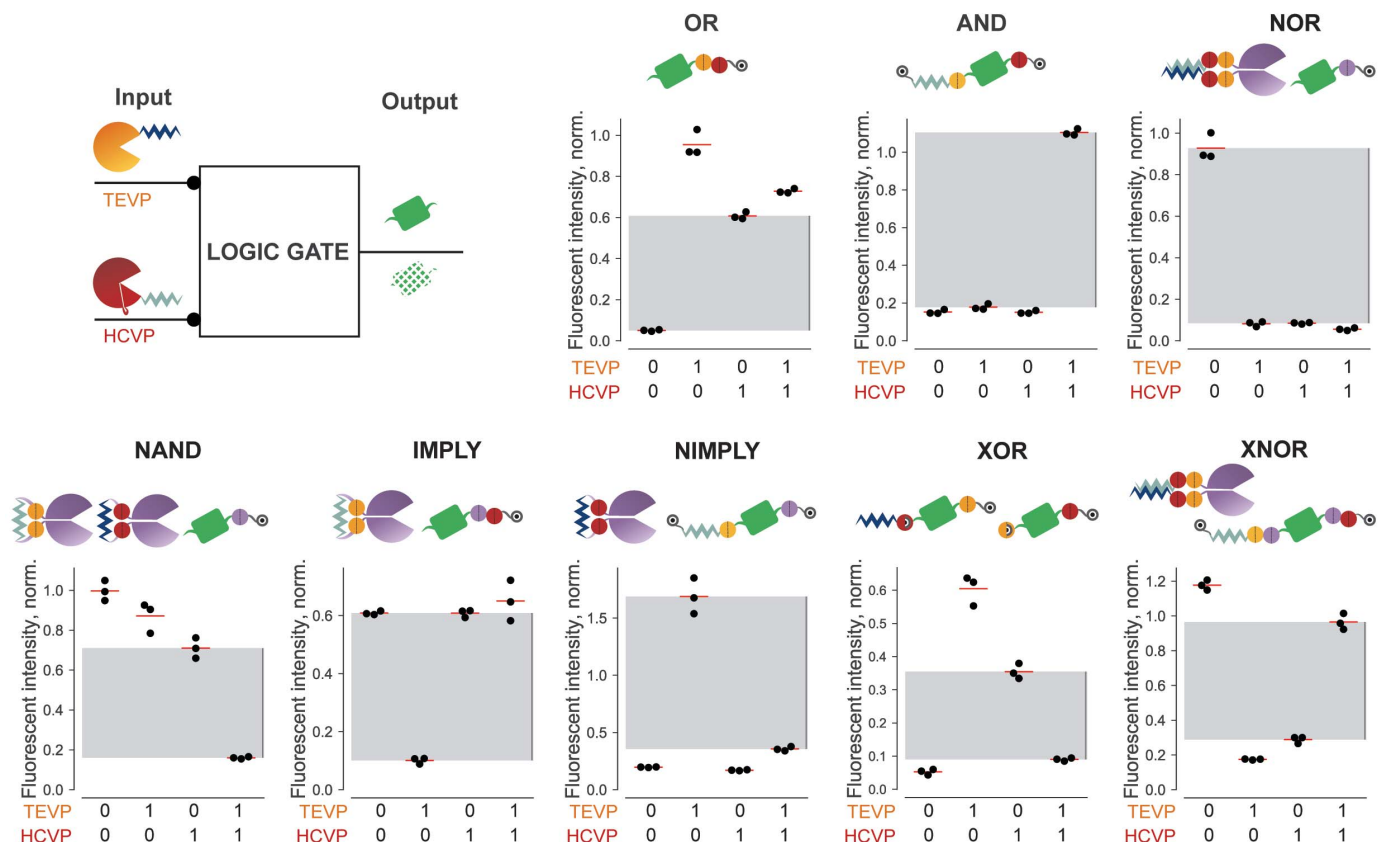


Fig. 2. CHOMP circuits implement binary logic gates. For each indicated gate, TEVP and HCVP serve as binary inputs, which are either included or excluded in transfections. Citrine fluorescence serves as gate output. The design and performance of each nontrivial two-input logic gate is shown for triplicate experiments (black dots).

Fluorescence intensity in each panel is normalized to the corresponding reporter stabilized with TMP (for gates containing only C-terminal degrons) or Shield-1 plus TMP (for gates containing degrons at both termini). Gray regions indicate the range from maximum "OFF" value to minimum "ON" value for that gate.

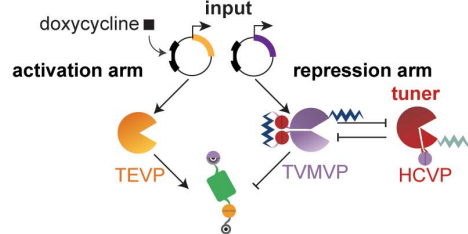
obtain a direct view of dynamics in individual cells, we also analyzed the same cell line by time-lapse fluorescence microscopy (Fig. 3G and movie S1). Analysis of individual cells revealed similar adaptive dynamics, responding maximally at 269 ± 68

(mean \pm SD) min after rapamycin addition, decaying to 50% of their peak values over the subsequent 491 ± 170 min, and eventually reaching fluorescence similar to that before induction (Fig. 3H). These results demonstrate the design of single-

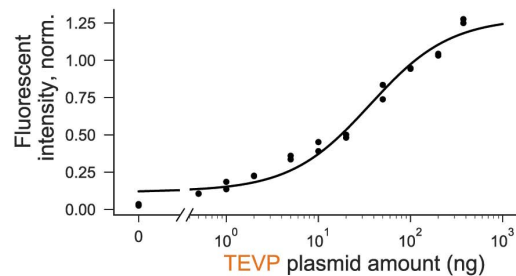
gene multicomponent circuits that generate dynamic signal responses.

By coupling directly to endogenous cellular outputs and inputs, protein-level circuits could act as programmable therapeutic devices. As

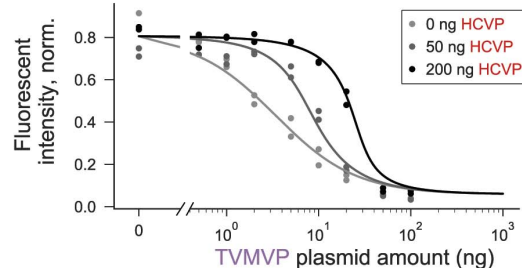
A Bandpass circuit design



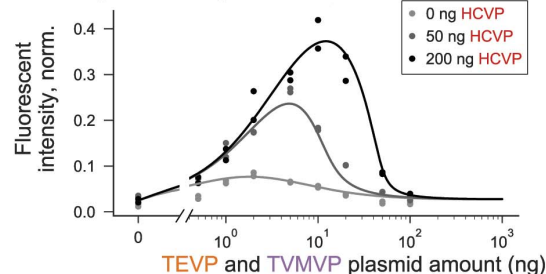
B Activation arm only



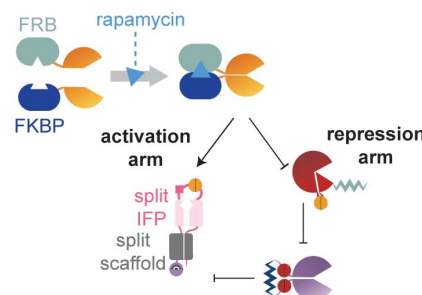
C Repression arm only



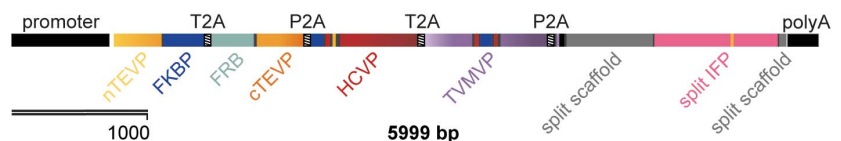
D Complete bandpass



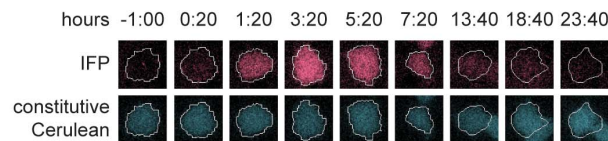
E Adaptive pulse circuit design



F Single-transcript adaptive pulse circuit



G Time-lapse images of adaptive pulse circuit



H Single-cell traces

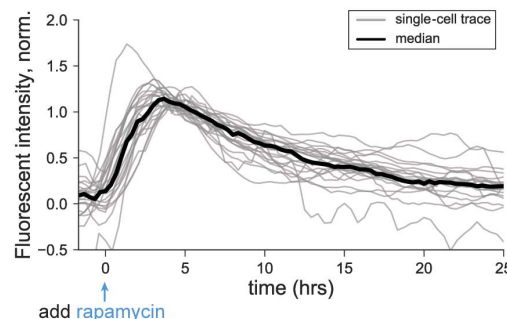


Fig. 3. Design of bandpass filtering and pulse-generation circuits.

(A) For bandpass filtering, the expression of co-regulated inputs TEVP (yellow) and TVMVP (purple) are controlled by the amount of transfected DNA or by doxycycline (square) induction. The amount of HCVF (red) plasmid can be varied to tune the repression arm. (B) Input-output curve of the activation arm in the absence of TVMVP. Here and in subsequent panels, dots indicate duplicate measurements, and the curve is a model fit (materials and methods). (C) Input-output curve of the repression arm, in the presence of constant TEVP and increasing levels of HCVF (gray shades), which increases the repression threshold and sharpens the response. (D) Bandpass behavior of the complete circuit. Increasing HCVF expression (gray shades) shifts the position and increases the amplitude of the peak response. Data in (B) to (D) are normalized to the TMP-stabilized reporter. (E) Delayed

repression can enable pulse generation. In this design, rapamycin-induced dimerization of FKBP and FRB domains reconstitutes TEVP. Cleavage of the reporter by TEVP allows maturation of far-red fluorescent protein (IFP, pink) (fig. S4D). (F) The pulse circuit was completely encoded on a single transcript, with protein components (indicated) separated by self-cleaving sequences (T2A and P2A) (47). (G) Filmstrips of a single cell stably incorporating both the pulse-generation circuit (pink) and a constitutive cerulean segmentation marker (blue). After rapamycin induction ($t = 0$), the output IFP signal (pink) increases and then decays, whereas the cerulean signal (blue) remains constant. (H) Traces of IFP fluorescence in 24 individual cells (gray lines). This analysis omits cells that exhibited phototoxicity or moved out of the field of view (see materials and methods). The black line indicates median fluorescence over all cells at each time point.

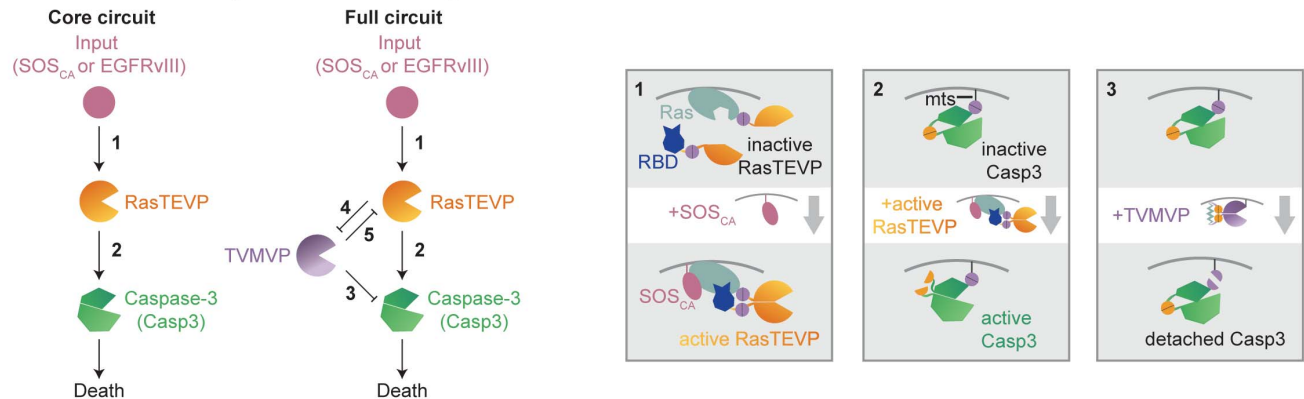
a proof of principle for such a strategy, we designed a circuit to selectively kill cells with elevated activation of Ras, a protein whose activity is increased in many cancers (53, 54). More specifically, we designed a core circuit that responds

to upstream activators of Ras, such as SOS and epidermal growth factor receptor (EGFR), by activating an engineered TEV protease, which in turn activates caspase-3 (Casp3) to induce cell death (11, 55) (Fig. 4A, core circuit). We

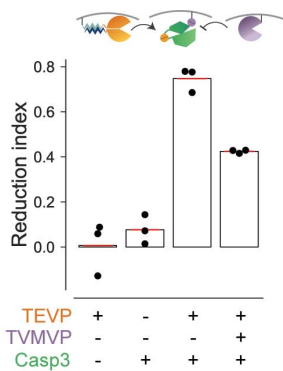
then improved this circuit by incorporating additional proteases and interactions (Fig. 4A, full circuit).

To enable efficient protease-dependent induction of cell death at the plasma membrane, where

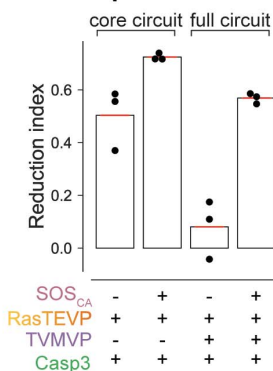
A Ras-conditional Caspase-3 circuit designs



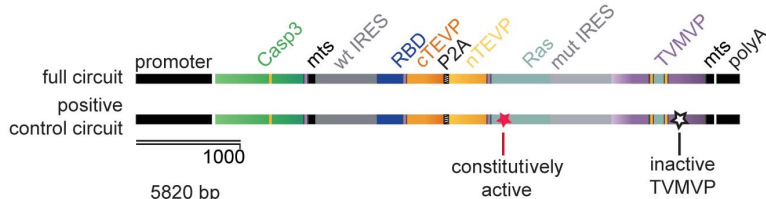
B Protease regulation of Caspase-3



C Comparison of core and complete circuits



D Single-transcript Ras-conditional Caspase-3 circuit



E Single-transcript circuit in mixed population

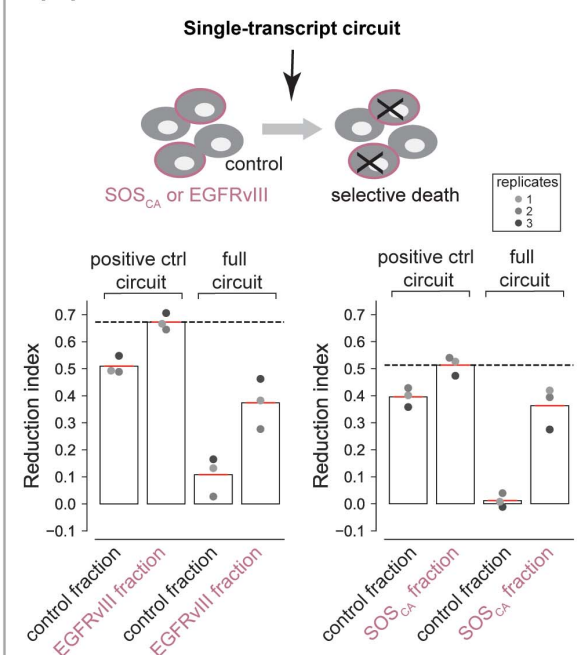


Fig. 4. CHOMP circuit enables conditional activation of Casp3 in Ras-activating cells.

(A) The core circuit (left) links Ras activation by SOS_{CA} or EGFRvIII to Casp3 activation. The full circuit (right) incorporates an additional TVMVP component to enhance selectivity. New regulatory features introduced in this circuit are explained schematically in the corresponding numbered boxes. Box 1: Input from upstream activators of Ras such as SOS_{CA} and EGFRvIII (pink) activates Ras (light blue), causing it to bind RBD (dark blue), reconstituting RasTEVP. Box 2: Engineered Casp3 (green) tagged with a membrane localization sequence (mts) can be converted from an inactive to an active state by TEVP cleavage. Box 3: TVMVP cleavage detaches Casp3 from the membrane, reducing its ability to be activated by membrane-localized TEVP. (B) TEVP activates the engineered Casp3, whereas TVMVP inhibits this activation. Cells transfected with the indicated components were analyzed to determine

the reduction index (percentage of cell number reduction compared to cells transfected with only a fluorescent marker; see materials and methods and fig. S5B). (C) The core circuit preferentially reduced cell number in the presence of ectopic SOS_{CA}. The full circuit exhibited improved selectivity. (D) The full circuit (top) and a positive-control circuit incorporating a Gly¹²→Val mutation that makes Ras constitutively active and a Cys¹⁵²→Ala mutation that abolishes TVMVP activity (bottom) were each encoded as a single transcript. (E) In a mixed population, the single-transcript circuit (D, top) conditionally reduced the number of EGFRvIII cells (left) and SOS_{CA} cells (right) compared with that of cocultured control cells. The positive-control circuit (D, bottom) reduced the number of both fractions. The dashed line indicates the upper limit of the reduction index measured with the positive-control circuit. Dots from the same well are color matched.

Ras activation occurs, we membrane localized a TEVP-activated Casp3 variant (55) by incorporating the 20-amino acid membrane-targeting sequence (mts) from the C terminus of human H-Ras (56) (Fig. 4A, box 2). Using flow cytometry, we quantified the effect of this Casp3 variant on cell numbers in terms of a "reduction index" whose value measures the relative reduction in cell number compared with a control condition (materials and methods and fig. S5B). The membrane-targeted Casp3 decreased cell numbers when cotransfected with a similarly membrane-localized TEVP variant (Fig. 4B), with higher efficiency than the original cytoplasmic Casp3 variant (fig. S5D). Further, to allow bidirectional regulation by TEVP and TVMVP, we also incorporated a TVMVP cleavage site adjacent to the mts tag (Fig. 4A, box 3), enabling membrane-localized TVMVP to remove Casp3 from the membrane and thereby attenuate its activation by TEVP (Fig. 4B).

Next, to couple Ras-activating inputs to TEVP, we fused the N-terminal half of TEVP to Ras and its C-terminal half to the Ras-binding domain (RBD) of Raf, which binds to the active form of Ras (57, 58). In this design, upstream activators of Ras should reconstitute RasTEVP (Fig. 4A, core circuit and box 1, and fig. S5C) and thereby activate Casp3. To validate this design, we constructed a HEK293 cell line stably expressing a constitutively active SOS (SOS_{CA}) variant with a membrane-localization myristoylation signal and no inhibitory C-terminal region (59). Transfection of the core circuit reduced cell numbers, both in this SOS_{CA} cell line and in its parental control line that lacks ectopic SOS_{CA}, but preferentially affected the SOS_{CA} cells (Fig. 4C, core circuit, and fig. S5F). This selectivity required the regulated Ras-RBD interaction (fig. S5E and supplementary text). However, though this core circuit provided some selectivity, it also exhibited a relatively high background rate of Casp3 activation in the control cells.

To improve the circuit's selectivity, we incorporated a TVMVP-TEVP reciprocal inhibition motif (fig. S5A, boxes 4 and 5) similar to the one used in the bandpass circuit, as well as feed-forward repression of Casp3 activation by TVMVP (Fig. 4A, box 3). In this full-circuit design, TVMVP should suppress activation of Casp3 in control cells, both directly and indirectly through TEVP. By contrast, in SOS_{CA} cells, elevated activation of TEVP should override the inhibitory effects of TVMVP. The full circuit indeed improved selectivity (Fig. 4C, figs. S5G and S6A, and supplementary text). More specifically, expressing TVMVP in amounts comparable to but lower than those of TEVP nearly abolished off-target effects in control cells while retaining most of the on-target reduction in cell number (Fig. 4C and fig. S5G).

To simulate a more biomedically relevant context, we encoded the full four-protein circuit on a single transcript, optimizing the relative abundance of components with internal ribosome entry site variants (60) (Fig. 4D, fig. S6B, and supplementary text), and transfected it into a mixed population of SOS_{CA} and control cells. At its optimal concentration (fig. S6C), the single-

transcript circuit reduced the number of SOS_{CA} cells by ~40%, approaching the ~50% upper limit achieved by a positive-control circuit that constitutively activates Casp3 (Fig. 4D, and Fig. 4E, right). (The upper limit is constrained by gene delivery and expression efficiency.) Notably, it exhibited minimal effects on the control population (Fig. 4E, right). SOS_{CA}-dependent killing could also be observed using annexin V staining as an independent readout of apoptosis (fig. S6D). Finally, to test the generality of the circuit, we considered the distinct and more biomedically relevant input EGFRvIII, an oncogenic EGFR mutant found in glioblastoma and other cancer types (61). The single-transcript full circuit also selectively killed EGFRvIII cells (Fig. 4E, left, and fig. S6D). Together, these results show that a CHOMP circuit can be engineered to detect and kill in response to upstream activators of Ras through rational iterative design optimization.

The considerable diversity of natural cellular behaviors stems from the flexibility with which regulatory components can form distinct circuits. Our results demonstrate how a set of composable protein regulators and circuit design principles can enable a broad range of protein-based circuits and functions. The use of a small number of composable components shifts the design problem, in part, from the level of the individual protein to the level of the protein circuit. Because the operation of CHOMP components does not depend on how they are expressed, they can be optimized through transient transfections, accelerating the overall design-build-test cycle. Although powerful, CHOMP could be improved with additional features. Protease-activating proteases would simplify some circuit designs and facilitate signal amplification. Protein design strategies to control the intrinsic nonlinearity (effective cooperativity) of input-output responses could enable the implementation of useful dynamics such as multistability (62) and oscillation (63, 64). With one exception, the circuits shown here were created with three proteases, but additional orthogonal proteases would allow larger and more complex circuits (25). Finally, future work could expand the range of CHOMP inputs and outputs, enabling direct sensing of the activities of Ras and other oncogenes, and allow for combinatorial sensing of multiple inputs.

CHOMP circuits could provide distinct capabilities compared with transcriptional systems. In terms of speed, proteases can respond rapidly to an increase in input protease activity (fig. S7 and supplementary text). CHOMP circuits can also operate in parallel at specific subcellular sites within a cell. Because CHOMP circuits have a relatively compact genetic design and do not require regulatory interactions with DNA, they could be introduced into differentiated and even postmitotic cells with gene therapy vectors or other viruses and could improve the specificity of oncolytic virotherapy (65). Synthetically, hybrid circuits combining transcriptional or translational regulation with engineered proteases could offer the programmability of base-pairing interactions

together with protein-level operation. For example, existing cancer-detection circuits (66, 67) could conditionally express CHOMP components to increase specificity and couple to protein-mediated inputs and outputs. Integrating these capabilities, one can envision smart therapeutics or sentinels based on CHOMP circuits (68, 69).

REFERENCES AND NOTES

1. J. Bonnet, P. Yin, M. E. Ortiz, P. Subsoontorn, D. Endy, *Science* **340**, 599–603 (2013).
2. B. H. Weinberg et al., *Nat. Biotechnol.* **35**, 453–462 (2017).
3. S. Ausländer, D. Ausländer, M. Müller, M. Wieland, M. Fussenegger, *Nature* **487**, 123–127 (2012).
4. K. Rinaudo et al., *Nat. Biotechnol.* **25**, 795–801 (2007).
5. L. Wroblewska et al., *Nat. Biotechnol.* **33**, 839–841 (2015).
6. A. S. Khalil et al., *Cell* **150**, 647–658 (2012).
7. N. Roquet, A. P. Soleimany, A. C. Ferris, S. Aaronson, T. K. Lu, *Science* **353**, aad8559 (2016).
8. A. A. K. Nielsen et al., *Science* **352**, aac7341 (2016).
9. B. Angelici, E. Mailand, B. Haefliger, Y. Benenson, *Cell Reports* **16**, 2525–2537 (2016).
10. J. J. Lohmueller, T. Z. Armel, P. A. Silver, *Nucleic Acids Res.* **40**, 5180–5187 (2012).
11. I. Budihardjo, H. Oliver, M. Lutter, X. Luo, X. Wang, *Annu. Rev. Cell Dev. Biol.* **15**, 269–290 (1999).
12. M. A. Marchisio, J. Stelling, *Bioinformatics* **24**, 1903–1910 (2008).
13. B. J. Yeh, R. J. Rutigliano, A. Deb, D. Bar-Sagi, W. A. Lim, *Nature* **447**, 596–600 (2007).
14. J. E. Dueber, B. J. Yeh, K. Chak, W. A. Lim, *Science* **301**, 1904–1908 (2003).
15. S.-H. Park, A. Zarrinpar, W. A. Lim, *Science* **299**, 1061–1064 (2003).
16. P. L. Howard, M. C. Chia, S. Del Rizzo, F.-F. Liu, T. Pawson, *Proc. Natl. Acad. Sci. U.S.A.* **100**, 11267–11272 (2003).
17. D. M. Barrett, N. Singh, D. L. Porter, S. A. Grupp, C. H. June, *Annu. Rev. Med.* **65**, 333–347 (2014).
18. L. Morsut et al., *Cell* **164**, 780–791 (2016).
19. K. T. Roybal et al., *Cell* **164**, 770–779 (2016).
20. V. Stein, M. N. N. K. Alexandrov, *ACS Synth. Biol.* **6**, 1337–1342 (2017).
21. V. Stein, K. Alexandrov, *Proc. Natl. Acad. Sci. U.S.A.* **111**, 15934–15939 (2014).
22. J. C. Carrington, W. G. Dougherty, *Proc. Natl. Acad. Sci. U.S.A.* **85**, 3391–3395 (1988).
23. J. Tózsér et al., *FEBS J.* **272**, 514–523 (2005).
24. R. Bartsch-Schlagler, *J. Viral Hepat.* **6**, 165–181 (1999).
25. M. J. Adams, J. F. Antonini, F. Beaudoin, *Mol. Plant Pathol.* **6**, 471–487 (2005).
26. C. Taxis, G. Stier, R. Spadaccini, M. Knop, *Mol. Syst. Biol.* **5**, 267 (2009).
27. M. T. Butko et al., *Nat. Neurosci.* **15**, 1742–1751 (2012).
28. H. K. Chung et al., *Nat. Chem. Biol.* **11**, 713–720 (2015).
29. J. Fernandez-Rodriguez, C. A. Voigt, *Nucleic Acids Res.* **44**, 6493–6502 (2016).
30. N. H. Kipniss et al., *Nat. Commun.* **8**, 2212 (2017).
31. G. Barnea et al., *Proc. Natl. Acad. Sci. U.S.A.* **105**, 64–69 (2008).
32. N. M. Daringer, R. M. Dudek, K. A. Schwarz, J. N. Leonard, *ACS Synth. Biol.* **3**, 892–902 (2014).
33. J. A. Gramespacher, A. J. Stevens, D. P. Nguyen, J. W. Chin, T. W. Muir, *J. Am. Chem. Soc.* **139**, 8074–8077 (2017).
34. D. S. Waugh, *Protein Expr. Purif.* **80**, 283–293 (2011).
35. M. Iwamoto, T. Björklund, C. Lundberg, D. Kirik, T. J. Wandless, *Chem. Biol.* **17**, 981–988 (2010).
36. A. Varshavsky, *Proc. Natl. Acad. Sci. U.S.A.* **93**, 12142–12149 (1996).
37. S. Nallamsetty et al., *Protein Expr. Purif.* **38**, 108–115 (2004).
38. S. S. Taremi et al., *Protein Sci.* **7**, 2143–2149 (1998).
39. I. Ghosh, A. D. Hamilton, L. Regan, *J. Am. Chem. Soc.* **122**, 5658–5659 (2000).
40. M. C. Wehr et al., *Nat. Methods* **3**, 985–993 (2006).
41. L. A. Banaszynski, L.-C. Chen, L. A. Maynard-Smith, A. G. L. Ooi, T. J. Wandless, *Cell* **126**, 995–1004 (2006).
42. F. Rossi, C. A. Charlton, H. M. Blau, *Proc. Natl. Acad. Sci. U.S.A.* **94**, 8405–8410 (1997).
43. S. A. Ghabrial, H. A. Smith, T. D. Parks, W. G. Dougherty, *J. Gen. Virol.* **71**, 1921–1927 (1990).
44. S. P. Weinheimer et al., *J. Virol.* **67**, 5813–5822 (1993).

45. Y. Hart, U. Alon, *Mol. Cell* **49**, 213–221 (2013).
46. A. Porcher, N. Dostatni, *Curr. Biol.* **20**, R249–R254 (2010).
47. S. Basu, Y. Gerchman, C. H. Collins, F. H. Arnold, R. Weiss, *Nature* **434**, 1130–1134 (2005).
48. D. Greber, M. Fussenegger, *Nucleic Acids Res.* **38**, e174 (2010).
49. W. Ma, A. Trusina, H. El-Samad, W. A. Lim, C. Tang, *Cell* **138**, 760–773 (2009).
50. S. Basu, R. Mehreja, S. Thiberge, M.-T. Chen, R. Weiss, *Proc. Natl. Acad. Sci. U.S.A.* **101**, 6355–6360 (2004).
51. T.-L. To *et al.*, *Proc. Natl. Acad. Sci. U.S.A.* **112**, 3338–3343 (2015).
52. A. L. Szymczak *et al.*, *Nat. Biotechnol.* **22**, 589–594 (2004).
53. A. D. Cox, S. W. Fesik, A. C. Kimmelman, J. Luo, C. J. Der, *Nat. Rev. Drug Discov.* **13**, 828–851 (2014).
54. J. Downward, *Nat. Rev. Cancer* **3**, 11–22 (2003).
55. D. C. Gray, S. Mahrus, J. A. Wells, *Cell* **142**, 637–646 (2010).
56. J. F. Hancock, K. Cadwallader, H. Paterson, C. J. Marshall, *EMBO J.* **10**, 4033–4039 (1991).
57. A. F. Oliveira, R. Yasuda, *PLOS ONE* **8**, e52874 (2013).
58. R. Yasuda *et al.*, *Nat. Neurosci.* **9**, 283–291 (2006).
59. A. Aronheim *et al.*, *Cell* **78**, 949–961 (1994).
60. E. Y. C. Koh *et al.*, *PLOS ONE* **8**, e82100 (2013).
61. C. J. Wikstrand, C. J. Reist, G. E. Archer, M. R. Zalutsky, D. D. Bigner, *J. Neurovirol.* **4**, 148–158 (1998).
62. T. S. Gardner, C. R. Cantor, J. J. Collins, *Nature* **403**, 339–342 (2000).
63. M. B. Elowitz, S. Leibler, *Nature* **403**, 335–338 (2000).
64. J. Stricker *et al.*, *Nature* **456**, 516–519 (2008).
65. S. J. Russell, K.-W. Peng, J. C. Bell, *Nat. Biotechnol.* **30**, 658–670 (2012).
66. L. Nissim, R. H. Bar-Ziv, *Mol. Syst. Biol.* **6**, 444 (2010).
67. Z. Xie, L. Wroblewska, L. Prochazka, R. Weiss, Y. Benenson, *Science* **333**, 1307–1311 (2011).
68. R. Kojima, D. Aubel, M. Fussenegger, *Adv. Drug Deliv. Rev.* **105** (Pt A), 66–76 (2016).
69. F. Lienert, J. J. Lohmueller, A. Garg, P. A. Silver, *Nat. Rev. Mol. Cell Biol.* **15**, 95–107 (2014).

ACKNOWLEDGEMENTS

We thank J. Markson, Y. Antebi, N. Nandagopal, and J. Ruan for technical assistance; A. Varshavsky, R. Deshaies, and P. Coffino for scientific input and advice; and R. Kishony, G. Seelig, J.G. Ojalvo, J. Markson, L. Potvin-Trottier, K. Frieda, R. Zhu, and A. Granados for critical feedback. **Funding:** The research was funded by DARPA (HR0011-17-2-0008, M.B.E.), the Gordon and Betty Moore Foundation (GMBF2809, M.B.E.), NIH (T32 GM07616, L.S.C.), and the Helen Hay Whitney Foundation (F1047, X.J.G.). M.B.E. is a Howard Hughes Medical Institute investigator. **Author contributions:** X.J.G. conceived of the project. X.J.G., L.S.C., M.S.K., and M.B.E.

designed experiments. X.J.G., L.S.C., and M.S.K. performed experiments. X.J.G., L.S.C., M.S.K., and M.B.E. analyzed data and did mathematical modeling. X.J.G., L.S.C., and M.B.E. wrote the manuscript, with input from all authors. **Competing interests:** All authors are inventors on U.S. patent application 62/619,001 ("A System for Programming Protein-level Circuits in Living Cells") submitted by Caltech. **Data and materials availability:** All DNA constructs are available from Addgene (www.addgene.org/depositing/75869/), and cell lines available from M.B.E. under a material transfer agreement with Caltech. The datasets generated and analyzed and the computer code used during the current study are available upon request from the corresponding author.

SUPPLEMENTARY MATERIALS

www.sciencemag.org/content/361/6408/1252/suppl/DC1
Materials and Methods
Supplementary Text
Figs. S1 to S7
Table S1
References (70–73)
Movie S1

5 March 2018; accepted 14 August 2018
10.1126/science.aat5062

BIOTECHNOLOGY

Engineered CRISPR-Cas9 nuclease with expanded targeting space

Hiroshi Nishimasu^{1*}, Xi Shi^{2,3}, Soh Ishiguro^{4,5,6}, Linyi Gao^{2,7}, Seichi Hirano¹, Sae Okazaki¹, Taichi Noda⁸, Omar O. Abudayyeh^{2,3,9}, Jonathan S. Gootenberg^{2,3,9}, Hideto Mori^{4,5,6}, Seiya Oura^{8,10}, Benjamin Holmes^{2,3}, Mamoru Tanaka⁴, Motoaki Seki⁴, Hisato Hirano¹, Hiroyuki Aburatani⁴, Ryuichiro Ishitani¹, Masahito Ikawa^{8,10,11}, Nozomu Yachie^{1,4,5,6}, Feng Zhang^{2,3,7,9}, Osamu Nureki^{1*}

The RNA-guided endonuclease Cas9 cleaves its target DNA and is a powerful genome-editing tool. However, the widely used *Streptococcus pyogenes* Cas9 enzyme (SpCas9) requires an NGG protospacer adjacent motif (PAM) for target recognition, thereby restricting the targetable genomic loci. Here, we report a rationally engineered SpCas9 variant (SpCas9-NG) that can recognize relaxed NG PAMs. The crystal structure revealed that the loss of the base-specific interaction with the third nucleobase is compensated by newly introduced non-base-specific interactions, thereby enabling the NG PAM recognition. We showed that SpCas9-NG induces indels at endogenous target sites bearing NG PAMs in human cells. Furthermore, we found that the fusion of SpCas9-NG and the activation-induced cytidine deaminase (AID) mediates the C-to-T conversion at target sites with NG PAMs in human cells.

The CRISPR RNA-guided endonuclease Cas9 cleaves double-stranded DNA targets complementary to the RNA guide (1) (fig. S1) and has been harnessed for genome editing in eukaryotic cells (2). However, the widely used Cas9 from *S. pyogenes* (SpCas9) strictly recognizes an NGG sequence (where N is any nucleobase) as the protospacer adjacent motif (PAM) (3), thereby restricting the targetable genomic loci. Structure-guided directed evolution approaches to address this limitation yielded several SpCas9 variants with altered PAM specificities, such as the SpCas9 VQR and VRER variants, which recognize the NGA and NGCG PAMs, respectively (4). In addition, Cas9 and Cas12a (also known as Cpf1) enzymes with distinct PAM specificities, such as *Staphylococcus aureus* Cas9 (SaCas9) (5),

Acidaminococcus sp. Cas12a (AsCas12a), and *Lachnospiraceae bacterium* Cas12a (LbCas12a) (6), have extended the targeting range in CRISPR-Cas-mediated genome editing.

To expand the targeting range of CRISPR-Cas9, we sought to engineer a SpCas9 variant with relaxed preferences for the third nucleobase of the PAM. Previous studies revealed that the second and third nucleobases in the NGG PAM are recognized by Arg¹³³³ and Arg¹³³⁵ of SpCas9, respectively (7) (fig. S2). We thus hypothesized that the PAM constraint can be reduced by eliminating the base-specific interaction between Arg¹³³⁵ and the third G, and compensating for the loss of this base-specific interaction by introducing non-base-specific interactions with the PAM duplex. We first measured the in vitro cleavage activities

of purified wild-type SpCas9 and the R1335A (Arg¹³³⁵ → Ala) mutant toward a target plasmid with the TGG PAM and confirmed that, whereas wild-type SpCas9 efficiently cleaves the TGG target, R1335A has almost no activity (fig. S3, A to C).

We next examined whether the R1335A activity is restored by the substitution of residues surrounding the PAM duplex, and found that the replacements of Leu¹¹¹¹, Gly¹²¹⁸, Ala¹³²², and Thr¹³³⁷ with Arg partially restored the activity of the R1335A mutant (fig. S3, A to C). Furthermore, the R1335A/L1111R/G1218R/A1322R/T1337R variant (referred to as ARRRR) efficiently cleaved the TGG target (fig. S3, A to C). However, the cleavage kinetics of ARRRR was slower than that of wild-type SpCas9 (fig. S3, D and E). In the previously reported VQR (D1135V/R1335Q/T1337R) and VRER (D1135V/G1218R/R1335E/T1337R) variants, the D1135V mutation provides interactions with the sugar-phosphate backbone of the PAM duplex (8, 9). In addition, molecular modeling suggested that the E1219F mutation forms hydrophobic interactions with the ribose moiety of the second G, and that the R1335V mutation stabilizes Arg¹³³³

¹Department of Biological Sciences, Graduate School of Science, The University of Tokyo, 7-3-1 Hongo, Bunkyo-ku, Tokyo 113-0033, Japan. ²Broad Institute of MIT and Harvard, Cambridge, MA 02142, USA. ³McGovern Institute for Brain Research, Cambridge, MA 02139, USA. ⁴Research Center for Advanced Science and Technology, The University of Tokyo, 4-6-1 Komaba, Meguro-ku, Tokyo 153-8904, Japan. ⁵Institute for Advanced Biosciences, Keio University, 14-1 Baba-cho, Tsuruoka, Yamagata 997-0035, Japan. ⁶Graduate School of Media and Governance, Keio University, 5322 Endo, Fujisawa, Kanagawa 252-0882, Japan. ⁷Department of Biological Engineering, Massachusetts Institute of Technology, Cambridge, MA 02139, USA. ⁸Research Institute for Microbial Diseases, Osaka University, 3-1 Yamadaoka, Suita, Osaka 565-0871, Japan. ⁹Department of Brain and Cognitive Sciences, Massachusetts Institute of Technology, Cambridge, MA 02139, USA. ¹⁰Graduate School of Pharmaceutical Sciences, Osaka University, 1-6 Yamadaoka, Suita, Osaka 565-0871, Japan. ¹¹Institute of Medical Science, The University of Tokyo, 4-6-1 Shirokanedai, Minato-ku, Tokyo 108-8639, Japan.

*Corresponding author. Email: nishimasu@bs.s.u-tokyo.ac.jp (H.N.); nureki@bs.s.u-tokyo.ac.jp (O.N.)

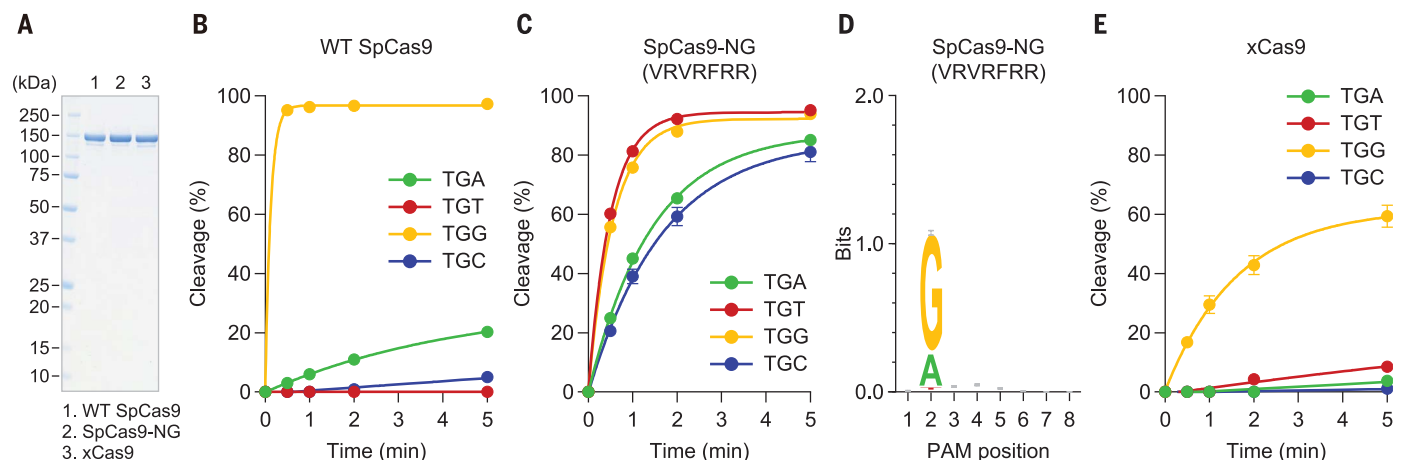
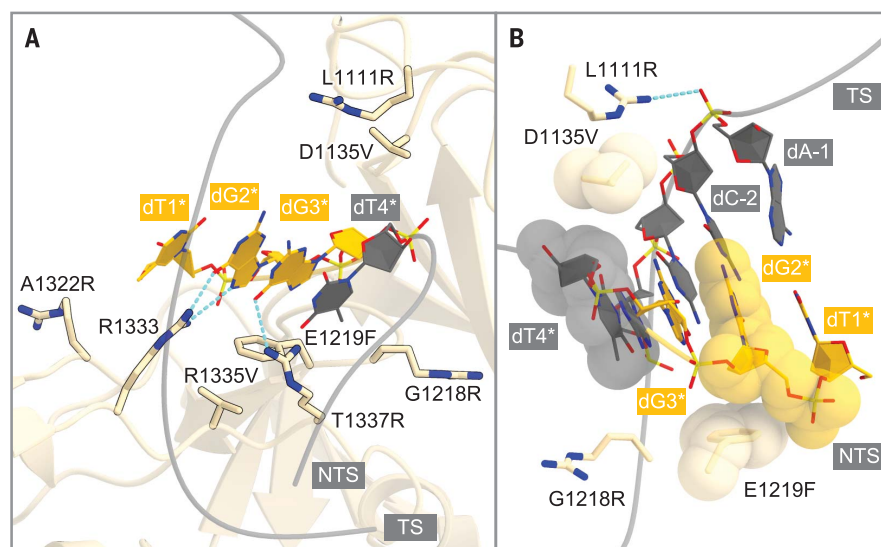


Fig. 1. In vitro cleavage activity. (A) SDS-polyacrylamide gel electrophoresis analysis of wild-type SpCas9, SpCas9-NG, and xCas9. (B, C, and E) In vitro DNA cleavage activities of wild-type SpCas9 (B), SpCas9-NG (C), and xCas9 (E) toward the TGN PAM targets. Data are means \pm SD ($n = 3$). (D) PAM preference of SpCas9-NG.

**Fig. 2. Crystal structure of SpCas9-NG.**

(A) Recognition of the PAM duplex. Arg¹³³³ and the substituted residues are shown as stick models. (B) Non-base-specific interactions between the PAM duplex and the substituted residues. TS, target strand; NTS, nontarget strand.

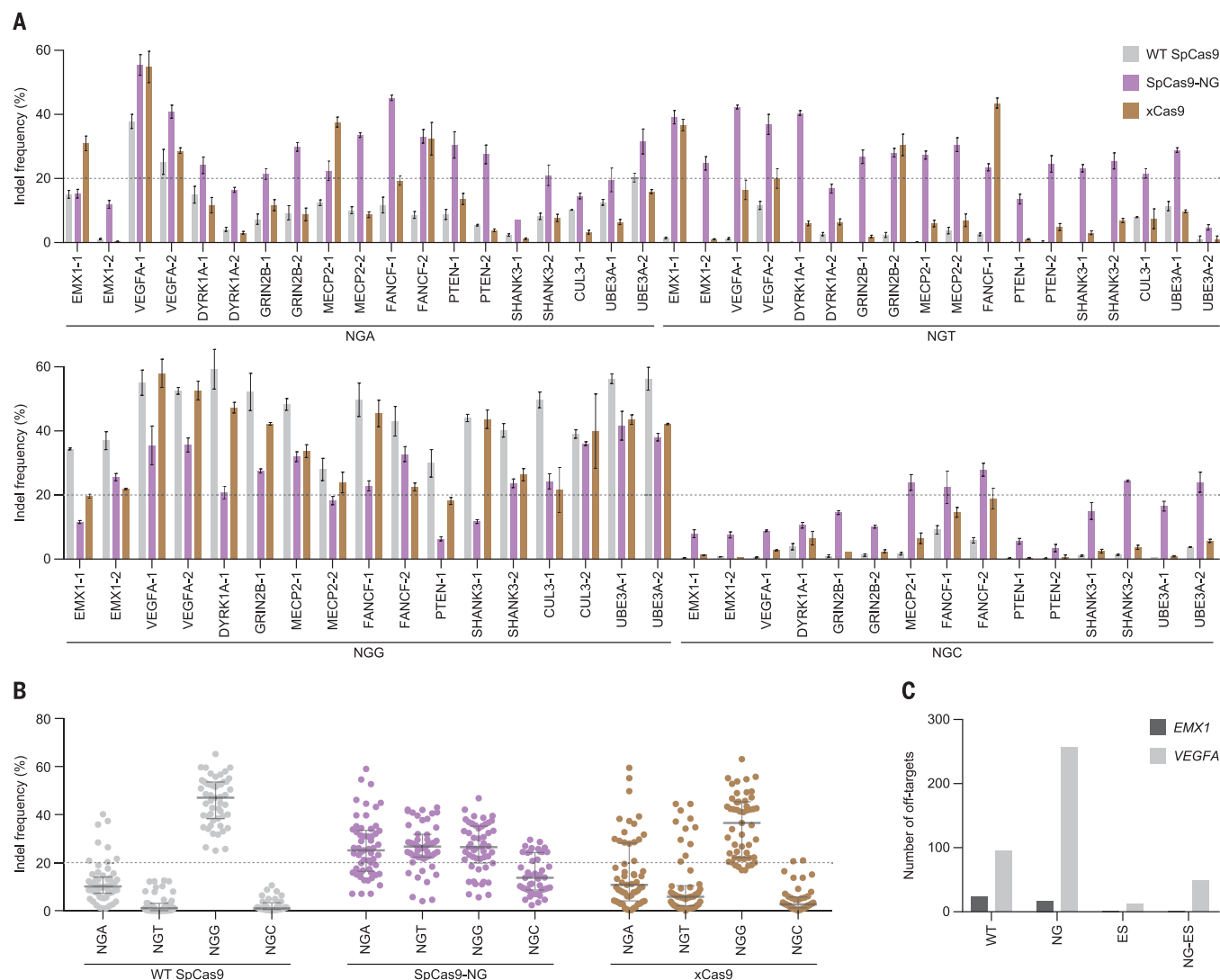
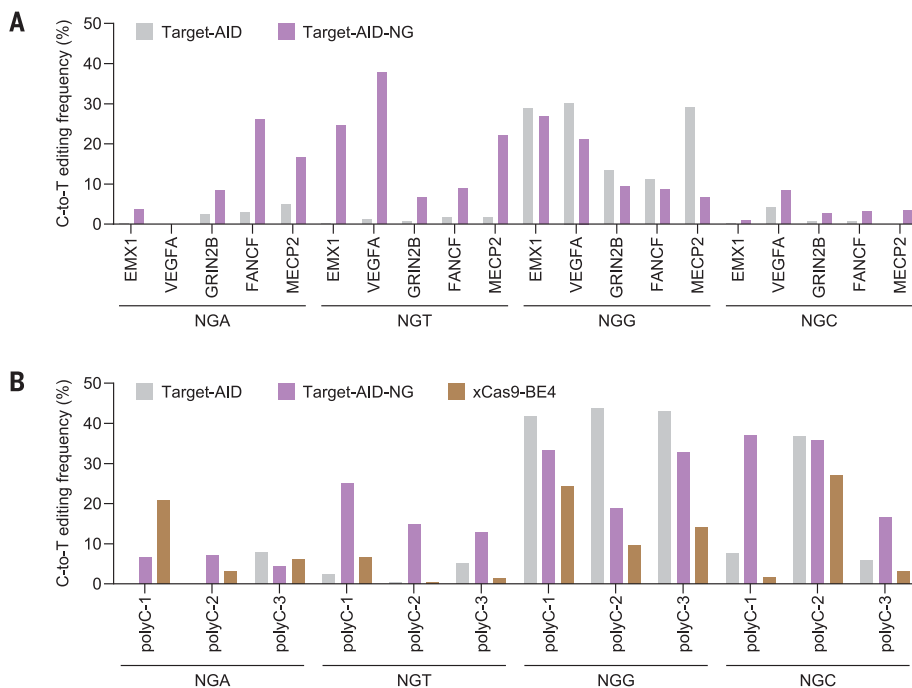


Fig. 3. Gene editing in human cells. (A) Indel formation efficiencies of wild-type SpCas9, SpCas9-NG, and xCas9 at the 69 endogenous target sites in HEK293FT cells. Data are means \pm SD ($n = 3$). (B) Summary of the editing efficiencies of SpCas9, SpCas9-NG, and xCas9. Medians and first and

third quartiles are shown. In (A) and (B), 20% indel frequency is indicated by dashed lines. (C) Specificities of wild-type SpCas9, SpCas9-NG, and the enhanced-specificity versions of SpCas9 (ES) and SpCas9-NG (NG-ES). The off-target cleavages were evaluated by GUIDE-seq.

**Fig. 4. Base editing in human cells.**

(A and B) C-to-T conversion efficiencies at the 20 endogenous target sites (Target-AID and Target-AID-NG) (A) and at the 12 poly-C-containing target sites (Target-AID, Target-AID-NG, and xCas9-BE4) (B) in HEK293T cells. The experiments were performed at least twice, and similar results were obtained.

and Phe¹²¹⁹ (E1219F) (fig. S3F). Indeed, the addition of the D1135V, E1219F, and R1335V mutations enhanced the cleavage activity (fig. S3, D and E). We designated the R1335V/L1111R/D1135V/G1218R/E1219F/A1322R/T1337R variant as VRVFRFR.

We next measured the cleavage activities of VRVFRFR toward the target plasmid with TGN PAMs. Relative to wild-type SpCas9, VRVFRFR slowly but more efficiently cleaved the TGA, TGT, and TGC targets (Fig. 1, A to C, and fig. S4). Although VRVFRFR is less active than wild-type SpCas9 and SaCas9, its cleavage activity was comparable to those of AsCas12a and LbCas12a (5, 6) (fig. S5). Using an in vitro PAM identification assay (10), we confirmed that whereas wild-type SpCas9 is specific to NGG PAMs, VRVFRFR preferentially recognizes NG PAMs (Fig. 1D and fig. S6). Although the PAM identification assay revealed that VRVFRFR slightly recognizes NAN PAMs (Fig. 1D), in vitro cleavage experiments demonstrated that VRVFRFR is less active toward TAN PAMs than toward TGN PAMs (fig. S7). Thus, we concluded that VRVFRFR recognizes a relaxed PAM, and we refer to this variant as SpCas9-NG, as it has increased activity on NGH (H = A, T, or C) PAMs, albeit with reduced relative activity on NGC.

We compared SpCas9-NG with the xCas9 enzyme (a SpCas9 variant with the A262T/R324L/S409I/E480K/E543D/M694I/E1219V mutations), which was engineered via directed evolution and recognizes NG PAMs (11) (fig. S8). We measured their in vitro cleavage activities toward the target plasmid with the TGN PAMs. Under our assay conditions (50 nM Cas9), xCas9 showed almost no activity toward the TGA, TGT, and TGC targets, and it cleaved the TGG target with lower efficiency than did SpCas9-NG (Fig. 1, A to C and E, and fig. S9A). At a higher concentration (200 nM Cas9), xCas9 cleaved the TGA, TGT, and

TGC targets (fig. S9, D and G); nonetheless, the cleavage kinetics of xCas9 was slower than that of SpCas9-NG (fig. S9, C, D, F, and G), and the cleavage activity of xCas9 toward the TGA target (fig. S9, B, D, E, and G). These results demonstrate that SpCas9-NG outperforms xCas9 in recognizing NGH PAMs in vitro.

To clarify the NG PAM recognition mechanism, we determined the crystal structure of SpCas9-NG, in complex with a single guide RNA and its target DNA containing the TGG PAM, at 2.7 Å resolution (fig. S10A and table S1). The second G in the PAM (dG2*) forms bidentate hydrogen bonds with Arg¹³³³ (Fig. 2A), which is stabilized by Val¹³³⁵ (R1335V). The third G (dG3*) forms a hydrogen bond with Arg¹³³⁷ (T1337R) (Fig. 2A), consistent with the preference of SpCas9-NG for the third G (Fig. 1C). Arg¹¹¹¹ (L1111R), Val¹¹³⁵ (D1135V), and Phe¹²¹⁹ (E1219F) interact with the sugar-phosphate backbone of the PAM duplex, whereas Arg¹²¹⁸ (G1218R) does not directly interact with the DNA backbone (Fig. 2B). A structural comparison with the SpCas9 R-loop complex (12) suggested that Arg¹³²² (A1322R) interacts with the nontarget DNA strand (fig. S10B).

To assess the activity of SpCas9-NG in mammalian cells, we next measured the formation of indels (insertions or deletions) induced by wild-type SpCas9, SpCas9-NG, and xCas9 at 69 endogenous target sites with NGN PAMs in human embryonic kidney (HEK) 293FT cells (table S2). As expected, wild-type SpCas9 induced indels predominantly at the NGG sites, with some recognition of NGA sites (Fig. 3, A and B). Wild-type SpCas9 achieved a >20% indel rate at NGG (17 of 17 sites) and NGA sites (3 of 19 sites), but not NGT (0 of 18 sites) or NGC sites (0 of 15 sites)

(Fig. 3, A and B). In contrast, SpCas9-NG edited NGA, NGT, and NGG sites, with lower activity at NGC (Fig. 3, A and B), consistent with the in vitro cleavage preference for the third D (D = A, T, or G) PAM nucleotide (Fig. 1C). SpCas9-NG achieved a >20% indel rate at 13 NGG, 13 NGA, 15 NGT, and 5 NGC sites (Fig. 3, A and B). Relative to SpCas9-NG, xCas9 had lower editing efficiency at all of the NGH sites (Fig. 3, A and B), consistent with our in vitro cleavage data (Fig. 1E). xCas9 induced a >20% indel rate at 15 NGG sites, five NGA sites, and four NGT sites, but none at NGC sites (Fig. 3, A and B).

Using GUIDE-seq (genome-wide, unbiased identification of double-stranded breaks enabled by sequencing) (13), we examined the specificity of wild-type SpCas9 and SpCas9-NG in human cells at two previously characterized target sites (*EMX1* and *VEGFA*). We found that wild-type SpCas9 and SpCas9-NG have comparable numbers of off-target sites for the *EMX1* target, and that the K848A/K1003A/R1060A mutations in the high-fidelity SpCas9 variant [eSpCas9(1.1)] (14) substantially reduced the off-target cleavage by SpCas9-NG (Fig. 3C and fig. S11). These results show that SpCas9-NG has cleavage specificity comparable to that of wild-type SpCas9, and that its specificity can be enhanced by the high-fidelity mutations. As expected, SpCas9-NG had a different off-target profile with off-target sites harboring NGH PAMs (fig. S11), further confirming the relaxed PAM recognition.

The nuclease-inactive version of SpCas9 can be applied to numerous technologies such as base editing (15, 16). We examined whether the SpCas9-NG D10A nickase fused to the activation-induced cytidine deaminase (nSpCas9-NG-AID, referred to as Target-AID-NG) mediates C-to-T conversion at 32 endogenous target sites with NG PAMs in

human cells (table S3). nSpCas9-AID (Target-AID) efficiently induced C-to-T conversion at the NGG sites, with lower activity at NGA sites and no activity at NGT or NGC sites (Fig. 4A and figs. S12A and S13). In contrast, Target-AID-NG showed base-editing activity toward all PAMs assessed, albeit with lower efficiency at NGC sites (Fig. 4A and figs. S12A and S13), consistent with the indel data (Fig. 3A). In addition, Target-AID-NG showed higher base-editing efficiencies than did the xCas9 D10A nickase fused to the APOBEC1 cytidine deaminase (xCas9-BE4) at most of the tested poly-C-containing target sites (Fig. 4B and figs. S12B and S13). These results demonstrate that the catalytically inactive version of SpCas9-NG can serve as a useful RNA-guided DNA targeting platform.

In this study, we engineered an SpCas9-NG variant with an increased targeting range (fig. S14). Nonetheless, the cleavage activity of SpCas9-NG is lower than that of wild-type SpCas9 at NGG sites, and SpCas9-NG is less active at NGC sites relative to NGD sites. Thus, it will be important to improve the activity of SpCas9-NG by further molecular engineering. Overall, the rationally designed SpCas9-NG and its high-fidelity variants can serve as useful genome-editing tools with increased versatility across genomes.

REFERENCES AND NOTES

1. M. Jinek *et al.*, *Science* **337**, 816–821 (2012).
2. L. Cong *et al.*, *Science* **339**, 819–823 (2013).
3. S. H. Sternberg, S. Redding, M. Jinek, E. C. Greene, J. A. Doudna, *Nature* **507**, 62–67 (2014).
4. B. P. Kleinstiver *et al.*, *Nature* **523**, 481–485 (2015).
5. F. A. Ran *et al.*, *Nature* **520**, 186–191 (2015).
6. B. Zetsche *et al.*, *Cell* **163**, 759–771 (2015).
7. C. Anders, O. Niewoehner, A. Duerst, M. Jinek, *Nature* **513**, 569–573 (2014).
8. C. Anders, K. Bargsten, M. Jinek, *Mol. Cell* **61**, 895–902 (2016).
9. S. Hirano, H. Nishimasu, R. Ishitani, O. Nureki, *Mol. Cell* **61**, 886–894 (2016).
10. L. Gao *et al.*, *Nat. Biotechnol.* **35**, 789–792 (2017).
11. J. H. Hu *et al.*, *Nature* **556**, 57–63 (2018).
12. F. Jiang *et al.*, *Science* **351**, 867–871 (2016).
13. S. Q. Tsai *et al.*, *Nat. Biotechnol.* **33**, 187–197 (2015).
14. I. M. Slaymaker *et al.*, *Science* **351**, 84–88 (2016).
15. A. C. Komor, Y. B. Kim, M. S. Packer, J. A. Zuris, D. R. Liu, *Nature* **533**, 420–424 (2016).
16. K. Nishida *et al.*, *Science* **353**, aaf8729 (2016).

ACKNOWLEDGMENTS

We thank A. Kurabayashi for assistance with sample preparation, T. Yamano for Cas12a preparation, B. P. Kleinstiver and J. K. Joung for assistance with GUIDE-seq, and the beamline scientists at BL41XU at SPring-8 for assistance with data collection. **Funding:** Supported by JST (JPMJPR13L8) and JSPS (26291010 and 15H01463) (H.N.); JSPS (16J06287) (S.I.); JSPS (17H01394), AMED (JP18gm5010001), Takeda Science Foundation, NICHD (P01HD087157 and R01HD088412), and the Bill & Melinda Gates Foundation (OPP1160866) (M.I.); NEDO (Genome Editing Program), AMED (17g6110007h0002), JST (10814) and JSPS (18H02428) (N.Y.); NIMH (5DP1-MH100706 and 1R01-MH110049), NIDDK (5R01DK097768-03), and the

New York Stem Cell, Simons, Paul G. Allen Family, and Vallee foundations (F.Z.); AMED (16am0301002h0003) and CSTI, SIP (O.N.). F.Z. is a New York Stem Cell Foundation Robertson Investigator. **Author contributions:** H.N. designed the variants, performed in vitro cleavage experiments, and determined the crystal structure; X.S., L.G., O.O.A., J.S.G., B.H., and F.Z. performed PAM screens, indel detection, and GUIDE-seq analyses; S.I., H.M., M.T., M.S., H.A., and N.Y. performed base-editing analyses; T.N., S.Ou., and M.I. performed indel detection; S.H. performed crystallization; H.N., S.H., S.Ok., and H.H. prepared the proteins; R.I. assisted with the structural determination; H.N. wrote the manuscript with help from all authors; and H.N. and O.N. supervised the research. **Competing interests:** H.N. is a scientific adviser for EdiGENE. F.Z. is a co-founder and scientific adviser for Editas Medicine, Pairwise Plants, Beam Therapeutics, and Arbor Biotechnologies. F.Z. serves as a director for Beam Therapeutics and Arbor Biotechnologies. O.N. is a co-founder, board member, and scientific adviser for EdiGENE. H.N., H.H., and O.N. have filed a patent application related to this work. **Data and materials availability:** The atomic coordinates of SpCas9-NG have been deposited in the Protein Data Bank with PDB code 6AI6. All data are available in the manuscript or the supplementary material.

SUPPLEMENTARY MATERIALS

www.sciencemag.org/content/361/6408/1259/suppl/DC1
Materials and Methods
Figs. S1 to S14
Tables S1 to S3
References (17–24)

4 January 2018; accepted 16 August 2018
Published online 30 August 2018
10.1126/science.aas9129



RESTORING HOPE



Since the first Deep Brain Stimulation initiative of Tsinghua University in 2000, PINS Medical has gradually established a multinational corporation with headquarters based in Beijing and international business center in Singapore. As an innovative high-tech enterprise with focus on neuromodulation, a variety of clinical products have been developed to date, which include stimulators for deep brain, vagus nerve, spinal cord and sacral nerve stimulation therapies. PINS Medical devotes itself to providing cutting-edge treatments for patients who suffer from neurological disorders such as Parkinson's Disease, Epilepsy, Chronic Pain and OAB, etc.

As part of the "National Engineering Laboratory for Neuromodulation", PINS Medical works in close cooperation with Tsinghua University and the numerous affiliated clinical centers, becoming a center of attraction for a wide range of professional talents in areas of clinical research, innovative R&D and business management. Since 2008, PINS Medical has developed rapidly in becoming a leading brand in neuromodulation within the Chinese market, due to the success of its creative research platform that efficiently links basic research, R&D of novel products, clinical testing and market entry.

With an outstanding reputation as a high-tech healthcare corporation, PINS Medical has a primary mission for providing innovative, high-quality products and services for patients to improve quality of life. PINS, which stands for Programmable Implanted Neuromodulation Stimulator, is also an abbreviation of "Patient Is No.1 always". This clearly presents the goal of PINS Medical for "restoring hope", not simply as an innovation company but also across society to citizens.

Looking into the future with the continuous rise in incidence of neuropsychiatric disorders and increased social burden across the globe, PINS Medical along with local governments, research centers, companies and top academic scientists, are now developing and promoting innovative therapies worldwide.

www.pinsmedical.com

info@pinsmedical.cn

ScienceAdvances



OPEN ACCESS, DIGITAL, AND FREE TO ALL READERS



Pushing the Boundaries of Knowledge

As AAAS's first multidisciplinary, open access journal, *Science Advances* publishes research that reflects the selectivity of high impact, innovative research you expect from the *Science* family of journals, published in an open access format to serve a vast and growing global audience. Check out the latest findings or learn how to submit your research: **ScienceAdvances.org**



Inception Institute of Artificial Intelligence:

A Bold Initiative to Foster Global AI Research and Innovation

The Inception Institute of Artificial Intelligence (IIAI), headquartered in Abu Dhabi, the capital of the United Arab Emirates, is an international research organization dedicated to achieving breakthroughs in fundamental and applied AI. IIAI consists of an elite team of handpicked scientists and engineers, led in their dedication to excellence by Oxford University trained CEO and Chief Scientist Dr. Ling Shao, the former Chair Professor of Computer Vision and Machine Learning at the United Kingdom's University of East Anglia.

Since its establishment earlier this year, IIAI has attracted over 60 members from leading universities and research organizations, including Oxford, MIT, ETH Zurich, Tsinghua University, Peking University, the Australian National University, the National University of Singapore, and New York University. IIAI continues to expand quickly, with plans to onboard hundreds of researchers and engineers in the near future. In addition to our full-time team, IIAI will also accept a large number of graduate student interns from world-renowned universities.

Artificial Intelligence: At the Heart of a Happier, Healthier, and More Productive Global Community

At IIAI, we believe AI is essential to tackling some of humanity's most challenging and pressing problems. To help our society reach its full potential, IIAI is leading fundamental and applied research across numerous domains, pushing the boundaries of AI capabilities. In

fundamental research, we focus primarily on machine learning, with a particular emphasis on deep learning. Within this domain, we are developing more efficient and intelligent learning models, including unsupervised or self-supervised learning, few-shot or zero-shot learning, and lifelong learning.

Because we believe in the profoundly positive impact AI can have on society, IIAI is also investing extensively in applied research, with the aim of fundamentally transforming the use of AI across domains. IIAI's current applied AI research is focused on two primary areas: smart cities and healthcare. For instance, to accelerate the evolution of smart cities, we are developing a world-class, intelligent video-analytics platform powered by thousands of computing clusters to revolutionize object re-identification and activity recognition. In the healthcare sector, we are leveraging medical imaging and electronic health records to optimize the early detection, diagnosis, and targeted treatment of ailments, including diabetic retinopathy, a complication of the type 1 or type 2 diabetes prevalent across the Middle East, and breast cancer, which is most commonly detected by digital mammography.

From Big Data to Cloud Computing, IIAI's Resources Keep it at the Forefront of Research and Innovation

To support its research, IIAI leverages powerful computing resources, including massive parallel-processing clusters with hundreds of NVIDIA DGX-class GPU

ADVERTISEMENT

servers, HPC resources consisting of thousands of CPU nodes, and petabytes of SSD-based data storage. In addition to these physical resources, IIAI also works with a wealth of big data from various domains, from text to audio, still images to full-motion video. The combination of our technological power and substantial data assets is instrumental in supporting not only the AI research being conducted, but also accelerating its application to multiple, wide-ranging fields and industries.

IIAI is rapidly making an impact on both the national and global levels, publishing numerous papers in top journals and at international conferences. Notably, four articles have been presented at this year's IEEE Conference on Computer Vision and Pattern Recognition (CVPR2018), over ten articles were presented at the 2018 European Conference of Computer Vision (ECCV2018), and two articles have been published in IEEE Transactions on Pattern Analysis and Machine Intelligence (TPAMI). Furthermore, in order to promote the development of fundamental research in AI, IIAI has sponsored several international conferences, including ECCV, the International Conference on Machine Learning (ICML), and the Conference on Neural Information Processing Systems (NIPS).

To support its mission of expanding AI research across disciplines, IIAI is forming long-term strategic partnerships with numerous internationally renowned universities and organizations. This enables important academic research and knowledge to be combined with the experience and extensive domain expertise particular to industry, establishing the foundations for the future of AI, while at the same time promoting AI in the region – and beyond. Thus far, IIAI has initiated the establishment of joint laboratories with the University of Edinburgh, the University of Amsterdam, and New York University Abu Dhabi. These collaborations include joint doctoral programs, exchanged researcher visits, as well as joint research and development. In addition to academic collaborations, IIAI also maintains a close relationship with various research institutions globally, from Europe to Asia.

Research within these collaborations is based on a broad spectrum of data resources, with the aim of promoting the rapid development of AI and data science for practical applications in a variety of fields.

Join IIAI and Be Part of a One-of-a-Kind Institute in a Visionary and Dynamic Nation

The IIAI office is located in an international financial center, the Abu Dhabi Global Market, which is surrounded by a wide range of businesses and entertainment facilities, as well as beautiful beaches and endless sunshine. In addition, IIAI's strategically central location at the intersection of the East and West offers the unique opportunity to work in a highly international community, which brings together a variety of perspectives and backgrounds while creating a diverse and open culture that is warm and welcoming to those from all backgrounds and nationalities.

IIAI is currently recruiting a select group of expert researchers and engineers highly specialized in the fields of deep learning, computer vision, natural language processing, and medical image analysis. Well-qualified researchers and engineers who are passionate about AI, driven towards excellence, and have a spirit for adventure are encouraged to contact IIAI.

Job portal:

(<https://www.jobs.ac.uk/enhanced/linking/inception-institute-of-artificial-intelligence/>)

IIAI website: <http://www.inceptioniai.org/>

Contact: jobs@inceptioniai.org



The Dreyfus Prize in the Chemical Sciences



The Dreyfus Prize in the Chemical Sciences recognizes exceptional and original research in a selected area of chemistry that has advanced the field in a major way.

The topic of the 2019 Dreyfus Prize is:

Chemistry in Support of Human Health

The Prize is open to international nominations of **an individual**, and consists of a monetary award of \$250,000, a medal, and a certificate.

The nomination deadline is February 28, 2019. For further information, see www.dreyfus.org.

The Camille
& Henry Dreyfus
Foundation

Visit SRI LANKA!

AAAS *Travels*



January 25 -February 7, 2019!
Visit the Jewel of the Indian Ocean

We invite you to join this botanical and cultural adventure of discovery to the lush tropical isle of Sri Lanka! Discover many of the scenic, natural and cultural wonders of this island paradise, with leadership by Sri Lanka naturalist Neela de Zoysa. Learn about the rich heritage of this land of serendipity. \$4,995 + air

For a detailed brochure, call (800) 252-4910
All prices are per person twin share + air



BETCHART EXPEDITIONS Inc.
17050 Montebello Rd, Cupertino, CA 95014
Email: AAASInfo@betchartexpeditions.com
www.betchartexpeditions.com

DOES YOUR LAB COMBINE COMPUTATIONAL AND EXPERIMENTAL STRATEGIES TO INVESTIGATE SIGNALING NETWORKS?



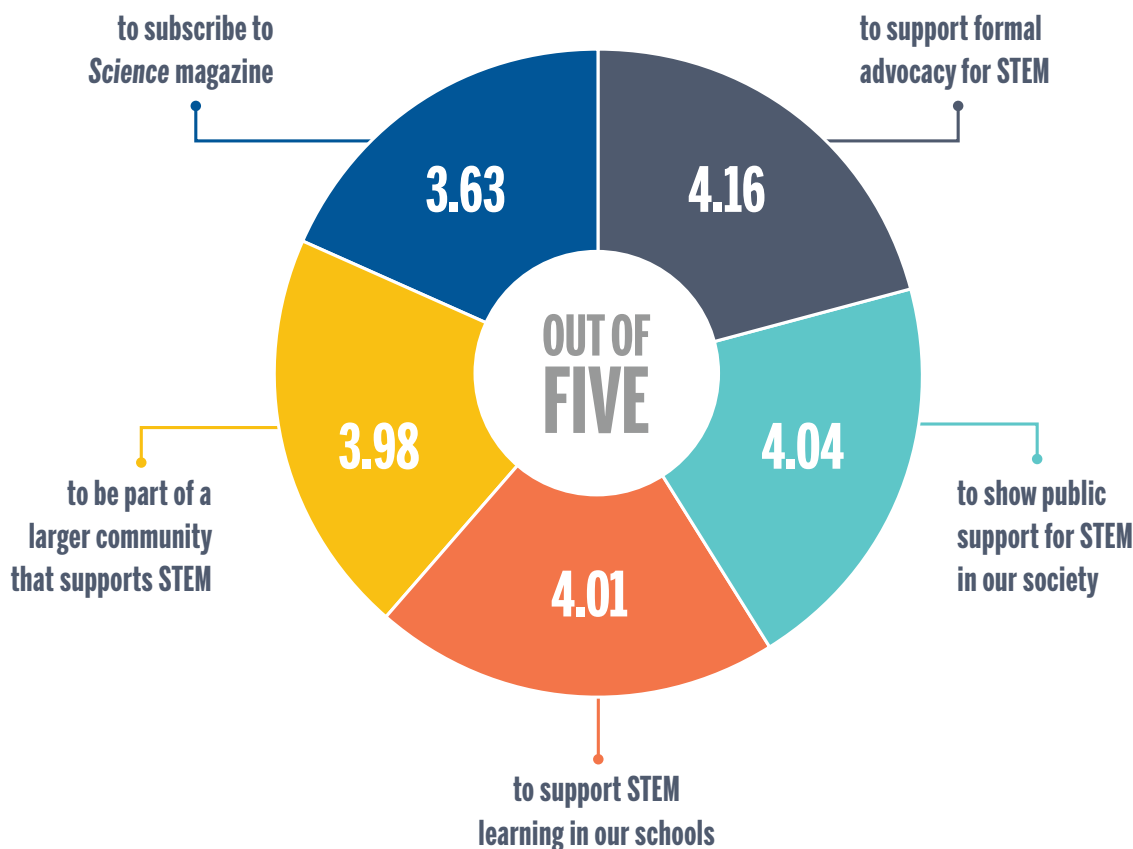
Michal Hershinkel, Elias Aizenman, Glen Andrews, and Israel Sekler *Sci. Signal.* 3, mr2 (6 July 2010) Image: Omer Barad, Department of Molecular Genetics, Weizmann Institute of Science, Rehovot, Israel.

ScienceSignaling | AAAS
CELL SIGNALING IN PHYSIOLOGY AND DISEASE

Find out more about the scope of the journal and submit your research today. **ScienceSignaling.org**

AAAS IS THE FORCE FOR SCIENCE

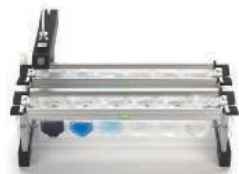
According to the 2017 Member Survey, you joined AAAS ...



TELL US WHAT'S IMPORTANT TO YOU!

The 2018 Member Survey is launching in September. Look in your inbox for a link.

Your responses help us to better serve science, scientists, and the global community.
Don't miss your chance to tell us what's most important to you!



Serial Diluter

The Inlabtec TA12 Serial Diluter was developed in response to the demand from food culture and probiotic producers undertaking final quality control with the standard plate count method. Because you are placing the sample into a sterile, empty Serial Dilution Bag instead of a prefilled test

tube, then adding the diluent at the touch of a button, performing serial dilutions with the TA12 is fast, reliable, and much less taxing than traditional procedures. The TA12 combines two lines of six dilution bags in parallel, and the telescopic dispensing arm makes changing between the two rows of bags easy and convenient. Any kind of diluent can be used, enabling probiotic producers to use preferred diluents such as skimmed milk, for which prefilled test tubes are not available. Serial Dilution Bags are made from high-purity polyethylene, guaranteed to be free of any substances that could inhibit proliferation of sensitive cells.

Inlabtec

For info: +41-(0)-71-222-4865

www.inlabtec.com

High-Throughput PARP Screening Assay

AMS Biotechnology offers an extensive portfolio of Poly (ADP-ribose) polymerase (PARP) isozymes such as assay kits, inhibitors, recombinant histone substrates, and screening/profiling services for over 10 different PARPs. PARPs play key signaling roles in apoptosis, DNA excision and repair, and chromatin structure. They are also involved in transcriptional regulation of several signaling pathways, including genes involved in inflammation. The latest addition to the range is the PARPtrap Assay Kit, which is designed to measure PARP1/DNA complex formation in a high-throughput screening assay using fluorescence polarization. The kit comes in a convenient 96-well format, supplied with purified PARP1 enzyme, fluorescent-labeled nicked DNA, and PARPtrap assay buffer for 100 enzyme reactions. Without the PAR reaction, PARP1 binds to the fluorescent-labeled nicked DNA, resulting in the emission of highly polarized light. However, after autoribosylation of PARP1, the nicked DNA is dissociated from PARP1 and rotates freely, emitting less polarized light.

AMS Biotechnology

For info: 44-(0)-1235-828200

www.amsbio.com/parp-assay-kits-enzymes.aspx

Confocal Microscope

With the Andor Dragonfly, you can image with an unrivaled combination of speed, sensitivity, confocality, and resolution beyond the diffraction limit. It is now available in the compact 200 series and the full-model 500 series. Dragonfly naturally benefits from Andor EMCCD and sCMOS technologies, and with its motorized optical zoom, the system delivers industry-leading signal-to-noise and image fidelity. Applications range from single-molecule to live-cell confocal, and from total internal reflection fluorescence microscopy (TIRFM) to whole-embryo and thick-tissue imaging, and all benefit from the system's speed and sensitivity. Dragonfly delivers real-time visualization for rapid specimen evaluation and ClearView-GPU (graphics processing unit) deconvolution to maximize resolution and throughput.

Andor

For info: +44-(28)-9023-7126

www.andor.com/microscopy-systems/dragonfly

Particle Analysis Platform

Micro-Flow Imaging (MFI) combines the direct-imaging capabilities of digital microscopy with the precise control of microfluidics. What does that get you? High-resolution images with 85% sampling efficiency, more precise counts and sizing with full morphological detail for all subvisible particles in your sample, and the complete confidence that you can accurately identify every possible particle type—from protein aggregates to air bubbles. Images of the sample are captured as it passes through the flow cell's sensing zone. Every particle in every image is then analyzed to create a database of particle count, size, transparency, and morphology (or shape). And you'll have visual verification on the spot, as images are displayed in real time. You can also display results for many samples at once, making it easy to monitor stability and comparability. If you're looking for broader, deeper analysis of your biotherapeutic products, MFI is the particle analysis tool for you.

ProteinSimple

For info: 888-607-9692

www.proteinsimple.com/mfi_5000.html

Lifetime Contrast Microscope

The SP8 FALCON (FAST Lifetime CONTRast) from Leica Microsystems can record lifetime contrast 10x faster than previous solutions. This lifetime information lets researchers monitor interactions between proteins in living cells as well as providing extra contrast to clearly separate a multitude of fluorophores. The FALCON offers lifetime imaging with fluorescence lifetime imaging (FLIM) in an instant. Detecting molecular interactions with biosensors using fluorescence resonance energy transfer (FRET) is as easy as recording standard confocal data. Even complex experiments are easy to perform, opening a wide range of applications. As the FALCON is part of the SP8 family, lifetime imaging can be easily combined with other modalities. For example, combine FLIM with the SP8 DIVE for deep imaging, the SP8 STED for nanoscopy resolution, or the LAS X Navigator software module for mosaic tiling, which ensures you always have a clear roadmap to brilliant data.

Leica Microsystems

For info: 800-248-0123

www.leica-microsystems.com

Pipette Quality Control and Calibration Service Kits

Our Good Liquid Handling (GLH) Kits provide users with everything necessary to verify and calibrate their systems to industry standards. They furnish reliable instrument services, products, and training, and are medically manufactured to ensure quality and performance. GLH Kits deliver liquid classes, methods, and recommendations for automated pipetting for any scenario. With three different kits available, you will surely find something to meet your needs. A unique feature included in the kits is Good Liquid Handling's integrated software, GLH Tracker, which allows results to be uploaded to a cloud-based resource accessible to additional team members as well as the Good Liquid Handling experts, who can offer troubleshooting or consultations. The tracker lets users drag and drop through a WebDAV (Web Distributed Authoring and Versioning) collaboration platform (BiotechCloud.org), to share methods and exchange data for processing or sharing through one's optional LinkedIn account. Kits support a wide range of volumetric measurements and are compatible with 96- or 384-well plates.

GoodPipetting.com

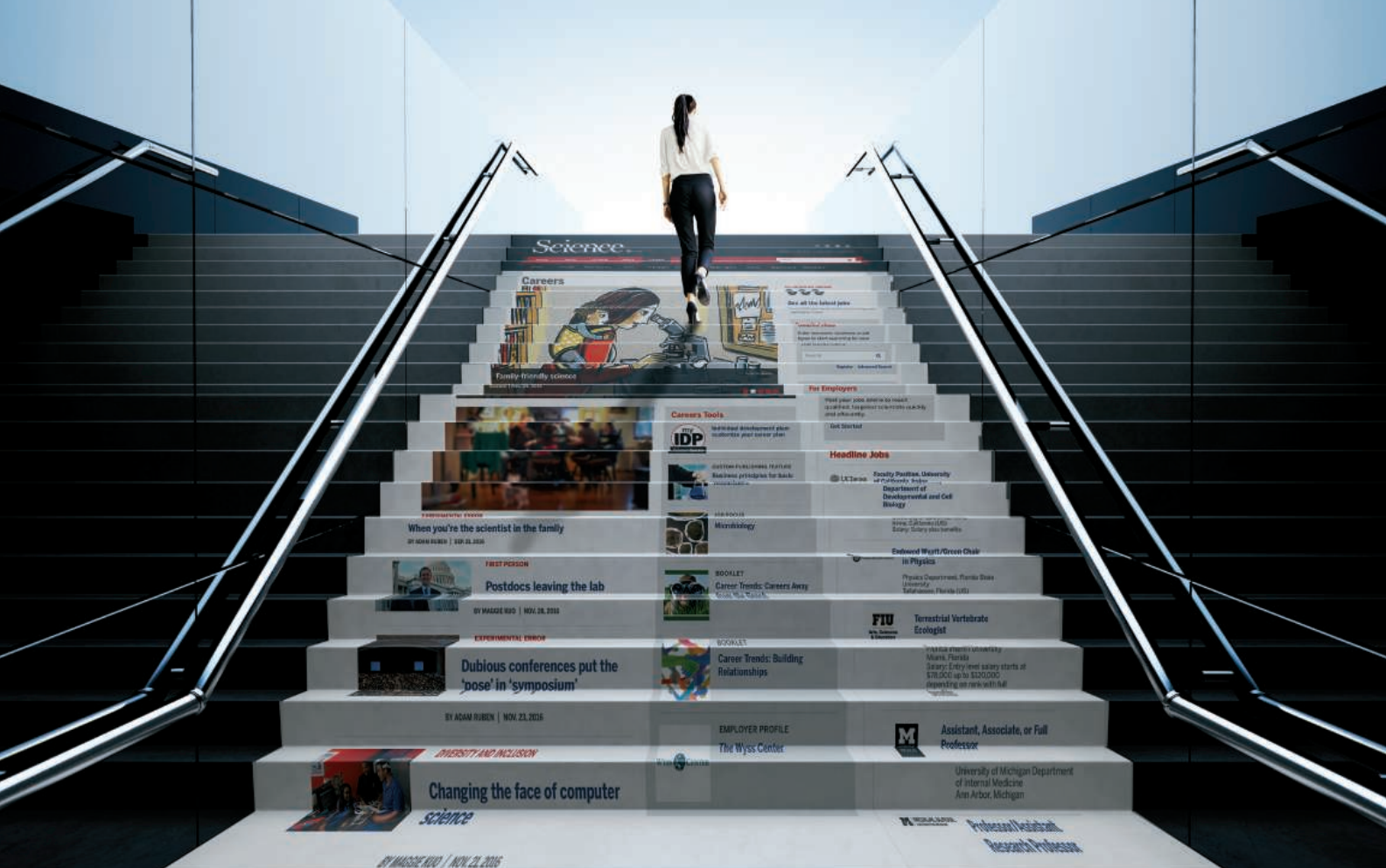
For info: 617-752-2288

www.goodpipetting.com

Electronically submit your new product description or product literature information! Go to www.sciencemag.org/about/new-products-section for more information.

Newly offered instrumentation, apparatus, and laboratory materials of interest to researchers in all disciplines in academic, industrial, and governmental organizations are featured in this space. Emphasis is given to purpose, chief characteristics, and availability of products and materials. Endorsement by *Science* or AAAS of any products or materials mentioned is not implied. Additional information may be obtained from the manufacturer or supplier.

Step up your job search with *Science Careers*



- Access thousands of job postings
- Sign up for job alerts
- Explore career development tools and resources



Search jobs on **ScienceCareers.org** today

Exceptional scientists wanted

Present your work to the world

Are you a representative of the upcoming generation of thought leaders in your field? Together we look forward to your application for the new Sartorius & Science Prize for Regenerative Medicine & Cell Therapy.

Apply now!

www.passionforscience.com/prize



The Sartorius & Science
Prize for Regenerative
Medicine & Cell Therapy

Awarded by



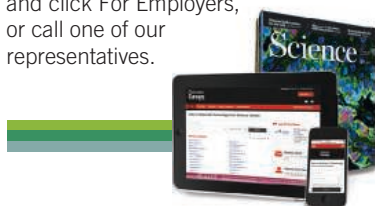
sartorius

Science

Science Careers

SCIENCE CAREERS ADVERTISING

For full advertising details, go to ScienceCareers.org and click For Employers, or call one of our representatives.



AMERICAS

+1 202 326-6577
+1 202 326-6578
advertise@sciencecareers.org

EUROPE, INDIA, AUSTRALIA, NEW ZEALAND, REST OF WORLD

+44 (0) 1223 326527
advertise@sciencecareers.org

CHINA, KOREA, SINGAPORE, TAIWAN, THAILAND

+86 131 4114 0012
advertise@sciencecareers.org

JAPAN

+81 3-6459-4174
advertise@sciencecareers.org

CUSTOMER SERVICE

AMERICAS

+1 202 326-6577
REST OF WORLD
+44 (0) 1223 326528

advertise@sciencecareers.org

All ads submitted for publication must comply with applicable U.S. and non-U.S. laws. *Science* reserves the right to refuse any advertisement at its sole discretion for any reason, including without limitation for offensive language or inappropriate content, and all advertising is subject to publisher approval. *Science* encourages our readers to alert us to any ads that they feel may be discriminatory or offensive.

Science Careers

FROM THE JOURNAL SCIENCE AAAS

ScienceCareers.org



Plant Community Ecology

Assistant Professor

School of Biological Sciences, College of Arts and Sciences
Washington State University

The School of Biological Sciences at Washington State University, Pullman, Washington, invites applications for a full-time, permanent, tenure-track faculty position in *Plant Community Ecology*. This position is to be filled at the Assistant Professor level and will begin in August of 2019.

Candidates should have a research program focused on plant community ecology, potential for collaborative research and training, and the ability to complement our faculty's research strengths. Area of expertise is open. The ideal candidate will use modern approaches to address pressing contemporary and future issues in plant community ecology.

Required qualifications include an earned doctorate at time of application, a record of research accomplishment in plant community ecology, evidence of a commitment to teaching excellence including the ability to teach undergraduate and graduate courses such as community ecology, effective communication skills, and demonstrated ability to collaborate with other scientists. Successful candidates will be expected to develop and maintain an active research program supported by extramural funding, train graduate and undergraduate students, participate in graduate and undergraduate teaching, participate in service, and advance our commitment to diversity and multiculturalism.

To apply, visit www.wsujobs.com to upload application materials. Applications must include a letter of application addressing qualifications, a curriculum vitae, separate teaching and research statements and up to three selected reprints of published or in press papers. Three (3) letters of recommendation that address the applicant's history of and potential for research, teaching and communication excellence are required. The reference letters will be automatically requested and obtained from the reference provider through our online application system. Review of applications begins **October 29, 2018**.

For information on the position or the status of your application, candidates may contact: Dr. Asaph B. Cousins Chair, Plant Community Ecology Search Committee School of Biological Sciences Washington State University Pullman, WA 99164; email: acousins@wsu.edu

Full notice of vacancy can be viewed at <https://www.wsujobs.com>

EEO/AA/AD

Science Careers

FROM THE JOURNAL SCIENCE AAAS

Follow us for jobs,
career advice
and more!



@ScienceCareers



/ScienceCareers



Science Careers

ScienceCareers.org

POSITIONS OPEN

Utah State UNIVERSITY

Assistant Professor – Inorganic Chemistry
Utah State University

The Department of Chemistry and Biochemistry at Utah State University invites applications for a tenure-track position at the Assistant Professor level in the area of inorganic chemistry. The successful applicant will be expected to develop and maintain a vibrant and impactful externally funded research program, effectively teach at the undergraduate and graduate levels, and participate in faculty service. Application information can be found on-line at <http://jobs.usu.edu> (REQ ID F1800392). Evaluation of applications will begin **October 15, 2018** and will continue until the position is filled. For further information please visit our website at <http://www.chem.usu.edu>. *Utah State University is an Equal Opportunity/Affirmative Action Employer committed to advancing diversity. Applications from minorities, women, people with disabilities and veterans are strongly encouraged.*

Search more jobs online

Access hundreds of job postings
on ScienceCareers.org.

Expand your search today.



Career Feature:

Artificial Intelligence

Issue date: November 30

Book ad by November 15

Ads accepted until November 21 if space allows

**129,562**subscribers in print
every week**503,472**monthly unique browsers
on ScienceCareers.org**56 %**of our weekly readers
are Ph.D.sTo book your ad:
advertise@sciencecareers.org**The Americas**

+ 202 326 6577

Europe

+44 (0) 1223 326527

Japan

+81 3 6459 4174

**China/Korea/Singapore/
Taiwan**

+86 131 4114 0012

Produced by the Science/AAAS
Custom Publishing Office.

SCIENCECAREERS.ORG

Artificial Intelligence (AI) is impacting science in new and exciting ways as scientists are using it to better understand society to find solutions to problems across diverse disciplines. This feature will give an overview of AI, and explore the hotspots/centers of excellence and applications for AI. Typical career paths for those working in AI will be explored as well as the opportunities that exist for careers in AI.

Your organization can brand itself as a leader in AI by raising your visibility alongside relevant content while attracting potential candidates. Contact us for further details.

What makes Science the best choice for recruiting?

- Read and respected by 400,000 readers around the globe
- Your ad dollars support AAAS and its programs, which strengthens the global scientific community.

Why choose this AI Feature for your advertisement?

- Relevant ads lead off the career section with a special "AI" banner.

Expand your exposure by posting your print ad online:

- Link on the job board homepage directly to AI jobs
- Dedicated landing page for AI positions.

**ScienceCareers**

FROM THE JOURNAL SCIENCE AAAS

FOR RECRUITMENT IN SCIENCE, THERE'S ONLY ONE SCIENCE.

UIC University of Illinois
at Chicago

The University of Illinois at Chicago invites applicants for a joint position at the rank of assistant professor in the departments of chemistry and biological sciences beginning August 2019. We seek applicants with a research record and interest in the area integrating chemical biology and microbiome research. Candidates may hold a doctorate in chemistry, biology or a closely related field. The successful candidate will be expected to carry out a full and active program of innovative research and to contribute to the teaching of graduate and undergraduate students in chemistry and biological sciences. Final authorization of the position depends upon availability of state funding.

For fullest consideration, please complete an on-line application, including the names and email addresses of three references, and upload a letter of application indicating applicant qualifications, a vita, and a separate one-page statements outlining future teaching and research plan at <https://jobs.uic.edu/job-board/job-details?jobID=102733&job=assistant-professor-chemistry-and-biological-sciences> by **October 31, 2018**. Review of applications will begin on **November 1, 2018** and continue until the position is filled.

The University of Illinois at Chicago is an Affirmative Action, Equal Opportunity Employer, dedicated to the goal of building a culturally diverse and pluralistic faculty and staff committed to teaching and working in a multicultural environment. We strongly encourage applications from women, minorities, individuals with disabilities and covered veterans. The University of Illinois may conduct background checks on all job candidates upon acceptance of a contingent offer. Background checks will be performed in compliance with the Fair Credit Reporting Act.

UIC University of Illinois
at Chicago

The University of Illinois at Chicago invites applicants for a position at the rank of assistant professor in chemistry and learning sciences beginning August 16, 2019. We seek applicants with a record of research and publication focusing at the nexus of an area of Chemistry Education Research and the Learning Sciences. Candidates may hold a doctorate in chemistry or may hold a master's degree in chemistry in addition to a doctorate in the Learning Sciences or a closely related field. Successful candidates should have a demonstrated record of research and scholarship focused on supporting college and/or pre-college level chemistry learners. Position responsibilities include programmatic research and scholarship with high potential for extramural funding. Final authorization of the position depends upon availability of state funding.

The UIC Chemistry Department offers undergraduate Bachelor of Science and Bachelor of Arts degrees, and graduate degrees that encompass a broad range of research areas in Chemistry including Chemistry Education Research. The department hosts excellent facilities to support teaching and learning experiences for undergraduate students with newly remodeled and updated classroom laboratories for instruction in addition to research space for the design and evaluation of new educational interventions related to chemistry instruction. More information can be found at <http://uic.chem.edu>. The UIC Learning Sciences Research Institute (LSRI) is a unit dedicated to the support of multidisciplinary research on learning and teaching in formal and informal contexts, and to the design, development and evaluation of learning environments, curriculum materials, and educational practices appropriate for the 21st century. The institute encompasses 100+ members including more than a dozen faculty, 40 research and administrative staff, 20 Learning Sciences graduate students, along with varying numbers of graduate and undergraduate students representing multiple disciplines. More information can be found at <http://lsri.uic.edu>.

For fullest consideration, please complete an on-line application, including the names and email addresses of three references, and upload a letter of application indicating applicant qualifications, a vitae, and a separate one-page statements outlining future teaching and research plan at <https://jobs.uic.edu/job-board/job-details?jobID=102789&job=assistant-professor-chemistry-and-learning-sciences> by **October 31, 2018**. Review of applications will begin on November 1, 2018 and continue until the position is filled.

The University of Illinois at Chicago is an Affirmative Action, Equal Opportunity Employer, dedicated to the goal of building a culturally diverse and pluralistic faculty and staff committed to teaching and working in a multicultural environment. We strongly encourage applications from women, minorities, individuals with disabilities and covered veterans. The University of Illinois may conduct background checks on all job candidates upon acceptance of a contingent offer. Background checks will be performed in compliance with the Fair Credit Reporting Act.

Advance
your career
with expert
advice from
Science
Careers.



Download Free Career
Advice Booklets!

ScienceCareers.org/booklets



ScienceCareers

FROM THE JOURNAL SCIENCE AAAS



DukeNUS
Medical School

Faculty Positions Cancer and Stem Cell Biology

The Programme in Cancer and Stem Cell Biology (CSCB) at the Duke-NUS Medical School (Duke-NUS) invites applications from outstanding physician-scientists and scientists for tenure track positions in the general areas of cancer and stem cell biology. We seek internationally competitive applicants, including those whose research programmes intersect with institutional initiatives in ageing, global health and Precision or Translational Medicine. Scientists with existing programmes that are translational in nature are especially encouraged to apply.

CSCB is one of the five Signature Research Programmes of Duke-NUS, a global partnership between Duke University in the United States and the National University of Singapore. Our faculty are expected to establish extramurally funded translational or basic science research programmes and to participate in medical education. Applicants should have a PhD, MD, or equivalent and a record of outstanding promise or achievement. New recruits will work alongside existing faculty and trainees with strong programmes in cancer signaling, genomics, bioinformatics, cell biology, and stem cell biology. Opportunities also exist for translational studies in collaboration with world-class clinical services including the Singapore General Hospital and National Cancer Centre Singapore, as well as other Research Institutes and Universities across the island. More information about CSCB faculty, facilities and research programmes can be found at www.duke-nus.edu.sg/cscb/.

Faculty positions at Duke-NUS include full salary support and generous start-up research funding, to be supplemented by competitive grant awards.

For full consideration, interested candidates should submit to: hr@duke-nus.edu.sg by **December 15th, 2018**, a cover letter, curriculum vitae, a summary of research accomplishments and outline of future plans. Candidates applying for the Assistant Professor position are requested to additionally arrange to have three letters of reference sent in support of their application.

**S. Tiong ONG, Chair,
Faculty Search Committee
Programme in Cancer and Stem Cell Biology
Duke-NUS Medical School
Website: www.duke-nus.edu.sg**

WORKING LIFE

By Barbara A. Wanchisen

Afraid to fail? Reach out

Many years ago, a trusted professor suggested I make a radical change in my academic path and pursue a doctorate in psychology. That sounded impossible! I was interested in the subject matter, but my training was in English and philosophy. I was petrified that seeking a science Ph.D. would bring rejection and failure. For months, I looked into programs, only to get cold feet and back away—until my curiosity spurred me down the road again. Now, years after successfully completing my doctorate, I realize that I was actually facing two distinct fears during that tortured time. And I realize that I could have eased my path by seeking outside perspectives.

One fear was simply that, in trying to make a dramatic career change, I would fail. Given my training and connections in the humanities, who could write letters recommending me for a science program? Who would mentor me along the way? What could I point to as evidence that I was a credible candidate? Even if I were accepted, did I really believe that I could succeed? The risk seemed overwhelming. I thought I would suffer for years, if not my entire life, if I didn't get into a program or was unprepared and had to leave.

My other fear was that such a bold move would disappoint important people in my life. This fear is not unique to academia, but university culture can make it hit particularly hard. Many advisers see students as academic progeny, and when we make career choices that don't match our advisers' ideas of what we should do, we may feel we are betraying them. When I told one of my humanities professors that I was serious about applying to doctoral programs in psychology, he expressed grave concern that I was making the wrong choice (although, to his credit, he wrote a wonderful letter of recommendation).

Beyond academic colleagues, it was difficult to face the prospect of disappointing family and friends who had supported me—emotionally and in some cases financially—during the ups and downs of my studies. I worried that if I pursued what might appear to be a pipe dream, they would feel I was turning my back on all they had done. Or they might conclude that all my efforts up to that point had been a failure. When I talked with my parents about making the leap to psychology, they questioned whether it was the right choice and wondered when I would be settled.

Now, though, I realize that I probably exaggerated the



“People who have no skin in the game ... can offer fresh perspectives.”

strength of others' feelings. My colleagues, friends, and family may have felt a bit rejected or confused by my actions, but they had their own lives to think about. Ultimately, I needed to make the decision that was right for me, not for them. My parents came around to the idea that I was going to be a “professional student” for a while, and many friends and colleagues eventually offered support, though I lost touch with that professor.

I didn't have a good strategy for dealing with my fears at that time. But I have since learned a valuable approach that I wish I had known then: Reach out to people beyond your immediate circle for input and advice. People who have no skin in the game—your neighbors, your hair stylist, even strangers you

strike up conversations with at the airport—can offer fresh perspectives that may help you see your options more clearly. Reach out to people in jobs you're interested in to find out how they got where they are. As someone who now receives these types of inquiries, I can tell you that it's not a burden at all. In fact, it's a compliment—plus I enjoy helping the next generation. If the first person you ask doesn't respond, try again. Chances are you will be pleasantly surprised.

There are more people than you may think who have made bold career moves. Talk to them. Your future is your own. Reach out and see what happens. ■

Barbara A. Wanchisen is the director of the Board on Behavioral, Cognitive, and Sensory Sciences at the National Academies of Sciences, Engineering, and Medicine in Washington, D.C. Do you have an interesting career story? Send it to SciCareerEditor@aaas.org.